

NATIONAL INSTITUTE FOR FUSION SCIENCE

Proceeding of A3 Foresight Program Seminar on Critical Physics Issues
Specific to Steady State Sustainment of High-Performance Plasmas
May 17-20, 2016, Yinchuan, China

Edited by Liqun HU, Shigeru MORITA and Yeong-Kook OH

(Received - Oct. 27. 2016)

NIFS-PROC-102

Jan. 23. 2017

This report was prepared as a preprint of work performed as a collaboration research of the National Institute for Fusion Science (NIFS) of Japan. The views presented here are solely those of the authors. This document is intended for information only and may be published in a journal after some rearrangement of its contents in the future.

Inquiries about copyright should be addressed to the NIFS Library, National Institute for Fusion Science, 322-6 Oroshi-cho, Toki-shi, Gifu-ken 509-5292 Japan.

E-mail: gakujutsujoho@nifs.ac.jp

<Notice about photocopying>

In order to photocopy and work from this publication, you or your organization must obtain permission from the following organization which has been delegated for copyright for clearance by the copyright owner of this publication.

Except in the USA

Japan Academic Association for Copyright Clearance (JAACC)
6-41 Akasaka 9-chome, Minato-ku, Tokyo 107-0052 Japan
Phone: 81-3-3475-5618 FAX: 81-3-3475-5619 E-mail: jaacc@mtd.biglobe.ne.jp

In the USA

Copyright Clearance Center, Inc.
222 Rosewood Drive, Danvers, MA 01923 USA
Phone: 1-978-750-8400 FAX: 1-978-646-8600

Proceeding of A3 Foresight Program Seminar on
Critical Physics Issues Specific to Steady State Sustainment
of High-Performance Plasmas

May 17-20, 2016, Yinchuan, China

Edited by

Liqun HU, Shigeru MORITA and Yeong-Kook OH

Abstract

A3 foresight program is a joint project on plasma physics research under the auspice of JSPS (Japan), NRF (Korea) and NSFC (China). Its main purpose is to solve several key physics issues specific to steady state high performance plasmas through joint experiments on three Asian advanced fully superconducting fusion devices (EAST in China, LHD in Japan, KSTAR in Korea) and other magnetic confinement devices. As a major activity of this A3 program, the academic workshop is held in Korea, Japan, and China in turn. Since the first coordinator meeting at Jeju Island, Korea in 2012, seven workshops have been held with three in Japan, three in Korea and two in China, A3 program has become an important platform for scientists of three countries to report and discuss the latest progress and achievement in steady-state sustainment of high-performance plasma. In the meanwhile, multi-faceted and complementary physics researches have been guided to carry out effectively on three devices. Thanks to harmonic and joint efforts, the mid-evaluation of the A3 program have been passed successfully last May. To make a better summary of last year's research result, optimize ongoing collaborations and maximize scientific outcomes, this 9th workshop is proposed. This workshop is also motivated by discussions on new collaborations and scientific supports needed in the near future to analyze the data and to improve the experiment including the instrumentation. The topics include current drive and profile control, transport of edge and divertor plasmas, stability of edge plasma, interaction between energetic particle and bulk plasma, and experimental and theoretical study in other relative fields.

Key words: magnetically confined devices, toroidal plasmas, high performance plasmas, steady state operation, edge plasma, divertor plasma, edge stability, high-energy particle, alpha particle and fusion plasma simulation.

Organizing Committee

Liqun HU (Institute of Plasma Physics, Chinese Academy of Sciences, China)

Shigeru MORITA (National Institute for Fusion Science, Japan)

Yeong-Kook OH (National Fusion Research Institute, Korea)

Program Committee

Liqun HU (Institute of Plasma Physics, Chinese Academy of Sciences, China)

Shigeru MORITA (National Institute for Fusion Science, Japan)

Yeong-Kook OH (National Fusion Research Institute, Korea)

Ge ZHUANG (Huazhong University of Science and Technology, China)

Hong QIN (University of Science and Technology of China, China)

Yi LIU (Southwestern Institute of Physics, China)

Ze GAO (Tsinghua University, China)

Houyang GUO (Institute of Plasma Physics, Chinese Academy of Sciences, China)

Nong Xiang (Institute of Plasma Physics, Chinese Academy of Sciences, China)

Bingjia Xiao (Institute of Plasma Physics, Chinese Academy of Sciences, China)

Conference Secretariat

Ruijie Zhou (Institute of Plasma Physics, Chinese Academy of Sciences, China)

Shaohua Dong (Institute of Plasma Physics, Chinese Academy of Sciences, China)

Preface

Steady-state sustainment of high-performance plasmas is one of the crucial issues needed to be addressed for fusion reactor development. To enhance close collaborations among scientists in three Asian countries (China, Japan and Korea), A3 foresight program on Plasma Physics was newly started from August 2012 under the auspice of JSPS (Japan), NRF (Korea) and NSFC (China). The main purpose of this project is to solve several key physics issues through joint experiments on three Asian advanced fully superconducting fusion devices (EAST in China, LHD in Japan and KSTAR in Korea) and other magnetic confinement devices to carry out multi-faceted and complementary physics researches.

The 1st coordinator meeting hosted by NFRI (Korea) was held in Jeju Island, Korea on August 22 in 2012. Since then, seven seminars have been held in Japan, China, and Korea in turn. More specifically, the second meeting hosted by NIFS (Japan) was held in Kushiro, Japan during January 22-25 in 2013, followed by third meeting hosted by ASIPP (China) in Beijing, China during May 20-23 in 2013, fourth meeting hosted by NFRI (Korea) in Gyeongju, Korea during November 3-4 in 2013, fifth meeting hosted by NIFS (Japan) in Kagoshima, Japan during June 23-26 in 2014, sixth meeting hosted by ASIPP (China) in Nanning, China during January 6-9 in 2015, seventh meeting hosted by NFRI (Korea) in Chuncheon, Korea during May 19-22 in 2015, and eighth meeting hosted by NIFS (Japan) in Tokyo, Japan during December 1-4 in 2015, respectively. Fruitful results from collaborative research have been summarized and discussed, and the foundations for further collaborations among scientists in China, Japan and Korea have been laid during those meetings. Also, many young scientists obtained the opportunity to get lots of valuable guidance and advices from experienced scientists.

To make a better summary of last year's research result, optimize ongoing collaborations and maximize scientific outcomes, the ninth meeting hosted by ASIPP (China) is held in Yinchuan, China during May 17-20 in 2016. In total 74 participants attended this meeting, among which 12 from Korea, 15 from Japan, and 47 from China.

In the meeting, participants gave 56 reports which focused on five categories (I: Current drive and profile control; II-a: Transport of edge and divertor plasmas; II-b: Stability of edge plasma; III: Interaction of energetic particle and bulk plasma; IV: Experimental and theoretical study in other relative fields). Those reports contain the latest achievements in physics research, collaboration results, and the status of system upgrade of the main magnetic confined fusion devices in China, Japan and Korea. To encourage the active participation of young scientists and promote their growth, half-day academic forum for young scientists was arranged specifically. Participants discussed ardently on issues of interest in the reports and on future collaboration plans. Results of the collaboration based on this meeting are published as the proceeding which can ensure better communication among the A3 community. In the proceeding, 44 papers are collected in the end. Order of the papers in the proceeding is arranged firstly according to their categories, then according to order of the presentations during the meeting.

The meeting was closed with great success, clarifying remarkable progress obtained through A3 collaboration in the researches concerning the above important topics and also contributing to the fostering of younger scientists in related field. The organizing and program committees are deeply grateful to all participants and to strong and continuous support from foundation of three countries (NSFS in China, JSPS in Japan, and NRF in Korea), with whose support and corporation the seminar was smoothly and successfully concluded.

Liqun HU, Shigeru MORITA and Yeong-Kook OH
Chairpersons of the Organizing Committee

Contents

Preface

Contents

Photo of Participants

Category I: Current drive and profile control

Jong-Gu KWAK (NFRI).....	1
Heating and plasma performance status in KSTAR 2015 campaign	
Ohjin KWON (Daegu Univ.).....	7
Dependence of pedestal properties on plasma parameters	
Haiqing LIU (ASIPP)	13
Current profile measurements by laser-based POLarimeter-INTerferometer (POINT) system on EAST	
Satoshi OHDACHI (NIFS).....	23
2D VUV camera on KSTAR and RMP study using imaging diagnostics	
Guoqiang ZHONG (ASIPP)	28
Nuclear radiation shielding and monitoring on the EAST device	
Yasuhiro SUZUKI (NIFS).....	31
Observation of ballooning mode in LHD and its theoretical analysis	
Dalong CHEN (ASIPP)	35
Halo current study on the EAST tokamak	
Hui LIAN (ASIPP)	43
Experimental study of the evolution for Faraday Rotation Angle by LHCD on EAST	
Takahiro BANDO (NIFS).....	49
Study on applicability of scintillator-based SX diagnostic for high neutron flux environments in EAST and LHD	
Guoliang XU (USTC).....	53
Preliminary Assessment of Tungsten as an Optional Plasma Facing Material in CFETR	

Yulei WANG (USTC)60
Multi-scale Full-orbit Dynamics of Runaway Electrons in Tokamak with Synchrotron Radiation

Jingbo CHEN (ASIPP)66
Radiative divertor experiments with Ar and Ne seeding on EAST

Category II-a: Transport of edge and divertor plasmas

Songlin LIU (ASIPP) 75
Ripple and error field analysis due to applying blanket with RAFM steel in CFETR

Shigeru MORITA (NIFS) 83
Steady divertor detachment operation assisted by $m/n=1/1$ RMP field with resonance in the stochastic magnetic field layer of LHD

Won-ha KO (NFRI)89
The H-mode power threshold to low error fields in KSTAR

Yi TAN (Tsinghua University)93
Recent progress in the SUNIST spherical tokamak

Suk-Ho HONG (NFRI)99
Inter-ELM heat loads on misaligned tungsten blocks in KSTAR

Jun-Gyo BAK (NFRI) 104
SOL widths of limiter plasmas in KSTAR and EAST tokamaks

Mamoru SHOJI (NIFS) 110
Simulation of the impurity transport by the emission of dusts at the termination of a long pulse discharge in the Large Helical Device

Seong-Heon SEO (NFRI) 115
Data analysis method of KSTAR reflectometer for density profile measurement

Tetsutarou OISHI (NIFS) 121
Observation of carbon impurity flow in the ergodic layer of LHD and its impact on the edge impurity screening

Ling ZHANG (ASIPP) 125
Experimental study of impurity transport coefficient based on the time behaviour measurements of impurity line emissions intensity on EAST

Category II-b: Stability of edge plasma

Kazuo TOI (NIFS)	132
Interactions between Edge Localized Modes (ELMs) and the Scrape-Off Layer (SOL) plasma in EAST and HL-2A Tokamaks and a Plan for the External Control	
Ahmet AYDEMIR (NFRI)	139
Explosive behavior of some pressure-driven modes	
Naoko ASHIKAWA (NIFS).....	144
Characterizations of deposited tungsten layer and their hydrogen isotope retention	
Bojiang DING (ASIPP)	148
LHCD optimization for high performance in EAST	

Category III: Interaction between energetic particle and bulk plasma

Deng ZHOU (ASIPP)	165
Magnetic components of GAMs in tokamak plasmas with a radial equilibrium electric field	
Youjun HU (ASIPP)	171
Simulation of fast-ion-driven Alfvén eigenmodes on EAST tokamak	
Yasushi TODO (NIFS)	179
Resonance overlap of multiple Alfvén eigenmodes leads to fast ion profile stiffness	
Tianyang XIA (ASIPP).....	183
Simulations of the particle and heat fluxes of ELM and inter-ELM phase on tokamaks with BOUT++	
Shouxin WANG (ASIPP)	195
Experimental study of density pump-out on EAST	
Jiao PENG (ASIPP)	209
Cleaning of first mirror surface of Charge Exchange Recombination Spectroscopy Diagnostics of EAST using radio frequency plasma	
Huajie WANG (USTC).....	214
Current status and data analysis of BES in EAST	
Li LIU (USTC)	219
Investigating of the heating transport models in DIII-D ITER ramp up experiments	

Xingjia YAO (ASIPP)	237
Snake perturbation during pellet injection on the EAST tokamak	

Xiuda YANG (ASIPP).....	241
Preliminary result of impurity density evaluation on EAST	

Category IV: Experimental and theoretical study in other relative

fields

Shuyu DAI (NIFS).....	250
Impact of the perpendicular diffusivity on impurity transport in the stochastic layer of LHD in comparison with EUV emission measurements	

Sang Gon LEE (NFRI).....	254
Long-lived pressure-driven MHD mode in KSTAR plasmas	

Yang He (USTC)	258
Hamiltonian particle-in-cell methods for Vlasov-Maxwell equations	

Xianli HUANG (NIFS).....	262
Comparison of impurity transport between Al and Fe in LHD based on space-resolved EUV spectroscopy	

Cheonho BAE (NFRI)	268
Plasma conditions for gyroviscous cancellation in flowing plasmas	

Liangbing HU (ASIPP).....	272
Dynamic behavior of cryogenic system under plasma discharge in EAST	

Daiji KATO (NIFS)	280
Tungsten ion distribution analysis based on visible M1 lines of highly charged tungsten ions in LHD	

Cunyun GAN (ASIPP).....	284
Simulations of parametric decay instability of ion Bernstein wave	

Program	291
----------------------	-----

List of Participants	297
-----------------------------------	-----



Heating and plasma performance status in KSTAR 2015 campaign

Jong-Gu Kwak

¹NFRI, Daejeon, Korea
jgkwak@nfri.re.kr

The main mission of KSTAR program is exploring the physics and technologies of high performance steady state tokamak operation that are essential for future fusion reactor. Since the successful long pulse operation of 25 sec at 0.5 MA exceeding conventional tokamak capabilities in 2013, the duration of H-mode has been extended to over 50s which corresponds to a few times of current diffusion time. In addition to long-pulse operation, the plasma performance is further extended on the high poloidal beta discharge which characterizes the fully non-inductive discharge over 12 s and achieves both ion and electron temperature over 5 keV simultaneously in line integrated density of $5 \times 10^{19}/\text{m}^3$.

For supporting above KSTAR performances, the main heating system consists of various asset of heating mixtures. Especially highly co-tangential 6 MW NBI consisting of three ion sources and 1 MW ECCD have been played in very important role in sustaining and achieving the high performance plasma as well as the startup. The innovative concept of current drive, helicon, was installed and its preliminary results show its high efficient coupling and ~ 300 kW high power system will be tested in 2016. In addition to heating systems, various diagnostics including the neutron measurements are also used for characterizing and interpreting the plasma performance. ECE imaging and beam emission spectroscopy on KSTAR provided the basic underlying physics of the ELMs and fluctuations. Since the unique success in ELM suppression using $n=1$ RMP, KSTAR has been focusing on extending operation window of ELM suppression and in parallel, by extending the duration of the ELM suppression up to 10 sec, the heat deposition in long-pulse state of RMP suppression is diagnosed by IR camera also.

Including above topics, the presentation will address the recent results on high ion temperature and neutron production discharge with the energy spectra of neutron.

1. Introduction

The KSTAR is a superconducting machine for exploring the physics and technologies of high performance steady state long pulse operation of the future fusion reactor. Since its successful long pulse operation of 25sec at 0.5MA H-mode in 2013, KSTAR has extended its performance in terms of pulse duration at H-mode, fully non-inductive and high beta-N discharges. The duration of H-mode has been extended to over 50s at plasma current of 0.6 MA and β_N reaches 2.9 transiently and sustained $\beta_N \sim 2.8$ for more than 1s in 2015.[1] β_N of 2.5 keeps constantly over 10s. For supporting AT(Advanced Tokamak) researches which is also one of final missions of KSTAR, a new constructing off-axis NBI beam system was scheduled to operate in 2018 and the high efficient innovative concept of helicon current drive is suggested as well. In addition to heating systems, various diagnostics including neutron measurement is also used for characterizing and interpreting the high performance plasma performance. MSE provided basic profile data of current distribution and ECE imaging and beam emission spectroscopy on KSTAR provided the basic underlying physics of the ELMs and

fluctuations. Since the unique success in ELM suppression using $n=1$ RMP, KSTAR has been focusing on extending operation window of ELM suppression and in parallel, by extending the duration of the ELM suppression up to 10 sec, the heat deposition in long-pulse state of RMP suppression is diagnosed by IR camera also.

2. KSTAR performance and present status

KSTAR already reached the high β_N of 2.9 transiently and sustained $\beta_N \sim 2.8$ for more than 1s exceeding MHD stability limit of no wall ideal limit. It was demonstrated transiently during the ramping period of plasma current by optimizing I_p/B_T with $P_{\text{ext}} \sim 3$ MW.[1] The long pulse discharge over 10s instead of the transient high beta operation was tested and β_N of 2.5 is sustained for 10s. The shot was designed to be consisting of two 10s phases. At phase I, ~ 4 MW NBI heating sources are firstly injected and after getting stable low beta($\beta_N \sim 2$) plasma, we can get the higher beta discharge after 10s at $q_{95}(\sim 3.8)$ phase II by applying additional the third 2 MW NBI ion source. Due to present limitation of available NBI power to reach the high β_N at 2T, the toroidal magnetic field is decreased to 1.5T. Whenever β_N exceeds 2.5, suddenly β_N drops and TM ($n=2$) also reduces core confinement at $\beta_N > 2$ and $q_{95}(\sim 3.8)$, but β_N keeps 2.4 after NB-c injection for 10s. Maximum $\beta_N \sim 2.9$ was reached transiently, but disrupted by (N)TM (2/1) at $q_{95} \sim 3.3$. Note that keeping β_N of 2.5 for 10s was demonstrated without error field correction coil in KSTAR. According to the measurement of intrinsic error field(EF) in KSTAR, the error field is estimated to be about 10^{-4} at $\beta_N \sim 2.6$ so that the low level of intrinsic EF is expected to allow easier access the no-wall stability limit in KSTAR without EF correction and KSTAR may not need any EF correction to realize ITER baseline scenario.

Inductively long pulse operation based on the standard H-mode has been conducted for 400 -600kA ranges of plasma current. Since the first H-mode plasma whose duration is 2s in 2010, H-mode plasma has been sustained more stably and the pulse-length is further increased year by year through overcoming the difficulty in many engineering issues and pulse length is about 40 s for 0.5 MA in 2014 and ~ 55 s discharge at 0.6 MA is sustained in 2015 successfully as shown in Figure 1. The peak stored energy is about 0.4 MJ and the line integrated density is about $\sim 4.5 \cdot 10^{19}/\text{m}^3$ and the electron and the ion temperature is ~ 8 keV and 2.6 keV around 15s respectively. The injected power is 4.2 MW NBI and 0.65 MW ECCD.

Nominal pulse length of the inductive discharge would be 40-60s where the diamagnetic energy during flat top is decreased sometimes. W_{mhd} drops 10% from 0.4 to 0.33 MJ as well as the electron temperature(8~6keV). It seems that the drift of vertical plasma position is one of causes, which seems to be related with the plasma position control scheme and long term drift of the integrator. During the variation of 0.4 at 15s to 0.28 MJ at 50s, the vertical position moves upward ~ 3.2 cm. Depending on the discharge condition of long pulse, plasma position changes time to time and sometimes showed

upward direction. The long pulse discharge is terminated around 60 s by interlock from over MVA limit of the circulating power and several shots also show the termination by NBI fault. Presently, MVA limit is the main reason for the long pulse interrupt, which limits the maximum available ohmic flux and is set to 120 MVA. The MVA constraint is set to prevent releasing mechanical preloading on central solenoid coils. Further engineering effort is required to get stationary inductive discharge to 100 s without Wmhd degradation including the plasma position control and maximum preloading coils.

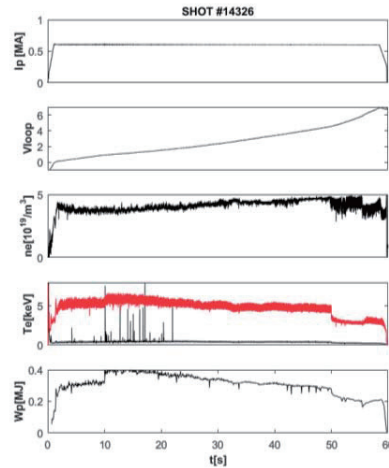


Fig.1. The time evolution of I_p , flux loop, line integrated density, electron temperature and stored energy(#14326). The NBI beam is interlocked at 50s, but the discharge continues with ECH and then terminated by MVA limit at 59s.

For steady state operation, it is strongly required for tokamak to keep the plasma current fully non-inductive so that KSTAR should demonstrate its non-inductive capability in 100 % to achieve its final goal. By decreasing the plasma current down to 400 kA, fully non-inductive discharge is obtained for 12 s at $2.5 \cdot 10^{19}/\text{cm}^2$ line density with NB power of 3.5 MW and 1 MW ECCD as shown in Figure 2. The toroidal magnetic field is set to 2.9T which is also the optimum magnetic field for central heating of 170 G ECH. The obtained β_p and β_N is about 3.5 and 2 respectively. The flux consumption is nearly zero and PF coil current keeps constant during the flat-top period. In advanced scenarios with $q_{95} \geq 8.5$, the plasma current was lowered to 300-400 kA to maximize the bootstrap fraction of non-inductive current drive by increasing β_p . The calculated bootstrap fraction would be $\sim 50\%$ where Sauter model is used and Te/ne profile data are from Thomson diagnostics. But due to overheating on the poloidal limiter, the discharge is interrupted for the machine safety. The temperature at the poloidal limiter is increased up to 450C and the similar temperature rise at limiter is seen by tangential IR camera as well. According to the calculation by 3D orbit code, the prompt ion loss of NB beam would be one of key contribution to the temperature rise at the limiter. Maximum 10 % of NB power would be deposited at the specific limiter position and more than $0.5 \text{ MW}/\text{m}^2$ heat load could hit the poloidal limiter(especially lower part of the limiter). The loss is the largest at relatively perpendicular injected beam C. More gas puff, NB-C turn-off and higher plasma current operation were suggested for options to reduce ion loss. The line density was increased up to $4 \cdot 10^{19} \text{ cm}^3$ by gas-puff and temperature at limiter comes

down to 75 °C(25% of #13008) even up to 22s, but the discharge changed to inductive mode. For case of turn off NB-C, the pulse length can be extended to 40 s without noticeable increase in limiter temperature, but the discharge is also changed to inductive. By increasing plasma current to 500 kA shows that the loop voltage is increased so that it indicates that there is optimum plasma current ranges for high β_p fully non-inductive discharge at present available heating resources.

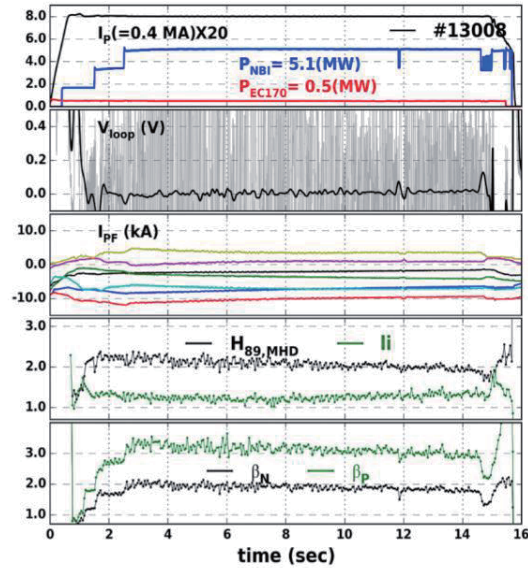


Fig.2. The time evolution of plasma current, injected heating power, loop voltage, current of PF coils, H-factor and beta values. The plasma is terminated around 15s by over-temperature limit at the poloidal limiters

Another interesting discharge is to demonstrate the high ion temperature by increasing plasma current to 800 kA with 4.5 MW NBI heating, the ion temperature reaches to about 5 keV with the electron temperature of 6 keV at $4 \times 10^{19} / \text{cm}^2$ line integrated density as shown in Figure 2. The calculated bootstrap current fraction is about 41% and the stored energy is about 0.5 MJ. At much higher plasma current of 1 MA, the ion temperature is decreased,

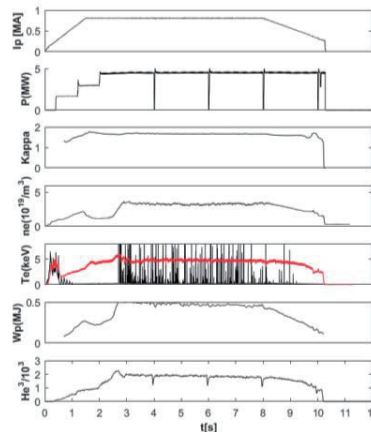


Fig.3. The time evolution of I_p , NBI heating power, kappa, density, electron temperature, stored energy and neutron counts(#14165). The nbi beam blips are used for CES measurements.

ECH has relatively no many resolving issues comparing with NBI in term of long pulse operation. Due to the vendor request of 170 G gyrotron, it only tested by 50 sec at 1 MW. 50 sec long-pulse injection with ~ 0.75 MW (avg. power at the window) achieved by heater boosting of 28 V and anode voltage control. Maximum collector surface temperature was ~ 150 °C with beam current of ~ 50 A. The temperature rise of water-cooled antenna mirror is about ~ 3 °C. Presently, 105/140 G dual frequency gyrotron is commissioned and 1MW and 0.8 MW is obtained for 300 s at 140 G and 105 G respectively. During 300 s, many issues are arising including overheat of transmission line. For the high beta operation above 2.5, NTM control is one of critical issues. The search and suppress and active q tracking method can run independently or change from one method to another in real time. EC power and mirror was successfully controlled by NTM control algorithm based on mode amplitude with not NTM in high beta plasma, but with very special tearing mode in L-mode plasma

3. Summary

KSTAR has successfully extended the operation boundary toward high performance, long-pulse H-mode (~ 55 Sec at 0.6 MA) but further efforts are still required to long stationary discharge in terms of vertical drift of plasma position and heating resources reliability. Present projection estimates that β_N is limited by internal MHD stability in conventional discharges and the max stable $\beta_N \sim 2.5$ ($I_p = 0.6$ MA, $B_T = 1.4$ T, $P_{NBI} \sim 5$ MW) far below no wall limit with $\beta_N \sim 4$ and $l_i \sim 3.5$ and (N)TM ($n=1$) leads to disruption

($q_{95} \sim 3.4$) or confinement loss up to 30-40 %. Fully non-inductive discharge with high poloidal beta condition is achieved with the max $\beta_p \sim 3$ but fully non-inductive state with duration of 12 s is demonstrated with issues of PFC overheating by fast prompt ion loss from NBI at low plasma current.

References

[1] Kwak et al., "An overview of KSTAR results", NF, 53(2013) 104005

Dependence of Pedestal Properties on Plasma Parameters

Ohjin Kwon¹ and S.K. Kim²

¹Department of Physics, Daegu University, Gyeongsan 38453, Gyeongbuk, Korea

²Department of Nuclear Engineering, Seoul National University, Gwanak 08826, Seoul, Korea

Abstract

We have numerically investigated the dependence of pedestal properties such as the pedestal height and the pedestal width on various global parameters. We have used EPED, a predictive model of the edge pedestal. Among global parameters we have chosen to vary, the triangularity, δ , the elongation, κ , and the poloidal beta have larger effect on the pedestal properties. Improvement of pedestal properties can be achieved for more shaped plasma boundary. However, the increase in the pedestal height and the width with δ saturates around $\delta \sim 0.6$. Also, the pedestal width saturates and the pedestal temperature starts to decrease for $\kappa > 1.9$. Improvement of the pedestal properties due to δ is larger at higher poloidal beta.

1. Introduction

High confinement mode (“H-mode”) in a tokamak device is achieved via formation of edge transport barrier related to pedestal structure of density and temperature near the outer region of plasma. The performance of H-mode is associated with plasma confinement in edge pedestal region and strongly affected by characteristics of pedestal such as width (Δ_{ped}) and temperature height (T_{ped}). To optimize the performance of current and future fusion devices, understanding the pedestal behavior is important, and finding the best plasma conditions that maximizing the pedestal performance is required for fusion study. However, the prediction of the pedestal temperature and width still has many uncertainties and understanding its physics remains as a challenge. Especially, prediction of pedestal structure is one of ongoing issues in designing the future fusion devices, ITER and DEMO. For these purposes, various approaches were done on this question and considerable progress has been achieved.

Among many approaches on pedestal prediction, one of successive model is EPED [1,2]; the edge pedestal predictive model based on the peeling-ballooning mode (PBM) and kinetic ballooning mode (KBM). Despite some limits on its’ theoretical model, it showed good agreement with experimental results and has been verified in previous studies. Since such methodology can be used to various tokamak plasma, it is also possible to estimate the pedestal structure of predicted plasma equilibrium which is calculated with numerical equilibrium solver. Based on this idea, we have investigated the dependence of pedestal properties such as the pedestal height and the pedestal width on various global parameters for a large tokamak.

2. Results

We have used HELENA code [3] for H-mode equilibrium generation and MISHKA code [4] for stability determination. The geometric characteristics of plasma boundary is usually defined by

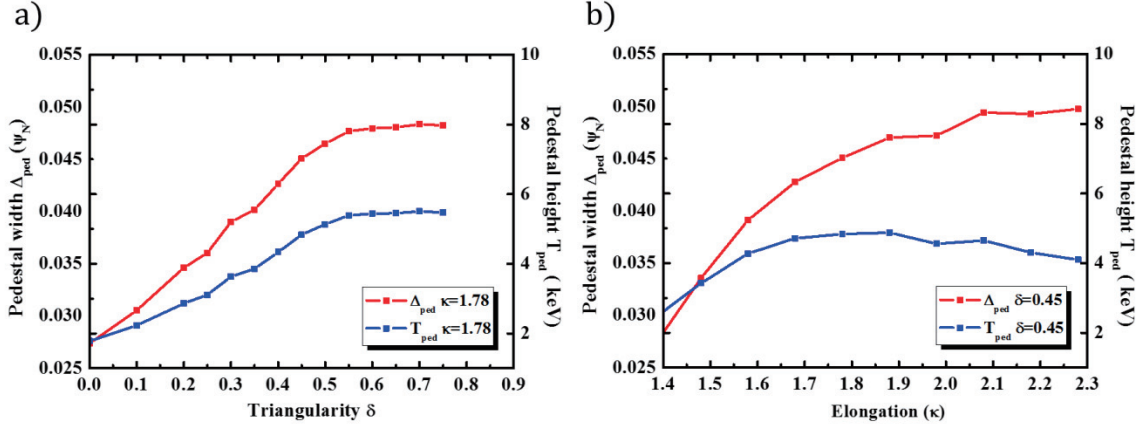


Fig. 1 Behavior of Δ_{ped} and T_{ped} with different δ (a) and κ (b). (Red) and (Blue) are Δ_{ped} and T_{ped} respectively.

triangularity (δ) and elongation (κ). Since δ and κ can change the safety factor, current density and pressure gradient at pedestal regions, they strongly affect MHD instabilities in edge region including PBM. As a result, pedestal structure strongly depends on the plasma shape, and experimental studies found that pedestal structure tends to grow as δ and κ increase. To compare this trend with our predictive modeling, we calculated pedestal structures via EPED with changing δ and κ separately from reference equilibrium. The results are shown in Fig. 1. From this figure, it can be seen that Δ_{ped} and T_{ped} largely vary with κ and δ . Both Δ_{ped} and T_{ped} tend to grow as shape parameters increase and it well agrees with previous experiment studies. In Fig. 1(a), Δ_{ped} increases by 70%, while T_{ped} increases threefold. as δ increase from 0 to 0.5 Also, Δ_{ped} and T_{ped} improve by 60% as κ increase from 1.4 to 1.8 as shown in Fig. 1(b). The reason for improved pedestal structure turned out to be the results of increased stabilization of PBM. Fig. 2 shows stability boundary of PBM on $j_\phi - \alpha$ diagram, where $\alpha = -(q^2/R_0 B_T)(\partial P/\partial \rho)$ is normalized pressure gradient, and j_ϕ is edge current density. Here, q is safety factor, ρ is normalized

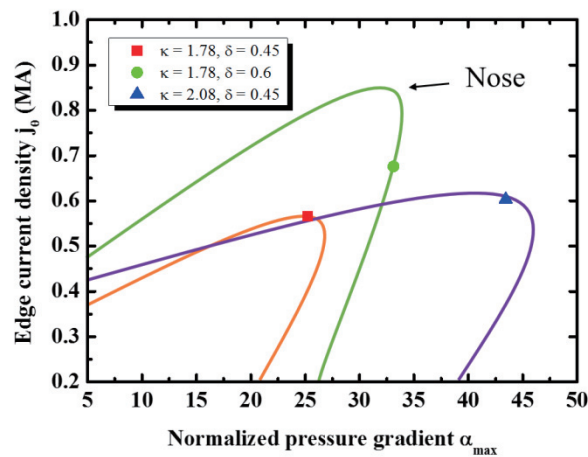


Fig. 2 Figure shows equilibrium points on $j_\phi - \alpha$ space for reference (red), large δ (green), and large κ (blue) case. Also peeling-ballooning stability boundaries for each case are drawn together. As κ and δ increase, PBM is strongly stabilized. Notice that edge of stability boundary is called as nose.

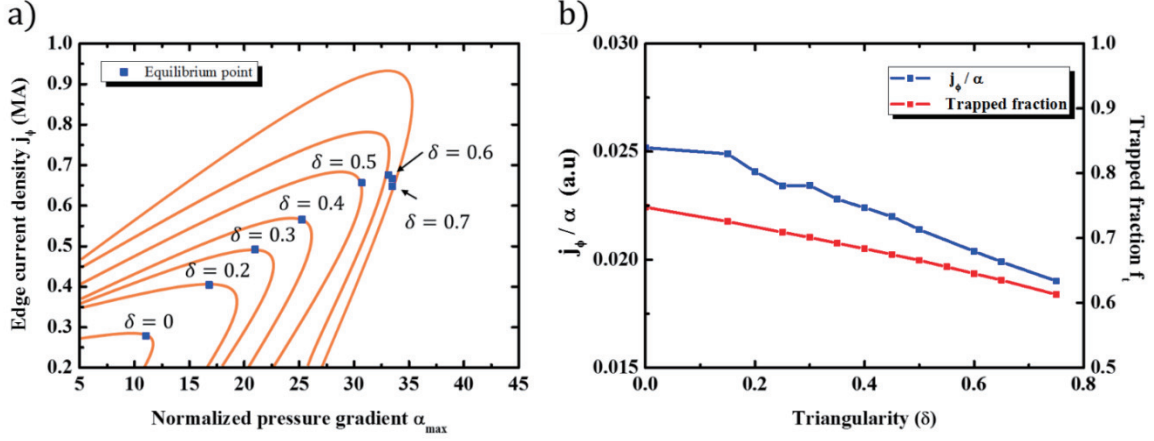


Fig. 3 Figure a) shows equilibrium points and corresponding stability boundary (orange) for different δ . In figure, up-right movement of equilibrium can be found. This movement stopped when $\delta \geq 0.6$. Also b) is plot that compares j_ϕ/α (equilibrium) and f_t for different δ . Good agreement was found between these two values.

radius, P is plasma pressure, B_T is toroidal field, and R_0 is major radius. As δ and κ increase, stability region widens and it allows plasma equilibrium to move diagonally to the region of larger α and j_ϕ . Since α and Δ_{ped} are correlated under KBM condition, Eq. (1) is satisfied, where P_{ped} is plasma pressure at pedestal top.

$$\alpha \propto P_{ped}/\Delta_{ped} \propto \beta_{p,ped}/\Delta_{ped} \propto \Delta_{ped} \propto T_{ped}^{1/2} \quad (1)$$

From Eq.(1), larger α means wider Δ_{ped} and higher T_{ped} , and T_{ped} increases much faster than Δ_{ped} because $T_{ped} \propto \Delta_{ped}^2$. As a consequence, both Δ_{ped} and T_{ped} increase as equilibrium moves to upper diagonal side and therefore, they grow with δ and κ . This is also consistent with previous studies of shaping effect on PBM.

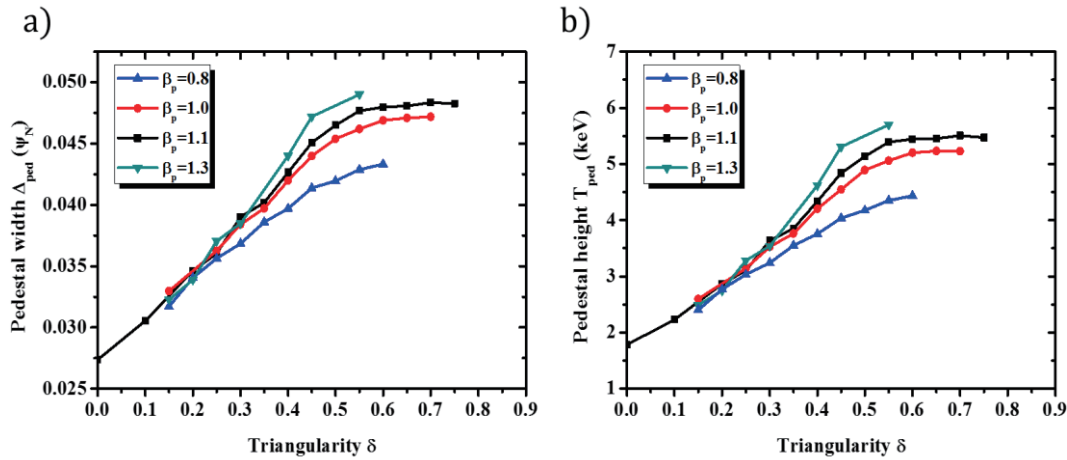


Fig. 4 This figure a) shows Δ_{ped} respect to β_p for different δ . Also b) is plot that shows T_{ped} respect to β_p in different δ . Both increase with β_p and δ , and saturate for $\delta \geq 0.6$.

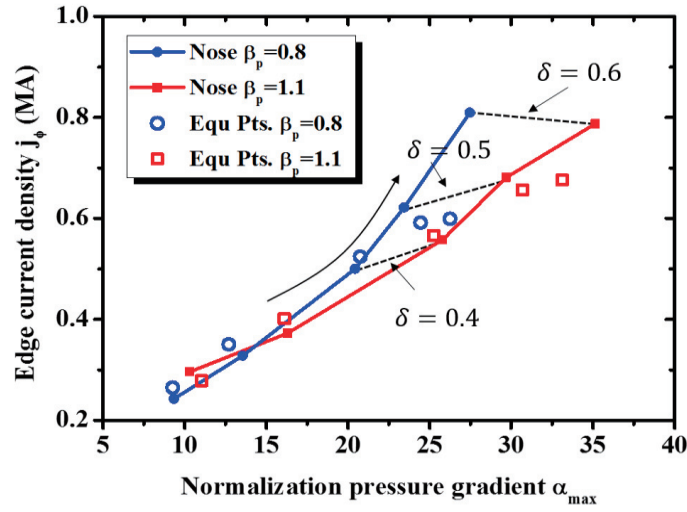


Fig. 5 This figure shows equilibrium points and location of corresponding nose of stability boundary for different δ . Arrows indicate location of boundary nose for each δ . As δ increases, these points are moving to top-right corner. It indicates that stability boundary widens as δ and β_p increases. Also, it is found that stabilization effect of δ is more stronger in higher β_p .

However, improvement in pedestal properties saturates as plasma boundary shaping becomes stronger. In Fig. 1(a), it can be seen that Δ_{ped} and T_{ped} saturates at $\delta > 0.6$. The saturation of pedestal structure with δ is related to trapped fraction (f_t). At pedestal region, bootstrap current (j_{bs}) plays dominant role in current distribution and it is proportional to pressure gradient ($\propto \alpha$) and f_t . Trapped fraction does not change much with δ when δ is small, so j_ϕ can increase with α in $j_\phi - \alpha$ space. But, for large δ , f_t considerably decreases, and $j_\phi \approx j_{bs}$ cannot grow further even α increases. Fig. 3(a) shows how reduction in f_t can affect the movement of equilibrium. In Fig. 3(a), equilibrium point moves up diagonally following the stability boundary for $\delta \leq 0.6$ because f_t remains almost same for small δ . When $\delta > 0.6$, however, j_{bs} decreases since f_t decreases with δ . The equilibrium point moves downward accordingly. Therefore, improvement of stability boundary for $\delta > 0.6$ cannot be fully utilized as j_ϕ decreases. As a result, Δ_{ped} and T_{ped} saturate for large δ . Comparison of $f_t(\delta)$ with j_ϕ/α ($\propto j_{bs}/\nabla P$) of equilibrium points of different δ (Fig. 3(b)) is also consistent with this explanation. These two values show similar tendency and it indicates that saturation of Δ_{ped} and T_{ped} in large δ is mainly due to f_t .

In Fig. 1(b), T_{ped} starts to decrease when $\kappa > 1.9$ while Δ_{ped} steadily increase with κ . When κ changes from 1.9 to 2.3, Δ_{ped} increases by 10% and T_{ped} decreases by 10%. To understand this tendency, we derived expression of T_{ped} with κ . From KBM constraint, T_{ped} and $\partial T_{ped}/\partial \kappa$ can be described as Eq.(2) and (3), where I_p is plasma current and L is perimeter of plasma boundary.

$$T_{\text{ped}} \propto \beta_{\text{p,ped}} I_p^2 / L^2 \propto \Delta_{\text{ped}}^2 I_p^2 / (\kappa^2 + 1) \quad (2)$$

$$\partial T_{\text{ped}} / \partial \kappa \propto \partial \Delta_{\text{ped}} / \partial \kappa - \Delta_{\text{ped}} / \kappa \quad (3)$$

In Fig. 1(b), Δ_{ped} strongly increases with κ for $\kappa \leq 1.9$ and $\partial \Delta_{\text{ped}} / \partial \kappa$ is larger than $\Delta_{\text{ped}} / \kappa$. Consequently, T_{ped} increases with κ from Eq.(3). For large κ , however, $\partial \Delta_{\text{ped}} / \partial \kappa$ become smaller than $\Delta_{\text{ped}} / \kappa$ because stabilization effect of κ saturates at large shaping. Therefore, $\partial T_{\text{ped}} / \partial \kappa$ has negative value when $\kappa > 1.9$ and T_{ped} decreases as κ increases. Thus, behavior of T_{ped} in Fig. 1(b) can be explained with Eq. (3) and change of $\partial \Delta_{\text{ped}} / \partial \kappa$.

Poloidal beta (β_p) is a major global parameter in tokamak plasma that indicates the performance of plasma confinement. Since β_p is highly related to pressure profile and poloidal flux distribution, it strongly affects PBM and pedestal structure. Especially, previous study found that β_p induces Shafranov shift (Δ_{sh}) and stabilizes the edge instability via Shafranov stabilization effect. To understand this tendency, similar analysis is performed on β_p and results are shown Fig. 4. As β_p increases, Δ_{ped} and T_{ped} increase. This agrees fairly well with previous studies. Here, change of Δ_{ped} and T_{ped} increases with δ when β_p varies from 0.8 to 1.3. In Fig.4, change in Δ_{ped} is less than 1 % at $\delta = 0.1$ while it is larger than 20% for $\delta = 0.5$. This indicates that effect of β_p on pedestal structure is enhanced by strong shaping. In other words, Δ_{ped} and T_{ped} more rapidly increase with δ at higher β_p . This behavior should be related to stabilization of PBM and it turned out that β_p enhances the stabilization effect of δ on ballooning mode. Fig.5 shows the nose of stability boundary (see Fig.2) of PBM and equilibrium points of different β_p . In Fig.5, equilibrium point in both cases move up-diagonally with similar slope as δ increases from 0.4 to 0.6. However, nose of higher β_p (= 1.1) case moves diagonally to upper region with smaller slope than lower β_p (= 0.8) case due to larger stabilization of ballooning mode. This results in considerable difference. Because equilibrium of high β_p plasma can proceed to further right region of larger α than that of small β_p , former case can have larger Δ_{ped} and T_{ped} as seen from Eq.(1). Also horizontal distance between noses in different β_p on $j_\phi - \alpha$ space widens as δ increase and therefore, difference of pedestal structure in two cases also grows. Thus, effect of δ on edge pedestal increases with β_p . However, the mechanism that describes how β_p changes stabilization effect of δ on PBM still remains as a question.

3. Conclusions

With predictive model EPED, we estimate the effect of global plasma parameters (δ , κ , β_p , v_{eff}) on the behavior of edge pedestal. Comparison between prediction results and experiments in conventional tokamak shows good agreement for the case of δ , κ and β_p . Δ_{ped} and T_{ped} increase with δ and κ , and saturates at strong shaping. To summarize the effect of the shaping parameters, δ and κ , they largely affect the pedestal structure, and predictions from EPED agree well with experimental tendencies. However, Δ_{ped} and T_{ped} start to saturate or decrease as δ and κ increase over the critical values. This implies that large shaping is less effective to edge pedestal. Furthermore, large shaping induces difficulties in plasma control and there is some limit in operation window and too large value of δ and κ will be negative.

Therefore, optimum shape parameters can be determined by considering control issues and predictive modeling.

We also found that β_p enhances the shaping effect. It seems that β_p reinforces the stabilization effect of δ and κ on ballooning mode via Shafranov shift. Considerable effect of β_p on pedestal structure is observed. Correlation of β_p with shaping parameter is found and it is expected that optimization of edge pedestal structure via shaping will be more effective in plasma with higher poloidal beta.

Acknowledgements

This work was partly supported by the JSPS-NRF-NSFC A3 Foresight Program in the field of Plasma Physics (NSFC No.11261140328).

References

- [1] P.B.Snyder, et al., *Physics of Plasmas*, **16** (2009) 056118.
- [2] P.B.Snyder et al., *Nuclear Fusion*, **51** (2011) 103016.
- [3] G.T.A.Huysmans, J.P.Goedbloed, and W.O.K.Kerner, *Proceeding of CP90 Conference on Computational Physics* (World Scientific, Singapore, 1991) p371.
- [4] A.B.Mikhailovskii, et al., *Plasma Phys. Rep.* **23** (1997) 844.

Current Profile Measurements by laser-based POLarimeter-INTerferometer(POINT) system on EAST

H. Q. Liu,¹ Y. X. Jie,¹ W. X. Ding,² D. L. Brower,² J. P. Qian,¹ Z. Y. Zou,¹ W. M. Li,¹ H. Lian,¹ S. X. Wang,¹ Y. Yang,¹ L. Zeng,¹ T. Lan,^{1,3} Y. Yao,¹ L. Q. Hu,¹ X. D. Zhang,¹ and B. N. Wan¹

¹Institute of Plasma Physics, Chinese Academy of Sciences, Hefei, Anhui 230031, P.R. China

²Department of Physics and Astronomy, University of California Los Angeles, Los Angeles, CA 90095, USA

³University of Science and Technology of China, Hefei, Anhui 230026, P.R. China

Abstract

A double-pass, radially-viewing, far-infrared laser-based POLarimeter-INTerferometer (POINT) system utilizing the three-wave technique has been implemented for fully diagnosing the plasma current and electron density profiles in the EAST tokamak. POINT has been operated routinely during the most recent experimental campaign and provides continuous 11 chord line-integrated Faraday effect and density throughout the entire plasma discharge for all heating scheme and all plasma conditions (including ITER relevant scenario development). Reliability of both the polarimetric and interferometric measurements are demonstrated in typical plasma on EAST.

1. Introduction

Achievement of long pulse and steady-state plasma regimes is a major challenge for both ITER and prospective fusion power reactors. A primary goal of the EAST device is to develop long-pulse high-performance plasmas near the operational (MHD and beta) limits using ITER relevant actuators (NBI, RF current drive and heating) and sensors. The goal of plasma discharge extension to long pulse is important for demonstrating that the current profile relaxes to a steady-state and that no stability boundary is crossed during this evolution that would compromise performance. This requires an accurate, time-resolved diagnosis of the internal magnetic field, current density and electron density profiles. Measuring the Faraday effect is an appealing candidate for internal magnetic field measurement as no neutral beams are required and information is provided continuously throughout the entire plasma discharge. In addition, the high temporal resolution measurements provided are indispensable for advanced tokamak operation as tracking fast equilibrium profile dynamics and magnetic field fluctuations can be utilized for plasma control. Polarimeter systems, with either poloidal, vertical, or toroidal viewing geometry, have been successfully demonstrated on many devices, including TEXTOR¹, TEXT², JET³, MST⁴, and Alcator C-Mod⁵. A laser-based, double-pass, radially-viewing, eleven channel Faraday effect POLarimetry-INTerferometry (POINT) diagnostic has been developed for current density and electron density profile measurements in the EAST tokamak.^{6,7} POINT, which provides a non-perturbing probe of the core magnetic and current density profiles of high-performance plasmas, will focus on real-time plasma control for up to 1000 second discharges in order to extend high-performance plasma regimes to long-pulse

and develop ITER-like scenarios. The realtime output of POINT will be used to monitor the fast profile dynamics of electron density, current density and q (safety factor) and ultimately be integrated into the real-time plasma control system. Since the 2015 experimental campaign, the 11 channel POINT system has been routinely operated to measure the electron density, current density and safety factor profiles for long-pulse EAST plasmas. In this paper, we present the instrumental technique, optical layout, calibration, and initial experimental results from the 11-chord POINT system. Equilibrium electron density, current density and q profiles are obtained equilibrium reconstruction using EFIT with POINT constraints. Measurements clearly demonstrate the low phase noise and fast time response of POINT thereby enabling the observation of both equilibrium dynamics and small-amplitude fluctuations.

2. POINT on EAST

The three-wave configuration has been demonstrated to work successfully on several plasma experiments including RTP⁸, MST⁴, J-TEXT⁹, Alcator C-Mod⁵. EAST POINT^{6,7} is configured using double-pass, radially-viewing chords which access the plasma via an equatorial midplane port. The measurement technique employed is based on three-wave technique. An initial five-chord test system installed in 2014 has been upgraded to 11 chords in 2015. The horizontal chords are situated at vertical locations above and below the midplane with $z = -42.5, -34, -25.5, -17, -8.5, 0, 8.5, 17, 25.5, 34, 42.5$ (0 cm denotes the vacuum vessel center). An overview of the optical layout is shown in Fig. 1. Three CW far-infrared gas lasers using formic acid (HCOOH) and operating at nominal wavelength 432.5 μm are used as the sources. Each FIR laser is optically pumped by independent infrared CO₂ lasers operating at 9.27 μm on the 9R20 line. Output power is up to 30 mW of per cavity. Two lasers, with slight frequency offset (~ 1 MHz), are made collinear with counter-rotating circular polarization (R- and L-waves) in order to determine the Faraday effect by measuring their phase difference upon transmission through the plasma,

$$\Psi_F = \frac{2\pi}{\lambda} \int \frac{(n_R - n_L)}{2} dz = 2.62 \times 10^{-13} \lambda^2 \int n_e(z) B_{\parallel}(z) dz, \quad (1)$$

where λ is the laser wavelength, dz is the plasma path length, and B_{\parallel} in Tesla is the magnetic field component along the beam. The third laser also frequency offset, is used as a reference providing local oscillator (LO) power to each detector so that one can obtain the phase shift caused by the plasma electron density.

$$\Phi = \frac{2\pi}{\lambda} \int \frac{n_R + n_L}{2} dz \approx 2.82 \times 10^{-15} \lambda \int n_e(z) dz. \quad (2)$$

All waves are detected using VDI Schottky planar-diode fundamental waveguide mixers with integrated conical horn optimized for high sensitivity, 750 V/W. This is sufficient to provide good signal quality for all eleven chords of the polarimeter-interferometer system.

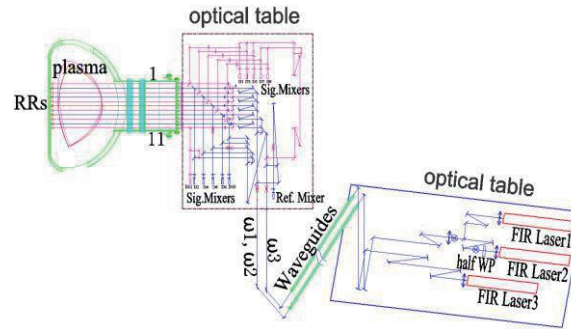


FIG. 1. 11 channels optical layout of the EAST POINT system, 5 channels (blue) is installed in 2014 with expansion to 11 channels (with added 6 channels in pink) in 2015.

The triple laser system is positioned on an optical table (20 tons) located in a humidity and temperature-controlled laser room outside the machine hall. The laser room provides a thermostatic, vibration-free, electromagnetic shielded environment for lasers. On the optical table, two laser beams are combined making them spatially-overlapped and collinear with orthogonal linear polarization. The combined beams are guided to the optical tower in the EAST machine hall, together with linearly-polarized LO beam using separate overmoded, dielectric, waveguides of ~ 20 m length. Optical stability is an important issue in FIR optical diagnostics. To avoid the vibration caused by the tokamak, a massive stainless steel tower (30 tons), mechanically independent of the EAST machine, is constructed to ensure the stability of beam-processing optics. All optical components (mirrors, beamsplitters, waveplates, lens, etc.), including the mixers and heterodyne receiver system, are mounted on an optical breadboard attached to this tower. The optical tower is located immediately adjacent to the EAST tokamak, by the diagnostic access window for the POINT system. It has been observed that mechanical vibration errors decrease up to two orders with highly stable optical table and tower. The probe beams are divided into individual 11 individual chord and a reference using wire-mesh beamsplitters. Probe beams for each chord are converted to orthogonal, counter-rotating circular polarization by a quarter waveplate before entering the plasma. The probe beams are combined with the LO beam after a double pass through plasma achieved by reflecting from corner-cube retro-reflectors mounted on the inside wall of EAST. The beams are then focused onto the mixers where signals are observed at the difference or intermediate frequencies of the lasers in the 1-2 MHz range. All intermediate frequency (IF) signals are processed by an amplifier and filter module and then sent into a high-speed digital phase detector to extract the phase shift information, from which Faraday rotation angle and density phase shift can be obtained.

In the POINT system (see Fig. 2), the in-vessel molybdenum retro-reflectors (RR) with 50 mm aperture are the major component determining the Gaussian beam size along the laser path. The surfaces of these RR are aligned accuracy up to 20 arcs to ensure high quality of the return beams. In addition, the retro-reflectors are designed to withstand baking temperature up to 350°C and discharge duration more than 1000 s without surface distortion. After two months of experimental operation on EAST, the mirror surface of the RR were

film coating materials reveals the sample includes 14% carbon, 79.5% oxygen, 0.5% silicon, 0.8% ferrum, and 5.2% molybdenum. The FIR probe beam signal reflected from the RR was recorded over a period of ~60 days, from March 10th to May 5th, where a gradual decrease was observed but sufficient power remained to conduct the POINT measurements of electron density and Faraday rotation. During this operation, it was also noted that no distortion of the FIR beam polarization was observed as determined from the system calibration. Despite the degradation of the RR, POINT was able to continue making measurements.

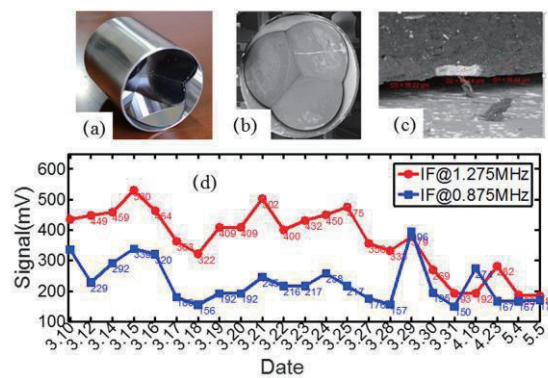


FIG. 2. (a) New retro reflector, (b) 2 months used retro reflector with film coating, (c) film on retro reflector, (d) reflected signal by retro-reflector versus date.

The long term goal of the EAST program is to use POINT data, in conjunction with other diagnostic systems, for realtime feedback control in order to maintain stable operation of high-performance tokamak plasmas while avoiding deleterious MHD events such as disruptions and ELMs. Stable intermediate frequencies (IFs) among the three FIR lasers is required for reliable real-time output of the electron density and current density to meet this requirement. To that end, a closed-loop control system is developed to stabilize the FIR laser IFs at a pre-set value based on an automatic control of the FIR laser cavity length using a piezo-electric transducer (PZT). A stable IF signal over a long time period (up to several hours) is obtained using this frequency control system. The output IF drift is lower than 0.6% for a 1 hour (3600 seconds) test. In addition, each CO₂ pump laser is frequency locked to a Fabry-Perot cavity.

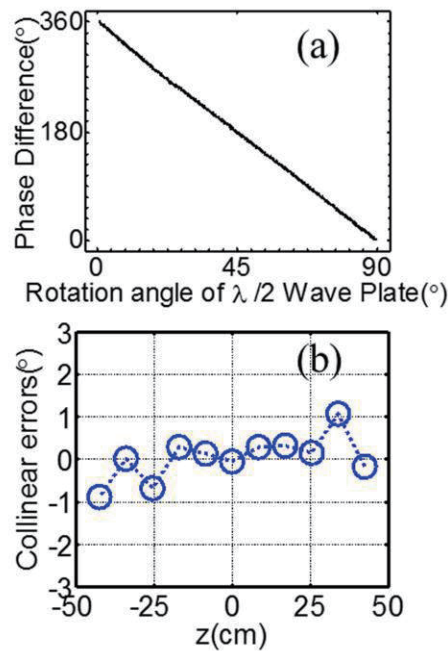


FIG. 3. Calibration results of (a) polarization of probe beams and (b) collinear error for 11 chords in high density EAST experiment.

Meanwhile, a Digital Phase Detector (DPD), prototype hardware based on a PCI card that combines a very high speed Field Programmable Gate Array (FPGA), has been developed to provide realtime output with 250 kHz bandwidth for POINT system. The DPD is used to perform phase demodulation and real-time phase calculations, provides real-time Faraday rotation angle and density phase shift output for use in the EAST plasma control system. Real-time EFIT with Faraday angle and density phase shift constraints is planned for implementation in the plasma control system in the near future. The DPD samples the reference and plasma signals each containing the three IF frequency bands of information, currently centered at 0.850, 1.275 and 2.125 MHz with about a 100 kHz tolerance. With input signals from the signal and reference mixers, DPD output for each chord corresponds to the plasma density (0.85 MHz) and Faraday-effect (1.275 MHz). Stability is necessary for POINT operation with the long term goal to provide real-time input to the plasma control system.

Measurement accuracy is directly determined by the identification and minimization of RMS and systematic errors. For interferometric measurement, mechanical vibration is a major error source which can easily induce error up to tens of degrees. As mentioned before, EAST POINT employs a massive, stable optical table and optical tower to decrease the mechanical error by up to two orders. After first alignment, in situ test without plasma reveals the electron density error is lower than $5 \times 10^{16} \text{ m}^{-2}$ (2°), while the Faraday rotation angle RMS phase noise is $< 0.1^\circ$.⁵ For polarimetric measurement, systematic errors come from non-collinear (spatially offset) probe beams, polarization distortion from non-ideal optical components, instability of intermediate frequency, misalignment to the toroidal field, finite-temperature

effects, Cotton-Mouton effect and geometric phase effects. The finite finite-temperature effects, IF stability (with feedback control), Cotton-Mouton and geometric phase effects are less than the RMS noise level of POINT. During the EAST operation, the toroidal field was scanned from 1.6 T to 2.8 T, and no misalignment to toroidal field was detected. The remaining polarization and collinearity errors are the major source of systematic errors for EAST POINT and will be discussed in more detail.

The polarization distortion results from non-ideal optical components primarily resulting from wire-mesh beamsplitters reflectance and transmission that is polarization sensitive. Distortion of laser beam circular polarization due to anisotropic reflectivity/transmissivity of optics is largely eliminated by a newly-developed optical configuration optimization. Calibration techniques for the double-pass system with zero-offset return beam have been developed, confirming polarization conservation. For examining the polarization of counter-rotating circularly-polarized probe beams, we add a rotating half-wave plate in the optical path to replace the plasma and modulate the polarization. If the probe beams' polarizations are counter-rotating circularly polarized, phase difference between the R- and L-waves will change linearly and equal four times the rotation angle of the half wave plate; any distortion of polarization will lead to a nonlinear response. As shown in figure 3(a), a linear calibration curve is observed indicating very small distortion of the probe beam polarization throughout the optical system. This calibration procedure is followed for each chord of the POINT system. The second important source of systematic error stems from non-collinearity and/or non-matched spatial overlap of the probe beams and is a unique issue to three-wave measurement technique. When the L-wave and R-wave are not collinear, phase error will be introduced by the difference of their optical path length and the different plasma regions probed in the presence of a finite density gradient. The collinearity error can be directly detected by placing a linear polarizer in the probe beam path prior to passing through the plasma. In this configuration, any phase difference measured results from the beam misalignment. The collinearity error can be directly examined in plasma experiment and is shown in figure 3 (b). All 11 chords are used in the test to obtain the error profile where the central line-averaged density for this case is $3 \times 10^{19} \text{ m}^{-3}$. As shown in the figure, the collinearity error is less than 0.3° for almost all chords, smaller than the Faraday angle. Chords positioned nearer the plasma edge where the density gradient is steepest show the largest error as expected.

3. Experimental results

For the most recent EAST experimental campaign, the POINT system alignment and calibration were optimized. The phase resolution for each of the 11 chords is about 0.1° for Faraday rotation angle and about 1° for line-integrated density averaged within a bandwidth of 50 kHz. An example of 11-chord measured data from the EAST POINT is presented in figure 4.

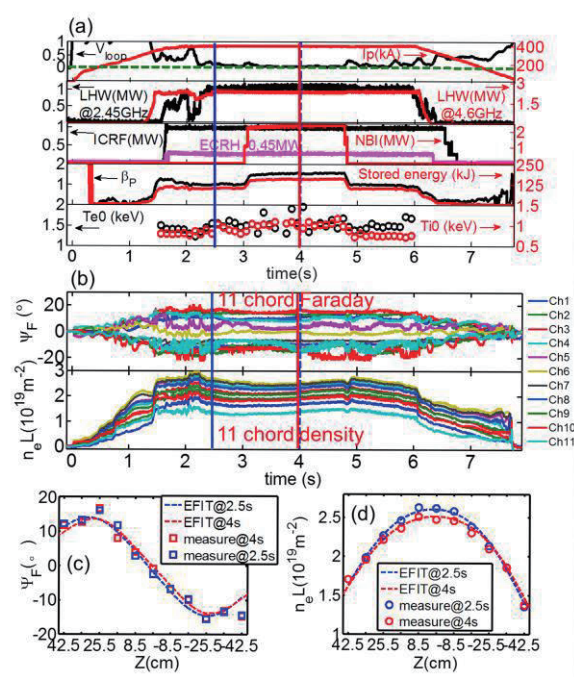


FIG 4. Typical plasma discharge (shot No. 62295) results from EAST POINT. (a) Plasma typical parameter, (b) 11 chords Faraday angle and 11 chords line-integrated density, (c) Faraday angle and (d) line-integrated density at $t = 2.5$ s and $t = 4$ s.

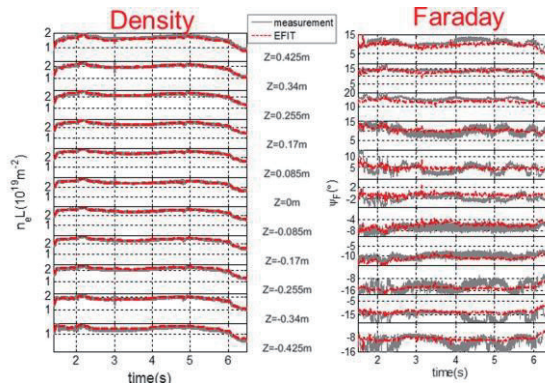


FIG 5 Typical EFIT equilibrium with POINT constraints. Overplotted using dashed lines are results from POINT measurement and EFIT reconstruction. (left), line-averaged density by POINT measurement (solid grey lines) and inverse integrated analysis by using EFIT reconstructed (dashed red lines), (right) line-integrated Faraday rotation angle by POINT measurement (solid grey lines) and inverse integrated analysis by using EFIT reconstructed (dashed red lines).

The discharge is a high-performance H-mode plasma with 2.4 MW neutron beam injection (NBI), $B_T=2.5$ T, $I_p=400$ kA, $T_{e0}=2$ keV, $T_{i0}=1.5$ keV, central line average density $3 \times 10^{19} \text{ m}^{-3}$, $\beta_p=1.5$, stored energy = 155 kJ, and $V_{loop}=0$, as shown in figure 4(a). The injection heating power includes 2.4 MW NBI, 1 MW ion cyclotron resonance heating (ICRH), 0.45 MW electron cyclotron resonance heating (ECRH), 2.3 MW low hybrid wave (LHW) @4.6GHz and 1 MW LHW @ 2.45 GHz. Figure 4 (b) shows the temporal evolution of the actual line-integrated density and Faraday effect measurements exhibiting no obvious interference from powerful NBI, LHW, ICRH and ECRH heating sources, indicating that POINT can operate for any heating scheme employed on EAST. Figure 4 (c) and (d) show profiles of measured Faraday angle and line-integrated density, respectively.

A comprehensive method to self-consistently reconstruct the current and density profiles with magnetic and POINT measurements by using the equilibrium fitting code EFIT was developed. The measured line-integrated profiles are compared with the results computed from EFIT (magnetic equilibrium reconstruction) for 11 channels at times $t = 2.5$ s (L mode) and $t = 4$ s (H mode). Figure 5 show the time evolution of the actual line-integrated density measurements and Faraday rotation measurements as compared with the results computed from EFIT (magnetic equilibrium reconstruction with POINT constraints) for 11 channels. At each chord location, the measurements are consistent with EFIT estimates of line average density and the Faraday angle within experimental error. This agreement also supports the claim that the toroidal magnetic field is having no deleterious effect on the measurements via either misalignment or the Cotton-Mouton effect.

At $t = 4$ s, the core electron temperature increases significantly up to 2 keV, higher than 1.5 keV before 3 s, as shown in figure 4 (a). The importance of adding POINT constraints to EFIT reconstruction is clearly seen in Fig. 6 (a), at $t=4$ s. Without internal constraint provided by POINT, EFIT is unable to resolve the hollow current profile and reversed shear q-profile. When the reversed shear condition develops in EAST, the electron density and temperature profile peak suggesting the possible presence of an internal transport barrier (ITB)-like structure, as shown in figure 6 (b). From these data it becomes clear that initial 11 chord POINT provides a reasonably accurate determination of the current and q profiles for the EAST tokamak. POINT can also be used in conjunction with MSE measurements and other internal information in future to further constrain EFIT.

Figure 7 shows the Faraday fluctuations spectrograph and density fluctuation spectrograph of the POINT at $Z = 25.5$ cm. It clearly indicates fast time response of POINT has allowed observation of both density and Faraday fluctuations associated with MHD and fast ion driven instabilities as well as POINT provides a very useful tool for EAST tokamak confinement and transport research.

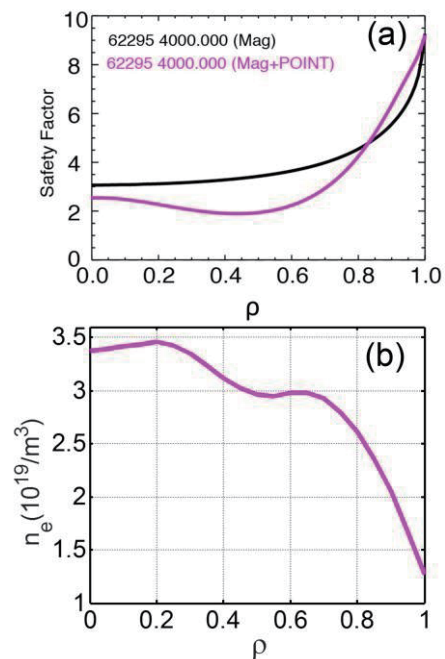


FIG. 6 Reverse shear q profile with ITB-like structure. (a) reverse shear q profile by EFIT constrained by POINT data, (b) electron density profile by POINT with ITB-like structure.

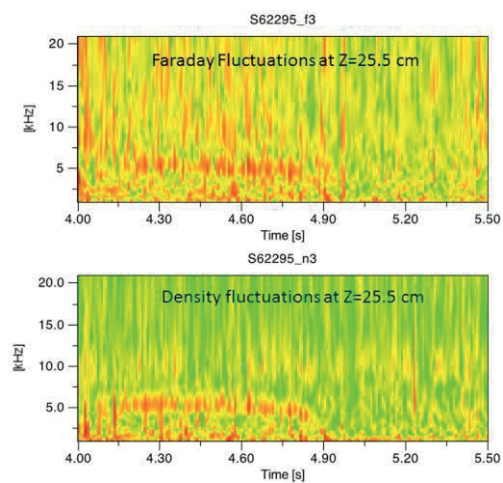


FIG. 7. (Top) Faraday fluctuations spectrograph and (Bottom) Density fluctuations spectrograph of the faraday angle and line-integrated density signal of POINT at $Z = 25.5$ cm.

4. Summary and Future Plan

An 11-chord, double-pass, radially-viewing, polarimeter-interferometer system has been developed and now routinely operated from 2015 to fully diagnose the core region of EAST plasmas. A Digital Phase Detector with 250 kHz bandwidth, which provides real-time Faraday rotation angle and density phase shift output for use in plasma control, have been developed for use on the POINT system. The electron line-integrated density resolution of POINT is better than $1 \times 10^{16} \text{ m}^{-2}$ ($< 1^\circ$), the Faraday rotation angle rms phase noise is $< 0.1^\circ$, and high temporal resolution, up to $\sim 1 \mu\text{sec}$, is achievable. Reliability of both the polarimetric and interferometric measurements are demonstrated during H mode discharges with four sources of auxiliary heating. Large density gradients present during H-mode operation not negatively impact POINT measurements and POINT works for all heating schemes tested on EAST to date. The current profile, density profile and safety factor (q) profile are reconstructed using the EFIT code. Comparison of EFIT output constrained by POINT data show good agreement with measurements serving to validate POINT data. POINT measurements can now be used to investigate plasma confinement and transport issue related to reversed magnetic shear and ITB-like structures. Future plans include integration of POINT measurements into real-time EFIT (rtEFIT). Long term goals include using POINT data, in conjunction with other diagnostic systems, for feedback control in order to maintain stable operation of long-pulse and high-performance tokamak plasmas while avoiding deleterious MHD events such as disruptions and ELMs in the future.

ACKNOWLEDGMENTS

This work is supported by the National Magnetic Confinement Fusion Program of China with contract No.2012GB101002, No.2014GB106002 and the National Nature Science Foundation of China with contract No.11375237. This work is also partly supported by the US D.O.E. contract DESC0010469. This work was partially supported by the JSPS-NRF-NSFC A3 Foresight Program in the field of Plasma Physics (NSFC No 11261140328).

¹ H. Soltwisch, *Rev. Sci. Instrum.* **57**, 1939 (1986).

² Zeng, L., D.L. Brower and Y. Jiang, *PPCF* **39**, 591-608 (1997).

³ G. Braithwaite et al., *Rev. Sci. Instrum.* **60**, 2825 (1989).

⁴ W.X. Ding et al., *Rev. Sci. Instrum.* **81**, 10D508 (2010); D.L. Brower, W.X. Ding, S.D. Terry, et al., *Rev. Sci. Instrum.* **74**, 1534 (2003).

⁵ W. F. Bergerson, et al., *Rev. Sci. Instrum.* **83**, 10E316 (2012).

⁶ H.Q. Liu *et al.*, et al., *Rev. Sci. Instrum.* **85**, 11D405 (2014).

⁷ H.Q. Liu *et al.*, *J. Instrum.* **11**, C01049 (2016).

⁸ J.H. Rommers et al., *Rev. Sci. Instrum.* **68**, 1217 (1997).

⁹ J. Chen et al., *Rev. Sci. Instrum.* **85**, 11D303 (2014).

2D VUV camera on KSTAR and RMP study using imaging diagnostics

S. Ohdachi^{1,2}, T. F. Ming³, Y. Suzuki^{1,2}, and S. Yamamoto⁴

¹National Institute for Fusion Science, Toki 509-5292, Gifu, Japan

²Graduate University for Advanced Studies, Toki 509-5292, Gifu, Japan

³ Institute of Plasma Physics, Chinese Academic Sciences, Hefei, China

⁴ Institute of Advanced Energy, Kyoto University, Gokasho, Uji 611-0011, Japan

Abstract

Imaging diagnostics is quite useful in studying the interaction of the RMP field and magnetically confined plasmas. Estimate of the deformation of the plasma using the tangentially viewing 2D VUV camera system is proposed. If there is gradient in the radiation profile at the rational surfaces, deformation of the flux surface can be detected. It is also possible to distinguish the kink-type response and tearing-type response.

1. Introduction – Why the effect of the RMP should be studied by the imaging diagnostics

Since the improved confinement mode is necessary for the fusion reactor, some kind of transport barrier in plasma is surely required. H-mode with edge transport barrier is therefore still the one of the most promising candidate for the scenario of the next generation Tokamak experiments. Edge localized modes (ELMs) observed in H-mode threaten this scenario because the energy released at a ELM collapse is so large that the divertor of the next generation devices is predicted to be damaged severely. Though several types of the mitigation method have been demonstrated, the application of the resonant magnetic field perturbation (RMP) has been considered as the most reliable method. However, though the effect of the application of the RMP is deniable, detailed physics mechanism of the mitigation has not been clarified yet. One of the reasons is that the interaction of the RMP to the plasma is very complicated and the equilibrium field with RMP was estimated so far. Without equilibrium, stabilities of the MHD instabilities which induce EMP crash cannot be discussed quantitatively. In this sense, to determine the equilibrium with RMP field is the one of the most important task for fusion reactor.

RMP is mainly shielded or amplified at the rational surface whose pitch of the magnetic field is resonant to the RMP. From an equilibrium estimated by HINT2 code with $n=3$ RMP, Br component of the $n=3$ field is decreased by the factor of three at $q = 3$ surface. This shielding is caused by the resonant current at the $q = 3$ surface. That means this current is the most visible effects of the RMP amplification. If we can detect this current, especially the radial profile of the shielding current, the largest part of the change in the equilibrium can be estimated.

Measurement by the magnetic probes is the first candidate to detect the current. However, the radial profile of the current cannot be estimated from the magnetic field measured outside the plasma; the tearing-like and kink-like response is not easy to be distinguished. However, if we measure the change of the shape of the plasma, we can distinguish the different response of the plasma. Fig. 1 shows an example, where the interchange mode are observed by the tangentially viewing SX camera system. If we compare

the observed mode structure (Fig. 1(E)) with the synthetic ones assuming tearing-like structure with magnetic island (Fig. 1(B)) and kink-like without island (Fig. 1(C)), the deformation of the plasma is found to be a kink-like without island [1]. Since the MHD mode is rotating, we can observe the structure with different phases. Though RMP is fixed to the laboratory frame, in the extreme case, this information can be obtained by two measurements at two locations shown by the Fig. 2. If we subtract the two images measured at two different toroidal angles, deformation of the plasma at the rational surface can be detected even though the difference is quite small. Tearing/kink response can be distinguished as well. The phase-shift pattern similar to the pattern shown in Fig. 1(B), indicate the tearing-like response together with the generation of the magnetic islands. When two cameras cannot be installed, the phase of the RMP can be shifted in a discharge and calculate the difference. The difference of the image at different phase has the same information with the two camera system if the plasma parameters are not largely changed.

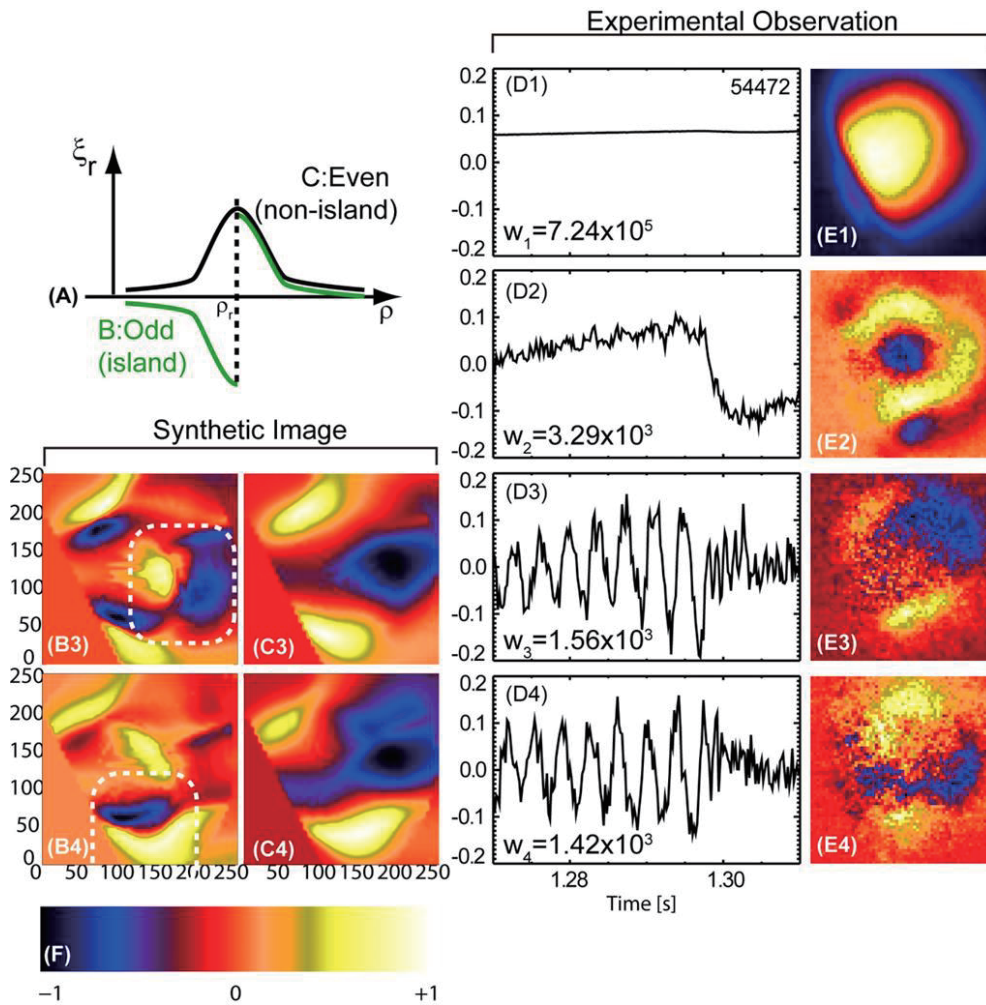


Fig. 1: Spatial structure of the interchange mode measured by the tangentially viewing soft X-ray camera is shown in Fig. (D) and (E). Spatial structure is obtained by the singular value decomposition method. Synthetic image assuming the displacement of the plasma at the mode rational surface (A) are shown in Fig. (B) and (C). Here, two components appear since this mode is a rotating mode.

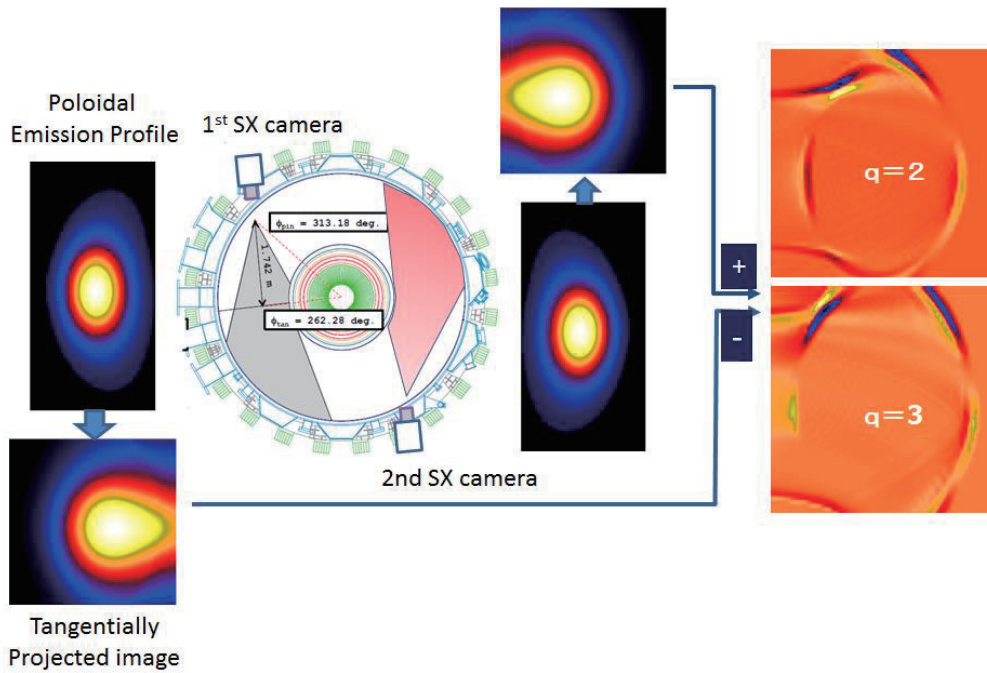


Fig. 2: Conceptual diagram of the diagnostics to detect the deformation with RMP from two point's measurement.

2. VUV camera system and viewing field in KSTAR

VUV camera is a kind of telescope having an inverse Schwarzschild type optical configuration, consisting of two mirrors. The mirrors, whose curvature lengths are 213.3mm and 79.53mm, respectively, are made of layers of molybdenum and silicon. VUV light with a wavelength of 13.5 nm ($\Delta\lambda \sim 1$ nm) is reflected. The distance between the mirrors is 133.8mm. The diameters of the mirrors are 23.2mm (first convex mirror) 147mm (second concave mirror). Image magnification factor is 1/80 with this optics. In order to exclude the low-energy VUV light, a Zr film of 200nm thickness is inserted. The maximum framing rate about 6 kHz when it is operated in LHD device. Images are detected by a two-stage micro-channel plate (MCP) with a phosphor screen (PHOTONIS, APD 2 PS 18/6/5/560:1 EDR 4.5" FM P47 type). A Vision Research Phantom V4.2 type CMOS camera is used to record the 2D image on the phosphor screen. Normally, images are recorded with 256×256 pixels. Line emission of CVI ($n=4$ to 2) can be measured with this system. It is suitable to measure the edge plasma where the rational surfaces resonant to the RMP field exist. It has been developed in the LHD [2, 3] and will be shipped to KSTAR device in near future.

The viewing field of the camera, we are considering, is shown in Fig. 3. From the tangential port of the KSTAR, most of the plasma is covered by this camera. Unfortunately outboard side of the plasma is blocked by the port (now shown). This plasma is also covered by two other tangentially viewing systems, the GEM detector system and SX-CCD camera.

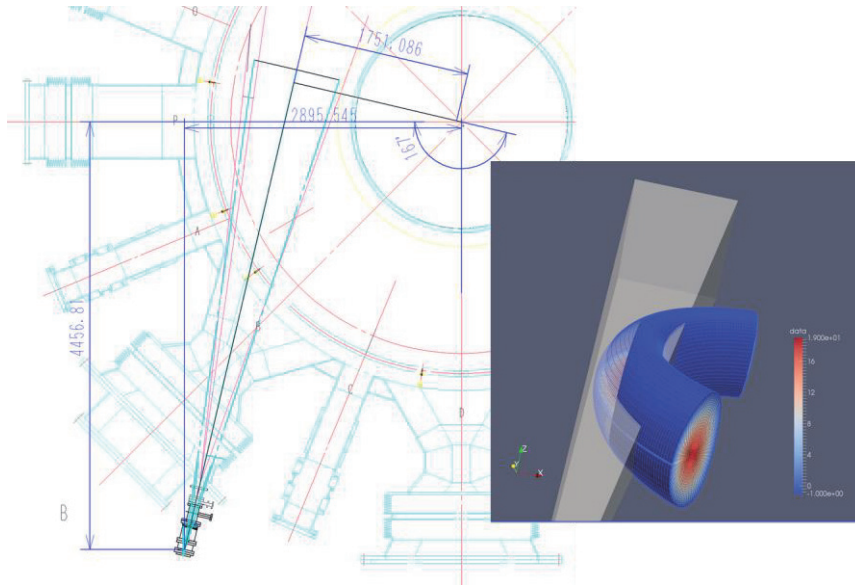


Fig. 3 Top view (left) and bird's view (right) of the viewing field of the VUV camera are shown.

3. Estimation of the image in KSTAR experiment

Image measured by the tangentially viewing VUV camera is estimated in this section. In order to calculate the image, the flux surfaces are approximated by the triangular mesh [1]. From this approximation, the calculation of the crossing point of the sight line with the flux surfaces becomes quite simple. The contribution to a pixel from the emission in a layer between the flux surfaces can be obtained. Thereby the relation of the radial emission profile and the 2D image is expressed by the matrix form. In order to interpret the images measured in the experiment, the synthetic image is obtained by integrating the VUV-light emission from the deformed magnetic surface with the radial plasma displacement. Moreover, the deformed structure is made assuming the radial displacement and difference of the image with different phase are shown in Fig. 4.

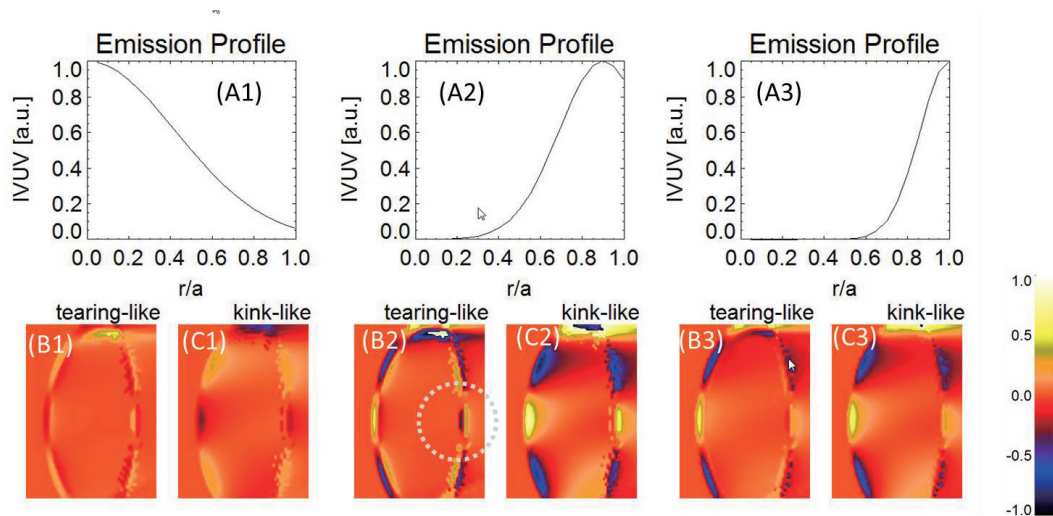


Fig. 4. Emission profile (A), difference of image with tearing-like resonance (B) and with kink-like resonance (C) is shown. Assumed profile is peaked one (1), hollow one (2) and another hollow (3), respectively

shown by (A).

Fig 4 shows the estimated image when $n=2$ fields with different field are applied. The image with 90deg difference with $n=2$ field ($m=6$, $n=2$) are shown. If the thickness of the perturbed area is large and there is gradient in the emission, deformation of the plasma will be detected as shown by these synthetic images. If the gradient is large enough, tearing-like and kink-like response are expected to be distinguished as shown in the dotted region of Fig. B(2).

In summary, it is shown that the penetration of the RMP can be studied by imaging diagnostics effectively. VUV camera system developed in LHD will be shipped to KSTAR this summer with frameworks of A3 and Japan-Korea diagnostics collaboration. If there is gradient in the radiation profile at the rational surface, deformation of the flux surface can be detected. It is also possible to distinguish the kink-type response and tearing-type response.

Acknowledgements

The authors are grateful to the kind collaboration of the KSTAR group, Dr. S. G. Lee and Dr. J. H. Kim, and KAIST Group, Mr. T. Jeon and Prof. W. Choe. This work was supported by NIFS budget code ULPP021, 028 and is also partially supported by the Ministry of Education, Science, Sports and Culture Grant-in-Aid for Scientific Research 26249144, by the JSPS-NRF-NSFC A3 Foresight Program (NSFC: No.11261140328, NRF: No. 2012K2A2A6000443), and by NIFS/NINS under the project of Formation of International Scientific Base and Network.

References

- [1] S. Ohdachi, T.F. Ming, K. Watanabe, and K. Toi, IEEE Transactions on Plasma Science **10**, 2732 (2014).
- [2] M. Takeuchi and S. Ohdachi, Plasma and Fusion Research **5**, S1037 (2010).
- [3] T.F. Ming, S. Ohdachi, S. Sakakibara, and Y. Suzuki, Review of Scientific Instruments **83**, 10E513 (2012).

Nuclear radiation shielding and monitoring on the EAST device

Guoqiang Zhong, Kai Li

Institute of Plasma Physics, Chinese Academy of Science, Anhui , Hefei 230031

The nuclear radiation have come an important issue after the NBI heating system successful operation on EAST device. Massive DD neutrons produce from beam-thermal reaction are need effective measurement and shielding to safeguard for human and environment. Thirteen sites of dose monitoring arrangement on the sensitive district to online acquisition the neutron and gamma dose rate, and provide light and sound alarm during the dose rate exceed configured threshold. The EAST device shielding by 1.5 meters of concrete wall and the vacuum chamber wall interbed injection water to prevent the fusion neutron leaking into the environment. The monitoring data show that the neutron and gamma ray dose rates are around the natural background level.

I . Introduction

Fusion energy is the best way to solve the energy crisis in the future. However, strong nuclear radiation such as neutron and gamma ray, which always accompanied with the fusion reaction. The ionizing radiation might cause huge damage to the human and the environment. Take active defense measure for radiation is very importance on fusion experiment research. The EAST is the first independent design and construction whole superconducting tokamak of china, it provide a good flat-form to explore the physical and engineering problems of fusion energy. The device locates in Hefei's western suburbs, in a peninsula of Dongpu reservoir, distance the downtown about 15 km. That project parameters is displayed on table 1, and the auxiliary heating systems occupy the ports are shown on Figure 1.

Table 1. Project parameters of EAST device

Toroidal magnetic (B_t)	3.5T	
Plasma current (I_p)	$\geq 1\text{MA}$	
Large radius (R)	1.7m	
Small radius (a)	0.4m	
Aspect ratio (R/a)	4.25	
Cross sectional shape	D	
Pulse length	1000 s	
Heating and driving mode	NBI	8 MW
	ICRH	3 MW
	ECRH	0.5MW
	LHCD	3.5MW

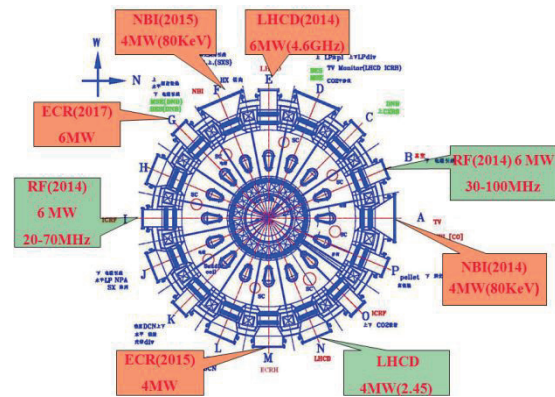


Figure 1. Heating system arrangement on EAST

At present, EAST fusion device mainly carries on deuterium plasma experiment, the main nuclear reaction process are as follows:



DD fusion neutrons (2.45MeV) emission occupy dominate, and a less of DT neutron (14.1MeV) from deuterium reaction with produce tritium. During high power of auxiliary heating injection, the neutron yield approach to $1.0 \times 10^{15} \text{n/s}$. Besides, secondary nuclear radiation such as gamma rays and X rays

generated by bremsstrahlung and plasma breakdown.

II. Radiation shielding

The neutron and gamma rays will cause huge damage to human and environment. For the protection of personal safety and environment, radiation released into the environment should be as low as possible, and below the safety limits prescribed by the government. Radiation shielding measures is introduced, shown in figure 2. First, the double vacuum chamber wall, with 5 cm boron water, which can reduce the neutron influence of magnet and peripheral devices. Second, the pipeline of experimental hall was designed with labyrinth, to avoid direct leakage of radiation from the experimental hall. Last, the experiment hall, made by steel reinforced concrete, the size of the experiment hall is 33m×28m×23m, the thickness of the concrete is up to 1.5m, the experimental hall is the most important and effective way to prevent the nuclear radiation from escaping into the environment, which may cause huge damage to the human and the environment.

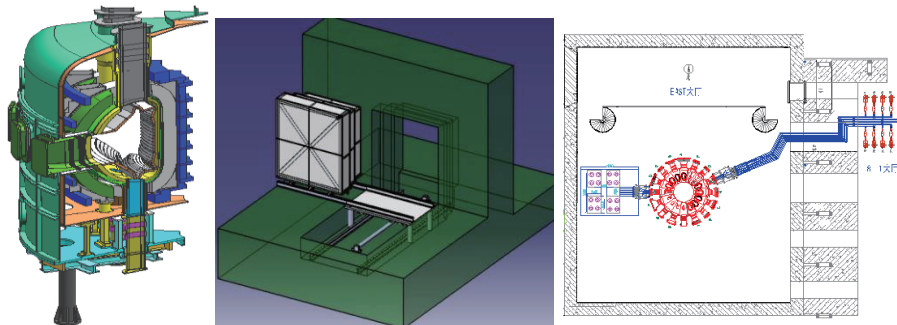


Figure 2. The radiation shielding measures on EAST device

III. Radiation monitoring and environmental evaluation

In order to obtain the radiation level around the EAST device, and evaluate the effect of EAST radiation shielding system. Thirteen fixed monitoring sites and one moving site were selected around the EAST, each site contains a neutron detector and a gamma ray detector (see Fig. 3).

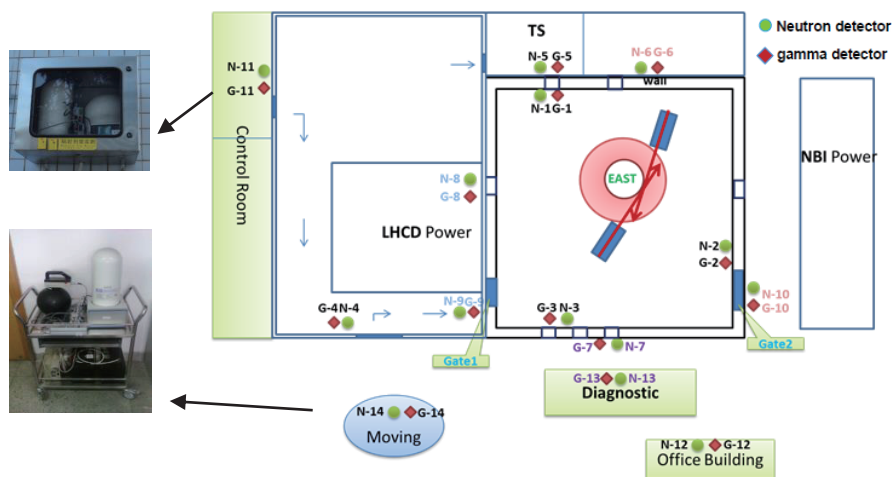


Figure 3. Distribution of the EAST radiation monitoring site

Moreover, a wide range of nuclear radiation investigation is executive, that items and position are shown in figure 4. Those survey include sound, electromagnetic and ionizing radiation. The ionizing radiation contain air absorbed dose rate, surface contamination, neutron cumulative dose and dose rate

monitoring. Soil and aerosol samples have been collection. This work is collaboration with the environmental protection department of Anhui province.

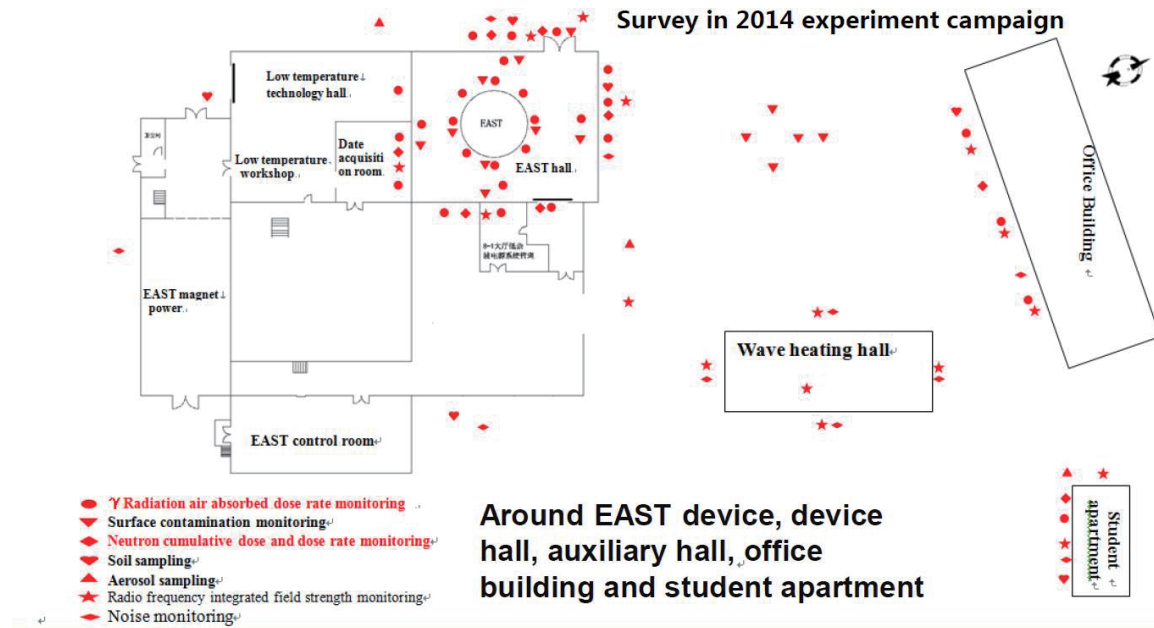


Figure 4. Radiation survey in 2014 experiment campaign

In order to intuitive evaluate the environment influence of the EAST experiment, the average radiation dose rate and the accumulated dose was given, as is shown in table 1, it respectively gives the comparison of radiation dose rate between pr-experiment and during the experiment. During the experiment the accumulated dose of G7、G10 is lower than pr-experiment, mainly affected by the different radiation background in different time. The neutron accumulated dose of N7、N10 during the experiment was both higher than before, but the difference is small. Overall, during the experiment, the dose rate is basically at the background level, the EAST shielding system provides good shielding for the neutron and gamma ray, EAST experiments will not cause additional radiation doses to the surrounding environment.

Table 1. Comparison of dose rate and accumulated dose before and during the experiment

Detector	Average dose rate before experiment/uGy·h ⁻¹	Average dose rate during experiment/ uGy·h ⁻¹	Accumulated dose before experiment /uGy	Accumulated dose during experiment/ uGy	Deviation of accumulated dose
G7	0.1489	0.1479	25.26	24.8473	-1.63%
N7	0.002305	0.002331	0.3910	0.3916	0.15%
G10	0.1120	0.1116	19.06	18.9930	-0.35%
N10	0.002218	0.002361	0.3763	0.3964	5.34%

IV. Summary

A large number of radiation dose rate data during the operation and the wide range of radiation survey data shows that the radiation shielding measures is effective, the radiation dose level of the surrounding environment is normal.

Acknowledgements

This work was partly supported by the JSPS-NRF-NSFC A3 Foresight Program in the field of Plasma Physics (NSFC: No.11261140328, NRF: No.2012K2A2A6000443).

Observation of ballooning mode in LHD and its theoretical analysis

Y. Suzuki^{1,2}, **S. Ohdachi**^{1,2}, **Y. Takemura**^{1,2}, **S. Sakakibara**^{1,2}, **K. Y. Watanabe**¹,
T. Nicolas^{1,3}, **K. Ichiguchi**^{1,2}, **Y. Todo**^{1,2}, **W. A. Cooper**³
and LHD experiment group

¹National Institute for Fusion Science, Toki 509-5292, Gifu, Japan

²SOKENDAI, Graduate University for Advanced Studies, Toki 509-5292, Gifu, Japan

³École Polytechnique Fédérale de Lausanne, Lausanne CH-1015, Switzerland

Abstract

Applying 3D nonlinear MHD simulation codes, a collapse event observed in the Large Helical Device (LHD) experiment is studied. In the experiment, the collapse of the plasma density in the plasma core was observed in a configuration, where the magnetic axis is shifted to the outward. At the collapse event, the density profile was sharply dropped but the temperature profile was flattened. This suggests a kind of the MHD instability drives the pump-out of the plasma density. The 3D MHD equilibrium is calculated by the 3D MHD equilibrium code then nonlinear MHD are simulated. In simulations, the ballooning-type MHD instability was found. Since the comparison of observed and calculated results is comparable, the calculated results is similar to one of the experiment.

1. Introduction

Nonlinear dynamics in Heliotron plasmas using a 3D nonlinear MHD simulation code in heliotron plasmas is studied. In the Large Helical Device (LHD) experiment, many MHD instabilities are observed. Especially, if the peaked pressure profile was sustained by the pellet injection, a collapse event, so-called the core density collapse (CDC), was happen. In nonlinear MHD simulations, it is expected the CDC is driven by the resistive ballooning mode [1]. Recently, a new imaging diagnostics of the two-dimensional soft-X ray arrays is installed in the LHD. Using the new diagnostics, perturbations localized at the outward of the torus. That is a characteristic of the ballooning mode. So, it seems the ballooning mode is observed in the LHD experiments. However, to interpret the experimental observation, we need to know what kind mode patterns should be observed.

In this study, we study 3D MHD equilibria with reconstructed pressure profile using a 3D MHD equilibrium code, which does not assume nested flux surfaces [2]. And then, we will study nonlinear MHD simulations based on the 3D MHD equilibrium with the magnetic island [3]. In this study, we note nonlinear saturation to compare with the experimental observation.

2. Nonlinear MHD modeling

Nonlinear MHD simulation is carried out by using the MIPS code (MHD Infrastructure for Plasma Simulation) which solves the following full MHD equations in the cylindrical coordinates (R, ϕ, Z) ,

$$\begin{aligned}
\partial_t \rho + \nabla \cdot (\rho \mathbf{v} + \rho \mathbf{v}_i^*) &= S_\rho + \nabla \cdot (D \nabla \rho) \\
\rho (\partial_t \mathbf{v} + \mathbf{v} \cdot \nabla \mathbf{v} + \mathbf{v}_i^* \cdot \nabla \mathbf{v}_i^*) &= \mathbf{J} \times \mathbf{B} - \nabla p + \nu \nabla^2 \mathbf{v} \\
\partial_t p + \mathbf{v} \cdot \nabla p + \Gamma p \nabla \cdot \mathbf{v} &= S_p + \nabla \cdot (\chi_\perp \nabla p) \\
\partial_t \mathbf{B} &= -\nabla \times \mathbf{E} \\
\mathbf{E} + \mathbf{v} \times \mathbf{B} &= \eta \mathbf{J} \\
\mathbf{v} = \mathbf{v}_E + \mathbf{v}_{\parallel, i}, \mathbf{v}_i &= \mathbf{v} + \mathbf{v}_i^*, \mathbf{v}_i^* = d_i \frac{\mathbf{B} \times \nabla p_i}{\rho B^2}, d_i = K / \sqrt{n_0}
\end{aligned}$$

where, ρ is the mass density, \mathbf{v} is the plasma velocity, p is the pressure, \mathbf{B} is the magnetic field, η is the resistivity, ν is the viscosity, χ is the thermal diffusion coefficient, and Γ is the adiabatic constant.

The original MIPS code uses the fourth-order finite difference scheme. The fourth-order Runge-Kutta method is used for the time integration. As the beta value increases, the equilibrium pressure gradient becomes steep in the outer torus due to the large Shafranov shift. For the high beta LHD plasmas, the pressure driven modes becomes unstable in the periphery region so that the perturbed plasma flow grows near the plasma boundary. This leads to the numerical oscillation when the convection terms are treated by the fourth-order finite difference scheme. Thus, in this study, the Kawamura-Kuwabara scheme (3rd order upwind scheme) is used for the convection terms in order to avoid numerical oscillation near the plasma boundary. In the nonlinear simulations, the number of grid points are (512,256,512). The MHD equilibrium is constructed by HINT2 without assuming existence of the nested flux surfaces.

3. Comparisons of nonlinear simulations and experimental observations

Figure 1 shows a reconstructed 3D MHD equilibrium for an experiment the CDC was happened. Flux surfaces, iota profile, and a profile of the Mercier criterion are shown. Since the pressure profile is peaked, the magnetic axis is shifted to the outward. Usually, the LHD configuration is the magnetic hill configuration in the plasma core. However, because of the large Shafranov shift, the Mercier criterion is positive in the plasma core. That means the large Shafranov shift makes the magnetic well in the plasma core and the ideal interchange mode should be stable. In this study, global ideal MHD stability is studied by an ideal MHD stability code TERPSICORE [4, 5, 6]. However, no any ideal modes are found. Therefore, the CDC event observed in the experiment might be the resistive mode.

Figure 2 shows the time evolution of the kinetic energy and the perturbed pressure in the MIPS simulation. The kinetic energy evolves linearly and then nonlinearly saturated. The perturbed pressure in the linear phase is studied. Clear mode structures are appeared and the amplitude of the perturbed pressure becomes strong in the outboard side. That is a characteristic of the ballooning mode

Figure 3 shows the line integrated density fluctuation measured by the CO2 laser interferometer and lines integrated pressure perturbation calculated from the MIPS simulation. For a comparison, sight lines of the CO2 laser interferometer and flux surfaces are shown. In the experimental observation, strong fluctuations are observed in only the outboard side. This is consistent to the ballooning mode. In addition, two peaks are observed by the CO2 laser interferometer. Since the mode structure of the ballooning mode in the LHD is

very sophisticated, the peak of the line integrated signal might not be only one. On the other hand, the MIPS simulation could reproduce two peaks of the line integrated perturbed plasma pressure. This means the physical picture, which is the CDC is driven by the resistive ballooning mode, is one good hypothesis. However, if the experimental observation and simulated result are compared carefully, some differences, which are the radial location and so on. To study more systematically, the scan of dissipations in the MIPS simulation is necessary. That will be discussed in a different paper.

4. Summary

In this study, the CDC event observed in the LHD experiment is simulated by the resistive nonlinear simulation code, MIPS. From the experimental observation, the CDC is driven by the ballooning mode because the large fluctuation is observed in only the outboard side. In the global ideal MHD simulation, no significant modes are observed. Therefore, the CDC might be driven by the resistive mode. The MIPS simulation with finite dissipation is performed and the resistive ballooning mode is nonlinearly saturated. In the linear phase, a simulated result is compared with the experimental observation. Both results are qualitatively agreed but differences are also found. Effects of finite dissipations should be studied more carefully.

Acknowledgements

This work was partly supported by the JSPS-NRF-NSFC A3 Foresight Program in the field of Plasma Physics (NSFC: No.11261140328, NRF: No.2012K2A2A6000443).

References

- [1] N. Mizuguchi, et al., Nucl. Fusion **49** (2009) 095023
- [2] Y. Suzuki, et al., Nucl. Fusion. **46** (2006) L19
- [3] Y. Todo, et al., Plasma Fusion Res. **5** (2010) S2062
- [4] D. V. Anderson, et al., International Journal of High Performance Computing Applications **4** (1990) 34.
- [5] D. V. Anderson, et al., Scientific Computing on Supercomputers II (1990)
- [6] G. Y. Fu, et al., Phys. Fluids B **4** (1992) 1401

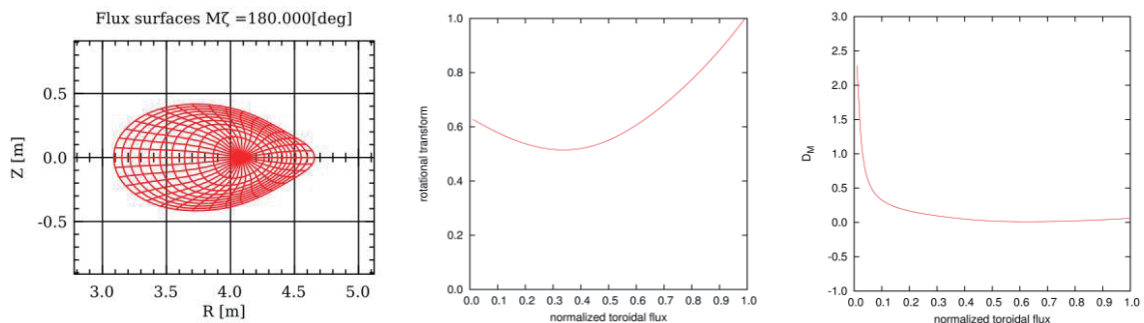


Fig. 1 a reconstructed 3D MHD equilibrium is shown for a shot of the CDC observed. Flux surfaces at the horizontally elongated cross section, the iota profile, and the profile of the Mercier criterion are shown.

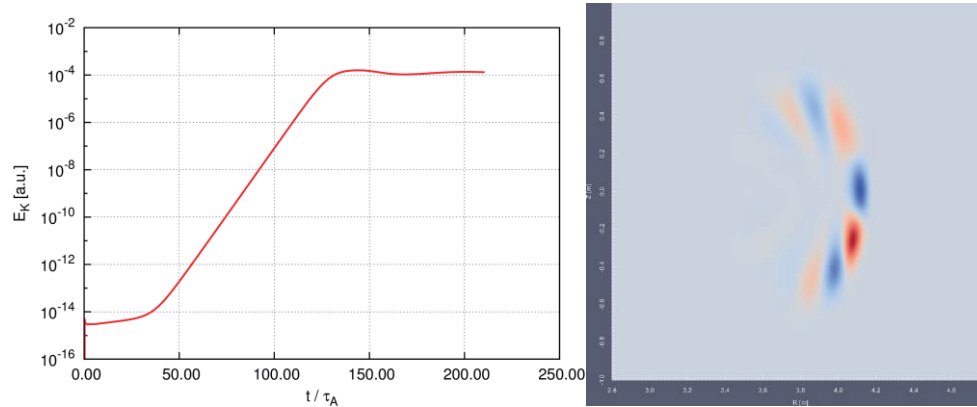


Fig. 2 The time evolution of the kinetic energy in the MIPS simulation and the mode structure of the perturbed pressure in the linear phase are shown.

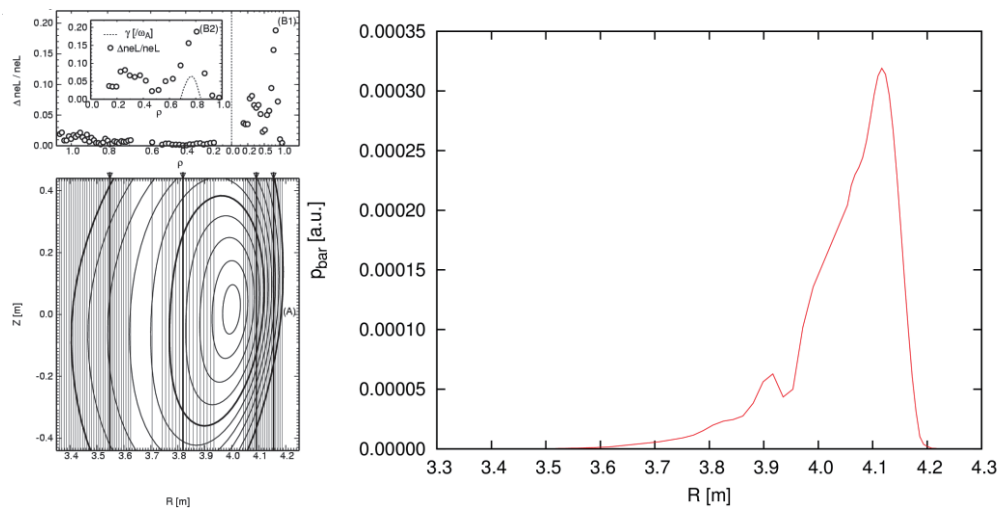


Fig. 3 A comparison of the measured density fluctuation by the CO₂ interferometer and line integrated perturbed pressure in the MIPS simulation is shown. For a comparison, flux surfaces and sight lines of the CO₂ interferometer are also shown. Both are qualitatively agreed.

Halo current study on the EAST tokamak

D. Chen^{1(a)}, B. Shen¹, J. Qian¹, R. S. Granetz² and B. Xiao^{1,3}

a) E-mail: cdaolong@ipp.ac.cn

1 Institute of Plasma Physics, Chinese Academy of Sciences, Hefei, China

2 MIT Plasma Science and Fusion Center, Cambridge, MA 02139, USA

3 School of Nuclear Science and Technology, University of Science and Technology of China, Hefei
230031, China

Abstract

Disruptions is unavoidable events for tokamak. In current quench period, a halo current is generated on the surface of plasma, which produce the magnetic field distribution required to maintain plasma force balance. When the safety factor of the plasma drops nearly to 2, the current can grow as large as tenths of the plasma current, this will be a severe threat for machine components because of $J \times B$ force.

For better understand halo current on EAST tokamak, we have developed a series of current diagnostics. All the sensors are Rogowski coils that surround conducting structures, and all the signals are analog integrated. Measurements from disruptions show that the halo current diagnostics are working well. The disruption experiments show that when plasma volume drift upward a significant amount of halo current flows in the top of the machine, while little is seen at the bottom. With the measurement of sensors installed on tungsten divertor, it is shown that the current flow into outer plate through cassette finally back from inward plate. The interesting thing is that litter current is observed in center column, this implies that almost all the halo current just ow through the divertor component not through center column. From the several sets of sensors, it is estimated the total halo current is up to 40% plasma current, with toroidal peaking factor less than 2.

Primary halo current mitigation is observed using helium gas injection with valve response time within 0.15 ms. It is demonstrated that nearly 1/3 halo currents were mitigated compared with non-mitigation. Noble gas jet injection can effectively shorten the vertical displacement, resulting in plasma volume non-contact completely with the wall, this can be clearly seen from reconstruction using filament code.

1. Introduction

Disruptions cause a sudden loss of plasma energy confinement, resulting in a rapid drop in temperature and increase in plasma resistivity. This causes the plasma current to decay quickly. The inductive voltage induced by this current quench can generate halo currents in the scrape-off layer just outside the plasma boundary. During the current quench, vertical position control of the plasma is usually lost, and the plasma often moves vertically, eventually becoming limited on the divertor. The halo currents in the scrape-off layer can then flow through the first wall (vessel and/or tiles), which generates

electromagnetic loads on the vessel, and is therefore a concern for tokamaks, particularly ITER [1][2]. This motivates us to study the evolution and scaling of halo currents on experimental advanced superconducting tokamak (EAST).

The halo current has been studied in a large number of tokamak devices, In EAST, many discharges were disrupted after failure of the feedback control of the vertical instability. For measuring the halo current, four sets of halo sensors were installed in the last EAST experiment, and these halo sensors were located at different toroidal positions. Experimentation showed that the halo current in EAST first lands on the outer baffle plate, goes through the dome and finally goes back to the plasma. Besides, EAST disruption database has been established, which is useful for quickly selecting disruptive shots and their relevant parameters. With the database it is clearly shown that most current quench time is in a range of 4 ms to 6 ms. Disruption rate is increasing with the increase of plasma current. With the halo current diagnostics, it is demonstrated that maximum halo current is 0.4 of plasma current and $TPF \times I_h / I_{p0}$ less than 0.65

Primary halo current mitigation is observed using helium gas injection with valve response time within 0.15 ms. It is demonstrated that nearly 1/3 halo currents were mitigated compared with non-mitigation.

The rest of this paper is organized as follows. In Section 2, the experimental set up and diagnostics, and the calibration of experimental data are described. In Section 3, experimental results including reversed current spike, halo current flow, and toroidal peaking factor are discussed. In Section 4, a test of the mitigation system is introduced. Finally, some conclusions are drawn from the present study in Section 5.

2. Design and installation of system

2.1. Location of diagnostics

At the end of 2013, the EAST upper divertor was upgraded with a new tungsten divertor consisting of 80 cassettes in the toroidal direction. The tungsten monoblock plates in each cassette are mechanically supported with pin-clevis attachments at a number of points. For determining where the halo currents actually flow in the tungsten divertor, we have installed 10 small-cross-section Rogowski coils in each of 4 cassettes at 90° intervals around the torus, as seen in Figure 1 [3].

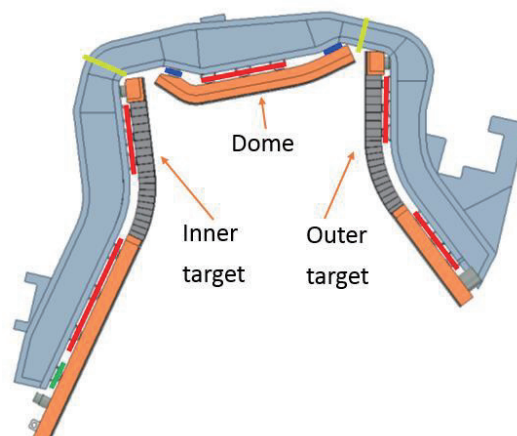


Fig. 1. Layout of halo current diagnostics in new upgraded upper divertor

The lower divertor, which still has carbon fiber composite tiles, consists of 16 modules in the toroidal direction. Each module has an inner vertical target plate, an outer vertical target plate, and a central dome (seen in Figure 2(left)). The target plates and dome are connected to the vacuum vessel by stainless steel supports. Halo current coils surround these supports. A pair of coils are on the inner plate supports at each of 4 toroidal locations, another pair are on the outer plate supports at each of the 4 toroidal locations, and 4 coils are on the support legs of the dome at each of the 4 toroidal locations. The arrangement of these coils allows for measurements of both halo currents and toroidal eddy currents flowing through the lower divertor structure. Reconstruction of plasma boundary using filament code shows that for downward-going disruptions, the plasma often touches just the dome, as shown in Fig. 2 (right). Therefore, it is possible that much of the halo current could flow into one side of the dome, through its copper tile support plates, and out of the other side of the dome, but not pass through the instrumented support legs of the dome

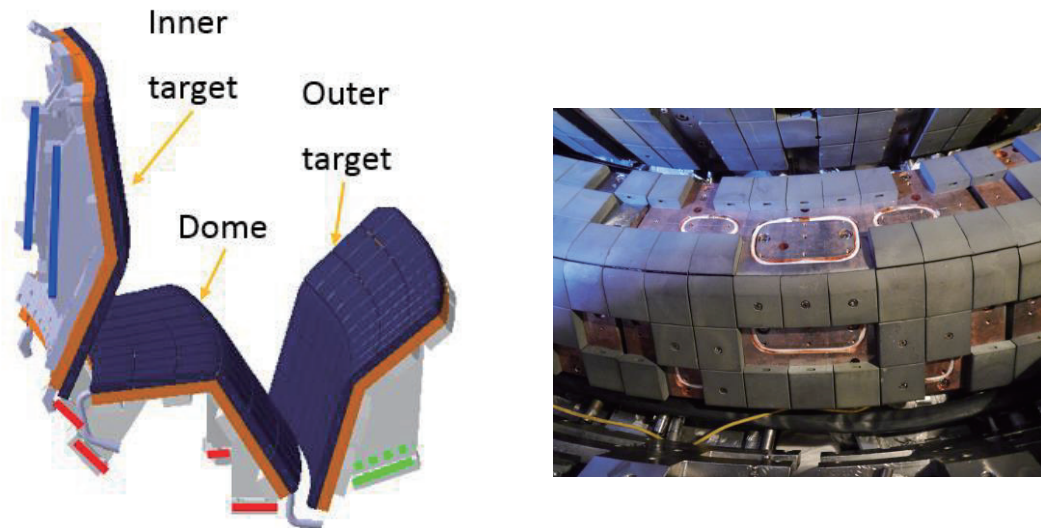


Fig. 2. Layout of halo current diagnostics in EAST lower divertor (left). The picture of halo current coils embedded in the groove of copper plate. For dome, 3 coils are on one side and another 3 are on other side (right).

2.2. Calibration of Rogowski coil

The Rogowski coils were calibrated by wrapping a selected subset of them around a current-carrying circuit consisting of 20 turns of wire. Current in the circuit was provided by a large power amplifier (60 VAC, 30 A p-p). A shunt resistor ($R = 10 \Omega$) was connected in series with the circuit, and the voltage drop, $\varepsilon_R(t)$, across it was measured to accurately determine the current, $I_{cal}(t) = I_{cal}^{max} \sin wt$. Nine different frequencies were used, ranging from 200 Hz to 1 kHz. The voltage output of each Rogowski coil is So, the mutual inductance of the Rogowski coil is

$$\varepsilon_{Rog}(t) = -L \frac{dI_{cal}(t)}{dt} \quad (1)$$

So, the mutual inductance of the Rogowski coil is

$$L = \frac{1}{w} \left| \frac{\varepsilon_{Rog}^{\max}}{I_{cal}^{\max}} \right| \quad \text{and} \quad w = 2\pi f \quad (2)$$

The coil mutual inductance depends on the coil winding density and cross-sectional area. The results of the calibrations are shown in Fig. 3(left). The mutual inductances of the large- and small-cross-section coils are $3.677 \times 10^{-7} H$ ($\sigma = 0.13\%$) and $2.323 \times 10^{-8} H$ ($\sigma = 0.31\%$), respectively.

The calibration of one of the Rogowski coil sensors was checked by comparing its measurement with a Hall sensor. Both sensors were wrapped around the same current-carrying cable, and the signals were simultaneously recorded and shown in Fig.3(right). The maximum current measured by both sensors differs by less than 1%.

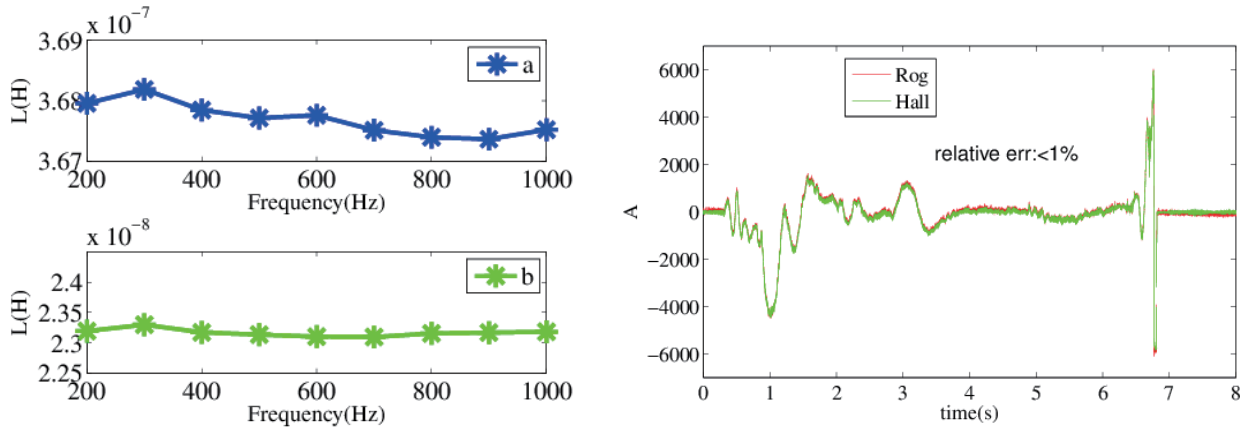


Fig. 3. Calibration of coils' inductances at several frequencies (f: 200 Hz - 1 kHz)(left).

Comparison of measured current using Hall sensor and Rogowski coil (right).

3. Disruption database

For better analysis disruption physics and extend present tokamak information to ITER device, a disruption database is urgent. The limited conditions for the disruption case should be adjusted by the criteria that are shown in Table 1. In this table it should be noted that (i) $\tau_{\text{discharge}}$ is the duration time of the discharge, the length of pulse must be more than 600 ms; (ii) τ_{CQ} is the CQ time, which means that the CQ time should be less than 50ms, typically this value is in 10 ms; (iii) $I_{p,\text{final}}$ is the minimum plasma current within 15ms after the discharge has disrupted, this criterion is for rejecting a minor disruption, such as some small crashes in the discharge; (iv) I_{p0} is the plasma current before CQ; (v) $I_{p,\text{max}}$ is the maximum plasma current; (vi) this criterion is for rejecting shots that disrupt late in current ramp down. Therefore, under these limited conditions, the disruption data are successfully obtained [4].

With the disruption database, it is clearly seen that in 2014 EAST campaign how many discharge move upward or downward, and it is easily to be searched the exactly discharge we want. Besides, from

which it is easily seen that 26.8% of discharges are disrupted. The interesting thing is that the disruptive rate in group I ($200 \text{ kA} < I_{p0} < 400 \text{ kA}$) is much higher than that in group II: this is because group I occurs in the beginning of the campaign: at that time the first wall was not clean enough for discharge, so many impurities were injected into the plasma volume, and after many clean shots, the discharge became normal. In group II it is easily seen that the plasma disruptive rate grows with the increase of plasma current, all are shown in Fig.4

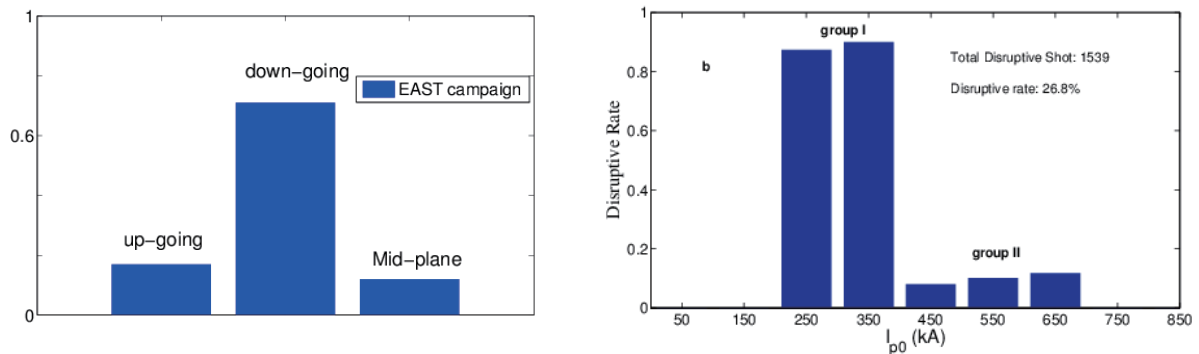


Fig. 4. The possibility of plasma volume movement (left) and disruptive rate with plasma current (right).

4. Analysis of halo current

4.1 Measurement of halo current

Elongated plasmas are vertically unstable, and when they disrupt, position control is lost, leading to vertical motion. In unmitigated disruptions, the plasma moves far enough to contact the divertor or $_rst$ wall at the top or bottom of the machine. The large loop voltage that is generated during the current quench can drive so-called halo current in the scrape-off layer (SOL) of the plasma. The halo current flows along the helical field lines in the SOL [6][7][8][9][10].

In plasma downward movement, the volume mostly touches the dome and this can be clearly seen from plasma reconstruction using filament. Also measurement from Rogowski coils, it is shown that the current flow into inward then back from outward of dome. The maximum total halo current estimated from toroidal sets is about 40% plasma current with TPF less than 2, as shown in Fig.5 [10].

In plasma upward going case, as the new up divertor is upgraded with monoblock and cassette structure, the plasma volume mostly contacted the inner and outer target. As shown in Fig... Besides, from the measurement only less currents through water cooling tube, this is mainly because the connect with the two part of tube is stainless bellow, and the resistivity is much large than copper. The maximum current measured in one cassette is 10 kA under plasma current in 500 kA with large current asymmetry, as shown in Fig.6.

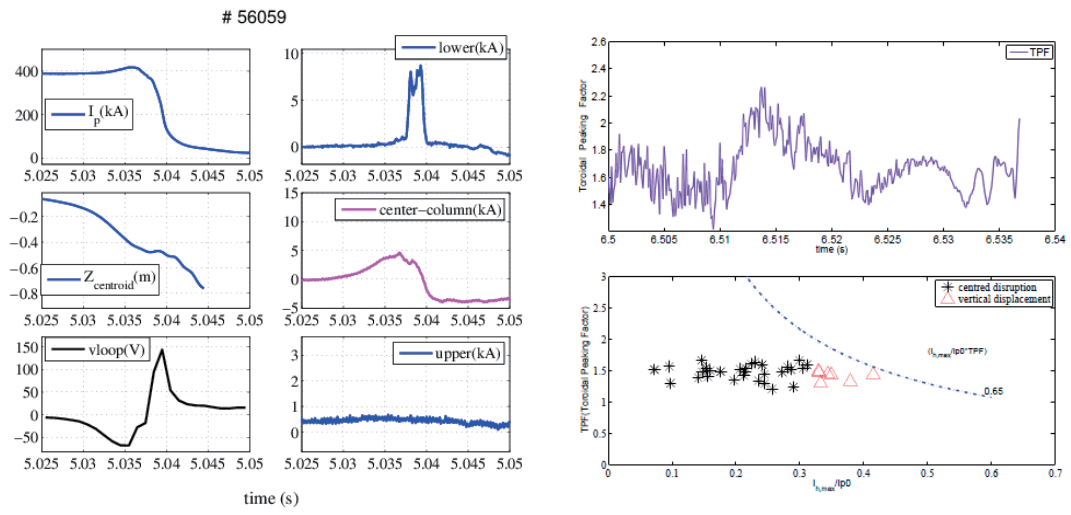


Fig. 5. Halo current flows in graphite divertor (left) and current asymmetry (right).

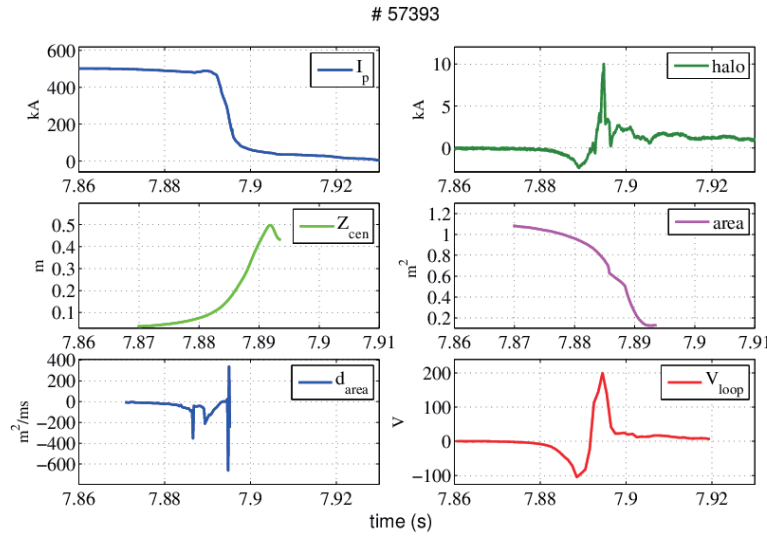


Fig. 6. Halo current flows in new upgraded divertor (left) and sketch of current flows (subplot).

4.2 Mitigation of halo current

In these initial experiments, it is found that the helium gas reaches the plasma edge less than 3 ms after the MGI valve is triggered [11], Figure 7 compares an unmitigated disruption with the He MGI disruption. Compared with He MGI on other tokamaks, the He MGI on EAST does not seem to radiate a large fraction of the thermal energy, perhaps because the amount of injected gas is an order of magnitude less.

Nevertheless, the He MGI on EAST effectively results in less vertical displacement, as seen in Fig 2b, which compares the vertical motion of an MGI mitigated disruption to an unmitigated disruption. This is

also seen in Fig. 2c, which shows the evolution of $B_r(\sim I_p/d)$ measured by a saddle sensor installed in the lower passive plate. ("d" is the distance between the plasma and the sensor.) The saddle signal implies that the mitigated disruption does not get as close to the wall as the unmitigation disruption.

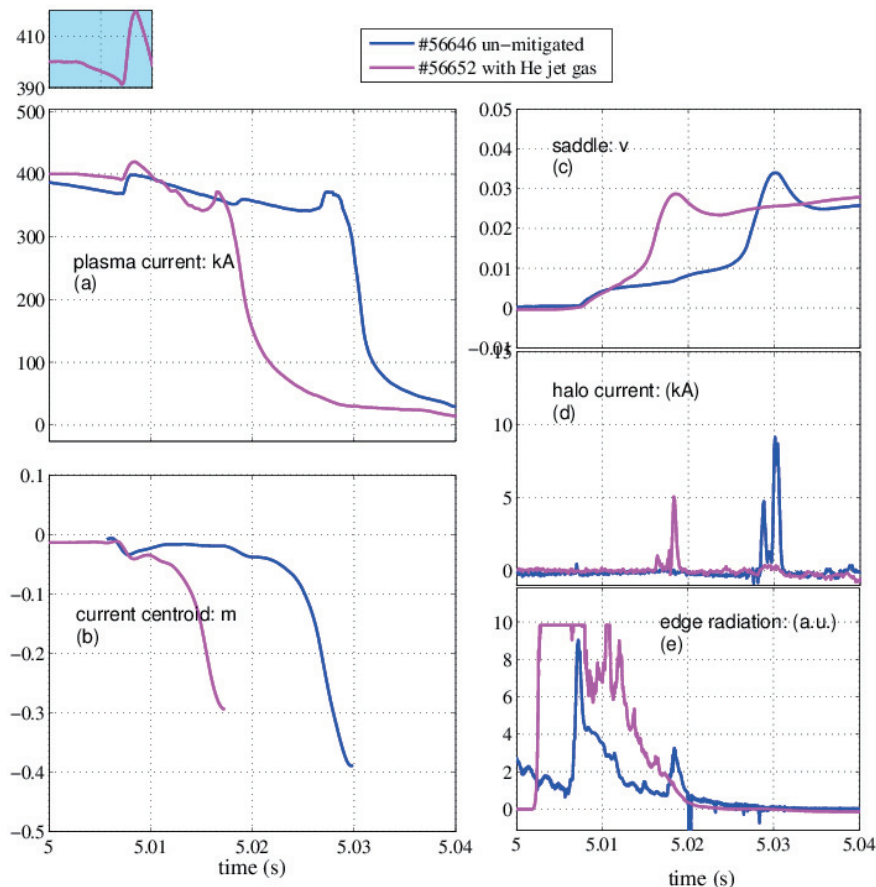


Fig. 7. Comparison of an mitigated halo current (line in pink) with the unmitigated (line in blue). (a) the plasma current; (b) vertical current centroid of the plasma; (c) saddle signal; (d) the evolution of halo current on the dome plate; (e) edge radiation power.

5. Summary Mitigation of halo current

The halo current have been measurement with the help of several sets of current sensors. With maximum halo current reached to 40% plasma current and TPF less than 2. However, the current measured in new upgraded divertor (monoblock+cassette) is with larger asymmetry, this is because of engineering installation, not driven from plasma asymmetry.

EAST disruption database has been successfully established, with 18 of these parameters are currently being populated, which is useful for quickly selecting disruptive shots and their relevant parameters (current quench characteristics, EFIT equilibrium characteristics, kinetic parameters, halo currents, vertical motion)

The fast MGI valve on EAST has been successfully tested. It has a response time of 150 microseconds, and is capable of _ring adjustable amounts of different noble gases. In the initial operation of the MGI system on EAST with helium gas, it is observed from _lament reconstructions, and from a saddle coil signal, that the plasma vertical displacement is reduced because the plasma is terminated much more quickly compared to an unmitigated midplane disruption. This reduces the contact time with the divertor, and the measured halo current in the divertor is reduced by about 50%. It is also seen that the edge radiated

power increases, and the edge temperature decreases.

Plans for the next campaign on EAST include operation at higher current and higher temperature (low q , low collisionality). This may require enhancements in the MGI system to protect the machine, including the use of higher Z noble gases such as argon, or Ar/He mixtures, and larger amounts of gas. In addition, we will also measure the radiated power during disruptions using AXUV detector arrays. Experiments to test these enhancements will to be done soon.

Acknowledgements

This work was partly supported by the the National Natural Science Foundation of China (Grant Nos. 11475002 and 11475224) and the National Magnetic Confinement Fusion Science Program of China (Grant Nos. 2014GB103000, 2013GB102000, and 2015GB102004)and JSPS-NRF-NSFC A3 Foresight Program in the field of Plasma Physics (NSFC: No.11261140328, NRF: No.2012K2A2A6000443)

References

- [1] ITER Physics Expert Group on Disruptions, Plasma Control and MHD and ITER Physics Basis Editors, Chapter 3 MHD stability, operational limits and disruptions. 1999 Nuclear Fusion 39(12) 2321 {2332
- [2] T. C. Hender and ITPA MHD, Disruption and Magnetic Control Topical Group.2007 Nuclear Fusion 47 S163
- [3] D. L. Chen, B. Shen, R. S. Granetz, Y. Sun, J. P. Qian, Y. Wang, and B. J. Xiao.2015 REVIEW OF SCIENTIFIC INSTRUMENTS 86, 103506
- [4] D. Chen, R. S. Granetz, B. Shen, F. Yang, J. Qian and B. Xiao.2015 Chinese Physics B 24 025205
- [5] E. M. Hollmann, P. B. Aleynikov et al.2015 Physics of Plasmas 22 021802
- [6] R.S. Granetz, E.M. Hollmann, D.G. Whyte et al.2007 Nuclear Fusion 47 1086C1091
- [7] O. Gruber, K. Lackner, G. Pautasso, U. Seidel, and B. Streibel.1993 Plasma Phys. Controlled Fusion 35 B191
- [8] R. Fitzpatrick. 2007 Phys. Plasmas 14 062505
- [9] A. H. Boozer.2013 Physics of Plasmas 20 082510
- [10] D. Chen,, B. Shen and et al.2014 Chinese Physics B 23 065205
- [11] H. D. Zhuang and X. D. Zhang.2015 Review of scienti_c instruments 86 053502

Experimental study of the evolution for Faraday Rotation Angle by LHCD on EAST

H.Lian¹, H.Q.Liu¹, Y.X.Jie¹, L.Zeng¹, B.J.Ding¹, M.H.Li¹, Y.C.Li¹, S.Y.Lin¹, Bo Lyu¹, S.B.Zhang¹, N.Shi¹, T.Lan¹, G.Li¹, Z.Y.Zou¹, W.M.Li¹, and the EAST team

¹ Institute of Plasma Physics, Chinese Academy of Science, Hefei, Anhui 230031, China

ABSTRACT: Lower Hybrid Wave Current Drive is one of the most effective ways to drive the plasma current on EAST. Based on the three-wave technique, the POLarimeter/INTerferometer (POINT) system on EAST can provide two signals with the contribution of plasma, in which the Faraday rotation angle is greatly relevant with the plasma current. The temporary job is focused on the evolution of the Faraday rotation angle, from which we can speculate the current deposition by LHCD, and the experiment result is consistent with the measurement of the Hard X-Ray(HXR) measurement system.

Key Words: Faraday rotation angle ; LHCD ; Current Deposition

1. Introduction

The plasma current driven is a key issue for a Tokamak fusion reactor, which is driven by the transformer traditionally. But the variable flux provided by the transformer is always limited, so many people put forward the idea of driving current through the non-inductive ways in 1970s. Then a large scale experiments about current driven by non-inductive ways has been carried out on a large tokamaks such as JET, JT-60U, DIII-D and so on, including NBI, ECCD, FWCD and LHCD. LHCD system is one of the most effective and steady ways to drive plasma current on EAST.

To achieve long-pulse H-mode steady discharges on EAST, the research of the current profile is essential as the reason of that LHW can drive the current effectively, which makes it very important to make the regime of current profile evolution by LHCD clear for EAST.

2. Experimental Setup

2.1. LHCD on EAST

Lower Hybrid Wave(LHW) can drive the plasma current through the regime of Landau Damping. EAST have installed two Lower Hybrid Wave(LHW) systems, the first one was applied in 2008, which frequency is 2.45GHz, and the frequency of the second system is 4.6GHz, which was applied in 2014. The two systems can drive the plasma current effectively, and also, H-mode plasma is obtained by either the 4.6GHz LHCD alone, or together with the 2.45GHz LHCD system (see Fig. 1), the NBI(neutral beam injection) system^[1].

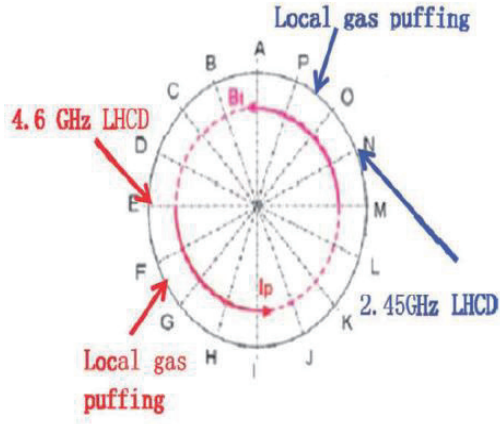


Fig 1. Top view of LHCD systems

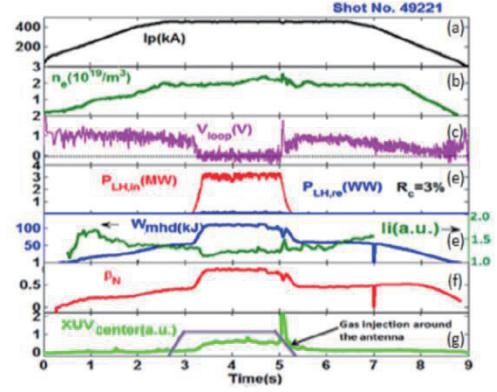


Fig 2. The discharge parameters for shot49221

As shown in the figure 2, when the LHW injects in, the loop voltage decreases quickly to zero approximately, and the internal inductance (\$I_i\$) decreases significantly, the plasma energy increases from 50kJ to 100kJ, which means the LHW couples to the plasma effectively^[1].

2.2. POINT on EAST

Based on the three-wave technique, which is demonstrated to work successfully on several tokamak reactors, such as JET^[2], MST^[3], TEXT^[4], the POINT system on EAST has a double-pass, horizontal, radially-viewing measurement configuration. In 2014, the POINT system was installed with 5 measurement chords originally, which was updated to 11 chords in 2015 experiment campaign, and the corresponding Z location is $Z = -42.5, -34, -25.5, -17, -8.5, 0, 8.5, 17, 25.5, 34, 42.5$ cm (fig3)^[5].

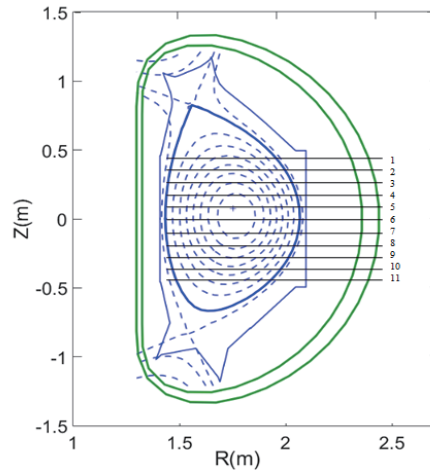


Fig 3. Location of the 11 POINT measurement channels

The plasma can contribute to phase shift and faraday rotation angle when the measure beam is reflected by retro-reflector, which is calculated with the formula:

$$\phi = 2.82 \times 10^{-15} \lambda \int n_e dl \quad (1)$$

$$\psi_F = 2.62 \times 10^{-13} \lambda^2 \int n_e B_{\parallel} dl \quad (2)$$

Where ϕ is phase shift, ψ_F is faraday rotation angle, λ is the wavelength of measure beam, which is equal to $432.5 \mu m$, n_e is electron density, B_{\parallel} is the magnetic component paralleled to the measurement direction, with which we can calculate the plasma current. Utilizing the measurement result of 11 channels, the profile of electron density and plasma current can be reconstructed.

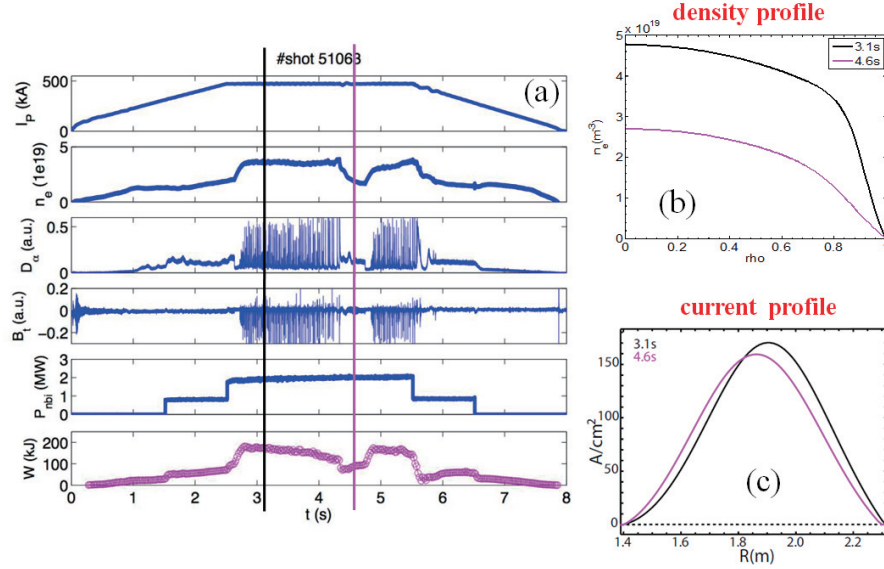


Fig 4. The parameters for shot 51063(a), and the reconstructed density profile(b) and current profile(c)

For shot #51063 (see Fig. 4), combined with the equilibrium fit(EFIT) code, the measurement result of POINT system provided the density and current profile successfully for the chosen time points of 3.1s and 4.6s^[6].

3. The evolution of faraday rotation with LHCD

Faraday Rotation angle is relevant with the plasma current, so we can obtain current information from which. LHCD can drive the plasma current effectively, the following part is on the study of the faraday rotation angle evolution only with LHCD.

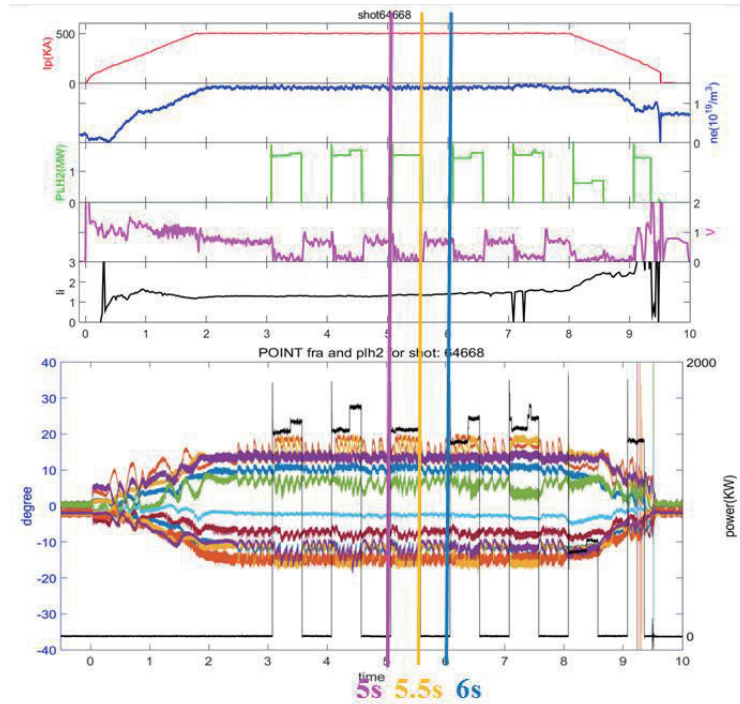


Fig 5. Parameters for shot 64668 and faraday rotation angle

On EAST, we have done the experiment about modulating the LHW injection with the frequency of 1Hz(fig5).The loop voltage decreases approximately to zero significantly when the LHW injects in, and the faraday rotation angle of some chords change obviously. The time points of 5s,5.5s and 6s are picked out for a deep research (see Fig. 6).

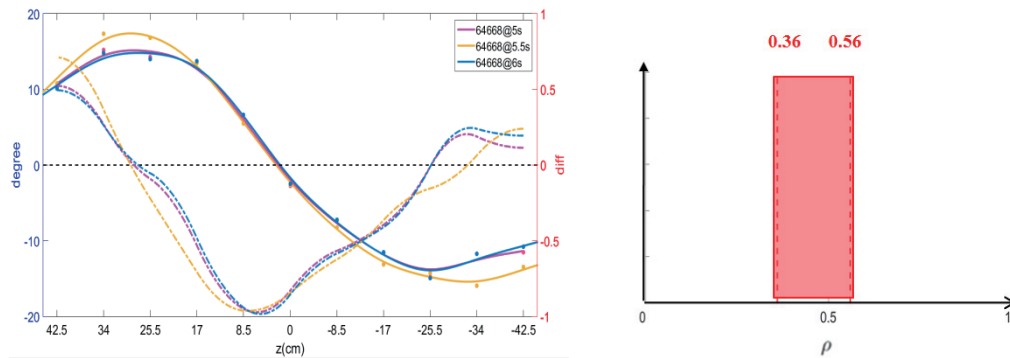


Fig 6. Smoothing data for the 11-chords faraday rotation angle (solid lines), and the corresponding derivatives(dash lines).

Fig 7. Corresponding ρ location

Comparing to the time points(5s,6s) without LHW, derivatives of the time point(5.5s) with LHW on decreases significantly. Obviously, it is the LHW that contributes to the difference, which means the deposition of the LHW is around the zone where the derivatives changes significantly. Accordingly, the ρ position of the region calculated out is between 0.36-0.56 (see Fig. 7).

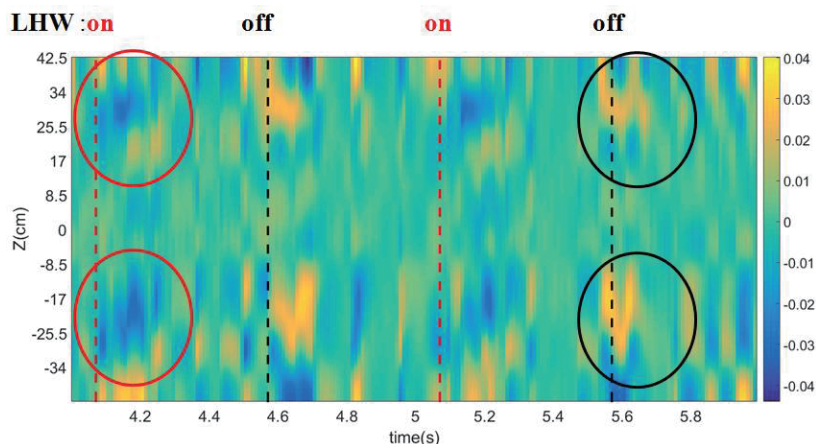


Fig 8. Time evolution of faraday rotation angle

The fig. 8 shows the time evolution of faraday rotation angle, in which we can see the deposition of the LHW more clearly. The derivative of the zone in red and black circle decreases and increases significantly when LHW injected in and cut off, which means the LHW deposition is around this section.

Hard X-Ray measurement system is a effective way to research the activity of the fast electron. On EAST, there are 20 channels of HXR measurement in total^[7]. The measure result for shot 64668 of HXR is shown in Fig. 9:

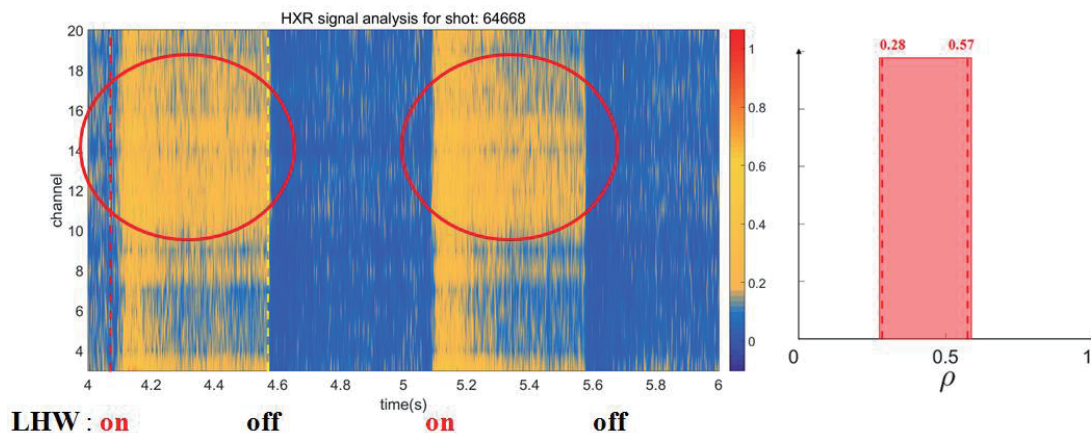


Fig 9. Time evolution of HXR signals and the corresponding ρ location

It is clearly that the intensity of the 20 channels signals are almost the same when LHW cut off, however, there is an obviously gap immediately the LHW turned on. Compared to the channels between 4-8, the intensity of the channels from 10-18 are bigger enough to indicate the LHW deposition is just around the area. The result is corresponding to the ρ location from 0.28 to 0.57, which is almost the same with the result from POINT.

4. Conclusion

The POINT system with the ability to measure electron density and plasma current was established successfully for the goal of long-pulse and high performance discharge on EAST.

To find out the current deposition by LHCD, we inject the LHW with a modulating frequency, and this leads to changes with different degree of faraday rotation angle for the 11 channels on POINT, which indicates the LHW deposition. The result is consistent with HXR measurement system.

5. Acknowledgments

This work is mainly supported by the National Magnetic Confinement Fusion Program of China with contract No. 2012GB101002, No. 2014GB106002 and the National Nature Science Foundation of China with contract No. 11375237, and we greatly appreciate the help from A3 foundation 11261140328. The author would like to infer the support from LHW group and HXR group in EAST, to whom we should say great thanks.

References

- [1]. Liu, F.K., et al., *First results of LHCD experiments with 4.6 GHz system toward steady-state plasma in EAST*. Nuclear Fusion, 2015. **55**(12): p. 123022.
- [2]. Braithwaite, G., et al., *JET polari-interferometer*. Review of Scientific Instruments, 1989. **60**(9): p. 2825-2834.
- [3]. Ding, W.X., et al., *Upgrade of far-infrared laser-based Faraday rotation measurement on MST*. Review of Scientific Instruments, 2010. **81**(10): p. 10D508 - 10D508-5.
- [4]. Zeng, L., D.L. Brower, and Y. Jiang, *Poloidal magnetic field measurements on TEXT-Upgrade*. Plasma Physics & Controlled Fusion, 1998. **39**(4): p. 591-608(18).
- [5]. Liu, H.Q., et al., *Faraday-effect polarimeter-interferometer system for current density measurement on EAST*. Rev Sci Instrum, 2014. **85**(11): p. 11D405.
- [6]. Liu, H.Q., et al., *Internal magnetic field measurements by laser-based POLarimeter-INTerferometer (POINT) system on EAST*. Journal of Instrumentation, 2016. **11**(1): p. C01049.
- [7]. Gao, X. and T.E. Team, *Overview of diagnostic system in the experimental advanced superconducting tokamak*. Instruments & Experimental Techniques, 2008. **51**(2): p. 246-250.

Study on applicability of scintillator-based SX diagnostic for high neutron flux environments in EAST and LHD

Bando Takahiro¹, Ohdachi Satoshi^{1,2} and Suzuki Yasuhiro^{1,2}

¹SOKENDAI(The Graduate University for Advanced Studies), 322-6 Oroshi-cho, Toki 509-5292, Japan

²National Institute for Fusion Science, 322-6 Oroshi-cho, Toki 509-5292, Japan

Abstract

Multi-channel soft x-ray (SX) diagnostic has been used in the Large Helical Device (LHD) to research MHD equilibria and activities. However, in the coming deuterium plasma experiments in LHD, it is difficult to use semiconductor systems near LHD. Therefore, a new type of SX diagnostic, a scintillator-based type, has been investigated to avoid the damage from radiations. From a comparison between scintillators, CsI:Tl and P47 scintillators are selected as candidates. A prototype with CsI:Tl has been developed in LHD and a test with P47 will be done in EAST.

1. Introduction

Multi-channel soft x-ray (SX) diagnostic has been used as one of main diagnostics in fusion plasma devices to research MHD equilibria and activities [1]. In hydrogen plasma experiments of LHD, semiconductor-based diagnostics were used for this purpose [2]. However, in the coming deuterium plasma experiments of LHD, it is difficult to use semiconductor detectors near LHD because neutrons produced by DD reactions damage semiconductors. In the upper part of LHD, photodiodes are estimated to survive only several hundreds of discharges [3]. Therefore, a new type of SX diagnostic, a scintillator-based type, has been investigated to avoid the damage from radiations. In this type, an SX from a plasma is converted to visible light by a scintillator. The light is then guided to a remote location and measured by detectors. It is reported that this kind of diagnostics is working well even in high neutron flux environments of NSTX [4].

In Ref. 5, CsI:Tl has been suggested as a candidate for scintillator-based SX diagnostic in LHD. From a comparison between CaF₂, CsI:Tl, GAGG (Gd₃Al₂Ga₃O₁₂:Ce), P43 (Gd₂O₂S:Tb), and P47 (Y₂SiO₅:Ce,Tb), CsI:Tl and P47 are selected as candidates considering the sensitivity to neutrons and decay time. We have developed the prototype with CsI:Tl in LHD and have a plan to test P47 in EAST.

2. The prototype of scintillator-based SX diagnostic in LHD

We have developed the prototype of scintillator-based SX diagnostic with CsI:Tl in hydrogen plasma experiments in LHD. The schematic view of the prototype is shown in Fig. 1. This system is essentially a pinhole camera with a scintillator screen. The system views a

vertical poloidal cross section of LHD. The size of the pinhole is 2 mm (toroidally) \times 6 mm (radially) with Be foil to cut low energy photons. The thickness of Be foil is 15 μ m. Photons which energies are smaller than 1.3 keV are cut with the foil. Three of the fiber optic plates with scintillator (FOS) J6673-01 using CsI:Tl (50 μ m in thickness) made by HAMAMATSU Photonics are used. Each effective area of FOS is 47 mm \times 7 mm. The scintillation light is converted by two lenses for one channel. In Fig. 1 (c), sensitive areas where the emission light is collected by the lenses are shown. The size of this area is about 64 mm². The converged light is transferred by pure silica core optical fibers (30 m in length) to the floor of the experimental hall. The scintillation light is then detected by C12703-01 avalanche photodiode (APD) modules, made by HAMAMATSU Photonics.

Time evolution of the signal obtained by this prototype with CsI:Tl is shown in Fig. 2 together with time evolution of the plasma parameters. From the comparison of signals from SXs between semiconductor-based diagnostic [6] (black line in Fig. 2(d)) and scintillator-based diagnostic (red line in Fig. 2(d)), functionality of the scintillator-based type is demonstrated. These two SX channels view the similar major radius on the equatorial plane and show similar time evolution. The signal to noise ratio of the scintillator-based system was not good due to the unexpected absorption of SX at the protection layer on the CsI:Tl. However, in the deuterium plasma experiments, a scintillator without the absorption layer will be used and this problem will be removed.

3. Experimental plan of scintillator-based diagnostic with P47 in EAST

We have a plan to test P47 in EAST experiments. There are two objectives for the test. First, we compare signals between that with SX shield and that without the shield. And, second objective is to examine the method to evaluate Signal Noise Ratio of the scintillator-based SX diagnostic in Ref. [5] for future devices.

The schematic view of the detector system is shown in Fig. 3. In the system, a P47 scintillator (50 μ m in thickness), made by ProxiVision, will be used. The scintillation light from the scintillator is converged by lenses and transferred by optic fibers. Then, the light is detected by H10723-210 PMT modules, made by HAMAMATSU Photonics. Remote power control device enable us to control the power supply on the Web. In this system, there are two channels. One of channels detects SXs, neutrons and γ -rays. However, the other channel cannot detect SXs due to SX shield. Then, we can know the noise level due to neutrons and γ -rays experimentally.

4. Summary and Future plan

From a comparison between some scintillators, CsI:Tl and P47 are selected as scintillators for the scintillator-based SX diagnostic on LHD. The prototype of the diagnostic with CsI:Tl showed promising results and reliability of the system. The test with P47 will be

done in EAST experiments.

Acknowledgements

This paper is the result of many fertile suggestion from Prof. T. Nishitani Prof. M. Isobe, and Dr. K. Ogawa. The authors acknowledge the help of Prof. T. Nishitani, who provided us his results of MCNP calculations. This work was supported by NIFS budget code ULPP021, 028 and is also partially supported by the Ministry of Education, Science, Sports and Culture Grant-in-Aid for Scientific Research 26249144, by the JSPS-NRF-NSFC A3 Foresight Program (NSFC: No.11261140328, NRF: No. 2012K2A2A6000443), and by NIFS/NINS under the project of Formation of International Scientific Base and Network.

References

- [1] LC Ingesson, B Alper, BJ Peterson, JC Vallet, Fusion Sci. Technol., **53**, 2 ,p. 528 (2008)
- [2] S. Ohdachi, F. Watanabe, S. Yamamoto, K. Toi, C. Suzuki, K. Ida, S. Muto, LHD Experiment Group, Fusion Sci. Technol., **58**, 418–425 (2010)
- [3] J.F. Baur, B. A. Engholm, M. P. Hacker, I. Maya, P. H. Miller, W. E. Toffolo, and S. S. Wojtowicz, GA-A-16614. General Atomic Co., San Diego, CA (USA, 1981).
- [4] L.F. Delgado-Aparicio, D. Stutman, K. Tritz, and M. Finkenthal, Rev. Sci. Instrum. **75**, 4020 (2004)
- [5] T. Bando, S. Ohdachi, and Y. Suzuki, Plasma Fusion Res., **10**, 1402090 (2015)
- [6] X. Du, S. Ohdachi, K. Toi, and LHD experiment group, Plasma Fusion Res. **7**. (2012)

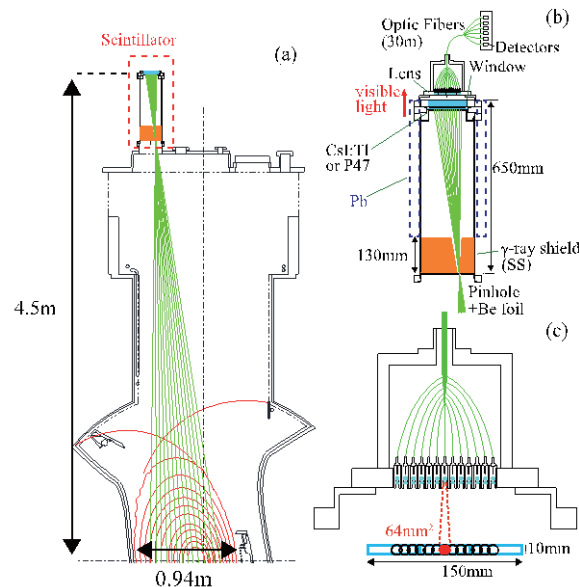


Fig. 1. Schematic design of the scintillator-based diagnostics. (a) Sight lines (green lines) at a vertically elongated cross sectional view at 3.5U port of LHD are shown. (b) An expanded view of the red box region of (a) is shown. (c) Sensitive areas on the scintillator screen are shown.

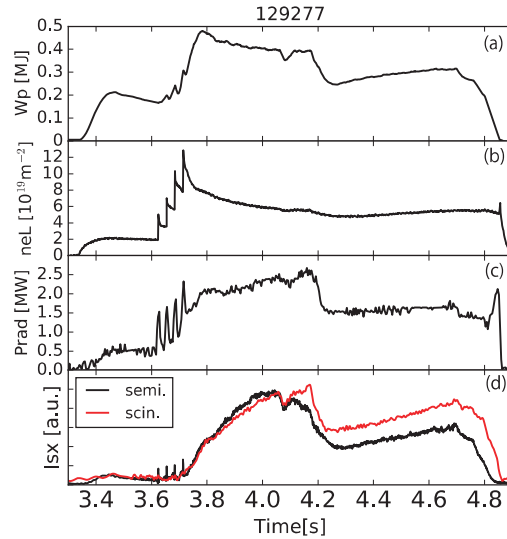


Fig. 2. Time evolutions of plasma parameters and a comparison of signals from SXs between semiconductor-based diagnostic [6] and scintillator-based diagnostic in hydrogen plasma experiments. (a) The plasma stored energy, (b) the line integrated electron density, (c) the radiation power and (d) signals from semiconductor-based diagnostic¹¹ and scintillator-based diagnostic are shown. The electron temperature at the plasma center is about 1keV.

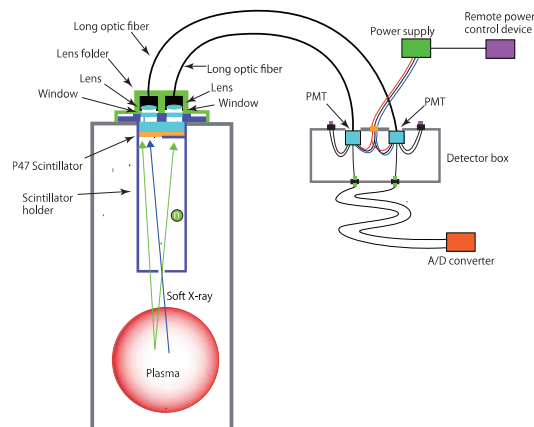


Fig. 3. The schematic view of the scintillator-based SX system with P47 in EAST.

Preliminary Assessment of Tungsten as an Optional Plasma Facing Material in CFETR

Guoliang Xu¹, Yifu Zhou¹, Defeng Kong², Shifeng Mao¹, Minyou Ye²

¹School of Nuclear Science and Technology, University of Science and Technology of China, 230026, Hefei, Anhui China

²Institute of Plasma Physics, Chinese Academy of Sciences, No.350 Shushanhu Road, Hefei, China

Abstract

The objective of this study is to assess whether the tungsten impurity from the divertor will adversely affect the CFETR steady state performance. The OEDGE (OSM-EIRENE-DIVIMP) code package is employed to do the simulation. OSM-EIRENE provide 2D steady-state background plasma, then DIVIMP code is used to determine the impurity distribution. The heat load of the tungsten divertor is assumed to be under the engineering heat load limit (10MW/m²). In order to sample a large area of plasma performance condition, a range of the edge plasma temperature and density decay length are assigned based on an empirical equation. The result reveals both the temperature and density decay length have a noteworthy effect on tungsten sputtering flux, divertor tungsten retention and core concentration. A larger impurity diffusion coefficient can also improve the impurity divertor retention thus reduce the tungsten core concentration. Results of the sensitivity scan over a range of plasma condition is showed in this paper.

1. Introduction

The China Fusion Engineering Test Reactor (CFETR), which is aiming at being an important complement of ITER to DEMO is now under conceptual design. The CFETR is expected to have a full-metal plasma facing materials to achieve low tritium retention. However, the strong radiation of high-Z impurities from plasma facing components (especially the divertor) may negatively influence the performance of core plasma. In this paper, we will evaluate the tungsten divertor's sputtering yields and tungsten concentration in the core plasma under a set of high-recycling divertor solutions.

This paper is organized as follow. In section 2, the code package we used is briefly introduced. Section 3 describes the method and Section 4 contains the results and discussion, followed by a conclusion in Section 5.

2. OEDGE code

The OEDGE code [1] is an interpretive modeling code for the edge plasma of magnetic fusion devices. It contains OSM, EIRENE, and DIVIMP. In the Onion skin model (OSM), the SOL is taken to consist of separate, along-B, flux tubes nested inside each other (onion skin) and 1D, along-B modeling is carried out for each flux tube separately, with the cross filed terms treated more or less simply. EIRENE (Monte Carlo neutral hydrogen code) provides hydrogen particle and power source terms for the fluid equations. DIVIMP (Divertor Impurities) is a Monte Carlo code which follows the trajectories of individual impurity particles in the edge plasma of a divertor tokamak.

In the OEDGE code, the background plasma of SOL is solved iteratively by using OSM and

EIRENE, then DIVIMP use the background plasma to calculate the tungsten sputtering yields and give the tungsten impurity distribution.

3. Method

3.1. Geometry

The first wall and grid geometry is showed in Fig.1. It is a lower single null CFETR geometry shape with an ITER-like divertor. The major radius and minor radius are 5.6m and 1.6m respectively. The toroidal field on the magnetic axis is 5T. The grid can be divided into two parts. The inner part, $0.9 < r/a < 1$, contains the pedestal information, and the outer part, $r/a > 1$, contains the scrap of layer information.

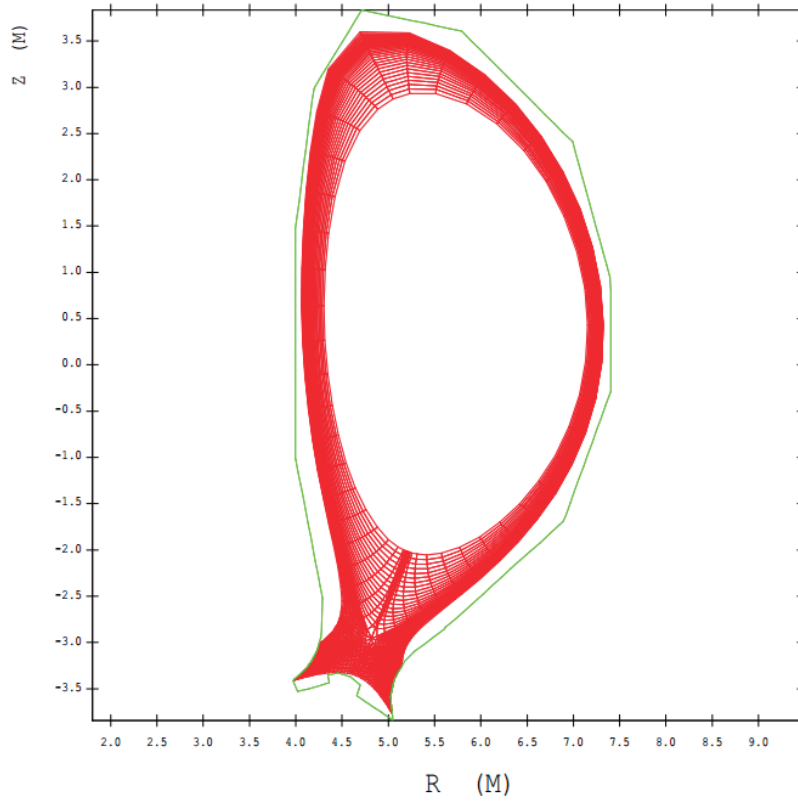


Fig. 1. The first wall and grid geometry

3.2. Background plasma

The background hydric plasma in the region $0.9 < r/a < 1.0$ is taken from EPED simulation with the pedestal top density set to be 8×10^{19} . To generate a set of edge plasma ($r/a > 1.0$), some assumptions are made.

- $T_{i_target} = T_{e_target}$
- Heat load of the targets' strike point $q_{str} = 10 \text{ MW/m}^2$
- Exponential target profiles, and the decay lengths satisfy:
 - $\lambda_{sol} = 4\lambda_{PFR}$ [2]
 - $\lambda_n = 1.4\lambda_T$ [3]
 - $\lambda_{target} = f^* \lambda_u$ (f : magnetic flux expansion)

With the assumption listed above, the plasma density and temperature at the target strike point can be decided by following the iteration logic in Fig. 2. We should mention that the value of the

decay lengths do not affect the iteration results. For a given middle plane temperature decay length a set of decay lengths of the SOL plasma can be determined. By choosing a strike point plasma density n_{str} , the plasma temperature at the strike point can be calculated. Then the temperature and density profiles on the divertor targets are determined and put into OSM-EIRENE to generate the background plasma in the SOL. If the plasma density and temperature and the outer middle plane matches the value from EPED simulation, the input n_{str} and T_{str} are accepted. In this presentation, the strike point density and temperature are $n_{str}=1.5 \times 10^{20}$ and $T_{str}=50\text{eV}$.

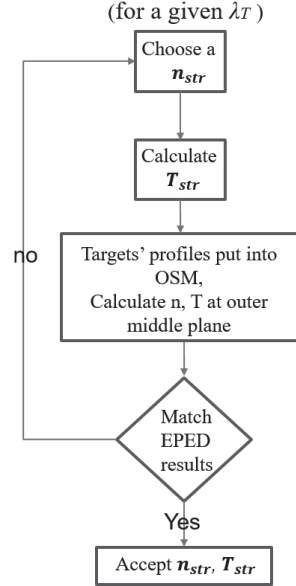


Fig. 2 The iteration logic

An empirical scaling reveals: [4]

$$\lambda_q = (0.73 \pm 0.38) B_T^{-0.78 \pm 0.25} q_{cyl}^{1.20 \pm 0.27} P_h^{0.1 \pm 0.11} R_{geo}^{0.02 \pm 0.2}$$

B_T : toroidal magnetic field

q_{cyl} : cylindrical safety factor, or q_{95}

P_h : power into SOL

R_{geo} : major radius

And in the flux limit regime (weak collisionality),

$$\lambda_q^{flux-limit} = \left(\frac{3/2}{\lambda_T} + \frac{1}{\lambda_n} \right)^{-1}$$

In the CFETR cases showed in this presentation, $B_T=5.0$, $q_{95}=4.0$, $P_h=98.0\text{MW}$, and $R_{geo}=5.6\text{m}$. Thus the plasma temperature decay length of the middle plane is in the region of $0.38\text{mm} < \lambda_T < 31\text{mm}$. To evaluate the influence of plasma decay lengths on the edge impurity transport, λ_T is chosen to be [5, 6, 10, 15, 20, 25, 30] mm. For different λ_T , different SOL background plasma can be generated.

3.3. Impurity transport

To radiate enough power and reduce the heat load on the divertor targets, Neon is injected from the private flux region. Since these ions are 100% recycling, the distribution in the plasma volume is independent of initial injection location. The neon concentration is set to be 0.5% [5] just inside the separatrix. Then the tungsten sputtering yields is calculated by taking the deuterium and neon flux into consideration. The DIVIMP code launches the tungsten impurity from the targets and

trace the transport process in the background plasma generated in Section 3.2. The cross field transport is assumed to be purely diffusion and diffusion coefficient is usually varied in the region of $0.1\sim 10\text{m}^2\text{s}^{-1}$. In this presentation the diffusion coefficient is set to be $D_{\perp}=[0.5\ 1\ 3\ 5\ 8\ 10]$.

4. Results and discussion

Divertor retention (DR) described by the ratio of the impurity content in the divertor region to the impurity content in the main plasma region. The DR of different background plasma temperature decay lengths and diffusion coefficients is showed in Fig. 4.

The results reveal the DR value increases with the diffusion coefficient increase. As shown in Fig. 5, the tungsten density is higher in the core plasma, thus a larger D_{\perp} value will increase the tungsten density in the SOL, then increase the impurity divertor retention.

Fig. 4 also reveals the λ_T influence on the divertor retention. With λ_T increasing, the divertor tungsten retention decreases when $\lambda_T < 10\text{mm}$, and increases when $\lambda_T > 10\text{mm}$. To understand this phenomenon, the tungsten sputtering flux and the background plasma temperature along the target is drawn in Fig. 6 and Fig. 7 respectively. In the $\lambda_T < 10\text{mm}$ cases, radial tungsten density gradient dominates, and in other cases, radial temperature gradient dominates.

The integrated tungsten sputtering flux for different λ_T cases is shown in Fig. 8, and the core tungsten concentration for different λ_T and D_{\perp} cases is shown in Fig.9. Unfortunately, in all the cases the tungsten concentration in the core plasma is above the 1×10^{-5} limit [6].

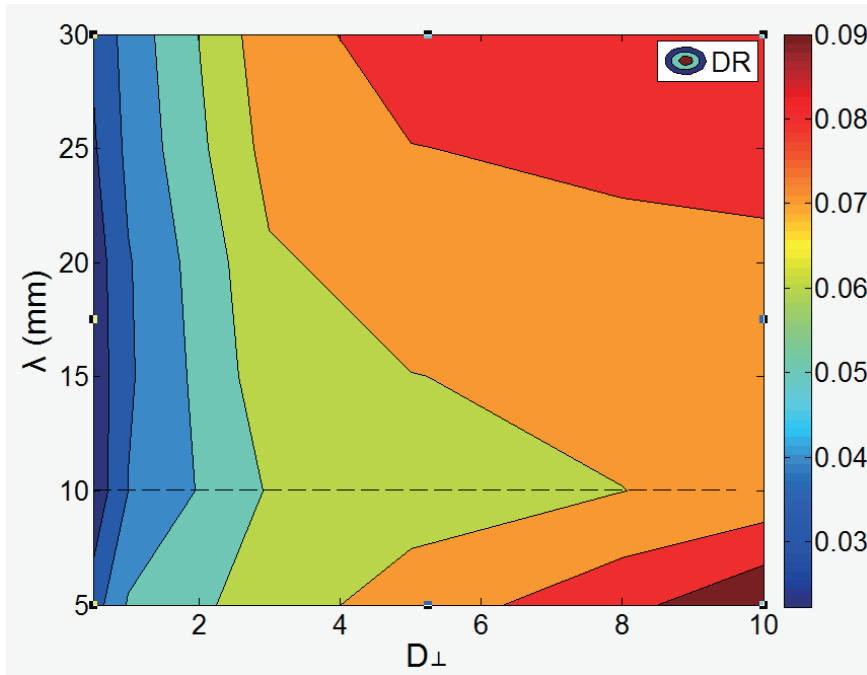


Fig. 4. DR of different background plasma temperature decay lengths and diffusion coefficients

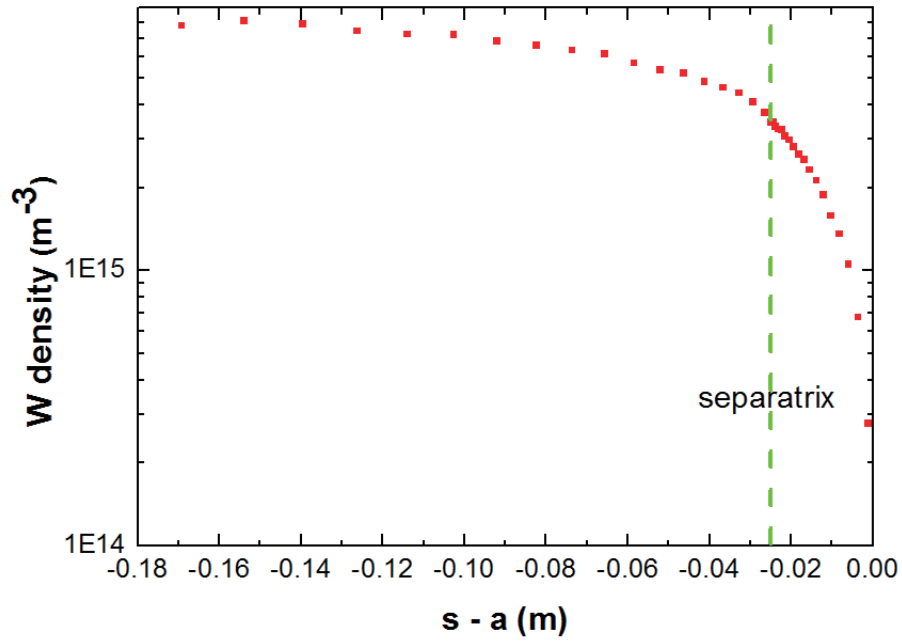
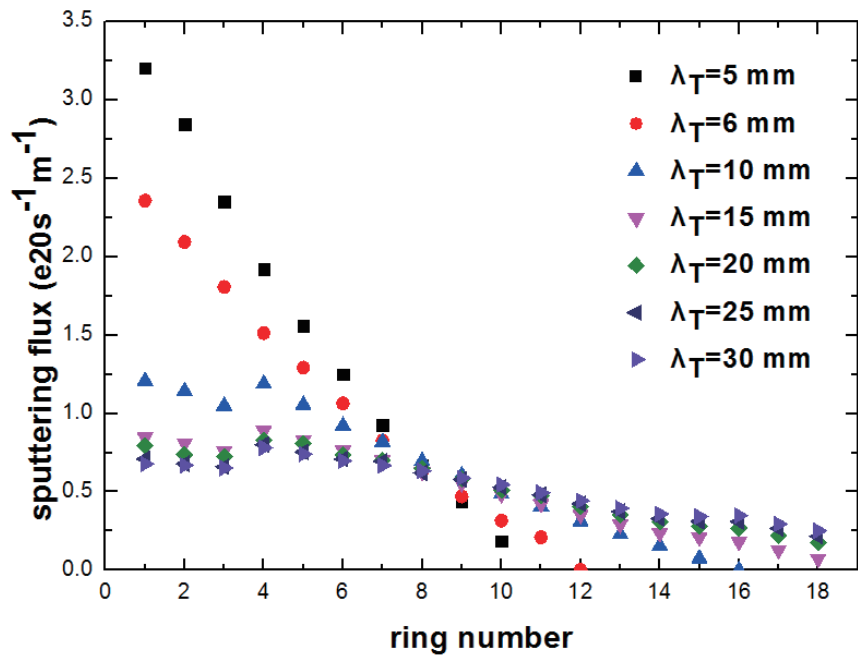


Fig. 5 Tungsten density of the middle plane

Fig. 6 Tungsten sputtering flux along the target (outside of the separatrix) for different λ_T cases.

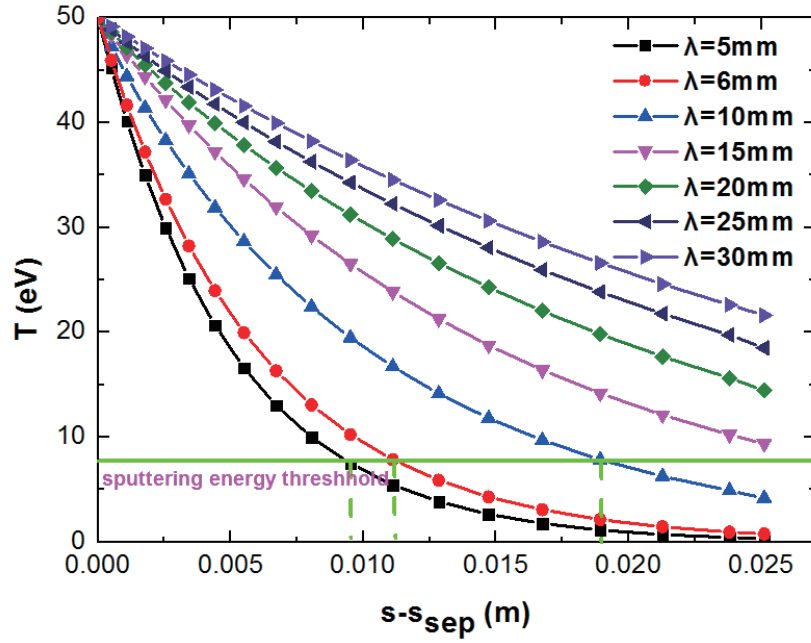


Fig. 7 Background plasma temperature along the divertor target (outside of the separatrix) for different λ_T and D_{\perp} cases.

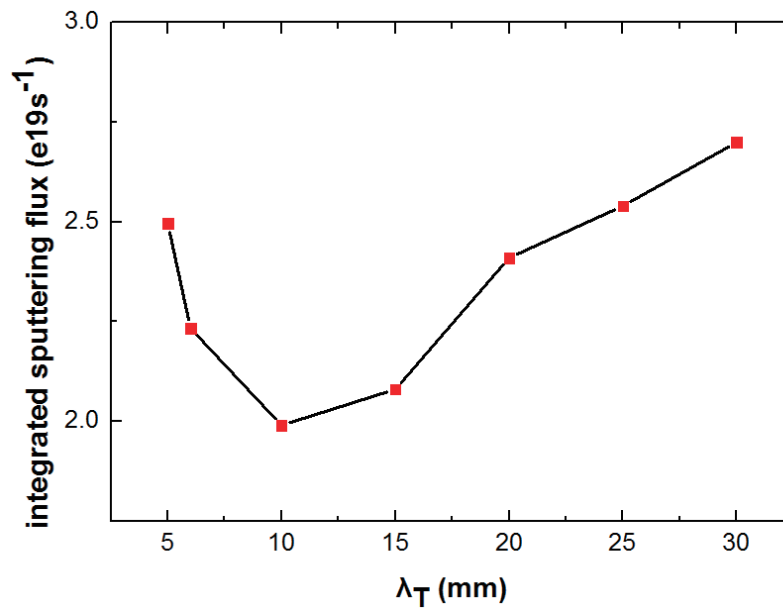


Fig. 8 Integrated tungsten sputtering flux for different λ_T cases.

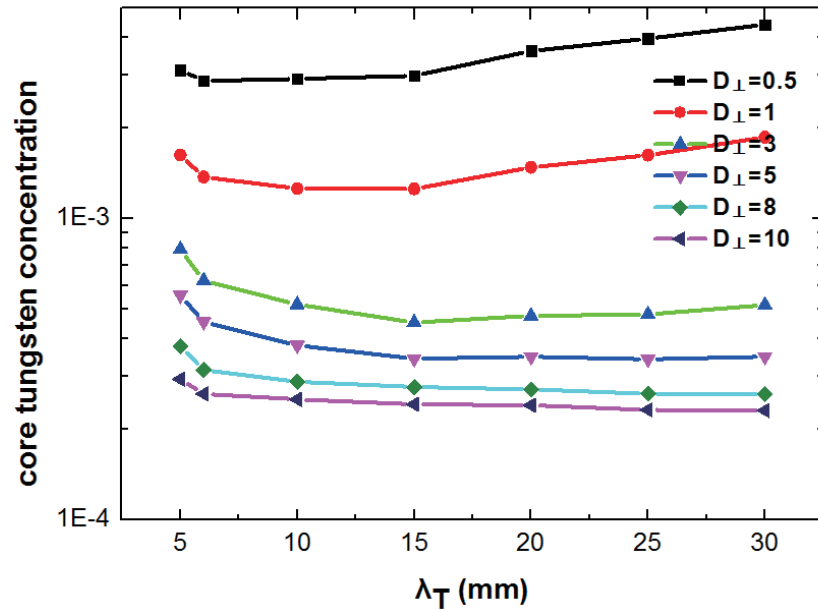


Fig. 9 Core tungsten concentration for different λ_T and D_{\perp} cases

5. Conclusion

This presentation shows the background plasma temperature and density exponential decay length have a noteworthy effect on tungsten sputtering flux, divertor tungsten retention and core concentration. A larger Impurity diffusion coefficient can improve the impurity divertor retention and reduce tungsten core concentration. And $10\text{MW}/\text{m}^2$ is an excessive heat load for tungsten divertor in all the cases. However, all the cases in the presentation are in the high-recycling regime, the cases in detachment will hopefully reduce the tungsten concentration in an acceptable level.

Acknowledgement

This work is supported by Nation Science Program (Grant Nos.:2014GB110001, 2014GB110002, 2014GB110003). We'd like to express our thanks to University of Toronto Institute for Aerospace Studies for their permission of using the OEDGE code and technical support.

References

- [1] Stangeby P C, Elder J D, Boedo J A, et al. Interpretive modeling of simple-as-possible-plasma discharges on DIII-D using the OEDGE code[J]. Journal of nuclear materials, 2003, 313: 883-887.
- [2] Pitcher, Charles Spencer, and P. C. Stangeby. Plasma Physics and Controlled Fusion 39.6 (1997): 779.
- [3] Sun H J, Wolfrum E, Eich T, et al. Plasma Physics and Controlled Fusion, 2015, 57(12): 125011.
- [4] Eich, T., et al. Physical Review Letters 107.21 (2011): 215001.
- [5] Braams B J. Radiative divertor modelling for ITER and TPX[J]. Contributions to Plasma Physics, 1996, 36(2 - 3): 276-281.
- [6] Pütterich T, Neu R, Dux R, et al. Nuclear Fusion, 2010, 50(2): 025012.

Multi-scale Full-orbit Dynamics of Runaway Electrons in Tokamak with Synchrotron Radiation

Yulei Wang¹, Hong Qin¹, Jian Liu¹

¹Department of Modern Physics and School of Nuclear Science and Technology,
University of Science and Technology of China, Hefei, Anhui 230026, China

Abstract

In this proceeding, we give a short introduction about our recent work on runaway electrons [Phys. Plasmas 23, 062505 (2016)]. The secular full-orbit simulations of runaway electrons with synchrotron radiation in tokamak fields are carried out using a relativistic volume-preserving algorithm. Detailed phase-space behaviors of runaway electrons are investigated in different dynamical timescales spanning 11 orders. In the small timescale, i.e., the characteristic timescale imposed by Lorentz force, the severely deformed helical trajectory of energetic runaway electron is witnessed. A qualitative analysis of the neoclassical scattering, a kind of collisionless pitch-angle scattering phenomena, is provided when considering the coupling between the rotation of momentum vector and the background magnetic field. In large timescale up to one second, it is found that the initial condition of runaway electrons in phase space globally influences the pitch-angle scattering, the momentum evolution, and the loss-gain ratio of runaway energy evidently. However, the initial value has little impact on the synchrotron energy limit. It is also discovered that the parameters of tokamak device, such as the toroidal magnetic field, the loop voltage, the safety factor profile, and the major radius, can modify the synchrotron energy limit as well as the strength of neoclassical scattering. The maximum runaway energy is also proved to be lower than the synchrotron limit when the magnetic field ripple is considered.

As a typical multi-scale process, the dynamics of runaway electrons in tokamak has emerged as an important topic in the study of magnetic confined fusion devices. During tokamak experiments, many operation phases, such as fast shutdown, disruptions, and strong current drive, are accompanied by the generation of runaway electrons [1–15]. The collisional friction from the background plasma cannot prevent the acceleration of these energetic electrons if the inductive loop electric field is larger than a critical value [16, 17]. Through the acceleration by the electric field, the velocity of runaway electrons can be sped up to nearly the light speed. Runaway electrons carrying energies from 10 to 100 MeVs have been observed in different experiments [18–21]. Once hitting the plasma-facing components (PFCs), these energetic electrons can damage the tokamak devices badly. Because of the strong relativistic effect, the synchrotron radiation becomes an important ingredient of runaway electron physics. For extremely energetic runaway electrons, their synchrotron radiation loss could be strong enough to balance out the acceleration by the loop electric field.

The radiation dissipation then provides runaway electrons an upper bound of energy, i.e., the synchrotron energy limit [22–25]. The typical duration for a runaway electron with low energy (1keV-1MeV) to reach the energy limit has the order of magnitude of one second while the smallest timescale of Lorentz force is 10^{-11} s [24, 26], which means the dynamical behavior of runaway electrons spans about 11 orders of magnitude in timescale. The multi-scale character poses great difficulty to a satisfying physical treatment of runaway dynamics.

Through averaging out the gyro-motion, the gyro-center theory can reduce the span of timescales by about three orders and is used widely in dealing with runaway electron dynamics. Fruitful results of this theory have been accomplished. Considering the gyro-center approximation regardless of the toroidal geometry, one can transfer the full-orbit dynamical equations of runaway electrons to a set of relaxation equations which are much easier to solve theoretically and numerically [24]. By use of relaxation equations, the momentum evolution structure as well as energy limit has been studied in detail under several kinds of dissipations, such as collision, synchrotron radiation, and bremsstrahlung radiation [22, 23, 27]. Meanwhile, the restriction effect of magnetic ripple on the maximum energy has also been discussed in this way [23]. If involving the toroidal geometry, some extra geometry-related phenomena arise, often dubbed neoclassical effects. The Ware-pinch effect shows an inward drift of trapped orbit [25, 28, 29], while the neoclassical drift provides an outward radial drift velocity of transit runaway orbits [30]. Both of these phenomena reflect the conservation of the toroidal canonical angular momentum. Recently, gyro-center simulations have been equipped with structure-preserving discrete methods and shown better long-term numerical accuracy than traditional methods [24, 25, 31].

Unlike gyro-center theory, the full-orbit analysis can keep entire physical information covering all timescales of runaway dynamics. Especially, a recent full-orbit simulation on runaway electrons has shown that the assumption of gyro-center theory no longer holds in tokamak magnetic field if the runaway electrons are accelerated to several tens of MeVs [26]. Because of the high energy, the change of background magnetic field direction encountered by runaway electrons is significant even within one gyro-period. The violent change of magnetic field causes a full-orbit effect, the collisionless neoclassical pitch-angle scattering, which arises from the toroidal geometry and causes a violent momentum exchange between parallel and perpendicular directions. It also leads to a drift in momentum space and the significant run-up of perpendicular momentum, which provides a new picture of runaway momentum structure. The energy limit is also found to be higher when the full-orbit effect is considered. Therefore, the full-orbit dynamical analysis is vital to obtain reasonable descriptions on runways.

In this paper, we discuss the detailed full-orbit runaway dynamics in views of both small (10^{-11} - 10^{-9} s) and large (1-3 s) timescales and analyze the influences of tokamak design parameters on the long-term motion of runaway electrons. A throughout simulation of the

multi-timescale behavior of runways requires more than 10^{12} time steps, which is an astronomically big number and cannot be properly implemented by traditional numerical methods. To tackle the global accumulation of coherent errors for such long-term simulation, we follow the method in Ref. [26] and use a relativistic volume-preserving algorithm (VPA) [32]. As a geometric algorithm, the relativistic VPA possesses long-term numerical accuracy and stability [24, 25, 31–41]. The secular full-orbit dynamics of runaway electrons is obtained through directly solving the Lorentz force equations. The synchrotron radiation is included in the physical model, when the collisional force is ignored.

The characteristic timescale imposed by magnetic force reflects the smallest timescale of runaway dynamics, which can be defined as the gyro-period

$$\mathcal{T}_c = \frac{2\pi\gamma m_0}{eB}, \quad (1)$$

where γ is the Lorentz factor, m_0 is the rest mass of electron, e is the unit charge, and B denotes the strength of magnetic field. Although gyro-center theory breaks down for energetic runaways in toroidal geometry, the gyro-period can still be used as an available characteristic parameter for the small timescale. This is because that the failure of the gyrocenter condition is mainly due to the rapid change of the direction of the magnetic field, while B doesn't vary a lot during each gyro-period. The practicability of \mathcal{T}_c can also be analyzed in the view of the rotation operator. We will show that in the gyro-period timescale the trajectory of an energetic runaway electron is elongated both toroidally and poloidally, and the corresponding \mathcal{T}_c will increase to about one twentieth of the transit period. As a result, the local magnetic field witnessed by an energetic runaway electron rotates rapidly, and the norm of magnetic rotation axial vector, namely, $|\boldsymbol{\Omega}_B| = |\mathbf{b} \times \dot{\mathbf{b}}|$, becomes comparable with $1/\mathcal{T}_c$, which leads to the collisionless neoclassical pitch-angle scattering. A qualitative description of the collisionless scattering is given through the coupling between the rotations of momentum and magnetic vector. The momentum drift caused by the long-term accumulation of collisionless scattering effect is analyzed. To be specific, the perpendicular momentum of a runaway electron increases in the direction of $\boldsymbol{\Omega}_B$ which is approximately in the direction of z-axis.

The long-term evolution of momentum and energy are investigated for runaways with different initial conditions in phase space. Four main characteristics of the momentum evolution structure are discussed: (a) the zero-point position of perpendicular momentum, (b) the oscillation amplitude when reaching energy limit, (c) maximum parallel momentum, and (d) maximum perpendicular momentum. Among these four characteristics, (a) and (b) correspond to the fine oscillating structures of runaway orbit, meanwhile (c) and (d) are related closely to the synchrotron energy limit [26]. It will be shown that the zero-point of perpendicular momentum and the amplitude of oscillation are impacted significantly by the initial pitch-angles. Larger initial perpendicular momentum will cause larger zero-point position and stronger oscillation in small timescale. However, the initial momentum samplings have little influence on the energy limit. The impact of the initial configuration

position on the long-term momentum evolution is also negligible. For a deeper insight, we define two quantities to describe the long-term integral behavior of runaway energies, i.e., the energy loss-gain ratio and the energy balance time. The energy loss-gain ratio is defined as the ratio of the total energy loss through radiation to the energy gained from the loop electric field. This ratio is influenced by the initial runaway momentum significantly but is nearly independent of the initial position. The evolutions of energy loss-gain ratio under different initial phase space samplings have similar behaviors in the vicinity of the energy limit. The energy balance time describes the time required for a new-born runaway electron to run up to its energy limit, which is approximately independent of its initial values in the phase space.

Finally, in order to describe tokamak experimental research on runaways, the influences of tokamak parameters, including the loop electric field, the background magnetic field, the major radius, and the safety factor q , on both the energy limit and the strength of neoclassical pitch-angle scattering are analyzed. Large loop inductive electric field can impel runaways with high energy in short time. On the other hand, the strength of magnetic field mainly contributes to the neoclassical effects. Smaller magnetic field will stall for the energy balance time but bump up the perpendicular momentum more significantly. As a key parameter of tokamaks, the major radius affects the energy limit and the balance time through changing the power of radiation. Smaller major radius results in stronger radiation and shorter balance time. The strength of neoclassical scattering decreases slightly as the growth of major radius. The influence of safety factor is also discussed. Involving several different effects, the maximum energy, the balance time, and the maximum perpendicular momentum roughly depend on the safety factor linearly. When q is small, the dependence of momentum oscillation on q is more sensitive. When q is larger than 2, the amplitude of oscillation approaches to a constant approximately. Lastly, we also study the effect of magnetic field ripple due to the finite number of toroidal coils. The energy limit is proved to be lower than the synchrotron limit when magnetic ripple exists, which is consistent with the theoretical analysis in Ref. [42].

References

- [1] R. Yoshino, T. Kondoh, Y. Neyatani, K. Itami, Y. Kawano, and N. Isei, *Plasma Phys. Control. Fusion* **39**, 313 (1997).
- [2] R. Jaspers, N. L. Cardozo, F. Schuller, K. Finken, T. Grewe, and G. Mank, *Nucl. Fusion* **36**, 367 (1996).
- [3] P. Helander, L.-G. Eriksson, and F. Andersson, *Phys. Plasmas* **7**, 4106 (2000).
- [4] P. Helander, L. Eriksson, and F. Andersson, *Plasma Phys. Contr. Fusion* **44**, B247 (2002).
- [5] T. Fülöp, H. Smith, and G. Pokol, *Phys. Plasmas* **16**, 022502 (2009).
- [6] R. Gill, B. Alper, A. Edwards, L. Ingesson, M. Johnson, and D. Ward, *Nucl. Fusion* **40**, 163 (2000).
- [7] R. Jaspers, K. Finken, G. Mank, F. Hoenen, J. Boedo, N. L. Cardozo, and F. Schuller, *Nucl. Fusion* **33**, 1775 (1993).

- [8] R. Nygren, T. Lutz, D. Walsh, G. Martin, M. Chatelier, T. Loarer, and D. Guilhem, *J. Nucl. Mater.* **241**, 522 (1997).
- [9] P. Parks, M. Rosenbluth, and S. Putvinski, *Phys. Plasmas* **6**, 2523 (1999).
- [10] M. Rosenbluth and S. Putvinski, *Nucl. Fusion* **37**, 1355 (1997).
- [11] R. Yoshino and S. Tokuda, *Nucl. Fusion* **40**, 1293 (2000).
- [12] H. Tamai, R. Yoshino, S. Tokuda, G. Kurita, Y. Neyatani, M. Bakhtiari, R. Khayrutdinov, V. Lukash, and M. Rosenbluth, *Nucl. Fusion* **42**, 290 (2002).
- [13] M. Lehnen, S. Bozhenkov, S. Abdullaev, and M. Jakubowski, *Phys. Rev. Lett.* **100**, 255003 (2008).
- [14] K. Finken, S. Abdullaev, M. Jakubowski, R. Jaspers, M. Lehnen, R. Schlickeiser, K. Spatschek, A. Wingen, and R. Wolf, *Nucl. Fusion* **47**, 91 (2007).
- [15] N. J. Fisch, *Rev. Mod. Phys.* **59**, 175 (1987).
- [16] H. Dreicer, *Phys. Rev.* **115**, 238 (1959).
- [17] J. Connor and R. Hastie, *Nucl. Fusion* **15**, 415 (1975).
- [18] H.-W. Bartels, *Fusion Eng. Des.* **23**, 323 (1994).
- [19] T. Kawamura, H. Obayashi, and A. Miyahara, *Fusion Eng. Des.* **9**, 39 (1989).
- [20] H. Bolt, A. Miyahara, M. Miyake, and T. Yamamoto, *J. Nucl. Mater.* **151**, 48 (1987).
- [21] R. Jaspers, N. L. Cardozo, A. Donne, H. Widdershoven, and K. Finken, *Rev. Sci. Instrum.* **72**, 466 (2001).
- [22] J. Martín-Solís, J. Alvarez, R. Sánchez, and B. Esposito, *Phys. Plasmas* **5**, 2370 (1998).
- [23] J. Martín-Solís, B. Esposito, R. Sánchez, and J. Alvarez, *Phys. Plasmas* **6**, 238 (1999).
- [24] J. Liu, H. Qin, N. J. Fisch, Q. Teng, and X. Wang, *Phys. Plasmas* **21**, 064503 (2014).
- [25] X. Guan, H. Qin, and N. J. Fisch, *Phys. Plasmas* **17**, 092502 (2010).
- [26] J. Liu, Y. Wang, and H. Qin, *Nucl. Fusion* **56**, 064002 (2016).
- [27] M. Bakhtiari, G. Kramer, and D. Whyte, *Phys. Plasmas* **12**, 102503 (2005).
- [28] A. Ware, *Phys. Rev. Lett.* **25**, 15 (1970).
- [29] N. J. Fisch and C. F. Karney, *Phys. Fluids* **24**, 27 (1981).
- [30] H. Qin, X. Guan, and N. J. Fisch, Report No. PPPL-4639, Princeton Plasma Physics Laboratory (PPPL), Princeton, NJ (United States) (2011).
- [31] R. Zhang, J. Liu, Y. Tang, H. Qin, J. Xiao, and B. Zhu, *Phys. Plasmas* **21**, 032504 (2014).
- [32] R. Zhang, J. Liu, H. Qin, Y. Wang, Y. He, and Y. Sun, *Phys. Plasmas* **22**, 044501 (2015).
- [33] Y. He, Y. Sun, J. Liu, and H. Qin, *J. Comput. Phys.* **281**, 135 (2015).
- [34] J. Xiao, J. Liu, H. Qin, and Z. Yu, *Phys. Plasmas* **20**, 102517 (2013).
- [35] H. Qin, S. Zhang, J. Xiao, J. Liu, Y. Sun, and W. M. Tang, *Phys. Plasmas* **20**, 084503 (2013).
- [36] H. Qin and X. Guan, *Phys. Rev. Lett.* **100**, 035006 (2008).
- [37] Y. He, H. Qin, Y. Sun, J. Xiao, R. Zhang, and J. Liu, *Phys. Plasmas* **22**, 124503 (2015).
- [38] Y. He, Y. Sun, J. Liu, and H. Qin, *J. Comput. Phys.* **305**, 172 (2016).
- [39] H. Qin, J. Liu, J. Xiao, R. Zhang, Y. He, Y. Wang, Y. Sun, J. W. Burby, L. Ellison, and Y. Zhou, *Nucl. Fusion* **56**, 014001 (2015).

- [40] J. Xiao, J. Liu, H. Qin, Z. Yu, and N. Xiang, *Phys. Plasmas* **22**, 092305 (2015).
- [41] J. Xiao, H. Qin, J. Liu, Y. He, R. Zhang, and Y. Sun, *Phys. Plasmas* **22**, 112504 (2015).
- [42] L. Laurent and J. Rax, *Europhys. Lett.* **11**, 219 (1990).

Radiative divertor experiments with Ar and Ne seeding on EAST

Jingbo Chen^{1,2}, Yanming Duan¹, Zhongshi Yang^{1*}, Liang Wang¹, Kai Wu^{1,2}, Fang Ding¹, Hongmin Mao¹, Jichan Xu^{1,2}, Ling Zhang¹, Jinhua Wu¹, Marco Wischmeier³, Lingyan Xiang^{1,3}, Sven Wiesen⁴, Guang-Nan Luo¹, and EAST Team^a

¹Institute of Plasma Physics, Chinese Academy of Sciences, P.O. Box 1126, Hefei, 230031, China

²Science Island Branch of Graduate School, University of Science & Technology of China, Hefei, China

³Max Planck Institute of Plasma Physics, D-85748 Garching, Germany

⁴Forschungszentrum Jülich, Jülich, Germany

Abstract

Radiative divertor experiments with Ar and Ne seeding have been carried out during recent EAST experimental campaigns. The results proved the high efficiency of Ar and Ne in reducing heat load and particle flux onto the divertor target. However, core plasma contamination and PFCs sputtering were observed with Ar seeding especially when the impurity was seeded from upper tungsten divertor. The experiments with different seeding pulse width proved Ar is a strong radiator for EAST, and excessive Ar seeding easily caused the burst of radiation in the plasma core region which led to a great loss of plasma stored energy. To compare with Ar seeding, Ne seeding experiment was carried out in EAST 2016 spring campaign. Its preliminary results showed Ne, compared with Ar, has advantages on radiation profile and less contamination in plasma core region.

1. Introduction

Increasing divertor radiation by injecting impurities is a general and effective method to reduce heat flux from scrape-off layer and to cool the divertor plasma to detachment. Impurities such as nitrogen (N₂), neon (Ne) and argon (Ar) have been widely used in radiative divertor experiments on several tokamaks. In ASDEX-Upgrade, in full tungsten divertor wall condition, complete and partial detached plasmas were achieved by feedback controlled N₂ seeding. In addition, Ar or Ne impurities were also used to control the heat flux onto the divertor successfully [1, 2]. In JET, N₂ seeding is used to compare the effect of reducing heat load on ITER-Like wall (ILW) to all-carbon wall conditions. N₂ seeding elicits different responses between them in raising plasma density, reducing ELM frequency and pedestal pressure [3]. In JT-60U, with Ne, Ar and a mixture of Ne and Ar injection in H-mode plasmas, the fractions of divertor radiation power by these impurities in addition to an intrinsic impurity, C, were investigated. It was found that Ne is the biggest radiator when plasma detached by Ne seeding but carbon acts as the biggest radiator with other impurities seeding in carbon wall condition [4].

Owing to the routine lithium wall coating conditioning before EAST discharges, Ar, instead of N₂, is used as the seeded impurity to achieve long-pulse high-performance operations in EAST [5-7]. In this work, the radiative divertor experiments by using the mixture of Ar/D₂ (1:4) as seeded impurity carried out during EAST 2014 and 2015 campaigns were introduced with more details in subsequent sections. Furthermore, EAST has upgraded its upper divertor into actively-cooled W/Cu plasma-facing components (PFCs) in 2014[8]. In recent discharges, excessive Ar seeding easily caused the contamination in core plasma region. Despite a reduction in electron temperature and power flux, Ar injection had led to a significant increase of the sputtered tungsten flux near the strike point, especially when the impurity was seeded from upper tungsten divertor target, which is discussed in section 3. Section 3.2 describes the differences of using long and short pulses for Ar seeding in upper single null (USN) divertor configuration. To compare with Ar seeding, Neon was used as the radiator in 2016 campaign. Its preliminary result will be shown on Section 3.3. Summary and future plan are presented in the last section.

2. Experimental setup and relevant diagnostics

During EAST 2014 and 2015 campaigns, radiative divertor experiments were carried out in L-mode discharges and H-mode discharges in order to compare the differences between these two confinement modes in distribution of heat load reduction, asymmetry and impurities behaviors in divertor region. As shown in Fig. 1, the controlled pulsed mixture of Ar/D₂ (1:4) was injected through a pipe located inside the

*Corresponding author: Zhongshi Yang (zsyang@ipp.ac.cn)

^aSee Appendix of B. N. Wan et al., Nucl. Fusion 55, 104015 (2015)

divertor target near the strike point. The delay time of Ar affecting on plasma was about 75ms-140ms limited by the length of pipes after the upgrade of divertor gas puff system in 2014[9]. Width of puffing pulse followed the PCS (plasma control system) program setting. According to lower single null (LSN) and upper single null (USN) configuration, the mixture was injected from different regions, i.e., lower carbon divertor and upper ITER-Like tungsten divertor, in several discharges. The results are discussed in section 3.

Information on electron temperature, electron density, and particle & heat flux on divertor targets can be provided by EAST divertor Langmuir probe diagnostic system[10, 11] consisting of 89 groups of triple probes of which the poloidal layout is shown in Fig. 1. The total and the profile of radiated power in bulk plasma can be provided by four 16-channels AXUV (absolute extreme ultraviolet) arrays, total 64 channels, installed in P horizontal port, and one 24-channels AXUV array, installed in the up-vertical C port[12]. Impurities, such as argon, neon, deuterium, lithium carbon, and tungsten, in upper divertor region (only inboard and outboard targets) can be observed by divertor tungsten spectroscopy with the range the range of 399-431 nm. These results have been also confirmed by a flat-field extreme ultraviolet (EUV) spectrometer working in 20-500 Å wavelength range with fast time at the mid-plane[13].

3. Results and discussions

3.1 Impurity seeding from lower(carbon) and upper(tungsten) divertor

Shot #56467 ran with conditions as follows: $I_p=0.5$ MA, $B_T=2.5$ T, line integrated density $n_e \approx 2.7 \times 10^{19}$ m⁻³. Fig.2 shows the time evolution of this L-mode discharge under the LSN divertor configuration with ∇B drift towards the upper divertor and the divertor cryo-pump being activated. The heating power was 1.4 MW by low hybrid waves. Ar mixture had been injected near the lower inboard target strike point at the rate of $2.0 \sim 2.6 \times 10^{20}$ e/s since 6.0s for 200ms. After a delay time of 100 ms, the effect of Ar actually started at about 6.1s. The heat flux, q_t , on the divertor target plate, was clearly reduced, i.e. by ~ 3 times, the ion saturation current I_s and electron temperature T_e , measured by divertor Langmuir probe, were decreased by 40% and 35% near the strike point, because the ionization of the seeded neutral gas had led to the rise of radiation to exhaust power in the divertor region. The plasma partially detached on lower inboard target. And a more interesting thing is that the rise of radiation, measured by AXUV, mainly distribute on upper and lower divertor region when the Ar impurity seeded from lower divertor. The main reason may be the transportation of the impurity ion along with ∇B drift direction and ionization in upper divertor region. Further experiments are required to confirm this phenomenon and its mechanism.

Like Shot #56467, Shot #56649 was an L-mode discharge under the LSN configuration, and the conditions are: $I_p=0.4$ MA, $B_T=2.5$ T, line averaged density $n_e \approx 2.0 \times 10^{19}$ m⁻³. These two discharges have similar parameters, but Ar injected from upper divertor target instead of lower divertor for 300 ms. Their results show clear difference on profile of radiation. The rise of radiation more concentrates on the core plasma region after the Ar mixture seeded from upper divertor target compared with the former. As Fig.3 shows, main reason is a great part of Ar impurity enter the plasma core region and bring a significant rise of radiation. It is considered that this result may have some association with plasma shape setting and divertor geometry type. In addition to, it is a notable challenge in tungsten wall condition that Ar injection led to an increase of the tungsten flux on upper divertor surface despite a reduction in electron temperature and power flux. It is difficult to observe tungsten sputtering by spectroscopy with EAST heavily Li-coating wall condition on tungsten divertor region. Fortunately, this result was founded at the end of daily discharges with the weakest of Li-coating. In that situation, the sputtered tungsten, observed by divertor tungsten spectroscopy, entered core plasma easily and thus resulted in the degradation of plasma confinement due to the burst of core radiation. Similar result for Ar seeding were discovered in ASDEX-Upgrade as well [14, 15]. It is deduced that the sputtering of tungsten is mainly ascribed to Ar impurity being ionized in boundary plasma and accelerated to the target due to sheath potential. However, the count of tungsten is still in commissioning because the tungsten and argon signals have an overlap in this wavelength range.

3.2 Different setting of puffing pulse

As is well-known, EAST upgraded its upper divertor into actively-cooled W/Cu PFCs in 2014[16]. To prove the capacity of heat load and find an effective way to control the heat flux on upper divertor target, impurity seeding experiments under USN divertor configuration H-mode condition carried out during 2015 campaign firstly. Injection method is the major factor with regard to the effect of impurity seeding from our

and other devices' experience. Experiment results show that the pulse width, amplitude and repetition frequency of gas puffing, as well as seeding position, had a significant influence on plasma performance[17]. Long pulse and short pulse were set before seeding in USN divertor configuration H-mode plasma. In Shot#57417 and #57423(see Fig. 5), B_t was set at 2.5 T and $I_p=0.4$ MA, and the heating power around 4.3 MW with ICRF of 1.5MW and LHW of 2.8 MW. The Ar impurity had been seeded from upper outboard target at the rate of $2.2\sim 2.7\times 10^{20}$ e⁻/s for 200 ms. During gas puffing, the rise of radiated power measured by AXUV was about 350 kW. So that the heat flux on divertor observed by LP was clearly reduced about 75%. However, the entire plasma energy decreased by less than 5%, and it returned to initial state very quick after gas puffing. The latter shot, as Fig.4 shown, with long pulse of Ar seeding set at the rate of $0.9\sim 1.4\times 10^{20}$ e⁻/s for 1000ms, this H-mode plasma lost 32 kJ energy, 35% of whole plasma stored energy, ascribed to the excessive loss of radiated power, and then H- to L-mode transition was observed. The main reason is Ar impurity enters the plasma core region easily and Ar is a quite strong radiator in electron temperature T_e at 2 to 3 hundreds eV. It indicated that using a single continuous long pulse Ar seeding is possibly of great risk when feedback controlled divertor gas puffing system is still underconstructed in EAST.

3.3 Preliminary results of Ne seeding experiment

To compare with Ar seeding, Ne seeding experiment was carried out in EAST 2016 spring campaign. Moreover, this is first time we take Ne as the radiator on EAST machine after EAST upgraded its upper tungsten divertor and divertor gas puffing system. In these L-mode USN divertor configuration discharges with 2.0 MW LHW heating, and the conditions are: $I_p=0.4$ MA, $B_t=2.3$ T, line integrated density $n_e\approx 2.2\times 10^{19}$ m⁻³. According to the cooling factor of Ne, a small amount of pure Ne was seeded from upper divertor outer target. After Ne seeded, the plasma electron temperature on upper divertor outer target decreased by less than 5 eV (see Fig. 6). There is a peak of Ne's cooling factor L_z in 20-40 eV[18], which is the electron temperature in the divertor region during this discharge. The experiment proved the efficiency of Ne impurity in reducing the heat load. In addition, compared with Ar seeding, as Fig.7 shows, the rise of radiation more located in the divertor region under similar parameters' condition and the same gas puff position. The experimental result on EAST shows that Ar seeding is prone to a core radiation compared to Ne seeding that Ar impurity enter core plasma more easily and its cooling factor much higher than Ne's in the plasma core region. Thus, Ne impurity will be preferred in the future radiative divertor experiment.

4. Summary

Radiative divertor experiments with Ar seeding have been carried out during recent EAST campaigns. The Ar mixture and Ne as the radiators were seeded from the divertor region under the different confinement modes and divertor. Experiments proved the high efficiency of Ar and Ne impurities in reducing heat load and particle flux. However, PFCs sputtering, especially tungsten sputtering, and core plasma contamination were observed with Ar seeding. Ar is also a strong radiator for EAST, and excessive Ar impurity will easily cause the burst of radiation and lead a great loss of stored energy in core plasma, which is unfavorable for long pulse high performance operation. Compared to Ar seeding, Ne shows advantages on distribution of radiation rise and control of core plasma contamination.

Thus, in the future, Ne will be used as the radiator preferentially. Not only Ne impurity but also other impurities such as nitrogen (without Li coating) will be tested for steady long-pulse partial detached plasma. Moreover, according to the result of setting different seeding pulse, modulation method of gas puffing will be tried out in future EAST campaign.

Acknowledgements

This work was supported by the National Natural Science Foundation of China No.11575242, No.11305214 and National Magnetic Confinement Fusion Science Program No. 2013GB105002.

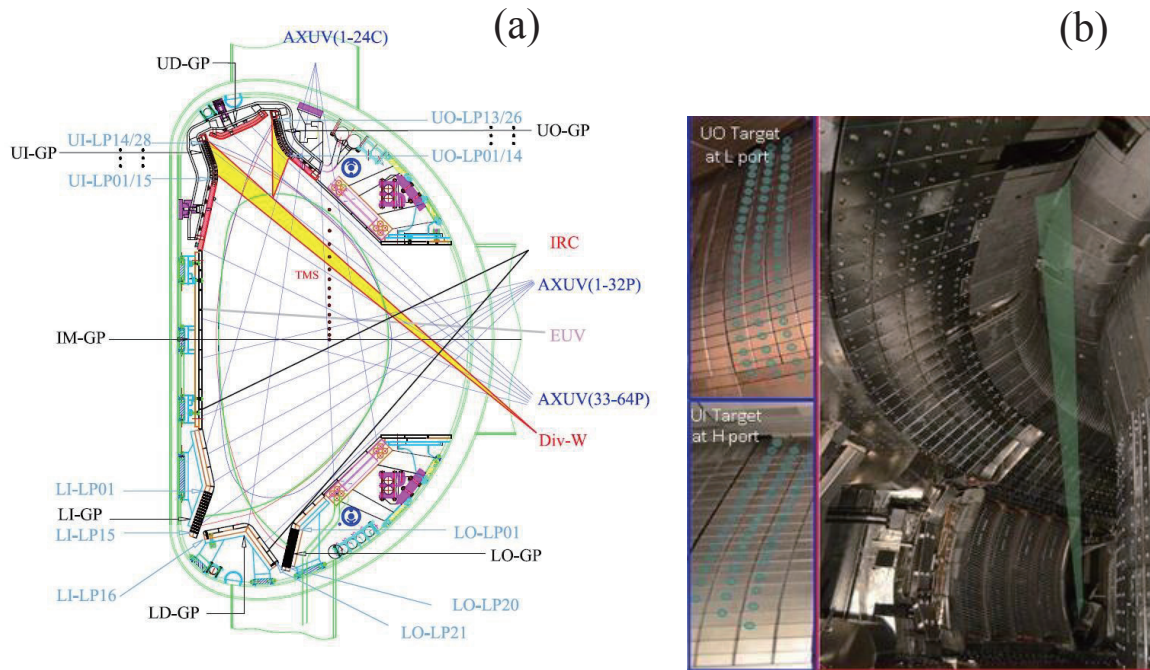


Figure 1. (a) Poloidal cross section of EAST showing relevant diagnostics of the experiments and divertor gas puff locations. AXUV- absolute extreme ultraviolet bolometer arrays; U(L)I-upper(lower) inboard divertor; U(L)O-upper(lower) outboard divertor; U(L)D- upper (lower) divertor dome; GP-gas puff inlet; IM- inner midplane; TMS-Thomson scattering; IRC-infrared camera; EUV- extreme ultraviolet spectrometer; Div-W: divertor tungsten spectroscopy. (b) EAST first wall and observable region of divertor tungsten spectroscopy.

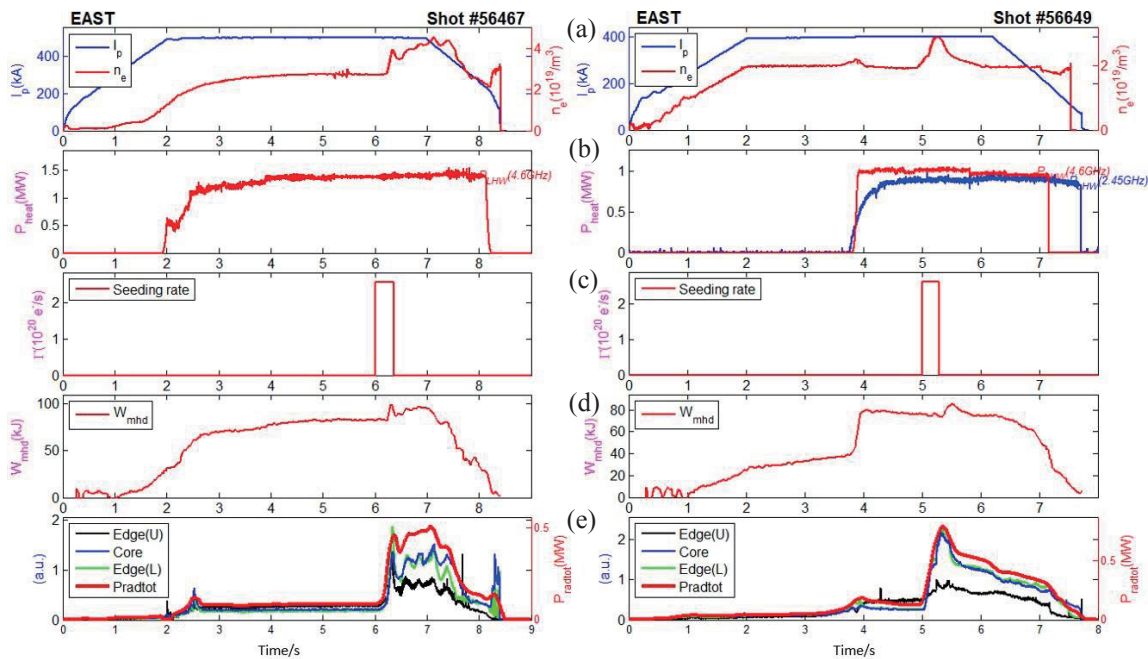


Figure 2. Time evolution of Shot#56467 and Shot#56649. (a) Line intergrated density (n_e) and plasma poloidal current (I_p). (b) Heating power: 2.45GHz LHW, 4.6GHz LHW and ICRF. (c) Impurity seeding rate. (d) Stroed energy of plasma: W_{mhd} (e) Core, upper divertor, lower divertor region line intergrated radiation and total radiation power.

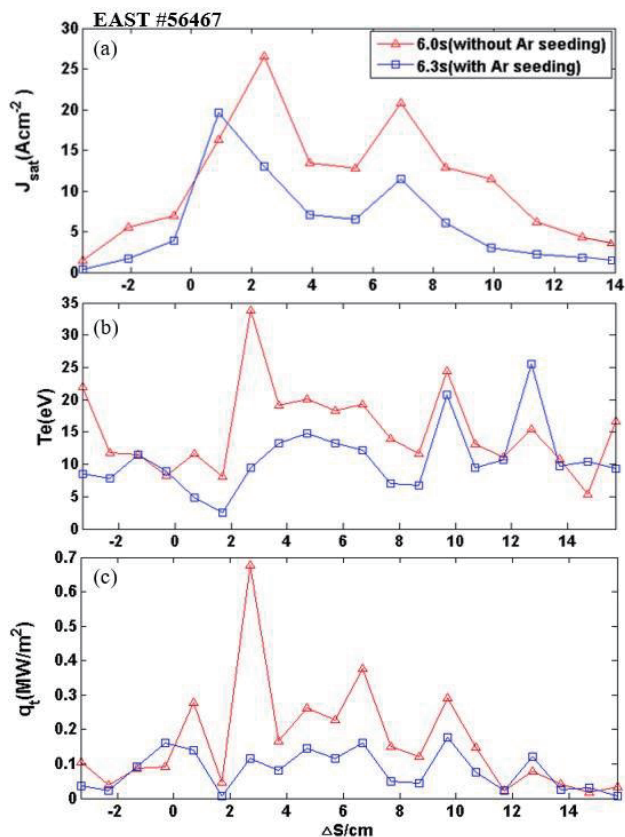
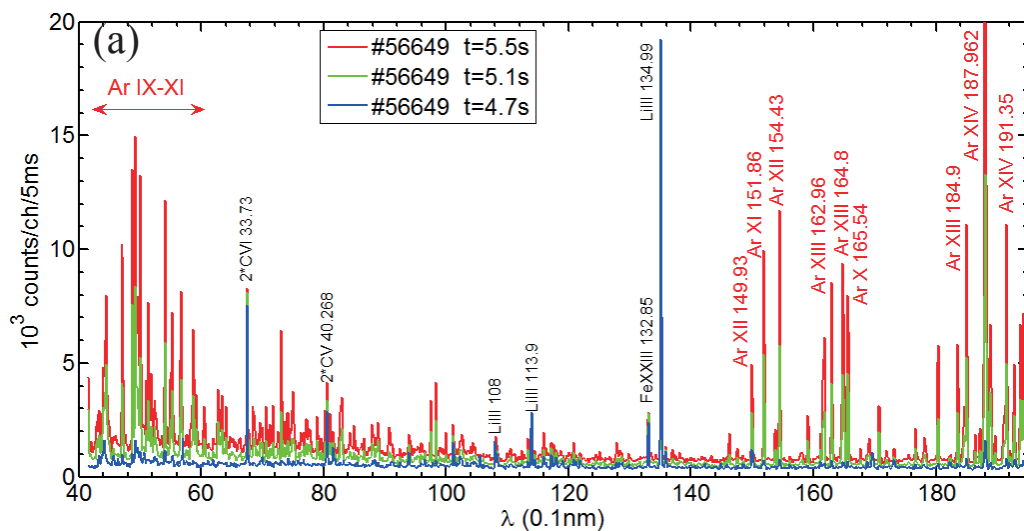


Figure 3. Shot #56467: Langmuir probe measurements on lower divertor target. (a) saturation ion current (b) electron temperature (c) vertical heat flux onto the target.



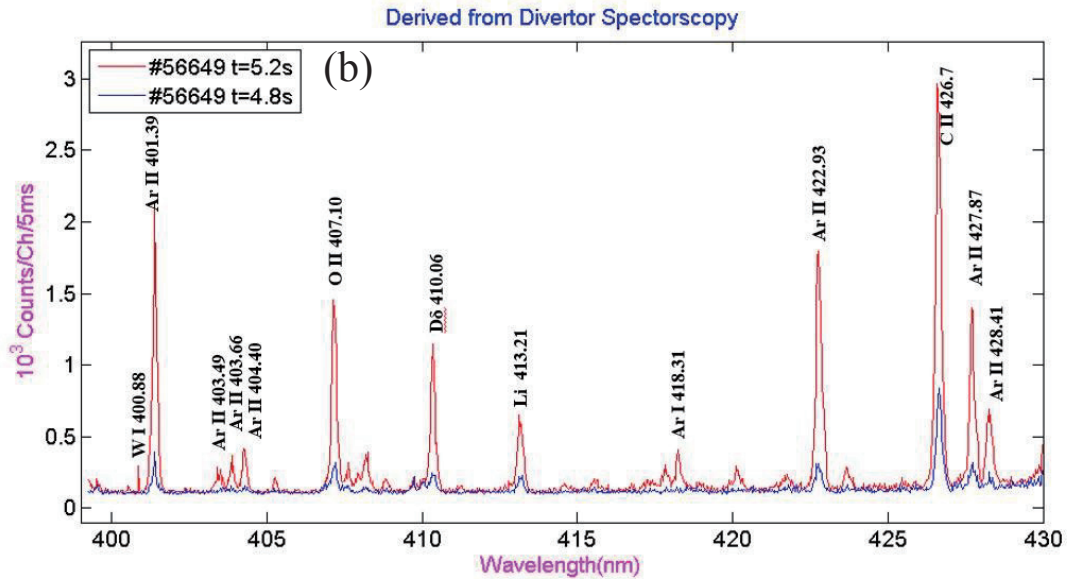


Figure 4. (a) Impurities at the mid-plane observed by EUV spectrometer before (4.7s), during (5.1s), and after (5.5s) Ar seeding (b) Impurities in upper divertor region observed by div-W spectroscopy without Ar seeding (4.8s) and with Ar seeding (5.2s).

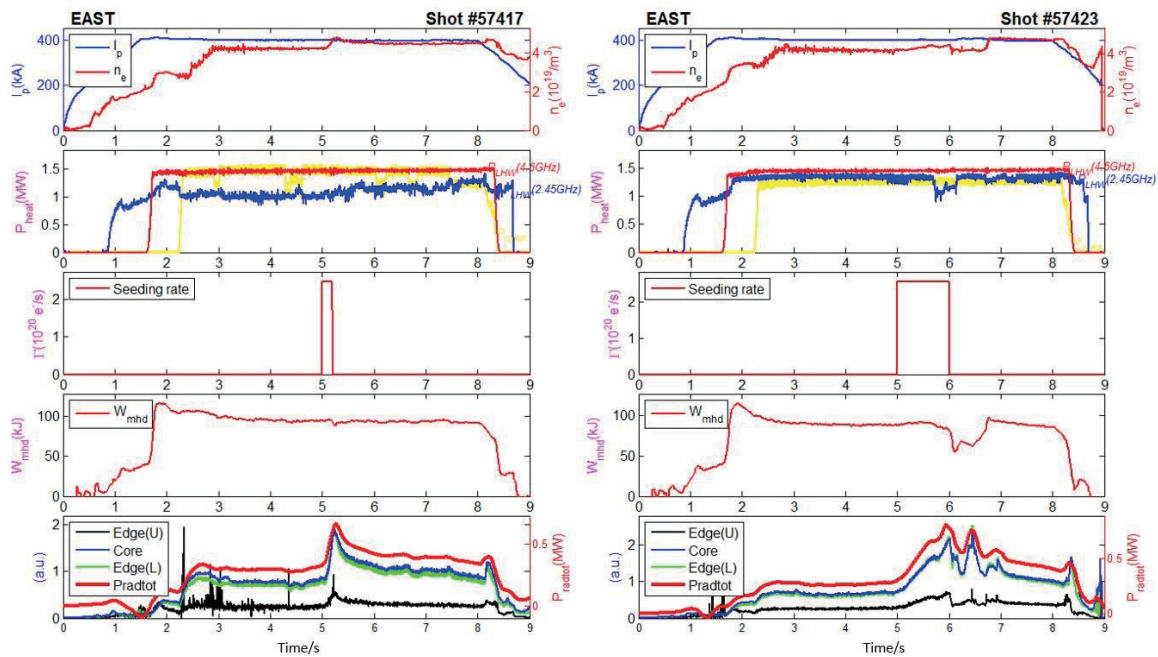


Figure 5. Time evolution of plasma parameters for Shot#57423. Same parameters as shown in Fig. 2.

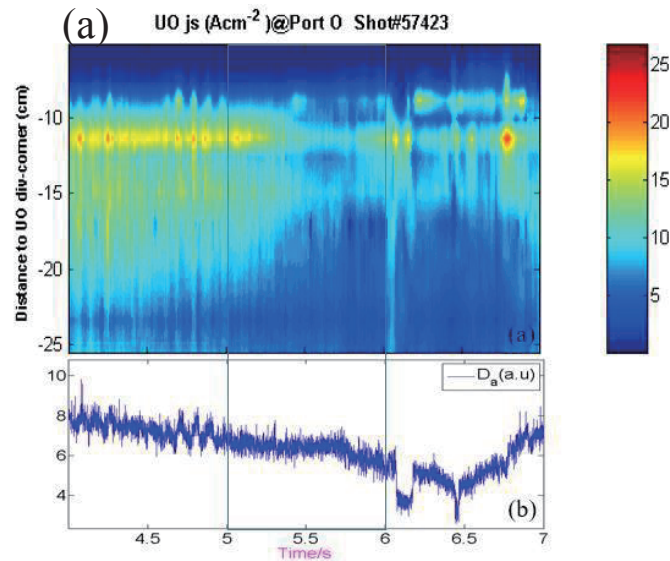


Figure 6. (a) Distribution of saturation ion current measured by Langmuir probe in upper divertor region (b) D_α signal.

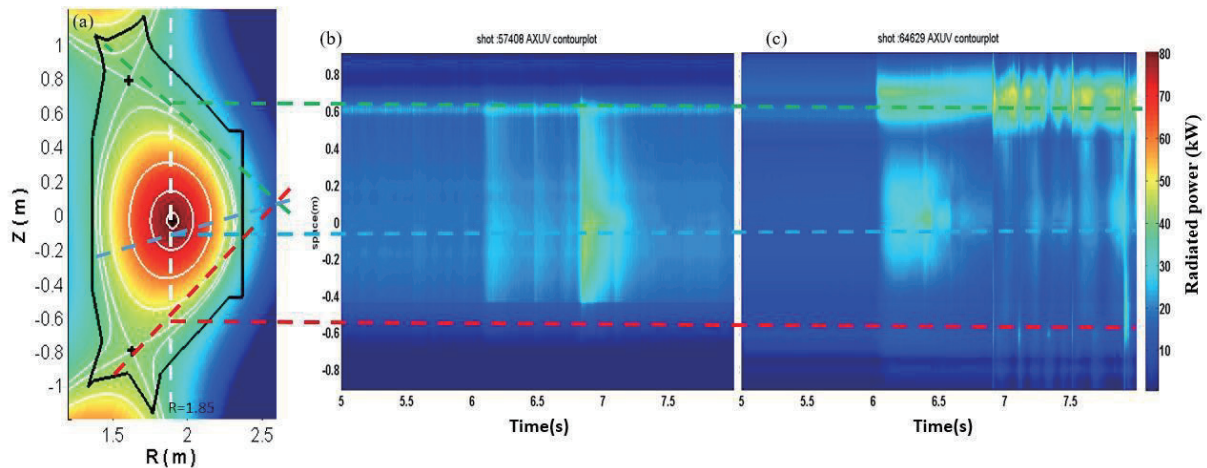


Figure 7. Radiation profile for Shot#57408(Ar seeding) and Shot#64629(Ne seeding). The dotted line in (a) represents the locations in (b) and (c).

References

- [1] F. Reimold, M. Wischmeier, M. Bernert, S. Potzel, A. Kallenbach, H.W. Müller, B. Sieglin, U. Stroth, Divertor studies in nitrogen induced completely detached H-modes in full tungsten ASDEX Upgrade, *Nuclear Fusion* 55 (2015) 033004.
- [2] A. Kallenbach, M. Bernert, M. Beurskens, L. Casali, M. Dunne, T. Eich, L. Giannone, A. Herrmann, M. Maraschek, S. Potzel, F. Reimold, V. Rohde, J. Schweinzer, E. Viezzer, M. Wischmeier, Partial detachment of high power discharges in ASDEX Upgrade, *Nuclear Fusion* 55 (2015) 053026.
- [3] G.P. Maddison, C. Giroud, B. Alper, G. Arnoux, I. Balboa, M.N.A. Beurskens, A. Boboc, S. Brezinsek, M. Brix, M. Clever, R. Coelho, J.W. Coenen, I. Coffey, P.C. da Silva Aresta Belo, S. Devaux, P. Devynck, T. Eich, R.C. Felton, J. Flanagan, L. Frassinetti, L. Garzotti, M. Groth, S.

- Jachmich, A. Jarvinen, E. Joffrin, M.A.H. Kempnaars, U. Kruezi, K.D. Lawson, M. Lehnen, M.J. Leyland, Y. Liu, P.J. Lomas, C.G. Lowry, S. Marsen, G.F. Matthews, G.K. McCormick, A.G. Meigs, A.W. Morris, R. Neu, I.M. Nunes, M. Oberkofler, F.G. Rimini, S. Saarelma, B. Sieglin, A.C.C. Sips, A. Sirinelli, M.F. Stamp, G.J. van Rooij, D.J. Ward, M. Wischmeier, J.E. Contributors, Contrasting H-mode behaviour with deuterium fuelling and nitrogen seeding in the all-carbon and metallic versions of JET, *Nuclear Fusion* 54 (2014).
- [4] T. Nakano, J.T. Team, Comparison of Ne and Ar seeded radiative divertor plasmas in JT-60U, *Journal of Nuclear Materials* 463 (2015) 555-560.
- [5] D.S. Wang, H.Y. Guo, Y.Z. Shang, K.F. Gan, H.Q. Wang, Y.J. Chen, S.C. Liu, L. Wang, W. Gao, L.Y. Xiang, Z.W. Wu, G.N. Luo, E. Team, Radiative Divertor Plasma Behavior in L- and H-Mode Discharges with Argon Injection in EAST, *Plasma Science & Technology* 15 (2013) 614-618.
- [6] H.Y. Guo, J. Li, X.Z. Gong, B.N. Wan, J.S. Hu, L. Wang, H.Q. Wang, J.E. Menard, M.A. Jaworski, K.F. Gan, S.C. Liu, G.S. Xu, S.Y. Ding, L.Q. Hu, Y.F. Liang, J.B. Liu, G.N. Luo, H. Si, D.S. Wang, Z.W. Wu, L.Y. Xiang, B.J. Xiao, L. Zhang, X.L. Zou, D.L. Hillis, A. Loarte, R. Maingi, Approaches towards long-pulse divertor operations on EAST by active control of plasma-wall interactions, *Nuclear Fusion* 54 (2014) 013002.
- [7] H.Y. Guo, J. Li, B.N. Wan, X.Z. Gong, Y.F. Liang, G.S. Xu, X.D. Zhang, S.Y. Ding, K.F. Gan, J.S. Hu, L.Q. Hu, S.C. Liu, J.P. Qian, Y.W. Sun, H.Q. Wang, L. Wang, T.Y. Xia, B.J. Xiao, L. Zeng, Y.P. Zhao, P. Denner, J.R. Ferron, A.M. Garofalo, C.T. Holcomb, A.W. Hyatt, G.L. Jackson, A. Loarte, R. Maingi, J.E. Menard, M. Rack, W.M. Solomon, X.Q. Xu, M. Van Zeeland, X.L. Zou, Recent advances in long-pulse high-confinement plasma operations in Experimental Advanced Superconducting Tokamak), *Physics of Plasmas* 21 (2014) 056107.
- [8] B.N. Wan, J.G. Li, H.Y. Guo, Y.F. Liang, G.S. Xu, L. Wang, X.Z. Gong, A. Garofalo, E.T. Collaborators, Advances in H-mode physics for long-pulse operation on EAST, *Nuclear Fusion* 55 (2015) 20.
- [9] W. Wang, Upgrade of gas puffing system and preliminary results in EAST radiative divertor experiment, University of Chinese Academy of Sciences, 2015.
- [10] J.C. Xu, L. Wang, G.S. Xu, e. al., Upgrade of Langmuir probe system for actively water-cooled, ITER-like tungsten mono-block divertor on the EAST superconducting tokamak, submitted to *Rev.Sci.Instrum* (2016).
- [11] T. Ming, W. Zhang, J. Chang, J. Wang, G.S. Xu, S. Ding, N. Yan, X. Gao, H.Y. Guo, Improvement of divertor triple probe system and its measurements under full graphite wall on EAST, *Fusion Engineering and Design* 84 (2009) 57-63.
- [12] Y.M. Duan, L.Q. Hu, S.T. Mao, P. Xu, K.Y. Chen, S.Y. Lin, G.Q. Zhong, J.Z. Zhang, L. Zhang, L. Wang, Measurement of Radiated Power Loss on EAST, *Plasma Science & Technology* 13 (2011) 546-549.
- [13] L. Zhang, S. Morita, Z. Xu, Z. Wu, P. Zhang, C. Wu, W. Gao, T. Ohishi, M. Goto, J. Shen, Y. Chen, X. Liu, Y. Wang, C. Dong, H. Zhang, X. Huang, X. Gong, L. Hu, J. Chen, X. Zhang, B. Wan, J. Li, A fast-time-response extreme ultraviolet spectrometer for measurement of impurity line emissions in the Experimental Advanced Superconducting Tokamak, *The Review of scientific instruments* 86 (2015) 123509-123509.
- [14] A. Kallenbach, M. Balden, R. Dux, T. Eich, C. Giroud, A. Huber, G.P. Maddison, M. Mayer, K. McCormick, R. Neu, T.W. Petrie, T. Pütterich, J. Rapp, M.L. Reinke, K. Schmid, J. Schweinzer, S. Wolfe, Plasma surface interactions in impurity seeded plasmas, *Journal of Nuclear Materials* 415 (2011) S19-S26.
- [15] A. Kallenbach, M. Bernert, T. Eich, J.C. Fuchs, L. Giannone, A. Herrmann, J. Schweinzer, W. Treutterer, Optimized tokamak power exhaust with double radiative feedback in ASDEX Upgrade, *Nuclear Fusion* 52 (2012) 122003.

- [16] D.M. Yao, G.N. Luo, Z.B. Zhou, L. Cao, Q. Li, W.J. Wang, L. Li, S.G. Qin, Y.L. Shi, G.H. Liu, J.G. Li, Design, R&D and commissioning of EAST tungsten divertor, *Physica Scripta* 2016 (2016) 014003.
- [17] D.S.Wang, Study of divertor plasma physics and impurity injection behavior on EAST, University of Science and Technology of China, 2012.
- [18] A. Kallenbach, M. Bernert, R. Dux, L. Casali, T. Eich, L. Giannone, A. Herrmann, R. McDermott, A. Mlynek, H.W. Müller, F. Reimold, J. Schweinzer, M. Sertoli, G. Tardini, W. Treutterer, E. Viezzer, R. Wenninger, M. Wischmeier, Impurity seeding for tokamak power exhaust: from present devices via ITER to DEMO, *Plasma Physics and Controlled Fusion* 55 (2013) 124041.

Ripple and error field analysis due to applying blanket with RAFM steel in CFETR

Songlin Liu^{1,2}, Guanying Yu², Xufeng Liu¹

¹ Institute of plasma physics, Chinese academy of sciences, Hefei 230031, China

² University of science and technology of China, Hefei 230026, China

Abstract

CFETR (Chinese Fusion Engineering Tokamak Reactor) is an important intermediate device between ITER and DEMO. The WCCB (Water Cooled Ceramic Breeder) blanket, whose structural material is made of RAFM (reduced activation ferritic/martensitic) steel, is one of the candidate conceptual blanket design for CFETR. An analysis of ripple and error field induced by RAFM steel used in WCCB is evaluated with the method of Static Magnetic Analysis in the ANSYS code. Significant additional magnetic field is produced by blanket and it leads to an increased ripple field. Maximum ripple along the separatrix line reaches 0.53% which is higher than 0.5% of the acceptable design value. Simultaneously, one blanket module is taken out for heating purpose and the resulting error field is calculated to be seriously against the requirement.

1. Introduction

The Chinese Fusion Engineering Test Reactor (CFETR) is a tokamak device that is proposed to be built in China as an intermediate stage between ITER and DEMO[1]. The most significant goal of CFETR is to get the steady state in high-performance plasma. Minimization of toroidal field ripple (TFR) and error field is an important factor to achieve the mission of high-performance plasma in CFETR.

During CFETR conceptual design, the TFR amplitude in CFETR has been calculated with the ANSYS code by Lei Wang et al[2] whose model only contains TF coils and ferromagnetic inserts installed in the vacuum vessel. The results show that TFR amplitude at the edge of plasma in CFETR is approximately 0.3%, which satisfies the design specification. However, the result did not take into account a large perturbation of the toroidal field (TF) at some space points induced by the tritium breeding blanket which is made of RAFM (reduced activation ferritic martensitic) steel as structural material. It is necessary to evaluate the ripple and error Field induced by blanket in CFETR because the blanket employs a large amount of RAFM steel which is ferromagnetic.

In this paper, the TF ripple field induced by blanket in CFETR is investigated based on WCCB blanket[3] design with the ANSYS code. The blanket refers to Water Cooled Ceramic Breeder blanket which is one of candidates[4] for CFETR. Furthermore, error field is evaluated when one blanket module is assumed to be taken out for the purpose of diagnostics or heating plasma. The resulting error field called B_{3-mode} is found to violate the requirement and need to be compensated with some methods.

2. The CFETR configuration and WCCB blanket

For CFETR, the major radius is 5.7m, the minor radius is 1.6m, plasma current is 8~10MA. CFETR has 16 large D-shape toroidal coils which determine 16 sectors of each 22.5° for blanket system. Each coil consists of 132 circuits with a current of 67.4kA. For WCCB blanket configuration, each sector along

toroidal direction is divided into 2 inboard and 2 outboard blanket segments. Along poloidal direction, each inboard segment has 4 modules and each outboard segment has 6 modules. Each module has different sizes in order to fit the plasma configuration. The configuration of CFETR in one sector is shown in Fig.1.

For the current version of WCCB blanket, each module box is enclosed by first wall (FW), Side wall (SW) and back plate (BP). The blanket box is divided into several breeding zones and it is enhanced by cooling plates (CP) and stiffening plates (SP). Fig.2 shows main structure scheme of typical blanket module[5]. RAFM (e.g. F82H, CLAM) steel is employed as structural material.

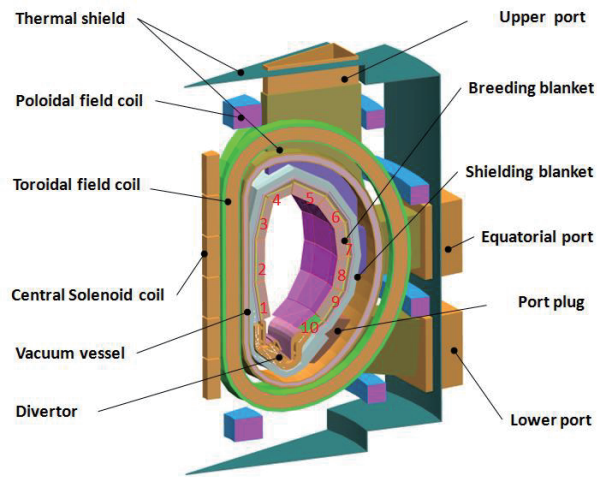


Fig.1. The configuration of CFETR with WCCB blankets

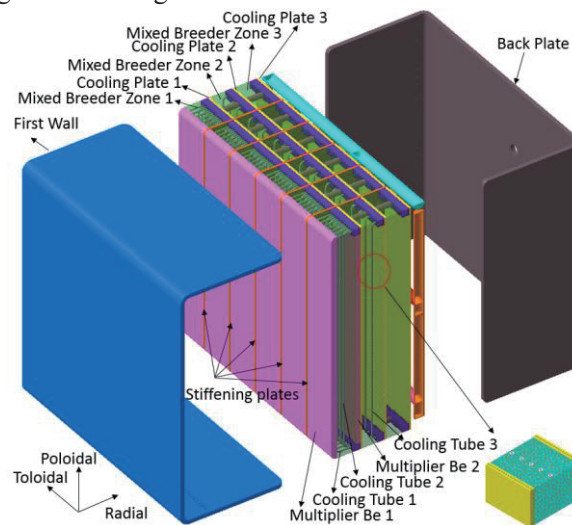


Fig.2. Schematic diagram of typical WCCB blanket module

3. Methodology and model

The 3-D scalar potential approach in ANSYS code was applied because it was suitable for ferromagnetic analysis[6-7].

The sixteen D-shaped toroidal field coils were modeled using source circuitual element according to toroidal field coil (TFC) geometry. Each coil consists of 132 circuits with a current of 67.4kA. According to WCCB blanket geometry, one finite element model of 22.5 toroidal angle was developed. Each blanket module was modeled in detail by the element of Solid96, including pebble beds, first wall (FW), cooling plates (CP), back plates (BP), stiffening plates (SP), and side wall (SW). Void was also modeled by the

element of Solid96. A layer of element Infi111 with far-field symbol was used to define the far-field boundary at the outermost of the whole model. The cyclic symmetry condition was assumed and modeled by coupling all DOFs at each node of low surface ($\phi = -11.25^\circ$) and high surface ($\phi = 11.25^\circ$). Fig.3 shows the finite element model of TFC and the blanket.

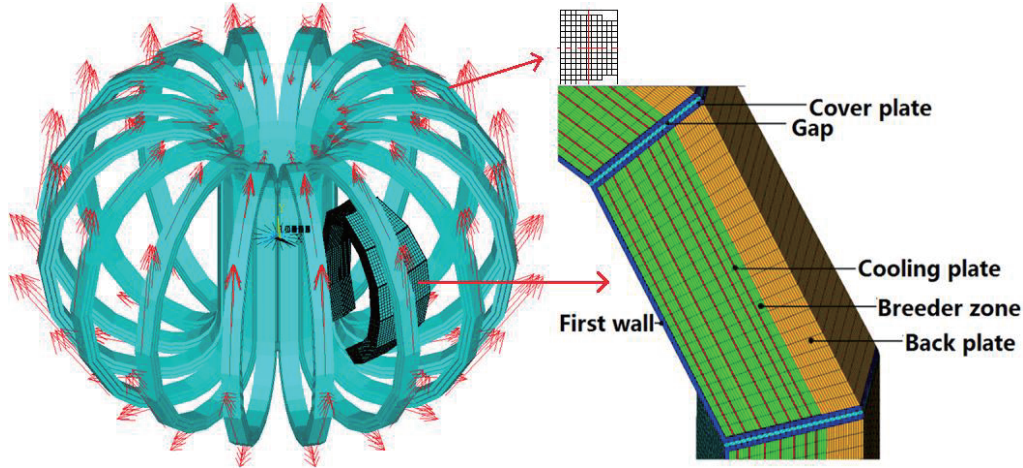


Fig.3. The ANSYS model of toroidal coil and blanket

The properties of RAFM steel refer that of F82H steel with saturated magnetization of approximate 1.7 T and its B-H curve is shown in Fig.4. The relative permeability of other materials, i.e. breeder, was all defined as 1.

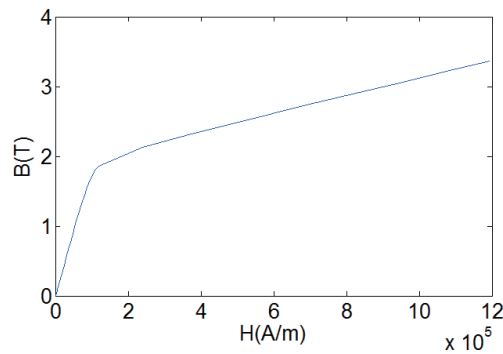


Fig.4. B-H curve of F82H

4. Calculation of magnetic field

Ferromagnetic material in blanket can produce an additional magnetic field and significantly increase the magnetic field in blanket area. Fig.5 shows that magnetic field in blanket area is unnaturally enhanced compared with previous studies[4]. In contrast to other areas of blanket, there is a more significant increase in back plate of inboard blanket, probably due to its larger mass of RAFM than that of other parts of the blanket.

Case of a model without blanket is also done for the purpose of comparison. Toroidal magnetic field distribution between two TFCs is similar to sine wave in a wave circle in plasma area when blanket is not applied. It comes to a difference after the installation of blanket, as shown in Fig.6, for distribution of toroidal magnetic field becomes irregular instead of a sine wave circle, especially when the position is close to blanket. And it can also be seen that the result of our calculation is not exactly symmetrical, which means the existence of computational error in our model, especially in the case which has the blanket. That is

because ANSYS applies certain physical assumptions in iron regions[7]. The assumptions may not be good approximations when the iron is heavily saturated and violated assumptions may degrade accuracy. However, since the magnitude of computational error ($\sim 0.0001\text{T}$ in Fig.6(a)) is so small compared with toroidal magnetic field, the effect of this error is negligible.

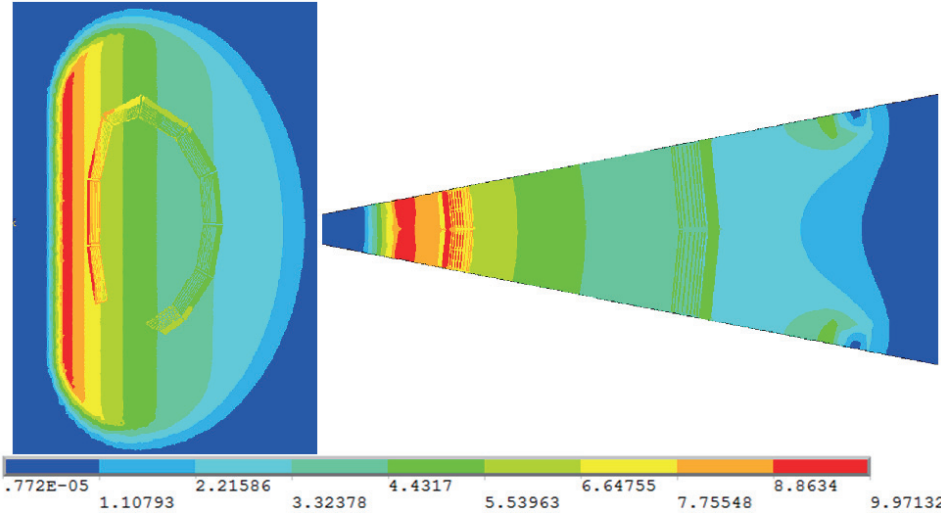


Fig.5. Magnetic field(T) distribution on $\phi = 5.625^\circ$ plane (left) and equatorial plane (right)

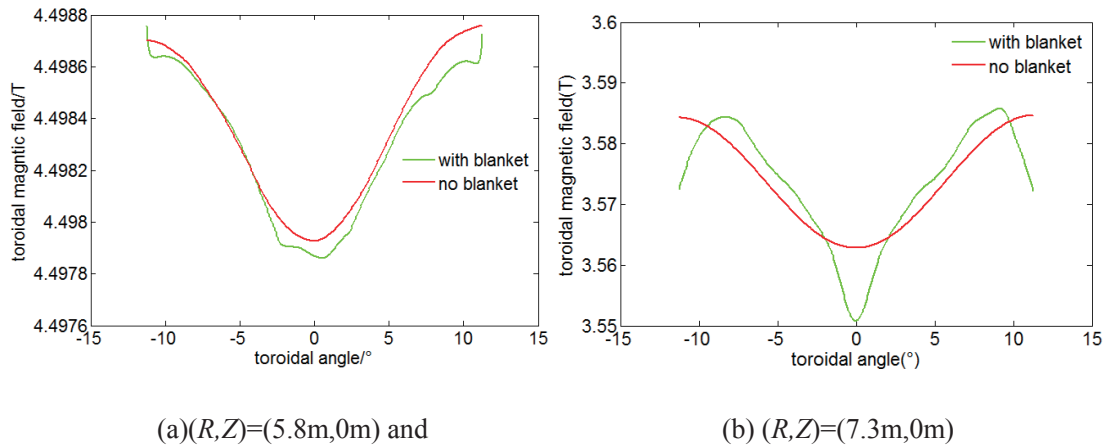


Fig.6: Toroidal magnetic field distribution at (a) $(R,Z)=(5.8\text{m},0\text{m})$ and (b) $(R,Z)=(7.3\text{m},0\text{m})$

4.1 Ripple field analysis

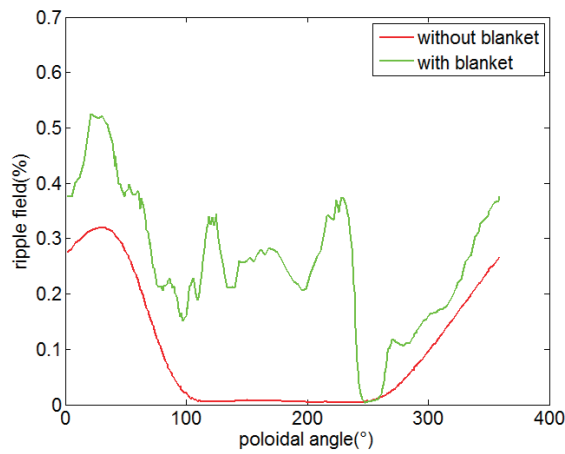
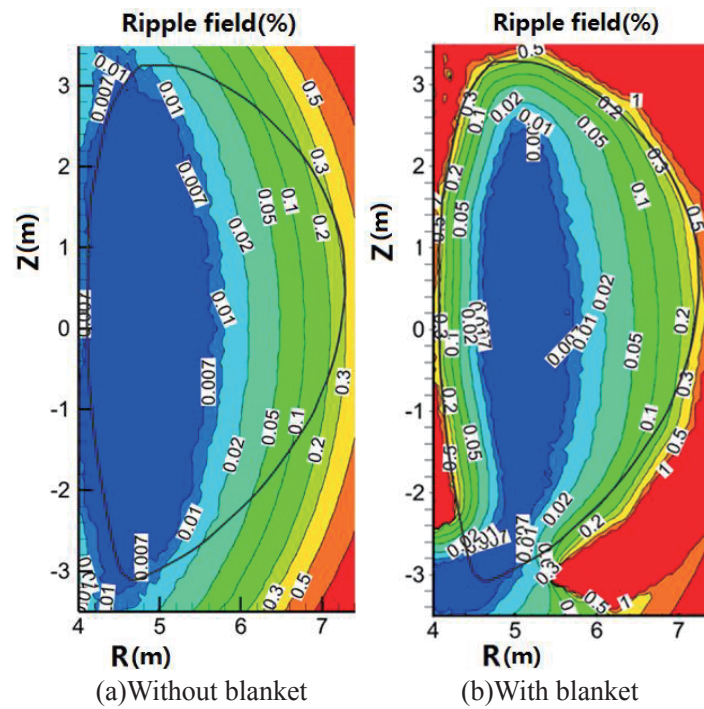
Ripple field is defined as follows:

$$\delta(R,Z) = \frac{B_{tmax} - B_{tmin}}{B_{tmax} + B_{tmin}} \tag{1}$$

where B_{tmax} and B_{tmin} are the maximum and minimum values of the toroidal magnetic field on the circle with coordinates (R,Z) , respectively.

The requirement of physical design for TFR amplitude should be less than 0.5% in the plasma area[4]. The requirement is satisfied when blanket is not applied (Fig.7(a)). However, after the installation of blanket, the requirement is slightly challenged. Ripple field bigger than 0.5% exists along the separatrix

line of plasma (Fig.7(b)). Fig.7(c) shows TFR distribution on the separatrix line. TFR on the separatrix line is more significantly enhanced near inboard blanket ($100^\circ < \text{poloidal angle} < 250^\circ$). However, the largest value of TFR, which reaches 0.53%, locates at $(R,Z)=(7.28\text{m},0.63\text{m})$ near outboard blanket.



(c) TFR amplitude along the separatrix of plasma
 Fig.7. Ripple field distribution in plasma zone

4.2 Error field analysis

Magnetic field produced by ferromagnetic material on $q=2$ magnetic surface is very low. However, this magnetic field represents an error field, a perturbation of axial symmetry of the tokamak magnetic field, and in spite of its low value must be evaluated with enough accuracy because it could produce plasma locking and at the end plasma disruptions. However, since the blanket configuration is axial symmetry in toroidal direction, the magnetic field produced on $q=2$ surface is still axial symmetry, which means no error field is produced by blanket.

In fact, the configuration of blanket modules can hardly be axial symmetry. For example, some blanket modules need to be replaced by ports for diagnostics or heating equipment, which results to a source of asymmetry. In this paper, one blanket module (Module 7, whose toroidal center is at 5.625°) is

assumed to be taken out for such purposes and the resulting error field is discussed. First we calculated the magnetic field on $q=2$ surface induced by all magnetized FEM elements in Module 7. Then error field was obtained based on the distribution of the induced magnetic field.

The induced magnetic field has been evaluated in two steps (methods presented in[8]):

i) Evaluation of the induced magnetization of the missing blanket module: the induced magnetization has been evaluated element by element using the FEM model.

ii) Each magnetized FEM element is regarded as an ideal magnetic dipole which is in the center P of that element. The magnetic moment M_P of the dipole is given by:

$$\mathbf{M}_P = (\mathbf{B}_P - \mu_0 \mathbf{H}_P) V \quad (2)$$

where H_P is magnetic field intensity and B_P is magnetic flux intensity, they are related according to B-H curve in Fig.4. All fields are in the FEM element center, μ_0 is the permeability of vacuum and V is the element volume; the field produced by the dipole in P at any position Q of $q=2$ magnetic surface was calculated by the formula.

$$\mathbf{B}(Q) = \frac{1}{4\pi|Q-P|^3} (\mathbf{M}_P + \frac{3(Q-P)(\mathbf{M}_P \cdot (Q-P))}{|Q-P|^2}) \quad (3)$$

A group of scattered points on $q=2$ surface was provided by our CFETR physics team. The detailed data is shown in Appendix A. Fig.8 shows the magnetic field at the missing blanket module and the field perturbation of B_\perp , where B_\perp is the induced magnetic field's component which is perpendicular to the magnetic surface on $q=2$ surface.

As can be seen, field perturbation produced by blanket module is consistent with that produced by TBM in ITER[9]. Basically, Module 7 produces a toroidally aligned, dipole-like magnetic field pattern, which is localized around the module. The magnetic field line emerges from one end of the module and terminates at the other end. The induced error field is then calculated by the following formula[3]:

$$B_{m,n} = \frac{1}{2\pi^2} \int_0^{2\pi} \int_0^{2\pi} B_\perp(\varphi, \theta) e^{(n\varphi - m\theta)} d\theta d\varphi \quad (4)$$

where φ θ is the toroidal angle and θ is the poloidal angle.

Although the (2, 1) mode typically is the most dangerous, recent experiments have shown that other lower order (m, n) modes, most notably the (1,1) and (3,1), exhibit a drag effect on the $q=2$ surface. A more general expression including this influence, based on DIII-D scaling is[3]

$$\frac{B_{3-mode}}{B_{t0}} = \sqrt{0.2B_{1,1}^2 + B_{2,1}^2 + 0.8B_{3,1}^2} < 2 \times 10^{-5} \quad (5)$$

Where B_{t0} is central magnetic field of CFETR

Table 1 shows important statistical properties of $B_{2,1}$ and B_{3-mode} induced by the Module 7. One can tell that the induced error field seriously violates the allowed range and need to be compensated with some methods.

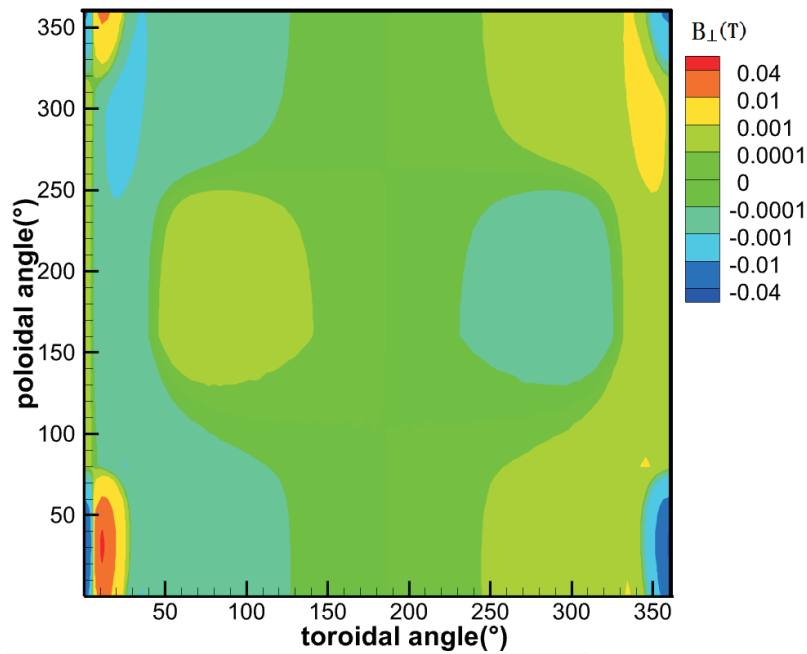
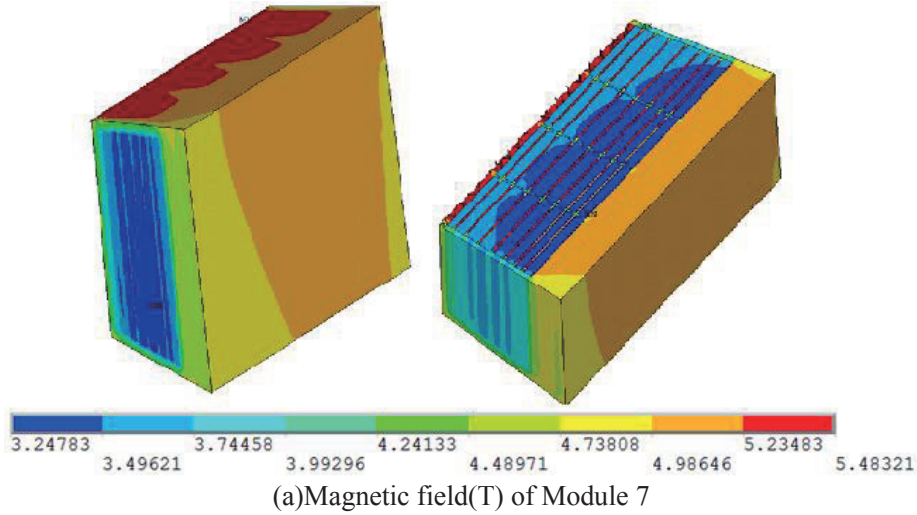


Fig.8. (a) Magnetic field (T) of Module 7 and (b) field perturbation of $B_{\perp}(T)$ on $q=2$ surface

Table.1. Typical error field value($\times 10^{-4}$)

$\frac{B_{1,1}}{B_{t0}}$	$\frac{B_{2,1}}{B_{t0}}$	$\frac{B_{3,1}}{B_{t0}}$	$\frac{B_{3-mode}}{B_{t0}}$
5.213	5.513	10.615	11.22

5. Summary

FEM model with blanket and TF coils is established to calculate ripple field in the paper. After the installation of blanket, TFR along the separatrix slightly violates the requirement of 0.5% and the largest value of TFR equals 0.53% where $(R,Z)=(7.28m,0.63m)$. An entire blanket module was assumed to be replaced by ports for the purpose of heating plasma or diagnostics and the resulting perturbation on magnetic surface using each magnetized FEM element of this blanket module was calculated. The

perturbation is constrained within a small area close to that blanket module and results to a significant error field which needs to be concerned and compensated with some methods.

Acknowledgments

This work was supported by National special project for magnetic confined nuclear fusion energy with Grant No. 2013 GB108004, and the Chinese National Natural Science Foundation under Grant Nos. 11175207, and was partly supported by the JSPS-NRF-NSFC A3 Foresight Program in the field of Plasma Physics (NSFC: No.11261140328, NRF: No.2012K2A2A6000443).

Note

Main work in this paper has been accepted by journal of plasma science and technology.

REFERENCES

- [1] Jiangang Li. 2015, Closing gaps to CFETR Readiness. IAEA TCM 3rd DEMO workshop.
- [2] Wang L, Zheng J, Hao J, et al. 2015, Fusion Engineering and Design, 100: 513-518
- [3] Liu S, Pu Y, Cheng X, et al. 2014, Fusion Engineering and Design, 89: 1380-1385
- [4] Xuebin M, Songlin L, Jia L, et al. 2014, Plasma Science and Technology, 16: 390
- [5] Xiaoman C, Xuebin M, Kecheng J, et al. 2015, Plasma Science and Technology, 17: 787
- [6] Liu S, Liu X, Ma X, et al. 2013, Fusion Engineering and Design, 88: 675-678
- [7] Electromagnetics, Theory Reference, Mechanical APDL, ANSYS Release 11 Documentation
- [8] M. Roccella, F. Lucca. 2008, 3D Magnetostatic Analyses. ITER IDM document, 2FMUUH.
- [9] Oh D K, Jhang H, Lee D K, et al. 2011, Fusion Engineering and Design, 86: 127-133

Steady divertor detachment operation assisted by $m/n=1/1$ RMP field with resonance in the stochastic magnetic field layer of LHD

S.Morita^{1,2}, H.M.Zhang², S.Y.Dai¹, T.Oishi^{1,2}, M.Kobayashi^{1,2}, X.L.Huang¹, Y.Liu² and M.Goto^{1,2}

¹National Institute for Fusion Science, Toki 509-5292, Gifu, Japan

²Graduate University for Advanced Studies, Toki 509-5292, Gifu, Japan

Abstract

In Large Helical Device (LHD), the detached plasma is obtained without external impurity gas feed by supplying the resonance magnetic perturbation (RMP) field with $m/n = 1/1$ mode at outwardly shifted plasma axis position of $R_{ax} = 3.90$ m where the resonance exists in the stochastic magnetic field layer, when the density is increased above a threshold value with hydrogen gas puff. The behavior of edge carbon ions originating in the graphite divertor plates is one of the important key issues to understand the RMP-assisted detached plasma. It is found that the CIII and CIV emissions located in the ergodic layer are drastically increased near the island O-point and in the vicinity of both the inboard and outboard X-points during the RMP-assisted detachment, while those emissions are enhanced only in the vicinity of the outboard X-point in attached plasmas without RMP. It clearly indicates a change in the magnetic field lines connecting to the divertor plates. In contrast, the CVI emission located inside the island entirely decreases the intensity during the detachment, suggesting the enhancement of the impurity screening.

1. Introduction

Heat load mitigation of divertor plates is one of critical issues in the future fusion device such as ITER. The peak power load on ITER divertor plates is estimated to be more than 20 MW/m^2 , which is almost two times higher than the present engineering limit ($\sim 10 \text{ MW/m}^2$). Formation of plasma detachment using working gas or gaseous impurities is a possible solution for the heat load mitigation. The H-mode plasma with complete detachment has been realized without deterioration of the energy confinement in ASDEX Upgrade with feedback-control gas puffing system using neon and deuterium. Total radiation reduction reaches 90% of the heating input power during plasma detachment. In the present tokamaks, however, a steady sustainment of the plasma detachment is difficult because a large heat flux during the edge localized mode (ELM) burst may penetrate the edge high radiation region and reach the divertor plates. In addition, the operation window of the plasma detachment with H-mode is very narrow.

In helical devices another technique for realizing the detached plasma has been attempted in Wendelstein 7-AS (W7-AS) and Large Helical Device (LHD) using the resonant magnetic perturbation (RMP) coils without any external impurity gas puffing. The heat load on divertor plates decreases by a factor of 3–10 during the detachment phase basically without degradation of energy confinement. This method seems to be attractive because the detached plasma with RMP may also mitigate a big ELM burst in tokamaks. Dedicated experiments have been performed in W7-AS and LHD to investigate the operation window for a

steady-state sustainment of high-performance plasma. In W7-AS, it is found that the island size and field line pitch in the island at the plasma edge region influence the stability of detached plasmas. It is also found in LHD that the radial location of $m/n = 1/1$ island supplied by RMP in the plasma edge is a critical factor for successful achievement of the detached plasma. In LHD the detached plasma can be only achieved when the $m/n = 1/1$ island is created in the edge stochastic magnetic field layer. At present, however, the reason why the radial location of $m/n = 1/1$ island is critical for achieving the plasma detachment in LHD is unclear. In addition, the concentration of iron impurity originating in the first wall protection tiles made of stainless steel is very low, in particular, at high-density discharges [1]. Carbon released from graphite divertor plates is thought to be a possible impurity source which can contribute to the high edge radiation during plasma detachment [2], although the energy loss channel in the RMP-assisted detached plasma without external impurity gas is still in open question. Therefore, the study of carbon behaviors during the plasma detachment in LHD is very important to find a cause triggering the detachment transition.

2. Radial position of $m/n=1/1$ island supplied by RMP coils

The magnetic field for plasma confinement in LHD is basically produced by two superconducting helical coils with poloidal and toroidal pitch numbers of $l = 2$ and $n = 10$, while three pairs of superconducting poloidal coils are used for controlling the plasma position and the shape of plasma cross section and cancelling the stray magnetic field. The magnetic axis position is varied at major radius between $R_{ax} = 3.50$ m and 4.00 m in general experiments. The averaged plasma minor radius defined by the last closed flux surface (LCFS) takes the maximum value of 64 cm at $R_{ax} = 3.60$ m. The core plasma in LHD is always accompanied by a stochastic magnetic layer formed outside the LCFS, which is originated in the presence of higher order Fourier components in the magnetic field created by the helical coils. Since the magnetic islands with different mode numbers are overlapped each other in the ergodic layer, the magnetic field structure becomes entirely three-dimensional. The magnetic field structure in the stochastic magnetic field layer is very different as a function of magnetic axis position. The thickness of the stochastic magnetic field layer, λ_{erg} , has the biggest value in the inboard edge X-point of the horizontally elongated plasma cross section ($\phi = 18^\circ$) at $R_{ax} = 3.90$ m configuration, e.g. $\lambda_{erg} \sim 60$ cm, while the magnetic field lines connecting to the divertor plates also becomes dominant in the outboard side. A lot of magnetic field lines with shorter L_c ($12 \leq L_c \leq 25$ m) appear in the vicinity of the outboard X-point together with the divertor legs in the $R_{ax} = 3.90$ m configuration [3].

Additional ten pairs of normal conducting coils to create a big magnetic island with $m/n=1/1$ poloidal and toroidal modes in the plasma edge, which are now called resonant magnetic perturbation (RMP) coils, are installed at the top and bottom in the LHD. The RMP coil system was originally used for the local island divertor experiment to demonstrate an efficient particle exhaust. As the island size can be easily controlled by the coil current, the maximum RMP coil current of $I_{coil} = 3340$ A is used in the present study to trigger the divertor detachment. The edge magnetic field structure with $m/n=1/1$ island is then kept constant during the discharge by presetting the coil current.

Radial profiles of the rotational transform ($\nu/2\pi$) in LHD are shown in Fig. 1 as a function of minor radius (ρ) for plasma axis positions of $R_{ax} = 3.60, 3.75$ and 3.90 m. The $\nu/2\pi$ profile becomes gradually

flat when the magnetic axis shifts outwardly. According to this change, the radial position of $\iota/2\pi = 1$ also moves outside, i.e. $\rho = 0.93$ inside LCFS ($\rho = 1$) at $R_{ax}=3.75$ m and $\rho = 1.03$ just inside the ergodic layer at $R_{ax} = 3.90$ m. In the case of $R_{ax} = 3.90$ m, however, the RMP coil has in principle no clear resonance to $m/n=1/1$ mode because of stochastic magnetic field lines in the ergodic layer, while a considerably big island can be created at the plasma edge in the $R_{ax}=3.60$ and 3.75 m configurations.

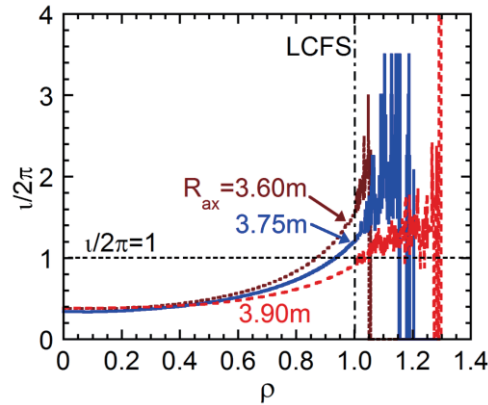


Fig. 1 $\iota/2\pi$ profile as a functions of minor radius (ρ) for $R_{ax} = 3.60, 3.75$ and 3.90 m. LCFS position is indicated with a dashed-dotted line.

3. RMP-assisted plasma detachment at $R_{ax}=3.90$ m in LHD

Vertical profiles and 2-D distributions of CIII–CVI are also studied in attached and detached plasmas at $R_{ax} = 3.90$ m configuration. Typical waveform of NBI discharges without (solid line) and with (dashed line) RMP at $R_{ax} = 3.90$ m and $B_t = 2.54$ T is shown in Fig. 2. The discharges initiated with ECH at $t = 3.0$ s are maintained with n-NBIs for 5 s at $t = 3.3 - 8.3$ s. In the discharge without RMP, the external gas feed is not utilized to avoid the radiation collapse at high density range. The line-averaged density and central electron temperature roughly keep constant, i.e. ($n_e \sim 5 \times 10^{13} \text{ cm}^{-3}$ and $T_{e0} \sim 1.2$ keV, during the discharge flattop at which the 2-D distribution is measured with the EUV_Long2 spectrometer. The ion saturation current, I_{is} , measured with Langmuir probe array embedded in the divertor plates at #6-O is constant at $I_{is} = 0.17$ A during the discharge. The effective plasma radius denoted with a_{99} shown in Fig. 14(f) is also constant at $r_{eff} = 0.55$ m during the discharge, indicating unchanged plasma volume. Here, the value of a_{99} often used in LHD is defined by a plasma radius in which 99% of the total plasma energy is confined. The effective plasma radius is then calculated based on the T_e and n_e profiles from Thomson scattering diagnostic.

When the RMP is supplied, the discharge changes into an entire different state. The electron density gradually increases with gas puffing and reaches the density threshold at which the discharge condition drastically changes. As shown in Fig. 14(e), the ion saturated current is suddenly decreased by 60% at $t = 5.1$ s denoted with vertical dotted line when the density meets the threshold, it keeps the low value until the end of discharge, indicating a specific feature of the plasma detachment. In the present discharge the density threshold is $n_e \sim 5 \times 10^{13} \text{ cm}^{-3}$, while it slight depends on the NBI input power. After the transition into the plasma detachment, the electron density continues to increase until $t = 6.3$ s and saturates at $n_e \sim 12 \times 10^{13} \text{ cm}^{-3}$. The central electron temperature start to decrease after the detachment transition reflecting the density increase and finally stays at $T_{e0} \sim 0.8$ keV. In contrast, the stored energy still continue to increase

even after the detachment transition and behaves similar to the density. Another specific feature for the detachment transition is appeared in the effective plasma radius. The effective plasma radius of $r_{\text{eff}} = 0.55$ m starts to decrease after the detachment transition. It finally reaches $r_{\text{eff}} = 0.48$ m and keeps the constant reduced plasma radius basically until the end of discharge. The radiation power is also increased and constantly kept a considerably high level during the plasma detachment phase.

The radial profiles of n_e and T_e measured at $t = 7.0$ s in Fig. 2 are shown in Fig. 3 for 3 different configurations, i.e. discharges without RMP (open circles), with 6-O island in detachment (solid circles) and with 7-O island in detachment (solid squares). The radial positions of $\iota/2\pi = 1$ and LCFS are denoted with vertical arrows and vertical dashed lines. The location of $m/n = 1/1$ island is denoted with shaded area. The density in the plasma core largely increases for both the 6-O or 7-O island cases after the detachment transition, which is two times larger than the density before the detachment transition. On the other hand, the temperature in the plasma core at the detachment phase is much lower than that at the attachment phase.

The important thing in the density and temperature profiles is in the effect of island. One of the specific features is observed in the edge density jump. The density increases at the vicinity of island toward the outside. The effect of island is also appeared in the edge temperature profile. Figure 16(c) shows the detailed T_e profile in the edge region. A flattened edge temperature ranging in $10 \leq T_e \leq 20$ eV is clearly seen near the island position. Although the temperature profile at 6-O island is broadened in the inboard side compared to the profile at 7-O island, it seems to be an effect of different deformation in the magnetic surface due to the plasma pressure.

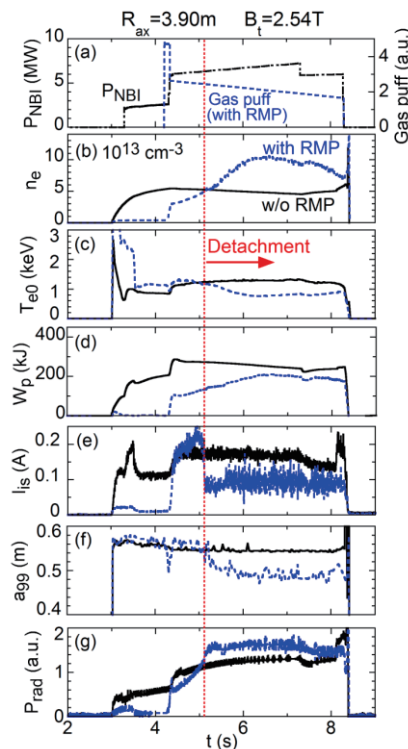


Fig. 2 Time behaviors of (a) NBI port-through power and gas puffing, (b) line-averaged electron density, (c) central electron temperature, (d) stored energy, (e) ion saturated current, (f) effective plasma radius and (g) radiation loss power in discharges at $R_{\text{ax}} = 3.90$ m without RMP (solid line) and with RMP (dashed line). The time of detachment transition is indicated with a dotted line.

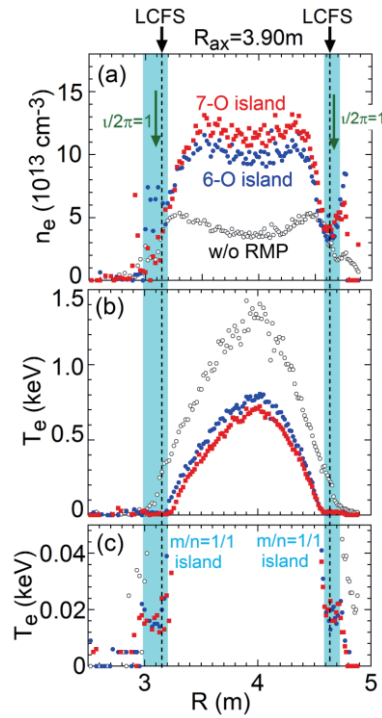


Fig. 3 Radial profiles of (a) n_e , (b) T_e and (c) detailed T_e in discharges at $R_{ax} = 3.90$ m without RMP, with 6-O island and with 7-O island. Radial locations of LCFS and $\nu/2\pi = 1$ are indicated with dashed lines and vertical arrows, respectively. The radial range of $m/n = 1/1$ island is denoted with shaded area.

4. Vertical profiles of carbon ions

The vertical profiles of $\nu/2\pi$ and CIII–CVI in $R_{ax} = 3.90$ m configuration are shown in Fig. 4 for attached plasma without RMP and detached plasmas with 6-O and 7-O islands. The CIII–CVI profiles at $t = 7.0$ s in Fig. 2 are plotted in Figs. 4(d)–(g). The radial position of $\nu/2\pi = 1$ is indicated with dashed line. In $R_{ax} = 3.90$ m configuration it is located just outside the LCFS denoted with vertical arrows. A local flattening of the $\nu/2\pi$ profile appeared near $\nu/2\pi = 1$ position is still visible for both the 6-O and 7-O islands, as shown in Figs. 4(b) and (c), respectively. The radial range of the $\nu/2\pi$ profile flattening is also indicated with shaded area in Figs. 4(b)–(g).

Since the stochastic magnetic field layer outside LCFS is thick in $R_{ax} = 3.90$ m configuration, the volume of low temperature plasma existing in the ergodic layer is large. The CIII emission can be measured with sufficient intensity at $R_{ax} = 3.90$ m, while the CIV, CV and CVI emissions are always strong as shown in Fig. 4(e), (f) and (g), respectively. The CIII and CIV profiles show an enhanced intensity in the vicinity of inboard or outboard side X-points at $-300 \leq Z \leq 300$ mm. The radial position of CIII–CV indicated by the top and bottom edge peaks in the vertical profiles is still outside the $\nu/2\pi = 1$ profile, the CVI is only located inside the $\nu/2\pi = 1$ position.

When the RMP is supplied in $R_{ax} = 3.90$ m configuration and the plasma detachment occurs, the profile of CIII–CVI totally changes due to the formation of $m/n = 1/1$ magnetic island and modification of stochastic magnetic field lines in the ergodic layer. For both the 6-O and 7-O island cases a new edge peak appears in the CIII and CIV profiles at the island location near $Z = \pm 400$ mm, while the original edge peak still remains at $Z \sim 420$ mm. Furthermore, the CIII and CIV emissions are also enhanced in the vicinity of edge X-points

at $-400 \leq Z \leq -250$ mm for the 6-O island case and at $-300 \leq Z \leq 300$ mm for both the 6-O or 7-O island cases. On the other hand, the CV moves inside the plasma at the detachment phase with keeping the same vertical profile shape. This change is basically caused by the change in the T_e profile shown in Fig. 3(b).

It is already known that the CIII and CIV are localized in temperature range of $T_e = 15\text{--}20$ eV. The flattened electron temperature at the island location also ranges in $T_e = 10\text{--}20$ eV in the detachment phase (see Fig. 3(b)), of which the result is also seen in Ref. [2]. This is a main reason why the CIII and CIV intensities are increased at the detachment phase. The intensity of CV is also stronger at the detachment phase as well as the CIII and CIV intensities, while the intensity of CVI decreases. It indicates an enhancement of the impurity screening effect similar to the $R_{ax} = 3.75$ m case. Therefore, it is concluded that the CIII–CV emissions located near the island are selectively enhanced by the effect of supplied RMP field, whereas the CVI emission decreases.

Acknowledgements

This work was partly supported by Grant-in-Aid for Scientific Research (B) 16H04088 and the JSPS-NRF-NSFC A3 Foresight Program in the field of Plasma Physics (NSFC: No.11261140328, NRF: No.2012K2A2A6000443).

References

- [1] S. Morita, C. F. Dong, M. Kobayashi, et. al., Nucl. Fusion **53** (2013) 093017.
- [2] M. Kobayashi, S. Masuzaki, I. Yamada, et. al., Phys. Plasmas **17** (2010) 056111.
- [3] S. Morita, E. H. Wang, et. al., Plasma Phys. Control. Fusion **56** (2014) 094007.

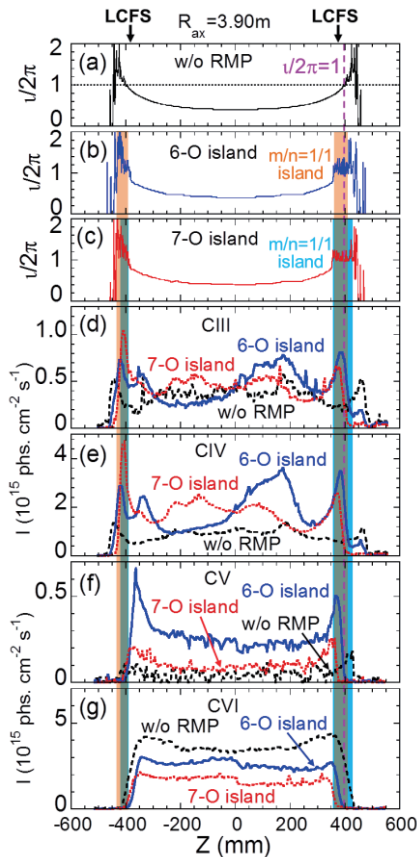


Fig.4 $u/2\pi$ profiles (a) without RMP, (b) with 6-O island, (c) 7-O island and vertical profiles of (d) CIII (386.203 \AA), (e) CIV (384.174 \AA) (f) CV (40.27 \AA) and (g) CVI (33.73 \AA) at the #10-O toroidal location in discharges at $R_{ax} = 3.90$ m without RMP (dashed line), with 6-O island (solid line) and with 7-O island (dotted line). Radial locations of LCFS and $u/2\pi = 1$ are indicated with vertical arrows and dashed line, respectively. The radial ranges of $m/n = 1/1$ island are indicated by shaded area with different colors for 6-O and 7-O island.

The H-mode power threshold to low error fields in KSTAR

Won-Ha Ko^{1*}, H.S. Kim¹, J.H. Lee¹, Y. In¹, H.H. Lee¹, J. Seol¹, Y.M. Jeon¹, K. Ida², S.W. Yoon¹, Y.K. Oh¹, and H. Park³

¹National Fusion Research Institute, Daejeon, Korea

²National Institute for Fusion Science, Toki, 509-5292, Gifu, Japan

³Ulsan National Institute of Science and Technology, Ulsan, Korea

*Email : whko@nfri.re.kr

Abstract

Non-axisymmetric magnetic field is actively employed in ELM control experiments [1, 2]. Generally, non-axisymmetric magnetic field can change pedestal transport and regulate pedestal profiles to stay below the thresholds for the peeling-ballooning instabilities [2]. Non-axisymmetric magnetic field is important role on the pedestal transport and confinement in KSTAR which has low error field ($\delta B/B_0 \sim 10^{-5}$) [3] and low toroidal field ripple ($\delta_{TF}=0.05\%$ [4]), as compared with other similar sized machine. KSTAR has lower H-mode power threshold than DIII-D with similar densities due to the low error field. It is the most important to estimate H-mode threshold power in future machine, ITER which should make low error field machine for saving LH transition power. The H-mode power threshold was obtained for different coil currents of non-axisymmetric field as a function of $\delta B/B_0$ from the experiments of power threshold, confinement, and pedestal transport by non-axisymmetric magnetic field scan in KSTAR. The confinement time and the normalized rotation pedestal were changed by non-axisymmetric magnetic field. Pedestal rotation profiles are of great importance for ITER, in the multiple contexts of confinement enhancement, the source of intrinsic torque in H-mode, and their response to ELMs and to ELM suppression techniques.

1. Introduction

The recent tokamak research has been emphasizing that the H-mode power threshold, which is related in radial electric field and rotation stability, plays an essential role in determining those of the next fusion machine such as ITER [1, 2].

The toroidal rotation behavior was shown from the effect of RMPs in KSTAR associated with the helical magnetics related to the RMPs. The RMPs make not only ELM suppression but also toroidal rotation decrease in KSTAR H-mode plasma. Changes of the toroidal rotation profiles show that there is the edge rotation which is related with the intrinsic torque. The physics model related RMP effect should be further studied. What interaction of RMP with H-mode threshold power torque is in ITER from the toroidal rotation behavior by RMPs. What further advancement in RMPs experiments is in pedestal and further studies are still needed to resolve the mechanism of it.

The effects of non-axisymmetric field on pedestal transport and confinement are important subject to study for better understanding of the underlying physical mechanisms of ELM suppression by

non-axisymmetric field. The more detail scan of H-mode threshold power is required for all range of non-axisymmetric field in KSTAR. It is the most important to estimate H-mode threshold power in ITER which should be made of low error field machine.

In Section 2, a description of H-mode threshold power in KSTAR plasma with low error field and RMPs, followed by the analysis of rotation pedestal, confinement time, and H-factor for the non-axisymmetric magnetic field. In Section 3, the effect of RMPs on ion temperature, toroidal rotation, poloidal shear flow effect on pedestal in pedestal region with RMPs are discussed. A summary is given in Section 4.

2. H-mode threshold power in KSTAR plasma with low error field and RMPs

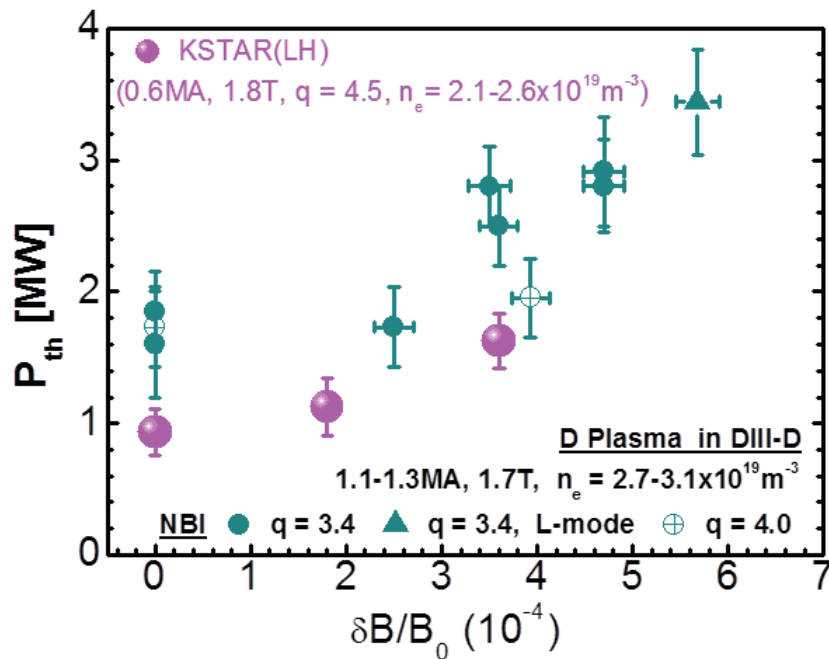


Figure 1. The threshold power for $\delta B/B_0$ in KSTAR shows a similar trend to DIII-D [5] KSTAR has low H-mode power threshold as compared with DIII-D which have similar size but with different error-field because of low intrinsic error field in KSTAR.

Threshold power was scan in low error field and non-axisymmetric magnetic field with $n=1$, 90 phasing in Fig. 1. Figure 1 shows unambiguously that H-mode threshold power increase when non-axisymmetric field increases in KSTAR. We have low threshold power as compared with DIII-D which have similar size but with different error-field because of low intrinsic error field in KSTAR. We showed that KSTAR has lower H-mode power threshold than DIII-D [5] with similar densities due to the low error field in Fig. 1. The threshold powers of KSTAR for $\delta B/B_0$ shows a similar trend to DIII-D under the condition of the same error field.

The target discharges we analyzed in this work are following in KSTAR: the toroidal magnetic field is $B_t =$

1.8 T, the plasma current is $I_p = 600$ kA, the line integrated density $ne = 2.1\sim 2.6 \times 10^{19}$ m⁻³ in L-mode, and the NBI heating power was changed depending on current of non-axisymmetric magnetic field. The L to H-mode transition was determined from Da signal and pedestal of ion temperature and rotation profiles. The net power threshold was determined from the sum of the input power of NBI and ohmic heating in KSTAR. The net threshold power was not considered the beam shine-through and ion orbit losses, the bulk radiated power from the plasma and the time derivative of the diammagnetic energy, dW/dt in KSTAR while that of DIII-D was determined from the sum of the input power (NBI, ECH, and ohmic) minus the beam shine-through and ion orbit losses, the bulk radiated power from the plasma and the time derivative of the diammagnetic energy, dW/dt in DIII-D [4]. If the net threshold power consider the minus terms, we can achieve less H-mode power threshold as compared now.

3. The effect of RMP on ion temperature, toroidal rotations and poloidal shear flow

Both toroidal rotation and ion temperature pedestal dropped by non-axis symmetric magnetic field and poloidal rotation peaked in pedestal foot with H-mode as compared with L-mode in Fig.2. Non-axisymmetric magnetic field reduced the both pedestal of toroidal rotation and ion temperature as shown in Fig. 2. We emphasize ion temperature and rotation profiles structure in L-mode, ELMing H-mode and H-mode with non-axis symmetric magnetic field. Traditional pedestal profiles of KSTAR are shown in Fig. 2. Electric field driven by poloidal rotation is shown in Fig. 2 (c). Large negative radial electric field and its shear are observed at the pedestal in H-mode plasma. Large positive electric field outside LCFS observed is consistent with the measurements in ASDEX and LHD in Fig. 2 (c). The disparity between the width of the toroidal rotation pedestal and that of the ion temperature pedestal is shown in Fig. 2 while conventionally the ion temperature pedestal should be broader, as the residual turbulence in H-mode is expected to drive quite modest levels of turbulent χ_ϕ . Thus, we expect the neoclassical ion thermal diffusivity in the pedestal to exceed the turbulent viscosity [2].

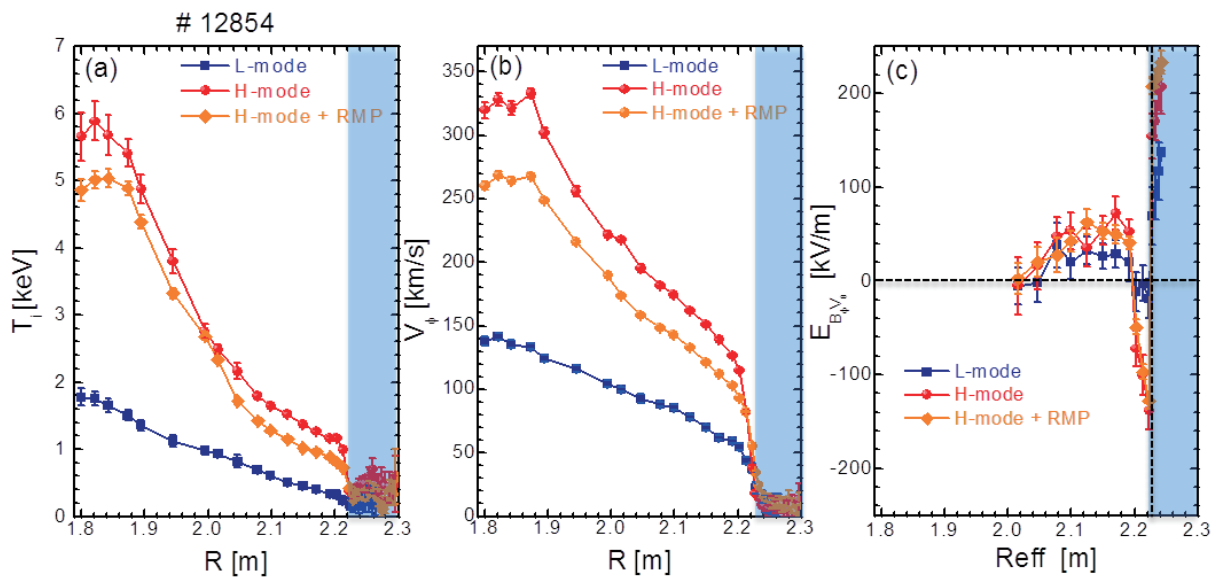


Figure 2. (a)The ion temperature, (b)toroidal rotation profile and (c)radial electric field driven by poloidal rotation

in L-mode, H-mode and H-mode with RMPs

4. Summary and future work

KSTAR has very lower H-mode power threshold than DIII-D with similar size due to the low error field. The H-mode power threshold and H-factor increased with $\delta B/B_0$ while the normalized rotation pedestal decreased and confinement time is almost constant or small degradation. A comparison study of $n=1$ vs $n>1$ δB is expected to address any differences between resonant and non-resonant influences on H-mode power threshold. Non-axisymmetric field reduced the toroidal pedestal rotation as shown in between rotation profiles and a scan of $\delta B/B_0$. The pedestal of ion temperature and toroidal rotation globally reduced and had strong reduction by $n=1$ +90 RMP and toroidal rotation has always globally big drop when $n=1$ and $n=2$ RMP applied before ELM suppression

Poloidal rotation dropped by RMPs and peaked in pedestal foot with H-mode as compared with L-mode. Rotation shear increased in H-mode without 3D field. Ongoing work is concerned primarily with H-mode threshold power to low error field and pedestal transport by non-axis symmetric magnetic field. Transport studies aim to determine the mechanism of non-axis symmetric magnetic field on pedestal.

Acknowledgements

This work was partly supported by the JSPS-NRF-NSFC A3 Foresight Program in the field of Plasma Physics (NSFC: No.11261140328, NRF: No.2012K2A2A6000443).

References

- [1] Jeon, Y.M. et al., Phys. Rev. Lett. 109, 035004 (2012)
- [2] Won-Ha Ko et al., Nucl. Fusion, 55, 083013 (2015).
- [3] Y. In et al, Nucl. Fusion 55 043004 (2015)
- [4] P. Gohil, et. al., Nucl. Fusion 51 103020 (2011)
- [5] S.W. Yoon et al, IAEA-FEC (2014)

Recent Progress in the SUNIST Spherical Tokamak

Y. Tan¹, Z. Gao¹, W. H. Wang¹, A. H. Zhao¹, H. Q. Xie¹, Y. Q. Liu¹, Y. Z. Jiang¹, S. Chai¹, R. Ke¹, H. Zhong¹, W. B. Liu¹, S. Z. Wang¹, G. Li¹, Y. Li¹, Z. Y. Liu¹, X. Y. Guo¹, Y. H. Luo¹, C. H. Feng², L. Wang², X. Z. Yang²

¹Department of Engineering Physics, Tsinghua University, Beijing, China

²Institute of Physics, Chinese Academy of Sciences, Beijing, China

Email of the main author: tanyi@sunist.org

Abstract

The recent experimental campaigns of the SUNIST spherical tokamak were focused on non-stationary plasma discharges, especially the ramp-up and ramp-down phases. The gas puffing was optimized in order to get a better repeatability of high ramp up rate operations. Eddy current distributions and its effects on equilibrium reconstructions were assessed. The properties of high frequency MHD activities during minor disruptions are investigated.

Optimization of high ramp up rate operations

The timing of gas puffing was found to have significant impacts on the repeatability of plasma discharges, especially for the ramp-up phase (Figure 1). If the timing of gas puffing was ahead of breakdown about 60 milliseconds, it was indicated by the simulation results of Molflow+ that the distribution of gas pressure in the vacuum vessel could be nearly uniform (Figure 2), which was thought to be the reason of better repeatability.

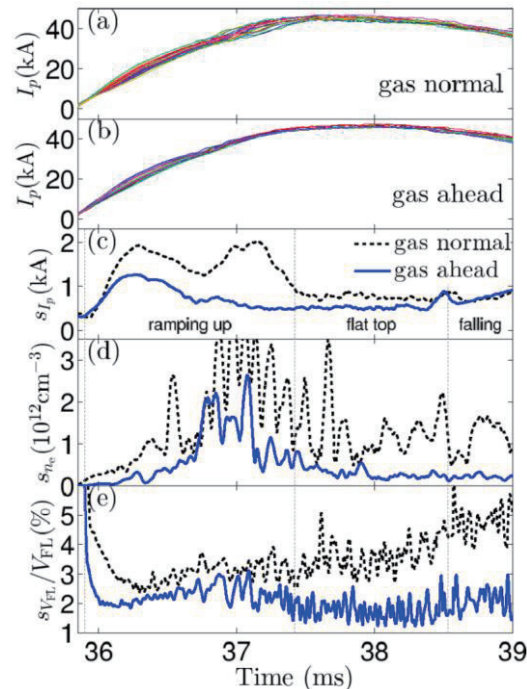


Figure 1 The plasma current of 20 shots of normal gas puffing timing (a) and of ahead timing (b), the standard deviation of plasma current (c) and electron density (d) of 20 shots, the relative standard deviation of loop voltages (e) of 20 shots.

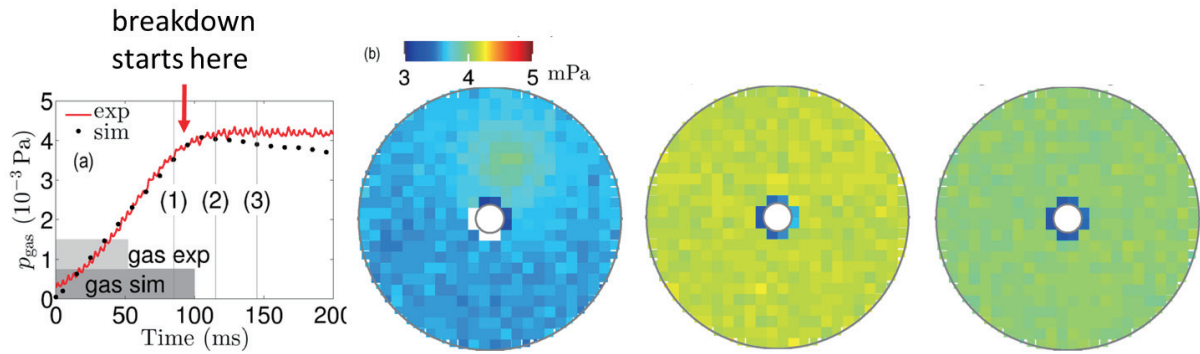


Figure 2 From left to right, the overall pressure vs time, the distribution of pressure in the vacuum vessel at time (1), (2) and (3) .

Eddy current distributions and its effects on equilibrium reconstructions

Eddy current plays an important role in high ramp-up discharges. This situation is particularly serious in SUNIST since it has a split vacuum vessel for the sake of saving the limited ohmic flux of the solenoid. Eddy current distribution in the split vacuum vessel becomes rather complicated (Figure 3).

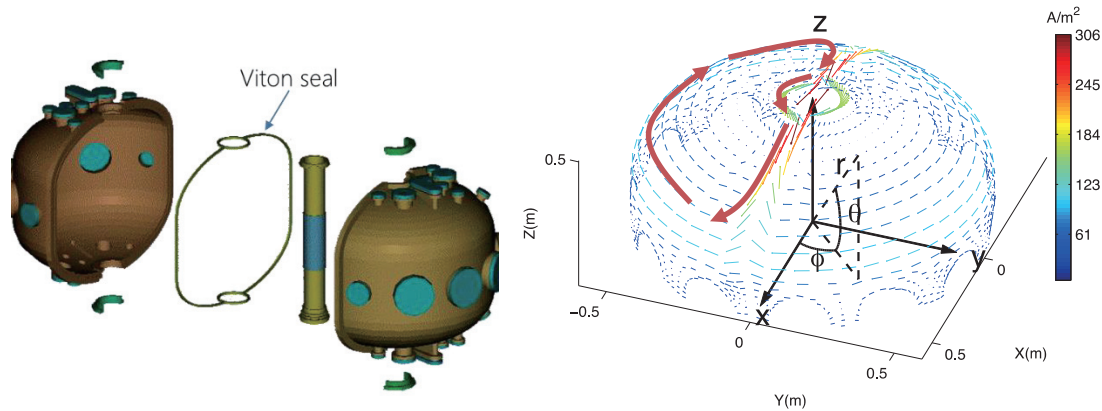


Figure 3 The split vacuum vessel of SUNIST (left), the distribution of eddy current in the wall of the vacuum vessel (right).

The asymmetrical eddy current brings an abnormal effect on the signals of flux loops. As show in Figure 4, the waveforms of the top and bottom flux loops have abnormal leading phases when compared with the waveforms of the excitation (PF current). This phenomenon makes the equilibrium reconstruction nearly impossible for the ramp-up phases. Therefore, a method called *complete response function* to estimate the temporal and the spatial evolutions of eddy current is developed in SUNIST. The basic equation of this method is shown in Figure 5. The second and the third terms in the right side of the equation represent the topology difference between eddy current and excitations, which greatly affect the signal of flux loops in SUNIST. This method is effective in extracting eddy current contribution from the raw signals of flux loop (Figure 6). The equilibrium reconstruction results become more reasonable when the eddy current contribution is included (Figure 7).

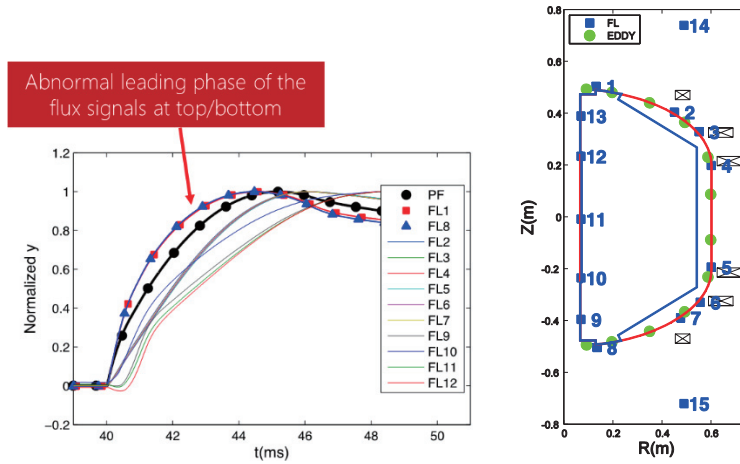


Figure 4 Temporal evolution of the measured fluxes and the current in PF coils (left), the flux loops installed in SUNIST (right).

$$\phi_{FL} = \int_0^t e^{-\frac{(t-u)G_1}{G_2}} \frac{i_{PF}(u)}{G_2} du + \frac{G_3}{G_2} i_{PF}(t) - \int_0^t e^{-\frac{(t-u)G_1}{G_2}} \frac{G_1 G_3 i_{PF}(u)}{G_2^2} du$$

the decay time effect
the topology difference between eddy current and excitations

Figure 5 The complete response function of flux loops, the first term in the right side represents the decay time effect, the second and the third terms represent the topology difference between eddy current and excitations

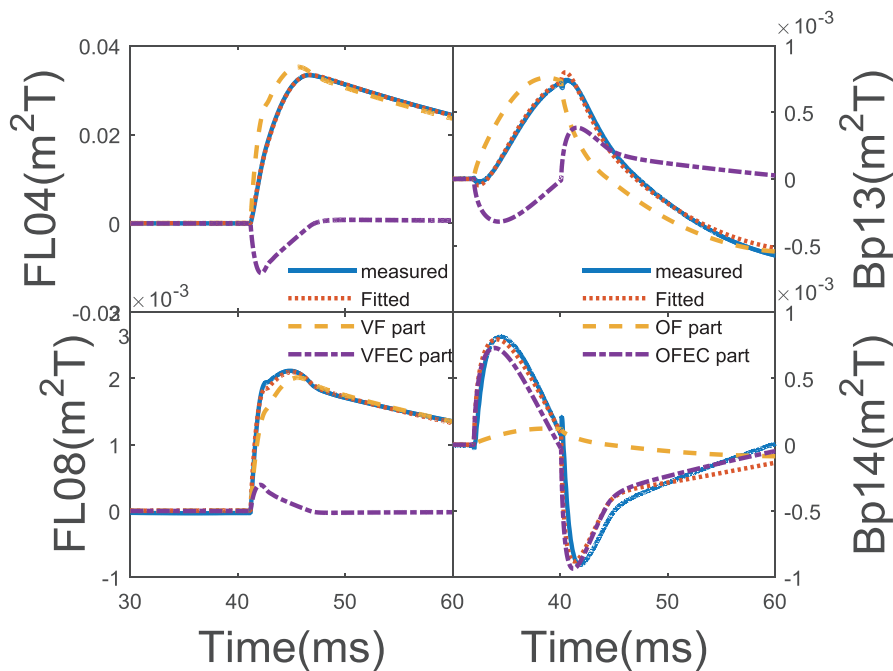


Figure 6 The normal (top) and abnormal (bottom) eddy current effect of flux loops (left) and magnetic

probes (right). The measured data (solid), the fitted value using the CRF (dotted), the drive source part (dashed) and the eddy current part (dash-dotted) are shown.

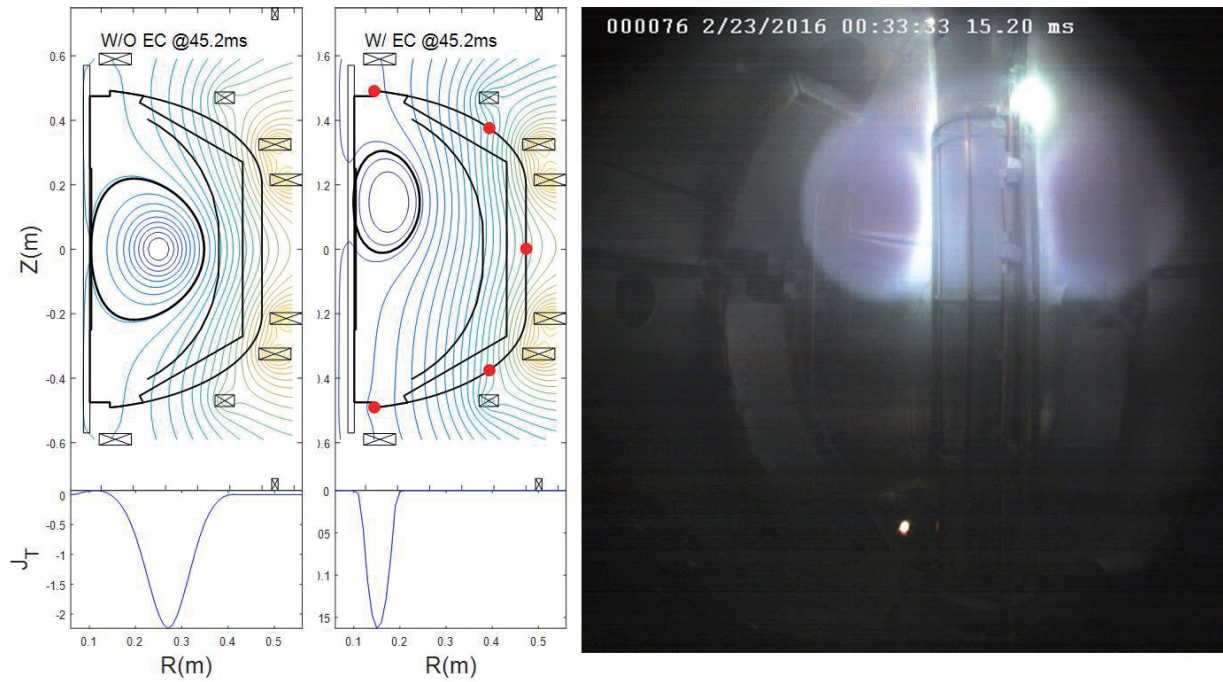


Figure 7 The reconstructed flux surfaces without (left) and with (middle) eddy current contributions. The right picture is captured by a fast camera.

The properties of high frequency MHD activities during minor disruptions

Owing to the ST configuration, ohmic discharges of SUNIST are seldom terminated by one major disruption. The plasma current often decreases in a stepwise form caused by a sequence of minor disruptions. High-frequency magnetic fluctuations have been observed during the minor disruptions from the signals detected by an array of high-frequency magnetic probes sampled at 15 MS/s. As shown in Figure 8, a kind of high frequency MHD modes occur during each minor disruptions which all have significant runaway plateaus. The frequency range of these modes are 150-400 kHz. Their toroidal and poloidal mode numbers are $n = -1$ and $-4 \leq m \leq -3$, respectively, as shown in Figure 9. The mode structure analysis indicates the co-existence of $m/n = -3/-1$ and $-4/-1$ harmonics, propagating toroidally opposite to the direction of plasma current and poloidally in the electron diamagnetic drift direction in the laboratory frame of reference.

There are several minor disruptions in one discharge shown in Figure 8. It can be found that the mode frequency is higher at low density and vice versa, suggesting that the modes may be Alfvén-type modes. In order to verify it, a statistical analysis with about 200 shots was made. Fig. 2 illustrates that the observed mode frequency scales linearly with the TAE frequency $f_{TAE} = v_A/4\pi qR$, where $v_A = B_T(\mu_0\rho)^{-1/2}$ is the Alfvén velocity, ρ is the mass density, q is the safety factor and R is the major radius. In the calculations, the line-averaged density and the on-axis toroidal field are used to estimate the Alfvén velocity. The safety factor is estimated by mode numbers. The scatter of data points in Figure 9 is mainly due to the variation of the size of plasma

column on which the line-averaged density is depended. Therefore, these high frequency MHD modes should be TAEs. The measured edge magnetic fluctuation level of the TAE is about one gauss, and $\delta B_\theta/B_T \sim 2 \times 10^{-3}$. Moreover, the signals measured on outboard coils are generally stronger than those measured on inboard coils suggesting that the TAE exhibits a ballooning feature.

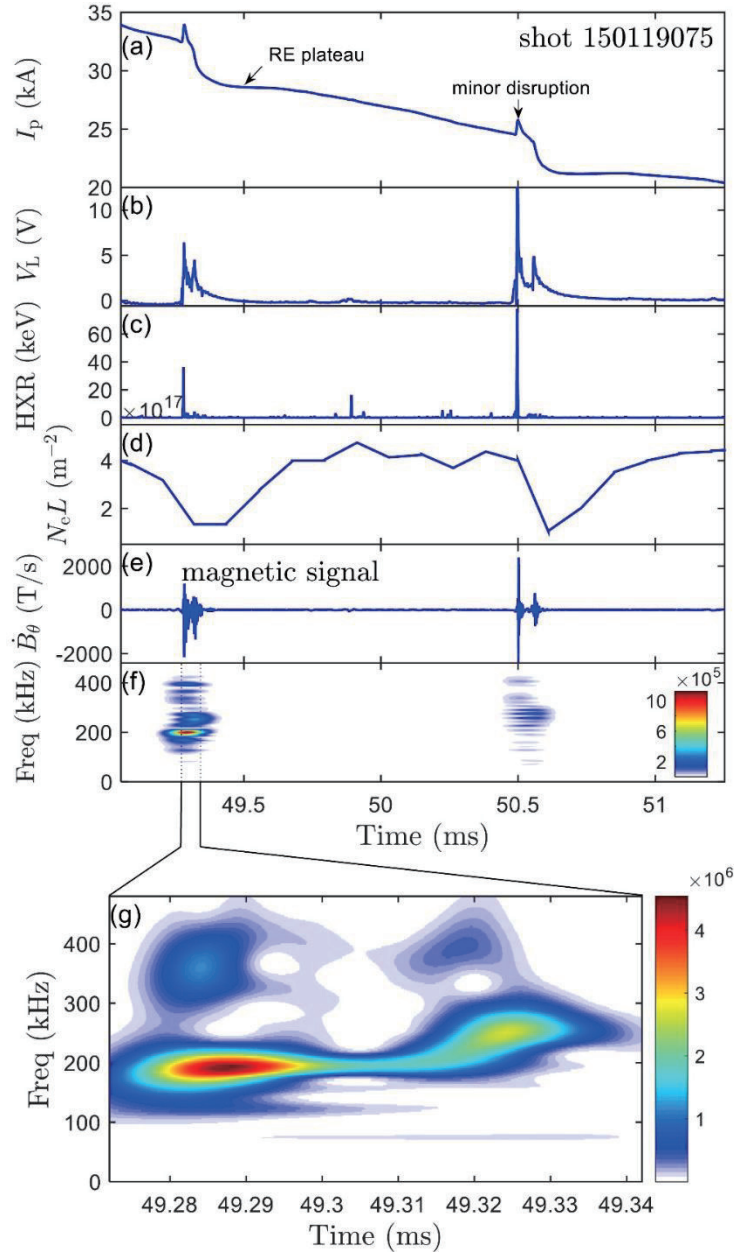


Figure 8 Time evolution of (a) plasma current, (b) loop voltage, (c) hard x-ray (HXR), (d) line-averaged electron density, (e) magnetic probe signal, (f) the spectrogram of a magnetic probe signal and (g) detail of the spectrogram of a magnetic probe signal in a minor disruption.

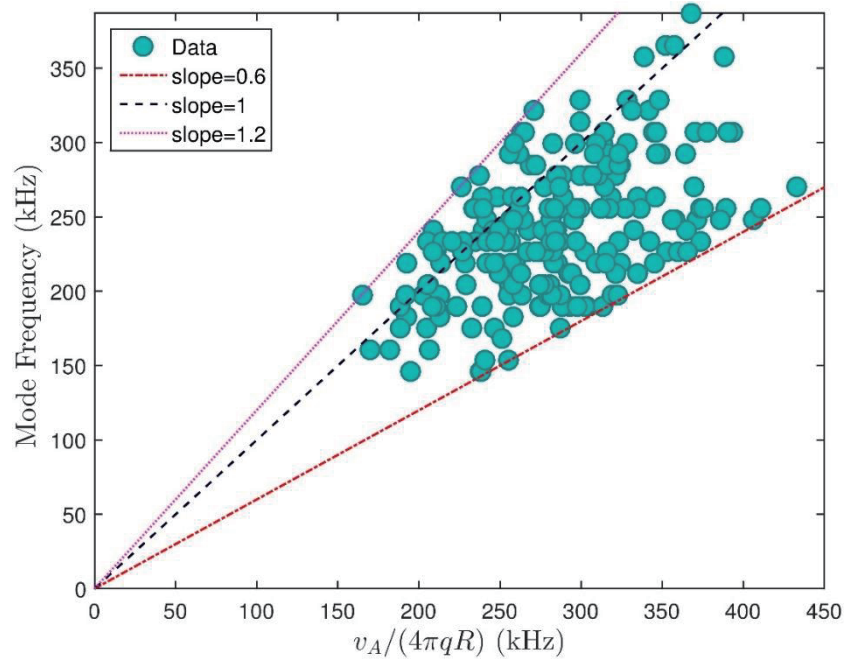


Figure 9 Comparison of the observed mode frequencies during minor disruptions with the expected TAE frequencies.

This work was supported by NSFC, under Grant Nos. 10990214, 11075092, 11261140327 and 11325524, MOST of China, under Contract No. 2013GB112001, 2013GB107001, Tsinghua University Initiative Scientific Research Program and 221 Program.

Inter-ELM heat loads on misaligned tungsten blocks in KSTAR

Suk-Ho Hong on behalf of KSTAR team and collaborators

National Fusion Research Institute, Daejeon, Korea

Email: sukhhong@nfri.re.kr

This paper gives a summary of inter-ELM (edge localized mode) heat loads on misaligned tungsten blocks in KSTAR divertor. The heat loads on the blocks were measured by zoomed-in divertor IR camera and compared with theoretical calculation performed by using COMSOL. The results indicate that there is no power balance discrepancy: Measured and modeled heat loads are consistent with each other.

1. Introduction

An important design issue for the ITER tungsten (W) divertor and in fact for all such components using metallic plasma-facing elements and which are exposed to high parallel power fluxes, is the question of surface shaping to avoid melting of leading edges. Different concepts and various designs have been proposed and tested [1]. However, there are inevitable engineering tolerances, especially with large scale, actively cooled systems, meaning that misalignments, usually at the level of hundreds of microns, cannot be avoided. During the fabrication of castellated tungsten blocks and their assembly in KSTAR, it is found that there is intrinsic misalignment of the order of 0.1 mm. In addition, entire graphite tile structures inside the KSTAR vacuum vessel have a misalignment level of ~ 0.5 mm caused by 3D tilting of individual tile [1], which is larger than engineering limit for ITER castellation (0.3 mm). In order to quantify the effect of such misalignment, a dedicated melting experiment and simulation of heat flux and surface temperature on the misaligned tungsten lamella during ELMs (edge localized modes) has been performed at JET [2]. Surprisingly, this experiment on JET cast some doubt on the power loading of extreme leading edges at glancing incidence [2], prompting the International Tokamak Physics Activity to launch a multi-machine effort to study leading edge physics in support of a shaping decision on ITER.

This paper reports on dedicated experiments which have been performed on KSTAR as a contribution to this coordinated task, especially inter-ELM phase. To study leading edge heat loads we have fabricated a series of multi-purpose, brazed W blocks (W-Cu-CuCrZr) and

monitored by divertor IR from the top. This paper is organized as follows. In section 2, the experimental setup and analysis methods will be briefly described. In section 3, results will be discussed in detail. Finally, a conclusion will be given.

2. Experimental Setup and thermal load analysis

In 2015 campaign, tungsten blocks with different leading edge heights were fabricated and installed at central divertor as shown in Fig. 1. The base design is a conventional castellated structure of right angled square structure with $30\text{ mm} \times 20\text{ mm} \times 12\text{ mm}$ size with a variety of leading edge heights (0.3, 0.6, 1.0, and 2.0 mm) with toroidal gap of 0.5 mm. The blocks were observed by an infra-red (IR) camera system from the top of the vacuum vessel as shown in Fig. 2. The spatial resolution of the system is $\sim 0.4\text{ mm/pixel}$ on the block surface in 2015 campaign with a zoom-in lens system.

Full 3D modeling of the heat flux on the blocks has been performed by using COMSOL multi-physics package. Each block is constructed in phase space, and modeled separately. From the IR measurements of “reference” discharges, we have measured heat flux on the tungsten blocks and used that as input parameters. The angle of incidence has been chosen as 3° , which is the same as ITER case.

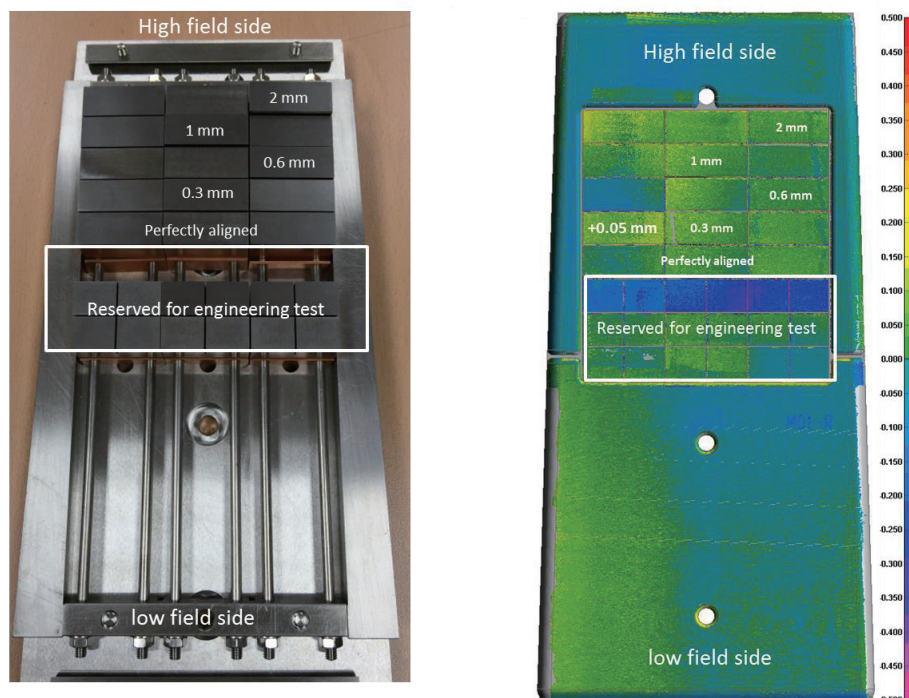


Fig. 1. Tungsten blocks for leading edge study in 2015 campaign.

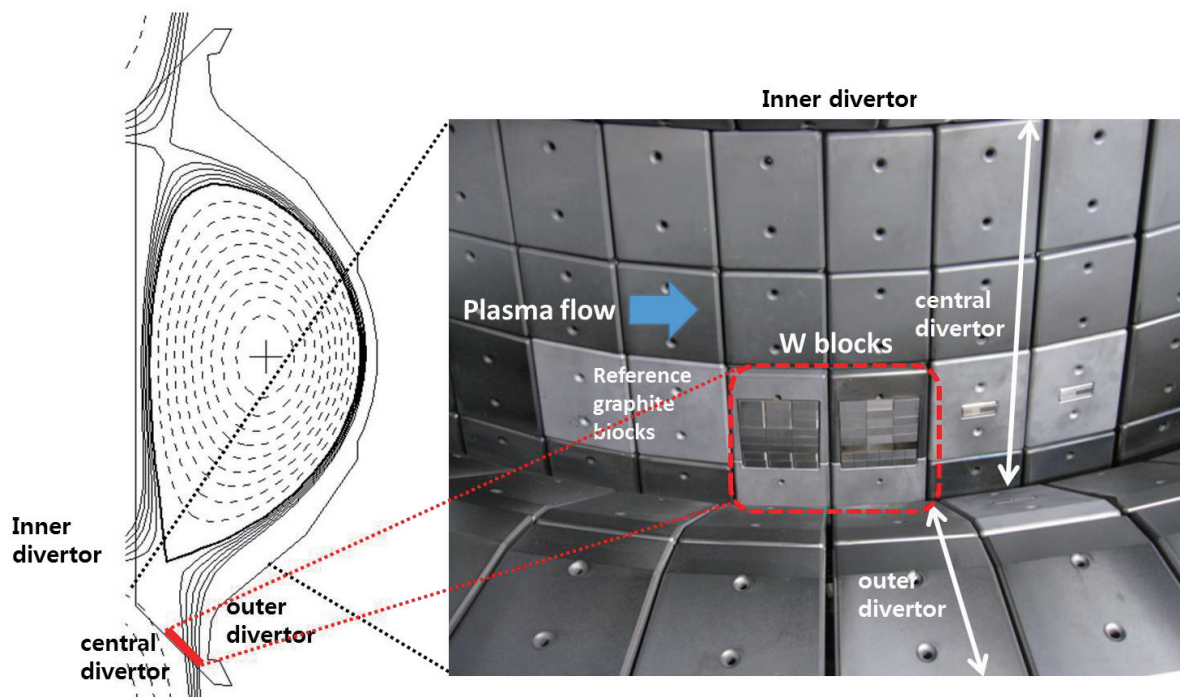


Fig. 2. Line of sight of divertor IR camera in 2015 campaign.

3. Results and discussion

Fig. 3. Shows an IR measurements during an ELMy H-mode (#13153). The IR image shows tungsten blocks (0.6 mm leading edge) under ELMy H-mode heat load. The peak heat flux on the block is 0.6 MW/m^2 . It is clearly seen that 0.6 mm leading edge is heavily bombarded by ions leading to a bright spot. Note that other leading edges of 0.3 mm and 1. mm are also illuminating due to wide strike point. Fig. 4 also shows the measured IR intensity profiles of three different time interval of 0.6 mm leading edge with the results obtained by COMSOL simulation. The temperature profiles obtained by COMSOL transient simulation and measured peak intensity matches very well with the calculation and show good agreement in shape. Both measurements and simulation match very well indicating the there is no power discrepancy found in KSTAR. Since the IR camera is not absolutely calibrated for tungsten surface, the intensity measured by IR camera is assumed to be proportional to the surface temperature. The results indicate that simple thermal analysis is very useful to predict heat load on castellated blocks with arbitrary shapes.

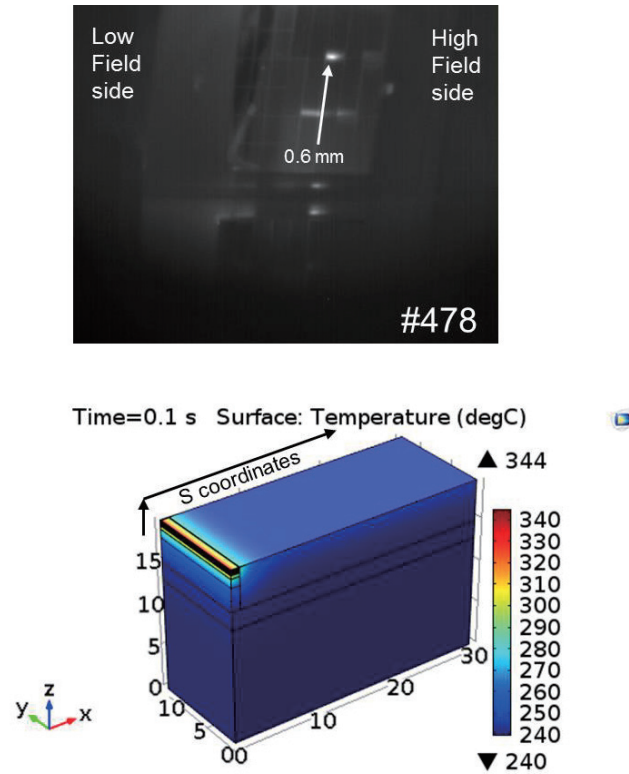


Fig. 3. An example of divertor IR measurement measurement during an ELMy H-mode. Corresponding inter-ELM COMSOL simulation is also shown.

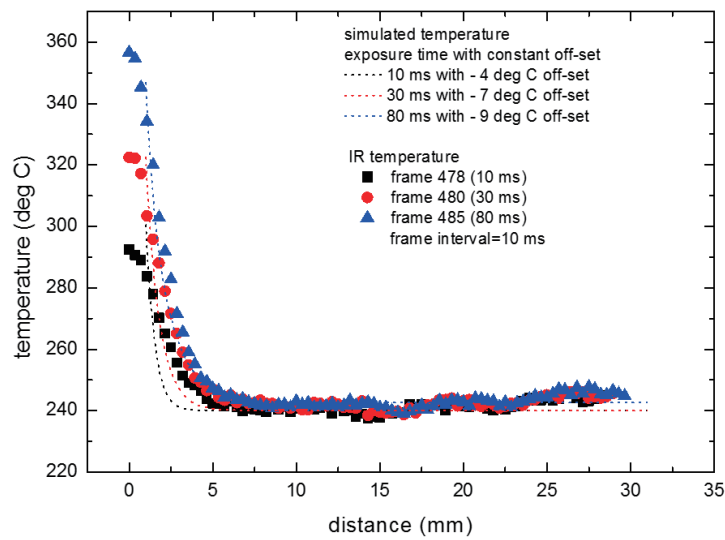


Fig. 4. Measured IR intensity profiles at three different time intervals with the results obtained by COMSOL simulation (0.6 MW/m^2)

4. Summary

Heat loads on misaligned edges calculated by COMSOL simulation compared with measured ones by divertor IR in KSTAR are reported. Peak temperature of each block depends strongly on the shape of the block. The heat load patterns on the tungsten blocks calculated by COMSOL simulation show qualitatively good agreement with measured ones by IR camera: Simple analysis can be used to predict the heat load patterns on a PFC block for the first order estimation.

Acknowledgement

This research was supported by Ministry of Science, ICT, and Future Planning under KSTAR project and was partly supported by the JSPS-NRF-NSFC A3 Foresight Program in the field of Plasma Physics (NSFC: No.11261140328, NRF : No. 2012K2A2A6000443).

References

- [1] S.-H. Hong et al., *Fus. Eng. Des.* 89 (2014) 1704.
- [2] J. W. Coenen et al., *Nucl. Fusion* **55** (2015) 023010

SOL widths of limiter plasmas in KSTAR and EAST tokamaks

J.G. Bak¹, H.S. Kim¹, J.W. Juhn¹, H.H. Lee¹, D.C. Seo¹, S.H. Hong¹,
L. Chen², L. Wang², J.B. Liu², B. Zhang², S. Liu²,
R. Pitts³
J.H. Jang⁴, W.H. Choi⁴

¹National Fusion Research Institute, Daejeon, Korea

²Academy of Sciences Institute of Plasma Physics, Hefei, Anhui, China

³ITER Organization, St. Paul Lez Durance Cedex, France

⁴Department of Physics, Korea Advanced Institute of Science and Technology, Korea

Email : jgbak@nfri.re.kr

The scrape-off layer (SOL) heat flux profiles $q_{||}(r)$ are measured by using the fast reciprocating Langmuir probe assembly (FRLPA) at the outboard mid-plane (OMP) during L-mode inner wall limiter (IWL) plasma in the KSTAR tokamak. There is a clear evidence of a double exponential decay (DED) structure in $q_{||}(r)$ ($= q_{||,near} + q_{||,main}$) such that a narrow feature, $\lambda_{q,near}$ ($= 5.3$ mm) is found close to the last closed flux surface (LCFS), followed by a broader width, $\lambda_{q,main}$ ($= 4.6$ cm) for 0.6 MA. The DED structure in $q_{||}(r)$ can be also found in the IWL plasmas from the infra-Red (IR) thermal images at inboard limiter tiles in the KSTAR. Interestingly, the SOL heat flux profile with the DED structure is also observed from the FRLPA measurement at the OMP during the IWL plasma in the EAST tokamak such as $\lambda_{q,near} = 7.0$ mm and $\lambda_{q,main} = 3.9$ cm for 0.3 MA. In this work, results from the experimental investigations of the SOL heat flux profiles for IWL plasmas in two superconducting tokamaks (KSTAR and EAST) from the FRLPA measurements at the OMP, together with the IR measurements, are presented.

1. Introduction

The issue of limiter scrape-off layer (SOL) heat flux widths has recently become of much greater importance following the realization that the previously simple approximation of a single exponential fall-off from the last closed flux surface (LCFS) assumed in the design of the ITER first wall panel toroidal shaping is invalid and that the SOL in present devices usually exhibits a more complex structure. That is, it was reported that double exponential decayed heat flux profiles in the SOL region, a narrow feature (few mm) near the LCFS followed with the broader e-folding length were observed from the fast reciprocating Langmuir probe assembly (FRLPA) and infra-red (IR) measurements for inner wall limiter (IWL) plasmas in several tokamaks [1-5]. Thus, a multi-machine effort, coordinated by the ITER Organization, has been conducted over the past 3 years, to gather as much data as possible regarding the scaling and physics understanding of this limiter heat flux profile [1,6]. Up to now, activities for the re-design of the ITER inner wall limiter tiles (required in the start-up phase) optimized for the double-exponential heat flux profile with a narrow feature has been carried out [1].

In the KSTAR tokamak, there were some activities on the evaluation of the SOL width from the fast reciprocating Langmuir probe assembly (FRLPA) measurements at the outboard mid-plane (OMP) for outboard wall-limited (OWL) ohmic and L-mode plasmas [7]. Here, radial profiles of electron temperature T_e and ion saturation current density J_{sat} obtained with the triple probe were used to compute the parallel heat flux profile $q_{||}(r)$ from which the heat flux width λ_q was able to be extracted. Secondly, in common with the technique employed elsewhere [2-5], measurements of the inboard limiter SOL heat flux profile with a narrow feature near the LCFS on the KSTAR have been obtained using the combination of infra-red (IR) thermography, with a tangentially viewing system whose field of view captures the graphite IWL tiles, and the FRLPA providing plasma profiles across the SOL at the OMP. There was a clear evidence of a double-exponential SOL heat flux profile from both the FRLPA and IR measurements such that a narrow feature, $\lambda_{q,near}$ was found close to the LCFS, followed by a broader width, $\lambda_{q,main}$. Interestingly, there was also the SOL heat flux profile with the double-exponential structure obtained from the FRLPA measurement during the IWL plasma in the EAST tokamak. Thus, we experimentally investigated the IWL SOL heat flux profiles in the KSTAR and EAST tokamaks to compare between SOL widths in two superconducting tokamaks. In this paper, diagnostics for the SOL profile measurements in the KSTAR and EAST are described in Sec. 2. The results from experimental investigations of the IWL SOL heat flux

profiles in two superconducting tokamaks are presented in Sec. 3. Finally, the summary is given in Sec. 4.

2. Diagnostics for SOL profile measurement in IWL plasma

Fig. 1(a) shows the FRLPA together with the probe head for radial profile measurements at the OMP and the IR camera together with thermal images at the IWL tiles in the KSTAR. There were five probe tips in the probe head of the FRLPA; three poloidally and two toroidally separated tips for the triple and Mach probe measurements, respectively. Details on the KSTAR FRLPA were described in Ref. 8. An IR camera (FLIR / ThermoVision SC6000) is used for measuring surface temperature on the graphite tiles used for inboard limiters and outer poloidal limiters during plasma discharges. The IR camera is a tangentially viewing system whose field of view (FOV) captures the graphite tiles. The IR camera has 640×512 pixels and a full frame rate of 125 FPS, and its noise equivalent temperature difference (NETD) is less than 25mK. The spatial resolution of the IR images was about 3.18 mm ~ 5.14 mm at the poloidal limiter. The region of interest covering with four tiles were selected for the IR thermography (see ‘rectangular box enclosed with white solid lines’ in Fig. 1(a)) by adjusting the FOV of the IR camera in order to capture mainly thermal images on the graphite IWL tiles. The thermal image size was $94 \times 117 \text{ mm}^2$, which was used for the evaluation of the IWL SOL heat flux profiles during IWL plasma discharges in the KSTAR.

Fig. 1(b) shows the FRLPA together with two different probe heads for radial profile measurements at the OMP in the EAST. There were two toroidally separated FRLPAs in the EAST. The FRLPA has a probe head with several tips, and measures radial profiles of the plasma parameters in the SOL region. Details on the EAST FRLPA were described in Ref. 9.

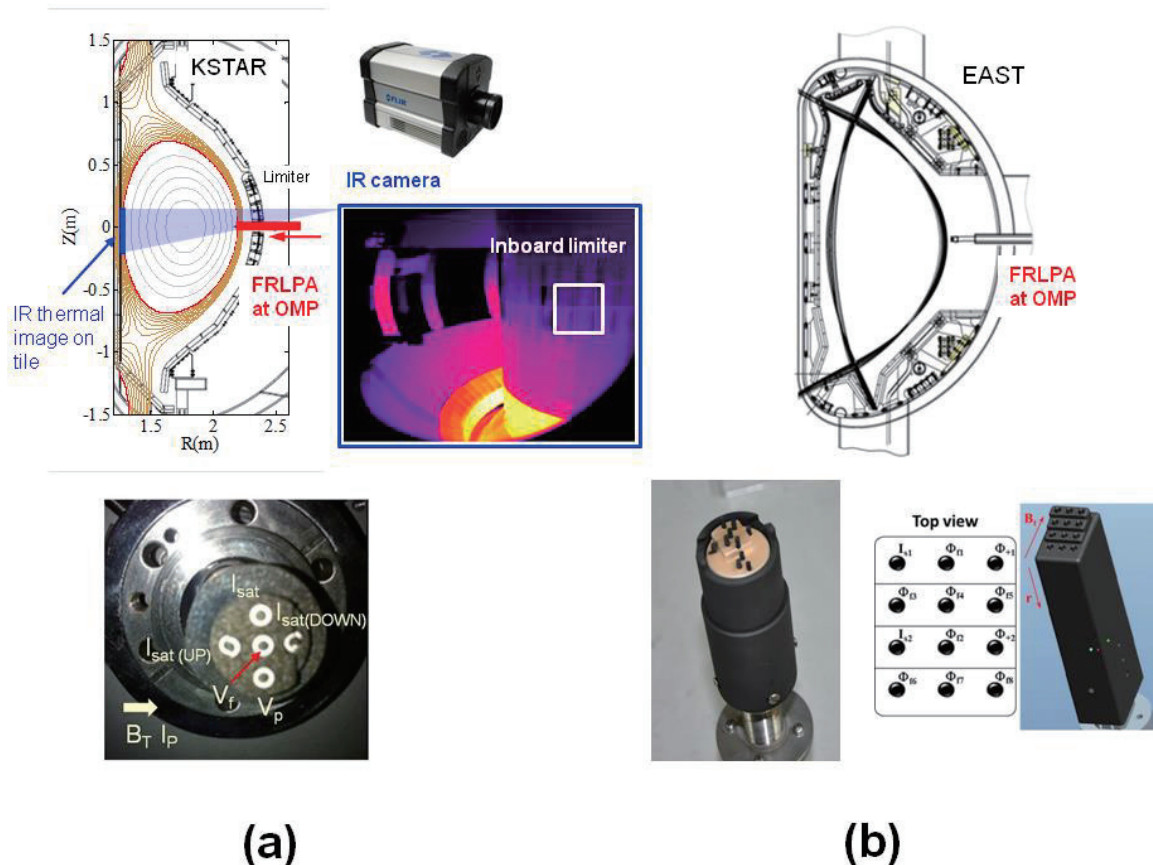


Fig. 1. Diagnostics for measuring IWL SOL widths in two tokamaks; (a) the FRLPA with a probe head and the IR camera with an IR thermal image during system check in the KSTAR, and (b) the FRLPA with two different probe heads in the EAST.

3. Experimental investigation of SOL heat flux in the KSTAR and EAST

The double-exponential SOL parallel heat flux $q_{\parallel}(r)$ with a narrow feature $\lambda_{q, near}$ near the LCFS is expressed as

$$q_{\parallel}(r) = q_{\parallel, near}(r) + q_{\parallel, main}(r) = q_{\parallel, near}(0) \exp\left(\frac{-\Delta r_{sep}}{\lambda_{q, near}}\right) + q_{\parallel, main}(0) \exp\left(\frac{-\Delta r_{sep}}{\lambda_{q, main}}\right), \quad (1)$$

where Δr_{sep} is the radial distance from the LCFS and $\lambda_{q, main}$ is the e-folding length (the broader width) in the main SOL region. $q_{\parallel, near}(r)$ and $q_{\parallel, main}(r)$ are the heat fluxes near the LCFS and in the main SOL region, respectively. By using the relationship as $R_q = q_{\parallel, near}(0)/q_{\parallel, main}(0)$ and the SOL power P_{SOL} , the parallel heat fluxes $q_{\parallel}(0)$ and $q_{\parallel, main}(0)$ at the LCFS are evaluated from simple SOL power balance at the OMP as following;

$$q_{\parallel}(0) = q_{\parallel, main}(0)(1 + R_q),$$

$$q_{\parallel, main}(0) = \frac{P_{SOL}}{4\pi R_{OMP} (R_q \cdot \lambda_{q, near} + \lambda_{q, main}) (B_{\theta} / B_{total})_{OMP}} \quad (2)$$

where R_{OMP} , B_{θ} and B_{total} are major radius, poloidal and total magnetic fields, respectively at the OMP. P_{SOL} is calculated as $P_{SOL} = P_{heating} - dW_{TOT}/dt - P_{rad}$ where $P_{heating}$, W_{TOT} and P_{rad} are the total heating power (ohmic + auxiliary heating), the stored energy and the radiative power, respectively. The neutral beam (NB) power P_{NB} was a major contributor of $P_{heating}$ in the KSTAR tokamak. The value of P_{rad} obtained from the bolometer measurement was ~ 0.5 MW for given heating powers as $P_{NB} = \sim 2.8$ MW, $I_p = 0.6$ MA during an L-mode plasma in shot #11398. Thus, $P_{SOL} = \sim 0.16 \cdot P_{heating}$ was used for the estimate of $q_{\parallel}(0)$ by using Eq.(2) to verify the parallel heat flux at the LCFS obtained from the FRLPA measurement.

3.1. SOL widths in KSTAR

The FRLPA measurement was performed in moderately elongated ($\kappa = \sim 1.55$) L-mode IWL plasma as shown in Fig. 2(a).

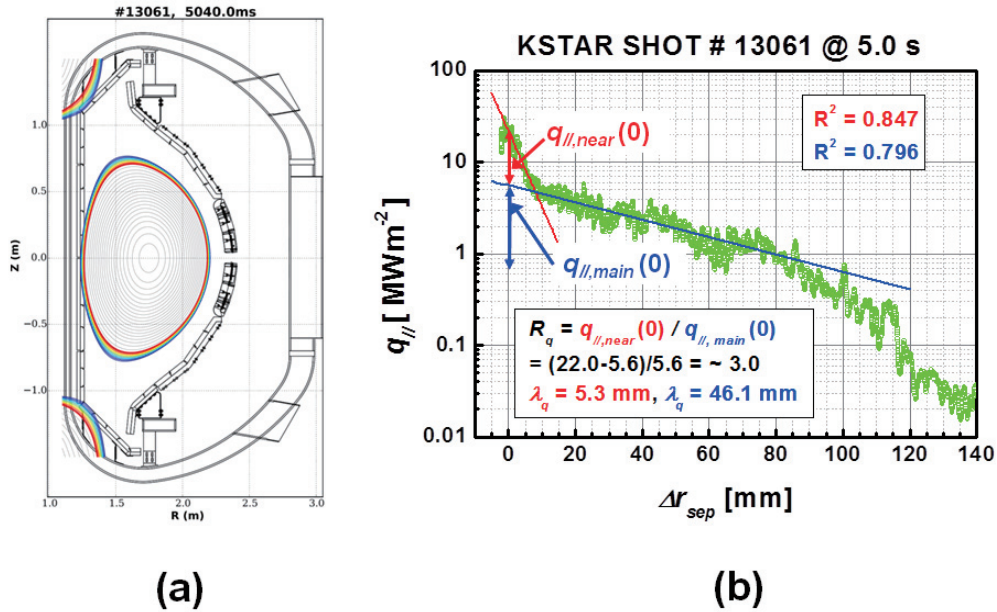


Fig. 2. (a) IWL plasma shape reconstructed by the EFIT, and (b) parallel SOL heat flux profiles from the FRLPA measurement at the OMP during the IWL plasma in the KSTAR.

The experimental conditions in the measurement were as following; toroidal magnetic field on the major axis, $B_T = 2.0$ T; plasma current, $I_p = 0.6$ MA; line averaged density, $n_e = \sim 4.0 \times 10^{19}$ m⁻³; safety factor at 95% flux surface, $q_{95} = \sim 3.9$; ohmic power, $P_{OH} = \sim 0.35$ MW; neutral beam (NB) power, $P_{NB} = \sim 1.4$ MW; major and minor radii, $R_0 = \sim 1.8$ m and $a = \sim 0.46$ m, respectively.

The radial profiles of the parallel heat flux $q_{||}(r)$ were evaluated from ones of electron temperature $T_e(r)$ and ion saturation current density $J_{sat}(r)$ obtained from the FRLPA measurement at the OMP as $q_{||}(r) = \gamma T_e(r) \cdot J_{sat}(r) / Z_{eff} e$ where γ is the heat transmission coefficient and its value was assumed as 7 ($T_e \approx T_i$). The ion effect charge Z_{eff} was evaluated from a bremsstrahlung diagnostic and $Z_{eff} = 3$ was used in the calculation of $q_{||}(r)$ in the IWL plasmas. The radial profiles obtained during the inward FRLPA movement were used to evaluate the SOL width. The profiles obtained during the outward radial scan were deformed, which might be due to interaction between plasma and probe tips. There is a clear evidence of a double exponential decay structure in $q_{||}(r)$ from the FRLPA measurement such that a narrow feature, $\lambda_{q,near}$ is found close to the LFCS, followed by a broader width, $\lambda_{q,main}$ during an IWL plasma as shown in Fig. 2(b). The two values of $\lambda_{q,near}$ and $\lambda_{q,main}$ are obtained as 5.3 mm and 4.6 cm, respectively from two single exponential fits ($R^2 = 0.847, 0.796$) for $q_{||}(r)$, and the value of R_q was about 3.0. Here, the value of $q_{||}(0)$ obtained from the FRLPA measurement was 22.0 MWm⁻², which matched well with the value calculated by using Eq. (2) within the discrepancy of 12 %. The calculated value was 23.9 (19.4) MWm⁻² for $P_{rad} / P_{heating} = 0.16$ (0.3). The IWL SOL heat channels with the double-exponential decay structure were also observed in other tokamaks [1-5].

Fig. 3(a) shows the IR thermal images on inboard limiter and outer poloidal limiter tiles during an inner wall limiter (IWL) plasma. The heat flux onto the inboard limiter tiles was evaluated by using a heat flux reconstruction code (called as ‘NANTHELOT’) solving the heat diffusion equation with the measured tile surface temperature by applying the finite volume method [10]. The NANTHELOT is the abbreviation for numerical analysis for thermal load onto target, and can provide 1D, 2D and 3D profiles of heat flux. Fig. 3 (b) shows the 2D perpendicular heat flux profile q_{\perp} evaluated by using the NANTHELOT code from the IR thermography at the inboard limiter tiles as shown in Fig. 3(a). Here, the x and y axes representing pixel numbers correspond to toroidal angle and vertical distance, respectively..

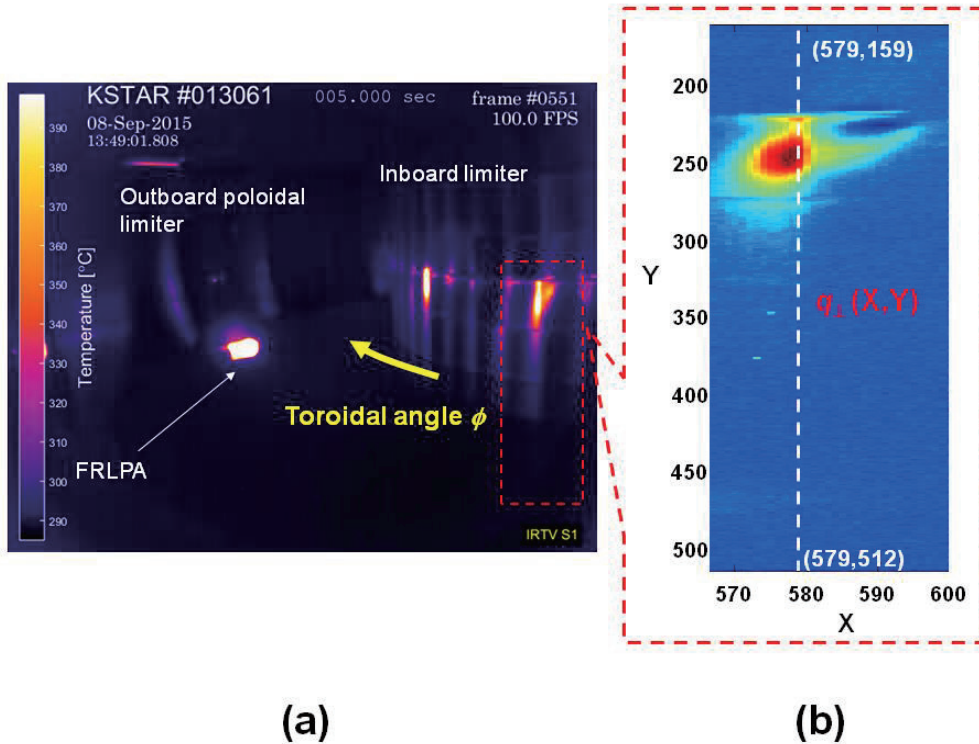


Fig. 3. (a) Thermal images taken by the IR camera located at the middle port of D and (b) 2D heat flux onto the inboard limiter tile from the IR thermal image by using the NANTHELOT code.

At the value of ‘579’ that corresponds to a toroidal angle of 202.7 degrees, the values of q_{\perp} versus vertical pixel is obtained as shown in Fig. 4(a). The profile of $q_{||}(r)$ was evaluated by using the relationship as $q_{||}(r) = q_{\perp}(r) / \sin \theta_{inc}$ after mapping to the OMP where incidence angle θ_{inc} was 1.5 degrees. The two values of $\lambda_{q,near}$ and $\lambda_{q,main}$ were obtained as 3.5 mm and 18.3 mm, respectively from two single exponential fits ($R^2 = 0.831, 0.423$)

for $q_{\parallel}(r)$, and the value of R_q was about 2.3 (see Fig. 4(b)).

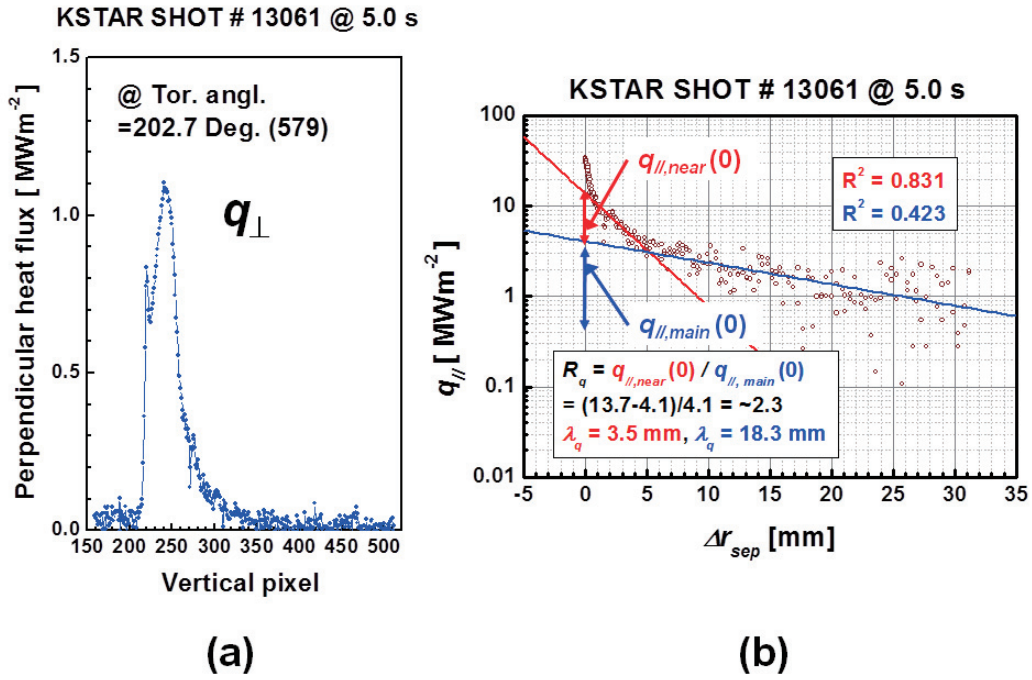


Fig. 4. (a) Perpendicular heat flux profile at a certain x pixel ('579') corresponding to a toroidal angle of 202.7 degrees, and (b) parallel heat flux mapped at the OMP from the IR thermal image at the inboard limiter tile in the IWL plasma.

3.2. SOL widths in EAST

The FRLPA measurement was performed in ohmic IWL plasma as shown in Fig. 5(a).

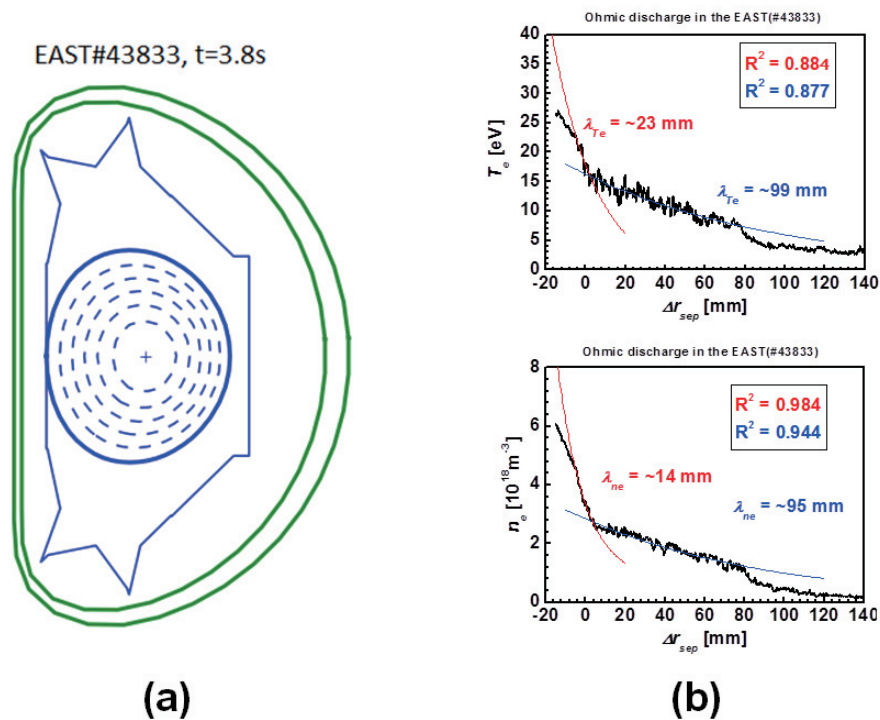


Fig. 5. (a) IWL plasma shape reconstructed by the EFIT, and (b) radial SOL profiles of T_e and n_e from the

FRLPA measurement at the OMP during the IWL plasma in the EAST for evaluation of SOL widths.

The experimental conditions in the measurement were as following; $B_T = 1.96$ T, $I_p = 0.3$ MA, $n_e = \sim 2.0 \times 10^{19}$ m⁻³, $q_{95} = \sim 4.1$, $P_{OH} = \sim 0.2$ MW, $\kappa = \sim 1.03$, $R_0 = \sim 1.85$ m, $a = \sim 0.46$ m.

The double-exponential SOL profiles are clearly observed in both $T_e(r)$ and $n_e(r)$ such as narrow e-folding lengths near the LCFS ($\lambda_{Te,near} = \sim 23$ mm and $\lambda_{ne,near} = \sim 14$ mm) and broader ones in SOL region ($\lambda_{Te,main} = \sim 99$ mm and $\lambda_{ne,main} = \sim 95$ mm) as shown in Fig. 5(b). The two values of λ_{near} and λ_{main} were obtained from two single exponential fits for $T_e(r)$ and $n_e(r)$. The SOL heat flux width λ_q can be evaluated from the relation in the flux limited regime with low collisionality ($q_{||e}^f \propto n_e \cdot T_e^{3/2}$) as

$$\lambda_q \approx \left(\frac{3}{2\lambda_{Te}} + \frac{1}{\lambda_{ne}} \right)^{-1}, \quad (3)$$

by using two characteristic e-folding lengths λ_{Te} and λ_{ne} obtained from the SOL profiles [11]. The values of $\lambda_{q,near}$ and $\lambda_{q,main}$ was evaluated as ~ 7.0 mm and ~ 3.9 cm, respectively.

4. Summary

There was a clear evidence of a double-exponential structure in $q_{||}(r)$ from the FRLPA measurement such that a narrow feature, $\lambda_{q,near}$ was found close to the LFCS, followed by a broader width, $\lambda_{q,main}$ during IWL plasmas ($B_T = \sim 2.0$ T, $q_{95} = \sim 4.0$, $R_0 = \sim 1.85$ m and $a = \sim 0.46$ m) in two superconducting tokamaks such as $\lambda_{q,near}$ ($\lambda_{q,main}$) = ~ 7.0 mm (~ 3.9 cm) for $I_p = 0.6$ MA, $n_e = \sim 4.0 \times 10^{19}$ m⁻³, $P_{OH} = \sim 0.35$ MW, $P_{NB} = \sim 1.4$ MW and $\kappa = \sim 1.55$ in the KSTAR, and $\lambda_{q,near}$ ($\lambda_{q,main}$) = ~ 7.0 mm (~ 3.9 cm) for $I_p = 0.3$ MA, $n_e = \sim 2.0 \times 10^{19}$ m⁻³, $P_{OH} = \sim 0.2$ MW and $\kappa = \sim 1.03$ in the EAST. Interestingly, the narrow and broader widths in $q_{||}(r)$ was also able to found from the IR thermal images at inboard limiter tiles in the KSTAR; $\lambda_{q,near} = \sim 3.5$ mm and $\lambda_{q,main} = \sim 1.8$ cm.

Further data from the FRLPA (or IR) measurements are needed for clearly investigating the comparison between the SOL widths under limited and diverted plasma configurations in the KSTAR and EAST tokamaks such as the dependence of I_p and $P_{heating}$ on λ_q .

Acknowledgements

This research was supported by Ministry of Science, ICT, and Future Planning under KSTAR project contract, and was partly supported by the JSPS-NRF-NSFC A3 Foresight Program in the field of Plasma Physics (NSFC: No. 11261140328, NRF: No. 2012K2A2A6000443).

References

- [1] D. M. Kocan *et al.*, Nucl. Fusion **55** (2015) 033019.
- [2] P.C. Stangeby *et al.*, J. Nucl. Mater. 463 (2015) 389.
- [3] J. Horacek *et al.*, J. Nucl. Mater. 463 (2015) 385.
- [4] R. Dejarnac *et al.*, J. Nucl. Mater. 463 (2015) 381.
- [5] F. Nespoli *et al.*, J. Nucl. Mater. 463 (2015) 393.
- [6] J. Horacek *et al.*, Plasma Phys. Control. Fusion 58 (2016) 074005.
- [7] J.G. Bak *et al.*, J. Nucl. Mater. 463 (2015) 424.
- [8] H.S. Kim *et al.*, available online 4 Feb 2016 in Fusion Eng. Des. (2016).
- [9] W. Zhang *et al.*, Rev. Sci. Instrum. 81(2010)113501.
- [10] C. S. Kang *et al.*, to be submitted to RSI, 2016.
- [11] P.C. Stangeby *et al.*, Nucl. Fusion 50 (2010)125003.

Simulation of the impurity transport by the emission of dusts at the termination of a long pulse discharge in the Large Helical Device

M.Shoji¹, G.Kawamura¹, R.Smirnov², A.Pigarov², Y.Tanaka³, S.Masuzaki¹, Y.Uesugi³
and the LHD Experiment Group¹

¹National Institute for Fusion Science, Toki 509-5292, Gifu, Japan

²University of California at San Diego, La Jolla 92093, CA, USA

³Kanazawa University, Kakuma 920-1192, Kanazawa, Japan

Abstract

The effect of dust emission in the LHD vacuum vessel on the sustainment of a long pulse discharge is investigated by a simulation using a three-dimensional edge plasma code (EMC3-EIRENE) coupled with a dust transport simulation code (DUSTT). The simulation is performed in the following two dust emission cases. One is carbon dust emission from a closed helical divertor region near a lower port. The other one is iron dust emission from a surface on the saddle portion on a helical coil can. It shows that the strong plasma flow in divertor legs is quite effective for preventing the dusts from terminating the long pulse discharge.

1. Introduction

A long pulse plasma discharge was successfully sustained for about 48min in FY2013 in the Large Helical Device (LHD) [1]. The plasma discharge was interrupted by emission of large amounts of carbon dusts from a closed helical divertor region near a lower port. Recent long pulse discharges in these two years have been interrupted by the emission of dusts, which is roughly categorized into two processes. One is the plasma termination by carbon dust emission from closed helical divertor regions [1]. The other one is that by iron dust emission from the surface on the saddle portion of a helical coil can in the vacuum vessel [2]. The investigation of the effect of the dust emission on the sustainment of the long pulse discharges is an essential issue for extending the duration time of the plasma discharges. In order to investigate the plasma termination induced by the dust emission, impurity transport simulation in the LHD peripheral plasma is performed using a three-dimensional edge plasma simulation code (EMC3-EIRENE) [3, 4] coupled with a dust transport simulation code (DUSTT) [5-7]. The simulation will contribute to sustainment of long pulse discharges in LHD and ITER and also future nuclear fusion reactors.

2. Preparation of impurity transport simulation by dust emission

The impurity transport simulation induced by the dust emission is performed in a fully three-dimensional grid model including the LHD main plasma, the peripheral plasma (ergodic layer), four helically twisted divertor leg structures, the vacuum vessel and closed helical divertor components [8, 9]. Figure 1 (a) indicates a bird's eye view of the grid model for a one half of the helical coil pitch angle (18° in toroidal direction) for a typical magnetic configuration ($R_{ax}=3.60\text{m}$). In this grid model, two positions for

the dust emission source are defined. One is on the surface of a dome structure in the closed helical divertor region near a lower port, and the other one is on the surface of the saddle portion of a helical coil can in the inboard side of the torus in the vacuum vessel, which are shown as broken yellow circles in Figure 1 (a). These two positions are assigned for carbon and iron dust emission sources, respectively.

The simulation tracks the dust trajectories (typically 2,000,000 test particles) from the dust sources using the DUSTT code. The enlarged views for showing representative dust trajectories released from the two dust sources are illustrated in Figure 1 (b) and (c) as colored lines, respectively. The simulation assumes that the initial dust velocity is 5m/s which is the typical value estimated by the analysis of the three-dimensional trajectories of dusts observed with stereoscopic fast framing cameras [1]. The dust radius is randomly chosen from a Junge distribution in the range from 1 μ m to 0.1mm which was experimentally found by a statistical analysis of the many dust sizes collected from the surface in the vacuum vessel after experimental campaigns [10]. In the simulation, it is assumed that all neutral impurity atoms produced by sublimated/evaporated dusts are promptly ionized at the positions of their production, and no production of impurities by sputtering on the divertor plates at the strike points is assumed for the simple simulation. The three-dimensional profile of the production rate of the neutral impurity atoms calculated by the DUSTT code is directly introduced into the EMC3-EIRENE code. The simulation provides a solution of the three-dimensional plasma parameter profiles in a case of continuous dust emission rates.

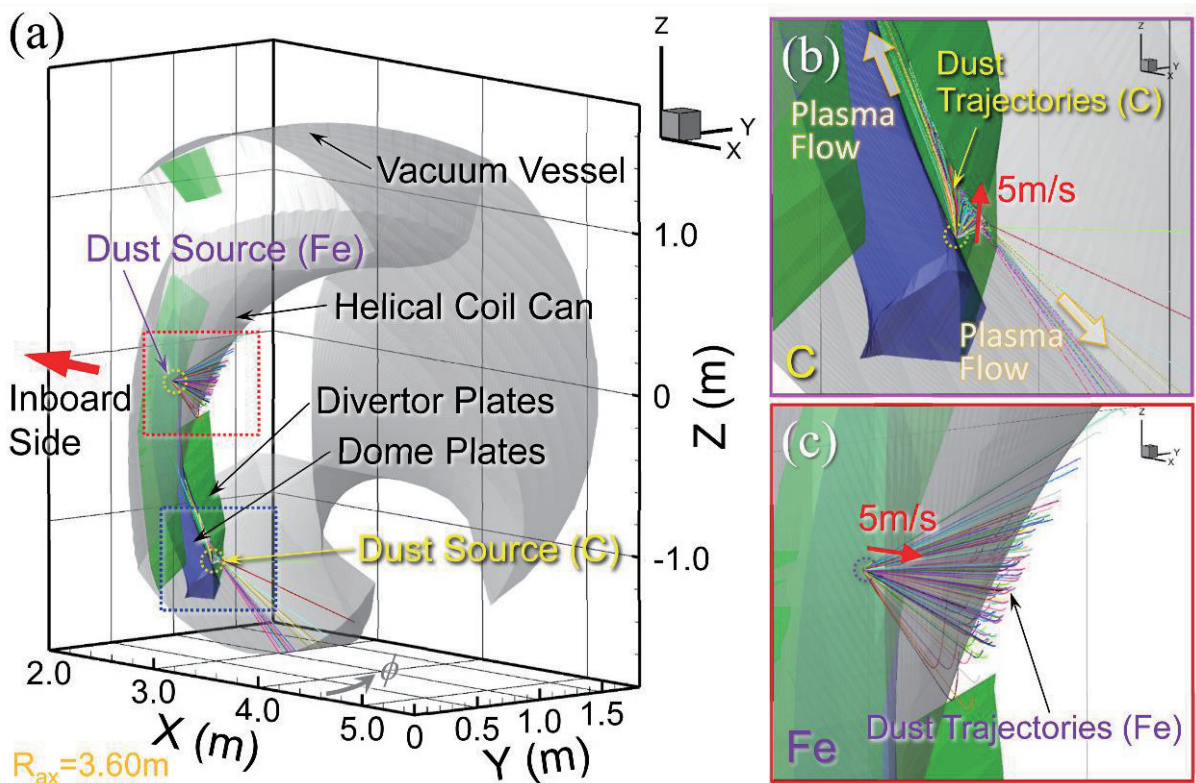


Fig.1 (a) A bird's eye view of a three dimensional model for the simulation. (b) An enlarged view of carbon dust trajectories released from a lower divertor region. (c) An enlarged view of the trajectories of the iron dusts released from the surface of the saddle portion of a helical coil can.

3. Results of the impurity transport simulation by dust emission

Figure 1 (b) shows that most of the carbon dust trajectories released from a lower divertor region is bent by the effect of the strong plasma flow in the divertor legs, which indicates that the divertor legs can

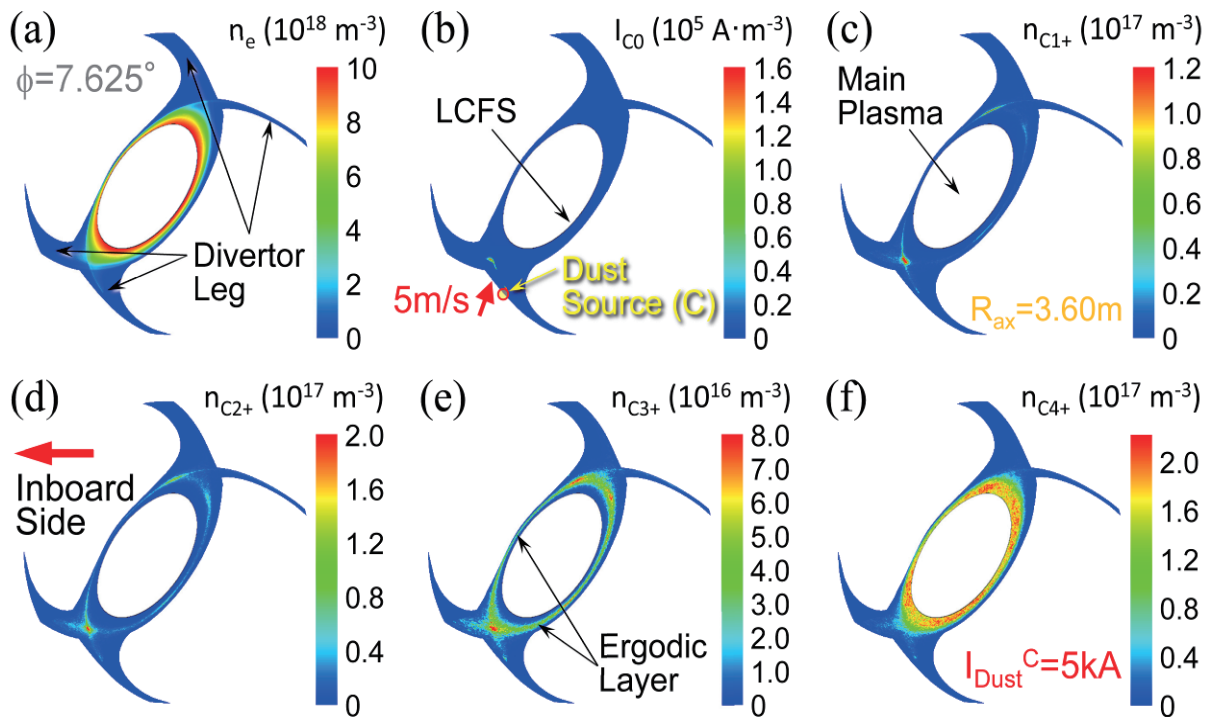


Fig.2 (a) The poloidal cross section of the plasma density profile, (b) the profile of the production rate of neutral carbon atoms induced by the dusts, (c-f) the profile of carbon ions at a toroidal angle close to the position of the carbon dust source.

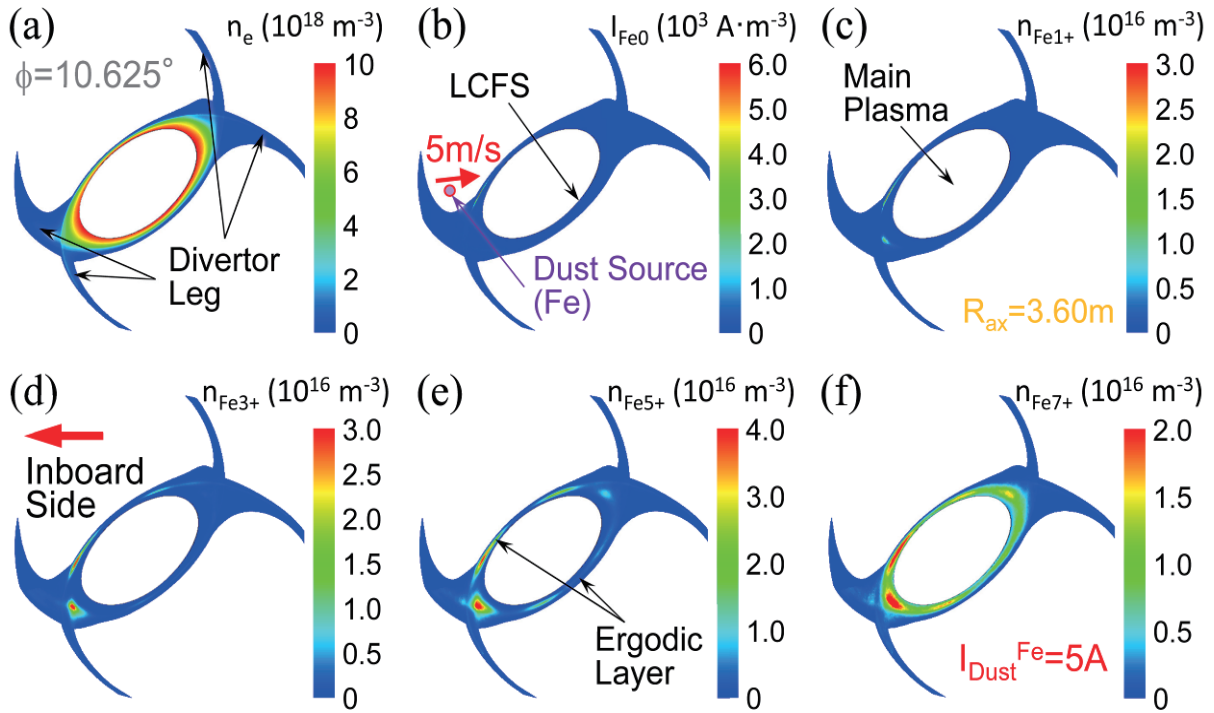


Fig.3 (a) The poloidal cross section of the plasma density profile, (b) the profile of the production rate of neutral iron atoms induced by the dusts, (c-f) the profile of iron ions at a toroidal angle close to the position of the iron dust source.

protect the main plasma from the dust emission. The simulation in the carbon dust emission case was carried out for a typical plasma heating power and electron density for long pulse discharges ($P_{LCFS}=1.0\text{MW}$ and $n_e^{LCFS}=1 \times 10^{19}\text{m}^{-3}$). Figure 2 indicates the poloidal cross section of the profile of the electron density, the production rate of neutral carbon atoms induced by the dust emission and carbon ion densities in the peripheral plasma at a toroidal angle close to the carbon dust source (toroidal angle $\phi=7.625^\circ$) in the case of a current of the carbon dust emission of 5kA. In the simulation, the profile of the production rate of the neutral carbon atoms is localized near the dust source. It is also shown that the carbon density profile for lower ionization stages (n_{C1+} and n_{C2+}) is localized near the dust source, and the carbon ions with higher ionization stages (n_{C3+} and n_{C4+}) are distributed in the peripheral plasma.

Figure 1 (c) shows that the iron dusts emitted from the helical coil directly reach the ergodic layer including the main plasma, which is because of no divertor legs on the trajectories from the dust source position. The simulation suggests that the long pulse discharges are subject to the iron dust emission from the saddle portion of a helical coil can. Figure 3 shows the poloidal cross section of the profile of the electron density, the production rate of neutral iron atoms induced by the dust emission and iron ion densities in the peripheral plasma at a toroidal angle close to the iron dust source (toroidal angle $\phi=10.625^\circ$) in the case of a current of the iron dust emission of 5A. Being similar to that for the carbon dust emission, the density profile of the iron ions for lower ionization stages (n_{Fe1+} and n_{Fe3+}) is localized near the dust source, and the iron ions with higher ionization stages (n_{Fe7+}) are distributed in the poloidal direction.

Acknowledgements

This work was partly supported by the JSPS-NRF-NSFC A3 Foresight Program in the field of Plasma Physics (NSFC: No.11261140328, NRF: No.2012K2A2A6000443). It is also financially supported by a NIFS budget (NIFSULPP015) and is performed with the support and under the auspices of the NIFS Collaboration Research program (NIFS12KNXN236) and NIFS/NINS under the project of Formation of International Scientific Base and Network (KEIN1111). One of the authors (M.S.) would like to thank Y. Feng for permission to use the EMC3-EIRENE code, and he is grateful for the computational resources of the LHD numerical analysis server and the plasma simulator in NIFS.

References

- [1] M. Shoji, et al., Nucl. Fusion **55** (2015) 053014.
- [2] M. Shoji, et al., Plasma and Fusion Res. **11** (2016) 2402056.
- [3] Y. Feng, et al., Plasma Phys. Control. Fusion **44** (2002) 611.
- [4] D. Reiter, et al., Fusion Science and Technology **47** (2005) 172.
- [5] A. Y. Pigarov, et al., J. Nucl. Mater. **363-365** (2007) 216.
- [6] R. D. Smirnov, et al., Plasma Phys. Control. Fusion **49** (2007) 347.
- [7] Y. Tanaka, et al., J. Nucl. Mater. **415** (2011) S1106.
- [8] G. Kawamura, et al., Contrib. Plasma Phys. **54** (2014) 437.
- [9] M. Shoji, et al., J. Nucl. Mater. **438** (2013) S559.
- [10] K. Koga, et al., Plasma and Fusion Res., **4** (2009) 034.

Data analysis method of KSTAR reflectometer for density profile measurement

Seong-Heon Seo¹

¹National Fusion Research Institute, Yuseong-Gu, Daejeon 34133, Korea

Abstract

KSTAR plasma density profile is measured by using a frequency modulation reflectometer. The time resolution of KSTAR reflectometer is 25 μ s. To achieve this fast time resolution, a new robust algorithm for the measurement of instantaneous frequency is developed based on wavelet transform. By applying this algorithm, the frequency of a highly amplitude modulated signal and of the signal contaminated with a similar frequency noise can be measured successfully. The data analysis methods are described in detail and the result of the plasma density profile measurement during ELM crash is presented.

1. Introduction

Frequency modulation (FM) reflectometer is a microwave diagnostics which measures the plasma density profile with fast time resolution. KSTAR reflectometer [1] launches microwave in the frequency range of 33-110 GHz through horn antennas installed in the middle of D-port. Since a single microwave component cannot cover such a broad band, the reflectometer is composed of 3 channels. Each channel covers Q band (33-50 GHz), V band (50-75 GHz), and W band (75-110 GHz), respectively. A channel consists of a launcher and a receiver. Therefore 6 horn antennas are installed in D-port. The whole frequency range is linearly swept in 20 μ s with a pause of 5 μ s before the next sweep.

The frequency sweep time determines the time resolution. The maximum time resolution can be achieved if the plasma remains stationary during the frequency sweep. Otherwise the determination of frequency becomes ambiguous. As a result, it is needed to average many measurements to clarify the frequency. This lowers the time resolution. Therefore it is important to develop a robust algorithm to measure the instantaneous frequency of non-stationary signals. In this paper, a new algorithm which utilizes the phase term of the wavelet transform (WT) coefficients is introduced in Sec. 2. In Sec. 3, it is demonstrated how the new algorithm works for a highly amplitude modulated signal and for the signal contaminated with a noise of similar frequency range. In Sec. 4, a hardware approach to reduce the noise is presented. In Sec. 5, the time evolution of the plasma density profile during ELM crash is shown in a time resolution of 25 μ s.

2. Frequency measurement based on wavelet transform

To obtain a plasma density profile, the total spatial phase variation as the wave propagates inside of plasma before being reflected back at the plasma cutoff density should be measured. The spatial phase

variation along the beam path cannot be measured directly in the high temperature plasmas. But the total spatial phase variation along the path can be calculated by measuring the temporal phase variations at two end points of the path and then subtracting them. Two end points are identical in reflectometry because the wave returns back at the cutoff density. The subtraction is easily accomplished by using a mixer. If the microwave launched to the antenna is power divided to feed the mixer local oscillator (LO) input and the microwave received from the antenna is fed to the mixer radio frequency (RF) input, the mixer IF output becomes the time derivative of the total phase variation. Once the total phase variation is obtained from the IF output measurement, it is easily converted to the plasma density profile by using Bottollier-Curtet algorithm [2]. The only issue is how to measure the mixer output frequency. The mixer IF output is a non-stationary signal, that is both the amplitude and the frequency are changing in time.

Normally spectrogram is used to measure the instantaneous frequency of non-stationary signal. Spectrogram is two dimensional amplitude graph of sliding fast Fourier transform (SFFT) coefficients. Ironically Fourier transform itself decomposes a signal into stationary sinusoidal functions, of which frequency and amplitude are constant in time. Therefore the analysis has an implicit assumption that the signal is stationary within the sliding window length. This implies that the frequency measurement based

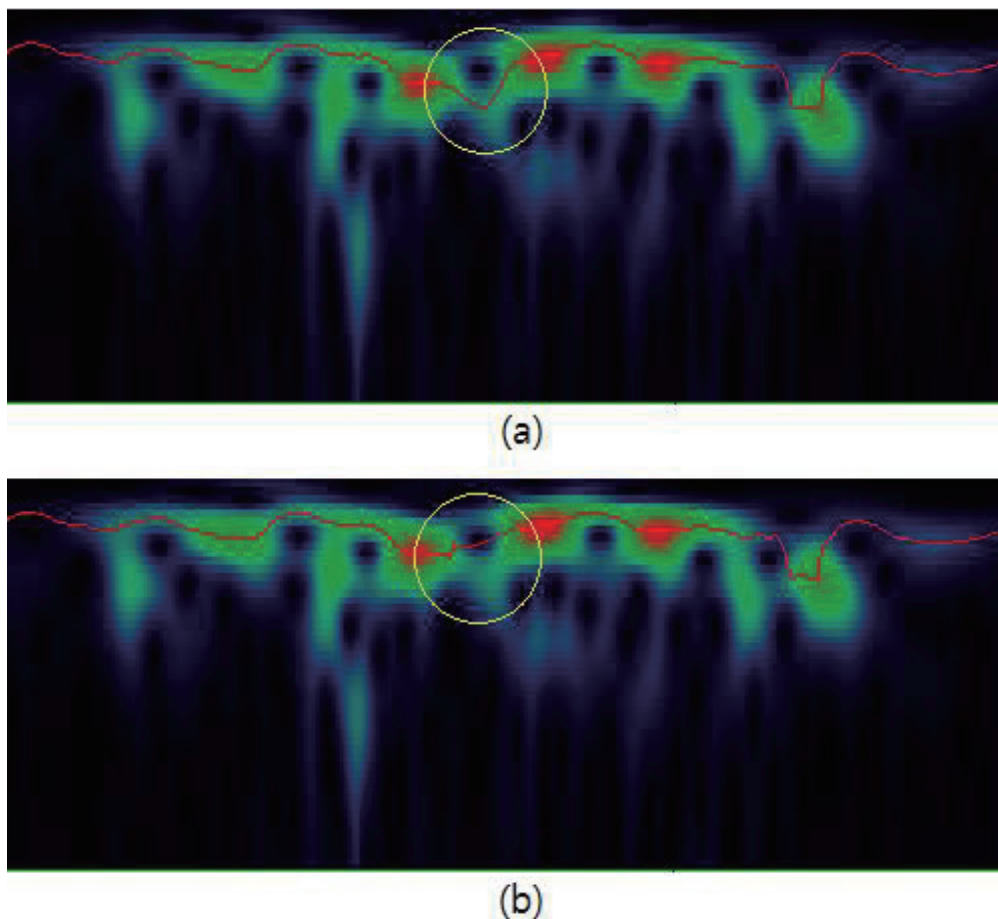


Fig.1 (a) There is a distortion in frequency measurement near amplitude zero crossing point (inside of a yellow circle). (b) Gaussian derivative wavelet transform straightens the frequency trace near zero crossing point.

on spectrogram might be incorrect for a fast varying signal. Scalogram is similar to spectrogram. The only difference is that WT substitutes SFFT. Actually SFFT can be considered as a subset of wavelet transform where a square windowed sinusoidal function acts as a wavelet. There exist three different frequencies in wavelet transform. The signal frequency ω_0 , the wavelet frequency $\frac{\omega}{a}$, and the time derivative of WT coefficient's phase $\frac{\partial \phi(a,b)}{\partial b}$, where a is scale and b is time shift in terms of wavelet transform. In Ref [3], it is shown that the true frequency of non-stationary signal can be obtained by finding the wavelet frequency where Eq. (1) is satisfied.

$$\frac{\partial \phi(a,b)}{\partial b} = \frac{\omega}{a} \tag{1}$$

It is also shown that the time derivative of WT coefficient's phase is a robust approximation of the true frequency for slowly varying signals.

$$\frac{\partial \phi(a,b)}{\partial b} \approx \omega_0 \tag{2}$$

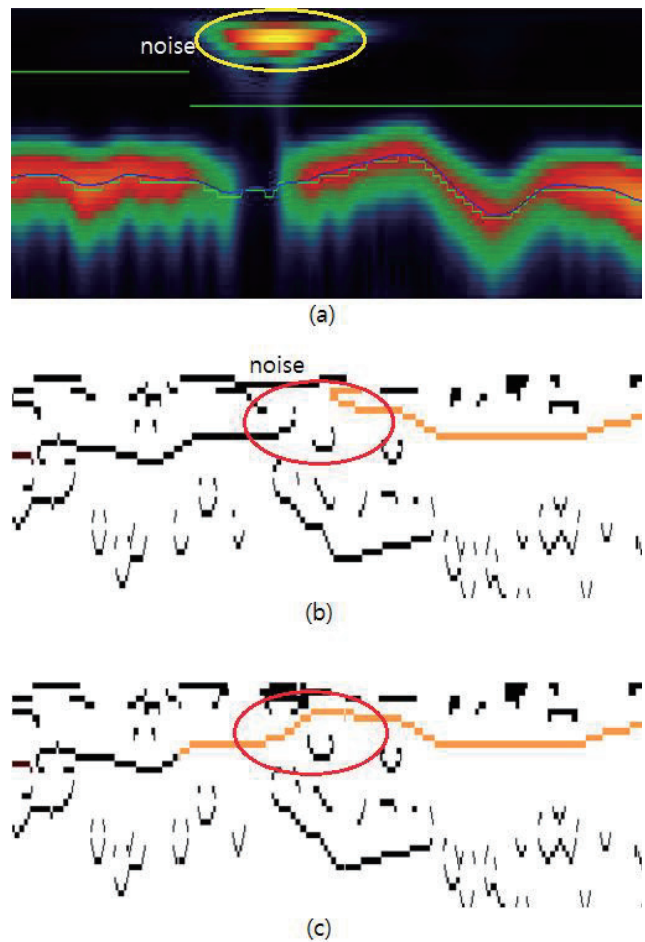


Fig.2 (a) A pseudo oscillation inside of a yellow circle acts as a noise. (b) The frequency cannot be determined around the noise. The frequency trace is broken as shown inside of a red circle. (c) The frequency trace is restored after the noise scalogram is subtracted from the scalogram of (b).

Table 1 The length of waveguides and delay lines

Band	Q (33-50 GHz)	V (50-75 GHz)	W (75-110 GHz)
Delay Line (ft)	23.6	23.6	22.3+3
DL effective length (m)	9.46	9.46	10.15
Waveguide (m)	4.0453	4.0833	4.0543
Waveguide for switch (m)	0.84901	0.682	0.49362

output frequency is determined by the path difference between the LO input and the RF input of mixer. The typical path lengths are summarized in table 1. The waveguide length includes the length of an electrical isolator that electrically isolates the reflectometer circuit from the waveguide connected to the vacuum vessel. The distance from the antenna input flange to the inner vacuum wall is 1.6963 m. When the full band width is swept in 20 μ s, the expected IF frequency of Q, V, and W band are 10.6, 14.4, 13.7 MHz, respectively. An additional delay line of 1 m (phase velocity = 76%) reduces the IF frequency by 3.73, 5.49, and 7.68 MHz for each channel. So if the delay line length is reduced, the IF frequency will be increased to make it easy to eliminate the pseudo noise by using a high pass filter. And then the frequency can be

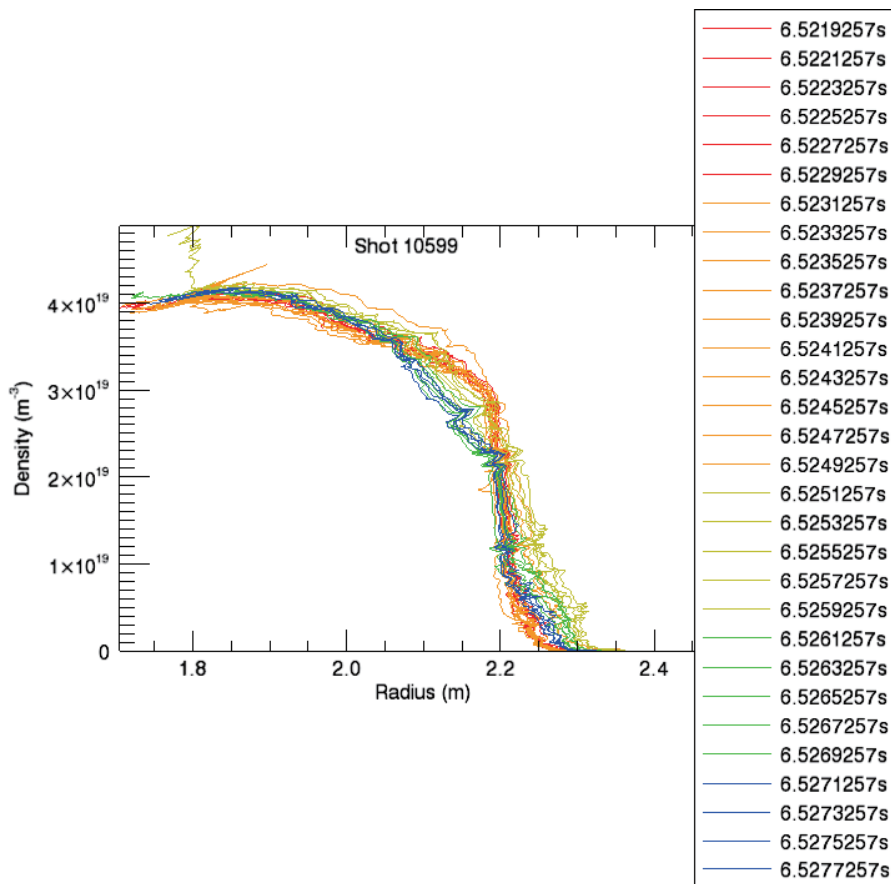


Fig.4 The time evolution of the plasma density profile during ELM crash

down-converted by using a mixer for digitization with 100 MSamples/s digitizers. A mixer generates two branches, that is, $f_{LO}-f_{IF}$ and $f_{LO}+f_{IF}$. The use of a higher IF frequency is good for filtering because the frequency difference between two branches is proportional to $2f_{IF}$. For the delay lines of -4.3, 0.3, 2.4 m for Q, V, and W band, the output frequency will be about 53 MHz. The minus length of delay line means that it should be located in the launching part. A high pass filter of 15 MHz can suppress the pseudo noise in the frequency range of < 6 MHz. An IF frequency of 45 MHz will down-convert the signal to the frequency range of 10 – 40 MHz for digitization. For the delay lines of 0.3, 3.21, and 4.77 m, the output frequency will be about 36 MHz.

4. Density profile measurement

By applying the developed algorithm, the plasma density profile can be measured with a time resolution of 25 μ s. Fig.4 shows the time evolution of the plasma density profile during ELM crash

Acknowledgements

This work was partly supported by the JSPS-NRF-NSFC A3 Foresight Program in the field of Plasma Physics (NSFC: No.11261140328, NRF: No.2012K2A2A6000443).

References

- [1] Seong-Heon Seo, Jinhyung Park, H. M. Wi, W. R. Lee, H. S. Kim, T. G. Lee, Y. S. Kim, Jin-Seob Kang, M. G. Bog, Y. Yokota, and A. Mase, Rev. Sci. Instrum. **84**, 084702, (2013).
- [2] Bottollier-Curtet and G. Ichtchenko, Rev. Sci. Instrum. **58**, 539 (1987).
- [3] Seong-Heon Seo and Dong Keun Oh, will be published in Rev. Sci. Instrum. **87** (2016).

Observation of carbon impurity flow in the ergodic layer of LHD and its impact on the edge impurity screening

**T. Oishi^{1,2}, S. Morita^{1,2}, S. Y. Dai^{1,3}, M. Kobayashi^{1,2}, G. Kawamura¹, X. L. Huang¹,
H. M. Zhang², Y. Liu², M. Goto^{1,2}, and the LHD Experiment Group¹**

¹National Institute for Fusion Science, Toki 509-5292, Gifu, Japan

²Graduate University for Advanced Studies, Toki 509-5292, Gifu, Japan

³School of Physics and Optoelectronic Technology, Dalian University of Technology, Dalian 116024, PR
China

Abstract

Spatial profiles of vacuum ultraviolet (VUV) lines from impurities emitted in the ergodic layer of the large helical device (LHD) were measured by a space-resolved VUV spectroscopy using a 3 m normal incidence spectrometer. Carbon impurity flows were derived by the Doppler shift of the CIV spectra with the wavelength of $1548.20 \times 2 \text{ \AA}$. Direction of the flows in the outward-shifted magnetic field configuration agrees with simulation results by a three-dimensional simulation code EMC3-EIRENE indicating flows which drive the impurity screening phenomena. Observation for carbon CIII-CVI lines suggests impurity screening is enhanced in high density discharges. It has no argument with the flow measurement and the simulation.

1. Introduction

Stochastization of edge magnetic fields is extensively studied not only for mitigation of the edge localized mode (ELM) but also for the plasma detachment and the impurity transport. The ergodic layer of LHD consists of stochastic magnetic fields with three-dimensional structure intrinsically formed by helical coils, while well-defined magnetic surfaces exist inside the last closed flux surface. It is therefore extremely important to study the impurity behavior and transport in the ergodic layer and to compare with those in the scrape-off layer of tokamaks. Recently, reduction of the parallel impurity transport, so called “impurity screening”, has been studied in LHD [1,2]. The theoretical modelling explains that a parallel momentum balance on impurity ions in the ergodic layer determines the direction and quantity of the impurity flow, which can be the key mechanism driving the impurity screening. Therefore, a precise profile measurement of the impurity flow is truly required to examine the validity of the theoretical modelling on the impurity transport in stochastic magnetic field layer.

2. Comparison of the experiment with the simulation for impurity flows in the ergodic layer

Figures 1(a) and (b) show the simulation results of C^{3+} impurity flow parallel to magnetic field lines calculated with a three-dimensional simulation code EMC3-EIRENE for different magnetic configurations of $(R_{ax}, B_t) = (3.6 \text{ m}, 2.75 \text{ T})$ and $(3.9 \text{ m}, 2.539 \text{ T})$, respectively, for hydrogen discharges with the electron density at the last closed flux surface (LCFS), $n_{e, LCFS}$, of $6.0 \times 10^{13} \text{ cm}^{-3}$ and the auxiliary heating power,

P_{in} , of 10 MW [3]. Radial thickness of the ergodic layer varies toroidally and poloidally. When the magnetic axis is shifted outwardly, the ergodic layer is wider and the plasma size within LCFS is smaller. The magnetic field lines at the top and bottom edges of the ergodic layer are illustrated by the black solid arrows as B_{top} and B_{bottom} , respectively. The blue and orange thick chain dashed arrows indicate the flow velocity parallel to the magnetic field line, $V_{||}$, at the top and bottom edges, respectively. It should be noted here that the toroidal component of $V_{||}$ has an opposite direction between the top and bottom edges, while the major radius component of $V_{||}$ has the same direction, namely, the direction toward outboard side for inward-shifted configuration with $R_{ax} = 3.6$ m while the direction toward inboard side for outward-shifted configuration with $R_{ax} = 3.9$ m.

Figure 2(a) shows an edge vertical profile of C^{3+} impurity flow evaluated from Doppler shift of the second order of CIV line emission ($2 \times 1548.20 \text{ \AA}$) measured by a VUV spectroscopy for $R_{ax} = 3.9$ m at a horizontally-elongated plasma position of LHD [4]. The observation range of the VUV spectroscopy is also illustrated in Fig. 2(b). The measured flow velocity in Fig. 2(a) is projection of the flow along the observation chord which can be approximately considered to be the direction of the plasma major radius.

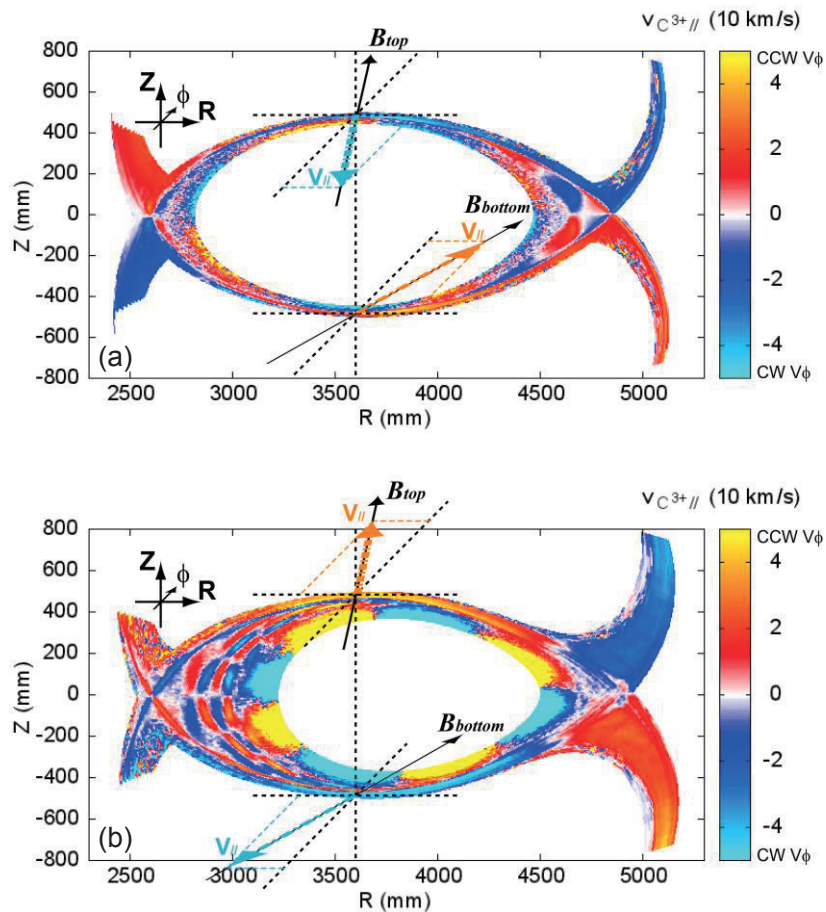


Fig. 1 Contour plot of C^{3+} impurity flow parallel to magnetic field lines calculated with EMC3-EIRENE code for (a) $R_{ax} = 3.6$ m and (b) $R_{ax} = 3.9$ m. Magnetic field lines at the top and bottom edges of the ergodic layer, B_{top} and B_{bottom} , and the flow velocity parallel to the magnetic field line, $V_{||}$, are illustrated together.

From the figure it is found that the flow direction is in the outboard direction in the outermost region in the observation range ($Z < -460$ mm). We have also already confirmed that a synthetic profile of the simulated flow obtained by integrating the Doppler-shifted CIV intensities along the observation chord agrees quantitatively with the experiment in the case of the inward-shifted configuration with $R_{ax} = 3.6$ m. The agreement concludes that the parallel flow in the ergodic layer can be well explained by the presently used theoretical modelling on the edge impurity transport.

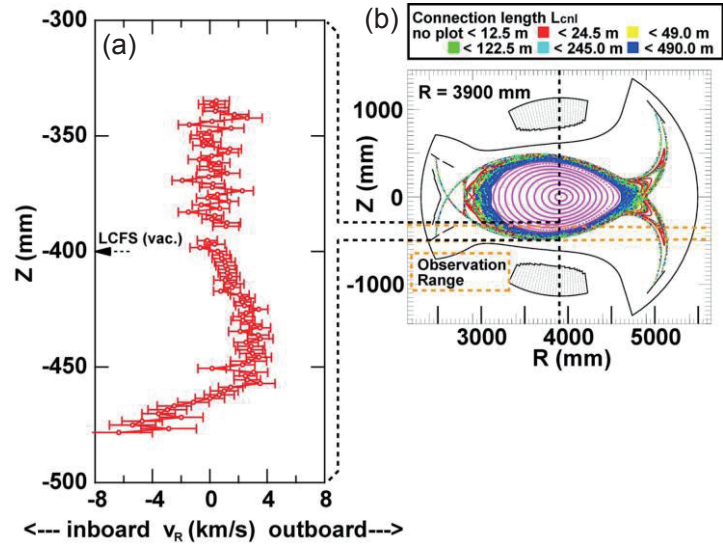


Fig. 2 (a) Vertical profile of C^{3+} impurity flow evaluated from Doppler shift of the second order of CIV line emission ($2 \times 1548.20 \text{ \AA}$) measured by VUV spectroscopy for $R_{ax} = 3.9$ m. (b) The observation range of the VUV spectroscopy.

3. Correlation between impurity flows and impurity screening

Figure 3 shows electron density dependence of carbon lines, (a) CIII and (b) CIV measured by VUV spectroscopy and (c) CV and (d) CVI measured by extreme ultraviolet (EUV) spectroscopy. The line emission intensities are normalized by the line-averaged electron density. CIII and CIV increase while CV and CVI decrease in higher n_e discharges. Carbon density profiles are calculated with EMC3-EIRENE code with $n_{e,LCFS} = 6.0 \times 10^{13} \text{ cm}^{-3}$, as shown in Figs. 3(e-h) for C^{2+} , C^{3+} , C^{4+} , and C^{5+} , respectively. C^{2+} and C^{3+} are localized at the outermost region of the ergodic layer while C^{4+} and C^{5+} are distributed close to LCFS. These results indicate that carbon lines emitted from outer region of the ergodic layer (CIII, CIV) increase while those from inner region (CV, CVI) decrease with density. The observation suggests enhancement of the impurity screening and has no argument with enhancement of friction-force dominated carbon flow directed to the divertor.

Acknowledgement

The authors thank all the members of the LHD team for their cooperation with the LHD operation. This work is partially conducted under the LHD project financial support (NIFS14ULPP010). This work was also supported by Grant-in-Aid for Young Scientists (B) 26800282 and partially supported by the JSPS-NRF-NSFC A3 Foresight Program in the Field of Plasma Physics (NSFC: No.11261140328, NRF: No.2012K2A2A6000443).

References

- [1] M. B. Chowdhuri, S. Morita, M. Kobayashi *et al.*, Phys. Plasmas **16** (2009) 062502.

[2] M. Kobayashi, S. Morita, C. F. Dong *et al.*, Nucl. Fusion **53** (2013) 033011.

[3] S. Y. Dai, M. Kobayashi, G. Kawamura *et al.*, Nucl. Fusion **56** (2016) 066005.

[4] T. Oishi, S. Morita, C. F. Dong *et al.*, Appl. Opt. **53** (2014) 6900.

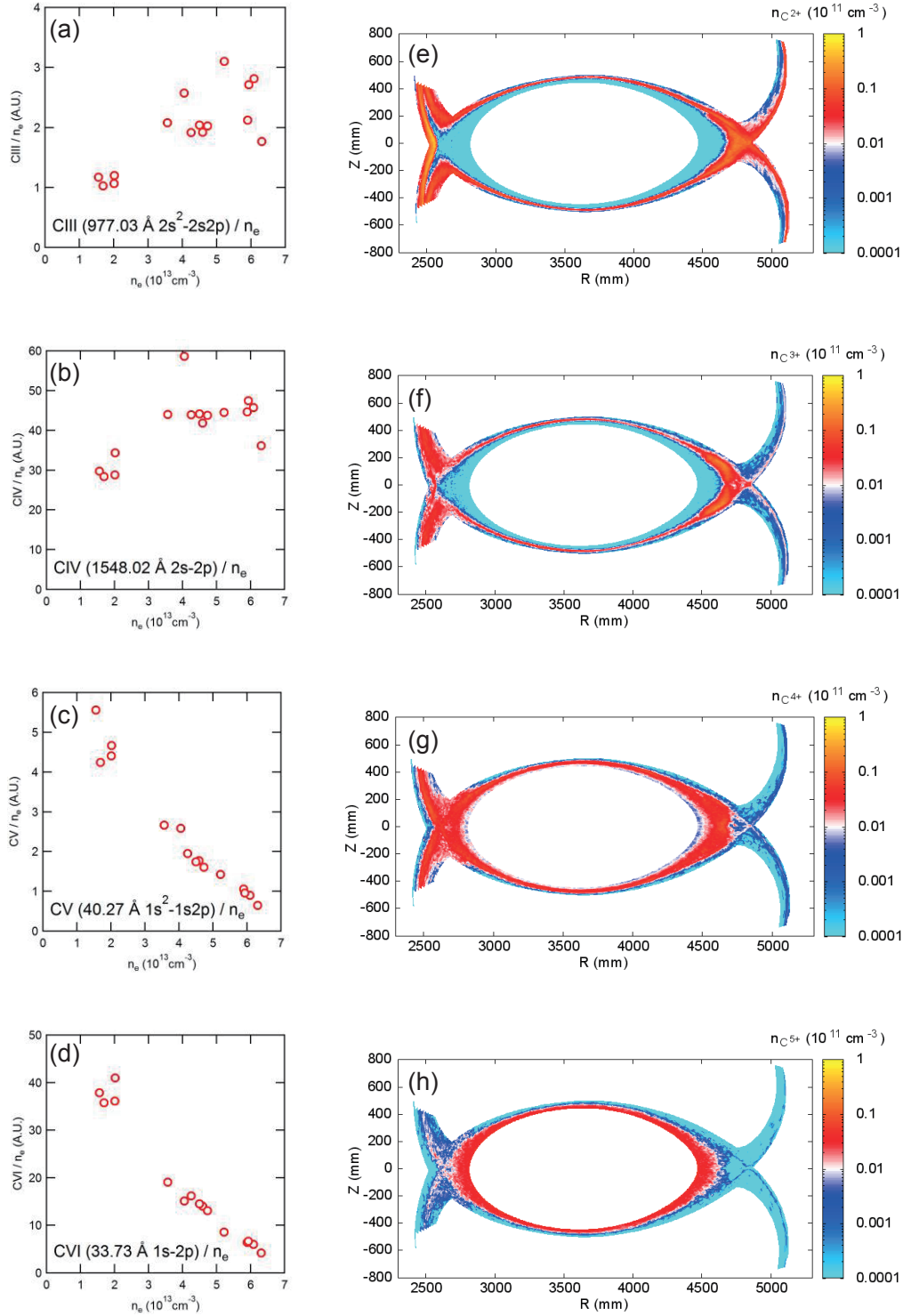


Fig. 3 Electron density dependence of carbon (a) CIII, (b) CIV, (c) CV, and (d) CVI line emission intensities normalized by line-averaged electron density and carbon density profiles for (e) C²⁺, (f) C³⁺, (g) C⁴⁺, and (h) C⁵⁺ calculated with EMC3-EIRENE code for $R_{ax} = 3.6$ m with $n_{e, LCFS} = 6.0 \times 10^{13}$ cm⁻³.

Experimental study of impurity transport coefficient based on the time behavior measurement of impurity line intensity on EAST

L. Zhang¹, S. Morita^{2,3}, Z. Xu¹, X. D. Yang¹, L. Q. Xu¹, Y. M. Duan¹, Y. Yuan¹, J. Huang¹,
P. F. Zhang¹, T. Ohishi^{2,3}, Z. W. Wu¹, J. L. Chen¹, L. Q. Hu¹ and EAST team

¹Institute of Plasma Physics Chinese Academy of Sciences, Hefei 230026, China

¹National Institute for Fusion Science, Toki 509-5292, Gifu, Japan

²Graduate University for Advanced Studies, Toki 509-5292, Gifu, Japan

Abstract

An analysis technique is introduced to determine the transport coefficients, D and V , for Cu using a sudden sputtering from LHW attanne based on the time behaviour measurements of impurity line emission from Cu ions with different ionization stages by a fast-response extreme ultraviolet (EUV) spectrometer as well as the time behaviour measurements of total radiation caused by Cu both at plasma edge and core by AXUV diode arrays (fast bolometer) and soft X-ray imaging system. The result on the impurity transport study is used for the impurity density calculation in EAST.

1. Introduction

Quantitative study on impurity behavior is very important. Since 2014 campaign EAST has been operated with graphite lower divertor, molybdenum first wall and tungsten upper divertor [1]. Quick increase of core radiation power loss during medium-high Z impurity accumulation always causes a periodic H-L back transition or even triggers a plasma disruption, which is the biggest issue to achieve the long pulse H-mode discharge in EAST. Therefore, the impurity density evaluation is urgently desired.

The impurity density profile, $n_{\text{imp}}(r)$, can be obtained from the space-resolved measurement of impurity line intensity [2]. The impurity transport coefficient D (diffusion coefficient) and V (convective velocity) in the core plasma is then determined by comparing the measured and simulated $n_{\text{imp}}(r)$ with 1D transport simulation. An absolutely calibrated fast-response extreme ultra violet (EUV) spectrometer (without space resolution) is used to measure the time behavior of line emission intensity on EAST [3]. The impurity density is also determined by comparing the measured and simulated chord-integral intensity of impurity line emissions [4]. In this case, however, the D and V need to be assumed in the simulation code.

Experimental study of impurity transport was often carried out by impurity injection with LBO, PI technique. Previous work on impurity transport study shows that a good fitting of the temporal intensity decay of line emissions is important in determining the impurity transport coefficient [5-6]. When a good agreement between computed and measured impurity intensity decay is attained, the intensity decay rate of

the chord-integral impurity emission is more sensitive to the D and V. Temporal evolutions can be therefore used to determine the D and V when a transient impurity source is given to plasma.

2. Analysis technique [6]

The 1-D model of impurity transport in the core plasma is used to describe the time-resolved density of impurity ions with ionization stage of z , n_z , as shown in equation (1) and (2),

$$\frac{\partial n_z}{\partial t} + \bar{V} \cdot \bar{\Gamma}_z = S_{z-1} n_e n_{z-1} + \alpha_{z+1} n_e n_{z+1} - (S_z n_e n_z + \alpha_z n_e n_z) \quad (1)$$

$$\Gamma_z = -D \nabla n_z - \frac{r}{a} V n_z \quad (2)$$

where Γ_z , S_z , α_z , D , V stand for transport flux, ionization rate coefficient, recombination rate coefficient, diffusion coefficient, and inward convective velocity, respectively. When the equation (1) is summed up for all the ionization stages, the equation (3) is obtained,

$$\frac{\partial N}{\partial t} = \frac{1}{r} \frac{\partial}{\partial r} \left[r \left(D \frac{\partial}{\partial r} + \frac{r}{a} V \right) N \right] \quad (3)$$

where N stand for the total impurity density for one impurity species. When equation (4) is considered to be the solution of equation (3),

$$N(r, t) = \sum_{m=0}^{\infty} A_m N_m(r) \exp(-\lambda t) \quad (4)$$

the Kummer's equation is obtained, as shown in equation (5).

$$-\lambda N(r) = \frac{1}{r} \left[\frac{\partial}{\partial r} \left(r D \frac{\partial N(r)}{\partial r} + \frac{r^2}{a} V N(r) \right) \right] \quad (5)$$

Then $W(z)=N(r)$, $z=-S(r/a)^2$, $S=(Va/2D)$ is used, the equation (5) is transformed to equation (6).

$$z \frac{\partial^2 w}{\partial z^2} + (1-z) \frac{\partial w}{\partial z} - \left(1 + \frac{\lambda a^2}{4SD} \right) w = 0 \quad (6)$$

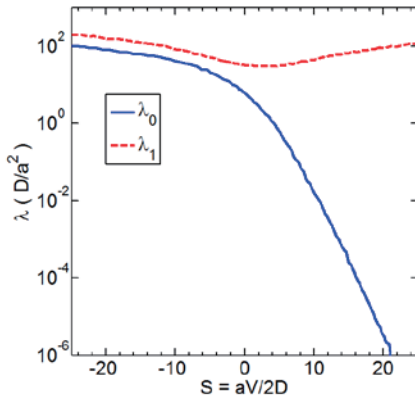


Fig. 1 λ_0 and λ_1 in the unit of D/a^2 as a function of $S=aV/2D$

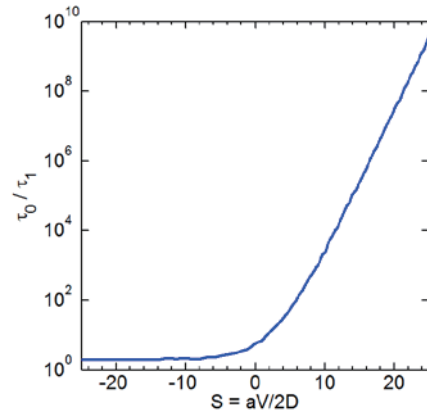


Fig. 2 The ratio of τ_0 and τ_1 as a function of $S=aV/2D$

There are two eigenvalues of equation (6), $\lambda_1 \equiv 1/\tau_1$, $\lambda_0 \equiv 1/\tau_0$, in Chebyshev polynomials ($\tau_0 \gg \tau_1$), as shown in Fig. 1 and Fig 2. λ_1 governs an initial temporal behavior of the injected impurity. Just after impurity injection deposited near the plasma edge, the initial distribution rapidly decays on the time scale of τ_1 and the impurity moves further toward the plasma core. On the other hand, λ_0 controls the long term

impurity behavior, and τ_0 describes the intensity temporal decay at the final impurity distribution which thus means the impurity confinement time. If both τ_1 and τ_0 are achieved experimentally, S could be determined based on the curve in Fig. 2, then D and V could be determined successively curves shown in Fig. 1.

3. Experimentally determined τ_1 and τ_0

3.1 τ_1 and τ_0 determined by impurity line emissions

In some discharges Cu is accidentally sputtered from LHW antenna similar to the impurity injection with LBO, PI. As shown in Fig.3, the long pulse ELM free H-mode plasma with lower single null (LSN) heated by 4.6GHz low hybrid wave (LHW) is achieved in shot #49825. The central electron temperature, $T_e(0)$, during the H-mode phase is about 2.5keV. It is clear that there are several spikes in the time trace of radiation intensity at plasma core indicating that the impurity is sputtered for several times. The sputtered impurity is proved to be dominated by Cu based on the measurement of EUV spectra. The biggest spike at $t \sim 16$ s shaded in Fig. 3 is analyzed.

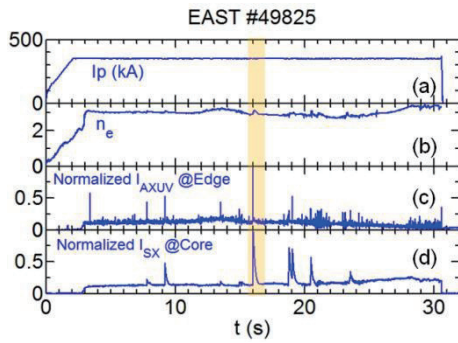


Fig. 3 Time evolution of (a) plasma current, I_p , (b) chord-averaged electron density, n_e , (c) and (d), normalized radiation intensity at plasma edge and core, respectively

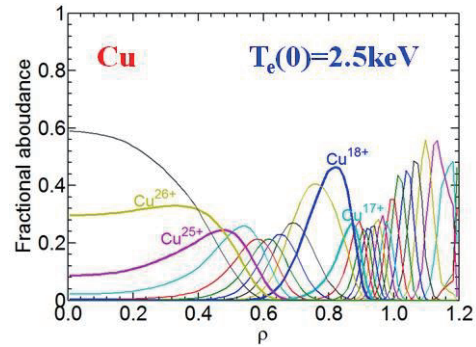


Fig. 4 Simulated fractional abundance of Cu using T_e and n_e profile and magnetic equilibrium configuration in the H-mode plasma in shot #49825

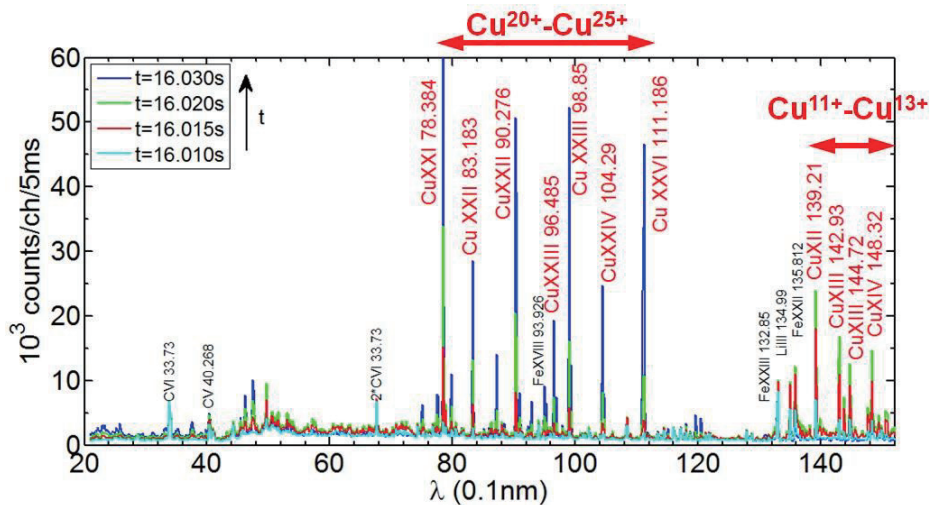


Fig. 5 EUV spectra at 20-150Å measured from 16.01 to 16.03s.

The simulated fractional abundance of Cu in plasma with similar T_e and n_e profile during the H-mode phase in shot #49825 are shown in Fig. 4. It is found that Cu^{10+} - Cu^{15+} exist in the range of $\rho=0.9$ -1.05, Cu^{25+} exist inside $\rho=0.6$. And it is found from Fig. 5 that line emissions from Cu^{11+} - Cu^{13+} appear in longer wavelength range of 140-150Å, while line emissions from Cu^{20+} - Cu^{25+} appear in shorter wavelength range of 80-110Å. Time evolutions of several line emissions intensity are plotted in Fig. 6. It is found that emission intensities from Cu ions with lower ionization stages show a sharp rise and quick drop after ‘injection’ indicating that Cu stays at plasma edge for a very short time. While for emissions from Cu ions with higher ionization stages, the intensity rise is not so quick, and the decay is apparently exponential and much slower compared to the lower ionization stage case. The impurity confinement times (τ_{imp}) of Cu^{11+} - Cu^{13+} , Cu^{20+} - Cu^{22+} and Cu^{25+} is determined by carrying the exponential decay fitting and are shown in Fig. 7. It is clear that the τ_{imp} could be divided into two group, i.e., the ions with the lower ionization stage and the ions with the lower ionization, and τ_1 and τ_0 could be determined by each group.

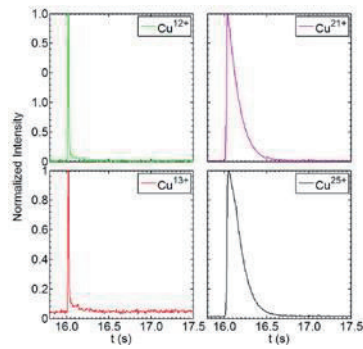


Fig. 6 Time evolution of line intensity of Cu^{12+} (142.93 Å), Cu^{13+} (148.32 Å), Cu^{21+} (90.276 Å) and Cu^{25+} (111.186 Å)

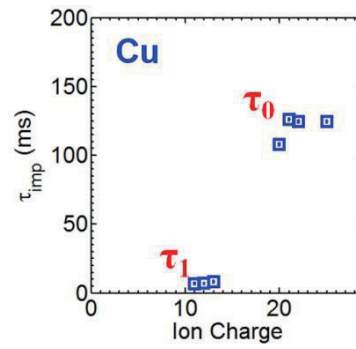


Fig. 7 Impurity confinement time of Cu ions, τ_1 and τ_0 are determined

3.2 τ_1 and τ_0 determined by total radiation

However, τ_1 and τ_0 cannot be determined by impurity line emissions correctly in all the discharges. For the low T_e case, e.g., $T_e(0)=1.0\text{keV}$, the Cu^{11+} - Cu^{13+} is located at $\rho\sim 0.8$, much deeper inside the LCFS, and is defined by impurity ions locating in the plasma core, as shown in Fig. 8 and 9. And the highest ionization stage seems to be Cu^{22+} . Line emissions from Cu^{23+} and Cu^{25+} are very weak. On the other hand, for the high T_e case, e.g., $T_e(0)=4.0\text{keV}$, fractional abundance of Cu^{26+} and Cu^{27+} is very high in plasma core, then the τ_{imp} of Cu^{25+} is lower than the correct τ_0 , as shown in Fig. 10 and 11. In these cases, the signal from AXUV diode array [7] and soft x-ray imaging diagnostics [8] can be useful in this analytical method. The line of sight of the horizontal AXUV diode arrays and vertical soft x-ray array are shown in Fig. 12 and 13.

As shown in Fig. 14, the τ_{imp} obtained from radiation measurement is compared with the τ_{imp} of Cu ions for the low T_e case in shot #49379. And it is found that signal from #48, 55 56 in AXUV array contributed by the impurity at plasma edge is good for τ_1 fitting and the signal from #9-16 in SX array is good for τ_0 fitting. Same comparison for the high T_e case in shot #62946 is shown in Fig. 15. And signal from #59-60 in AXUV array is good for τ_1 fitting and signal from #9-18 in SX array is good for τ_0 fitting.

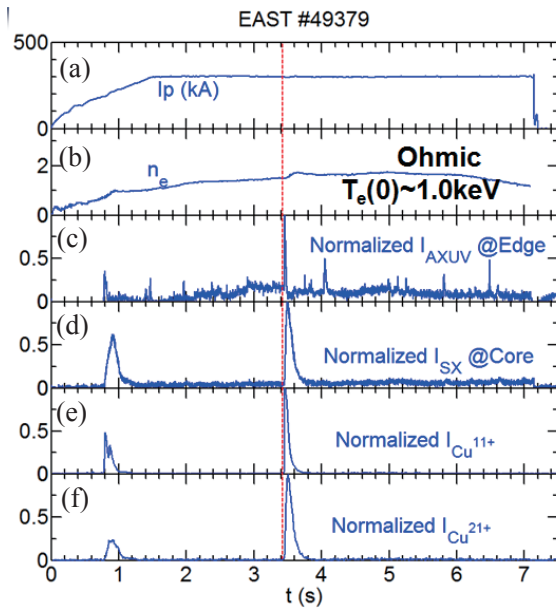


Fig. 8 Time evolution of (a) I_p , (b) chord-averaged n_e , (c) and (d), normalized radiation intensity at plasma edge and core, (e) and (f), normalized line emission intensity from Cu^{11+} (139.21 Å) and Cu^{21+} (90.276 Å)

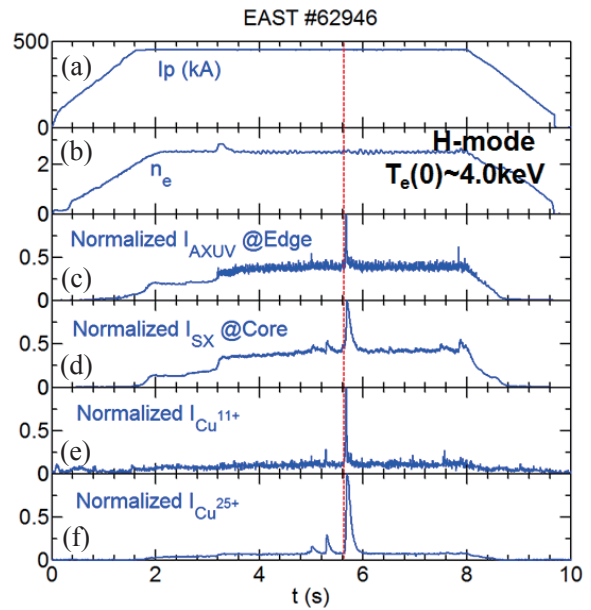


Fig. 10 Time evolution of (a) I_p , (b) chord-averaged n_e , (c) and (d) normalized radiation intensity at plasma edge and core, (e) and (f), normalized line emission intensity from Cu^{11+} (139.21 Å) and Cu^{25+} (111.186 Å) in shot #62946

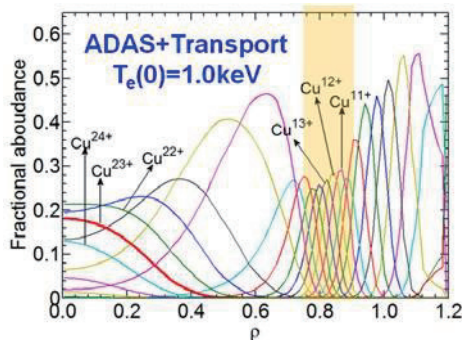


Fig. 9 Simulated fractional abundance of Cu in plasma with $T_e(0)=1.0\text{keV}$ for shot #49379

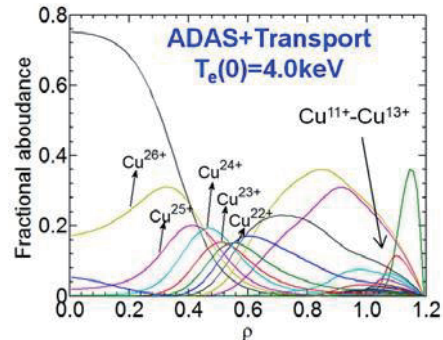


Fig. 11 Simulated fractional abundance of Cu in plasma with $T_e(0)=4.0\text{keV}$ for shot #62946

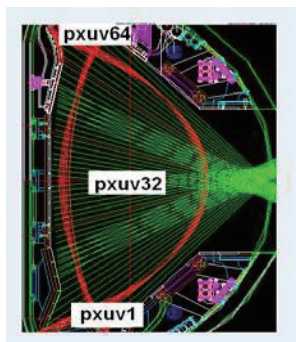


Fig. 12 The line of sights of the horizontal AXUV diode arrays

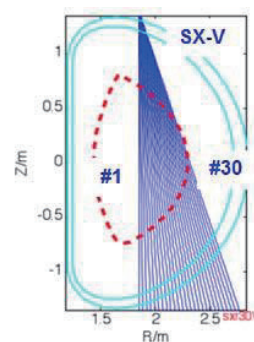


Fig. 13 The line of sights of the vertical soft x-ray array

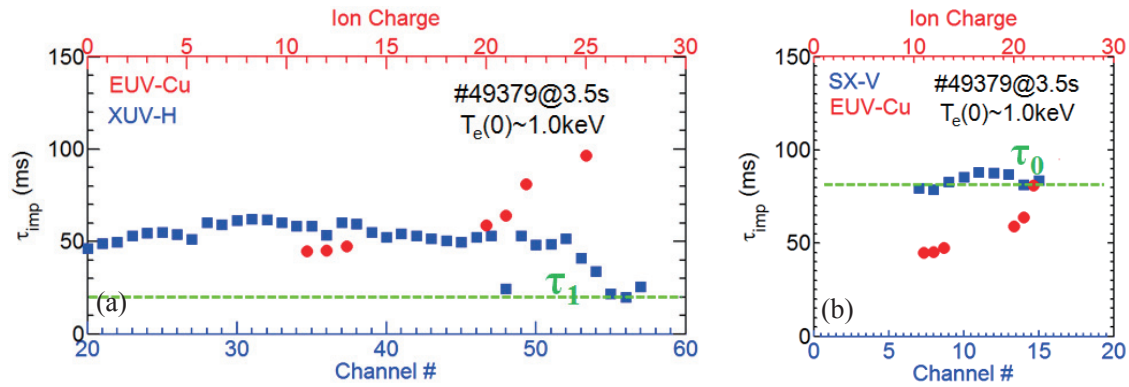


Fig. 14 (a) τ_1 is determined by edge radiation, (b) τ_0 is determined by core radiation in shot #49379

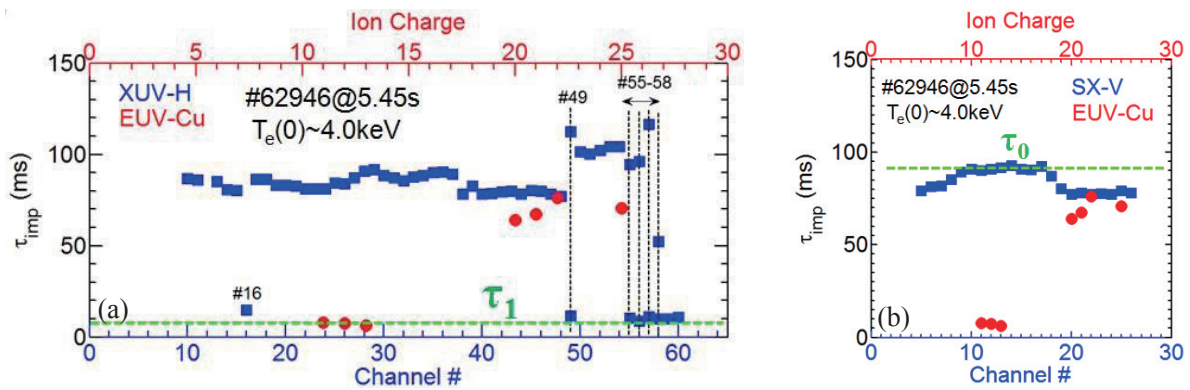


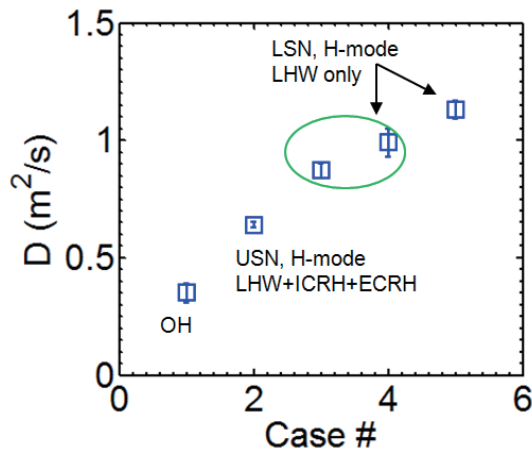
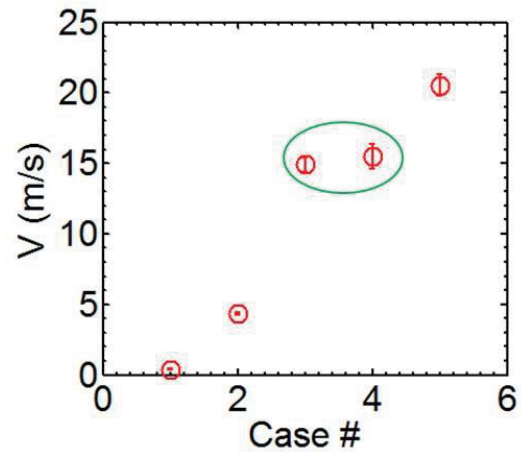
Fig. 15 (a) τ_1 is determined by edge radiation, (b) τ_0 is determined by core radiation in shot #62946

4. Results

Totally, 5 cases are analyzed in this work. The experimental conditions and plasma parameters are listed on table 1. Among them, Case No. 3 and No. 4 is in the ELM-free H-mode phase, and Case No. 5 is in ELM-H mode phase. The averaged transport coefficients, D (diffusion coefficient) and V (convective velocity, inward as positive), are deduced for these 5 cases, and plotted in Fig. 16 and 17. It is found from the results that the D and V is $0.35\text{m}^2/\text{s}$ and 0.38 m/s for the Ohmic case, while in the range of $0.8\text{-}1.2\text{ m}^2/\text{s}$ and $15\text{-}20\text{ m/s}$ for 4.6GHz LHW-heated H-mode cases. More and further data need to be accumulated to explain the difference between the H-mode case with additional ECRH or ICRH and with LHW heating only.

Table 1. The experimental conditions and plasma parameters of the 5 cases

Case	Shot@time(s)	Conf.	$P_{\text{LHW}1,2}$ (MW)	P_{HBI} (MW)	P_{ICRH} (MW)	P_{ECRH} (MW)	W_{MHD} (kJ)	Imp.	
1	49379@3.5	OH	LSN	0	0	0	-	Cu	
2	62946@5.45	H	USN	0.6+2.0	0	1.0	0.4	140	Cu
3	49585@11	H	LSN	0.0+2.1	0	0	0	115	Cu
4	49825@16	H	LSN	0.0+2.1	0	0	0	104	Cu
5	49894@10	H	LSN	0.0+2.1	0	0	0	92	Cu

Fig. 16 The experimental diffusion coefficients, D Fig. 17 The convective velocity, V

5. Summary and outlook

A simple analysis technique is introduced to determine the D and V for Cu ions using a sudden sputtering from LHW attanne based on time behaviour measurements of impurity line emission and total radiation. The result on the impurity transport study is used for the impurity density calculation in EAST.

The result will be checked by the simulation with space-resolved measurement of line emissions in the near future. More discharges will be analyzed to verify the variation of D and V including different heating schemes and more discharges will be analyzed for different impurity species to study the Z -dependence of the D and V .

Acknowledgements

This work was partly supported by the JSPS-NRF-NSFC A3 Foresight Program in the field of Plasma Physics (NSFC: No.11261140328, NRF: No.2012K2A2A6000443).

References

- [1] B. N. Wan et al., Nucl. Fusion 55 (2015)104015
- [2] C. F. Dong et al., Plasma Sci. Technol. 15(3) (2013)230
- [3] L. Zhang et al., Rev. Sci. Instrum. 86 (2015)123509
- [4] X. D. Yang, et al., A3 Foresight Program Workshop, 17-20th May 2016, Yinchuan, China
- [5] M. L. Reinke, PPPL seminar, 2nd February, 2015
- [6] W. K. Leung, Plasma Phys. Control. Fusion 28 (1986)1753
- [7] Y. M. Duan et al., Plasma Sci. Technol. 13(5) (2011)546
- [8] K. Y. Chen et al., Rev. Sci. Instrum. 87 (2016) 063504

**Interactions between Edge Localized Modes (ELMs) and
the Scrape-Off Layer (SOL) plasma in EAST and HL-2A Tokamaks
and a Plan for the External Control**

**K. Toi¹,
L.Q. Xu², L.Q. Hu², J.M. Gao³, Y. Liu³,
EAST² and HL-2A³ teams**

¹NIFS, Toki, Japan, ²ASIPP, Hefei, China, ³SWIP, Chengdu, China,

Abstract

In the divertor tokamaks EAST and HL-2A, interactions between edge localized modes (ELMs) and the scrape-off layer (SOL) plasma were studied to clarify the existence of ELM-induced filamentary currents driven along the magnetic field line in the SOL. In both tokamaks, small toroidal plasma current spikes of the order of a few percentages of the total plasma current have been observed in H-mode plasmas with large amplitude ELMs. The characteristics of the current spikes were studied in various divertor configurations by changing the direction of the toroidal drift with the fixed direction of the plasma current. The observed current spikes have a similar waveform with those of Da emission light in the divertor region and the ion saturation currents on the divertor targets. In all shots analyzed, the current spikes are positive to the total plasma current. Sharp drop in the loop voltage immediately induced as an action of the poloidal magnetic flux conservation. The origin of the observed plasma current spikes is discussed, based on thermoelectric current and other SOL current driving mechanisms. A possibility of active control of SOL currents by electric biasing of toroidally separated two divertor targets on HL-2A is also discussed.

1. Research background and objectives

Global stability of plasma with high plasma confinement is crucially important for steady-state sustainment of deuterium-tritium (D-T) burning plasmas. An H-mode which has an edge transport barrier (ETB) or so-called “pedestal” in the plasma edge is thought to be the most promising candidate operation scenario in the International Thermonuclear Experimental reactor (ITER). The steep pressure gradient and high edge toroidal current density in the pedestal or ETB can excite edge localized modes (ELMs) which lead to large transient heat load to the divertor target plates and serious damages of them. The heat load due to “type-I ELMs is inferred to increase sharply with the decrease in the pedestal

collisionality. The ELM impacts on the divertor plates are very serious for the life time of the divertor targets in ITER [1]. Accordingly, the characteristics of ELMs and the impacts on the divertor targets are intensively investigated experimentally and theoretically. In addition to these efforts, various active control techniques of ELMs are being developed in many toroidal devices. ELM suppression and/or mitigation by using resonant magnetic perturbations (RMPs) and non-resonant perturbations are successfully performed in some tokamaks and spherical tori [2], and also a stellarator/helical device LHD[3]. The characteristics of ELMs and ELM control mechanisms, however, are still not fully clarified. This collaboration is planned twofold, i.e., (1) understanding of ELM characteristics focusing on the ELM-SOL interaction, and (2) ELM control by application of externally applied magnetic perturbations.

2. Plasma current spikes induced by large amplitude ELMs

As a signature of the ELM-SOL interaction, we

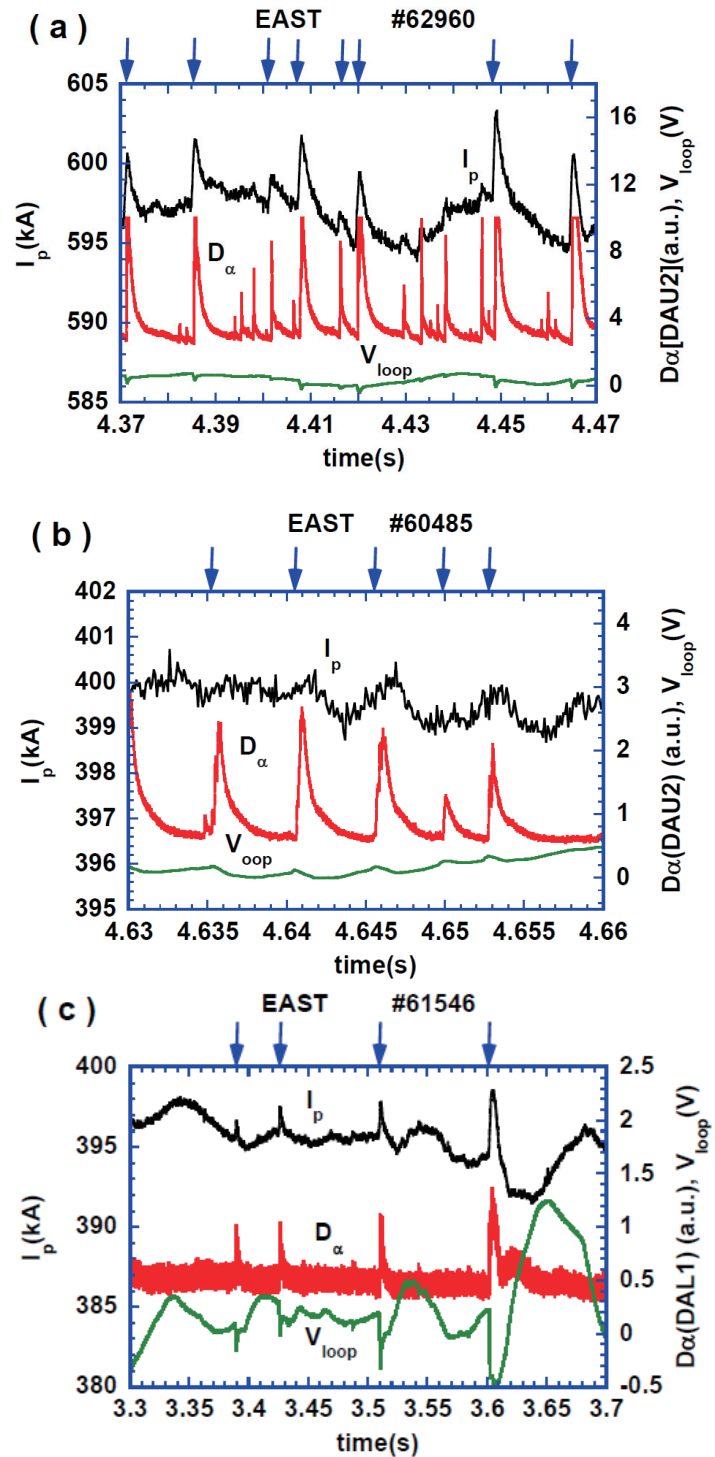


Fig.1 Zoomed toroidal plasma current (I_p) waveform in the H-modes with large ELMs together with the D_α emission from the divertor region and the loop voltage in the USN (a), DN (b) and LSN (c) divertor configurations of EAST. The vertical arrows indicate the ELMs paid attention. The ∇B -drift direction is downward.

focused on the toroidal current spikes induced by large amplitude ELMs incorporating the divertor plasma data. The current spikes are observed in the H-mode plasmas of EAST and HL-2A.

(2.1) Results from the EAST tokamak

In EAST, the toroidal current spikes were investigated in H-modes plasmas with large amplitude ELMs in various divertor configurations, of which shots the plasma current I_p is 400 kA or 600 kA at the fixed toroidal field magnitude $|B_t|=2.4$ T. The direction of toroidal field is changed in the clockwise ($B_t < 0$) or counter-clockwise ($B_t > 0$) direction, while the direction of the plasma current is fixed in the counter-clockwise. The fuel gas is deuterium. By adjusting the vertical plasma position, three divertor configurations are chosen, i.e., upper single null (USN), double null (DN) and lower single null (LSN). ELM size and strength may be determined by collisionality of the pedestal as mentioned above, but may be also affected by the divertor configuration and so on.

Figures 1(a), (b) and (c) show typical zoomed waveforms of the toroidal plasma current (I_p) together with the D_α emission from the divertor region and the loop voltage (V_{loop}) in the H-mode plasmas with large amplitude ELMs in the USN, DN and LSN configurations. The toroidal current spikes induced by large ELMs (ΔI_p) reaches up to ~ 5 kA (positive pulse) in the shots of the USN and LSN configurations. The

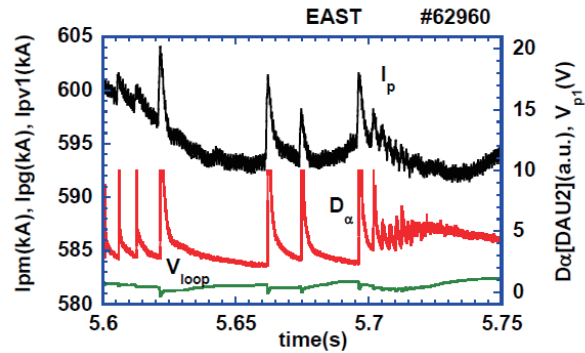


Fig.2 typical example of a shot where the current spikes induced by ELMs have a quite similar waveform with that of D_α emission from the divertor region. The USN configuration is employed and the ∇B -drift direction is downward.

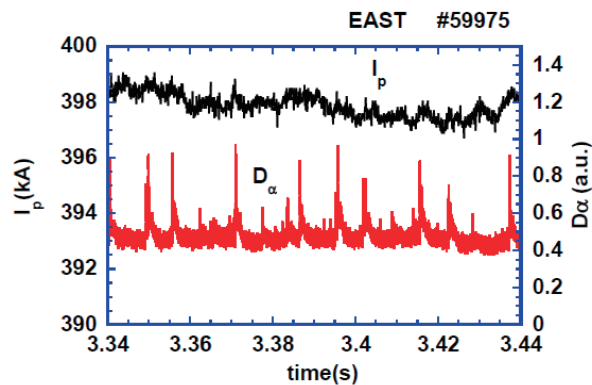


Fig.3 Zoomed I_p waveform in the H-modes with large ELMs together with the D_α emission from the divertor dome in the USN configurations. Here, the direction of B_t is reversed (counter clockwise) to that in the shots shown in Figs.1 and 2. The ∇B -drift direction is upward and points toward the X-point of the USN configuration.

characteristic rise time of ΔI_p is fairly short less than 1 ms. The loop voltage suddenly drops by about 0.3 V to 0.7V due to a reaction of the poloidal flux conservation. For the shot in the DN configuration, no clear current spikes in the plasma current are observed as seen from Fig.1(b). This may be explained by small plasma potential difference between upper and lower targets in outboard or inboard side. In the DN configuration, heat load to both targets is expected to be nearly balanced. For all analyzed shots, the largest current spike reaches $\Delta I_p \sim +10$ kA at $I_p=600$ kA. It should be noted that the I_p spikes induced by ELMs are similar to the waveform of the D_α emission from the divertor region, as seen from Figs. 1(a) and 1(c). In Fig.2, we add another typical example where the clear correlation between the waveforms of ΔI_p and D_α emission is seen for various shapes of ELMs. The positive current spikes with fast rise time of the order of ~ 1 ms suggest uni-directional current induced by ELMs along the field line in the SOL. The effect of the direction of the toroidal field on the ΔI_p is investigated for the cases of the clockwise ($B_t > 0$) and counter clockwise directions ($B_t < 0$). The waveforms of I_p and the D_α emission in the latter case of the counter clockwise are shown in Fig.3. No current spike is observed. This may be due to excitation of rather small ELMs.

(2.2) Results from the HL-2A tokamak

The positive current spikes are also detected in the H-modes obtained with neutral beam injection on HL-2A. The divertor configuration is the LSN configuration having the closed type of the divertor. The direction of B_t is clockwise and the ∇B drift directs toward the X-point of the LSN configuration. The direction of the plasma current is in the counter-clockwise. The zoomed

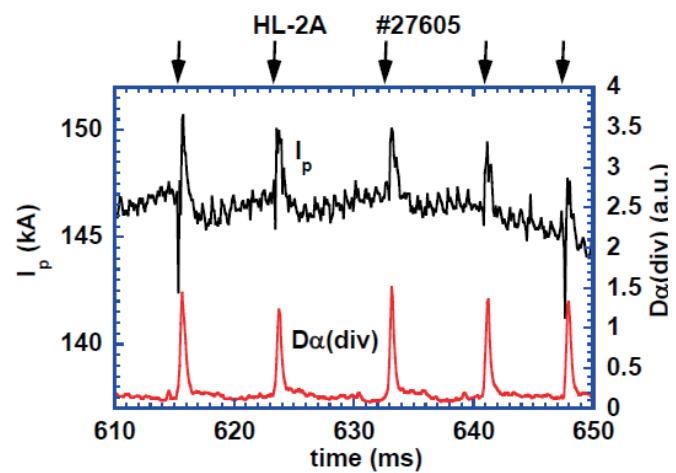


Fig.4 Positive plasma current spikes induced by ELMs in the HL-2A H-mode shot, where the LSN closed divertor configuration is adopted.

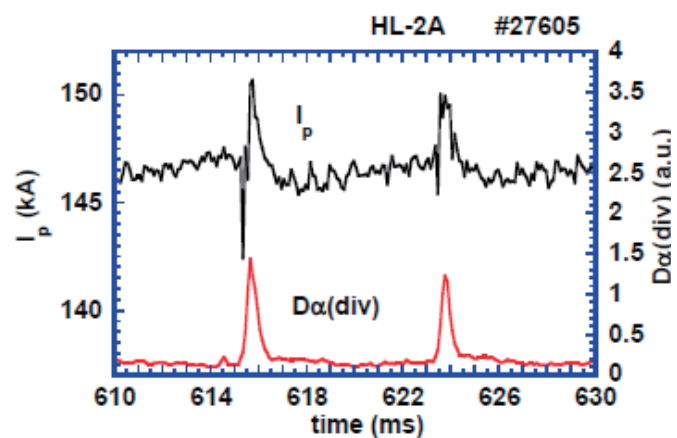


Fig.5 Zoomed waveforms of the plasma current and D_α emission signal in the H-mode of HL-2A..

waveform of I_p is shown in Fig.4 together with the D_α emission. The magnitude of the positive current spikes is up to ~ 5 kA for the $I_p=145$ kA plasma. The relative change in I_p is about 3 % which is about double of that in the EAST H-mode discussed in the subsection (2.1). The signals of I_p and D_α emission are acquired with the same trigger signal, so that the causality between the I_p disturbances and the D_α emission signal should be possible. Just after the onset of ELM the positive current spike is induced as seen from Fig.5. As seen from Figs. 4 and 5, a short negative current pulse is sometimes generated at the onset of an ELM and is followed by a positive spike. The negative current pulse is not observed in the H-modes in EAST. Large particle and heat loads to the divertor targets can drive the SOL current which is uni-directional and flows to the direction to increase the toroidal plasma current, as same as in EAST.

(2.3) Discussion on the origin of the positive current spikes

As mentioned above, large ELMs often generate positive spikes in the plasma current waveform in the LSN and USN divertor configurations of EAST and in LSN configuration of HL-2A. The waveform of the current spike (ΔI_p) is quite similar to that of the D_α emission signal from the divertor region. It should be noted that the rise time of ΔI_p is quite short in the order of sub-millisecond, typically ~ 0.5 ms. This fact indicates that the positive current spikes are not due to the increase in the pedestal region with high temperature just inside the LCFS. The likely candidate of the current spikes is the generation of the current flowing along the field line in the SOL as thermoelectric current driven by the sheath potential difference caused by ELM-induced heat and particle fluxes [4,5]. The thermoelectric current flows usually from the outboard side to inboard side of the divertor targets, because the ELM induced heat and particle fluxes are dominantly loaded to the outboard side targets. On the discharge conditions of the shots where clear positive current spikes are observed in EAST and HL-2A, the thermoelectric current is predicted to flow in the same direction of the toroidal plasma current. In the EAST plasma case shown in Fig.3 where the direction of B_t is reversed in the USN configuration, the current spike ΔI_p should be positive. However, clear positive spikes are not generated by ELMs. One main reason is thought that the ELMs are not strong enough to enhance the sheath potential difference in front of the outboard and inboard side targets. The Pfirsch-Schlüter current in the SOL and the current induced by the parallel gradient of electron pressure are also the possible candidates [6, 7]. In the DN configuration of EAST no clear current spikes are detected. In HL-2A, a short negative current spike is often observed at the ELM onset and then followed with the positive spike as shown in Figs. 4 and 5. This reason is not clarified yet. The negative current pulse may be related to the toroidal current loss due to peeling off the ELM-induced filament from the last closed flux surface (LCFS) [8]. It is known that multi-filament structures are formed by ELMs and they carry appreciable parallel currents to the divertor targets [8]. In MAST, the number of the filaments generated by an ELM is determined to be $n=7-15$ [8]. The field line in the SOL winds round the SOL with the effective safety factor q_{SOL} at the SOL. If the

parallel current of each filament is I_{fil} , the ELM induced current spike ΔI_p will be expressed as $\Delta I_p \sim nq_{SOL}I_{fil}$. In the EAST, I_{fil} is estimated to be ~ 160 A for the $\Delta I_p \sim 5$ kA shown in Fig.1(a) on the assumption of $q_{SOL} \sim 4$ and $n \sim 8$ which is inferred from the numbers of the bursts in the ion saturation current signals measured at the target plates. The current would produce the resonant magnetic perturbations of ~ 10 G at the pedestal near the SOL current layer.

3. Plan of a new ELM control method in HL-2A

Substantial SOL current is induced by ELM events and is thought that it can generate resonant magnetic perturbations (RMPs). If the SOL current is controlled externally, the RMPs can be generated for the control of the pressure gradient and edge toroidal current density at the pedestal.

We are discussing a possibility to apply toroidally segmented divertor biasing to the HL-2A plasma for generation of RMPs. It is not so easy to install the new divertor targets to which electrical biasing voltage can be applied, because the divertor of HL-2A is a

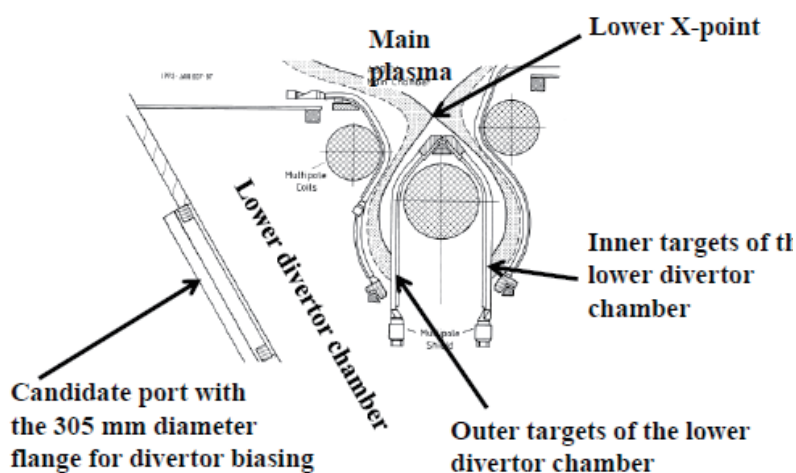


Fig.6 Layout of a candidate port placed on the lower divertor dome of HL-2A.

closed type. For the first step, a port of the 305 mm diameter attached in the lower divertor dome is available for the purpose, as shown in Fig.6. Two ways are possible: (1) to place several electrically floated divertor targets using a moving platform, and (2) to weld a new plate holder on the original divertor target, on which holder several electrically floated targets are attached. In the port, several diagnostics can be installed to get the information of the plasma near the biased and unbiased targets newly installed. That is, Langmuire probes, Infra-red thermography, visible spectrometer and thermocouples and so on are the candidates.

4. Summary and outlook

In ELMy H-modes of EAST and HL-2A, the positive spikes of the toroidal plasma current induced by ELMs are observed having a quite similar waveform of the D_α emission from the divertor region. It is found that the positive current spikes become a good indicator of the SOL current formed by multi filamentary structures generated by ELMs. Further detailed analyses are needed to confirm the generation mechanisms of the SOL current by large ELMs. A new active control method of the SOL current for ELM control is planned to

test in HL-2A. The technique is based on the toroidally segmented divertor biasing.

Acknowledgements

This research is partly supported by the Grant-in-Aid for Challenging Exploratory Research from JSPS (No. 26630476) and the JSPS-NRF-NSFC A3 Foresight Program in the field of Plasma Physics (NSFC: No.11261140328, NRF: No.2012K2A2A6000443).

References

- [1] A. Loarte et al., Plasma Phys. Control. Fusion **45**, 1549 (2003).
- [2] E. J. Doyle et al., Nucl. Fusion **47**, S18 (2007).
- [3] K. Toi et al., Nucl Fusion **54**, 033001 (2014).
- [4] G.M. Staebler and F.L. Hinton, Nucl. Fusion **29**, 1820 (1989).
- [5] A. Kallenbach et al., J. Nucl. Matters. **290-293**, 639 (2001).
- [6] A.V. Chankin et al., J. Nucl. Matters **196-198**, 739 (1992).
- [7] M.J. Schaffer et al., Nucl. Fusion **37**, 83 (1997).
- [8] A. Kirk et al., Plasma Phys. Control. Fusion **48**, B433 (2006).

Explosive behavior of some pressure-driven modes

A. Y. Aydemir, H. H. Lee, S. G. Lee, J. Seol, B. H. Park, and Y. K. In

National Fusion Research Institute, Daejeon 305-806, Korea

E-mail: aydemir@nfri.re.kr

Abstract. The quadrupole geometry of the $m/n = 2/1$ component of an $n = 1$ kink-ballooning mode is shown to result in an explosive ballooning finger that leads to a very fast, almost precursor-free disruption. The ballooning finger convects the hot plasma from the core to the edge on Alfvén time scales, in agreement with some experimental observations. The fast time scale of the ensuing disruption would make any mitigation attempt difficult if not impossible; thus, this type of disruption has to be avoided, which can only be achieved with a thorough understanding of the underlying physics.

Some disruptions at high- β tend to have very fast-growing precursors or no discernible precursors at all[1, 2]. When they are present, the precursor oscillations precede the thermal quench typically by less than a millisecond; time evolution of the signals suggests a mode growing at least exponentially and possibly explosively (faster than exponentially) well into the nonlinear regime.

An ideal MHD mode going through its marginal point as the plasma β increases linearly due to external heating may grow as $\exp(t/\tau)^{3/2}$ [3] [4], thus providing a possible explanation for the short time-scale of the precursors. However, this particular path to explosive growth was shown to be implausible, requiring an unrealistically small initial perturbation amplitude to generate Alfvénic growth, due to the vast separation in time scales between the Alfvén and heating time scales[5].

Here we show computationally that the ideal $m/n = 2/1$ mode, because of its unique geometric characteristics, may provide a generic mechanism for an explosive instability directly and thus may be responsible for those high- β disruptions with very fast precursors. The numerical tool used is the CTD code (see [6] and the references therein) that solves the nonlinear, resistive MHD equations in toroidal geometry.

Experimental context for these calculations is, ironically, not disruptions but highly stable discharges that last many tens of seconds while exhibiting a long-lived $2/1$ mode in the KSTAR tokamak[7], under conditions similar to “advanced/hybrid scenarios”[8], with high edge safety factor q_{q5} and a low inductive current fraction. During investigations into the nature of this mode, it was discovered that in equilibria with peaked pressure profiles, either a benign $2/1$ mode that saturates at a small

amplitude, or an explosively growing $2/1$ is possible, depending on the details of the pressure profile. Leaving a more comprehensive treatment to a future publication, this Letter will focus only on the explosively growing mode.

The equilibrium safety factor and pressure profiles used in the calculations, representative of the advanced/hybrid scenarios in KSTAR, are shown in Fig. 1. The edge and central safety factors are $q_{95} \sim 7, q_0 \sim 2$, respectively. The pressure profiles tend to be peaked due to on-axis electron cyclotron resonance heating (ECRH). Although the plasma- β is moderate for the cases considered here ($\beta_N \approx 1.4$), the $n = 1$ mode is ideally unstable for both q -profiles shown in Fig. 1. The pressure pedestal typical of the H(igh)-mode discharges is avoided numerically to prevent complications introduced by the edge-localized modes (ELM's).

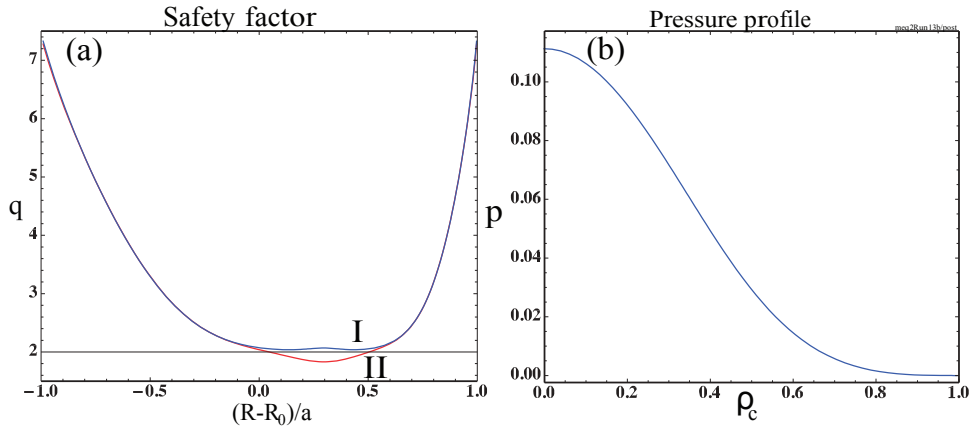


Figure 1: *Equilibrium profiles. The q -profiles in (a) are calculated by field-line tracing and are shown as a function of $(R - R_0)/a$, where a, R_0 are the minor and major radius, respectively. The slightly non-monotonic profile q_I has $q_{min} = 2.04, q_0 = 2.11$. The monotonic profile q_{II} has $q_0 = 1.83$. For both profiles, $q_{95} = 7.3$. The dashed line is at $q = 2$. (b) The pressure profile at the mid-plane as a function of ρ_c , the normalized radial variable of the conformal coordinate system (ρ_c, θ_c) .*

The $n = 1$ eigenfunction for the pressure field is shown in Fig. 2 (a) for the q_I profile (q_{II} gives similar results). As seen in the figure, the poloidal structure of the mode is dominated by an $m = 2$ component, although smaller $m = 3$ effects are also visible. The high and low-field side asymmetry of the perturbed pressure is indicative of a kink-ballooning mode, a low- n version of infernal modes[9]. The ballooning character of the mode is apparent also in its poloidal energy spectrum in Fig. 2 (b), showing a coupling that goes much beyond the immediate sidebands at $m = 2 \pm 1$.

The quadrupole geometry of the perturbed pressure (due to the dominance of the $m = 2$ component) in Fig. 2 (a) plays a crucial role in the subsequent nonlinear evolution of the mode. At the toroidal location with this particular phase of the perturbation ($\zeta = 0$ poloidal plane in this calculation), the flux and pressure surfaces that are nearly circular initially become elongated in the direction of the major radius ($+R$) as a result

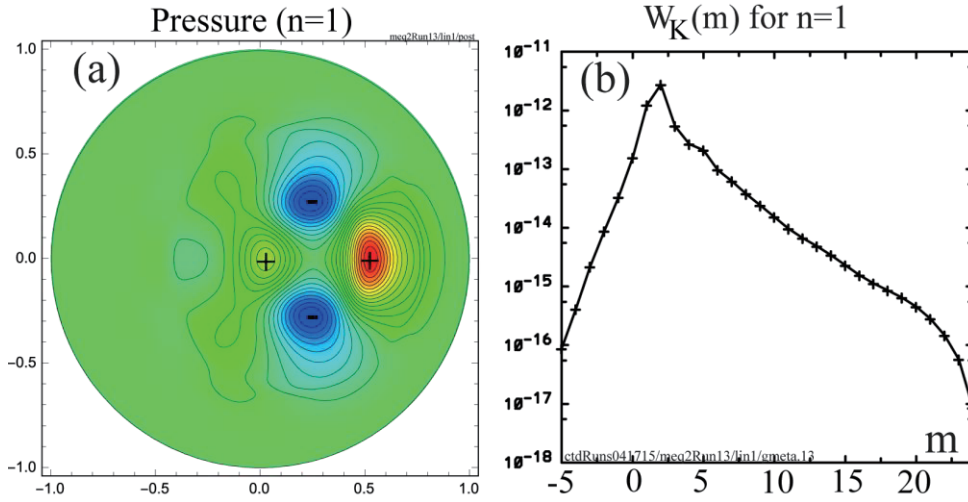


Figure 2: (a) Perturbed pressure contours for the $n = 1$ mode using the safety factor profile q_r in Fig. 1 (a). Note the ballooning nature of the eigenfunction. (b) Poloidal spectrum of the kinetic energy for the $n = 1$ mode.

of this perturbation. Continuing elliptical deformation eventually leads to the formation of a ballooning finger on the low-field side, as seen in Fig. 3 (a).

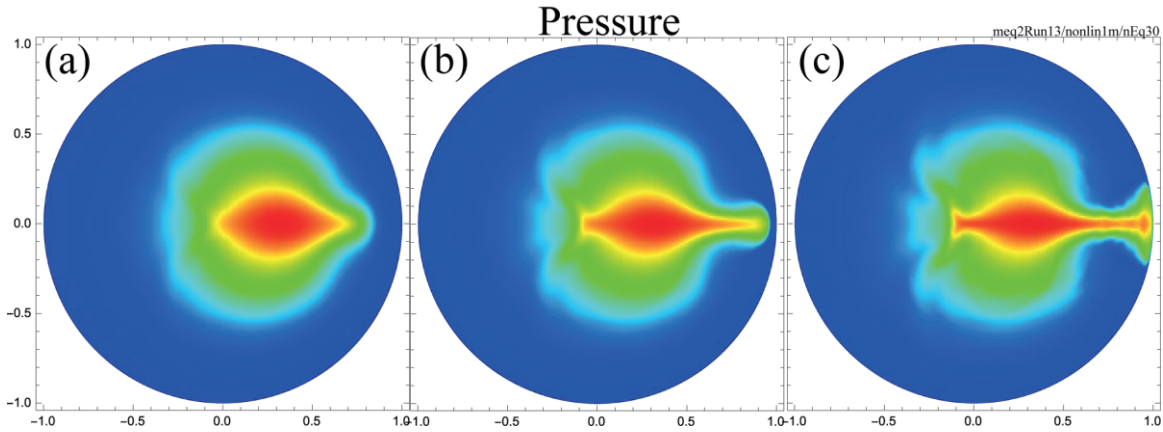


Figure 3: Formation and nonlinear evolution of the “explosive finger” at the $\zeta = 0$ poloidal plane. Figures (a) and (c) are separated by approximately 20 Alfvén times: $t_a = 1483$, $t_c = 1502$ in units of poloidal Alfvén time (See also Fig. 4).

Well before the nonlinear evolution of the $n = 1$ mode reaches the stage in Fig. 3 (a), with a well-defined $m = 2$ ballooning finger, its growth becomes explosive. The finger proceeds to get narrower and more elongated, reaching in ~ 20 Alfvén times the final stage seen in panel (c), where the hot plasma from the core has splashed against the wall. The end result, of course, is a disruption.

Explosive nature of the instability is seen in plots of the total kinetic energy (without the $n = 0$ contribution) in Fig. 4. Panel (a) shows that the growth rate starts increasing

early in the nonlinear evolution beginning around $t_c \approx 1420$ (normalized to the poloidal Alfvén time). In this explosive stage, $W_K(t)$ can be fitted with a curve of the form $W_K(t) = W_K(t_i)[(t_f - t_i)/(t_f - t)]^\nu$, where $t_i = 1417$, $t_f = 1502$, and the exponent $\nu = 3.37$ (panel (b)). Note that the finite-time singularity model is a very good fit to the numerical results except at the very end when the plasma starts coming in contact with the wall. Panel (c) shows the flux surfaces at the beginning of the nonlinear stage. Except for some high- m resistive modes near the edge, the core plasma is still intact, indicating the small amplitude of the $m = 2$ perturbation at this time. This point is confirmed by the energy plots in (a) and (b), which show that at the beginning of the nonlinear behavior, the total kinetic energy is still approximately four orders of magnitude smaller than its final value. Note that the evolution of the explosive finger seen in Fig. 3 occurs in approximately 20 Alfvén times at the very end of the plots in Fig. 4. Thus, this disruption would have only a very brief precursor, much too little to be of practical experimental use.

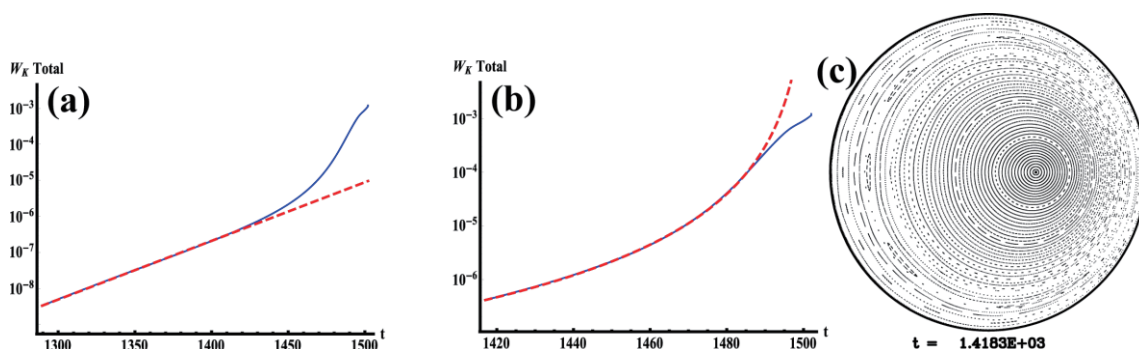


Figure 4: (a) The solid curve (blue) shows the growth of the total kinetic energy in $n \geq 1$ modes ($n_{max} = 30$ in this calculation). For $t \geq 1420$, the growth rate starts deviating from the purely exponential growth of the dashed line (red). (b) The dashed curve (red) shows a numerical fit to the end phase of the disruption of the form $W_K(t) = W_K(t_i)[(t_f - t_i)/(t_f - t)]^\nu$ where $\nu = 3.37$. (c) Poincaré plot of the field lines at the beginning of the explosive growth phase.

In summary, inherently explosive growth of an ideal $n = 1$ mode-driven ballooning finger, with a predominantly $m/n = 2/1$ component, has been demonstrated in nonlinear toroidal simulations. Transition from exponential to explosive growth is driven nonlinearly by the characteristic quadrupole geometry of the $m = 2$ pressure perturbation, which encourages the formation of a ballooning finger. The finger becomes narrower as it explosively pushes through flux surfaces, in qualitative agreement with published theories. This rapid convective loss of mass and energy from the core to the exterior, in some tens of Alfvén times, provides an explanation for fast high- β disruptions that occur with little or no precursors. Although the thermal quench starts with the explosive ejection of the hot core, it is also aided, on a slower time scale, by parallel transport along stochastic fields that are generated during the explosive phase.

Acknowledgments

This research was supported by Ministry of Science, ICT, and Future Planning under KSTAR project and was partly supported by the JSPS-NRF-NSFC A3 Foresight Program (NRF No. 2012K2A2A6000443). This manuscript is an abridged version of a paper published in *Nucl. Fusion* **56** (2016) 054001.

References

- [1] E. D. Fredrickson, K. McGuire, Z. Chang, A. Janos, M. Bell, R. V. Budny, C. E. Bush, J. Manickam, H. Mynick, R. Nazikian, and G. Taylor. Beta-limit disruptions in the tokamak fusion test reactor. *Phys. Plasmas*, 2:4216, 1995.
- [2] R. Yoshino. Neural-net predictor for beta limit disruptions in jt-60u. *Nucl. Fusion*, 45:1232, 2005.
- [3] R. J. Hastie, T. C. Hender, B. A. Carreras, L. A. Charlton, and J. A. Holmes. Stability of ideal and resistive internal kink modes in toroidal geometry. *Phys. Fluids*, 30:1756, 1987.
- [4] J. D. Callen, C. C. Hegna, B. W. Rice, E. J. Strait, and A. D. Turnbull. Growth of ideal magnetohydrodynamic modes driven slowly through their instability threshold: Application to disruption precursors. *Phys. Plasmas*, 6:2963, 1999.
- [5] Steven C. Cowley and Mehmet Artun. Explosive instabilities and detonation in magnetohydrodynamics. *Phys. Reports*, 283:185, 1997.
- [6] A. Y. Aydemir, J. Y. Kim, B. H. Park, and J. Seol. On resistive magnetohydrodynamic studies of sawtooth oscillations in tokamaks. *Phys. Plasmas*, 22:032304, 2015.
- [7] S. G. Lee, J. Seol, H. H. Lee, A. Y. Aydemir, L. Terzolo, K. D. Lee, Y. S. Bae, J. G. Bak, G. H. Choe, G. S. Yun, J. W. Yoo, and the KSTAR Team. Long-lived pressure-driven coherent structures in kstar plasmas. *Submitted for publication*, 9999:9999, 2015. The results were briefly summarized at the 26th Meeting of the ITPA Topical Group on MHD, Disruptions and Control, Oct. 19-22, 2015, Naples, Italy.
- [8] A. C. C. Sips for the Steady State Operation and the Transport Physics topical groups of the International Tokamak Physics Activity. Advanced scenarios for iter operation. *Plasma Phys. Control. Fusion*, 47:19, 2005.

Characterizations of deposited tungsten layer and their hydrogen isotope retention

N. Ashikawa^{1,2}, K. Katayama³, S. Saito⁴, S.H. Son⁵, M.K. Bae⁵, J.G. Bak⁵, S.H. Hong⁵, Y.W. Yu⁶, F. Ding⁶, J.Wu⁶, S.H.Zhou⁶, J.S.Hu⁶, G.N.Luo⁶

¹*National Institute for Fusion Science, Toki, Japan*

²*SOKENDAI, Toki, Japan*

³*Kyushu University, Kasuga, Japan,*

⁴*NIT Kushiro College, Kushiro, Japan*

⁵*National Fusion Research Institute, Daejeon, Korea*

⁶*Institute of Plasma Physics Chinese Academy of Science, Hefei, China*

E-mail: ashikawa@LHD.nifs.ac.jp

1. Introduction

Areas of controllable wall retention are limited region (not fully thickness of walls) in fusion devices [1-3]. Hence, to understand a range of controllable thickness into plasma facing materials (PFMs) is important. However, tools of wall retention are limited, such as baking, wall conditioning discharges for the PFMs.

Tungsten (W) is a candidate material for plasma-facing components because of low solubility and low sputtering yield for hydrogen isotopes. During fusion plasma discharges, the W surface will be modified due to sputtering and re-deposition. The deposited W layer has a different structure from the original W material. Therefore, the evaluation of tritium retention in not only original materials but also in deposited layers is required. Moreover, tritium desorption property from deposited W layers has to be also understood for tritium recovery. Lab-scale experiments on hydrogen isotope behavior in deposited W layer formed by plasma sputtering has been performed in Kyushu University. However, in order to discuss tritium behavior in deposited W layers formed in a fusion reactor, the characterized deposited layer should be exposed to energetic particles having energy distribution in the fusion experimental devices. In this work, the common target materials of deposited W layers produced by hydrogen plasma sputtering in Kyushu University are exposed to deuterium plasma in EAST and KSTAR, and surface analyses are planned in Kyushu University and NIFS. An advantage of this deposited W layer is to use characterized target materials with the known parameters. Amounts of tritium inventory on deposited W layer on the plasma facing materials are evaluated and the proper tritium recovery method will be proposed. The obtained results will be useful also for understanding hydrogen isotope retention in fusion devices.

2. Experimental setup

Figure 1 shows the schematic drawing of cross-section at the equatorial plane in KSTAR. The poloidal electric probe system is located at the low field side around the equatorial planes at different positions on torus and measured particle fluxes [4]. Poloidal limiter probes array

locates about 160~170 mm away from the last closed flux surface (LCFS) and 74 mm behind the poloidal limiter. The deposition probe system is located at the section C in KSTAR [5]. The head position of the deposition probe system is about 10 cm below from the equatorial plane. At this position, target samples did not attach to plasmas directly. Three samples holders were set on the circular plate of 78 mm diameter, it was made by the stainless steel 316, and this was connected to the deposition probe system. Fig.2 shows a picture of sample holders. In this experiment, bulk W, deposited W on the bulk W, titanium, silicon, stainless steel 316 targets were installed in the sample holders. In addition, three kinds of different W targets, Nilaco Corp., A.L.M.T. Corp., EAST-divertor type, were used. Two thermocouples were connected to side planes of sample holders, but data could not be detected due to damages of these thermocouples.

Samples exposed to deuterium plasmas during two experimental date in KSTAR. Typical plasma duration is about 30 seconds and plasma shot numbers are from 13775 to 13851. Effective plasma discharges are about 25 shots and an effective exposure time during H-mode plasmas was counted about 120 seconds in this experiment. Particle fluxes were measured by the poloidal limiter probes around the equatorial plane and a distance from the LCFS to the head of probes is similar to that from the LCFS to the surface of target materials. From analytical results, particle fluences of $1E23 D^+/m^2$ were calculated using above total exposure time.

X-ray photoelectron spectroscopy (XPS), which type is ESCA1600, analyzed surface contaminations and their chemical bindings on the target materials. An Al X-ray source of 400 W and a spot size of 800 μm were used. An argon (Ar) ion gun was used to etch the target samples and analysis of their depth profiles. Material structures were measured by X-ray diffraction (XRD) analyzer, which type is RINT-2200 with Cu source. Deuterium depth profiles were measured by a glow discharge optical emission spectroscopy (GD-OES) using Ar working gas. Eroded depth by GD-OES on bulk W specimens were measured by a profilometer and a sputtering rate of GD-OES was calibrated. Total deuterium retention after plasma exposures was evaluated by thermal desorption spectrometry (TDS) measurements. The thermal desorption of molecules was measured by quadrupole mass spectroscopy (QMS). In laboratory experiments, it was reported that results of deuterium

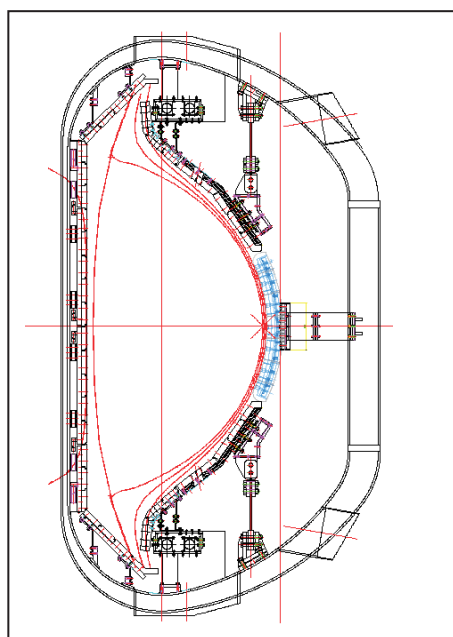


Fig.1 Poloidal cross section and poloidal probe system at the equatorial plane in KSTAR



Fig.2 A picture of the sample holder in KSTAR.

retention show clearly fluence dependences. As additional experiments, common tungsten target materials exposed to deuterium plasmas in tokamaks, EAST and KSTAR, in this A3 collaboration work.

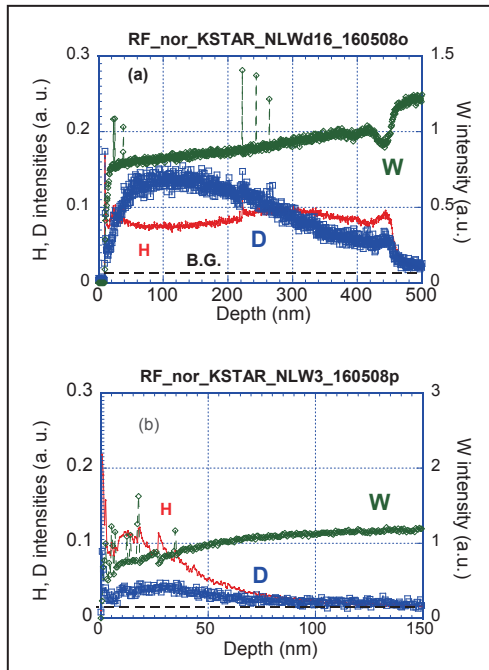


Fig.3 D, H, W depth profiles measured by top surface. In deposited W layer such as in Fig.3 GD-OES (a) with deposited W layer on bulk W and (b) bulk W.

3. Results and discussion

After deuterium plasma exposures in KSTAR, deuterium retention with and without deposited W layers were measured by thermal desorption spectrometry (TDS). deuterium retention on deposited W layer was 4×10^{20} D/m² and bulk W without deposited W layer was 2×10^{29} D/m² after deuterium plasma exposures.. incident fluence was estimated about 1×10^{22} D⁺/m² measured by the poloidal probes at the lower field side in KSTAR. D retention in deposited W layer is one order of magnitude higher than bulk W.

Figure 3 shows deuterium(D), hydrogen(H), W depth profiles after plasma exposure in KSTAR. In bulk W such as in Fig3 (b), small amounts of deuterium were increasing below 70 nm from the top surface. In deposited W layer such as in Fig.3 (a), deuterium was widely observed until 450 nm from the top surface and this thickness is similar to a thickness of the deposited W layer. GD-OES is

qualitative analysis and detected signals in Fig.3 are arbitrary unit. In the case of stable discharge parameters for specimens, a relative composition using these counts is available. From a comparison between with deposited W layer and without one, a difference of integrated counts is about 10 times and this result is similar to the result by TDS. A based bulk W, below deposited W layer, shown lower D intensities such as shown in Fig. 3 (a).

Fig. 4 shows XRD patterns for (a) bulk W made by A.L.M.L, (b) bulk W designed for EAST divertor and (c) deposited W based on bulk W. Bulk W made by A.L.M.L and EAST -type are similar patterns are shown. Deposited W shows the same positions of each peaks from a comparison with two bulk W. But width of peaks are wider than bulk W. Inharmonious compositional substance is considered for a reason of this pattern.

Bulk W samples with and without deposited W layers were exposed to deuterium plasma in EAST in 2012. Initial amounts of hydrogen were implanted by working gassed during sputtering to make deposition layer and a ratio between tungsten and hydrogen, H/W, is 0.032. These amounts of W/H before and after plasma exposures are the same. Retained deuterium after plasma exposure was implanted by deuterium plasma and the ratio between tungsten and deuterium, D/W, is 0.002. The retained deuterium in deposited W layer is at least one order of magnitude higher than that in bulk W [6-7]. In general, metal oxide layers on metal targets are regarded as one of trapping sites for hydrogen isotopes. In this experiment, initial oxide layers produced by air contaminations were removed during plasma exposures and influences of oxide layers for deuterium trappings are a few in this experiment. As other possibility of

trapping sites for deuterium isotopes, a grain boundary is considered in W. Deuterium trapping site into deposited W layers will be discussed later with a comparison with a numerical simulation.

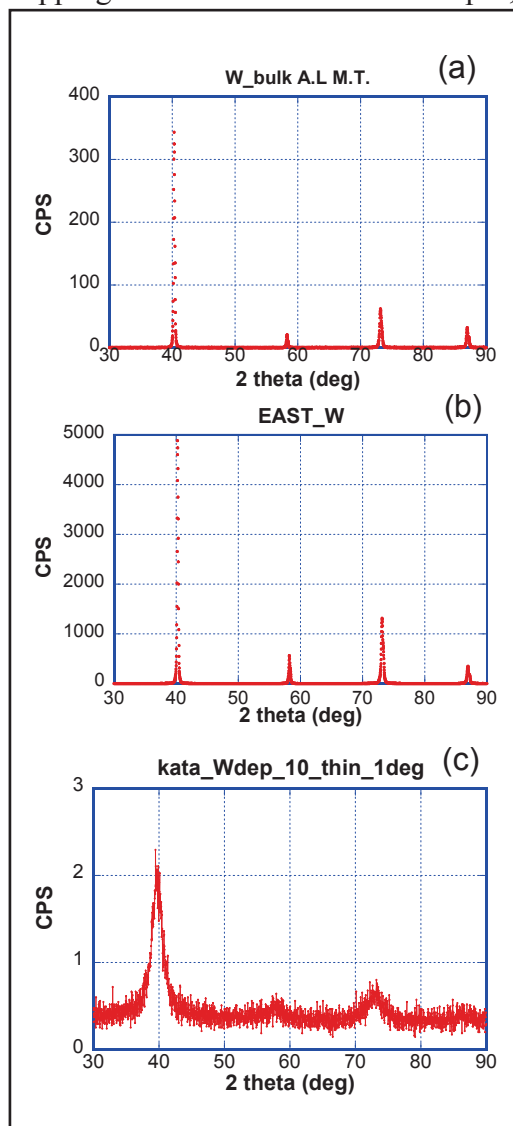


Fig.4 XRD patterns for (a) bulk W made by A.L.M.L, (b) bulk W designed for EAST divertor and (c) deposited W based on bulk W.

4. Summary

Deuterium retention on deposited W samples exposed to deuterium plasmas have been investigated.

D retention in the specimen with deposited W layer is higher than that of bulk W. D depth profiles show a similar results between deposited W layer and bulk W. D intensities was detected in deep regions of the layer. Two kinds of reasons are considered about higher D retention in deposited W layer. One is small grains with inharmonious compositional substance. Second is initial implanted hydrogen during sputtering process of W coating, which is estimated as interactions between metals and hydrogen such as isotope exchanges.

5. Acknowledgements

This research was partly supported by the JSPS-NRF-NSFC A3 Foresight Program in the field of Plasma Physics (NSFC: No.11261140328, NRF: No.2012K2A2A6000443) and NIFS budget KUHR010 and ULFF004.

- [1] J.S.Hu et al., Fusion Engineering and Design, 84(2009) 2167.
- [2] T. Wauters at al., 39th EPS Conference on Plasma Phys., Stockholm, July 2-6, 2012.
- [3] N. Ashikawa et al., Plasma and Fusion Research, 6, (2011) 2402138.
- [4] J.G. Bak, Y.S. Ho, H.S. Kim, et al., Contrib. Plasma Phys., 53(2013) 69.
- [5] S.K.Hong, et al., Fusion Sci. and Tech., 63 (2015) 36.
- [6] K.Katayama, N. Ashikawa, et al., Annual report of NIFS (2012 April - 2013 March).
- [7] K.Katayama, N. Ashikawa, F.Ding et al., 22th PSI conference (2016).

LHCD optimization for high performance in EAST

Bojiang Ding for LHCD group

Institute of Plasma Physics, Chinese Academy of Sciences, Hefei 230031, P. R. China

Abstract Lower hybrid current drive (LHCD) is one effective tool to achieve high performance plasma in EAST. To utilize LHCD for accessing high performance effort has been made to improve LHW-plasma coupling and current drive capability at high density. LHW-plasma coupling is improved by means of local gas puffing and gas puffing from the electron side is routinely used during EAST operation with LHCD. High density experiments suggest that low recycling and high LH frequency are preferred for the LHCD experiments at high density, consistent with previous results in other machines. Effect of LHCD on current profile in EAST demonstrates that it is possible to control the plasma profile by optimizing the LHW spectrum. Repeatable H-mode plasma is obtained by LHCD and the maximum density during the H-mode with the combination of 2.45GHz and 4.6GHz LH wave is up to $4.5 \times 10^{19} \text{m}^{-3}$.

1. Introduction

Lower hybrid current drive (LHCD) [1–3] plays a key role in controlling the current profile in tokamak experiments aimed at improving confinement and stability of fusion plasmas. The first H-mode plasma by LHCD was obtained in a limiter configuration in JT-60 [4]. In JET, long lasting ITB was sustained during high confinement (H-mode) using LHCD [5,6]. Recently, LHCD H-mode has been extensively obtained in EAST [7–10]. Existing results show that relatively high density is preferred for the LHCD H-mode plasma since more fast electrons driven by lower hybrid wave (LHW) are subjected to be slowed down by thermal electrons through collision, hence heating plasma and enhancing stored energy. However, there are at least two problems in the H-mode operation to be fixed. One is the LHW-plasma coupling, the other is current drive (CD) capability. As we know, good LHW-plasma coupling is the first necessary condition for LHCD experiment and high CD efficiency is important for driving plasma current and controlling current profile, especially for sustaining a long pulse H-mode

plasma. In the H-mode plasma, the edge density would decrease rapidly enough that the density at the grill mouth would not satisfy the wave-plasma coupling condition [11, 12], resulting in a large reflection. It requires the grill density to be above a cut-off density determined by $n_{e,co} = (\omega^2 m_e) / (4\pi e^2)$, where ω is the wave frequency, m_e is the electron mass and e is the electron charge. Consequently, the LHW power cannot be effectively coupled to the plasma if the plasma density at the grill is below the cut-off density. Usually, as reported in JT-60U, ASDEX, JET, Tore-supra, HT-7[13-19], local gas puffing near the antenna is an effective method for the coupling. In addition, reactor relevant high plasma density regimes have faced the LHCD tool with the challenge of effectively penetrating the main plasma without excessive power dissipation of the coupled radio frequency (RF) power at the edge. LHCD experiments on many tokamaks [20-23] have observed a decrease in non-thermal tails and a drop in bremsstrahlung emission much steeper than $1/n_e$ at high densities, which is stronger than expected based on current models. Similar results [7, 24] have also been reported in EAST.

In order to obtain EAST scientific goal (long pulse and high performance), two LHCD systems with 2.45GHz (4MW) [24-26] and 4.6GHz (6MW) [8] have been developed and exploited on EAST. Aiming at H-mode in EAST, related efforts including coupling and current drive capability toward to high performance have been done and continued. Main results in EAST are summarized as follows: 1) Local gas puffing from electron-drift side is more efficient to improve LHW-plasma coupling and taken as a routine way for the EAST operation with LHCD. 2) High temperature and low density in edge region is preferred for the LHCD experiments at high density. 3) High LH frequency is useful to improve RF power propagation into core region and enhance CD efficiency at high density. 4) Effect of LHCD on current profile in EAST suggests it is possible to control the plasma profile by adjusting the LHW spectrum.

2. Study for improving LHW-plasma coupling

Theory studies [11,12] indicate that plasma density at the grill mouth (grill density) and its gradient are two key factors determining wave-plasma coupling. The coupling

should be more outstanding in H-mode discharge since the steep density gradient near the pedestal will lower the grill density and was fixed by local gas puffing near the antenna. With 2.45GHz LHCD system in EAST, further experimental comparisons [27] of local gas puffing (D_2) from electron drift side (GIM_e) and ion drift side (GIM_i), as displayed in Fig. 1, are shown in Fig. 2, indicating that the effect of gas puffing from the electron drift side is better than that from the ion drift side. It is seen that, for a same gas flow, local gas puffing from the electron drift side reduces the reflection coefficient (RC) more than gas puffing from the ion drift side, as shown in Fig. 2(a). The enhanced coupling is due to higher density in edge region, as seen in Figs. 2(b) and (c). The difference in edge density between electron- and ion-side cases suggests that local ionization of puffed gas plays a dominant role in affecting the density at the grill due to different movement direction of ionized electrons and that part of gas has been locally ionized near the gas pipe before diffusing into the grill region.

Similar experiments in JET show that local gas puffing (D_2) near the LH antenna in the outer mid-plane is efficient to improve LH coupling. However, the gas flow rate in EAST is about one order smaller than that in JET[17,18], where a good coupling was obtained when using a flow rate of 5×10^{21} el./s with the dedicated gas pipe (GIM6) set in the outer wall. The reason for the difference is not very clear, possibly being related to puffed gas, global ionization, edge recycling, and particle transport.

Referenced from the above study, only the local gas puffing structure from electron drift side are installed on EAST, both for 2.45GHz and 4.6GHz, so as to save the space inside the device. Similar to 2.45GHz LHCD, as shown in Fig. 3, it is seen that the coupling with 4.6GHz LHW is improved by means of the local gas puffing.

The coupling characteristics in H-mode with and without local gas puffing is shown in Fig. 4. It shows that, by means of local gas puffing, the RCs in H-mode both decrease for 2.45GHz and 4.6GHz LHWs. The averaged reflection coefficient remains relative low ($<10\%$), indicating that the coupling is acceptable. Therefore, in the routine experiments in EAST, the local gas puffing from electron drift side is utilized for a good LHW-plasma coupling.

3. Exploration of high LHCD capability at high density

High density is a challenge of LHCD experiments. Especially, density will increase in H-mode discharges, leading to low CD efficiency. Some possible mechanisms (collisional absorption (CA) [28], parametric instabilities (PI) [29,6], scattering from density fluctuations (SDF) [30, 31]), individually or simultaneously, have been identified to preclude the penetration of LHWs, dissipating the power in the plasma periphery and degrading LH efficiency: In order to explore the experimental condition for high CD efficiency at high density in EAST, experiments with 2.45GHz LHW ($N_{//}^{\text{peak}}=2.1$) at a double null configuration were studied [7] by increasing density in one discharge with poor and strong lithisation, following the method assessed on FTU of reduced PI effect under higher edge temperature consequent to wall lithiation [6,20]. As mentioned above, the local gas puffing from GIM_e was utilized in the experiments. The effect of density on driven current was estimated by the count of hard X-ray rate (60keV~200keV) normalized by the injected LHW power, which is proportional to current drive efficiency. Seen from the deviation of HXR count rates from the curve of $1/n_e$ shown in Fig. 5 (a), in the strongly lithized discharge, there is no sudden decrease in the driven current until density up to $3.0 \times 10^{19} \text{ m}^{-3}$, which is much larger than the value of $2.0 \times 10^{19} \text{ m}^{-3}$ in the case of poor lithisation. This suggests that the use of wall lithisation promotes the occurrence of the LHCD effect at high density, in agreement with previous results [20] reported in FTU.

The trends of LHCD with plasma density and PI signatures, documented by frequency power spectrum of the signal collected by a RF probe located outside the machine in the mid-plane, have been analyzed. Such RF spectrum consists a broadening at around the LH wave operating frequency, and a sideband shift in the range of the ion-cyclotron frequency (IC-sideband). Seen from Fig. 5(b), compared to the strong lithiation, the IC sideband frequency in the case of poor lithiation decreases faster with density to a low value of ~14.5MHz, which corresponds to the local IC frequency in edge region where PI is subject to occur. The observed trend of decreasing IC sideband frequency with density (see Fig. 5(b)) is consistent with the sharp decay of HXR counts, supporting the

conclusion that the PI mechanism could play a key role in affecting LHCD. Higher temperature and lower electron density in the edge region in the case of strong lithiation (see Fig. 6) reduce PI [6] as well CA [21], thus providing condition favorable for the occurrence of the LHCD effect into the plasma core. As reported in Figs. 14, 15 and 16 in Ref. 24, the measured RF spectra indicating PI behaviour are qualitatively in agreement the preliminary PI modelings by the LHPI code [32] and the code developed by MIT group[33,34]. Note that since both codes do not fully take into account effect of plasma inhomogeneity, it only partly demonstrates the influence of PI on LHCD efficiency in EAST . Studies indicate that low recycling is preferred for high density LHCD operation and, more in general, for improving confinement and stability [6,20,32,35].

4. Effect of LHCD on current profile

To explore long pulse and high performance with LHCD, the capability of controlling current profile is necessary. Effect of LH spectrum with 4.6GHz system on LHCD characteristics was investigated [24] in EAST. The experiments were carried out with different toroidal phase differences ($\varphi_{\Delta}=0^{\circ}$, 90° , 180° , -90°) between the main waveguides and the corresponding spectrum calculated by ALOHA is shown in Fig. 7. The target plasmas and plasma configurations are kept the same for all the cases. Experimental results are shown in Fig.8, with the same plasma current, plasma density and LH power (see Fig. 8(a)-(c)). It is seen that the smallest consumptions of magnetic flux in Fig. 8(d) occurs with $\varphi_{\Delta}=90^{\circ}$, suggesting the highest CD efficiency. The internal inductance (l_i), shown in Fig. 8 (e), is the largest with $\varphi_{\Delta}=90^{\circ}$, whereas it is the lowest with $\varphi_{\Delta}=-90^{\circ}$, implying the most peaked current density profile with $\varphi_{\Delta}=90^{\circ}$. Possible reason for the discrepancy in the CD characteristic between the four cases could be that the spectrum in the main lobe with $\varphi_{\Delta}=90^{\circ}$ has a single main peak, whereas the others are compound, especially in the case of $\varphi_{\Delta}=-90^{\circ}$. Such preliminary results indicate the possibility of profile control by changing the wave spectrum. This could be clearer with the performance enhancement, eg., electron temperature.

A typical discharge with 4.6GHz LHW with 90^0 phasing are shown in Fig. 9, in which the loop voltage decreases quickly to zero approximately, meaning that LHW can drive plasma current effectively. Also, the energy increase from 50kJ to 100kJ due to LHCD, suggesting that LH power is effectively coupled to plasma and transferred plasma. In addition, the internal inductance (l_i) decreases after LHCD is applied compared to Ohmic plasma, implying the plasma current profile is broadened by the LHW application. The electron temperature profiles measured by Thomson scattering (TS) [36] with Ohmic and LHCD plasma are plotted in Fig.10. As compared to the Ohmic plasma, the electron temperature increases much during the LHCD phase. It is seen that the temperature in core region increases from 1.0keV to 4.5keV and an electron internal transport barrier (ITB) is well observed. As discussed in [37, 38], ITB formation could be due to weak magnetic shear modified current profile by LHCD. Unfortunately, measurement of current profile is unavailable yet. Another possible candidate is that the wave is mainly deposited in core region and effectively heats plasma by means of slowing down of fast electrons. Further physics needs to be understood, in particular, in regard to the direct effect of LHCD in improving plasma confinement and stability.

5. LHCD H-mode at high density

Based on the studies of coupling and LHCD characteristics, repeatable H-mode was obtained by LHCD. With 4.6 GHz and 2.45 GHz LHCD systems, high density H-mode was obtained and the typical waveforms are shown in Fig. 11. The electron cyclotron emission (ECE) signal drops quickly at the L-H transition, implying the decrease of LH driven current, possibly due to the concomitant density increase. Seen from the loop voltage and ECE signal, it is inferred that part of current is driven by LHW even if at the density of $4.5 \times 10^{19} \text{m}^{-3}$. Such density is higher than that of $1.5\text{-}2.5 \times 10^{19} \text{m}^{-3}$ obtained by 2.45 GHz LH alone[7].

Possible reason for the discrepancy between the two systems could be the different LHCD characteristics, since wave propagation in plasma is related to the wave frequency. In order to study the effect of frequency on LHCD, two different frequency waves (2.45 GHz and 4.6GHz) with the same power ($P_{\text{LH}} = 1.05\text{MW}$) were injected

successively in one discharge with almost constant density ($n_e = 2.0 \times 10^{19} \text{m}^{-3}$) and the typical waveform are shown in Fig. 12. It is seen that the residual voltages (V_{loop}) are 0.49V and 0.36V respectively during LH application of 2.45 GHz and 4.6 GHz, implying better CD efficiency for 4.6 GHz wave. Better plasma heating effect for 4.6 GHz can be inferred from the time evolution of plasma stored energy ($W_{\text{MHD}} \sim 68.3 \text{kJ}$ and 74.8kJ , respectively for 2.45 GHz and 4.6 GHz). Also, the internal inductance is higher with the 4.6 GHz LH wave injection, indicating the occurrence of more effective LHCD in the plasma core with respect to the 2.45 GHz case [39, 40]. In the experiments, as shown in Fig. 13 (a), the launched spectra are shown in and the peak value of the main lobe is 2.1 and 2.04 for 2.45 GHz and 4.6 GHz waves respectively. Since power spectrum is an important parameter affecting wave propagation and power deposition, using a ray-tracing/Fokker-Planck code (C3PO/LUKE)[41,42], power deposition and driven current profile are calculated (see Fig. 13(b, c)) without considering the spectrum broadening. The different power depositions via C3PO indicate some difference in the propagation characteristics. Note that though the total driven current is somewhat small with the 2.45GHz LHW, it cannot completely account for the experimental discrepancy ($\sim 100 \text{kA}$) estimated by the loop voltage. Therefore, the discrepancy in the initial spectrum could not dominate the difference in current drive. In addition, a comparison of frequency spectra measured by the RF probe between two waves is illustrated in Fig. 14, from which it is seen that larger spectral broadening occurs for 2.45 GHz case, indicating a stronger PI behaviour. This could partly explain the better CD effect with 4.6 GHz LH wave in terms of reduced parasitic PI effect, as previously reported [6,20]. The related results indicate that the 4.6 GHz frequency is more favorable for producing stronger LHCD on EAST, and that the 2.45 GHz operation would require an optimization in terms of PI effect mitigation, by exploiting the available know how in regard [20]. This search will be carried out in future campaigns.

6. Conclusion and discussion

In order to produce H-mode plasma in EAST, effort has been done to improve LHW-plasma coupling and current drive capability at high density as follows. 1) LHW-plasma

coupling is improved by means of local gas puffing and gas puffing from electron side is taken as a routine way for the EAST operation with LHCD. 2) High density experiments suggest that, due to PI effect and collisional absorption in edge region, high temperature and low density is preferred for the LHCD experiments at high density. 3) High LH frequency is useful to improve RF power propagation into core region and enhance CD efficiency at high density. 4) It is possible to control the plasma profile by optimizing the LHW spectrum. Repeatable H-mode plasma is obtained by LHCD. Up to now, the H-mode with maximum density (of $4.5 \times 10^{19} \text{m}^{-3}$) is obtained with the combination of the two LHCD systems (2.45 GHz and 4.6 GHz).

Note that the use of LHCD represents only one of the necessary conditions for obtaining the H-mode plasma. The H-mode plasma is indeed produced also only via appropriate conditions of plasma configuration, impurity radiation, etc. In addition, high temperature in edge region should be very important for LHCD at high density. As done in the experiments, lowering recycling by means of lithiation could be one effective way. Another one could be the direct heating electrons near the edge region. Since electron cyclotron resonance heating (ECRH) is available in EAST, it could be an effective tool to enhance current drive capability in H-mode at high density.

Acknowledgements:

This work is supported by the National Magnetic Confinement Fusion Science Program of China (Grant No. 2015GB102003, 2013GB106001B, 2013GB112003), the National Natural Science Foundation of China under Grant No. 11175206, 11305211 and 11275233, Hefei Science Center CAS (2015HSC-UE005), and the JSPS-NRF-NSFC A3 Foresight Program in the field of Plasma Physics (NSFC No. 11261140328). It is partly supported by the China-France and the China-Italy Collaboration program.

References

- [1] Fisch N.J. 1978 *Phys. Rev. Lett.* **41** 873.
- [2] Bernabei S. *et al* 1982 *Phys. Rev. Lett.* **49** 1255.
- [3] Fisch N.J. 1987 *Rev. Mod. Phys.* **59** 175.

- [4] S Tusji, K Ushigusa, Y Ikeda, et al., 1990 *Phys. Rev. Lett.* **64** 1023.
- [5] Crisanti F *et al* 2002 *Phys. Rev. Lett.* **88** 145004.
- [6] Cesario R, et al., *Phys. Rev. Letters*, **92** 17 (2004) 175002
- [7] Ding B. J., et al., 2013 *Nucl. Fusion* **55** 113027.
- [8] Liu F K, et al., 2015 *Nucl. Fusion* **55** 123022.
- [9] Wan B N et al., 2015 *Nucl. Fusion* **55** 104015.
- [10] Xu G S et al., 2011 *Phys. Rev. Lett.* **107** 125001
- [11] Brambilla M, 1976 *Nucl. Fusion* **16** 47.
- [12] Petržilka V. A., Leuterer F., Söldner F.-X., *et al* 1991 *Nucl. Fusion* **31**, 1758.
- [13] Leuterer F., Söldner F., Brambilla M., et al., 1991, *Plasma Phys. Controlled Fusion* **33** 169.
- [14] Ikeda Y., Naito O., Kondoh T., et al., in Proceedings of the 15th IAEA Conference on Plasma Physics and Controlled Nuclear Fusion Research 1994, Seville, Spain (1994), Vol. 1, p. 415.
- [15] Ekedahl A., et al., 2005, *Nucl. Fusion* **45** 351.
- [16] Pericoli Ridolfini V., Ekedahl A., Erements S. K., et al., 2004, *Plasma Phys. Controlled Fusion* **46** 349.
- [17] Ekedahl A., Petržilka V., Baranov Y., et al., 2012, *Plasma Phys. Controlled Fusion* **54** 074004.
- [18] Ekedahl A., Rantamäki K., Goniche M., et al., 2009, *Plasma Phys. Controlled Fusion* **51** 044001.
- [19] Ding B. J., Li M. H., Qin Y. L., et al., 2010, *Phys. Plasma* **17** 022504.
- [20] Cesario R. *et al* 2010 *Nature Commun.* **55** 1
- [21] Pericoli-Ridolfini V. *et al* 1994 *Nucl. Fusion* **34** 469
- [22] Cesario R. *et al* 2011 *Plasma Phys. Control. Fusion* **53** 085011
- [23] Wallace G.M. *et al* 2010 *Phys. Plasmas* **17** 082508
- [24] Ding B J et al., 2015 *Nucl. Fusion* **55** 093030.
- [25] Ding B. J., Qin Y. L., Li W. K., et al 2011 *Phys. Plasma* **18** 082510.

- [26] Zhao L. M., et al 2010 *Plasma Sci. Tec.* **12** 118.
- [27] Ding B J et al., 2013 *Phys Plasmas*, *20* 102504.
- [28] Bonoli P.T., and Englande, R.C. 1986 *Phys. Fluids***29** 2937.
- [29] Liu C.S., and TRIPATHI, V.K. 1986 *Phys. Rep.***130**143.
- [30] Peysson Y., et al 2011 *Plasma Phys. Contr. Fusion* **53** 124028.
- [31] Bonoli, P.T., and OTT, E. 1982*Phys. Fluids***25** 359.
- [32] R. Cesario, et al., 2014 *Nucl. Fusion* **54** 043002.
- [33] Takase Y. and Porkolab M., 1983, *Phys. Fluids* **26** 2992.
- [34] Baek S. G., Parker R. R., Shiraiwa S. et al., 2014, *Phys. Plasmas* **21**, 061511.
- [35] R Cesario, et al., *Plasma Phys Control. Fusion* 55 (2013) 045005
- [36] Zang Q. et al., 2011 *Rev. Sci. Instrum.* **82** 063502.
- [37] Challis C.D. et al 2001 *Plasma Phys. Control. Fusion* **43** 861
- [38] Joffrin E. et al 2002 *Nucl. Fusion* **42** 235
- [39] Takase Y., Porkolab M., Schuss J. J., et al 1985 *Phys. Fluids* **28** 983.
- [40] Hooke W. 1984 *Plasma Phys. Contr. Fusion* **26** 133.
- [41] Peysson Y. et al., 2012 *Plasma Phys. Control. Fusion* **54** 045003.
- [42] Peysson Y. et al., Theory of Fusion Plasmas, in AIP Conference Proceedings, 2008, Vol. **1069** pp. 176–187.

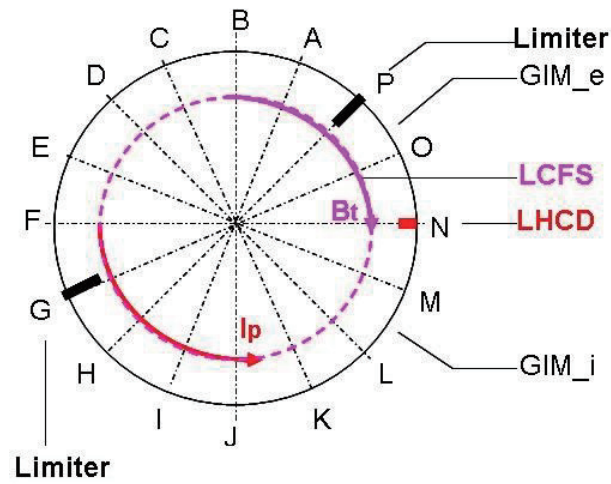


Fig. 1 Top view of local gas puffing for electron drift side and ion drift side

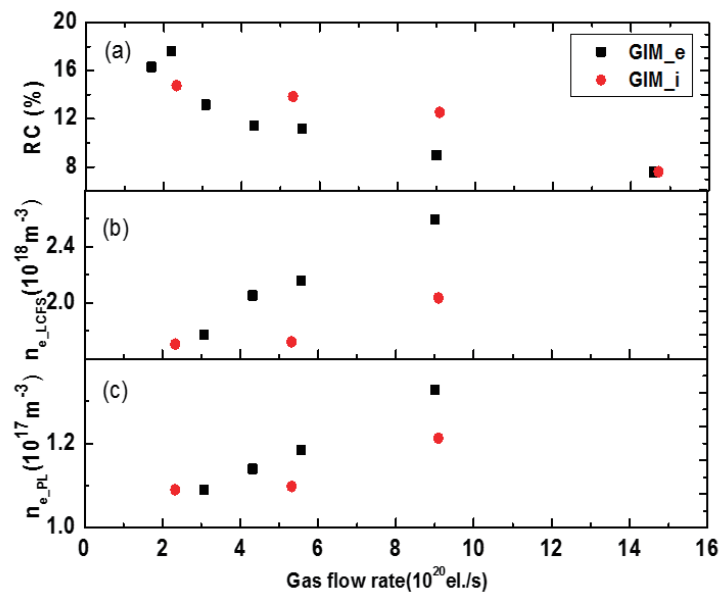


Fig. 2 Coupling comparison between gas puffing from electron side (GIM_e) and ion side (GIM_i) (a) reflection coefficient (b) density at the LCFS and (c) density at the poloidal limiter ($f=2.45$ GHz)

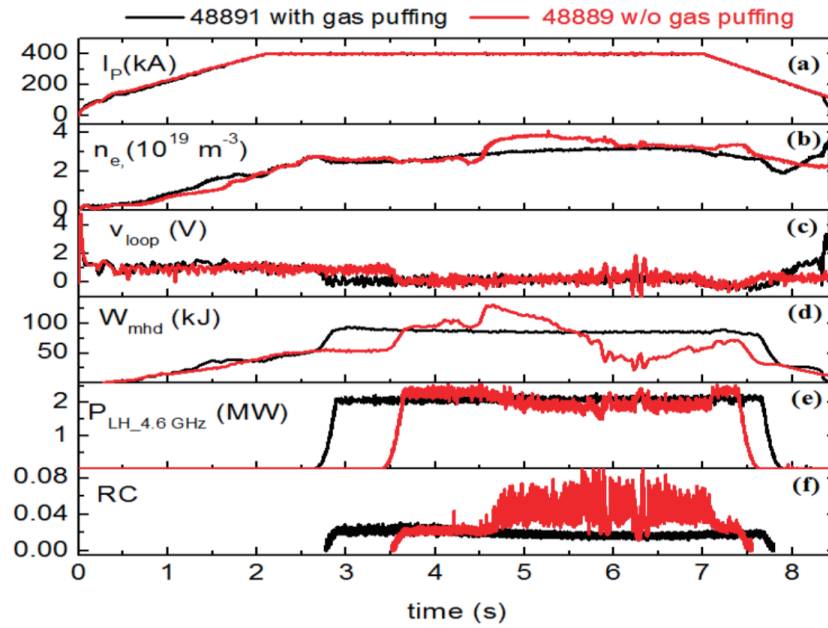


Fig. 3 Coupling improved by means of local gas puffing ($f=4.6\text{GHz}$)

- (a) plasma current (I_p), (b) central line averaged density (n_e), (c) loop voltage (V_{loop}),
- (d) stored energy (W_{mhd}) calculated with magnetic measurement, (e) internal inductance (l_i), and (f) reflection coefficient (RC)

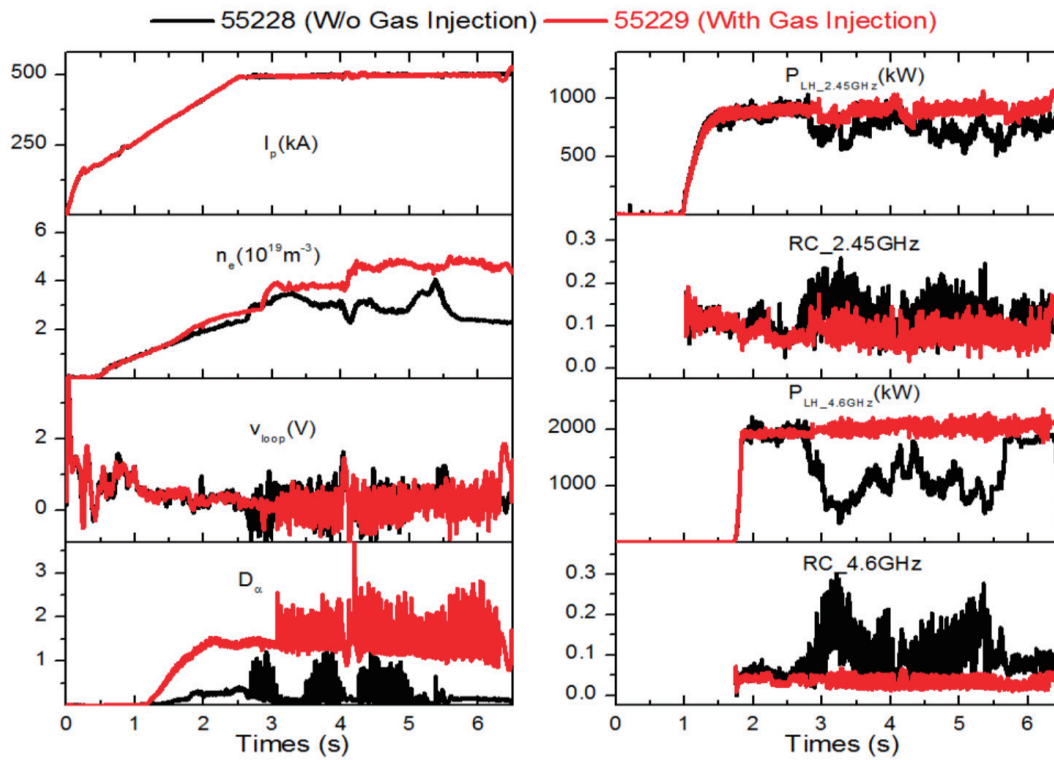


Fig. 4 Coupling characteristics in H-mode with and without local gas puffing

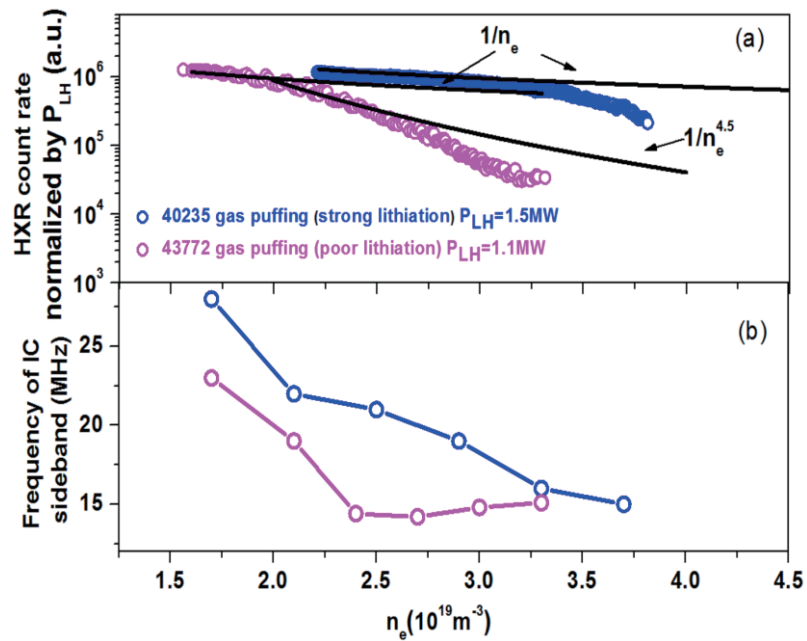


Fig. 5 (a) Relationship between HXR counts and density with strong and poor lithiation (b) Frequency of IC sidebands with strong and poor lithiation

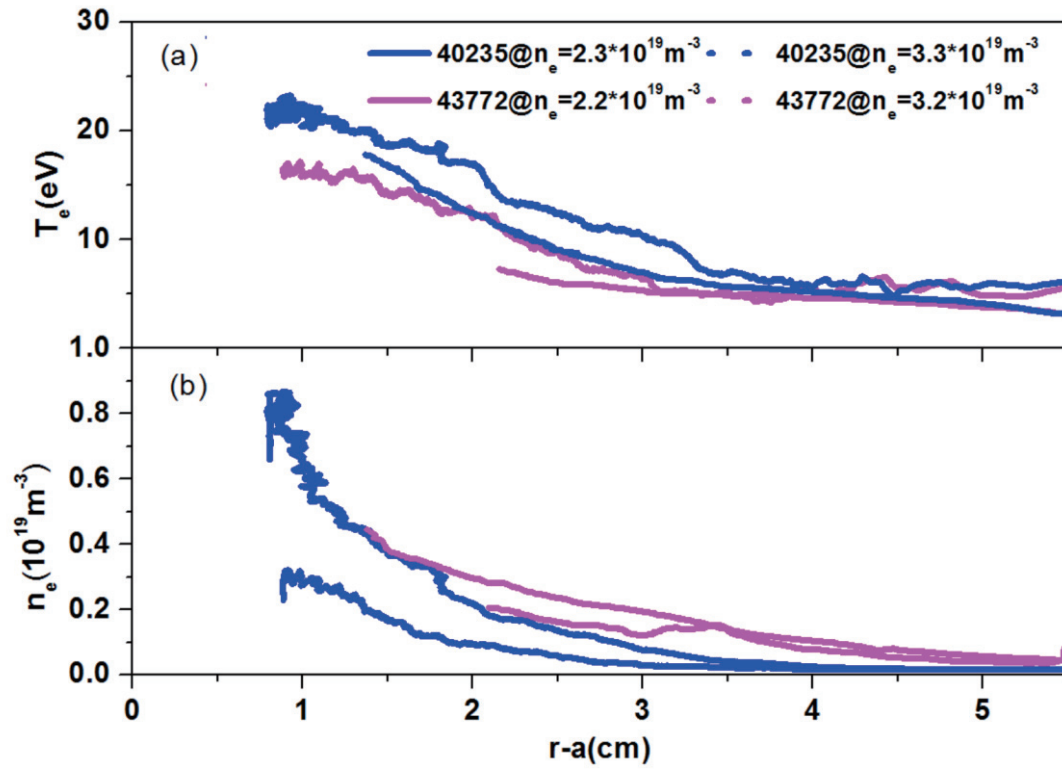


Fig. 6 Edge temperature (a) and (b) density profile measured by Langmuir probe ($r-a=0$ means the last closed flux surface)

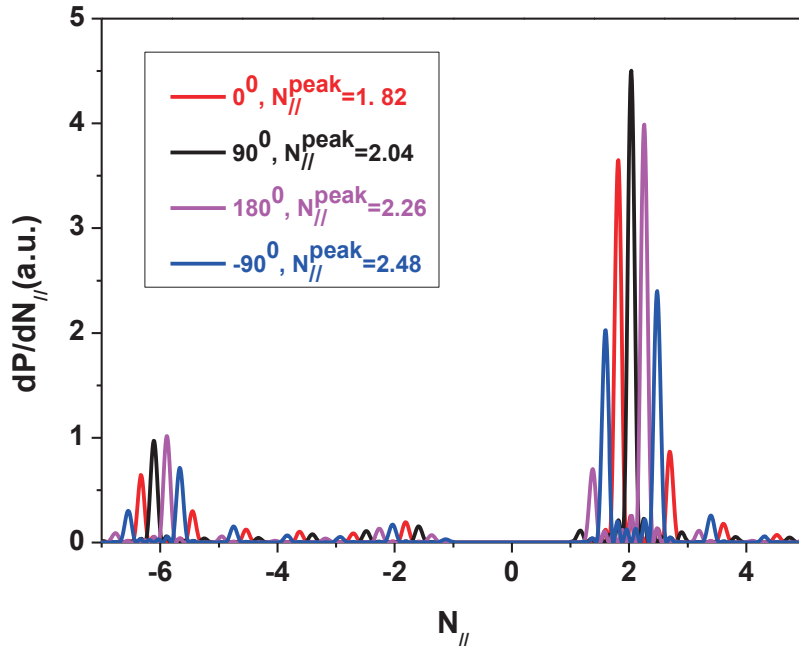


Fig. 7 Calculated spectrum for 4.6GHz LH antenna using ALOHA code ($N_{//}$ is the refractive index in parallel direction, $N_{//}^{peak}$ is the corresponding peak value)

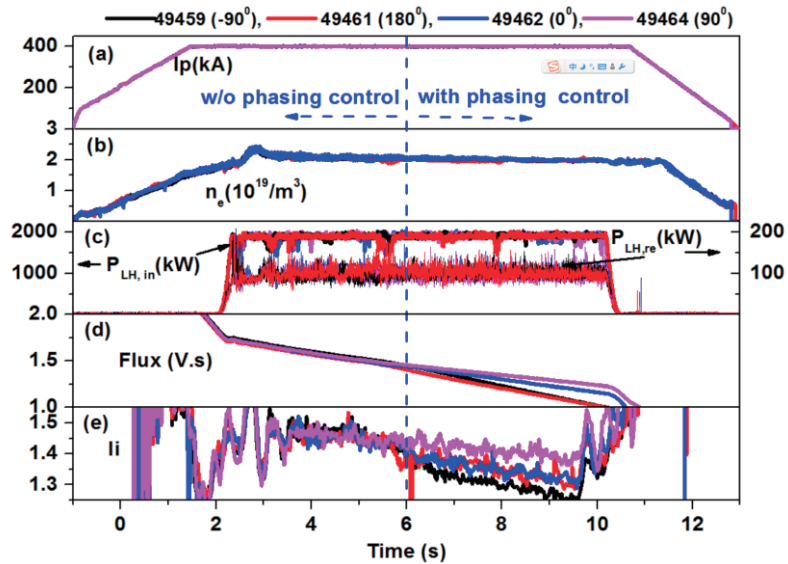


Fig. 8 Effect of spectrum on CD efficiency and current profile ($f=4.6\text{GHz}$, the vertical dashed line refers to the time at which the phasing is controlled)

- (a) plasma current (I_p), (b) central line averaged density (n_e), (c) injected LH power ($P_{LH,in}$) and reflected LH power ($P_{LH,re}$), (d) consumption of magnetic flux (flux), and (e) internal inductance (li)

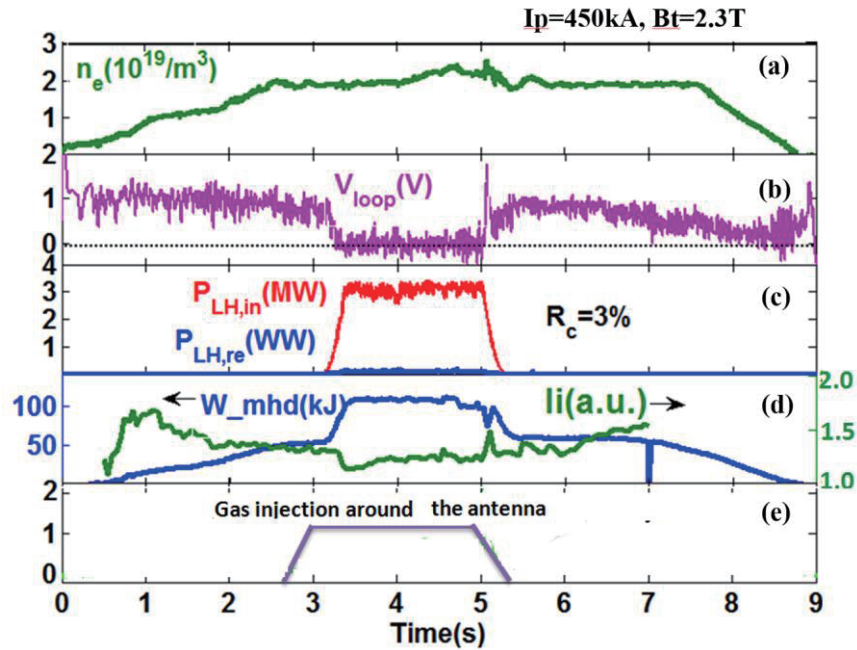


Fig. 9 Typical waveform of current drive and plasma heating ($f=4.6\text{GHz}$)
 (a) central line averaged density (n_e), (b) loop voltage (V_{loop}), (c) injected LH power ($P_{\text{LH,in}}$) and reflected LH power ($P_{\text{LH,re}}$), (d) stored energy (W_{mhd}) calculated with magnetic measurement and internal inductance (l_i), (e) local gas puffing (Gas injection around the antenna)

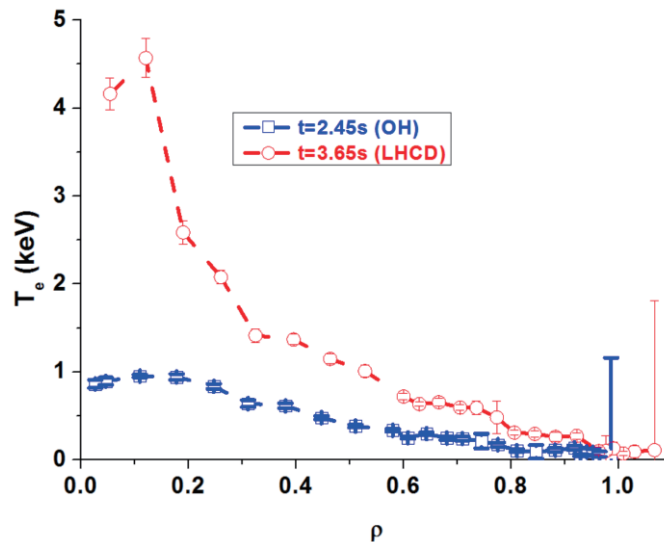


Fig. 10 Electron temperature profile measured with Thomson scattering system
 ($f=4.6\text{GHz}$) (ρ is the normalized minor radius.)

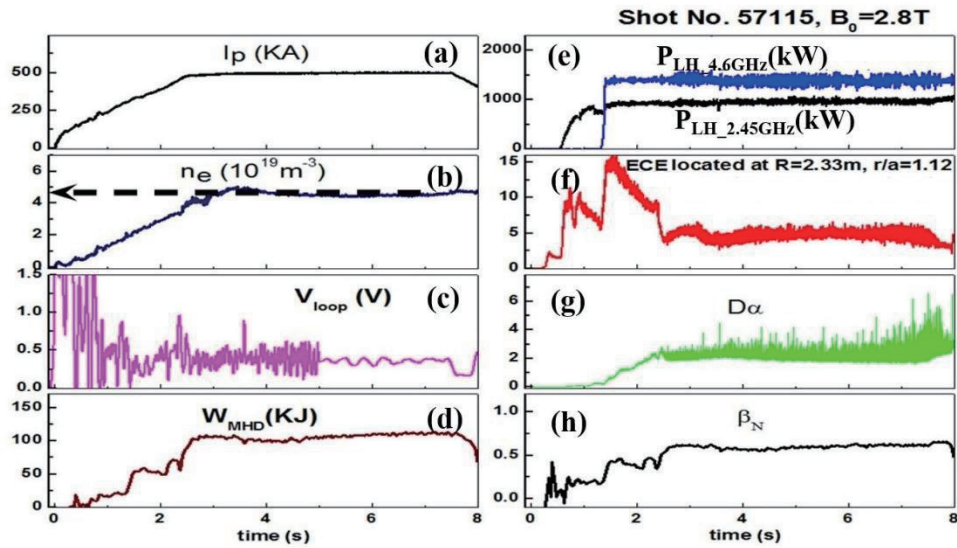


Fig. 11 Typical LHCD H-mode plasma at high density

- (a) plasma current (I_p), (b) central line averaged density (n_e), (c) loop voltage (V_{loop}),
- (d) stored energy (W_{mhd}) calculated with magnetic measurement, (e) LH power (f) ECE Supra-electron emission measured by ECE in edge region, (g) neutral hydrogen radiation (D_α), (h) normalized beta (β_N)

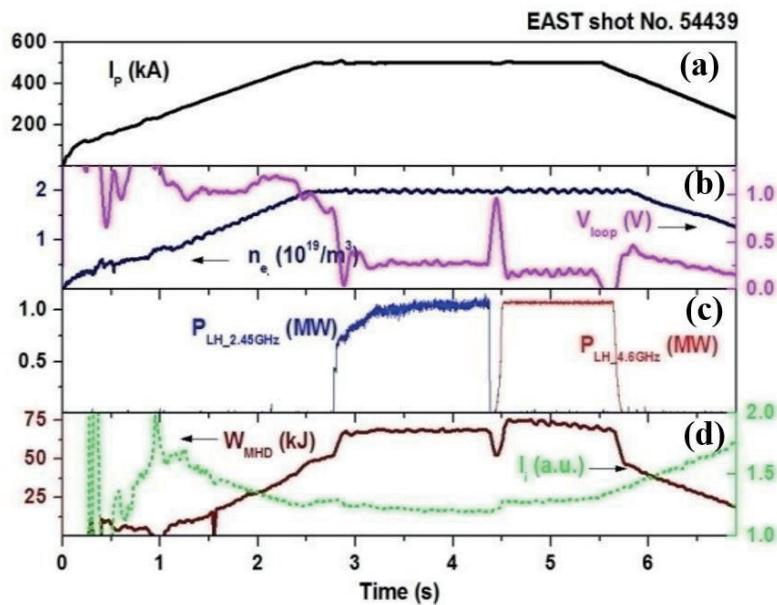


Fig. 12 Effect of LH frequency on LHCD characteristics

- (a) plasma current (I_p), (b) central line averaged density (n_e) and loop voltage (V_{loop}),
- (c) LH power, (d) stored energy (W_{mhd}) calculated with magnetic measurement and internal inductance (l_i)

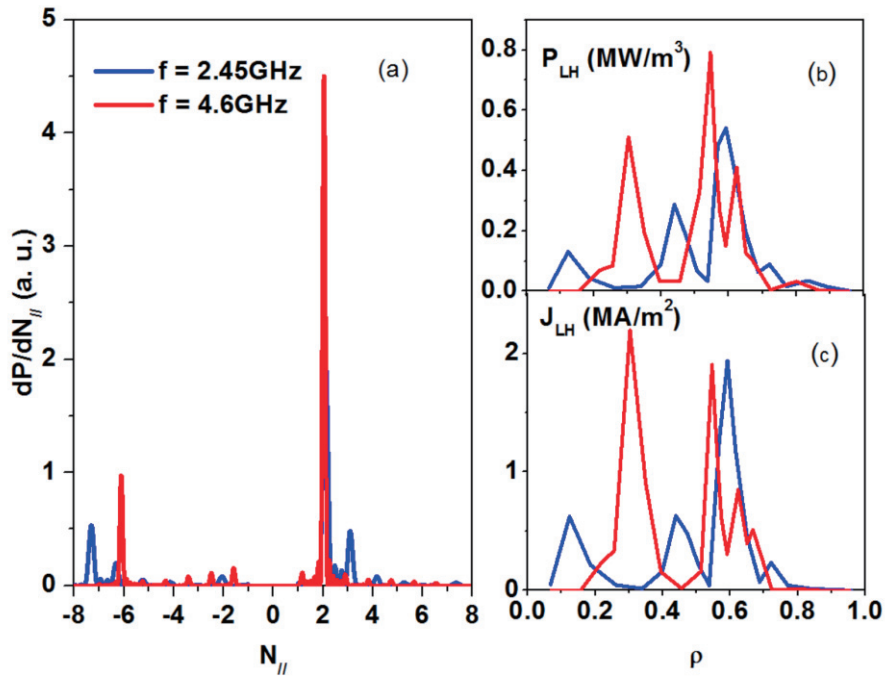


Fig. 13 (a) LH spectrum calculated by ALOHA , (b) Power deposition and (c) LH driven current with C3PO/LUKE without spectrum broadening

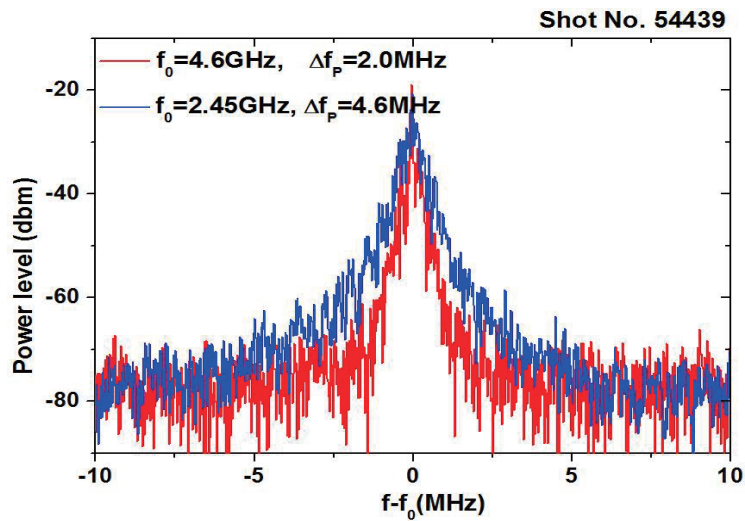


Fig.14 Spectrum broadening measured by loop antenna

Magnetic components of GAMs in tokamak plasmas with a radial equilibrium electric field**Deng Zhou^{1,2}**¹Institute of Plasma Physics, Chinese Academy of Sciences, Hefei 230031, P. R. China²Centre for Magnetic Fusion Theory, Chinese Academy of Sciences, Hefei 230031, P. R. China

The dispersion relation of geodesic acoustic modes with a magnetic component in the tokamak plasma with an equilibrium radial electric field is derived. The dispersion relation is analyzed for very low field strength. The mode frequency decreases with increasing field strength. There exists an $m=1$ magnetic component which is absent when no radial electric field is taken into account. The ratio between the $m=1$ and $m=2$ magnetic components increases with the Mach number.

1. Introduction

Geodesic acoustic modes (GAMs)¹, which are axi-symmetric oscillations observed in toroidal magnetic confinement devices, have been under active investigations in the past two decades^{2,3}. Normally, GAMs are considered as an electrostatic eigenmode which is sustained by the coupling of radial electrostatic field and the poloidal variational density perturbation. They are excited by the modulation instabilities of drift waves and usually detected at the edge region of tokamaks or stellarators through the diagnostics of electrostatic potentials. However, turbulence in a magnetically confined plasma is not always electrostatic, the electromagnetic perturbation may appear due to the finite β effect, where $\beta = p/(B^2/2\mu_0)$ is the ratio between the thermal pressure and the magnetic energy density. Hence, it quite possible in some situations that the electromagnetic turbulence self organizes to form not only the symmetric scalar electric potential, but also a symmetric magnetic perturbation, referred to as zonal field in literatures. Indeed, experiments have observed the magnetic component with poloidal mode number $m=2$ almost a decade ago^{4,5}. Recent experiments on tokamak DIII-D⁶ and spherical tokamak Globus-M⁷ also reported the existence of magnetic perturbation in GAMs with new features. Hence, it is necessary to consider the electromagnetic perturbation in the theoretical investigation of GAMs.

A previous theoretical work explained the $m=2$ magnetic perturbation as a result of the coupling between the $m=1$ radial curvature drift of ions and the $m=1$ density distribution adherent in GAMs⁸. Later work further revealed that the $m=1$ magnetic perturbation is an order higher than the $m=2$ component in the series expansion of $k_r \rho_i$ where k_r is the radial wave number and ρ_i is the ion Lamor radius⁹.

Usually, GAMs are observed at the edge region of tokamaks where a radial equilibrium

electric field may develop. So it is of practical importance to include the effect of radial equilibrium electric field in the study of GAMs. In a recent work¹⁰, the effect was taken into account in the study of pure electrostatic GAMs. Both the real frequency and the damping rate increases with the strength of radial electric fields. In this work, we investigate the electromagnetic GAMs with the effect of equilibrium field included. The dispersion relation is derived by treating $qk_r\rho_i$ as a small parameter, where q is the usual safety factor. The dispersion relation is analyzed for small mach number and it is found that the real frequency decreases with the increasing Mach number which is different from the electrostatic GAMs. An $m=1$ magnetic perturbation proportional to the beta value develops and increases with Mach number.

2. Basic Equations and the Derivation of Dispersion Relation

The starting point is the gyro-kinetic equation for both ion and electrons

$$\frac{\partial}{\partial t} \delta h + (\mathbf{v}_{\parallel} \mathbf{b} + \mathbf{v}_E + \mathbf{v}_{D\alpha}) \cdot \frac{\partial}{\partial \mathbf{X}} \delta h = \frac{q_{\alpha}}{T_{\alpha}} \left(\frac{\partial}{\partial t} \phi - v_{\parallel} \frac{\partial}{\partial t} \psi \right) F_0 \quad (1)$$

where the perturbation of distribution is $\delta f = -(q_{\alpha}/T_{\alpha})\phi F_0 + \delta h$, ϕ is the perturbation of electrostatic potential and $\psi = \mathbf{A} \cdot \mathbf{b}$ is the perturbation of the parallel vector potential.

We consider a large aspect ratio tokamak with a circular cross section, and the equilibrium magnetic field is written as $\bar{\mathbf{B}} = B_{\phi} \hat{\phi} + B_{\theta} \hat{\theta} = B_0 [(1 - \varepsilon \cos \theta) \hat{\phi} + (q^{-1} \varepsilon) \hat{\theta}]$, then the magnetic drift is given approximately by $\mathbf{v}_D = -\hat{v}_D \sin \theta \hat{r} - \hat{v}_D \cos \theta \hat{\theta}$ with

$\hat{v}_D = (v_{\parallel}^2 + v_{\perp}^2/2)/\Omega R$, $\Omega = eB/m$. The perturbation is expanded in the harmonic form

$$\phi = \sum_{l=0,\pm 1,\dots} \phi_l \exp[-i(\omega t - k_r x - l\theta)] \quad (2a)$$

$$\mathbf{A} = \mathbf{b} \sum_{l=0,\pm 1,\dots} \psi_l \exp[-i(\omega t - k_r x - l\theta)] \quad (2b)$$

$$\delta h = \sum_{l=0,\pm 1,\dots} \delta h_l \exp[-i(\omega t - k_r x - l\theta)] \quad (2c)$$

Substituting Eq. (2a-c) into (1) and dropping the harmonic components with $|l| > 2$, we obtains

$$\omega \delta h_0 - \frac{i\omega_{d\alpha}}{2} (\delta h_{-1} - \delta h_{+1}) = \frac{q_{\alpha} \omega}{T_{\alpha}} (\phi_0 - v_{\parallel} \psi_0) F_{0\alpha} \quad (3a)$$

$$(\omega \mp \omega_l) \delta h_{\pm 1} - \frac{i\omega_{d\alpha}}{2} (\pm \delta h_0 \mp \delta h_{\pm 2}) = \frac{q_{\alpha} \omega}{T_{\alpha}} (\phi_{\pm 1} - v_{\parallel} \psi_{\pm 1}) F_{0\alpha} \quad (3b)$$

$$(\omega \mp 2\omega_l) \delta h_{\pm 2} \mp \frac{i\omega_{d\alpha}}{2} \delta h_{\pm 1} = \frac{q_{\alpha} \omega}{T_{\alpha}} (\phi_{\pm 2} - v_{\parallel} \psi_{\pm 2}) F_{0\alpha} \quad (3c)$$

For small parameter $k_r \rho_{\alpha} \ll 1$, we can solve equations (3) iteratively to get

$$\delta h_0 = (\phi_0 - v_{\parallel} \psi_0) F_{0\alpha} + \frac{i\omega_{d\alpha}}{2} \left[\frac{\phi_{-1} - v_{\parallel} \psi_{-1}}{\omega + \omega_l} - \frac{\phi_{+1} - v_{\parallel} \psi_{+1}}{\omega - \omega_l} \right] F_{0\alpha} + \frac{\omega_{d\alpha}^2}{4\omega} \left[\frac{\phi_0 - v_{\parallel} \psi_0}{\omega + \omega_l} + \frac{\phi_0 - v_{\parallel} \psi_0}{\omega - \omega_l} \right] F_{0\alpha} \quad (4a)$$

$$\delta h_{\pm 1} = \frac{\omega}{\omega \mp \omega_l} (\phi_{\pm 1} - v_{\parallel} \psi_{\pm 1}) F_{0\alpha} \pm \frac{i\omega_{d\alpha}}{2(\omega \mp \omega_l)} \left[(\phi_0 - v_{\parallel} \psi_0) F_{0\alpha} - \frac{\omega}{\omega \mp 2\omega_l} (\phi_{\pm 2} - v_{\parallel} \psi_{\pm 2}) F_{0\alpha} \right] \quad (4b)$$

$$\delta h_{\pm 2} = \frac{\omega}{\omega \mp 2\omega_l} (\phi_{\pm 2} - v_{\parallel} \psi_{\pm 2}) F_{0\alpha} - \frac{\omega_{d\alpha}}{(\omega \mp \omega_l)\omega \mp 2\omega_l} \left[\frac{\omega_{d\alpha}}{2} (\phi_0 - v_{\parallel} \psi_0) F_{0\alpha} \mp \frac{\omega}{2} (\phi_{\pm 1} - v_{\parallel} \psi_{\pm 1}) F_{0\alpha} \right] \quad (4c)$$

Equations (4), the quasi-neutrality condition plus the Ampere's law

$$q_i \delta n_i + q_e \delta n_e = 0 \quad (5a)$$

$$k_r^2 \psi = \mu_0 \delta j_{\parallel} \quad (5b)$$

form a closure system to derive the dispersion relation and perturbation components.

We take the first order velocity moment of the distribution function to get the current, $l=0$ the components contributed from the α species is

$$\begin{aligned} \delta j_0 = & -\frac{1}{2} q_{\alpha} n_0 v_{T\alpha} \psi_0 + \\ & \frac{i}{2} q k_r \rho_{\alpha} q_{\alpha} n_0 v_{T\alpha} [Z_3(\xi_{-}) \phi_{-1} + Z_3(\xi_{-}) \phi_{+1} - \xi_{-} Z_3(\xi_{-}) \psi_{+1} - \xi_{+} Z_3(\xi_{+}) \psi_{-1}] + O[(k_r \rho_{\alpha})^2] \end{aligned} \quad (6)$$

It is obvious that, due to the prompt response of electrons to the $l=0$ parallel electric field, the homogeneous component of magnetic vector potential is much smaller than the inhomogeneous components, *i. e.* $\psi_0 \ll \psi_{\pm 1}$. So in the following, we take $\psi_0 \sim 0$.

Taking the 0-th order moment of the distribution function, we have the $l=0$ perturbation of density

$$\begin{aligned} \delta n_0 = & -\frac{1}{2} (k_r \rho_{\alpha})^2 n_0 \phi_0 + \\ & \frac{i}{2} q k_r \rho_{\alpha} n_0 [Z_2(\xi_{-}) \phi_{+1} - Z_2(\xi_{+}) \phi_{-1} - Z_3(\xi_{-}) \psi_{+1} - Z_3(\xi_{+}) \psi_{-1}] \\ & - \frac{(q k_r \rho_{\alpha})^2 n_0}{4\xi} [Z_4(\xi_{+}) + Z_4(\xi_{-})] \phi_0 \end{aligned} \quad (7)$$

where the first term on the right hand side is the polarization density. If we can solve for $\phi_{\pm 1}$ and $\psi_{\pm 1}$ in terms of ϕ_0 we can then derive the dispersion relation from (5a) and (7).

From the $l=\pm 1$ quasi-neutrality and Ampere's law, one obtains

$$\begin{aligned} & [1 + \tau^{-1} + \xi Z_p(\xi_{\mp})] \phi_{\pm 1} \mp \xi [\tau^{-1} + Z_1(\xi_{\mp})] \psi_{\pm 1} \pm \frac{i}{2} q k_r \rho_i [Z_2(\xi_{\mp}) - Z_2(\hat{\xi}_{\mp})] \phi_{\pm 2} \\ & + \frac{i}{2} q k_r \rho_i [Z_3(\hat{\xi}_{\mp}) - Z_3(\xi_{\mp})] \psi_{\pm 2} = \mp \frac{i}{2} q k_r \rho_i Z_2(\xi_{\mp}) \phi_0 \end{aligned} \quad (8a)$$

$$\begin{aligned} & \pm 2\xi [\tau^{-1} + Z_1(\xi_{\mp})] \phi_{\pm 1} + [\Delta - 2\tau^{-1} \xi \hat{\xi}_{\mp} - 2\xi \hat{\xi}_{\mp} Z_1(\xi_{\mp})] \psi_{\pm 1} + i q k_r \rho_i [Z_3(\xi_{\mp}) - Z_3(\hat{\xi}_{\mp})] \phi_{\pm 2} \\ & \pm i q k_r \rho_i [\hat{\xi}_{\mp} - \xi_{\mp} Z_3(\xi_{\mp}) + \hat{\xi}_{\mp} Z_3(\hat{\xi}_{\mp})] \psi_{\pm 2} = -i q k_r \rho_i \xi_{\mp} Z_2(\xi_{\mp}) \phi_0 \end{aligned} \quad (8b)$$

The $l=\pm 2$ quasi-neutrality and Ampere's law yields

$$\begin{aligned}
& \left[1 + \tau^{-1} + \frac{1}{2} \xi Z_p(\hat{\xi}_{\mp}) \right] \phi_{\pm 2} \mp \frac{1}{2} \xi \left[\tau^{-1} + Z_1(\hat{\xi}_{\mp}) \right] \psi_{\pm 2} \mp \frac{i}{2} q k_r \rho_i \left[Z_2(\xi_{\mp}) - Z_2(\hat{\xi}_{\mp}) \right] \phi_{\pm 1} \\
& + \frac{i}{2} q k_r \rho_i \left[Z_3(\xi_{\mp}) - Z_3(\hat{\xi}_{\mp}) \right] \psi_{\pm 1} = - \frac{(q k_r \rho_i)^2}{4 \xi} \left[Z_4(\xi_{\mp}) - Z_4(\hat{\xi}_{\mp}) \right] \phi_0 \quad (9a) \\
& \pm 2 \xi \left[\tau^{-1} + Z_1(\hat{\xi}_{\mp}) \right] \phi_{\pm 2} + \left[\Delta - \tau^{-1} \xi \hat{\xi}_{\mp} - 2 \xi \hat{\xi}_{\mp} Z_1(\hat{\xi}_{\mp}) \right] \psi_{\pm 2} - i q k_r \rho_i \left[Z_3(\xi_{\mp}) - Z_3(\hat{\xi}_{\mp}) \right] \phi_{\pm 1} \\
& \mp i q k_r \rho_i \left[\hat{\xi}_{\mp} - \xi_{\mp} Z_3(\xi_{\mp}) + \hat{\xi}_{\mp} Z_3(\hat{\xi}_{\mp}) \right] \psi_{\pm 1} = \mp \frac{(q k_r \rho_i)^2}{2 \xi} \left[\xi_{\mp} Z_4(\xi_{\mp}) - \hat{\xi}_{\mp} Z_4(\hat{\xi}_{\mp}) \right] \phi_0 \quad (9b)
\end{aligned}$$

The exact solution of (8) and (9) is very complicated. We can solve (8) and (9) iteratively to get an approximate series of the solution by treating $\varepsilon = q k_r \rho_i$ as a small parameter. The first step is to drop the second terms on the left hand side of (8a,b) and one obtains

$$\phi_{\pm 1} = i q k_r \rho_i \phi_0 \frac{\mp \Delta Z_2(\xi_{\mp})}{2 G(\xi_{\mp})} \quad (10a)$$

$$\psi_{\pm 1} = i q k_r \rho_i \phi_0 \frac{\pm (1 + \tau^{-1}) M_p \xi_{\mp} Z_p(\xi_{\mp})}{G(\xi_{\mp})} \quad (10b)$$

Then substitution of (10) into (9) yields $\phi_{\pm 2}$ and $\psi_{\pm 2}$ in the order of $O(\varepsilon^2)$ which is too complex to write out explicitly. One get the higher order correction to $\phi_{\pm 1}$ and $\psi_{\pm 1}$ by solving Eqs. (8) with the solution of $\phi_{\pm 2}$ and $\psi_{\pm 2}$ included, the correction is of order $O(\varepsilon^3)$.

The dispersion relation is obtained by inserting (10) into (7) and using the $l = 0$ component to be

$$\frac{[Z_2(\xi_{\mp})]^2}{G(\xi_{\mp})} \left[\frac{\Delta}{2} - \xi_{\mp} (1 + \tau^{-1}) M_p \right] + \frac{[Z_2(\xi_{\mp})]^2}{G(\xi_{\mp})} \left[\frac{\Delta}{2} + \xi_{\mp} (1 + \tau^{-1}) M_p \right] - \frac{Z_4(\xi_{\mp}) + Z_4(\xi_{\mp})}{2 \xi} - \frac{1}{q^2} = 0 \quad (11)$$

3. Analysis of dispersion relation

An approximate analysis is carried out by assuming $M_p < 1$ and $|\xi| \sim |\xi_{\pm}| \gg 1$, to yield

$$\begin{aligned}
& \frac{4(1 + \tau^{-1})^2 \tau^{-1} M_p^2}{\Delta^2 q^2} (\xi^2 - M_p^2) - \frac{\tau^{-1}}{q^2} - \frac{4(1 + \tau^{-1})^2 M_p^2}{\Delta^2} \left(1 + \frac{7}{4} \tau^{-1} \right) \\
& - \frac{4(1 + \tau^{-1})^2 M_p^2}{\Delta^2 q^2} \left(1 + \frac{\Delta}{1 + \tau^{-1}} + \tau^{-1} M_p^2 \right) + \left(1 + \frac{7}{4} \tau^{-1} + \frac{1}{q^2} \right) \frac{1}{(\xi^2 - M_p^2)} = 0 \quad (12)
\end{aligned}$$

We notice that the dispersion relation is qualitatively modified by the radial electric field different than that in the electrostatic cases. The usual perturbative expansion is no longer applicable. The approximate solution to (12) for $M_p \sim 0$

$$\xi^2 \approx \frac{\frac{7}{4} + \tau + \frac{\tau}{q^2}}{\frac{4(1 + \tau^{-1})^2 M_p^2 \tau \left(\frac{7}{4} + \tau \right) + \frac{1}{q^2}}{\Delta^2}} + M_p^2 \quad (13)$$

In Fig. 1, the exact solution to (12) and the approximate form (13) are plotted with respect to Mach number. $\psi_{\pm 1}$ and $\psi_{\pm 2}$ are plotted in Fig. 2. The ratio $\psi_{\pm 1}/\psi_{\pm 2}$ is plotted in Fig. 3

4. Summary

The electromagnetic GAMs is studied in tokamaks with a radial equilibrium electric field. The dispersion relation is qualitatively changed by E_r , and the mode frequency decreases with increasing Mach number.

Acknowledgements

This work was partly supported by the JSPS-NRF-NSFC A3 Foresight Program in the field of Plasma Physics.

References

- [1] N. Winsor, J. L. Johnson, and J. M. Dawson, *Phys. Fluids* 11, 2448 (1968)..
- [2] P. H. Diamond, S. -I. Itoh, K. Itoh, and T. S. Hahm, *Plasma phys. Contr. Fusion* 47, R35 (2005).
- [3] A. Fujisawa, *Nucl. Fusion* 49, 013001 (2009).
- [4] A. V. Melnikov, V. A. Vershkov, L. G. Eliseev, *et al.*, *Plasma Phys. Control. Fusion* 87, S41 (2006).
- [5] H. L. Berk, C. J. Boswell, D. Borba, *et al.*, *Nucl. Fusion* 46, S888 (2006).
- [6] G. Wang, W. A. Peebles, T. L. Rhodes, M. E. Austin, Z. Yan, G. R. McKee, R. J. La Haye, K. H. Burrell, E. J. Doyle, J. C. Hillesheim, M. J. Lanctot, R. Nazikian, C. C. Petty, L. Schmitz, S. Smith, E. J. Strait, M. Van Zeeland, and L. Zeng, *Phys. Plasmas* 20, 092501 (2013).
- [7] V. V. Bulanin, V. K. Gusev, A. D. Iblyaminova, N. A. Khromov, G. S. Kurskiev, V. B. Minaev, M. I. Patrov, A. V. Petrov, Yu. V. Petrov, N. V. Sakharov, P. B. Shchegolev, S. Yu. Tolstyakov, V. I. Varfolomeev, F. Wagner and Yu. Yashin, *Nucl. Fusion* 56, 016017 (2016).
- [8] Deng Zhou, *Phys. Plasmas* 14, 104502 (2007).
- [9] Lingfeng Wang, J. Q. Dong, Y. Shen, and H. D. He, *Phys. Plasmas* 18, 052506 (2011).
- [10] D. Zhou, *Phys. Plasmas* 22, 092504 (2015).

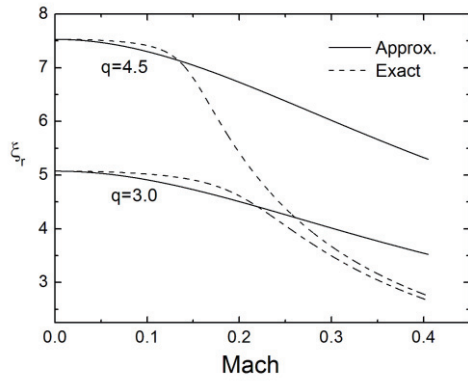


Fig. 1 The frequency changes with Mach number

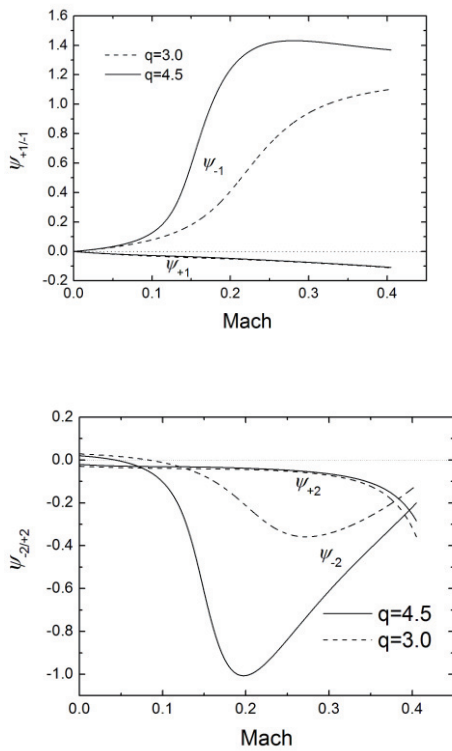


Fig. 2 The magnetic components

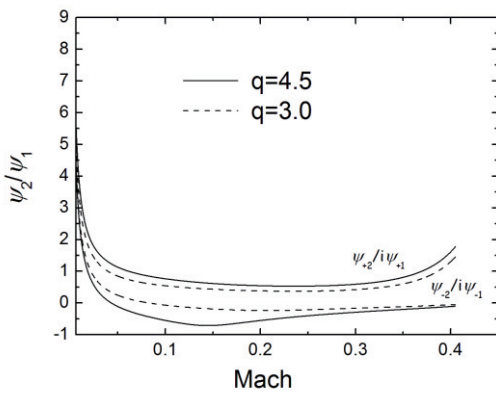


Fig.3 The ratio of magnetic components between different harmonics.

Simulation of fast-ion-driven Alfvén eigenmodes on EAST tokamak

YOUJUN HU¹, Y. TODO², N. XIANG¹, YOUNBIN PEI¹, AND JINPING QIAN¹

1. Institute of Plasma Physics, Chinese Academy of Sciences, Hefei, Anhui 230031, China
2. National Institute for Fusion Science, Toki, Gifu 509-5292, Japan

Abstract

Kinetic-MHD hybrid simulations are carried out to investigate possible fast-ion-driven modes on the Experimental Advanced Superconducting Tokamak (EAST). Three typical kinds of fast-ion-driven modes, namely Toroidicity-induced Alfvén Eigenmodes (TAEs), Reversed Shear Alfvén Eigenmodes (RSAEs), and Energetic-Particle continuum Modes (EPMs), are observed simultaneously in the simulations. The simulation results are compared with the results of an ideal MHD eigenvalue code, which shows agreement with respect to the mode frequency, dominant poloidal mode numbers, and radial location. However, the modes in the hybrid simulations take a twisted structure on the poloidal plane, which is different from the results of the ideal MHD eigenvalue code. The twist is due to the radial phase variation of the eigenfunction, which is attributed to the non-perturbative kinetic effects of the fast ions. By varying the stored energy of fast ions to change the fast ion drive in the simulations, it is demonstrated that the twist (i.e., the radial phase variation) is positively correlated with the fast ion drive.

1 Introduction

Alfvén eigenmodes (AEs) can be excited in tokamak plasmas by fast ions from various sources including neutral beam injection (NBI), RF heating, and fusion reactions[1, 2, 3, 4]. The electromagnetic fluctuations of the AEs have the possibility of influencing the transport of fast ions and thus are important in determining the performance of NBI/RF heating and future burning plasmas[5]. The Experimental Advanced Superconducting Tokamak (EAST)[6] has recently been upgraded to include four deuterium neutral beam lines. It is expected that, with the NBI generated fast ions, various AEs will be routinely observed on EAST. In the present work, kinetic-MHD hybrid simulations using MEGA code[7, 8, 9] are carried out to investigate possible fast-ion-driven Alfvén eigenmodes on EAST. The simulations use an equilibrium with a flat profile of safety factor. Anisotropic slowing down distributions are used to model the distribution of the fast ions from the neutral beam injection. Perturbations of multiple toroidal mode numbers are included in the simulations. Plenty of modes in the Alfvén frequency range are found in the simulation.

The frequency and radial width of the modes observed in the simulations are compared with the Alfvén continua to categorize the modes, which indicates the modes include the Toroidicity-induced Alfvén Eigenmodes (TAEs), Reversed Shear Alfvén Eigenmodes (RSAEs), and Energetic-Particle continuum Modes (EPMs). The simulation results are also compared with the results of a MHD eigenvalue code[10], which shows agreement with respect to the frequency, dominant poloidal mode number, and radial location of the modes.

Measurements from the electron cyclotron emission radiometer show that the phase of AEs usually changes across the radius[11]. The radial phase variation makes the two-dimensional mode structure on the poloidal plane take a twisted structure. The cause of the twist (or radial phase variation) is usually attributed to the non-perturbative kinetic effects of energetic particles[12]. In the present hybrid simulations, two-dimensional mode twist on the poloidal plane is observed, which is different from the results of the ideal MHD eigenvalue code. By varying the stored energy of fast ions to change the fast ions drive in the simulations, the dependence of the radial phase variation on the energetic particles drive is examined, which indicates that the radial phase variation is positively correlated with the fast ions drive.

The remainder of this paper is organized as follows. Section 2 discusses the model used in the simulation code MEGA and the equilibrium used in the simulation. The simulation results are given in Sec. 3. A brief summary is given in Sec. 4.

2 Simulation model and plasma equilibrium

These simulations use MEGA, which is a numerical code calculating the interaction of thermal plasmas and energetic particles (EPs) in toroidal geometries[8]. In MEGA, the thermal plasmas are described by the nonlinear full MHD equations while the EPs are described by the drift-kinetic equation. The EAST equilibrium used here was reconstructed by the EFIT code[13] by using the constraints from experimental diagnostics in EAST discharge #48916 at 4.5s. Figure 1 plots the flux surfaces shape of the equilibrium and the computational box on the poloidal plane used in the simulation.

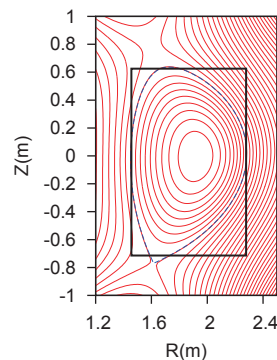


Figure 1. Flux surfaces shape of EAST discharge #48916 at 4.5s. The black rectangle indicates the computational box on the poloidal plane used in the simulation. The magnetic field at the magnetic axis $B_{\varphi 0} = +1.72$ Tesla, the toroidal plasma current $I_{p\phi} = -417$ kA.

The profiles of the safety factor q , plasma pressure p_0 , and electron number density n_{e0} of the equilibrium are plotted in Fig. 2. The profile of the safety factor has a weak negative shear in the region $\sqrt{\Psi_t} \leq 0.4$.

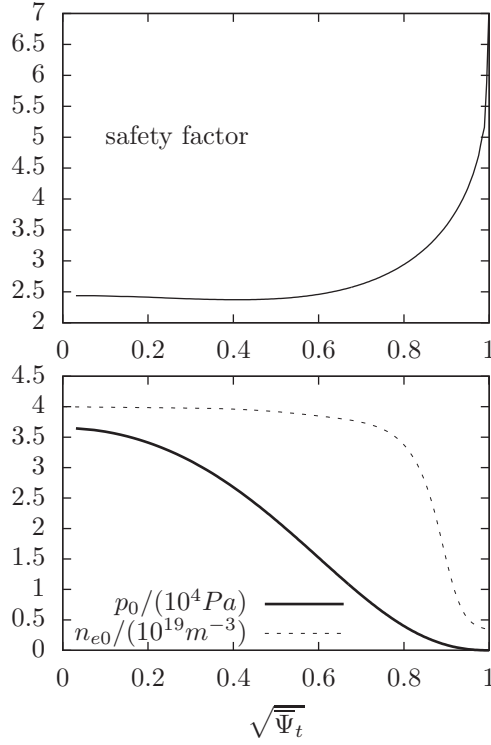


Figure 2. The radial profiles of the safety factor, plasma pressure, and electron number density for EAST discharge #48916 at 4.5s.

In this work, the equilibrium distribution of the fast ions from the Deuterium neutral beam injection is modeled by the anisotropic slowing down distributions, which takes the following form

$$f_{\text{eq}}(\psi, v, \lambda) = C \exp\left(-\frac{\psi_p}{\psi_{\text{scale}}}\right) \frac{1}{v^3 + v_{\text{crit}}^3} \frac{1}{2} \text{erfc}\left(\frac{v - v_b}{\Delta_v}\right) \exp\left(-\frac{(\lambda - \lambda_0)^2}{\Delta_\lambda^2}\right), \quad (1)$$

where C is a constant, which is chosen to achieve desired stored energy of fast ions; ψ_p is the normalized poloidal flux, ψ_{scale} is a quantity characterizing the radial gradient, v is the velocity of fast ions, v_b is the injection velocity of the neutral beam, Δ_v is a small velocity (compared with v_b), which is used to set the cutoff width near v_b ; λ is the the normalized magnetic moment defined by $\lambda = \mu B_0 / \varepsilon$, where B_0 is the strength of the equilibrium magnetic field at the magnetic axis, ε is the kinetic energy of fast ions, λ_0 and Δ_λ characterize the peak location and the width of the distribution over the pitch angle, v_{crit} is the critical velocity for the collisional friction of fast ions with thermal electrons and ions being equal, which is given by[14]

$$v_{\text{crit}} = \left(\frac{m_e}{m_i} \frac{3\sqrt{\pi}}{4}\right)^{1/3} v_{te}, \quad (2)$$

where m_e and v_{te} are the mass and thermal velocity of the electrons. In this work the beam velocity is chosen $v_b = 2.35 \times 10^6 \text{ m/s}$, which is the velocity of a Deuteron with kinetic energy of 58keV; $v_{\text{crit}} = 1.89 \times 10^6 \text{ m/s}$, which corresponds to the critical velocity given by Eq. (2) evaluated with the electron temperature $T_e = 2\text{keV}$. The small cutoff width near the beam velocity is chosen as $\Delta_v = 0.21 \times 10^6 \text{ m/s}$. The central pitch angle variable λ_0 is chosen as $\lambda_0 = 0.5$ with the expansion width Δ_λ chosen as $\Delta_\lambda = 0.3$, which represents a reasonable distribution over the pitch angle based on the beam injection geometry on EAST. The parameter ψ_{scale} , characterizing the radial gradient

of the fast ion pressure, is chosen as $\psi_{\text{scale}} = 0.4$.

3 Simulation results

The radial structures of the various poloidal harmonics of the $n = -2$ modes are plotted in Fig. 3, which shows that the $m = 5$ harmonics is dominant and the mode amplitude reaches its peak at the radial location $\sqrt{\Psi_t} = 0.2$.

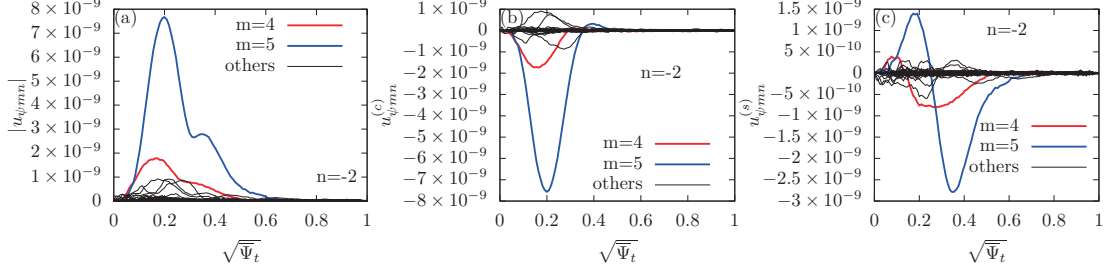


Figure 3. The radial profiles of (a) amplitude $|u_{\psi mn}|$, (b) cosine components $u_{\psi mn}^{(c)}$, and (c) sine components $u_{\psi mn}^{(s)}$ of the $n = -2$ mode.

To identify which kind of fast-ions driven mode the $n = -2$ mode discussed above belongs to, we plot the frequency and the Half Height Full Width (HHFW) of the mode on the graphic of the Alfvén continua, as shown in Fig. 4, which indicates that the mode lies in the TAE gap. Also plotted on Fig. 4a is the $m = 4$ and $m = 5$ Alfvén continua in the cylindrical limit, which shows that the two continua are well separated from each other, indicating there will be only weak coupling between these two harmonics in the corresponding toroidal geometry. Furthermore, as shown in Fig. 3, the mode is dominated by the $m = 5$ harmonic with the $m = 4$ harmonic being much smaller, thus excluding the possibility of being an TAE mode. Also note that the radial location of the mode is near the location where the safety factor reaches its minimal value ($\sqrt{\Psi_t} = 0.4$). Considering these characteristics of the mode, it is reasonable to identify the mode as a RSAE.

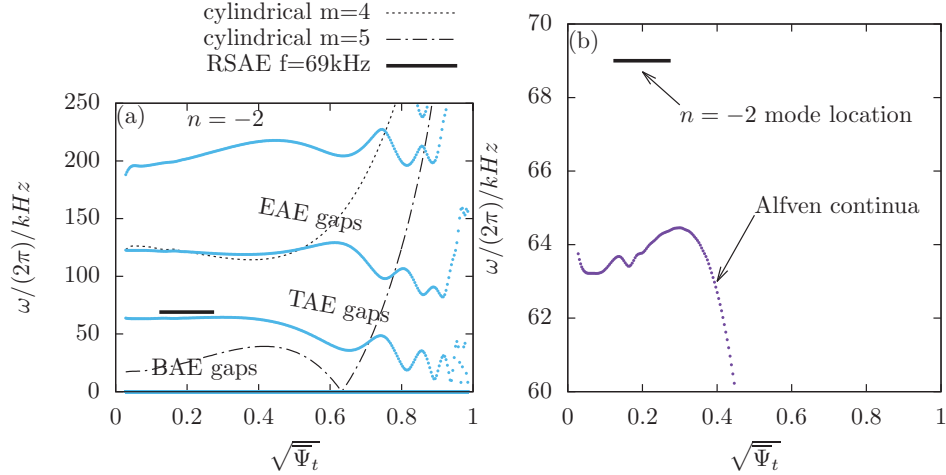


Figure 4. (a) $n = -2$ Alfvén continua with the frequency and the HHFW of the $n = -2$ mode plotted on. Also plotted on (a) are the $m = 4$ and $m = 5$ Alfvén continua in the cylindrical geometry limit. (b) Enlarged part of the Alfvén continua in the frequency range [60kHz: 70kHz] to show the tip of the continua near the zero magnetic shear point. The Alfvén continua is calculated in the slow-sound approximation[15, 16].

Similar analysis can be applied to the $n = -3$ mode. Figure 5 plots the frequency and the half height full width of the dominant $m = 7$ harmonics on the graphic of the Alfvén continua, which indicates the mode intersect with the $m = 7$ Alfvén continua. Considering these characteristics of the mode, it is reasonable to identify the mode as an Energetic-Particle continuum Mode (EPM), instead of a gap mode.

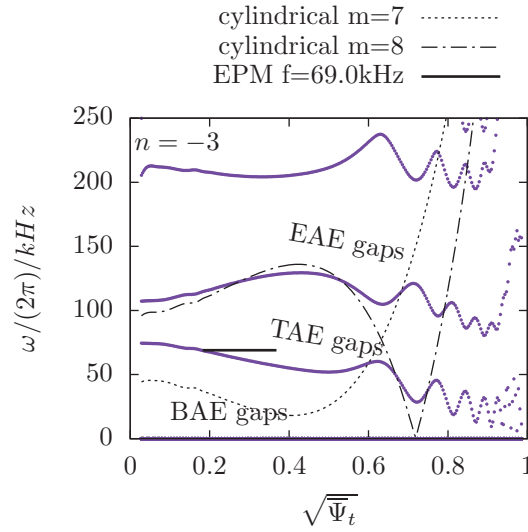


Figure 5. $n = -3$ Alfvén continua with the frequency and the HHFW of the $n = -3$ mode plotted on. Also plotted are the $m = 7$ and $m = 8$ Alfvén continua in the cylindrical geometry limit.

Similar analysis can also be applied to the $n = -4$ mode. Figure 6 plots the frequency and the HHFW of the dominant $m = 10$ harmonic on the graphic of the MHD continua, which indicates the mode lies in the TAE gap formed due to the coupling of the $m = 9$ and $m = 10$ harmonics. Considering this and that the two dominant harmonics $m = 9$ and $m = 10$ are comparable in amplitude, it is reasonable to identify the mode as a TAE.

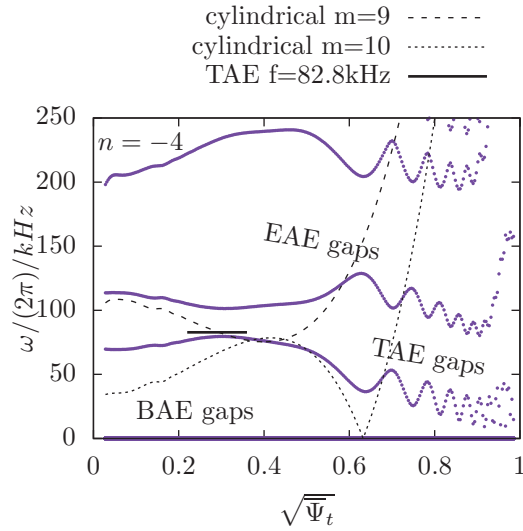


Figure 6. $n = -4$ Alfvén continua with the frequency and the HHFW of the $n = -4$ mode plotted on. Also plotted on (a) are the $m = 9$ and $m = 10$ Alfvén continua in the cylindrical geometry limit.

Figure 7 compares the two-dimensional mode structures calculated by MEGA and GTAW (an ideal MHD eigenvalue code[10]), which shows agreement with respect to the radial location and dominant poloidal harmonics of the modes. However, the $n = -4$ mode in the hybrid simulation takes a twisted structure on the poloidal plane, which is different from the results of the ideal MHD eigenvalue code. The twist is due to the radial phase variation of the eigenfunctions, which may be

attributed to the non-perturbative kinetic effects of the fast ions[12, 17, 18]. By varying the stored energy of fast ions to change the fast ions drive in the simulations, we examined the dependence of the radial phase difference of the $n = -4$ TAE on the fast ions drive, which is shown in Fig. 8a. The radial phase difference is defined to be the phase difference of the $m = 10$ harmonic between the radial location $\sqrt{\Psi_t} = 0.173$ and $\sqrt{\Psi_t} = 0.356$, which is the radial range where the mode amplitude is significant, as is shown in Fig. 9. Figure 8b shows that the growth rate (indication of the fast ions drive) increases with the increasing of the stored energy of fast ions while the frequency remains the same. Figure 8a shows that the phase difference increases with the increasing of the stored energy of fast ions, i.e., the mode twist is positively correlated with the fast ions drive.

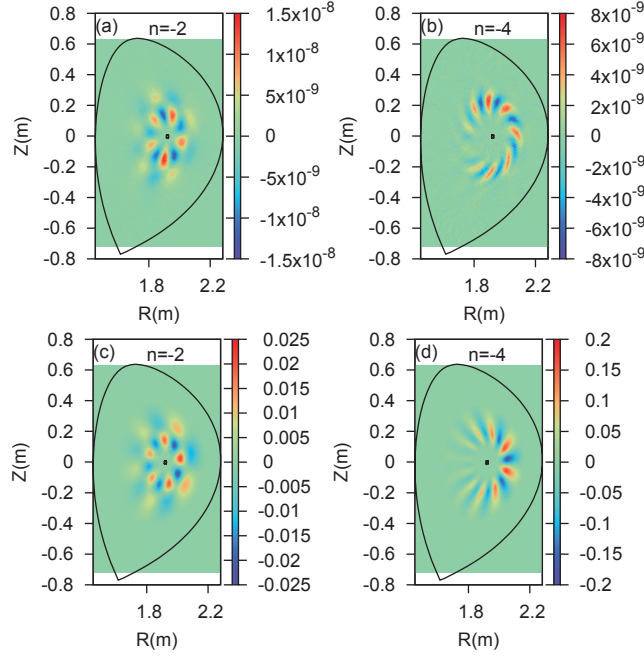


Figure 7. Contour of the radial fluid velocity on the poloidal plane calculated by MEGA ((a) and (b)) and GTAW ((c) and (d)). The $n = -2$ mode is an RSAE with frequency $f = 69.0\text{kHz}$ (67.9kHz given by GTAW). The $n = -4$ mode is a TAE with frequency $f = 82\text{kHz}$ (83kHz given by GTAW). The initial stored energy of fast ions used in the MEGA simulations is 36kJ .

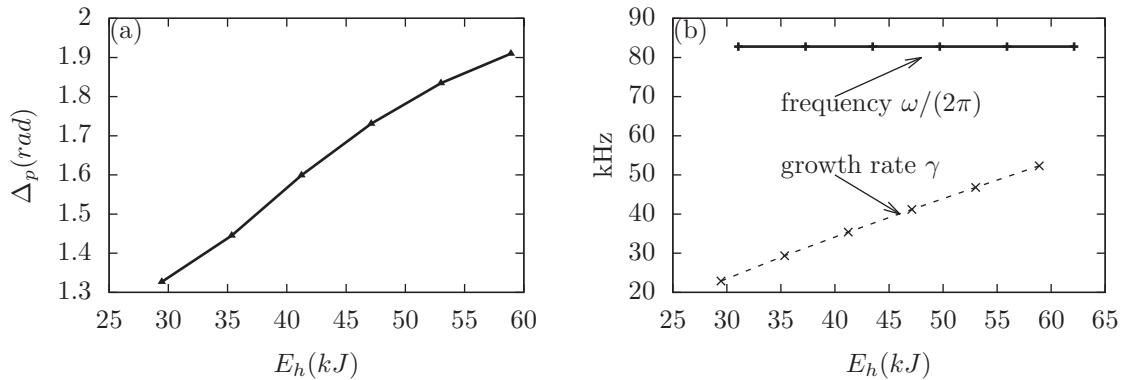


Figure 8. The dependence of (a) the phase difference, (b) mode frequency, and (b) growth rate on the initial stored energy of fast ions for the $n = -4$ TAE mode. The phase difference is defined as the phase difference of the $m = 10$ harmonic between the radial location $\sqrt{\Psi_t} = 0.173$ and $\sqrt{\Psi_t} = 0.356$, as is shown in Fig. 9.

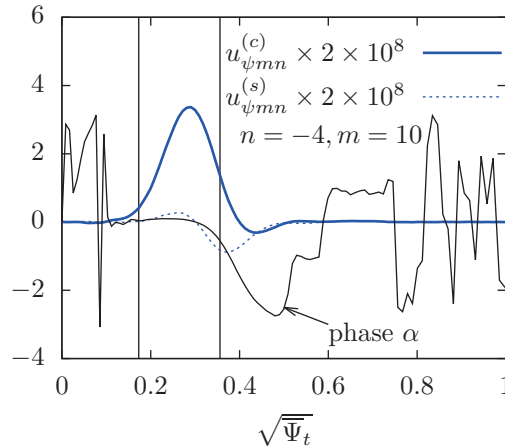


Figure 9. The radial profiles of the radial phase, cosine components $u_{\psi mn}^{(c)}$, and sine components $u_{\psi mn}^{(s)}$ of the dominant $m = 10$ harmonic of the $n = -4$ TAE. The two vertical lines indicate the radial region used in calculating the phase difference given in Fig. 8.

4 Summary

Kinetic-MHD hybrid simulations are carried out to investigate possible fast-ion-driven modes on the EAST tokamak. Toroidicity-induced Alfvén eigenmodes, reversed shear Alfvén eigenmodes, and energetic-particle continuum modes are observed simultaneously in the simulations. The slow-sound approximation of the Alfvén continua proves to be useful in identifying the modes found in the simulations. The agreement between the hybrid simulations and linear eigenvalue analysis provides confidence in the simulation results. It is demonstrated numerically that the radial phase variation of the toroidicity-induced Alfvén eigenmodes is positively correlated with the fast ion drive in the hybrid simulations.

5 ACKNOWLEDGMENTS

One of the authors (Y. Hu) acknowledges useful discussions with H. Wang, Shaojie Wang, W. Chen, H. S. Xie, W. Shen, J. Zhu, and Sheng Wang. Numerical computations were performed on the ShenMa High Performance Computing Cluster in Institute of Plasma Physics, Chinese Academy of Sciences. This work was partially supported by the JSPS-NRF-NSFC A3 Foresight Program in the field of Plasma Physics (NSFC No. 11261140328).

Bibliography

- [1] C. Z. Cheng, L. Chen, and M. S. Chance, *Ann. Phys. (NY)* **161** **21** (1984).
- [2] G. Y. Fu and J. W. Van Dam, *Phys. Fluids B* **1**, 1949 (1989).
- [3] K. L. Wong, R. J. Fonck, S. F. Paul, D. R. Roberts, E. D. Fredrickson, R. Nazikian, H. K. Park, M. Bell, N. L. Bretz, R. Budny, S. Cohen, G. W. Hammett, F. C. Jobes, D. M. Meade, S. S. Medley, D. Mueller, Y. Nagayama, D. K. Owens, and E. J. Synakowski, *Phys. Rev. Lett.* **66**, 1874 (1991).
- [4] W. Heidbrink, E. Strait, E. Doyle, G. Sager, and R. Snider, *Nucl. Fusion* **31**, 1635 (1991).
- [5] W. W. Heidbrink, N. N. Gorelenkov, Y. Luo, M. A. Van Zeeland, R. B. White, M. E. Austin, K. H. Burrell, G. J. Kramer, M. A. Makowski, G. R. McKee, and R. Nazikian, *Phys. Rev. Lett.* **99**, 245002 (2007).
- [6] B. Wan, J. Li, H. Guo, Y. Liang, G. Xu, L. Wang, X. Gong, A. G. for the EAST Team, and Collaborators, *Nucl. Fusion* **55**, 104015 (2015).
- [7] Y. Todo and T. Sato, *Phys. Plasmas* **5**, 1321 (1998).
- [8] Y. Todo, *Phys. Plasmas* (1994-present) **13**, (2006).
- [9] Y. Todo, M. V. Zeeland, A. Bierwage, and W. Heidbrink, *Nucl. Fusion* **54**, 104012 (2014).

- [10] Y. Hu, G. Li, N. N. Gorelenkov, H. Cai, W. Yang, D. Zhou, and Q. Ren, *Phys. Plasmas* **21**, 052510 (2014).
- [11] B. Tobias, E. Bass, I. Classen, C. Domier, B. Grierson, W. Heidbrink, N. L. Jr, R. Nazikian, H. Park, D. Spong, and M. V. Zeeland, *Nucl. Fusion* **52**, 103009 (2012).
- [12] Z. Wang, Z. Lin, I. Holod, W. W. Heidbrink, B. Tobias, M. V. Zeeland, and M. E. Austin, *Phys. Rev. Lett* **111**, 145003 (2013).
- [13] L. Lao, H. S. John, R. Stambaugh, A. Kellman, and W. Pfeiffer, *Nucl. Fusion* **25**, 1611 (1985).
- [14] I. physics basis editors, *Nucl. Fusion* **39**, 2471 (1999).
- [15] M. S. Chu, J. M. Greene, L. L. Lao, A. D. Turnbull, and M. S. Chance, *Phys. Fluids B* **4**, 3713 (1992).
- [16] W. Deng, Z. Lin, I. Holod, Z. Wang, Y. Xiao, and H. Zhang, *Nucl. Fusion* **52**, 043006 (2012).
- [17] W. Zhang, I. Holod, Z. Lin, and Y. Xiao, *Phys. Plasmas* **19**, 022507 (2012).
- [18] R. Ma, F. Zonca, and L. Chen, *Phys. Plasmas* **22**, 092501 (2015).

Resonance overlap of multiple Alfvén eigenmodes leads to fast ion profile stiffness**Y. Todo^{1,2}, M. A. Van Zeeland³ and W. W. Heidbrink⁴**¹National Institute for Fusion Science, Toki 509-5292, Gifu, Japan²SOKENDAI (Graduate University for Advanced Studies), Toki 509-5292, Gifu, Japan³General Atomics, San Diego, CA 92186-5608, USA⁴Department of Physics and Astronomy, University for California, Irvine, CA 92697, USA**Abstract**

Fast ion pressure profiles flattened by multiple Alfvén eigenmodes are investigated for various neutral beam deposition powers with a multi-phase simulation, which is a combination of classical simulation and hybrid simulation for energetic particles interacting with a magnetohydrodynamic fluid. A monotonic degradation of fast ion confinement and the fast ion profile stiffness are found with increasing beam deposition power. The confinement degradation and the profile stiffness are caused by a sudden increase in fast ion transport flux brought about by Alfvén eigenmodes for the fast ion pressure gradient above a critical value. The critical pressure gradient and the corresponding beam deposition power depend on the radial location. The fast ion pressure gradient stays moderately above the critical value, and the profiles of the fast ion pressure and the fast ion transport flux spread radially outward from the inner region where the beam is injected. It is found that the square root of the MHD fluctuation energy is proportional to the beam deposition power. An analysis of the time evolutions of the fast ion energy flux profiles reveals that intermittent avalanches take place with contributions from the multiple eigenmodes. Surface of section plots demonstrate that the resonance overlap of multiple eigenmodes accounts for the sudden increase in fast ion transport with increasing beam power. The critical gradient and the critical beam power for the profile stiffness are substantially higher than the marginal stability threshold.

1. Introduction

Alfvén eigenmodes (AEs) are one of the major concerns of burning plasmas because they can transport energetic alpha particles and reduce the alpha heating efficiency leading to deterioration of the plasma performance. Comparison among DIII-D experiments with different beam injection powers revealed the stiffness of the fast ion pressure profile with critical beam powers for sudden increase in fast ion transport flux [1]. We regard fast ion profile as “stiff” when the increase of the fast ion profile gradient above a critical value is lower than the proportional increase to the beam power. Critical gradient models based on linear stability analysis have been proposed for the prediction of the fast ion stiff profile [2,3]. However, we would like to point out that the resonance overlap of multiple eigenmodes [4] can be another mechanism of the critical gradient formation. What is important is that the degree of resonance overlap depends on the mode amplitudes. If the mode amplitudes are not large enough for the resonance overlap, the fast ion flux may not be able to keep the fast ion distribution close to the marginal stability where the fast ion drive is balanced with the intrinsic damping of the modes.

In DIII-D experiments, significant flattening of the fast ion profile was observed during Alfvén eigenmode (AE) activity. In the experiments, a rich spectrum of toroidal Alfvén eigenmodes (TAEs) and reversed shear Alfvén eigenmodes (RSAEs) driven by ~ 80 keV neutral beam injection is observed during the current ramp-up phase with reversed magnetic shear. Since the fast ion distribution in the DIII-D experiments is significantly affected by AEs, a comprehensive simulation, which deals with both the AEs and the fast ion transport as self-consistently and realistically as possible, yet attainable on a tractable timescale, is needed. We have developed a multi-phase simulation, which is a combination of classical simulation and hybrid simulation for energetic particles interacting with an MHD fluid, in order to investigate a fast ion distribution formation process with beam injection, collisions, losses, and transport due to the AEs [5]. It was demonstrated with the multi-phase simulation of DIII-D discharge #142111 that the fast ion spatial profile is significantly flattened due to the interaction with the multiple AEs and that the fast ion pressure profile is in agreement with that of the experiment with the root-mean-square of the deviations same as the error bar [6]. The predicted temperature fluctuation profiles of $n=3, 4,$ and 5 modes were quantitatively compared with ECE measurements, and it was found that the fluctuation profiles as well as phase profiles are in very good agreement with the measurements. Additionally, the saturated amplitudes are within a factor of 2 of those measured. The fast ion spatial profile is significantly flattened due to the interaction with the multiple AEs with amplitude $\delta B/B \sim O(10^{-4})$.

In the present work [7], we investigate the fast ion pressure profile and the fast ion transport flux brought about by AEs for different beam deposition powers in order to clarify how the fast ion pressure profile and the fast ion transport vary with increasing beam deposition power.

2. Simulation Results

The fast ion pressure profile and the AE-induced fast ion transport flux are investigated for 8 runs with different beam powers using the equilibrium data for DIII-D shot #142111. Figure 1(a) and (b) indicate that the increase of the fast ion pressure profile is lower than the proportional increase to the beam power, and the fast ion confinement degrades monotonically with increasing beam power. This is the profile stiffness. We see in Fig. 1(c) and (d) that the fast ion transport suddenly increases above a critical pressure gradient and a critical beam power that depend on the radial location. This is similar to the observation in the DIII-D experiments. Resonant particles with each AE are plotted in phase space for different beam powers in Fig. 1(e) and (f). We see in Fig. 1(f) that the resonance regions represented by the particles overlap each other for the higher beam power.

We conclude that the resonance overlap of multiple AEs accounts for the sudden increase in fast ion transport flux and leads to the fast ion profile stiffness. This is an important property for the prediction of the energetic alpha particle distribution in burning plasmas. For the plasmas we have investigated in this article, the critical gradient for the resonance overlap is substantially higher than that for the AE stability. The resonance overlap depends on the AE amplitude, which is determined by the balance between the intrinsic damping and the energy transfer from energetic particles to the AE. This indicates both the intrinsic AE damping rate and the nonlinear interaction between energetic particles and AEs should be analyzed for the prediction of energetic alpha particle distribution in burning plasmas.

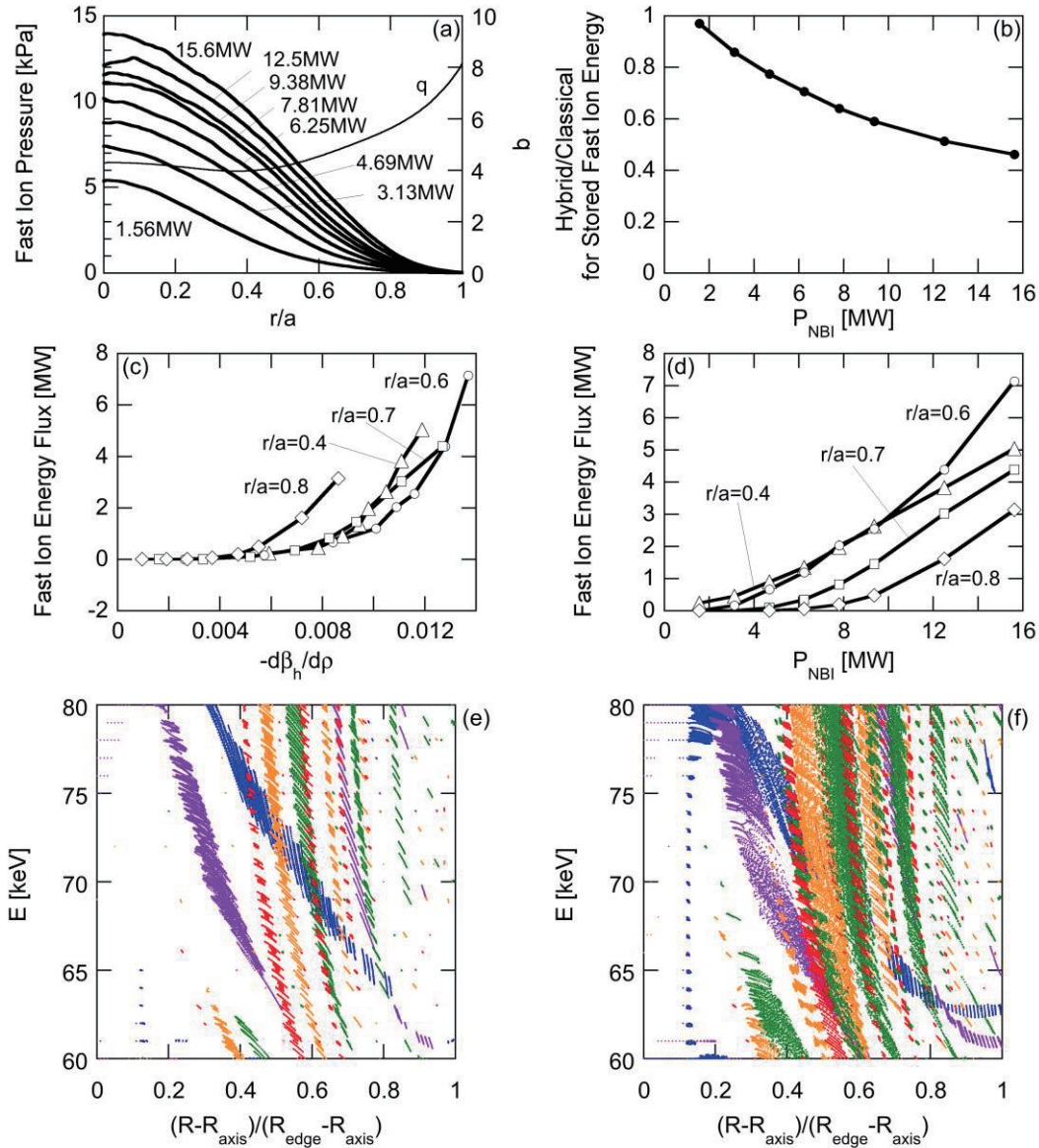


Fig.1 (a) Comparison of fast ion pressure profiles among different beam deposition powers, (b) ratio of stored fast ion energy in multi-phase hybrid simulation to that in classical simulation versus beam deposition power, (c) fast ion energy flux versus fast ion pressure gradient, (d) fast ion energy flux versus beam deposition power, and resonant particles in the phase space of normalized major radius and energy for beam deposition power (e) 1.56MW and (f) 6.25MW with Alfvén eigenmodes represented by colors: $n=1$ (blue), $n=2$ (purple), $n=3$ (green), $n=4$ (orange), and $n=5$ (red).

3. Summary

We investigated the fast ion pressure profile flattened by multiple Alfvén eigenmodes for various neutral beam deposition powers with a multi-phase simulation, which is a combination of classical simulation and hybrid simulation for energetic particles interacting with a magnetohydrodynamic fluid. A

monotonic degradation of fast ion confinement and the fast ion profile stiffness were found with increasing beam deposition power. The confinement degradation and the profile stiffness are caused by a sudden increase in fast ion transport flux brought about by Alfvén eigenmodes for the fast ion pressure gradient above a critical value. The critical pressure gradient and the corresponding beam deposition power depend on the radial location. The fast ion pressure gradient stays moderately above the critical value, and the profiles of the fast ion pressure and the fast ion transport flux spread radially outward from the inner region where the beam is injected. We found that the square root of the MHD fluctuation energy is proportional to the beam deposition power. We analyzed the time evolutions of the fast ion energy flux profiles, and found that intermittent avalanches take place with the contributions from the multiple eigenmodes. The surface of section plots demonstrated that the resonance overlap of multiple eigenmodes accounts for the sudden increase in fast ion transport with increasing beam power. The TAEs with $n=1-5$ are observed for all the runs including the lowest beam deposition power. This indicates that the critical gradient and the critical beam power for the profile stiffness are substantially higher than the marginal stability threshold. The overlap of the resonance regions of a single TAE was also found for the largest beam power.

Acknowledgements

This work was partly supported by the JSPS-NRF-NSFC A3 Foresight Program in the field of Plasma Physics (NSFC: No.11261140328, NRF: No.2012K2A2A6000443), MEXT as a priority issue to be tackled by using Post 'K' Computer, and JSPS KAKENHI Grant Number 15K06652. Numerical computations were performed at the Helios of the International Fusion Energy Center, the Plasma Simulator of the National Institute for Fusion Science, and the K Computer of the RIKEN Advanced Institute for Computational Science (Project ID: hp120212).

References

- [1] Collins C. S. *et al* 2016 *Phys. Rev. Lett.* **116** 095001
- [2] Ghantous K. *et al* 2012 *Phys. Plasmas* **19** 092511
- [3] Bass E. M. and Waltz R. E. 2013 *Phys. Plasmas* **20** 012508
- [4] Berk H. L., Breizman B. N. and Pekker M. S. 1995 *Nucl. Fusion* **35** 1713
- [5] Todo Y., Van Zeeland M. A., Bierwage A. and Heidbrink W. W. 2014 *Nucl. Fusion* **54** 104012
- [6] Todo Y., Van Zeeland M. A., Bierwage A., Heidbrink W. and Austin M. 2015 *Nucl. Fusion* **55** 073020
- [7] Todo Y., Van Zeeland M. A. and Heidbrink W. W. 2016 to appear in *Nucl. Fusion* **56**.

Simulations of the particle and heat fluxes of ELM and inter-ELM phase on tokamaks with BOUT++

T.Y. Xia^{1,2}, Y.B. Wu^{1,3,4}, X.Q. Xu², Z. Zheng¹, J.B. Liu and EAST Team¹

¹Institute of Plasma Physics, Chinese Academy of Sciences, Hefei, China (10.5pt)

²Lawrence Livermore National Laboratory, Livermore, USA (10.5pt)

³Donghua University, Shanghai, China

⁴Anqing Normal University, Anqing, China

Abstract (10.5pt, single line space)

A six-field two-fluid model based on the Braginskii equations with non-ideal physics effects in BOUT++ framework is used to simulate pedestal collapse in divertor geometry. The profiles from the DIII-D and EAST ELMy H-mode discharges are used as the initial conditions for the simulations. The evolution of the density profile during the burst of ELMs of DIII-D discharge #144382 is simulated. The growing process of the profiles for the heat flux at divertor targets during the burst of ELMs is also reproduced by this model. The widths of heat fluxes towards targets are a little narrower, and the peak amplitudes are as twice as the measurements possibly due to the lack of a model of divertor radiation which can effectively reduce the heat fluxes. For the EAST ELMy H-mode discharges, this model gives the consistent asymmetric particle distributions on divertor targets in double null geometry with the diagnostics. The simulations show that the asymmetric distribution of the particle flux is induced by the turbulent ExB drift in SOL near the two X-point regions where the strong convection plays an important role on the direction of ExB drift. The thermal sheath boundary conditions (SBC) have been implemented into the model for the divertor heat flux simulations. SBC does not affect the pedestal region obviously, but it is able to change the dominant toroidal mode number of the divertor heat flux to the zonal component due to inverse cascade.

1. Introduction

To assess the performance requirements of future tokamaks, such as ITER, one must study [1] discharges in the high edge particle and energy confinement regime known as H-mode [2]. In H-mode the steep pressure gradients can drive ballooning modes and bootstrap current generates peeling modes [3], and these two modes are considered to explain the trigger of Type-I edge-localized modes (ELMs) [4] successfully. However, unmitigated Type-I ELMs can lead to the impulsive heat and particle losses, which are predicted to cause excessive erosion and damage to plasma facing components (PFCs) in future tokamaks [5]. The nonlinear simulation of peeling-ballooning (P-B) modes is necessary to understand the ELM physics and find the methods to mitigate the heat flux problem to PFCs. SOLPS [6] and UEDGE [7] are widely used to simulate the steady-state energy depositions on divertor targets in the present and future tokamak design work. The transient heat fluxes during ELMs can be simulated with the modeled transport coefficients with SOLPS [8] and UEDGE. The self-consistent understanding of the transient evolution of ELMs is important and urgent to be studied.

The high-fidelity BOUT++ 2-fluid code suite has demonstrated significant recent progress toward integrated multi-scale simulations, including ELM dynamics, evolution of ELM cycles, and continuous fluctuations. The initial-value BOUT++ code has successfully simulated the nonlinear crash phase of ELMs [9, 10]. An emerging understanding of dynamics of edge localized mode (ELM) crashes and the consistent collisionality scaling of ELM energy losses with the world multi-tokamak database are studied within BOUT++ [11]. The 6-field 2-fluid module has been developed to simulate the ELM crash in shifted-circular geometry [12, 13] and in real tokamak geometry [14]. The theoretical and simulation results of a gyro-Landau-fluid (GLF) extension of the BOUT++ code are summarized in Ref. [13, 15], which contributes to increasing the physics understanding of ELMs.

In this paper, the electromagnetic 2-fluid 6-field mode under BOUT++ framework is used to study the ELM burst and inter-ELM turbulence on DIII-D and EAST. Starting from the Braginskii equations, within the flute-reduction, our 6-field model is constituted of 6 evolving equations of vorticity, parallel momentum, magnetic potential, density, ion and electron temperatures, which are written in drift ordering. In this model, the pressure is assumed to be isotropic, and the parallel collisionality is described by the parallel Spitzer resistivity. The Spitzer-Harm parallel thermal conductivities are used for the high collisional region, and flux-limited expressions are used for the low collisionality in order to take the kinetic effects into the consideration. The first order Finite Larmor Radius (FLR) effects are taken into account as the diamagnetic effects and gyro-viscous terms. The whole set of the equations is solved using the field aligned (flux) coordinate system with the shift radial derivatives [16].

The organization of the paper is: the validation with DIII-D ELMy H-mode diagnostics are presented in Sec. 2. In Sec. 3 the asymmetric distributions of the diverotr particle flux in double null geometry is discussed. Sec. 4 is the study on the effects of the thermal sheath boundary condition for the divertor heat flux simulations.

2. Validations with DIII-D ELMy H-mode experiments

The equilibrium of DIII-D ELMy H-mode discharge No. 144382 is used for the simulations. The discharge parameters are $I_p=1.16\text{MA}$, $B_T=2.15\text{ T}$, average $P_{\text{NBI}}=5.8\text{ MW}$, $R=1.78\text{m}$ and $a=0.58\text{m}$ [17]. The geometry of this discharge is lower single-null and the triangularity is low ($\delta=0.35$). The ELM frequency at the stationary phase is $f_{\text{ELM}}\sim 150\text{Hz}$. The constant normalized beta, $\beta_N=1.9$ and steady density are held by input power feedback during the ELMs. The crash and recovery of the small Type-I ELM at 2544.5ms were detected with multiple fast acquisition data chords in the pedestal, scrape-off layer (SOL) and divertor. This ELM produced a drop in the plasma stored energy of 2% (17kJ from a 0.8 MJ plasma). The fast target heat flux measurements by infrared television (IRTV) at 12kHz are also applied in this discharge to get the evolution of the heat flux on targets during the ELM cycle, so it is convenient to validate our model.

From the linear analysis, this discharge is ideal MHD stable, but unstable for resistive ballooning mode. Within the 6-field model with all the non-ideal physics, the growth rates peaked at $n=50$. The higher n modes are stabilized by the ion diamagnetic stabilizing effects. The experimental measurements indicate that this is a small ELM event. This small ELM event is very close to the ideal P-B instability threshold, therefore it is sensitive to both the equilibrium profiles and physics models. The small error from the profile measurements

leads to the uncertainty to determine if unstable modes are ideal or resistive in the actual experiments.

Fig. 1 shows the evolution of the electron density profiles n_e at outer mid-plane after the start of ELM [17]. Panel (a) is the measured profiles at the start of the ELM event, 0.29ms and 0.35ms after the ELM crash. Panel (b) is the simulated n_e profiles at the same time interval after the start of ELM event. In both panels, the black curves represent the initial profile at the start of the ELM. The magenta curves are for the n_e at 0.29ms after the ELM start and red are at 0.35ms. The simulation shows the similar crash range that the profile drops to the inner boundary $\Psi_N=0.8$ or $\rho_N=0.89$. The difference from the measurement is mostly because that the density profile is measured at 3007.1ms, which is different from the equilibrium reconstructed at 2544.5ms, the initial n_{e0} is not exactly the same as the simulation.

Fig. 2 shows the evolution of the profiles of the heat flux to the lower target during the ELM event for the simulated discharge [17]. Panel (a) is derived by the fast target heat flux measurements of 12kHz IRTV. Panel (b) is obtained from the 6-field 2-fluid model described in previous sections. The magenta curves for both panels are the heat flux profiles at the start of ELM. The black curves are at 200 μ s after the ELM burst, the red are at 280 μ s and the blue at 370 μ s. At the outer target, the simulated peak heat fluxes show the similar expansion to the measurements, from the strike point at $R\sim 1.56$ m to $R\sim 1.65$ m. The increasing progress of the peak heat flux is also shown in the simulation. The peak value keeps growing from the magenta curves to black, red and blue in both panels. The magenta curve in Panel (b) is too small to be seen because there is no energy flow into the SOL at the beginning of the simulation. The out-moving of the peak position at outer target is observed in our model. In panel (a), the peak of the heat flux is moved to $R\sim 1.62$ m for the blue curve from the strike point at $R\sim 1.56$ m for the black and magenta curves. In Panel (b) this out-moving effect is not so obvious as Panel (a) because the magnetic flutter terms in parallel thermal conduction, which are able to broaden the heat flux distribution, is not fully considered in this simulation yet. The present model leads to $\sim 40\%$ narrower of the width of the heat flux to outer target than the measurements. The amplitudes of the simulated heat fluxes in Fig. 2(b) are as twice as the measured values because there are only ions and electrons in our simulation. The low-temperature neutrals and impurities near the targets are not taken into consideration in this model, which can effectively dissipate the incoming energy flow through radiation and recombination. Therefore, the heat fluxes simulated here is the amplitude towards the targets and they should be much higher than the measurements. The amplitudes of the heat fluxes in the private flux region between the inner and outer separatrix in Panel (a) are due to reflections in the IRTV, which have been significantly reduced in the 2013 DIII-D campaign. There should be very low heat loads here, which is correctly simulated in Panel (b). The reason why the simulated heat fluxes at inner target show the similar amplitudes to measurements is that the reflection influences the precision for small fluxes, so the peaks at inner target in Panel (a) should be smaller. Another possible reason is that the simulated heat flux at inner target is underestimated because the magnetic flutter terms in thermal conduction are not considered in Panel (b) which are able to increase the inner heat flux.

One possible reason that the simulated energy loss is always larger than the measured value is the lack of energy and particle input in the simulation domain. The inner boundary condition applied in the simulation sets no flux flowing into the pedestal region, so there is no additional source in this model. However, in the experiments, the auxiliary heating, such as NBI and RF, is necessary to maintain H-mode. This indicates that

the additional particle and energy source should be considered in the ELM simulations. One simple method to consider the external source is to add the particle and energy flux via the inner boundary condition. This flux-driven boundary condition is able to prevent the fluctuations propagating into the inner boundary. When the fluctuations grow to the inner boundary with the zero-flux boundary condition, the energy stored near the boundary will be lost outwards to the separatrix and no mechanism could stop the lost. Therefore, the total energy loss will keep growing slowly and be very difficult to get saturated. The external source at the inner boundary might be able to constraint the slowly increasing of the total energy loss and obtain the smaller simulated energy loss. Another possible effect of the flux-driven boundary condition is to solve the issue that the simulated ELM bursts faster than the experiments. As shown in Fig. 1 and 2, both the crash of n_e and the increase of heat flux before $200 \mu s$ are much faster than the measurements. The particle flux-driven boundary can bring additional particles into pedestal and may slow down the crash of n_e . Similarly, the energy flux-driven boundary may decrease the energy loss and slow down the heat flux growing at the beginning of the ELM burst near targets. The implementation of the flux-driven boundary condition will be our next-step work.

3. The validations of the particle flux distributions on divertor of EAST ELMy H-mode

For the study of the ELMy H-mode on EAST, the 6-field 2=fluid model in BOUT++ is also used to simulate the burst of one ELM event as well as the distribution of particle and heat fluxes induced by ELM. The setup of the code is completely the same as the previous DIII-D simulations in last section. The quasi-neutral condition $n_i=n_e$ is assumed and there is no impurities considered in the simulation domain during the evolution of ELMs. The inner boundary conditions on radial direction are set to be Nuemann for density and temperature perturbations. The parallel momentum, vorticity and current is set to be zero at the inner boundary. For the outer boundary, the density, temperatures, vorticity, current and parallel momentum are all set to be Dirichlet. The domain of y directions inside the separatrix is twisted-shifted periodic and z is periodic. The sheath boundary conditions are applied at the divertor plates and the effects will be discussed late in this paper.

EAST ELMy H-mode discharge #38300 [18] is a double null geometry, but close to lower single null with $dR_{sep} = 0.8cm$. For this simulation, the density and temperature profiles from experiments are used as the input, and the electric field is calculated form the assumption of zero equilibrium net flow, which means that the equilibrium ExB flow is balanced with the ion diamagnetic flow. The linear analyses indicate that this discharge is ideal peeling-ballooning unstable. The nonlinear simulation shows the evolution of the formation of ELM filaments, as Fig. 3 shows. The dominant toroidal mode number is changed to a lower value with $n=5$ due to inverse cascade, which tells that the nonlinear ELM filaments are not consistent with the linear dominant mode. The power loss of the simulation is around 0.7MW, which is consistent with the typical value of EAST discharges with LHCD. In the EAST experiments, the distributions of the particle fluxes on divertor targets are found to be dependent on the direction of toroidal field B_T [19]. This simulation shows that the particle flux on upper outer target during ELM is larger than that on lower outer target for normal B_T case, and for reversed B_T case, the flux on upper outer target is smaller than that on lower outer target, which is consistent with the EAST experiments shown in Fig. 4. This direction of the particle flux is consistent with the Pfirsch-Schluter flow at low field side, which is opposite to ExB and ∇

B drift. The rough analysis shows that the asymmetric distribution of the particle flux is induced by the turbulent ExB drift in SOL near the two X-point regions where the strong convection plays an important role on the direction of ExB drift [20].

4. The effects of the sheath boundary condition on EAST ELMy H-mode simulations

In order to simulate the heat flux and particle flux on divertor targets, the effects of the plasma sheath near PFCs are necessary to be taken into the consideration. The sheath boundary condition (SBC) has been applied in BOUT++ framework to describe the effects of sheath for both thermal and radio frequency waves [21]. In the 6-field 2-fluid model, the thermal SBC is also implemented at divertor targets for the parallel velocity, ion and electron temperatures, vorticity, density and parallel current..

$$\begin{aligned}
 V_j &= C_s, \\
 q_{se} &= -\kappa_{||e} \partial_{||} T_e = \gamma_e n_i T_e C_s, \\
 q_{si} &= -\kappa_{||i} \partial_{||} T_i = \gamma_i n_i T_i C_s, \\
 \partial_{||} \varpi &= 0, \\
 \partial_{||} n_i &= 0, \\
 j_{||} &= n_i e \left[C_s - \frac{v_{Te}}{2\sqrt{\pi}} \exp\left(-\frac{e\phi}{T_e}\right) \right].
 \end{aligned}$$

Where C_s represents the sound speed, $\kappa_{||j}$ is the thermal conduction, γ_j is the energy transmission coefficient.

To study the SBC in the simulations, the equilibrium of EAST ELMy H-mode #56129 at 5550ms is used for its simple LSN geometry. Fig. 5 shows the linear growth rate for this equilibrium. This equilibrium is ideal MHD stable, but unstable for the resistive ballooning mode and drift Alfvén wave. These two modes contribute nearly the total linear growth rate even with other non-ideal MHD instabilities. The profile scan shows the linear growth rate is most affected by the electron temperature, but nearly not affected by density. This characteristic is also consistent with the resistive ballooning and drift Alfvén mode. Within SBC, the time evolution of the heat fluxes onto divertor plates during the burst of ELM are shown in Fig. 6. The profiles of the heat fluxes on outer (Panel (a)) and inner (Panel (b)) targets are shown at different times. At outer target, the heat flux profiles get increased with time when the ELM bursts and pumps out the energy from the pedestal region into SOL. The peak of the heat flux profiles are also moving outwards, because the magnetic flutter introduces the enhanced radial transport near the separatrix. This moving behavior is also observed on DIII-D diagnostics [17]. Although the peak of the heat flux is changed from $\Psi_N=1$ to 1.01, the change of the distance is just ~ 5 mm align the outer target plate. This value is much smaller than the spatial resolution of the divertor probes on EAST, so this small change of the peak position is difficult to be seen from diagnostics. Compared with the outer targets, Panel (b) shows much smaller heat fluxes, around one order of magnitude smaller than that on outer target. This is because that the ELM pumps out the energy from the outer mid-plane which is more close to the outer target. Since the inner target is far from the outer mid-plane, the peak of the heat flux is affected little by the magnetic flutter and the peak position is still at the separatrix. For this simulations, only 0.4ms is obtained and this time is still shorter than the free streaming time scale from the outer mid-plane to inner target. Therefore, it is still not enough to study the asymmetric

distribution of the particle flux.

Fig. 7 shows the effects of the SBC on heat flux simulations. The Dirichlet boundary condition is applied for all the evolving variables for the w/o SBC case. Fig. 7(a) shows that SBCs nearly do not change the behaviors in the linear phase, no matter which position is investigated. Fig. 7(b) shows that SBCs only affect the heat flux amplitude at outer mid-plane and inner target a little. The whole spectra are very close to the w/o SBC case. The peak of the toroidal mode number at these two positions are not changed. This indicates that the SBC does not show much influence on the pedestal region. However, the dominant toroidal number of the heat flux at out mid-plane is changed from $n=5$ to $n=0$, and the amplitude of the spectrum w/ SBC is changed a lot from the w/o SBC case. From this result, it indicated that SBC introduced a large zonal part of the heat flux which generate an obvious inverse cascade. More energy from the turbulent part is concentrated to the zonal part, so all the spectra for the high toroidal modes are damped due to SBC.

5. Summary

In order to study the distribution and evolution of the transient heat flux during ELMy H-mode in divertor geometry in tokamaks, the electromagnetic 6-field 2-fluid model is revised. The nonideal physics effects, such as Spitzer resistivity, ion FLR effects, parallel thermal conductions, hyper-resistivity, etc., are taken into the consideration. The DIII-D ELMy H-mode discharge #144382 is used as the lower single-null equilibrium of the validation. The linear analysis shows that this ELM is ideal MHD stable and destabilized by resistive-ballooning mode. The simulated total energy loss is close the measurement. The crash of the density profile and the increase of the divertor heat flux are simulated by this model. The simulated heat flux width is $\sim 40\%$ narrower than the measurements and the amplitude is around two times larger because there are no recombination and radiation effects of neutrals near the targets considered in this model. The evolution of the heat fluxes towards targets is much faster in the simulation than the measurements because the lack of the auxiliary heating source in the model, which is able to constrain the speed of the energy loss at pedestal region and can be simulated by flux-driven boundary conditions.

For the EAST ELMy H-mode simulations, the asymmetric distribution of particle flux on divertors in double null geometry are simulated by the 6-field 2 fluid model. The distributions under normal and reversed toroidal field in simulations show the consistent trend with the measurement. The direction of the particle flux is consistent with the Pfirsch-Schluter flow at low field side. The rough analysis shows that the asymmetric distribution of the particle flux is induced by the turbulent ExB drift in SOL near the two X-point regions where the strong convection plays an important role on the direction of ExB drift.

The thermal sheath boundary condition has been implemented at divertor plates in BOUT++ for the heat flux simulations. The study on the SBC effects shows that SBC does not affect the pedestal region at linear phase because the perturbations grow up at the pressure peak gradient region, which is far away from divertors. At nonlinear phase, the pedestal region is affected by SBC, but not very obviously. The divertor which is the most close to the outer mid-plane is affected by SBC dramatically. The dominant toroidal mode number of the divertor heat flux is changed to zero due to inverse cascade.

Acknowledgements

We gratefully acknowledge X.Q. Xu, Max Fenstermacher, Charles Lasnier and Lei Zeng (UCLA) for providing the pedestal profiles, IRTV heat flux and fast reflectometer profile data used in this work. This work was partly supported by the JSPS-NRF-NSFC A3 Foresight Program in the field of Plasma Physics (NSFC: No.11261140328, NRF: No.2012K2A2A6000443). This work was performed under the auspices of the U.S. Department of Energy by Lawrence Livermore National Laboratory under Contract DE-AC52-07NA27344, LLNL LDRD project 12-ERD-022, and LDRD project 11-ERD-058. It was supported by the China Natural Science Foundation under Contract No.11405215 and 11405217, the National Magnetic Confinement Fusion Science Program of China under Contracts No. 2014GB106001 and 2013GB111002. Numerical computations were performed on the ShenMa High Performance Computing Cluster in Institute of Plasma Physics, Chinese Academy of Sciences.

References

- [1] E.J. Doyle, R.V. Budny, J.C. DeBoo, et al., September 22nd IAEA Fusion Energy Conf. (Geneva, Switzerland), (2008).
- [2] M. Keilhacker, G. Becker, K. Bernhardt, et al., Plasma Phys. Control. Fusion **26** (1984) 49 .
- [3] P.B. Snyder, N. Aiba, M. Beurskens, et al., Nucl. Fusion **49**, (2009) 085035.
- [4] H. Zohm, Plasma Phys. Control. Fusion **38** (1996) 105.
- [5] A. Loarte et al., Proc. 23rd IAEA fusion energy conference, Daejeon, Korea (2010).
- [6] R. Schneider, X. Bonnin, K. Borrass, D. P. Coster, H. Kastelewicz, et al., Contrib. Plasma Phys. **46** (2006) 3.
- [7] T.D. Rognlien, D.D. Ryutov, N. Mattor, and G.D. Porter, Phys. Plasmas, **6**, (1999) 1851.
- [8] D.P. Coster, A.V. Chankin, H.-J. Klingshirn, X. Bonnin, A. Kukushkin and A. Loarte, 40th EPS Conference on Plasma Physics, (2013) P1.104.
- [9] X.Q. Xu, B.D. Dudson, P.B. Snyder, M.V. Umansky and H.R. Wilson, Phys. Rev. Lett. **105**, (2010) 175005.
- [10] P.W. Xi, X. Q. Xu and P.H. Diamond, Phys. Rev. Lett. **112**, (2014) 085001.
- [11] X. Q. Xu, J. F. Ma, and G. Q. Li, Phys. Plasmas, **21**, (2014) 120704.
- [12] T.Y. Xia, X.Q. Xu and P.W. Xi, Nucl. Fusion **53**, (2013) 073009.
- [13] C. H. Ma, X. Q. Xu, P. W. Xi and T. Y. Xia, Phys. Plasmas **22**, (2015) 010702.
- [14] T.Y. Xia and X.Q. Xu, Nucl. Fusion **55** (2015) 113030.
- [15] X.Q. Xu, et al., Phys. Plasmas, **20** (2013) 056113.
- [16] B.D. Dudson, M.V. Umansky, X.Q. Xu, P.B. Snyder, H.R. Wilson., Comput. Phys. Commun. **180**, (2009) 1467.
- [17] M.E.Fenstermacher, X.Q. Xu, T.Y. Xia, T. D. Rognlien, M. Umansky, I. Joseph, C.J. Lasnier, T.H. Osborne and L. Zeng, 40th EPS Conference on Plasma Physics, (2013) P4.104.
- [18] G.Q. Li et al. Plasma Phys. Control. Fusion **55** (2013) 125008.

[19] H.Y. Guo et al. Phys. of Plasmas **21**, 056107 (2014);

[20] B.N. Wan et al., Nucl. Fusion **55** (2015) 104015.

[21] B. Gui, X. Q. Xu, J. R. Myra, and D. A. D'Ippolito, Phys. Plasmas **21**, 112302

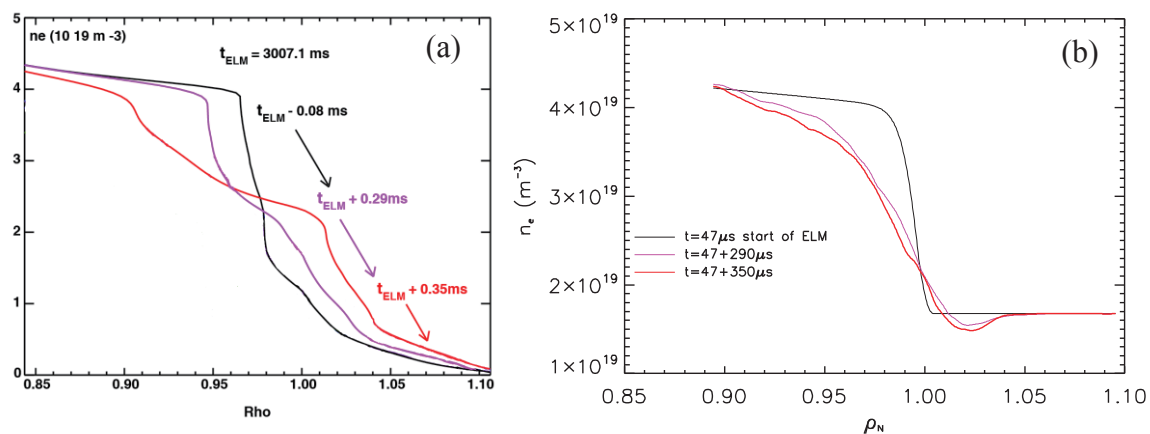


Figure 1: (a) The measured evolution of the density profiles at outer mid-plane during the crash of ELM. (b) The simulated evolution of the density profiles at the same time as Panel (a). The crash region of the density is well repeated by the simulation [14].

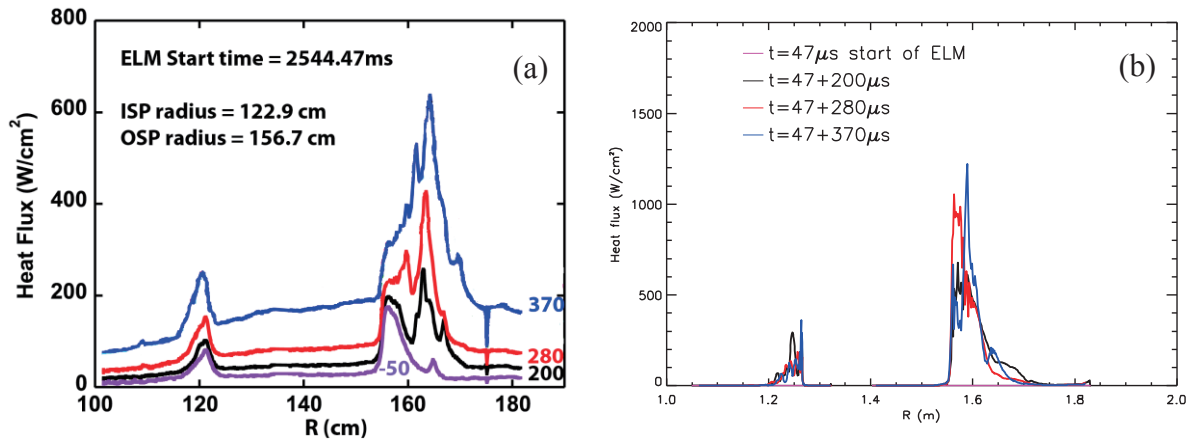


Figure 2: (a) The measured evolution of the heat flux profiles on lower targets during the burst of ELM event of DIII-D discharge #144382. (b) The evolution of the heat flux profiles obtained from BOUT++ simulation. The simulation derives the similar heat flux expansion on targets. The amplitudes are larger than the measurements because there are no neutrals and impurities in the model [14].

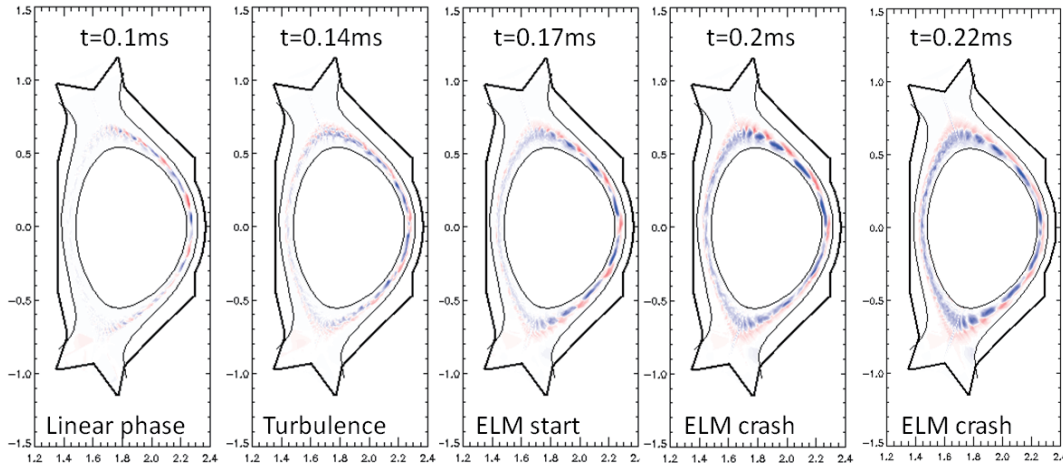


Figure 3: Figure 1: The simulated evolution of the ELM filamentary structures of EAST ELMy H-mode #38300. The toroidal mode number is changed from $n=15$ at linear phase to $n=5$ at the crash time [19, 20].

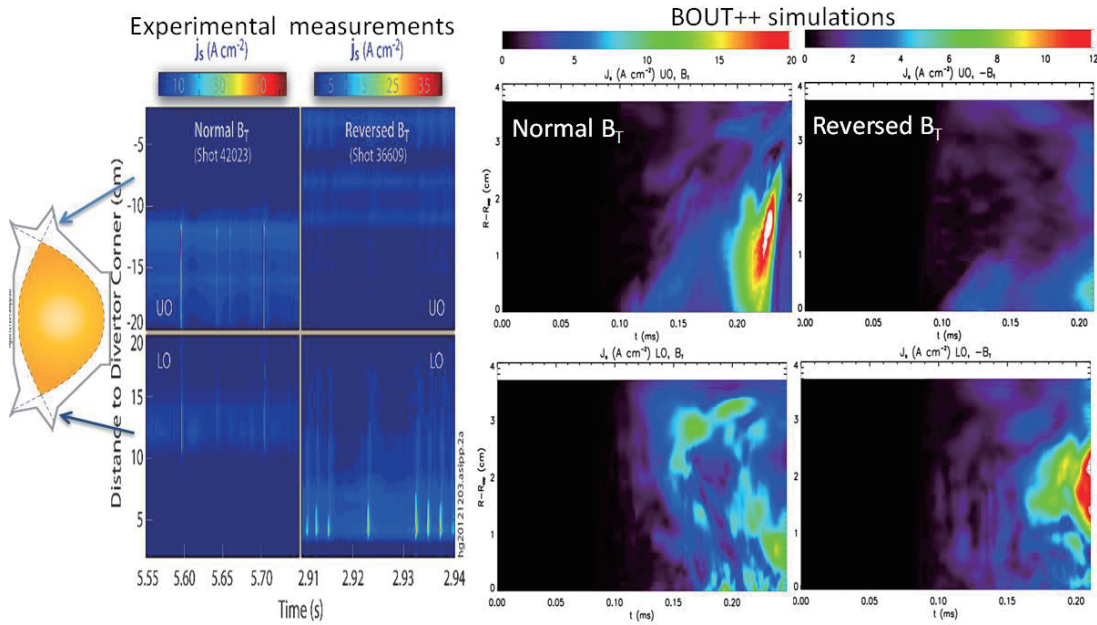


Figure 4: The asymmetric particle flux distribution on upper and lower outer divertor targets are measured in left panels. The right panels are derived from BOUT++ simulations. The consistent distributions are obtained with the measurement [19, 20].

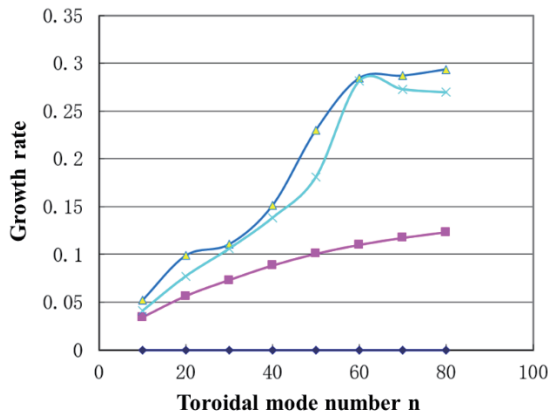


Figure 5: The linear growth rate of EAST #56129. The instability is mainly from resistive ballooning mode and drift Alfvén mode.

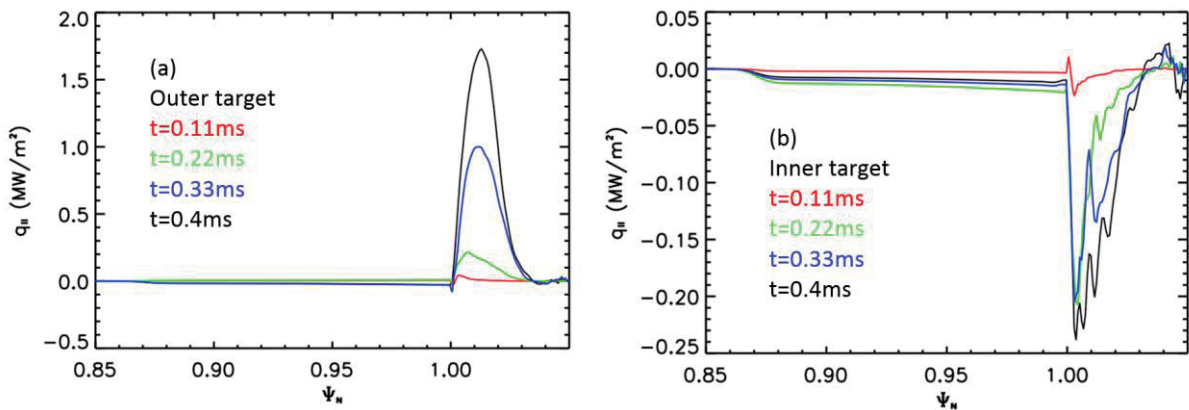


Figure 6: The time evolution of the heat flux distributions (a) and (b) at the burst of ELM for EAST #56129. The increasing of the heat flux is repeated by the simulation.

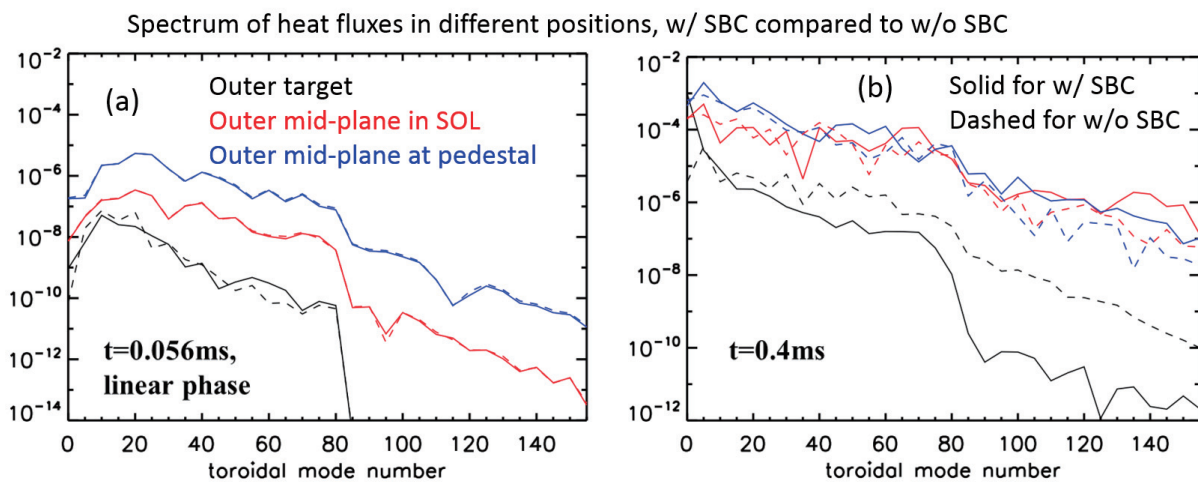


Figure 7: The power spectrum of the heat fluxes with different boundary conditions. The spectra are plotted at different time. Panel (a) is at linear phase and Panel (b) at nonlinear phase. SBCs affect the linear behaviors little, but leads to a much higher zonal component for the heat fluxes at outer target.

Experimental study of density pump-out on EAST*

S.X.Wang¹, H.Q.Liu¹, Y.X.Jie¹, Q.Zang¹, B.Lyu¹, T.Zhang¹, L.Zeng¹, S.B.Zhang¹, S.Nan¹, T.Lan², Z.Y.Zou¹, W.M.Li¹, Y.Yao¹, X.C.We¹, H.Lian¹, G.Li³, H.D.Xu¹, X.J.Zhang¹, B.Wu¹, Y.W.Sun¹ and the EAST team

¹Institute of Plasma Physics, Chinese Academy of Sciences, Hefei 230031, China

²University of Science and Technology of China, Hefei, Anhui 230026, China

³Tianjin University of Technology, Tianjin 300384, China

Abstract: In the Experimental Advanced Superconducting Tokamak (EAST), density pump-out phenomena were observed by using a multi-channel POLarimeter-INTerferometer (POINT) system under different heating schemes of Ion Cyclotron Resonant Heating (ICRF), Electron Cyclotron Resonance Heating (ECRH), Neutral Beam Injection (NBI). The density pump-out was also induced with application of resonant magnetic perturbation (RMP), company with a degradation of particle confinement. For the comparison analysis in all heating schemes, the typical plasma parameters are plasma current 400 kA, toroidal field 2T, and line average density $2 \times 10^{19} \text{ m}^{-3}$. The experimental results show that the degree of pump-out is concerned with electron density and heating power. Low density deuterium low confinement (L-mode) plasmas ($< 3.5 \times 10^{19} \text{ m}^{-3}$) show strong pump-out effects. The density pump-out correlated with a significant drop of particle confinement.

Keywords: density pump-out, particle confinement, ECRH, ICRF, NBI, RMP

PACS: 52.55.Fa, 52.25.Xz

1. Introduction

The phenomenon of density pump-out, also dubbed as density flattening, has been observed on both tokamaks and stellarators. It indicates the particle depletion from the plasma core and thus leads to the degradation of particle confinement. In nuclear fusion, the confinement time and density are of great importance and are affected by density pump-out in some experimental observation [1-4]. The research on density pump-out has an important significance on improving particle confinement time and density profile control [5]. Moreover, it may provide an available tool for high-Z impurities pump-out from the core plasma for achieving the goal that tokamak can

operate steadily with long pulse and high-performance plasma.

Several explanations of the confinement degradation due to density pump-out have been given in different devices. In Tore Supra, these density redistributions are ascribed to an $E \times B$ convection process linked with rf sheaths in condition of ICRH [6]; in MAST, a possible explanation of the phenomenon would be an enhancement of the particle turbulent transport in the outer plasma due to the magnetic perturbation [7]; in CHS, density pump-out is possibly triggered by the production of the electrons accelerated perpendicularly to the magnetic field with ECRH [8]. Apart from these reasons for this phenomenon, the self-consistent electric fields in the region near the isolated island chains [9], neoclassical outward thermodiffusion [10], the decrease of the Ware pinch [11], have been put forward as well. But the underlying physics mechanism is still not well understood due to the difficulty of measuring the sources for particle transport with sufficient accuracy.

In the EAST, density pump-out was observed clearly with ICRF [12], ECRH, NBI plasma. The density pump-out was also induced with application of RMP on EAST, company with a degradation of particle confinement. This paper presents the observation of the density pump-out and hence the confinement degradation on EAST. A brief description of the Far-infrared polarimeter/interferometer system for density pump-out phenomena observation on EAST is presented in section 2. Section 3 describe the observation of density pump-out with ECRH, ICRF, NBI and RMP plasma on EAST. Then the statistical results of the relation between relative density drop and line-averaged density or heating power are showed in section 4. Finally, summary and discussions are presented.

2. Far-infrared polarimeter/interferometer system on EAST

Density pump-out is mainly observed by HCN interferometer and POINT, which can provide the density profile with high time resolution.

Since 2006, the HCN interferometer has been setup as the primary diagnostic system to measure density. The wavelength of HCN laser is $337\mu\text{m}$ and output power is about 100mW. Three-chord probing beams passing through the EAST in vertical direction. The three beams are located at $R=1.64\text{m}$, 1.82m , 1.91m , R is major radius, as shown in Fig.1. The details of HCN interferometer are described in Ref. [13]. A double pass, radially-viewing, multichannel far-infrared (FIR)

polarimeter/interferometer system is developed to measure the current density profile and electron density profile on EAST from 2014. There are three FIR lasers and each of them can generate more than 30mW power by utilizing three 432.5 μm formic acid FIR lasers pumped by three CO₂ lasers. To determine the Gaussian beam propagation size along the laser beam path, the cube corner retro-reflectors are used behind the inner-wall tiles which can withstand 350°C baking temperature and 1000 s discharge. In 2014, a five-chord POINT system was installed on EAST. The five chords were located at $Z = -34, -17, 0, 17, 34\text{cm}$ along the horizontal direction. Then, an eleven-chord system was upgraded and routinely operated from 2015. Eleven chords were located at $Z = -42.5, -34, -25.5, -17, -8.5, 0, 8.5, 17, 25.5, 34, 42.5\text{cm}$, as shown in Fig.1. Initial calibration indicated the electron line-integrated density resolution is less than $5 \times 10^{16} \text{ m}^{-2}$. The detailed information about the POINT system are described in Ref [14].

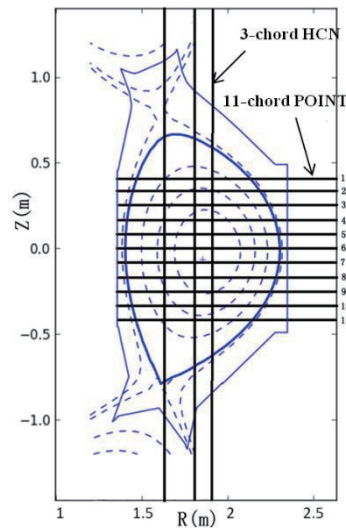


Fig.1 The schematic of the 3-chord HCN and the 11-chord POINT.

Fig.2 shows the operational region of EAST in 2014 and 2015. n_{gw} is Greenwald limit which is defined as $n_{gw} = I_p / \pi a^2$, I_p is the plasma current, a is the minor radius.

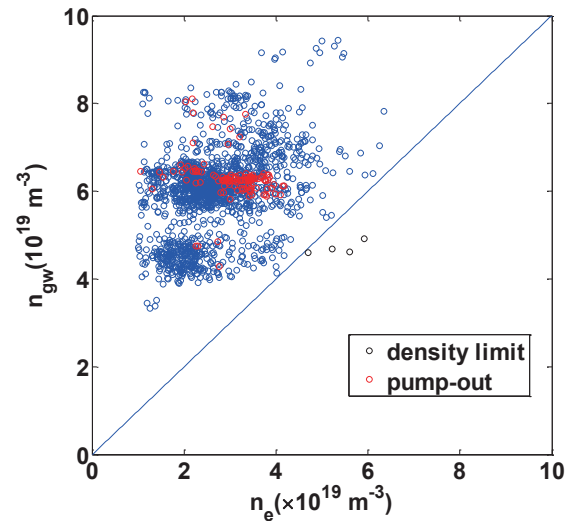


Fig.2 Operational region of EAST in 2014 and 2015

The density used in this paper is line-averaged density and what measured by POINT is line-integrated density, the chord length or the minor radius used to calculate line-averaged density is critical to density pump-out. We should aware and confirm that the minor given by equilibrium fitting (EFIT) code is correct. The red circles in Fig.2 represent the density pump-out discharges.

3. Density pump-out

3.1 Density pump-out induced by ECRH, ICRF, NBI

Here, the time evolution of the signals from the central chord of POINT and the density peaking factor, defined as the ratio of the central (n_6) to the peripheral (n_2) chord of POINT signal, n_6/n_2 , as well as the signals of other diagnostics, are plotted in a short time window around some heating scheme switch-on, as shown in Fig.3, Fig.4 and Fig.5.

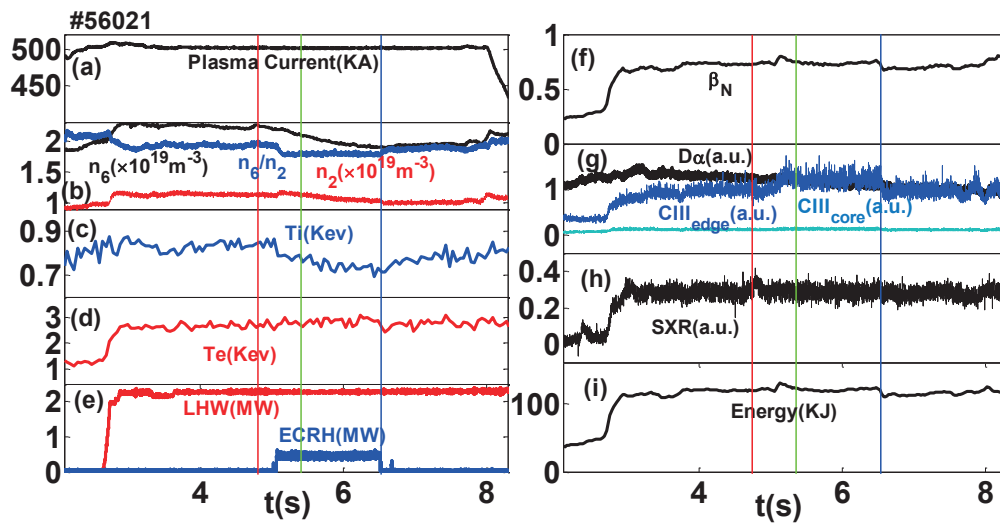


Fig.3 Time evolution of ECRH pump-out (#56021). The data from the top to the bottom are plasma current (a), central and edge line averaged density and density peaking factor (b), temperature of ions (c), and electron temperature measured by X-ray Crystal Spectrometer (XCS) (d), injected power of ECRH and Low Hybrid Wave (LHW) (e), normalized beta (f), intensity of Dα emission and edge and core CIII emission (g), intensity of soft x-ray (SXR) (h), and the plasma stored energy (i).

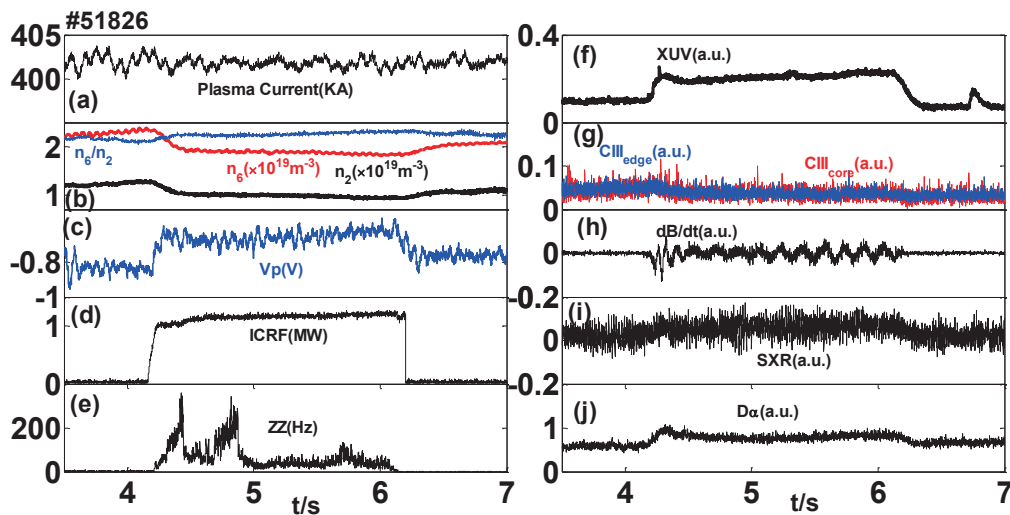


Fig.4 Time evolution of ICRF pump-out (#51826). The data from the top to the bottom are plasma current (a), central and edge line averaged density and density peaking factor (b), loop voltage (c), injected ICRF power (d), production of neutrons (e), intensity of radiation measured by Fast bolometer (f), edge and core CIII emission (g), spectrogram of the Mirnov coil signals (h), intensity of soft X-ray (i), and intensity of Dα emission (j).

(j).

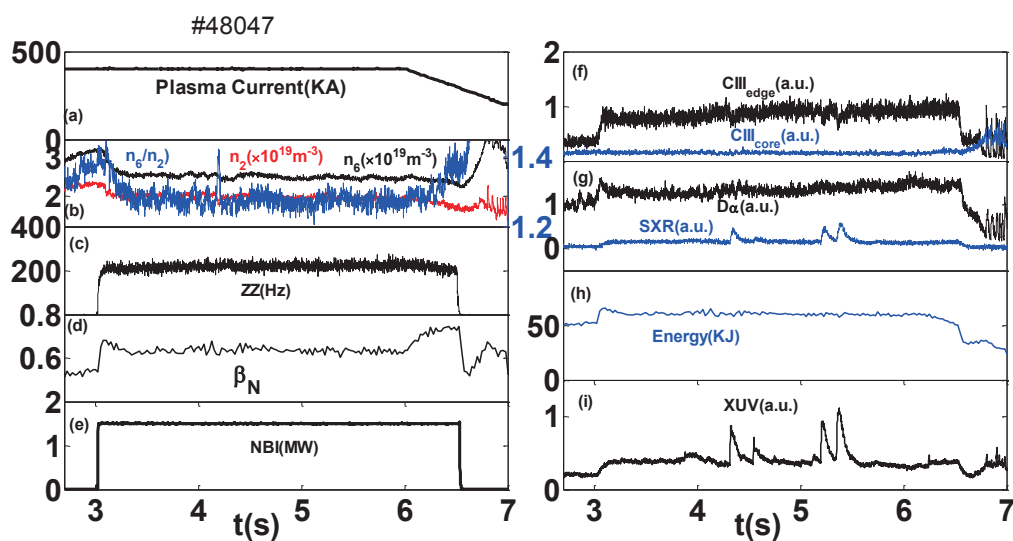


Fig.5 Time evolution of NBI pump-out (#48047). The data from the top to the bottom are plasma current (a), central and edge line averaged density and density peaking factor (b), production of neutrons (c), normalized beta (d), injected NBI power (e), intensity of edge and core CIII emission (f), intensity of Da emission and soft X-ray (g), plasma stored energy (h) and intensity of radiation measured by Fast bolometer (i).

ECRH, and NBI caused the density and density peaking factor decreased, as shown in Fig.3, and Fig.5. But the ICRF caused the density decreased and the density peaking a little increased, as shown in Fig.4. After ICRF launched into plasma, the radiation, neutron production and Da signal increased. Loop voltage decreased. Spectrogram of the mirnov coil signals indicates that some MHD activity may occurred in ICRF plasma. The results is agreement with most of shots with density pump-out caused by ICRF in 2010, which was observed with ICRF heating during L-mode discharges at high electron density of $4 \times 10^{19} m^{-3}$ [12]. Also, NBI caused the radiation, β_N and stored energy as well as the neutron production increased. Next, ECRH induced density pump-out will be emphasized.

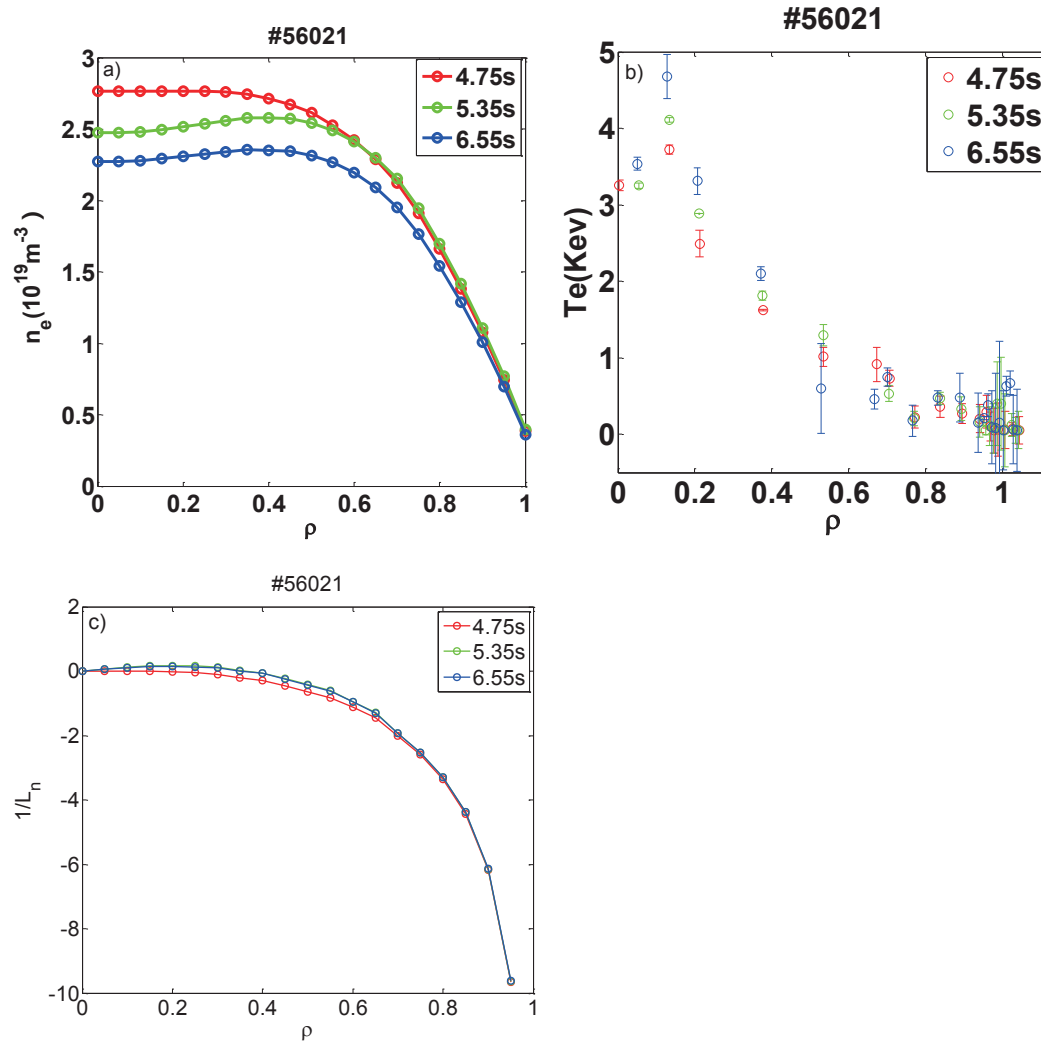


Fig.6 a) Electron density profile, b) electron temperature profile, c) inversed electron density gradient length $1/L_n$ at 4.75s (red marks), 5.35s (green marks), 6.55s (blue marks).

The effect of ECRH on the plasma density may become of high importance for future long-pulse or steady-state plasma operation, because it may provide a tool for density control. The impurity confinement is also affected by ECRH, which may provide a tool for impurity control [10]. Despite the obvious importance of the effect, there is still little understanding of the underlying physical process. On EAST, a new ECRH system has been routinely operated from 2015. With the application of ECRH, the central electron density decreased and density peaking also decreased, which means the density profile became flat. Fig.6(a) and Fig.6(b) illustrate the electron density and temperature of L-mode plasma in steady conditions during the Ohmic phase(4.75s), while density decreasing phase(5.35s) and after density decrease phase(6.55s). The

electron density in the plasma core decreased apparently while density increased in the edge, which is in accordance with the time evolution of density peaking that the density profile became flat. Density profile is obtained by combining the core profile from the POINT and edge profile from reflectometer. The line averaged density is $2 \times 10^{19} \text{ m}^{-3}$, providing a clear example of density pump-out on EAST caused by ECRH.

Figure 6(c) represents the values of inverse electron density gradient length $1/L_n(\rho) = \nabla n_e(\rho)/n_e(\rho)$ profiles in different heating phase. Obviously, the length profile is slightly changed after ECRH applied in the domain $\rho=0.2\sim 0.6$. While for large values of density gradient length, the dominant instability is a TEM and density gradients are a drive for TEMs [15], the ECRH density pump-out may related to the TEM instability.

3.2 Density pump-out induced by RMP

Edge-localized modes (ELMs) is an important phenomenon of edge higher confinement mode (H-mode) and H-mode can maintain for a long time under good control due to ELM expelling impurities. ELM is a disadvantage for facing plasma component because it can lead to energy lost and this will have an effect on the operation of inner part in tokamaks. RMP is a useful way to control ELMs and affect its frequency and size. But under some conditions, when RMP was used, density pump-out will happen, seen in Fig.8. There are not ELMs in this shot because H mode was not obtained.

Different from radio frequency (RF) heating and NBI heating cases, resonant magnetic perturbations mainly act on the plasma edge. From the time evolution of the density peaking plotted in Fig.7(f), we can see the signal n_0/n_2 increased after using RMP. This is because the peripheral density n_2 dropped more than the central density. The electron temperature profile remained unchanged, which means the RMP cannot influence the temperature of plasma core effectively, as seen in Fig.8(b). The decreasing of the β_N and the stored energy mainly due to the density pump-out.

Fig.8(a) and Fig.8(c) show the density profile and the inversed electron density gradient length in different time. Density profile becomes flattening while the density gradient length remained nearly unchanged, which is slightly different with the ECRH induced density pump-out.

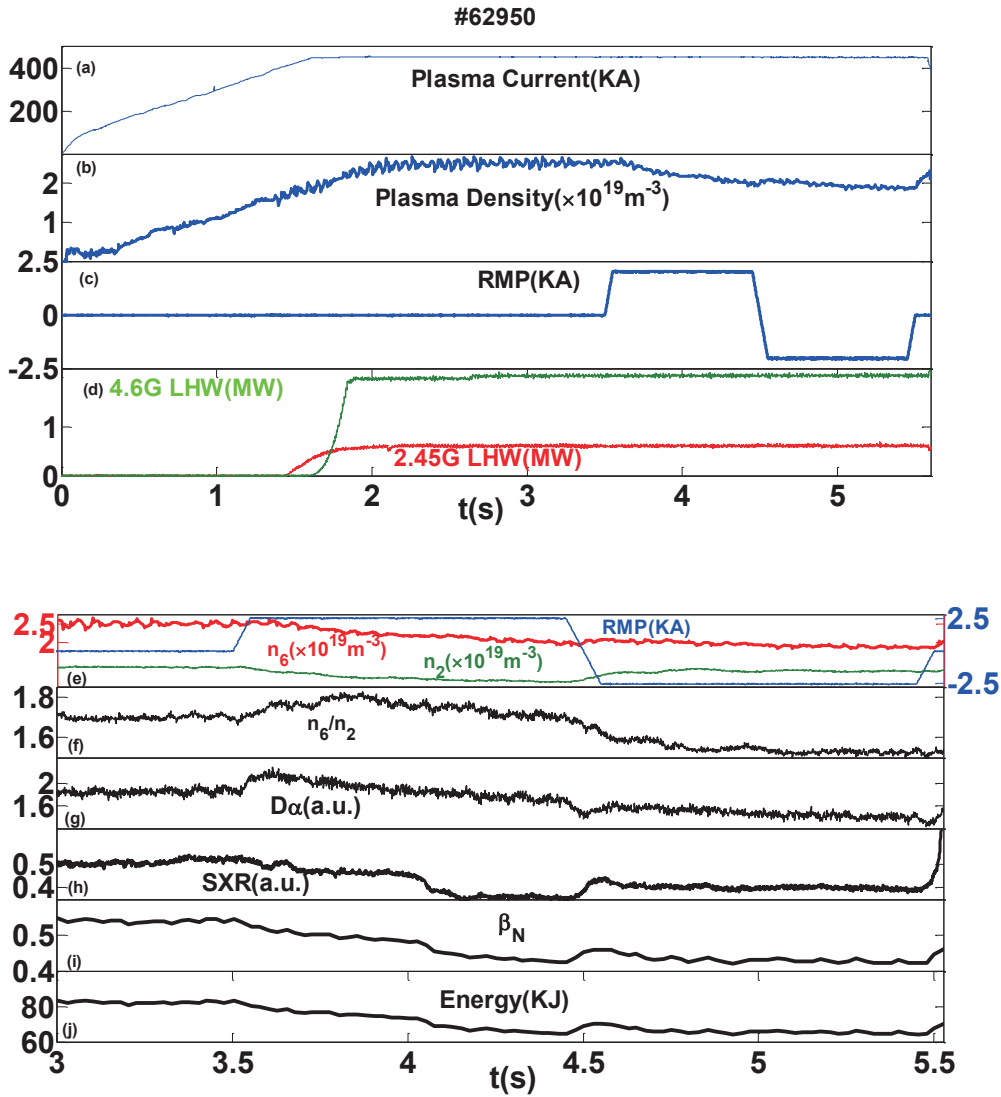
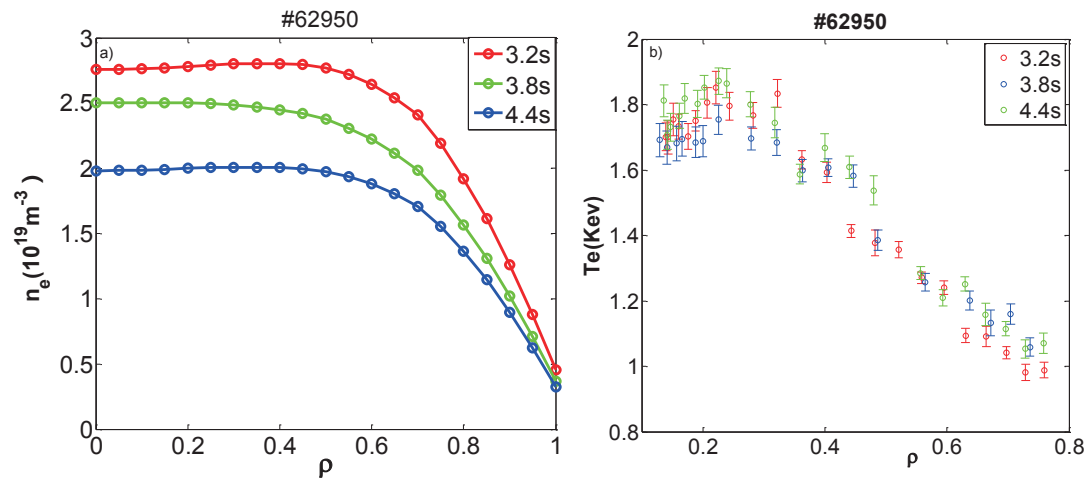


Fig.7 Time evolution of RMP($n=1$) pump-out (#55276). The data from the top to the bottom are plasma current (a), line averaged density (b), RMP current (c), injected LHW power (d), and short time window of central and edge electron density and RMP current (e), density peaking factor (f), intensity of $D\alpha$ emission (g), soft X-ray (h), normalized beta (i) and plasma stored energy (j).



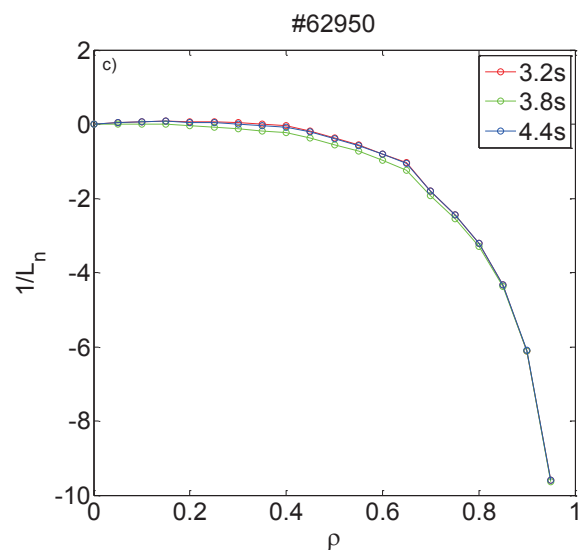


Fig.8 a) Electron density profile, b) temperature profile and c) inversed electron density gradient length $1/L_n$ at 3.2s (red marks), 3.8s (green marks), 4.4s (blue marks).

4. The statistics result of density pump-out

Quantities of shots with electron density pump-out were observed under specified conditions of heating method or magnetic perturbations. Nearly all of the shots with density pump-out are in L-mode with low density of $1.5\text{-}3.5 \times 10^{19} \text{ m}^{-3}$. As is shown in Fig.9, the relative peaking, defined as the ratio of the central (n_0) to the peripheral (n_2) chord of POINT signal, and normalized to the value during ohmic heating phase, decreased when some heating method applied, which shows strong density pump-out effect. This effect occurs at intermediate densities ($n_0 \sim 4 \times 10^{19} \text{ m}^{-2}$), but there are few data available in this domain, and in L-mode no data can be obtained at larger densities. In AUG, the H-mode with higher densities shows a small but still significant pump-out at the lowest densities ($n_e < 4.5$), a very well documented and reproducible absence of pump-out at intermediate densities ($4.5 < n_e < 6.5$), while a small effect of pump-out appears again at high densities ($n_e > 6.5$) [15].

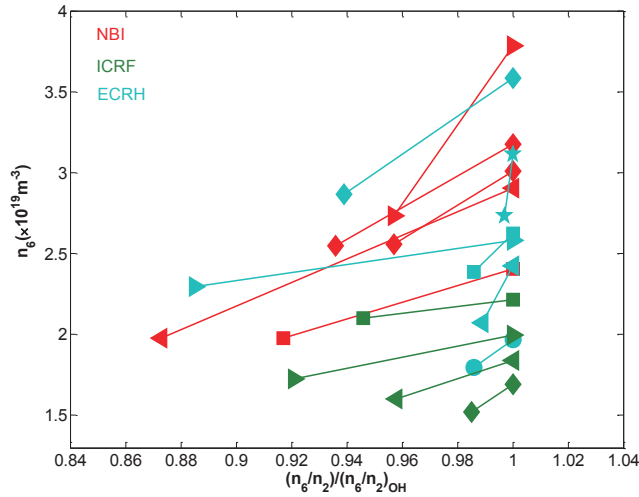


Fig.9 Line-averaged density as a function of relative peaking in L-mode

Fig.10 chooses two current platforms to study the relation between line-averaged density with the normalized line-averaged density drop. Obviously, larger densities has stronger density pump-out.

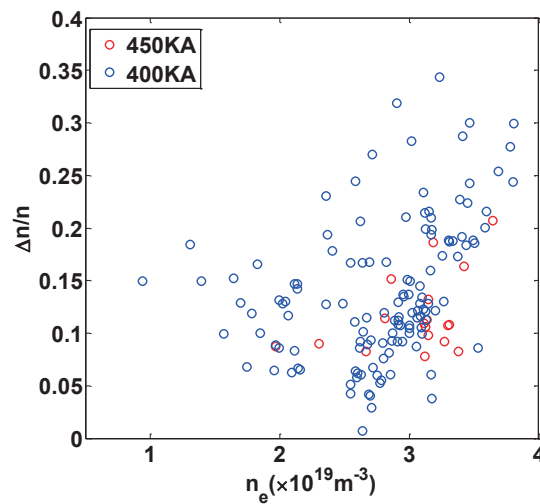


Fig.10 Relative density drop as a function of line-averaged density

Most of the shots with obvious density pump-out were caused by application of NBI and ICRF. As shown in Fig.11, all of the shots with density pump-out caused by ICRF and NBI were plotted. Fig.11(a) shows if the shots have lower density, the density pump-out become weaker with the increase of ICRF power. In contrary, this phenomenon gets more obviously. Fig.11(b) shows the relative density drops less with the NBI power increase.

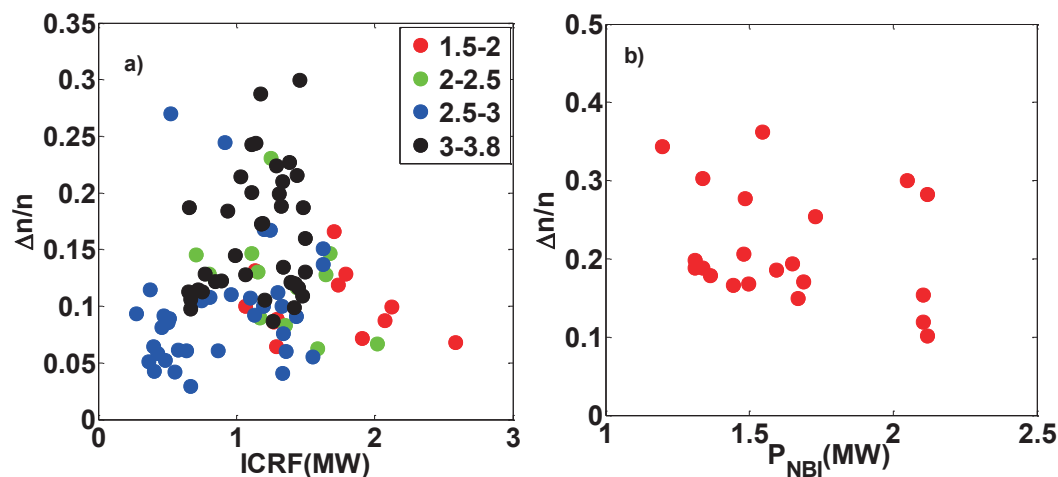


Fig.11 Relative density drop versus the power of ICRF (a) and NBI (b)

5. Summary and discussion

Density pump-out caused by ICRF, NBI and ECRH. When these heating method used, the line-averaged density decreased and density peaking also dropped. Density profile became flattening because the particle in the plasma core was expelled to the edge. Meanwhile, the electron temperature measured by Thomson Scattering increased apparently especially in the core due to the effective heating.

RMP is an effective way to control ELMs and it is responsible for the particle loss unavoidably, especially in the plasma edge. So the density peaking increased when the density dropped just because particle in the edge lost more than in the core.

The statistical data gives the relation between the relative density change and density or the heating power. This change went up with the increase of line-averaged density and dropped with the increase of NBI power. But lower density has weaker density pump-out and higher density have stronger pump-out with the increase of ICRF power.

It is difficult to explain this phenomenon because of uncertainties of recycling coefficients and neutral density profiles and, as a result, the underlying physical processes are still not understood. Even though, several explanations have been proposed in past years. Among the proposed explanations for density pump-out, one is based on neoclassical outward thermodiffusion, involving locally trapped particles in the presence of $m = n = 1$ MHD modes. The presence of MHD activity may be responsible for the observed striking difference between the peaking obeying the general scaling and peaking in discharges with pump-out^[10]. Another result shows the

central electron density pump-out is due both to the decrease of the Ware pinch (caused by the decrease of electric field) and to an increase of the diffusion coefficient. Besides, simulations of the behavior of the electron density during ECRH showed that the observed central electron density pump-out could be explained by the combined effect of a decrease of the collisional inward ('Ware') pinch and an increase of the diffusivity in TFR [11]. In TEXT, the self-consistent electric fields in the region near the isolated island chains may explain the observed density pump-out and thus, $E \times B$ convection maybe responsible for the enhanced particle transport^[9]. On EAST, the conceivable mechanism is MHD activity, which can be seen from the time evolution of dB/dt measured by mirnov coils, caused by ICRF application, as shown in Fig.5(h). Also, heating can make the impurity in the edge raised up and the core impurity didn't drop from the time evolution of density pump-out induced by ICRF, ECRH and NBI in L mode plasma, which indicates that no obviously impurity elimination effect exist in L mode plasma. Thus the particles lost in the core is mainly deuterium. The density pump-out and hence the impurities pump-out after using the ECRH, ICRF etc. will be focused on in the next step. The confinement evaluation after using RMP in ELMs H-mode plasma will be another key issue of study on density pump-out in near future.

6. Acknowledgments

This work is supported by the National Magnetic Confinement Fusion Program of China (Nos.2012GB101002 and 2014GB106002), and the National Nature Science Foundation of China (Nos.11375237 and 11105184). Also, the author appreciate the help from A3 foundation 11261140328.

REFERENCES

- [1] Liang Y, Koslowski H R, Thomas P R, et al. 2007, Physical Review Letters, 98: 265004
- [2] Pietrzyk Z A, Pochelon A, BehnR, et al. 1993, Nuclear Fusion, 33: 197
- [3] Mordijck S, Moyer R A, Evans T E, et al. 2009, Journal of Nuclear Materials, 390-391: 299
- [4] Schmitz O, Coenen J W, Frerichs H, et al. 2009, Journal of Nuclear Materials, 390-391: 330
- [5] Erckmann V, Gasparino U. 1994, Plasma Physics Control. Fusion, 36: 1869
- [6] Bécoulet M, Colas L, Pécoul S, et al. 2002, Physics of Plasmas, 9: 2619

- [7] Tamain P, Kirk1 A, Nardon E, et al. 2010, Plasma Physics Control. Fusion, 52: 075017
- [8] Idei H, Kubo S, Sanuki H, et al. 1995, Fusion Engineering and Design, 26: 167
- [9] Mccool S C, Wootton A J, Kotschenreuther M, et al. 1990, Nuclear Fusion, 30: 167
- [10] Weisen H, Furno I, and TCV Team. 2001, Nuclear Fusion, 41: 1230
- [11] TFR Group. 1988, Nuclear Fusion, 28: 1995
- [12] Zhang Xinjun, Zhao Yanping, WanBaonian, et al. 2012, Nuclear Fusion, 52: 032002
- [13] Shen Jie, Jie Yinxian, Liu Haiqing, et al. 2014, Fusion Eng. Des., 88: 2830
- [14] Liu Haiqing, Jie Yinxian, Ding Weixing, et al. 2014, Rev. Sci. Instrum., 85: 11D405
- [15] Angioni C, Peeters A G, Garbet X, et al. 2004, Nuclear Fusion, 44: 827

Cleaning of first mirror surface of Charge Exchange Recombination Spectroscopy Diagnostics of EAST using radio frequency plasma

J. Peng^{1,2}, J. L. Chen¹, R. Yan¹, Y. Y. Li¹, X. H. Y²

¹ Institute of Plasma Physics, Chinese Academy of Sciences, Hefei 230031, China

² University of Science and Technology of China, Hefei 230029, P. R. China

Abstract

Re-deposition of impurities eroded from the plasma facing components is a serious threat to the reflectance performance of the first mirrors (FMs) used for the optical diagnostic systems in ITER. In EAST, the reflectivity of FM of charge exchange recombination system (CXRS) dramatically decreased down to <14% after two experiment campaigns in 2015 due to the deposits on FM surface, degrading the intensity of the signal of this diagnostic system to an unacceptably low level. To remove the deposits and to recover the reflectivity of FM, radio frequency plasma cleaning has been conducted in the laboratory. After optimizing cleaning parameters through a series of cleaning tests, the real FM was cleaned by argon plasma with self-bias of -200V, the gas pressure of 0.5Pa during exposure for 168 hours. The complete removal of contamination was observed and the mirror surface became metal luster. Meanwhile, the specular reflectivity was partially recovered to > 86% of its initial value at 532nm. Under the cleaning parameters in the experiment, it gives a positive result for the uniformity of cleaning and sputtering damage due to excessive cleaning by cleaning the only polished FM samples.

1. Introduction

Most optical diagnostic systems in ITER will be used metallic mirrors which are also called first mirrors (FM) to guide light path and view the burning plasma. In the harsh environment, there are main competitive effects—erosion and re-deposition will change the surface structure of FMs, degrading the reflectivity performance[1]. Erosion from the charge exchange atoms could be mitigated significantly by manufacturing appropriate FM materials of those constructive plasma facing components (PFCs) which are bombarded most dramatically by the energetic plasma[2].

However, re-deposition of impurities eroded from the PFCs is still a devastating threat, impairing the intensity of signal and even distorting the reflective spectra due to the interference effect of the contaminant layers. It is reported that the even extremely thin (10 nm) and transparent deposits on FM are intolerable[3].

In Experimental Advanced Superconducting Tokamak (EAST), the reflective mirrors of some optical diagnostics are suffering from damaging deposition[4]. The main chemical compositions of the deposits consist of Lithium, carbon, oxygen. Li comes from the wall conditioning elements and is the maximum content of the deposits. C is from the re-deposition of the eroded graphite of lower divertor. Similarly, the Charge Exchange Recombination Spectroscopy (CXRS) Diagnostics is under threat of serious deposition. The schematic diagram of CXRS is shown in Fig.1. The poloidal CXRS locates at the A port. Two mirrors symmetrically installed at the distance of 960 mm are protected by a mechanical shutter. The shutter keeps shut during the Glow Discharge Cleaning (GDC) as well as wall conditioning to avoid the reduction of the transmission of the viewport[5]. The reflectivity of FM of charge exchange recombination system (CXRS) dramatically decreased down to <14% at the wavelength of 532 nm after two experiment campaigns in 2015 due to the deposits on FM surface, degrading the intensity of the signal of this diagnostic system to an unacceptably low level. The effective cleaning technique has to be developed to remove the deposits and to recover the reflectivity of FM. Radio frequency plasma

cleaning is the most promising method and has been investigating over the world[6].

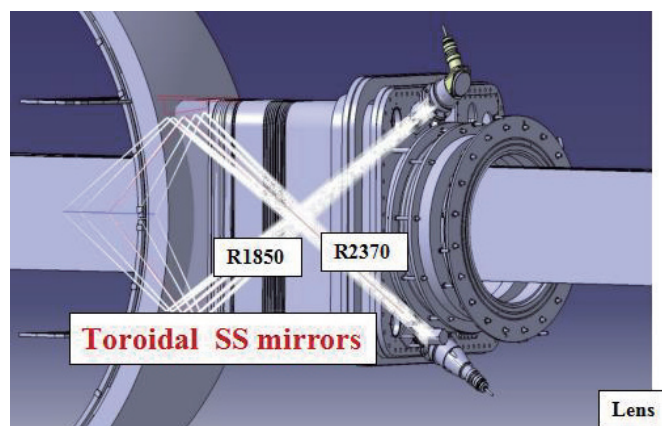


Fig. 1 The schematic diagram of CXRS

2. Experimental

2.1 Exposure of CXRS first mirror in the EAST tokamak

The CXRS first mirror is made of SS316L ($C \leq 0.03\%$, $Si \leq 1.00\%$, $Mn \leq 2.0\%$, $P \leq 0.035\%$, $S \leq 0.03\%$, $Ni: 12.0\%-15.0\%$, $Cr: 20.0\%-20.0\%$, $Mo: 2.0\%-3.0\%$) and has the dimension of $303 \times 86 \times 76 \text{ mm}^3$ with a small curvature of 0.008 mm^{-1} . FM was exposed in 2015 EAST experiment campaign with the protection of shutter from the wall conditioning under the deposition dominated conditions. In 2015, FM was exposed for 3977 shots with the current in the range 220-250KA, the electron density of $(2 - 3) \times 10^{19} \text{ m}^{-3}$.

2.2 Characterization of the optical and morphology properties

During the coating and cleaning procedure, the optical and morphology performance of mirrors were characterized with different methods. The evolution of total and diffuse reflectivity were monitored by an UV-VIS-NIR UV 3600-MPC 3100 spectrophotometer under the incidence angle of 8° for the total reflectivity and 0° for the diffuse reflectivity, respectively, in the wavelength range of 300-1200nm which was the most affected by coating and cleaning treatment [13]. The ellipsometer (J.A.woollam Co.Inc.M-2000U) was used to get the thickness of carbon film with the wavelength range of 264-1686nm for incident angle of 70° . Field emission scanning electron microscopy (FE-SEM) and energy dispersive spectroscopy (EDS) were carried on a Σ IGMA to detect the morphology performance of mirrors. The penetration depth of XPS was 6-10nm. The surface roughness of mirror surface before and after cleaning was detected by Innova Atomic Force Microscope (AFM).

3. Results and discussion

After exposure, the FM surface was covered by seriously non-uniform colorful deposits and some parts of them have been peeled off. To confirm the chemical composition of the deposits on the CXRS FM, XPS measurements were made. However, it is well known that FM is too large to be directly detected by XPS. In order to know qualitatively the elements of the contaminants, a small percentage of CXRS shutter was cut down as test sample. The main elements of the deposits were C, O. When the CXRS FM underwent cleaning treatment, the self bias was decreased to negative 200V maintaining other cleaning parameters unchanged. It is because there is a little difference between the deposits formed in the Tokamak and laboratory environment. The surface of the former looked like more loose

and porous, but the latter was relatively more even.

After cleaning of 168 hours, most deposits on FM were deposited and the surface developed a metallic luster again, but there still existed small amounts of film from visual inspection. Taking count into damage of FM due to excessive sputtering, we stopped the cleaning treatment.

The specular reflectivity of FM before and after cleaning was performed using He-Ne laser in the wavelength of 532nm. To reflect the value of reflectivity on such a big mirror as accurately as possible, the measurement points were gathered as the Fig.2. Square The hollow and solid red diamond, blue circle and green down triangle represent the upper, middle and lower location of FM, respectively. The upper, middle and lower were set as the location where FM was installed. From the evolution of the reflectivity which was given in Fig.3, it was found that the reflectivity of the whole exposed FM degraded dramatically and was below 14% at 532nm. After cleaning, the specular reflectivity was partially recovered higher than 86% of its initial value. However, there was still cleaning inhomogeneity on the large mirror in the identical location along the longitude.

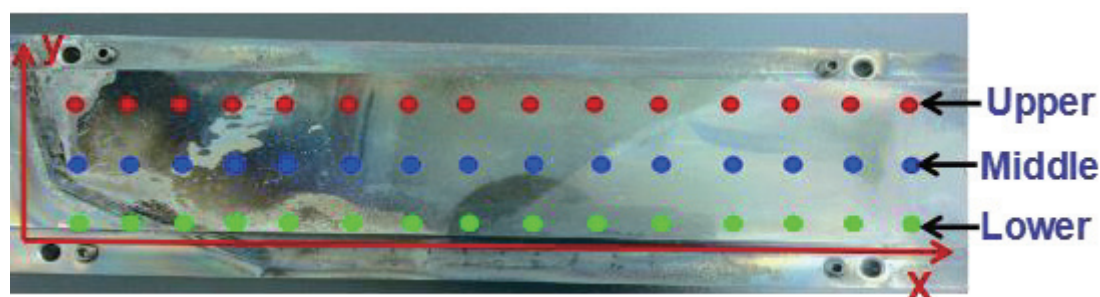


Fig.2 The measurement points of reflectivity in CXRS FM

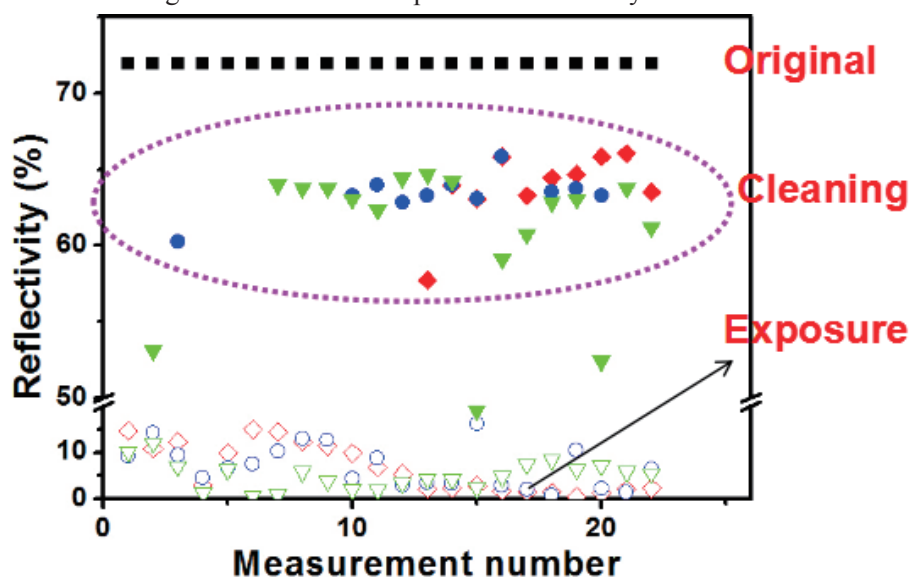


Fig.3 The evolution of the reflectivity of CXRS FM before and after cleaning

The cleaning uniformity of FM surface is significantly important, directly affecting the morphology property, subsequently degrading the reflectivity. It is impossible to calculate the cleaning efficiency due to the severe non-uniformity of the deposits. To evaluate the cleaning uniformity, the only polished SS mirror samples with the dimensions of 10mm10mm1mm were

embedded into the different location of the CXRS FM-like samples we manufactured as the size of the real FM, we can see that in Fig. 4. Due to the completely symmetric structure, the generated plasma on the surface will be symmetric, hence the middle and edge position are chosen for investigation. After plasma treatment with the same parameters with the CXRS FM cleaning, the roughness of the samples on the middle and edge position will be compared. Fig.5 gives the results of roughness for the different sputtering time. The roughness at the same position will grow with the increase of sputtering time. Because the longer the sputtering time, the larger the surface structure of samples. The roughness almost keeps stable at different position under the identical sputtering time.

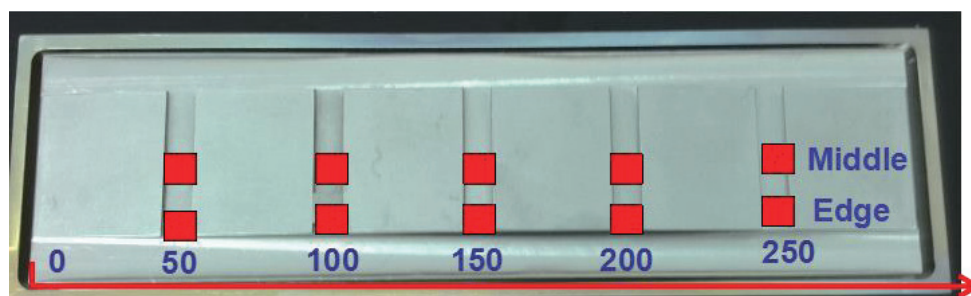


Fig.4 The distribution of FM samples

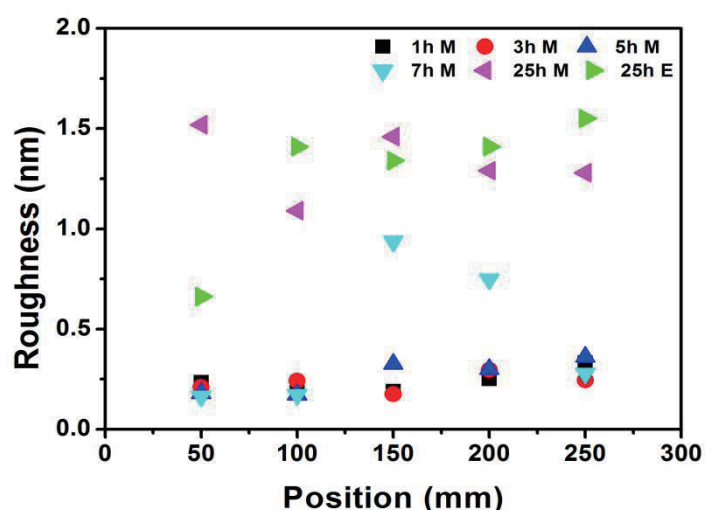


Fig. 5 The roughness in the different position

It is noted that the roughness increases slightly with the increase of cleaning time and keeps an low value. Even though the surface of the samples are sputtering for 25 hours, the roughness is only less than 2 nm for 25h. It means that excessive sputtering has little influence on surface damage. As we know, in our experiment, the cleaning uniformity mainly results from the inhomogeneous deposits--that is to say, some areas of FM surface are supposed to be sputtered excessively when the deposits of other areas have not been removed completely. It is expected that excessive sputtering is inevitable.

The change of specular reflectivity due to the roughness of surface is shown in Table 1. The reflectivity keeps almost stable, despite of different position and time. The excessive sputtering did not affect the specular reflectivity significantly.

Table 1 The change of reflectivity at different positions and different cleaning time

Cleaning time /h	Location	Position /mm				
		50	100	150	200	250
Original	-	73.89				
1	M	69.49	68.97	68.97	69.46	69.95
3	M	69.46	68.97	68.97	69.46	69.95
5	M	68.47	68.47	69.95	68.47	69.46
7	M	69.46	67.98	68.97	69.95	70.44
25	M	68.47	68.97	69.46	69.46	69.95
25	E	69.46	68.97	69.95	68.97	69.46

4. Conclusion

Radio frequency plasma cleaning has been conducted in the laboratory to remove the deposits with the thickness of about a few micrometers on the CXRS mirrors. After cleaning for 168 hours with the gas pressure of 0.5Pa, the self-bias of negative 200 V, the contamination layer was successfully removed and the specular reflectivity was partially recovered to > 86% of its initial value at 532nm. By cleaning the only polished FM samples under the same cleaning parameters in the experiment at different position and for different cleaning time to investigate the cleaning uniformity and sputtering damage, respectively, it was found that sputtering is inevitable for samples and cleaning is positively uniformity.

Acknowledgements

This work has been supported by the National Magnetic Confinement Fusion Science Program of China under contract Nos 2013GB107004 as well as 2013GB105003, the National Natural Science Foundation of China under Contract Nos 11475218, 11505321 and 11375010.

References

- [1] A. Litnovsky¹, V. Voitsenya², T. Sugie, Nucl. Fusion 49 (2009) 075014 (8pp)
- [2] V. Voitsenya, A.E. Costley, V. Bandourko, et al., Rev. Sci. Instrum. 72 (2001) 475
- [3] I. Arkhipov, A. Gorodetsky, R. Zalavutdinov, Journal of Nuclear Materials 415 (2011) S1210-S1213
- [4] T. Lan, S.X. Wang, H.Q. Liu. 17th International Symposium on Laser-Aided Plasma Diagnostics,
- [5] H. Y. Guo, J. Li, B. N. Wan, PHYSICS OF PLASMAS 21, 056107 (2014)
- [6] Moser, L, Steiner, R, Leipold, F, et al., Journal of Nuclear Materials 463 (2015) 940–943

Current status and data analysis of BES in EAST

H.J, Wang^{1,2}, Y, Yu¹, R, Chen², B, Lyu², Y.F, Wu¹, B.D, Yuan¹, S.Y, Feng^{1,2}, Y.M, Hou^{1,2}, Y.J, Shi¹, M.Y, Ye¹, B.N, Wan²

¹ School of Nuclear Science and Technology, University of Science and Technology of China, Hefei, Anhui, China

² Institute of Plasma Physics Chinese Academy of Sciences, Hefei, Anhui, China

ABSTRACT: Beam Emission Spectroscopy (BES [1, 2]) diagnostic based on neutral beam injection (NBI) has recently been developed in EAST TOKAMAK. Three cavity interference filter with a center frequency of 659.33nm and a bandwidth of 1.59nm is used to eliminate the interference $D\alpha$ signal and carbon impurities radiation. This BES system diagnoses the plasma density fluctuation with a sample rate of 1MHz and a spatial resolution of 1-3cm. It can diagnose a rectangular area in one shot, with a radial length of 20cm and a vertical length of 10cm. In the plasma cross section, which is movable from the core plasma to the edge of low field side of EAST by means of changing the angle of the first mirror. Filter test are also presented. Data in the recent experiments of BES show the great change of density fluctuations in the L-H transition.

Keywords: parameters and structures, filter, L-H transition

1. Introduction

Tokamak plasma physics achieved a lot of progress, but from realizing the controllable fusion in tokamak still has a long way to go. Many theory problems are there unknown. 2D Plasma density fluctuation is a very important parameter which can be used to study the formation of ITB, sheer flows, pedestal physics (3) and so on in tokamak fusion plasma physics. BES diagnostic can get high spatial resolution 2D plasma fluctuation efficiently which has built in EAST tokamak successfully.

2. Parameters and structures of BES

2.1 Basic parameters

BES diagnostic is used to detect red Doppler shifted $D\alpha$ $\lambda = 659\text{nm}$ filtered from background $D\alpha$ $\lambda = 656.1\text{nm}$ from the interaction place between NBI and plasma. NBI (80keV and 40A) tangential one of the two NBI in EAST port A is best to the BES system. Temporal and spatial resolution is 1~3cm according to the view sight with sampling frequency 2MHz, this is a very high spatial resolution. And the most important part is the detection channels and area, 128 APD detection channels with 16(radial)*8(poloidal) to get a 2D area in plasma cross section. Range of view sight is from core to the edge of plasma $\rho = 0.33\text{--}1.2$.

2.2 Control system of BES diagnostics

The control system contains three part: control computer, control box, BES observation optics. Fig.1 Control computer is the dominant control system located in EAST server room. It can control all the other system when taking experiment.

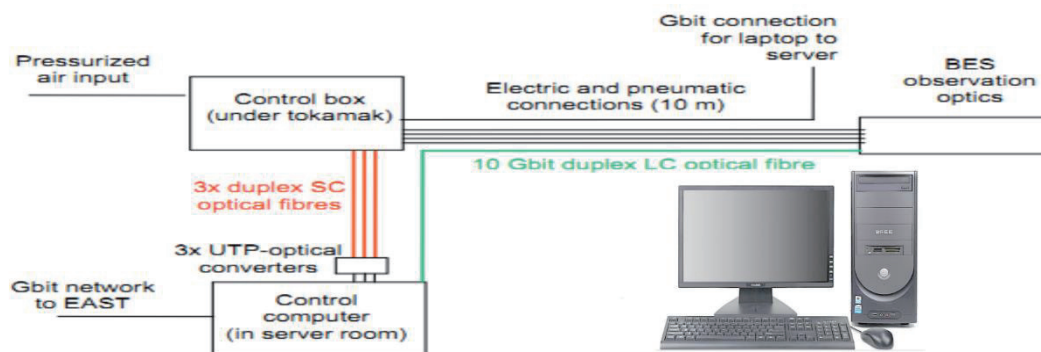


Figure 1. BES mainly control system

2.3 optical structure design of BES diagnostics

The structure has two branches, one is APD branch and the other is CMOS branch, Fig.2. APD branch detects BES signal. CMOS branch is used for space calibration and takes photos of EAST vacuum wall as a camera. The two branches share the same optical light path by first mirror which has a hole in the center. Light passes through the hole to the CMOS camera and reflects to the ADP branch.

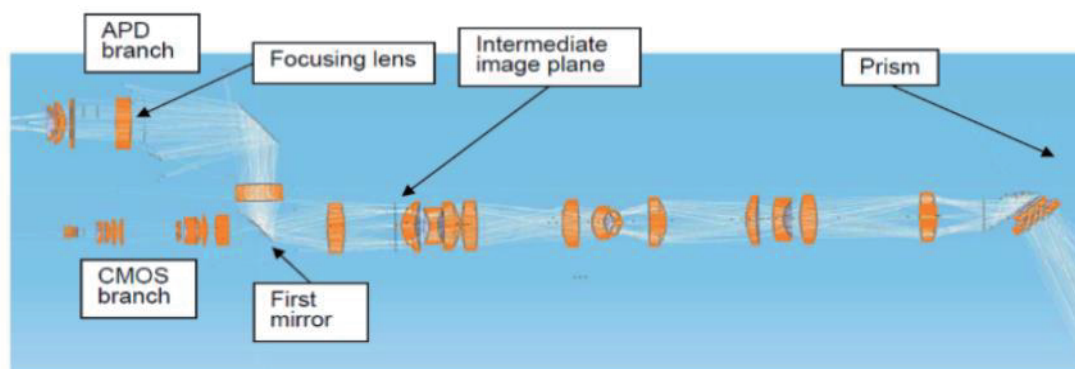


Figure 2. BES optical structure and the material objects of two branches

3. First result

These results get from EAST 2015-2016 spring experiment plan. BES system works when NBI injected. We take signal from low NBI to high NBI in different EAST discharge conditions. LHW, ICRF, ECRH, NBI are all EAST auxiliary heating methods. Here we give some basic results in system check and 2D plasma density fluctuation in L-H transition.

3.1 Filter filtration check

Filter is the most important element in the whole optical structure which is used to get Doppler shifted D_a signal from a broad band spectrum when tangential NBI injected. It's efficiency directly relates to signal to noise ratio (SNR). As NBI injection parameter (voltage and current) is from low to high condition. The BES system takes all the shot whenever NBI injected. Here we give two filter filtration check results in low and high NBI condition respectively.

3.1.1 Filter filtration in low NBI

Here shows the result in low NBI with voltage 52keV. The spectrum gets by a spectrograph. Signal light passes through the filter and guide to a spectrograph by an optical fiber which installed just beside the APD detection channels. We choose two shot with the same NBI parameters. Firstly, take off the filter from the light path in one shot and then turn in the filter in another shot.

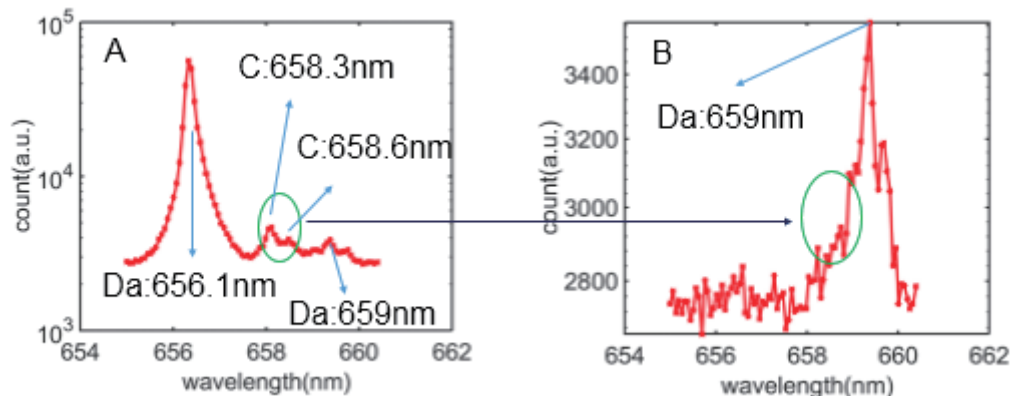


Figure 3. A and B are got from a spectrograph without and with filter respectively in a low NBI with 52keV.

In the Fig.3, A is without filter and B has a filter. Background Da, two carbon spectrum and BES interested signal are all marked out in A and B respectively. Green circle is the same wavelength part which contains the carbon spectrum. From the result, it can clearly see that BES signal is filter out efficiently.

3.1.2 Filter filtration in high NBI

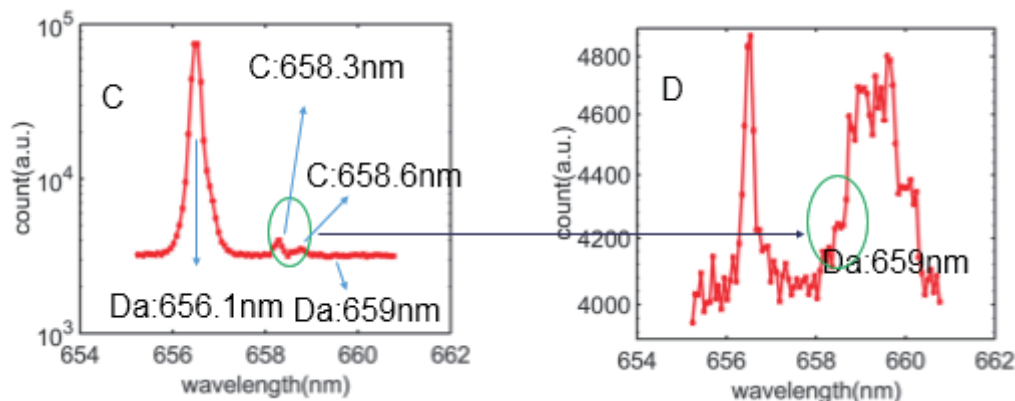


Figure 4. C and D are got from a spectrograph without and with filter respectively in a relative higher NBI with 65keV.

Do the same way in 2.1.1 in a high NBI parameter with voltage 65keV (see Fig. 4). From the result, that filter don't work well which background Da is comparable to the interested signal. This is because when NBI rises to a high voltage condition, that background Da rises sharply at the same time which surpasses the filter filtration capability. So in the next time, the filter will be replaced by a new one.

3.2 2D plasma fluctuation in L-H transition

This is a briefly density fluctuation in L-H transition detected by BES system. It can easily find out when L-H happened from the result.

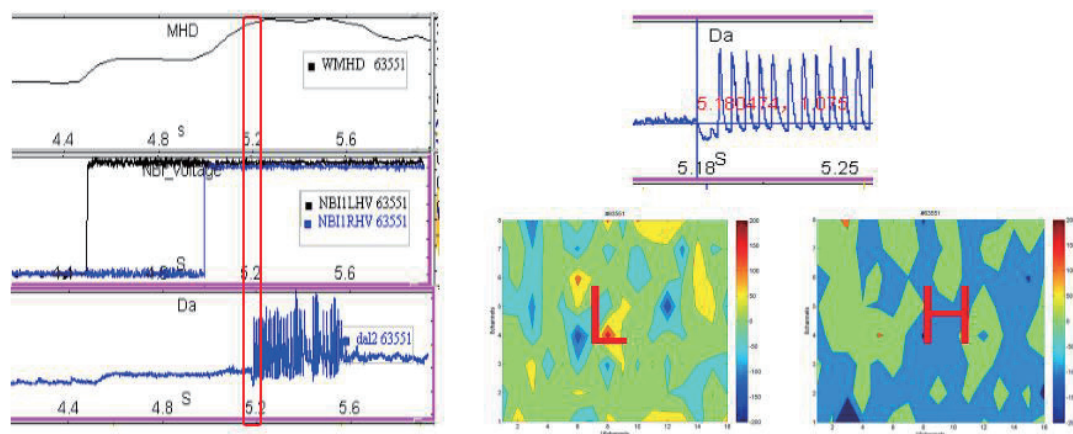


Figure 5. Left picture shows the EAST discharge condition. MHD, NBI, Da signal from top to down respectively in shot #63551. Right top picture is a fine structure of Da signal in the left one which marked with a red rectangle. From the last two pictures, it can easily find out that L-H happened at 5.179925—5.179926s

This result is from shot #63551(see Fig. 5). Tangential NBI is injected at 4.5s and another one injected at 5s. The MHD increases sharply when NBI applied. From the Da signal, when both NBI injected, Elmy appears obviously and L-H transition happens. In the last two plasma density fluctuation pictures, it can easily figure out that L-H transition happens at 5.179925-5.179926s.

4. Conclusion

BES has been build in EAST successfully. Some calibration has been done. 2D density fluctuation can clearly show the L-H transition.

Acknowledgements

This work was supported by the National Magnetic Confinement Fusion Energy Research Project (Grant No.2015GB120002, 2012GB101001, 2013GB107000), the National Natural Science Foundation of China (Grant No.11375053, 11535013), and the Innovative Program of Development Foundation of Hefei Center for Physical Science and Technology (Grant No. 2014FXCX003).

References

- [1]M. Lampert, M. J. Choi, D. Guszejnov, I. Kiss, A. Kovacsik, Y. U. Nam, H. Park, G. I. Pokol, G. Veres, S. Zoletnik, in *39th EPS Conference on Plasma Physics 2012, EPS 2012 and the 16th International Congress on Plasma Physics, July 2, 2012 - July 6, 2012*. (European Physical Society (EPS), Stockholm, Sweden, 2012), vol. 1, pp. 393-396.
- [2]G. McKee, R. Ashley, R. Durst, R. Fonck, M. Jakubowski, K. Tritz, K. Burrell, C. Greenfield, J. Robinson, Erratum: 'The beam emission spectroscopy diagnostic on the DIII-D tokamak' [Rev. Sci. Instrum. 70, 913 (1999)]. *Review of Scientific Instruments* **70**, 2179-2179 (1999)10.1063/1.1149732).

[3]P. B. Snyder, K. H. Burrell, H. R. Wilson, M. S. Chu, M. E. Fenstermacher, A. W. Leonard, R. A. Moyer, T. H. Osborne, M. Umansky, W. P. West, X. Q. Xu, Stability and dynamics of the edge pedestal in the low collisionality regime: physics mechanisms for steady-state ELM-free operation. *Nucl. Fusion* **47**, 961-968 (2007); published online EpubAug (10.1088/0029-5515/47/8/030).

Investigating of the heating transport models in DIII-D ITER ramp up experiments

Li Liu^a, Yong Guo^b, Vincent Chan^a, Shifeng Mao^a, Yifeng Wang^a, Chengkang Pan^b,
Zhengping Luo^b, Minyou Ye^{a*}

^aSchool of Nuclear Science and Technology, University of Science and Technology of China, Hefei, China

^bInstitute of Plasma Physics, Chinese Academy of Sciences, No.350 Shushanhu Road, Hefei, China

Abstract

The confidence in ramp up scenario design of the China Fusion Engineering Test Reactor (CFETR) can be significantly enhanced using validated transport models to predict the current profile and temperature profile. In the Tokamak Simulation Code (TSC), two semi-empirical energy transport models (the Coppi-Tang and BGB model) and three theory-based models (the GLF23, MMM95 and CDBM model) are validated on several CFETR relevant ramp up discharges, including three DIII-D ITER-like ramp up discharges. The plasma shape is controlled to be in good agreement with experiments using the RZIP control system. For the ohmic heating phase of DIII-D discharges (L-mode), the MMM95 and BGB model overestimate the ℓ_i within a maximum discrepancy of 12.56%, while the GLF23, Coppi-Tang and CDBM models underestimate the ℓ_i within a maximum discrepancy of -3.94%. For NBI heating phase of DIII-D discharges (H-mode), the experimental pedestal, NBI heating information and the Sauter current model are used in simulation. Including the influence of toroidal rotation during the NBI heating phase, the CDBM and GLF23 model can give good predictions for both the electron and ion temperature profiles, while the BGB and MMM95 model without rotation factor can only give good predictions for the electron temperature and underestimate β_p . Simulations with CDBM model yield the smallest discrepancy for ℓ_i and β_p . Comparing all models using standardized metrics, the Coppi-Tang model and CDBM model seem to be the favorable choices for the CFETR ramp up design in L- and H-mode, respectively.

1. Introduction

Scenario design of future tokamaks involves research to predict the plasma performance and optimize the operation space subject to available device capabilities, as well as to improve on the conceptual engineering design. The China Fusion Engineering Test Reactor (CFETR) [1] is performing ramp up scenario design to resolve critical physics and engineering design issues, such as controlling vertical instability, β_p limits, and ensuring the PF coils' ability to provide enough flux relative to predicted consumption. The challenge of future tokamak ramp up scenario design is to develop an interactive design and control platform for physics and engineering, which couples the poloidal field system controller with passive structures, a free boundary equilibrium solver, and the current and temperature profile evolution dynamics. All of these components are very sensitive to the energy transport models in the ramp up phase, since the current profile is directly

*Corresponding Author : Minyou Ye, Email : yemy@ustc.edu.cn

affected by the evolution of temperature profiles driven by the energy transport models. The current and temperature profiles in turn determine the plasma internal inductance ℓ_i and poloidal beta β_p , which are used to design the plasma controller. The accurate prediction of ℓ_i and β_p can improve our confidence to map out the stable operational space of different scenarios, especially with the addition of auxiliary heating in the ramp up phase. In order to develop confidence in the CFETR ramp up scenario design, several reference shots relevant to CFETR from DIII-D experiments have been studied to validate different heating and transport models during ramp up, while the plasma shape is constrained to be in good agreement with experiments. For this study we are using an equilibrium and time-dependent transport code, Tokamak Simulation Code (TSC) [2] coupled with several auxiliary heating modules.

TSC is a free-boundary axisymmetric equilibrium transport code coupled with a simplified practical control system. It computes the magnetic field evolution and plasma equilibrium on a two-dimensional rectangular grid with the circuit conditions of PF coils and passive structures. The evolution of the flux surface averaged temperature profile is solved with specified different transport models, such as the Coppi-Tang (CT) model[3], Bohm-gyroBohm (BGB) model[4], the Gyro-Landau-Fluid (GLF23) model[5], Multi-Mode Transport Model (MMM95)[6] and Current Diffusive Ballooning Mode (CDBM) model[7, 8]. The TSC code has been used not only to reproduce discharges from past experiments, such as representative discharges in TFTR [3] and EAST [9], the VDE and disruptions in ASDEX Upgrade[10], but also to predictively model the steady-state and hybrid scenarios in ITER[11-13].

In this work TSC is used to interpretatively analyze the ramp up phase of several DIII-D [14] experiments with various proposed thermal transport models. The DIII-D relevant experiments are a series of DIII-D ITER-like ramp up cases. These discharges undergo different ramp rates in current ramp up phase and neutral beam injection (NBI) heating in the rapid density ramp up phase, while the other operational parameters are set similar with ITER 15MA baseline to produce ‘ITER-like’ plasmas in the DIII-D tokamak. The DIII-D structures have been reconstructed in TSC acting as a numerical tokamak simulator. The plasma current and PF coil currents are preprogrammed in TSC for feedback control of the plasma shape and position. The temperature profiles and current profiles are evolved according to the different energy transport models, while the density and effective Z evolution are set from experimental data. The internal inductance ℓ_i and poloidal beta β_p are also obtained and comprehensively analyzed in our work. The resulting agreements of the different transport models with experiments are compared under common metrics over the entire set of experiments.

This paper is organized as follows. Section 2 presents the models we use in TSC, such as the geometry structure, the plasma control system, details of the transport models and the list of simulation assumptions. The simulation results and analyses of DIII-D ITER-like ramp up are presented in Section 3. Conclusions are given in Section 4.

2. TSC model

2.1. Geometry structure

The geometry structure of DIII-D has been built into the TSC code. The geometry model not only contains

coils connected to power supplies, like OH coils, PF coils, and internal shaping coils, but also passive structures, like vacuum vessel and passive plates, where eddy currents are induced during the plasma current ramp-up. The induced currents can influence the plasma equilibrium and change the controllability of the plasma control system, especially in an abnormal event like VDE or disruption[15].

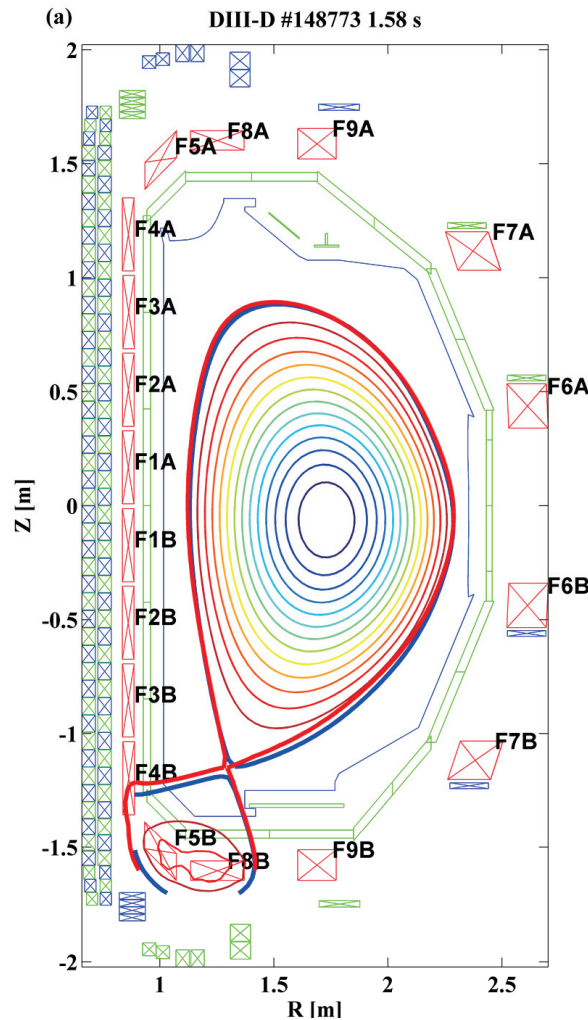


Figure 1. Geometry of DIII-D. PF coils (red boxes with inscribed ‘x’), OH coils (blue and green boxes with inscribed ‘x’), vacuum vessels and passive plates (green parallelograms) and first wall (thin blue lines) are shown. The contour line is the 2D poloidal flux distribution for DIII-D #148773 at 1.58s. The plasma shape constructed by the TSC (thick blue line) are compared with the one reconstructed by EFIT (thick red line).

The DIII-D tokamak (as shown in figure 1) is a D-shape tokamak with a significant number of active coils to shape the required flexible plasma equilibrium[14]. The toroidal field coils are not built into the TSC model, while the toroidal flux produced by TF coil is considered by setting the central magnetic field strength. The outermost ohmic heating coil system, which induces current in the plasma through transformer action, contains 122 turns electrically connected in two parallel sets (indicated by blue and green boxes) of 61 turns. The poloidal field coils, which are used to control shape and position of plasma,

consist of a set of 18 independent coils F1A-F9B (indicated by red boxes), the twelve inner coils having 58 turns and the six outer 55 turns. The vacuum vessel and passive support structures (indicated by green parallelograms) are modeled as the toroidal current filament with different equivalent resistances. The geometry of the first wall is set as limiters (indicated by blue line). The co-ordinates of all the structures are set according to the Toksys geometry data[16] of the experimental device.

2.2. Plasma control system

RZIP control consists of radial position control, vertical position control, and plasma current control. Gains in the real time algorithm are typically controlled using a rigid minimal response model applied and validated on many DIII-D and EAST experiments [17].

In the plasma current control, the preprogrammed current and feedback on the total plasma current with a Proportional Integration Derivative (PID) controller determine the PF or OH coil currents. Both the radial position control and vertical position control also use PID controller feedback on the flux difference at the two observation points. The PF feedback current is decided by

$$\sum_{i=1}^n W_{R,V}^i \cdot dI_{R,V}^i = g_P^{R,V} \cdot \psi_{o1} - \psi_{o2} + g_D^{R,V} \cdot \int \dot{\psi}_{o1} - \dot{\psi}_{o2} dt, \quad (1)$$

where $dI_{R,V}^i$ is the i th coil correction current due to the feedback of plasma radial and vertical control, $g_P^{R,V}$ and $g_D^{R,V}$ are the proportional and derivative gains of PID controller, $W_{R,V}^i$ is the weight of the i th shape control PF coil, ψ_{o1} and ψ_{o2} are the poloidal flux of the two observation points, $o1$ r_{o1}, z_{o1} and $o2$ r_{o2}, z_{o2} , respectively. To force the plasma shape evolution in agreement with experiment, the two observation points are selected near the plasma boundary and on the same poloidal flux in the reconstructed equilibrium, determined with EFIT[18] algorithm. Usually, the two observation points are set at the same radial coordinate for vertical control and the same vertical coordinate for radial control (see Table 1).

Table 1. The coordinates in the R-Z plan of observation pairs chosen for RZIP control of DIII-D #148773 discharge.

time (s)	Radial [m]		Vertical [m]	
	o1	o2	o1	o2
0.3	(1.3, 0.0)	(2.0030, 0.0)	(2.3, 0.2296)	(2.3, -0.2)
0.5	(1.3, 0.0)	(2.0727, 0.0)	(2.3, 0.1705)	(2.3, -0.2)
1.0	(1.3, 0.0)	(2.1129, 0.0)	(2.3, 0.1006)	(2.3, -0.2)
1.5	(1.3, 0.0)	(2.1331, 0.0)	(2.3, 0.1034)	(2.3, -0.2)
2.0	(1.3, 0.0)	(2.1680, 0.0)	(2.3, 0.1040)	(2.3, -0.2)
2.5	(1.3, 0.0)	(2.1889, 0.0)	(2.3, 0.1038)	(2.3, -0.2)
3.0	(1.3, 0.0)	(2.1893, 0.0)	(2.3, 0.1043)	(2.3, -0.2)
3.5	(1.3, 0.0)	(2.1897, 0.0)	(2.3, 0.1052)	(2.3, -0.2)
4.0	(1.3, 0.0)	(2.1901, 0.0)	(2.3, 0.1060)	(2.3, -0.2)

2.3. Physics models

External auxiliary heating and current drive are necessary for future tokamaks, like ITER and CFETR, to achieve fusion conditions and to sustain the plasma current for steady-state operation. In this work, the external heating sources are calculated by a variety of heating modules in ONETWO [19]. TSC, acting as a digital tokamak, provides experiment like conditions (plasma equilibrium, density profile, and ion and electron temperature profile) as input to ONETWO. In return ONETWO computes the heating and current profiles and sends these back to TSC to recalculate discharge conditions in an iterative loop. In our simulation, NUBEAM [20], an orbit following Monte Carlo code, is adopted as the neutral beam injection (NBI) source module.

Bypassing the complexity of simulating fueling and particle transport, the density evolution is set to match the density profile measured by the Thomson scattering diagnostic on DIII-D. The effective Z profile is also set to match the CER diagnostic results to omit the impurity evolution calculation. Neoclassical resistivity is used to better model the physics in the current ramp up phase. Sawtooth instability is taken into account by a time-averaged model [3]. Lastly, the bootstrap current is calculated by the Sauter bootstrap current model [21] consistent with the plasma evolution.

In this work, TSC code version 10.8 is used, where only the Coppi-Tang model, GLF23, and MMM95 are available for transport simulation. The CDBM and BGB are added into the version 10.8 in order to assess a broader spectrum of proposed transport models. It must be mentioned that toroidal rotation due to momentum injection by NBI is taken into account in the GLF23 model and CDBM model, while the other three models have no interface for toroidal rotation. These models are briefly described below.

Coppi-Tang model. The Coppi-Tang model is a semi-empirical model which has demonstrated good agreement with selected experiments on TFTR[3], JET [22], and ASDEX[23]. It has been extensively used in TSC simulations. The original adjustable parameters ($a_{121} = 0.08$ for auxiliary heating transport factor, $a_{122} = 0.4$ for ohmic heating transport factor) was used to scaling the confinement of TFTR[3]. To match the 0-D confinement predictions for ITER[24], a scale factor 2.5 is adopted to adjust the overall transport based on various studies[11, 12, 25], which matched current ramp up phases very well in DIII-D[25]. For JET discharges, simulations without overall transport adjustment strongly overestimated the temperature profiles[22, 26]. In our work, the original adjustable parameters in TFTR with overall transport adjustment are used in the Coppi-Tang model for L-mode. And for H-mode in the NBI heating phase, a smaller auxiliary heating transport coefficient ($a_{121} = 0.05$) is used to match the improved experimental confinement driven by the strong rotation.

GLF23 model. The Gyro-Landau-Fluid model (GLF23) is a quasilinear transport model based on the Gyro-Landau-Fluid equations, fitted to linear gyro-kinetic stability and with coefficients originally normalized using nonlinear gyro-Landau-fluid turbulence simulations [5]. The GLF23 model includes ITG/TEM turbulence at low wavenumber and ETG modes at high wavenumber with $E \times B$ shear suppression. In the following simulation, the version of GLF23 model is the retuned one, which is renormalized to the full gyro-kinetic turbulence simulation results. The influences of $E \times B$ shear and α stabilization are also considered in the simulation. Mindful of the limitation of the GLF23 model when

extended out to the separatrix for L-mode plasmas, in this work, the model is designed to apply either to the pedestal for H-mode or with the addition of a constant diffusion coefficient of $4 \text{ m}^2\text{s}^{-1}$ in the plasma edge ($0.85 \leq \rho \leq 1$) for L-mode. The same constant diffusion coefficient is also used in the MMM95 model and CDBM model.

MMM95 model. The Multi-Mode transport model (MMM95) [6] is a simplified mixed-physics model which consists of a series of theory transport models, such as (i) the Weiland model that calculates the ITG and ETG and usually provides the largest input to the transport, (ii) the Guzdar-Drake model that calculates the drift-resistance ballooning model, and (iii) the contributions of neoclassical transport and kinetic ballooning effects.

CDBM model. The current diffusive ballooning mode model (CDBM) [13], is a self-sustained turbulence model induced by current diffusivity constructed by solving the eigenvalue problem for the ballooning mode and the interchange mode. The thermal transport is considered as the sum of the neoclassical transport and the turbulence transport. The turbulent thermal diffusivity is expressed as:

$$\chi_{CDBM} = CF \hat{s}, \alpha F_k F_E \alpha^{3/2} \frac{c^2 v_A}{w_{pe}^2 qR} \quad (2)$$

Where $C = 12$ is the constant fitting parameter decided by comparing the energy confinement time with the level of ITER-89P L-model scaling law [8]. And $s = r q^{-1} dq/dr$ is the magnetic shear, $\alpha = -q^2 R d\beta/dr$ the normalized pressure gradient, $k = -r/R (1-1/q^2)$ the magnetic curvature, c the speed of light, w_{pe} the electron plasma frequency, and v_A the toroidal Alfvén velocity. The factor $F \hat{s}, \alpha$ reduces the heat transport due to weak or negative magnetic shear and the Shafranov shift, which is extremely important in the high ramp rate ramp up case because of the hollow or nearly hollow current profile. The term F_k is the correction for plasma shape. The term $F_E = 1 + G s, \alpha \cdot w_E^2^{-1}$ is the reduction by $E \times B$ rotation shear, which contributes significantly to the transport reduction when there is a strong toroidal rotation induced by NBI in existing tokamaks.

BGB model. The Mixed Bohm/gyro-Bohm model (BGB) is also a semi-empirical transport model with a mix of Bohm type and gyro-Bohm type transport [4]. The original L-mode version of BGB model [27] is used in our simulations. The BGB model has been demonstrated to model the internal inductance reasonably in the L-mode ramp up phase of at least two different tokamaks [26].

3. DIII-D relevant experiments

We have done validation studies with five transport models using the three DIII-D ITER-like ramp up cases. These discharges are originally proposed for simulations of the ITER 15MA baseline large-bore [28] ramp up scenarios, which means that the plasma shape is maintained as closely as possible to the ITER designed shape and the key physical parameters followed dimensionless parameter scaling from DIII-D to ITER [29]. The normalized current $I_N = I_p / aB_T$ and pressure $\beta_N = \beta_T / I_N$ in these discharges are the same as ITER 15 MA baseline, which leads to a similar trajectory of ℓ_i . Being able to reliably simulate the

evolution of pressures and densities in these ITER-like discharges is an important step in the extrapolation to ITER and CFETR scenario modeling. These discharges contain two phases from startup to steady state. In the first phase, pure ohmic heating is applied and the tokamak operates with low plasma pressure and low plasma confinement mode (L-mode). In the second phase, while the NBI heating is turned on, the plasma pressure increases rapidly and the plasma confinement transits to H-mode. The three discharges with 1.25 MA peak plasma current in DIII-D are characterized by similar steady state target and different ramp up designs (as shown in table 2). The different current ramp rates are in the range of 0.67 – 1.3 MA/s.

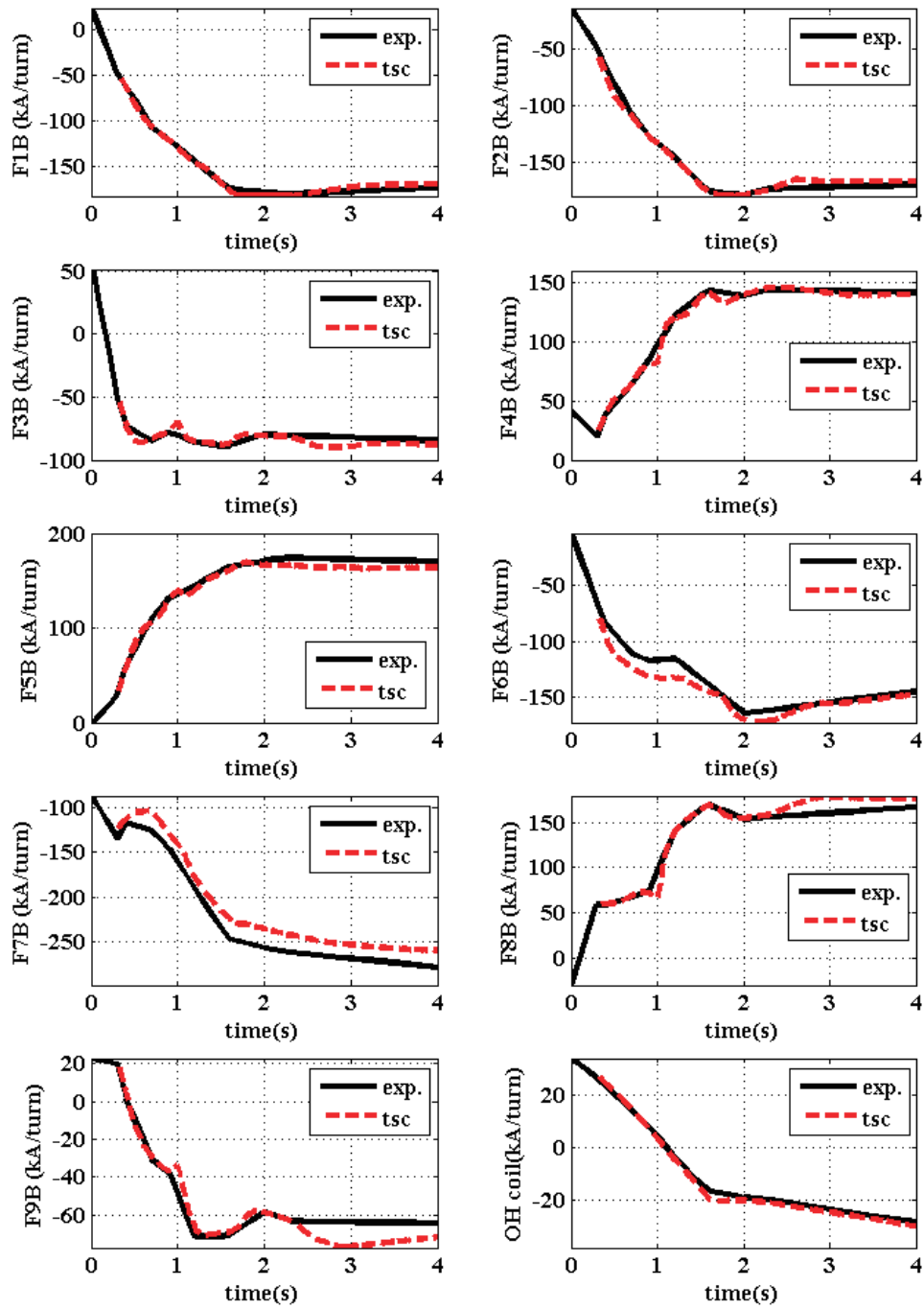


Figure2. Comparisons of the PF coil currents responded to RZIP control in simulation using the GLF23 model (red dash line) with that measured in DIII-D #148773 discharge (black solid line).

Table 2. List of begin time t_{begin} and end time t_{end} of TSC simulation, as well as start time of current flattop t_{flattop} and steady state t_{ss} , for the three DIII-D discharges. Related ramp rates are also given in the last column.

Shoot	t_{begin} (s)	t_{flattop} (s)	t_{ss} (s)	t_{end} (s)	Ramp rate (MA/s)
148773	0.3	1.574	2.308	4.0	0.67
148786	0.3	1.2	1.852	4.0	0.83
148793	0.3	0.8	1.398	4.0	1.3

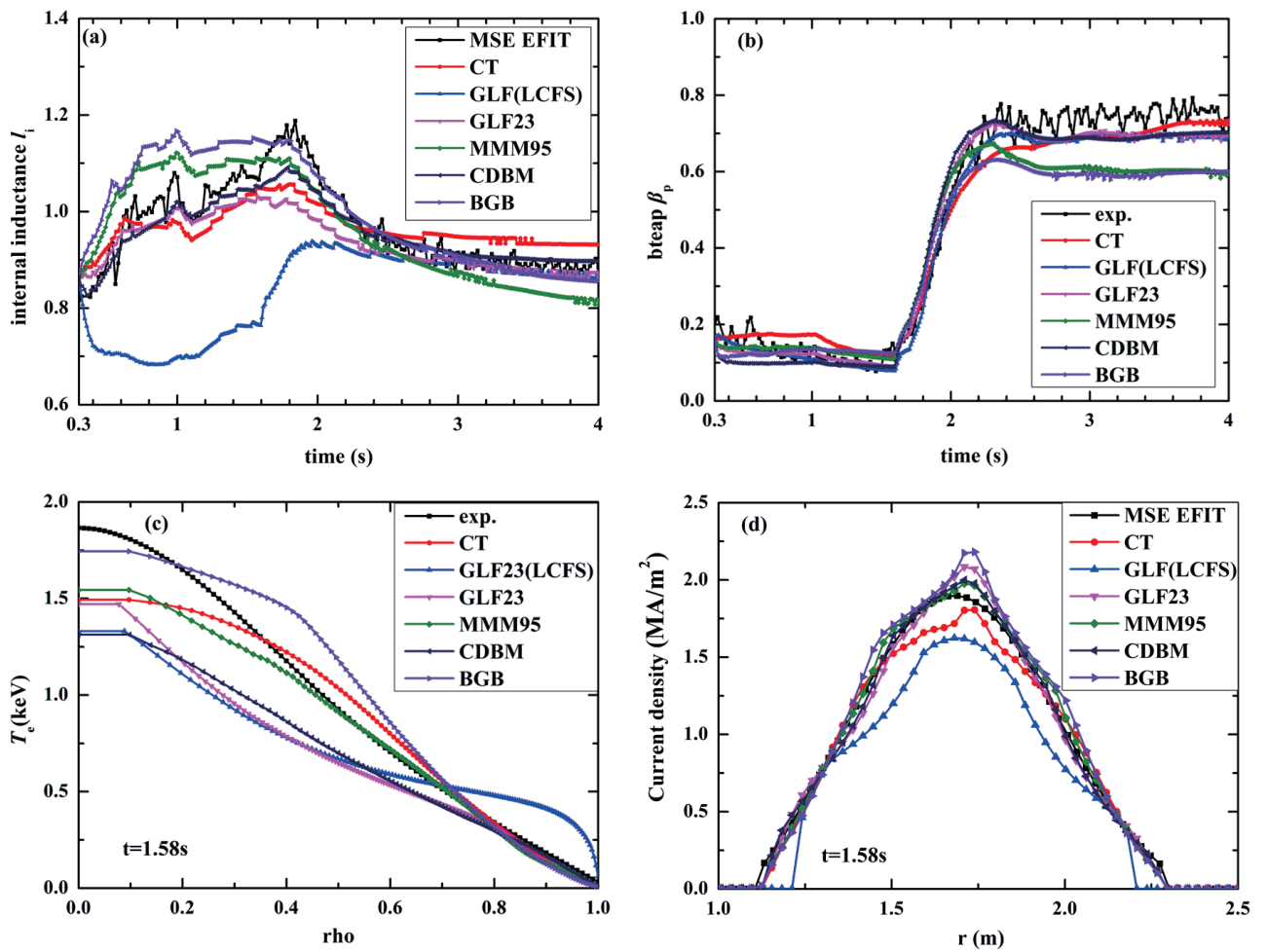


Figure 3. Comparisons of (a) internal inductance ℓ_i evolution, (b) β_p evolution, (c) electron temperature profile ($t = 1.58$ s) and (d) current density profile ($t = 1.58$ s) between experiment results of the DIII-D #148773 discharge (black line with square) with simulation results by introducing different energy transport models. Five transport model used in simulation are CT (red line with circles), GLF23 (magenta line with downward triangles), MMM95 (green line with diamonds), CDBM (navy line with leftward triangles) and BGB (purple line with rightward triangles), respectively. The ramp rate of DIII-D #148773 discharge is 0.67 MA/s.

3.1. Simulation of ohmic heating phase

For the three DIII-D discharges, the simulation is started from 0.3s, when X-point has been shaped and the plasma equilibrium can be reconstructed by MSE EFIT[18]. The initial plasma pressure is set to match the experimental measured ion and electron temperature profiles, based on the analytical form of $P \psi = P_0 \cdot x^{\alpha_P}$, where x is the normalized poloidal flux varying from 0 at the magnetic axis to 1 at the plasma boundary. It is found that the influence of initial current profile on the temperature predictions is very strong for some transport models in ASDEX Upgrade current ramps [23]. And the MSE EFIT allows good kinetic reconstruction of the current profile on DIII-D. In our work, the toroidal field function $FF' \psi$ is also constructed by TSC with two shape factors and the central safety factor to match the current profile reconstructed by the MSE EFIT.

The plasma shape and position evolutions mainly depend on the programmed plasma current and PF coils currents, and the RZIP control system. The programmed PF coils and total plasma current come from the experimental database. The observation points for plasma shape control are selected near the reconstructed EFIT plasma boundary (as shown in table 1 for #148773), which mainly depend on the signals of flux loops and magnetic probes mounted on the vacuum vessel. The controlled plasma shape (blue line) agrees well with the MSE EFIT boundary (red line) as shown in figure 1(a) at 1.58s. The deviations of the TSC results and MSE EFIT plasma boundary are no more than several centimeters. The calculated PF coil currents evolutions using the GLF23 model are shown in figure 2. The differences between the experimental data (black line) and the TSC results (red line) are smaller than 1% except for F7B and F6B (about 5%), which are of high weights in the RZIP systems. And this small simulation error is insensitive to the profile effects we focus on.

The normalized internal inductance ℓ_i is often introduced as an essential parameter to validate the current profile and transport model in the tokamak ramp up phases. Note that there are several definitions of ℓ_i . When comparing among tokamaks or free boundary simulations, some definitions that estimate the length of the poloidal circumference of the LCFS (the last closed flux surface) with basic parameters (like aspect ratios, elongation, magnetic axis position) of a device, are no longer suitable. In this paper, the generally agreed definition of ℓ_i computed from quantitative evaluations is used for all the simulations presented. The computational formula is $\ell_i = \langle B_p^2 \rangle / \mu_0 I / L_p^2$, where the numerator is the average of the square of the poloidal field in the plasma volume, while the denominator is the square of the average of poloidal field at the boundary. L_p is the length of the poloidal circumference of the LCFS from the equilibrium. Since $\langle B_p^2 \rangle$ is the plasma volume averaged parameter, the outer half of the plasma current profile dominates the normalized internal inductance, while it is sensitive to the transport model coefficients near the plasma edge.

In the ohmic heating phase with L-mode, the three theory-based core transport models, the GLF23 model, the MMM95 and CDBM model, are insufficient to model the very edge of the plasma. The three transport models are usually applied with a fixed boundary condition inside LCFS for static simulation [5,

30, 31] or fixed boundary transport coefficients for time-dependent simulation [26]. As shown in figure 3(a), simulations with the GLF23 model (applied up to the LCFS) underestimate the internal inductance ℓ_i (maximum -0.4 discrepancies) in this case. Similar situations are also mentioned in the JET and AUG ramp up simulations [26]. As shown in figure 3(d), the outer current profile calculated by the GLF23 model (applied up to the LCFS) is overestimated, while the central current is underestimated. This is because the transport coefficient calculated by the GLF23 model is very small (almost 0) and severely underestimates the transport at the edge, which causes an abnormal electron and ion temperature rise near the plasma boundary. The higher temperature decreases the neoclassical resistivity and changes the current profile by slowing the current penetration. In contrast, the MMM95 model and CDBM model overestimate the transport coefficients and as a result obtain an inflated internal inductance compared with the experimental values. To address this deficiency, a fixed boundary transport coefficient is introduced in the three theory-based models to fit the experimental temperature near the plasma boundary. In order to make clear the impact of the fixed boundary coefficient, a sensitivity study has been done with a coefficient ranging from $1 \text{ m}^2\text{s}^{-1}$ to $15 \text{ m}^2\text{s}^{-1}$ using the GLF23 model with the discharge #148773 data.

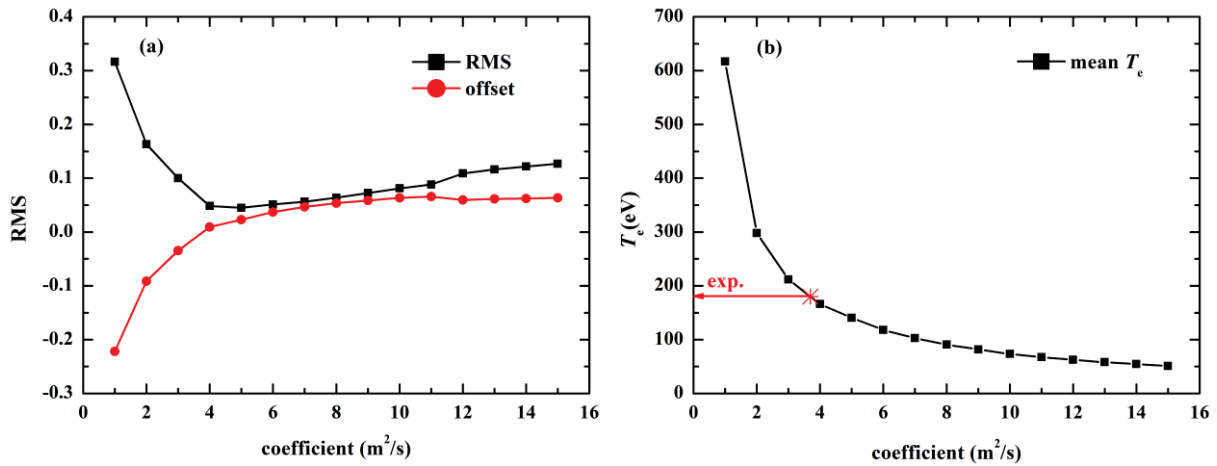


Figure 4. (a) The root mean square (RMS) deviations and offsets for the simulated ℓ_i in ohmic heating phase of DIII-D #148773 discharge, where the GLF23 model is introduced with different fixed coefficients in the region of $\rho > 0.85$. (b) The simulated time-averaged electron temperature at $\rho = 0.85$ with different fixed boundary coefficients. The red asterisk on the line has the experimental value of time-averaged T_e , therefore the coefficient used in this work is then chosen as $4.0 \text{ m}^2\text{s}^{-1}$.

To compare the simulation results in different discharges or same discharge with different condition assumes, standard metrics for ℓ_i and β_p are defined by the following two expressions:

$$RMS = \left[\frac{1}{N} \sum_{t=t_0}^{t_N} \frac{(P_{sim} - P_{exp})^2}{P_{exp}^2} \right]^{1/2}, \quad (3)$$

$$offset = \frac{1}{N} \sum_{t=t_0}^{t_N} \frac{P_{sim} - P_{exp}}{P_{exp}}, \quad (4)$$

where P_{sim} and P_{exp} are the simulated value and the experimental value of the analyzed parameter, t_0 and t_N are the start time and end time of analyzed phase, and N is the number of the time points. The RMS (Root Mean Square) and offset for the ℓ_i in the ohmic heating phase with different fixed boundary coefficients are shown in figure 4(a). With the increase of the fixed boundary coefficient, the boundary temperature (at $\rho = 0.85$) decreases as a result of the higher level of transport as shown in figure 4(b). As a consequence, higher neoclassical resistivity ($\eta_c = 1.03 \times 10^{-4} \cdot \ln \Lambda \cdot T_e^{-1.5}$) and faster current diffusion inward occur and result in the increase of ℓ_i . The obtained results show the RMS and offset are strongly sensitive to the fixed coefficient in the range of (1-3 m²s⁻¹), where the boundary temperature changes rapidly (as shown in fig. 4(b)). When the simulated edge temperature matches the experimental data (the red asterisk), the simulated ℓ_i agrees well with the experiments with the boundary coefficient of 4 m²s⁻¹. Therefore, the transport coefficients $\chi_e = \chi_i = 4 \text{ m}^2 \text{ s}^{-1}$ are fixed in the region of $0.85 < \rho < 1$, to give a reasonable description of this region, where various factors, such as divertor operation, impurity transport, wall conditions and so on, play more or less a role. The three transport models in the discussions that follow will all be referring to the transport models with the fixed boundary coefficient except when specified.

3.2. Analysis of ℓ_i and β_p for ohmic heating phase

Figure 3 also provides a comparison of other transport models with the experimental data. Overall, the GLF23, CDBM and Coppi-Tang model simulate the dynamic ℓ_i within ± 0.1 during the current ramp up phase, while the BGB and MMM95 model overestimate the dynamic ℓ_i (about 0.2 deviations) in this case. The calculated current profiles with different transport models are depicted at the end of the pure ohmic heating phase (1.58s) as shown in figure 3(d). The shapes of these current profiles are similar to each other except for the GLF23 applied out to the last closed flux surface (LCFS), but differ quantitatively across the minor radius. The dynamic ℓ_i , which summarizes the current profile evolution, provides crucial information for designing and optimizing plasma ramp up scenarios. Figure 3(b) shows the dynamic poloidal beta β_p evolution while figure 3(c) shows electron temperature profiles of different transport models at 1.58s. The GLF23 model and the CDBM model underestimate the electron temperature profiles in the plasma core, while the BGB model, Coppi-Tang model and MMM95 model fare much better. This seems to be consistent with previous static analyses of some DIII-D L-mode cases[31] with the GLF23 model or CDBM model in the ITPA profiles database.

For DIII-D discharge #148786 (as shown in figure 5), the five transport models yield the dynamic ℓ_i and electron temperature profile with similar features to #148773 because of the small difference in the current ramp rates (0.83 MA/s for #148786 and 0.67 MA/s for #148773). For the DIII-D discharge #148793 with 1.3 MA/s current ramp rates, the biggest deviation in ℓ_i simulation for all models does not

exceed 0.1 as shown in figure 6. With high current ramp rates, the simulated plasma current tends to have a flat profile, even a hollow current profile, which causes the simulated electron temperature profile also to be flat as shown in figure 6 as expected from ohmic heating.

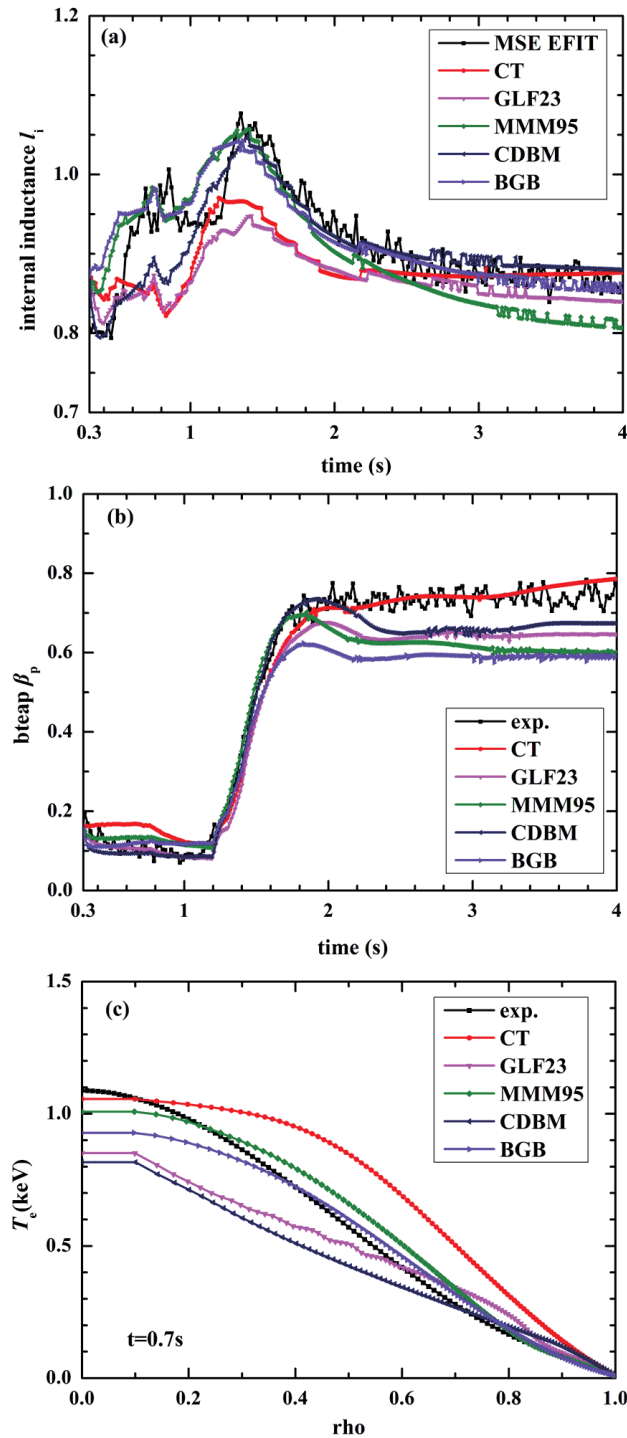


Figure 5. Comparisons of (a) internal inductance ℓ_i evolution, (b) β_p evolution and (c) electron temperature profile ($t = 0.7$ s) between experiment results of the DIII-D #148786 discharge with simulation results by introducing different energy transport models. The ramp rate is 0.83 MA/s. (The meaning of color and symbols for individual line is the same as in Figure 3).

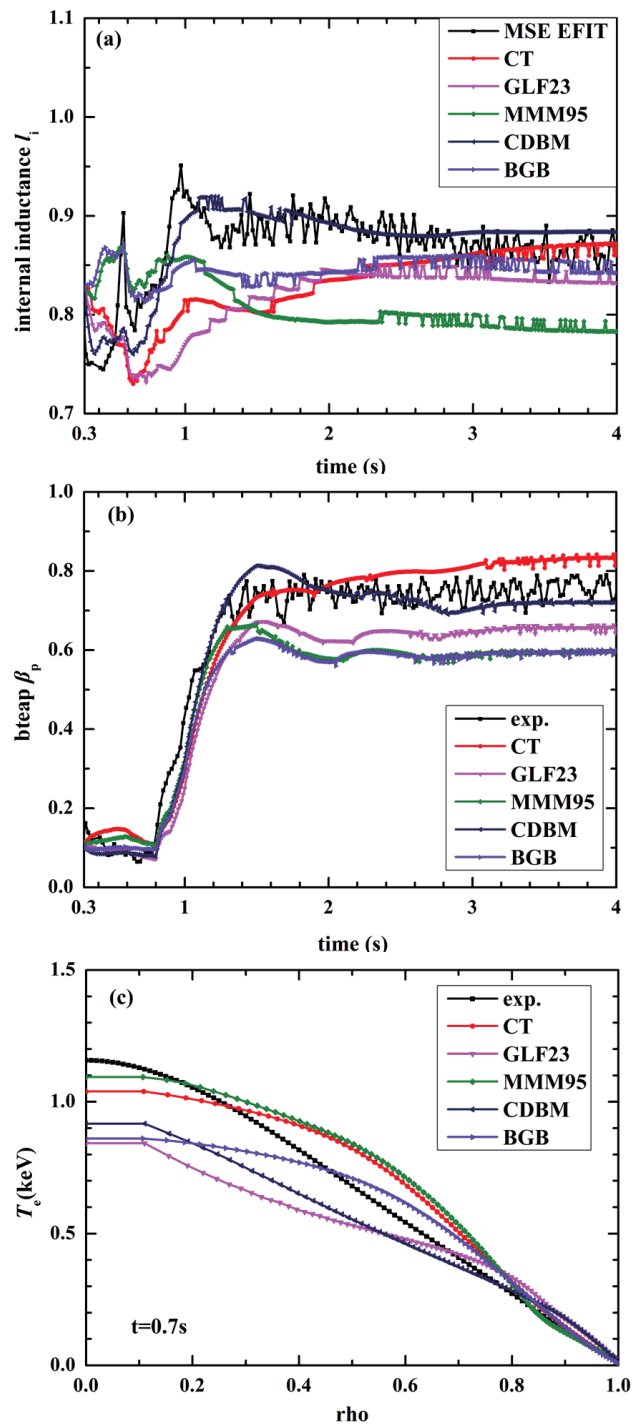


Figure 6. Comparisons of (a) internal inductance ℓ_i evolution, (b) β_p evolution and (c) electron temperature profile ($t = 0.7s$) between experiment results of the DIII-D #148793 discharge with simulation results by introducing different energy transport models. The ramp rate is 1.3 MA/s. (The meaning of color and symbols for individual line is the same as in Figure 3).

Table 3 shows the RMS and offset for ℓ_i and β_p in the three OH heating phases with different models. Because of the large error bar and low value of β_p , we just compare the ℓ_i here. For Coppi-Tang, GLF23 and CDBM models, the largest RMS and offset of ℓ_i are 7.96%/-3.11%, 7.87%/-3.94% and 4.96%/-2.35%, respectively in #148793 with high ramp rates. These deviations are smaller in the lower ramp rates cases. On the contrary, the RMS and offset obtained for the MMM95 and BGB model decrease with increasing ramp rate, but the minimum RMS and offset (7.82%/6.05% from MMM95, 8.37%/5.62% from BGB) are still larger than the maximum deviation from CDBM. We can conclude that the Coppi-Tang, GLF23 and CDBM are the reasonable models to predict ℓ_i for modeling the DIII-D ITER-like ohmic ramp up phase (L-mode). And for CFETR ramp up design in L-mode, without experimental edge temperature to fix the transport near LCFS, the Coppi-Tang seems to be our favorable choice. For the GLF23 and CDBM model, to have the edge information from the core-edge coupling simulation [32] will improve the confidence for CFETR L-mode simulation.

Table 3. The RMS deviations and offsets of simulated dynamic ℓ_i and β_p with five different transport model in ohmic heating (OH) phases of DIII-D discharges. The relative ramp rates are listed in Table 2.

OH phase L-mode		CT		GLF23		MMM95		CDBM		BGB	
		RMS	offset	RMS	offset	RMS	offset	RMS	offset	RMS	Offset
148773	ℓ_i	4.64%	-1.14%	4.26%	0.93%	10.14%	9.32%	1.31%	-0.51%	13.32%	12.56%
	β_p	8.87%	1.47%	18.49%	-15.47%	11.54%	-9.49%	32.94%	-27.86%	20.68%	-17.46%
148786	ℓ_i	6.72%	-2.05%	4.80%	-1.52%	8.23%	7.73%	3.11%	-1.75%	9.69%	9.02%
	β_p	62.15%	65.37%	15.20%	2.07%	34.95%	29.58%	18.40%	-12.60%	24.21%	12.99%
148793	ℓ_i	7.96%	-3.11%	7.87%	-3.94%	7.82%	6.05%	4.96%	-2.35%	8.37%	5.62%
	β_p	43.76%	32.5%	13.69%	0.39%	38.98%	29.13%	12.61%	-0.95%	19.97%	11.57%

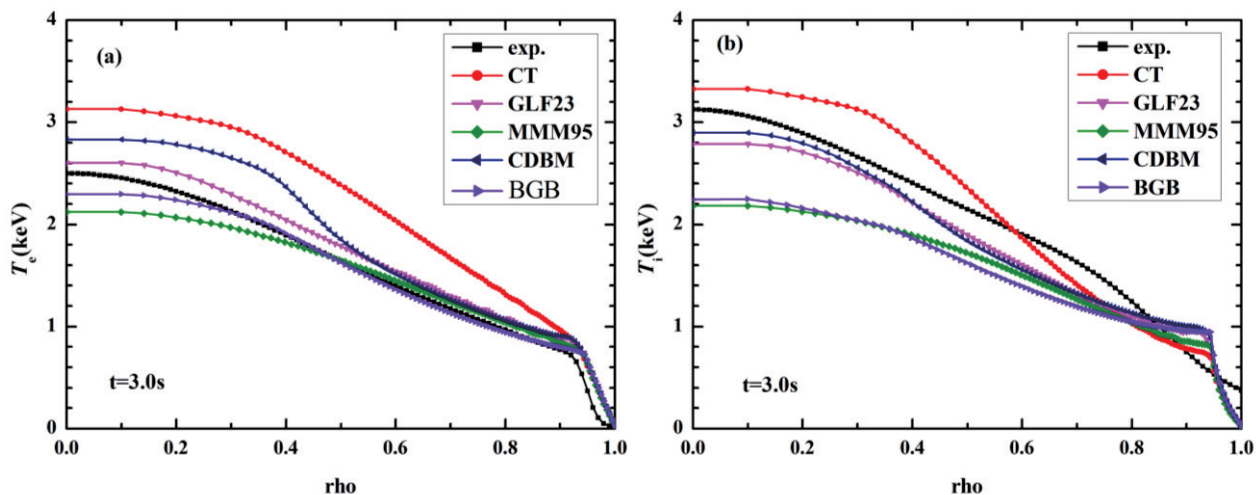


Figure 7. Comparisons of (a) electron temperature profiles and (b) ion temperature profiles ($t = 3.0$ s) between experiment results of the DIII-D #148786 discharge with simulation results by introducing different energy transport models. (The meaning of color and symbols for individual line is the same as in Figure 3)

3.3. NBI heating phase

During the NBI heating phase, the plasma confinement mode transits from L-mode to the H-mode, in which case the boundary temperature depends on the complex pedestal physics. For our model validation, the electron and ion transport in the pedestal region are reduced to increase the electron and ion temperature to match the experimental boundary temperature. The Sauter bootstrap current model is used to calculate the bootstrap current profiles. With a pedestal structure, the bootstrap current becomes a significant quantity, driven by the pressure gradient at the pedestal. The internal inductances of all transport models are reduced in different degrees because of the edge bootstrap current as shown in figure 3(a), 5(a) and 6(a).

The NBI heating profiles and beam driven current profiles are calculated by ONETWO with NFREYA[33] or NUBEAM, and then given to TSC to calculate the current profiles and the temperature profiles. For the three DIII-D discharges, about 3MW on-axis NBI is injected into the tokamak, which significantly increases the average temperature and β_p in 0.2~0.3 s as shown in figure 3(b), 5(b) and 6(b). Figure 7 shows the electron and ion temperature profiles at 3.0s in DIII-D #148786. All the transport models agree reasonably well with experiments within 10% deviation in the $\rho > 0.85$ region. Large deviations only exist in the central temperature profile. The Coppi-Tang model overestimates the central electron temperature by about 1 keV, while the MMM95 model and BGB model underestimate the central ion temperature by about 1 keV. For these NBI heating discharges, the measured maximum central toroidal rotation frequency reaches 1.4×10^5 rad/s. With the lack of rotation, the MMM95 and BGB model predict well the electron temperature profile but underestimate the ion temperature and β_p . Only the GLF23 model and the CDBM model, which account for the reduced transport induced by toroidal rotation, can well predict the ion temperature.

Table 4. The RMS deviations and offsets of simulated dynamic l_i and β_p with five different transport model in NBI heating phases of DIII-D discharges.

NBI heating H-mode	CT		GLF23		MMM95		CDBM		BGB		
	RMS	offset	RMS	offset	RMS	offset	RMS	offset	RMS	offset	
148773	l_i	3.49%	-1.14%	3.96%	-1.92%	1.80%	-0.13%	3.14%	1.86%	3.83%	3.54%
	β_p	8.85%	2.28%	10.16%	-0.15%	21.87%	-3.49%	12.31%	0.00%	23.74%	-4.67%
148786	l_i	4.33%	-2.42%	5.28%	-4.36%	3.63%	0.44%	2.87%	2.48%	2.93%	1.58%
	β_p	5.79%	-0.94%	12.58%	-12.07%	14.90%	-12.53%	9.19%	-7.17%	18.66%	-18.21%
148793	l_i	6.40%	-4.68%	7.79%	-6.70%	9.50%	-9.13%	2.47%	0.54%	5.33%	-4.57%
	β_p	8.37%	5.27%	13.90%	-13.45%	19.83%	-19.16%	6.34%	-0.78%	20.62%	-20.35%

The RMS and offset for l_i and β_p in NBI heating phase are also listed in table 4. The RMS and offset for l_i in all the simulations are less than 10%. The CDBM model with maximum RMS deviation 3.14% and offset 1.86% for l_i agrees best with experiments. The largest deviations of β_p simulation are obtained in the MMM95 and BGB simulations approximately with RMS 20% and offset -20%. This is probably caused by the lack of rotation influence on transport in the two models. The RMS and offset for β_p in the simulations using Coppi-Tang and CDBM model are no less than 10% as shown in table 4.

Simulations with Coppi-Tang model usually describe a higher β_p than others because of the higher electron temperature.

4. Conclusion

Five transport models have been applied to several DIII-D ITER-like ramp-up cases using the TSC code. The plasma shape evolution controlled by RZIP system agrees well with the EFIT reconstructed results. The plasma internal inductance ℓ_i , poloidal beta β_p , current profile and temperature profile calculated by different transport models have been obtained and compared with each other. Two key parameters, i.e., dynamic ℓ_i and β_p , are comprehensive analyzed to give an overall estimation of simulation results by different energy transport models.

The two empirical energy transport models, the BGB and Coppi-Tang model, can match simulations of dynamic ℓ_i with experiments both in the L-mode in the DIII-D ITER-like ramp up case with the TSC code, while the three theory based models must rely on a fixed boundary coefficient to fit the experimental boundary temperature. For example, simulation with GLF23 model extended to the LCFS underestimates the dynamic ℓ_i by predicting excessive electron and ion temperature rise near the plasma boundary to slow the current penetration; whereas, the sensitivity study shows GLF23 can reasonably model the dynamic ℓ_i with the fixed boundary coefficient. The edge temperature is influenced by many factors and only a full core-edge coupled simulation can predict it. We have demonstrated in the time-dependent simulations that using a fixed boundary transport coefficient is an acceptable simplifying assumption in order to match the experimental measured temperature across the entire minor radius.

To compare the five transport models, the RMS and offset for ℓ_i and β_p are analyzed. For OH heating on the DIII-D L-mode simulations, the MMM95 and BGB model overestimate the ℓ_i within maximum 12.56% discrepancies, while the GLF23, Coppi-Tang and CDBM model underestimate the ℓ_i within maximum -3.94% discrepancies. With a much lower ramp rate (0.25 MA/s) and similar tokamak size, the maximum deviation (about 0.4) among different models in this case is larger than that in DIII-D simulations. Qualitative analysis of the differences in the simulation of ℓ_i using different models has been shown to be consistent with the physics included in the models. Comparing all results in our simulations above, the Coppi-Tang model seems to be the favorable choice for the CFETR ramp up design in the L-mode. And the GLF23 and CDBM model with the predicted edge temperature are also very attractive models for CFETR L-mode simulation.

For simulation of NBI heating on a DIII-D H-mode discharge, the experimental pedestal, NBI heating information and the Sauter current model are used. With the same transport at the edge reduced to construct the pedestal for all models, simulations with the CDBM model yield ℓ_i and β_p with the smallest discrepancy. Including the influence of toroidal rotation during the NBI heating phase, the CDBM and GLF23 model predict accurately both the electron and ion temperature profiles, while the BGB and MMM95 model without rotation factor can only accurately predict the electron temperature and

underestimate β_p . For the Coppi-Tang model, the simulated ℓ_i and β_p agree well with experiments after the auxiliary heating transport coefficient has been adjusted to fit the experiments confinement for all the simulations. Comparing all models using a standardized metrics, the CDBM model seems to be the favorable choice for the CFETR ramp up design in the H-mode.

In the future, we will do the work to validate the transport model in CFETR-relevant experiments operating with some other auxiliary heating sources, such as ECRH and ICRH. More complete physics based models such as TGLF will be also researched in future studies. Tokamak size is also a crucial parameter. We will also focus on tokamaks with larger or smaller sizes, such as JET and TCV. It would significantly enhance the confidence to choose the appropriate transport models to design the CFETR ramp up scenarios.

5. Acknowledgements

This work is supported by National Magnetic Confinement Fusion Research Program of China (Grant Nos.:2014GB110000, 2014GB110003 and 2014GB103000) and the National Natural Science Foundation of China (Grant No. 11305216). We would like to express our thanks to all members of the CFETR physics team. We acknowledge the Princeton Plasma Physics Laboratory for permission to use the TSC code, the General Atomics theory group for permission to use the OMFIT framework and GA code suite like ONETWO and Toksys, and for their valuable technical support. Lastly, the permission of the DIII-D group for use of their experimental data is greatly appreciated. Numerical computations were performed on the ShenMa High Performance Computing Cluster in Institute of Plasma Physics, Chinese Academy of Sciences and supercomputing system in the Supercomputing Center of University of Science and Technology of China.

References

- [1] Wan Y., presented at the Proc. IEEE 25th Symp. Fusion Eng. (SOFE), 2013 (unpublished).
- [2] Jardin S., Pomphrey N., et al., *Journal of Computational Physics* **66** (2), 481-507 (1986).
- [3] Jardin S., Bell M., et al., *Nuclear Fusion* **33** (3), 371 (1993).
- [4] Erba M., Aniel T., et al., *Nuclear Fusion* **38** (7), 1013 (1998).
- [5] Kinsey J., Staebler G., et al., *Physics of Plasmas* **12** (5), 052503 (2005).
- [6] Hannum D., Bateman G., et al., *Physics of Plasmas (1994-present)* **8** (3), 964-974 (2001).
- [7] Poli F., Kessel C., et al., *Nuclear Fusion* **52** (6), 063027 (2012).
- [8] Takei N., Nakamura Y., et al., *Plasma Physics and Controlled Fusion* **49** (3), 335 (2007).
- [9] Guo Y., Xiao B., et al., *Plasma Physics and Controlled Fusion* **54** (8), 085022 (2012).
- [10] Bandyopadhyay I., Gerhardt S., et al., 2010.
- [11] Kessel C.E., Giruzzi G., et al., *Nuclear Fusion* **47** (9), 1274 (2007).
- [12] Kessel C.E., Campbell D., et al., *Nuclear Fusion* **49** (8), 085034 (2009).
- [13] Poli F., Kessel C., et al., *Nuclear Fusion* **54** (7), 073007 (2014).
- [14] Luxon J.L., *Nuclear Fusion* **42** (5), 614 (2002).
- [15] Putvinski S., Barabaschi P., et al., *Plasma Physics and Controlled Fusion* **39** (12B), 0741-3335 (1997).

- [16] Humphreys D.A., Ferron J.R., et al., Nuclear Fusion **47** (8), 943-953 (2007).
- [17] Xiao B., Humphreys D., et al., Fusion Engineering and Design **83** (2), 181-187 (2008).
- [18] Lao L., John H.S., et al., Fusion Science and Technology **48** (2), 968-977 (2005).
- [19] Pfeiffer W., Davidson R., et al., 1980.
- [20] Goldston R.J., Mccune D., et al., Journal of Computational Physics **43** (1), 61-78 (1981).
- [21] Sauter O., Angioni C., et al., Physics of Plasmas **6** (7), 2834-2839 (1999).
- [22] Voitsekhovitch I., Sips A., et al., Plasma Physics and Controlled Fusion **52** (10), 105011 (2010).
- [23] Fietz S., Fable E., et al., Nuclear Fusion **53** (5), 053004 (2013).
- [24] Shimada M., Nuclear Fusion **48** (0029-5515) (2008).
- [25] Casper T.A., Meyer W.H., et al., Nuclear Fusion **51** (1), 0029-5515 (2010).
- [26] Imbeaux F., Citrin J., et al., Nuclear Fusion **51** (8), 083026 (2011).
- [27] Erba M., Cherubini A., et al., Plasma Physics and Controlled Fusion **39** (2), 0741-3335 (1997).
- [28] Sips A.C.C., Casper T.A., et al., Nuclear Fusion **49** (8), 0029-5515 (2009).
- [29] Luce T., Humphreys D., et al., Nuclear Fusion **54** (9), 093005 (2014).
- [30] Kinsey J.E., Staebler G.M., et al., Physics of Plasmas (1994-present) **9** (5), 1676-1691 (2002).
- [31] Honda M. and Fukuyama A., Nuclear Fusion **46** (5), 580 (2006).
- [32] Xu G., Shi N., et al., Fusion Engineering and Design. 0920-3796 (2016).
- [33] Fowler R.H., Holmes J.A., et al., (Oak Ridge National Lab., TN (USA), No. ORNL/TM-6845. , 1979).

Snake perturbation during pellet injection on the EAST tokamak

Xingjia Yao^{1,2}, Jiansheng Hu^{1,*}, Liqing Xu¹, Zong Xu^{1,2}, Yue Chen¹, Changzheng Li¹, Haiqing Liu¹, Hailing Zhao¹, Yanmin Duan¹, Tonghui Shi¹, Wei Shen¹ and EAST team.

¹ Institute of Plasma Physics, Chinese Academy of Sciences, Hefei 230031, China

² Science Island Branch of Graduate School, University of Science and Technology of China, Hefei 230029, P. R. China

Abstract

The pellet-induced snake oscillation was observed by Soft X-ray diagnostic in the EAST for the first time after a fueling sized pellet penetrated inside the $q = 1$ surface. The snake phenomenon has a long lifetime with a helicity of $m = 1$ and $n = 1$. Basic behaviors of the snake, including triggering condition, interaction with the sawtooth and snake rotation frequency, were discussed in details by multiple core diagnostics. The snake location was also analyzed through observation of the vertical Soft X-ray arrays and raw Soft X-ray brightness profiles. It's clear that the snake resided in a broad region between the magnetic axis and the $q = 1$ surface derived from equilibrium reconstruction. This investigation is beneficial for the understanding of the snake formation for EAST and future devices, like ITER and DEMO.

1. Introduction

Snake phenomenon, a special type of core magnetohydrodynamic (MHD) activity, was first found after deuterium pellet injection in JET [1-3] discharges with an $m = 1$, $n = 1$ topology. This snake oscillation, which usually takes place inside the $q = 1$ surface and is characterized by a small region of high density and low temperature formed by pellet ablation [1], is also observed in ASDEX [4], Tore Supra [5, 6] and JT-60 [7]. Except for pellet induction, snake perturbation has also been observed to arise spontaneously in discharges exhibiting impurity accumulation at an early stage in JET [8]. It has a spatial helical structure and is closely associated with the $q = 1$ magnetic surface [9]. The behavior of the snake oscillation and its resonance effect can be used as a diagnostic to determine the position of the $q = 1$ surface and study some of central region properties [10]. Besides, snake is also a possible way to mitigate the central impurity accumulation.

Since the pellet injector [11] installed and tested on EAST [12] in 2012, lots of pellet injection experiments have been carried out. Recently, pellet injection on EAST, except for fueling and ELM triggering effects, was first found to excite snake oscillation. Snake could be detected by SXR emission, absolute extreme ultraviolet (AXUV), electron cyclotron emission (ECE) systems and other core diagnostics. The formation of the snake is under the necessary but not sufficient condition that pellet crosses the $q = 1$ surface [13]. A significant dip in $H\alpha$ emission was observed in JET discharge when the pellet crosses the $q = 1$ surface [14]. It is related to the reduction of hot electron reservoir available for ablating the pellet within the flux tube. And this pellet-induced snake shows a strong relationship with the sawtooth instability. A detailed analysis of the snake behavior and its location through observation, which gives a new angle of studying the snake in EAST, is carried out. It must be realized that comprehending the snake is potentially important not only for EAST but also for ITER [15] where the $q = 1$ surface can be as large as half the minor radius.

2. The pellet-induced snake oscillation on EAST

The deuterium pellet with atoms of 3.78×10^{20} and with velocity of about 280 m/s was injected radially from the low field side (LFS) into the Ohmic plasma with the following parameters: $I_p =$

400 kA, $B_t = 2.7$ T, $T_e(0) = 900$ eV and $n_e \approx 2.4 \times 10^{19} \text{ m}^{-3}$. The pellet touched the plasma at about 5.06s and the $D\alpha$ intensity and magnetic perturbations responded significantly. The pellet penetrates to about $r = 3$ cm and ablates inside the $q = 1$ surface causing a drop of the core electron temperature (950 eV to 850 eV). A small region, which was a breeding ground for the snake, of low temperature and high density inside the $q = 1$ surface was built. With pellet successfully penetrating to and beyond the $q = 1$ surface, snakes were detected by SXR system and other core diagnostics with characteristic oscillatory signals in Fig. 1. And within about 10 ms after pellet injection a snakelike periodic oscillation was gradually appeared on the SXR core signal showing an unusual waveform. The snake persisted 16 sawtooth cycles for nearly 1 s and changed periodically as the sawtooth grown and collapsed over and over again. This oscillation phenomenon was also recorded by XUV and ECE signal where the similar pattern could be found.

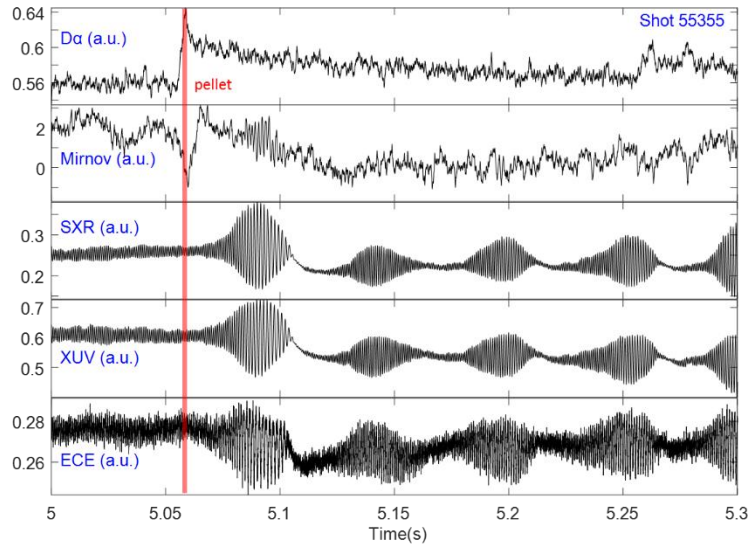


Fig. 1 Temporal evolution of characteristic oscillatory signals recorded after pellet injection. The signal from the top to the bottom are $D\alpha$ intensity, magnetic perturbations, soft X-ray intensity, plasma radiation intensity and raw signal from one ECE channel. The red solid line indicates the time of pellet injection.

Snakes were seen from different radial positions by vertical SXR array after pellet injection in Fig. 2 (oscillations in top two signals are noises). It's easy to find out that the snakes invert between $r = 6.1$ cm and $r = 4.8$ cm where the snake minor radius ($r_s \approx 5.5$ cm) locates (later it also finds out to be the magnetic axis in Fig. 4). Using the appropriate SXR arrays, the radial and poloidal dimensions of the snake were figured out as $1 r = 22$ cm and $1 \theta = 26$ cm respectively. According to JET [1], Tore Supra [6] and HT-7 [10], the pellet-induced snake oscillation occurs well inside the $q = 1$ surface. The q -profile during the snake oscillation at 5.1 s is calculated by the equilibrium reconstruction (see Fig. 3). And the radial location of the $q = 1$ surface, which has a value of $R_{q=1} = 1.84/2.02$ m ($Z = 0$ m), is revealed by the enlarged detail. Combining the location information of the $q = 1$ surface and the time history of raw SXR brightness profile, Fig. 4 appropriately demonstrates the radial relationship between the snake oscillation and the $q = 1$ surface (As the radial location of the $q = 1$ surface changes very little, its radial value at 5.1 s can well represent its true value during the whole process). It's clearly seen that the $q = 1$ surface almost cover the whole snake area and the snake mode periphery is well consistent with the radial location of the $q = 1$ surface. So in this case the snake mode periphery can roughly describe or help to find the location of the $q = 1$ surface. So in this case the snake mode periphery can roughly describe or help to find the location of $q = 1$ surface.

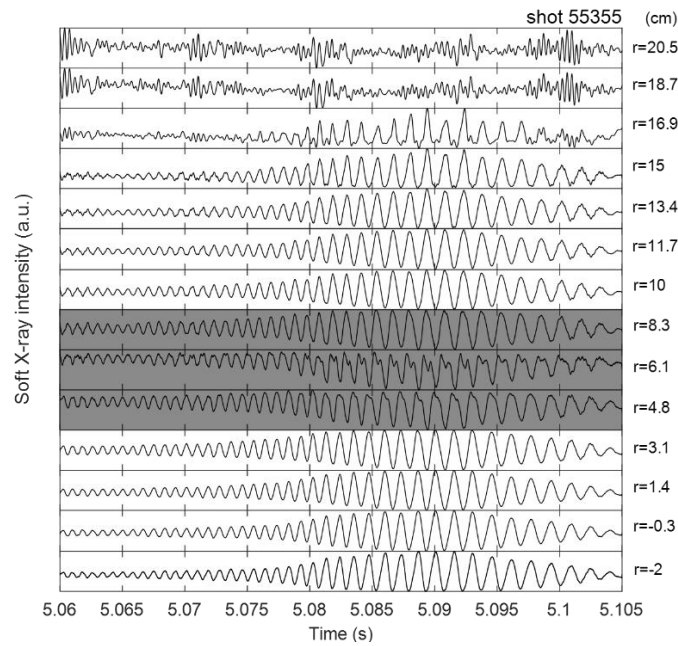


Fig.2 . Time evolution of SXR signals in a sawtooth cycle of the pellet-produced snake at different radial positions.

Like JET [1], there is also a gradual shrinkage of the location of maximum SXR brightness, which is generally used as a symbol for the position of $q = 1$ surface, at the time of sawtooth collapse (see Fig. 9). About 33% inward shift of the snake occurs in minus radius. After sawtooth collapse, a following outward behavior of the snake takes place until it gets back to the original position. However, the first shrinkage of the snake was much bigger than the later ones. Maybe it's due to the pellet strong residual effect on the surrounding plasma. This phenomenon goes along with the sawtooth until it disappears.

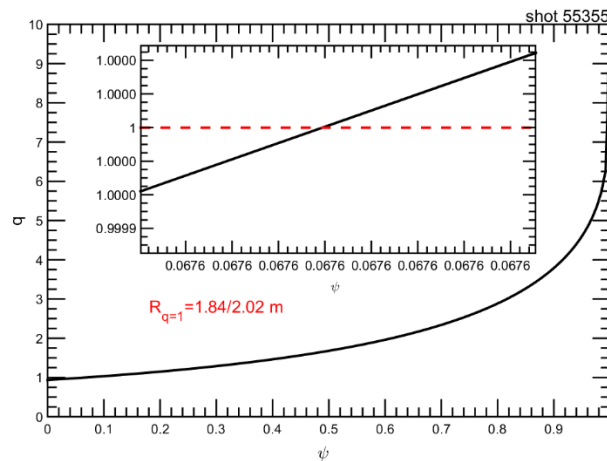


Fig. 3. Equilibrium reconstructed q -profile at 5.1 s during the snake oscillation.

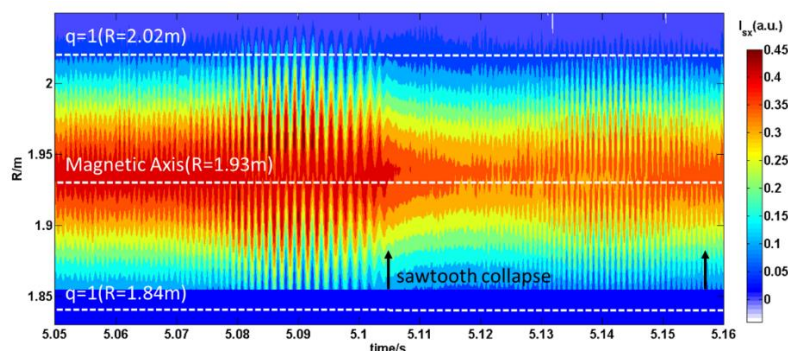


Fig. 4. Time evolution of raw SXR brightness profile of the pellet-induced snake.

3. Summary and discussion

In a summary, the pellet-induced snake oscillation was observed on the EAST for the first time after a fueling sized pellet penetrates inside the $q = 1$ surface. The snake phenomenon has a long lifetime with a helicity of $m = 1$ and $n = 1$. It's clear that the snake resided in a broad region between the magnetic axis and the $q = 1$ surface whose location derived from equilibrium reconstruction. The snake may be a possible way to mitigate the impurity accumulation and provides a new way to identify the position of the $q = 1$ surface on EAST. This investigation is beneficial for the understanding of the snake formation for EAST and future devices, like ITER and DEMO. Further experiments are needed to explore the nature of this process on EAST. And the triggering condition and mechanism of snakes should also be tested and discussed in the next campaign with more data support from the upgraded diagnostics, which have higher temporal and spatial resolution.

Acknowledgements

This work was partly supported by the JSPS-NRF-NSFC A3 Foresight Program in the field of Plasma Physics (NSFC: No.11261140328, NRF: No.2012K2A2A6000443).

References

- [1] Weller A *et al* 1987 *Phys. Rev. Lett.* 59 2303
- [2] Edwards A W *et al* 1988 Proc. 15th European Physical Society Conf. on Controlled Fusion and Plasma Physics p 342
- [3] Kupschus P *et al* 1988 Proc. 15th European Physical Society Conf. on Controlled Fusion and Plasma Physics p 143
- [4] Naujoks D *et al* 1996 *Nucl. Fusion* 36 671
- [5] Cristofani P *et al* 1994 Proc. 21st European Physical Society Conf. on Controlled Fusion and Plasma Physics p 210
- [6] Pecquet A L *et al* 1997 *Nucl. Fusion* 37 451
- [7] Kamada Y *et al* 1992 *Phys. Fluids B* 4 124
- [8] Gill R D *et al* 1992 *Nucl. Fusion* 32 7239
- [9] Delgado-Aparicio L *et al* 2013 *Phys. Rev. Lett.* 110 065006-1
- [10] Hu L Q *et al* 2003 *Plasma Physics and Controlled Fusion* 45 349
- [11] Li C Z *et al* 2012 *Fusion engineering and design* 89 99
- [12] Li J *et al* 2013 *Nat. Phys.* 9 817
- [13] Liu Y *et al* 2004 *Plasma Physics and Controlled Fusion* 46 455
- [14] Gill R D *et al* 1992 *Nucl. Fusion* 32 723
- [15] Shimomura Y Proc. 18th International Conference on Magnet Technology (Morioka City, Japan, 20-24 October 2003)

Preliminary result of impurity Density Evaluation on EAST

**X. D. Yang¹, L. Zhang¹, Z. Xu¹, J. Huang¹, Y. J. Chen, Y. M. Duan¹, P. F. Zhang¹,
P. Monier-garbet², N. Fedorczak², S. Morita³, T. Oishi⁴, Z. W. Wu¹, X. Z. Gong¹**

¹Institute of Plasma Physics Chinese Academy of Sciences (ASIPP), Hefei 230026, China

²Institute for Magnetic Fusion Research (IRFM), Cadarache, France

³National Institute for fusion science, Toki 509-5292, Gifu, Japan

⁴Department of fusion Science, Graduate University for Advanced studies, Toki 509-5292, Gifu,
Japan

Abstract

The evaluation of impurity densities in EAST (Experimental Advanced Superconducting Tokamak) plasma is carried out with combination of the impurity line emission intensities measured by a fast-response EUV spectrometer, a one-dimensional impurity transport code and the atomic data of photon emissivity coefficients (PECs) from Atomic Data and Analysis Structure (ADAS) database. In this paper, the preliminary results of impurity densities in EAST steady state H-mode discharge with high T_e ($T_e \sim 4.0$ keV) and upper single-null (USN) configuration (tungsten upper divertor) and Li coating wall conditioning is presented. The uncertainty of the results is discussed and the contributions from each impurity species to the effective ion charge (Z_{eff}) and radiation power loss are calculated. A set of discharges with different configuration and heating scheme are being further attempted.

1. Introduction

Since 2014 campaign, EAST have been operated with graphite lower divertor, molybdenum first wall, tungsten upper divertor. The intrinsic impurity contains low-high Z species, e.g. Li, C, N, O, Fe, Cu, Mo and W. The impurity density evaluation is urgently desired in EAST operation, which is very important for understanding of their influences on the plasma performance and the transport of high Z impurities especially for tungsten.

Generally, the impurity density profile $n_{\text{imp}}(r)$ can be obtained from the space-resolved measurement of impurity line intensity. The impurity transport coefficient in the core plasma is then determined by comparing the measured and simulated $n_{\text{imp}}(r)$ with 1D transport simulation. The impurity density could also be determined by comparing the measured and simulated chord-integrate intensity of impurity line emission. The measured intensity can be measured by an absolutely calibrated fast-response extreme ultra violet (EUV) spectrometer on EAST while the simulated intensity is calculated by combining the impurity transport code developed at IRFM and the data of ADAS. In this case, however, determining the profiles of transport coefficient is an empirical procedure, being derived from observation on existing tokamaks in the simulation code, under condition that the averaged transport coefficients are evaluated by a newly introduced analysis technique [2].

In this paper, the characteristic and performance of EUV spectrometer are described in section 2. In section 3, the 1D impurity transport code is exposed. In section 4, a new method to estimate the concentration of tungsten is introduced. In section 5, the resulting impurities concentrations are presented with their respective contributions to the radiation power (P_{rad}) and effective ion charge

(Z_{eff}) being addressed. In addition, the influence of transport coefficient on the impurity concentration deduced by the model that we establish is investigated and the uncertainty of the results is discussed. Finally, the paper is summarized in section 6.

2. Experimental setup

The fast-time-response EUV spectrometer has been newly constructed for monitoring several impurities in EAST discharges by measuring the EUV line emission in the wavelength range of 20-500 Å. A Schematic drawing of the EUV spectrometer working on EAST is illustrated in Fig. 1, showing that the sight line of the spectrometer is tilted upward to observe the center plasma. The high-time resolution (5ms) spectra have been successfully observed with good spectral resolution (0.22 Å @200 Å) by the present EUV spectrometer system.

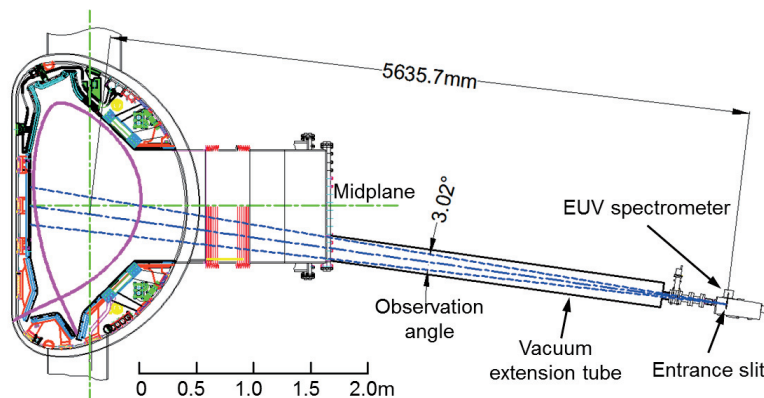


Fig. 1. Side view of fast-response EUV spectrometer installed on EAST. The elevation angle of the viewing axis is 8. The view area of the spectrometer is about 30cm in the vertical direction and 5 cm in the horizontal direction.

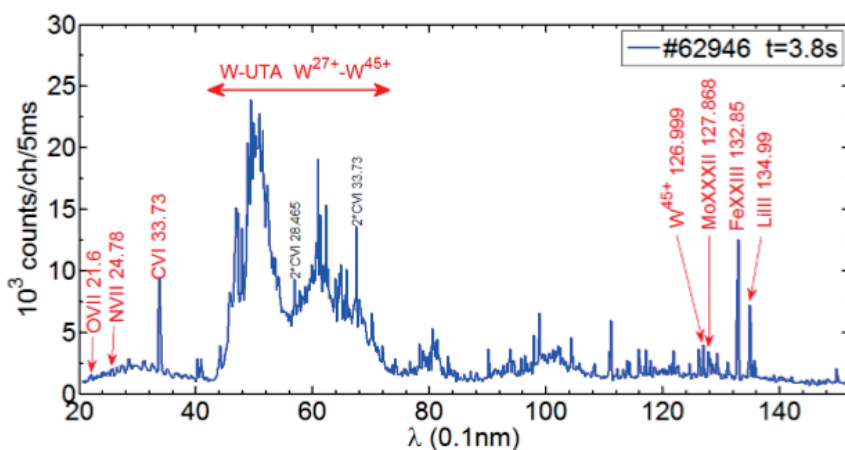


Fig. 2. Typical EUV spectra from EAST H-mode discharge in wavelength ranges of 20-150 Å

The ions charge states used to estimate the concentration of impurities are LiIII, CVI, NVII, OVII, FeXXIII, CuXXVI, MoXXXII and WXLVI, respectively, which correspond to the specific wavelengths shown in Fig. 2. Lyman α of H-like LiIII is strongly emitted due to the Li-coating for the wall conditioning. Line emissions from light impurities of H- and He-like carbon, nitrogen, and oxygen ions can be always observed at the shorter wavelength side of 20-40 Å while those from metallic impurities appear at the longer wavelength side. The UTA of W, whose structure is a

strong function of electron temperature, is clearly observed in the wavelength range of 45-70 Å consisting of ionization stage in W27+-W44+.

To realize the quantitative analysis of impurity line emissions, the absolute intensity of calibration of the EUV spectrometer is inevitably necessary. Here, the method of EUV bremsstrahlung continuum has been applied, which can give extremely accurate calibration factor as a function wavelength in the wavelength range of $20 \leq \lambda \leq 300$ Å shown in Fig. 3a. The time revolution of the absolutely calibrated intensities of impurities line emission is shown in Fig. 3b during the EAST discharge #62946 which is a typical ELMy H-mode discharge with lithium coating, USN configuration and high central electronic temperature.

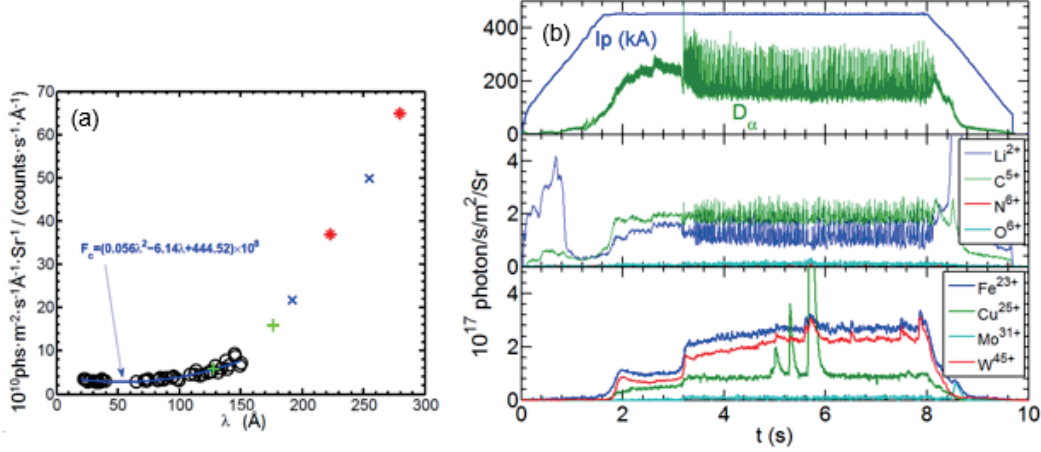


Fig. 3. (a) The calibration factor and fitting curve with polynomial expression (solid line) as a function of wavelength. (b) The time revolution of plasma current, divertor D_α and absolutely calibrated intensities of impurities line emissions during the EAST discharge #62946.

3. 1D impurity transport

As mentioned previously, the evaluation of impurity concentration can be obtained by comparing the measured and simulated the line-of-sight integrated value of the brightness. The latter could be calculated as

$$I_{calc} = \frac{1}{4\pi} \int n_f n_{tot} n_e PEC dl \quad (1)$$

where n_f is the fractional abundance of ions charging Z for a given element, n_e is radial profiles of electronic density, n_{tot} signifies the profile of the total density of the element Z and PEC here means the Photon emissivity coefficients which could be found in ADAS.

The detailed spatial distribution of n_f and n_{tot} could be calculated by solving the impurity transport equation:

$$\frac{\partial n_z}{\partial t} + \vec{\nabla} \cdot \vec{\Gamma}_z = S_{z-1} n_z n_{z-1} + \alpha_{z+1} n_z n_{z+1} - (S_z n_z n_z + \alpha_z n_z n_z) \quad 0 \leq z \leq Z \quad (2)$$

Where Γ_z is the radial impurity flux, which can be expressed by the pinch velocity V and diffusion coefficient D as: $\Gamma_z = -D \nabla \cdot n_z + V n_z$. S and α indicate ionization rate coefficient and recombination rate coefficient, respectively, supported by the ADAS.

Under the condition of steady case, deducing $\frac{\partial n_z}{\partial t} = 0$, the distribution of impurities is just determined by the process transport $\vec{\nabla} \cdot \vec{\Gamma}_z$ and the atomic process (ionization and recombination).

In this case, finite volume method is used to discretize the plasma in N cell in the radial direction during the simulation process. As refer to the boundary conditions, firstly, at the plasma edge, the flux is expressed as: $\Gamma_{edge}^z = S_s + \frac{n_z^{edge}}{\tau}$ where S_s and τ are the source for the neutral particles and the loss rate for all ions, respectively. Secondly, the flux in the center plasma is equal to zero. Assuming that the transport coefficients are in common for all charge states of a certain element, the total flux could be deduced as: $\Gamma_c = -D\nabla \cdot n_c + Vn_c = 0$ where n_c is the profile of total impurities density in the code. Considering the boundary condition, we can deduce the profile of the total impurities densities in the exponential form:

$$n_c = S_s \tau e^{(r - \frac{a^2}{r}) \frac{V}{2D}} \quad (3)$$

where a and r are the minor radius and the spatial position, respectively. So the n_{tot} in the equation (1) can be written as: $n_{tot} = A \cdot n_c$ where A is the coefficient that will be eventually calculated by comparing the simulated impurity emission line with the measured impurity emission line.

4. The methods to estimate the concentration of tungsten

In addition to comparing the measured and simulated chord-integrate intensity of impurity line emission to determine the concentration of tungsten, another way to evaluate is to apply the cooling rate of tungsten [1] shown in Fig. 4a and measurement of the radiation power of the tungsten from the fast bolometer.

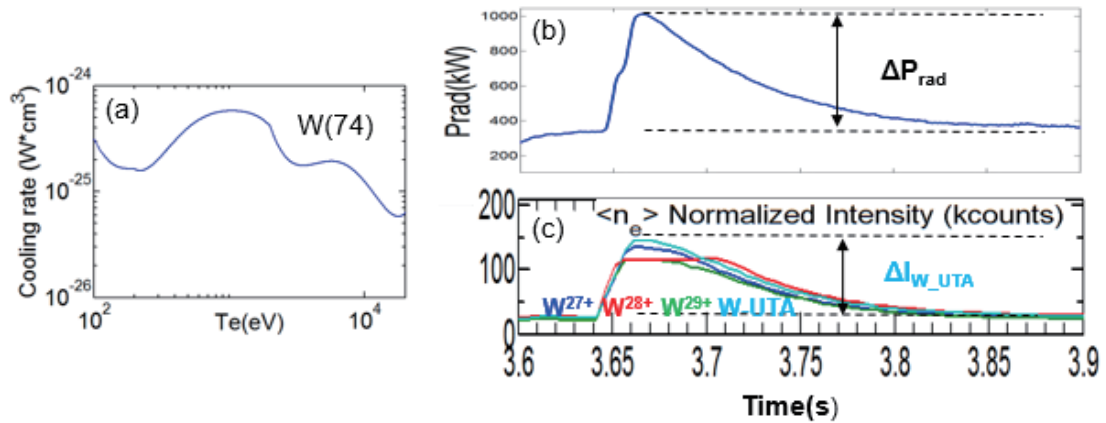


Fig. 4. (a) Cooling rate of tungsten as the function of electronic temperature. (b) and (c) are the time evaluations of the radiation power of plasma and the intensities of tungsten normalized to the line-averaged electronic density during 3.6-3.9s for the EAST discharge #63873, respectively.

This method has to be implemented in two steps. In the first step, the calibration factor P_{cali_W} should be calculated which could be expressed as: $P_{cali_W} = \Delta P_{rad} / \Delta I_{W-UTA}$ where ΔP_{rad} and ΔI_{W-UTA} are the increased radiation power loss by tungsten only and the correspondingly increased UTA of tungsten, respectively. Fig. 4b and Fig. 4c show another similar discharge whose contributor to the increased radiation power is just tungsten, which has been verified by examining the time evaluation of others impurities line emissions during the corresponding period.

In the second step, after obtaining the calibration factor, by comparing the simulated and the calibrated measured radiation power loss due to the tungsten, the concentration of the tungsten can

be estimated as expressed in the following equation:

$$P_W = A \int L_W(r) n_e(r) n_c(r) dV = P_{cali_W} I_{W-UTA} \quad (4)$$

where P_W , A , L_W , n_e , n_c , P_{cali_W} and I_{W-UTA} are power loss due to tungsten, the coefficient that we finally calculate, the cooling rate of tungsten, the profile of the impurity in the impurity transport code, the calibration factor and the intensity of tungsten UTA, respectively.

5. Results & Discussion

5.1 The result of concentration

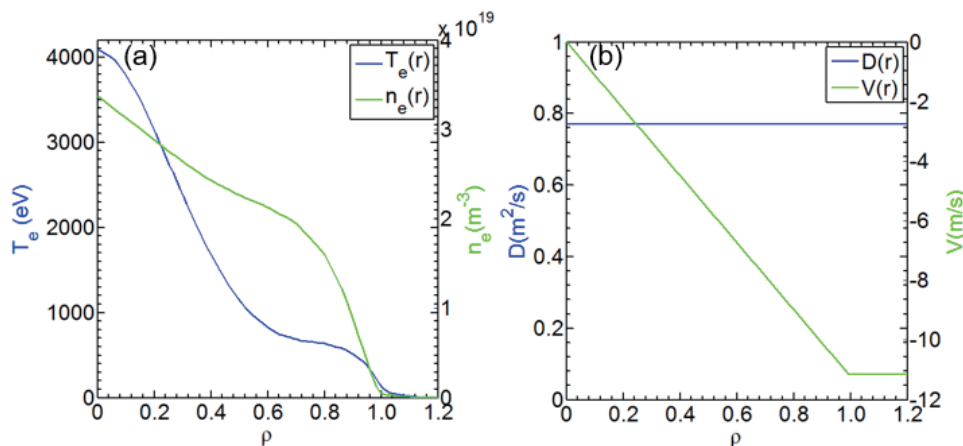


Fig. 5. (a) The profiles of n_e and T_e for the discharge #62946 at 3.8s. (b) The profiles of the pinch velocity V and diffusion coefficient D .

Table. 1. The concentration of the impurities for the EAST discharge 62946@3.8s

	Li	C	N	O	Fe	Cu	Mo	W		Total
								C_L	PEC	
$n_{imp}(0)/n_e(0)$	18	4.3	0.03	1.5	0.016	0.006	0.0004	0.002	0.008	23.9
	%	%	%	%	%	%	%	%	%	%
N_{imp}/N_e	10.	2.65	0.018	0.9	0.0096	0.0039	0.0002	0.001	0.005	14.5
	9%	%	%	%	%	%	6%	2%	6%	%

A typical ELMy discharge (#62946) with USN and Li coating in EAST steady state high T_e H-mode is firstly analyzed. This scenario with $I_p=450$ kA and $\bar{n}_e=3.0 \times 10^{19} \text{ m}^{-3}$ is achieved by electron cyclotron resonance heating (ECRH), LHCD consisting of the 2.45 GHz LHCD (LHI1) and 4.6 GHz LHCD (LHI1) and ion cyclotron resonance heating (ICRH) with PECH=0.5 MW, PLHI1=0.6 MW, PLHI2=2.1 MW, and PICRH=1.0 MW, respectively. Fig. 5a shows radial profiles of electron density measured by microwave reflectometry and electron temperature measured by Thomson scattering (TS) which are taken at 3.8s for discharge 62946. As shown in the Fig. 5b, the form of the radial profiles of D , whose average value \bar{D} is equal to 0.77 m^2/s , is flat and the inward pinch velocity V with the average value $\bar{V}=5.57$ m/s increase with the radius in the core plasma and is uniform at the edge plasma. In the following calculation, we suppose these profiles of transport coefficient are adapted to all the charge states for the different elements. By the method introduced in section 2, the results of concentrations of impurities relative to the

electronic density are shown in Table.1. N_{imp}/N_e and $n_{imp}(0)/n_e(0)$ stand for the concentration in the core plasma and that for the center plasma (N means the quantity of the particle), respectively. It can be seen that the concentration of lithium is in the order of 10%, which exceeds much more than expected and is comparable to that of carbon. Besides, the concentration of tungsten is in 10^{-5} % both by welding cooling rate (C_L) and PEC, although, the result of the former is four times higher than that of the latter. As for the reliability of the results, we will discuss in the section of 5.3 and 5.4.

Generally speaking, the simulation results suggest that impurities accumulate towards the center, accompanied by a reduction of the density of less ionized peripheral ions as shown in the Fig. 6, especially for the medium and high Z impurities, which have been observed in the experiments.

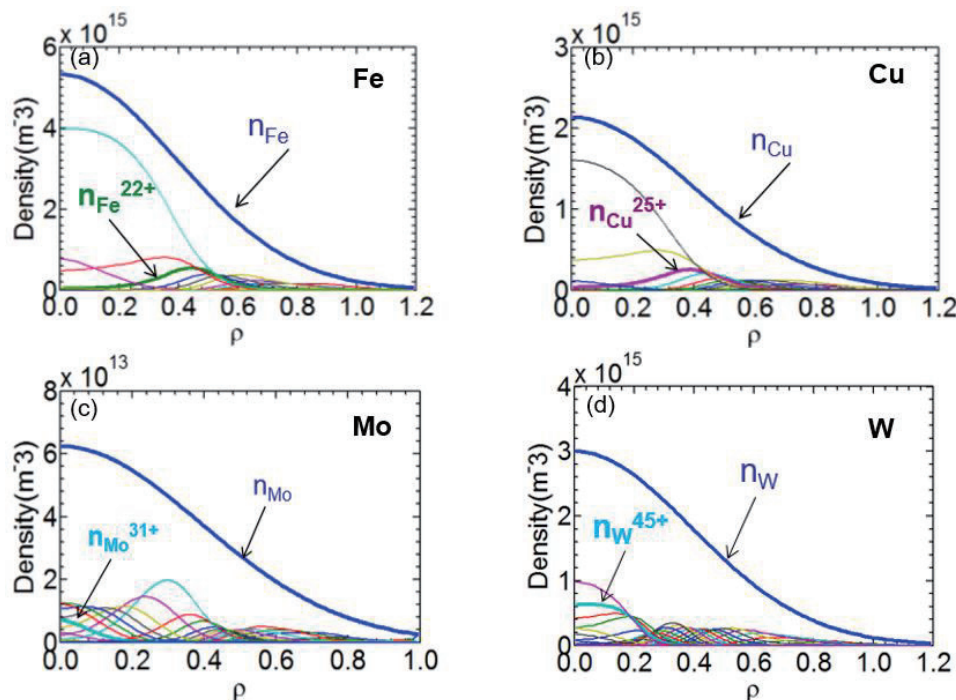


Fig. 6. The radial profiles of the total impurities density and the density of the relevantly different charge states (a). Fe. (b). Cu. (c) Mo. (d). W.

5.2 P_{rad} & Z_{eff}

Table. 2. ΔP_{rad} and ΔZ_{eff} for the EAST discharge 62946@3.8s

	Li	C	N	O	Fe	Cu	Mo	W		Total
								C_L	PEC	
$\Delta P_{rad}(kW)$	2.9	4.7	0.1	4.8	9.1	3.2	0.7	61.9	13.6	87/39
ΔZ_{eff}	0.95	0.93	0.008	0.56	0.044	0.021	0.001	0.029	0.135	3.5

For the purpose of verifying the rationality of the results, the contributions to Z_{eff} and the radiation power P_{rad} of the impurities are evaluated respectively by using the following calculation:

$$\Delta Z_{eff} = \sum_j Z_j^2 N_j / N_e \quad (5)$$

$$\Delta P = \int L(r) n_e(r) N_z(r) dV \quad (6)$$

with j the ionic charge states, the Z_j the ionic charge, N_j the quantity of the ions, N_e the quantity of the electron, L the cooling rate which could be found in ADAS and seen [1], n_e the electronic

density and N_z the total impurity density for element Z .

The final results are shown in Table 2, which could be concluded that the radiation power of the core plasma is dominated by tungsten and iron and the mainly contributors to the Z_{eff} are low impurities especially the carbon, lithium and oxygen. Due to the accumulation of the medium and high impurities in the center plasma, excessive power is radiated by them in that region as shown in Fig. 7a, which may decrease the overall plasma performance as well as the plasma duration. The Fig. 7b shows the simulated profiles of total Z_{eff} , the contributions to the Z_{eff} of carbon and lithium.

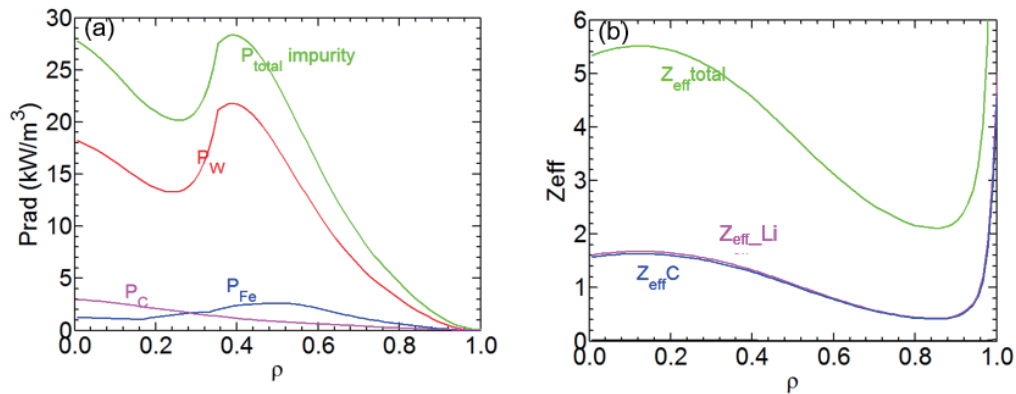


Fig. 7. (a) The profiles of density of the radiation power of all impurities $P_{total\ impurity}$ (green), of the tungsten (red) by using cooling rate, of iron (blue) and of carbon (marron). (b) The profiles of Z_{eff} of all impurities (green), of lithium (marron) and of carbon (blue).

5.3 The influence of transport coefficients

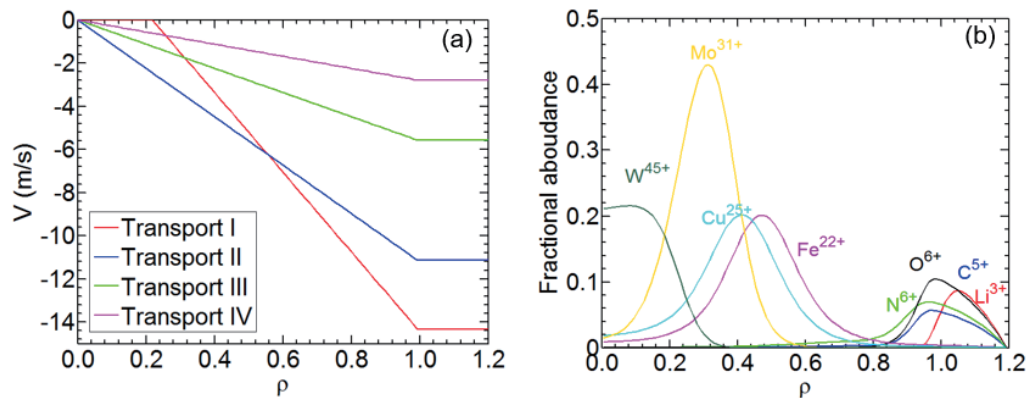


Fig. 8. (a) The different profiles of pinch velocity V . (b) The profiles of the fractional abundance of different impurities.

We vary the radial profiles of pinch velocity as shown in Fig. 8a fixing the profile of diffusion coefficient D to investigate the influence of transport in our established model. The Table. 3 show the result of the concentration of lithium, carbon and iron for the different transport cases including the coronal equilibrium model. It can be observed that the concentration of lithium is highly sensitive to the value V and also its profile, however, the variation of the concentration of iron isn't obvious, which could be concluded that the veracity of concentration of high and medium Z impurities is higher than that of the low Z impurities. Besides, the distributions of the

fractional abundance of ions of high and medium Z impurities, used to estimate the concentration, are located in much more center region while those of low Z impurities distribute in the plus edge region as shown in Fig. 8b.

Table. 3. The results of the concentration of the different transport model

		Transport I	Transport II	Transport III	Transport IV	Coronal equilibrium
Li	$n_{\text{imp}}(0)/n_e(0)$	17.4%	18.3%	4.3%	1.8%	5.2%
	N_{imp}/N_e	13.4%	10.7%	4.2%	2.4%	10.2%
C	$n_{\text{imp}}(0)/n_e(0)$	3.5%	4.4%	2.1%	1.3%	1.6%
	N_{imp}/N_e	2.7%	2.6%	2.1%	1.7%	4.5%
Fe	$n_{\text{imp}}(0)/n_e(0)$	0.012%	0.016%	0.012%	0.0098%	0.0091%
	N_{imp}/N_e	0.0089%	0.0093%	0.011%	0.013%	0.026%

5.4 discussion of the uncertainty

The uncertainty arise from three aspects. Firstly, since light impurities are fully ionized in the hot plasma core and therefore do not emit any line radiation and are not observed by conventional spectroscopy, the application of the H- and He-like ions of low Z impurities, especially lithium, to evaluate the central light impurity content and behavior, which is obviously unreliable. However this problem can now be experimentally solved by using the optical excitation of fully stripped light ions via charge exchange with neutrals from neutral beams. In addition, the variation of D , V and their profiles need to be considered for different impurities. Secondly, the error of experimental measurement is inevitable. The measurement of T_e profile at plasma edge is particularly important for low Z impurities concentration. Besides, the appearance of W-UTA in 20-45Å influence the intensity of weak lines e.g. NVII, OVII and The line OVII (21.6 Å) is contaminated by the line OVII (21.8 Å) because of the limitation of the spectra resolution of EUV_Long at short wavelength range, which will be carefully checked with the spectra recorded by EUV_short. Lastly, as for the evacuation of the tungsten concentration, there are still uncertainty of ionization rate and recombination rate, especially the latter one. Until now, we don't know the uncertainty of the cooling rate for W and PEC for W line. Moreover, the calibration between the UTA of tungsten and its corresponding radiation power need to be enhanced.

6. Conclusion

The impurity density in EAST stead state high Te H-mode discharge with USN and Li coating is preliminarily evaluated. The results of concentration of medium Z or high Z impurity is more accurate while the uncertainty for low Z impurity is relatively higher. Based on the result, the Zeff is mainly contributed by C and Li whose concentration is higher than our expectation. Tungsten density is evaluated by using cooling rate and PEC, and its concentration is in the 10^{-5} order relative to the electronic density, and its contribution to radiation power loss is dominate over other impurities.

More discharges with different condition will be investigated, including different configuration and heating schemes. Impurity density evaluation of low- Z impurity will be compared with the

result from charge exchange recombination spectrometer diagnostic. Since the temporal evolution of the chord averaged impurity emission was highly sensitive to variation in the transport coefficient, which led to an investigation of the degree to which temporal evolutions could be used to determine D and V , more accurate transport coefficient profiles will be applied in the simulation to calculate the contents of impurities and their transport behavior in the core plasma. The more precious atomic data of tungsten will be used to improve the accuracy of the density of W .

Acknowledgements

This work was supported by the National Magnetic Confinement Fusion Science Program of China (Grant Nos. 2014GB124006, 2013GB105003, and 2015GB101000) and National Natural Science Foundation of China (Grant Nos. 11575244, 11105181, and 11305207) and was partly supported by the JSPS-NRF-NSFC A3 Foresight Program in the field of Plasma Physics (NSFC No. 11261140328, NRF No. 2012K2A2A6000443).

References

- [1] W. K. LEUNG, W. L. ROWAN and J. C. WILEY, Plasma Physics and Controlled Fusion, Vol. 28, No.12A, pp. 1753 to 1763. 1986.
- [2] Ling Zhang, Shigeru Morita and Zong Xu, REVIEW OF SCIENTIFIC INSTRUMENTS 86, 123509, 2015.
- [3] C De Michelis and M Mattioli, Rep. Prog. Phys, Vol 47, pp 1233-1346, 1984, Printed in Great Britain.
- [4] N. Fedorczak, P. Monier-Carbet and T. Pütterich, Journal of Nuclear Materials 463 (2015) 85-90.
- [5] D. E. POST, R. V. JENSEN, C. B. TARTER, W. H. GRASBERGER, W. A. LOKKE, ATOMIC DATA AND NUCLEAR DATA TABLES 20, 397-439 (1977).
- [6] N J Peacock, R Barnsley, N C Hawkes, K D Lawson, M G O'Mullane, Diagnostics for Experimental Thermonuclear Fusion Reactors, 291-305 (1995)
- [7] D.G. WHYTE, M.R. WADE, D.F. FINKENTHAL, K.H. BURRELL, P. MONIER-GARBET, NUCLEAR FUSION, Vol. 38, No. 3 (1997).
- [8] Ling Zhang, 'Experimental study of impurity Transport Coefficient Based on the time Behaviour Measurement of impurity Line Intensity on EAST ', A3 seminar, Yinchuan, China, 17-20 May 2016.

Impact of the perpendicular diffusivity on impurity transport in the stochastic layer of LHD in comparison with EUV emission measurements

S. Y. Dai^{1,2*}, M. Kobayashi^{1,3}, G. Kawamura¹, H. M. Zhang³, S. Morita^{1,3}, T. Oishi^{1,3}, Y.

Feng⁴, Y. Suzuki^{1,3} and the LHD experiment group¹

¹ National Institute for Fusion Science, Toki 509-5292, Japan

² Key Laboratory of Materials Modification by Laser, Ion and Electron Beams (Ministry of Education), School of Physics and Optoelectronic Technology, Dalian University of Technology, Dalian 116024, PR China

³ SOKENDAI (The Graduate University for Advanced Studies), Toki 509-5292, Japan

⁴ Max-Planck-Institute für Plasmaphysik, D-17491 Greifswald, Germany

Abstract

The transport properties and line emissions of the intrinsic carbon in the stochastic layer of the Large Helical Device have been investigated with the three-dimensional edge transport code EMC3-EIRENE. The simulations of impurity transport and emissivity have been performed to study the dedicated experiment in which the carbon emission distributions are measured by a space-resolved EUV spectrometer system. A discrepancy of the CIV impurity emission between the measurement and simulation is obtained, which is studied with the variation of the perpendicular transport coefficient. The simulation results have shown that the deeper penetration of impurity into the higher plasma density region due to the enhanced D_{imp} is responsible for the change of emission pattern as well as the intensity.

1. Introduction

The transport behavior of impurities in the edge plasma is one of the most critical issues for the operation and performance of the fusion devices. In the Large Helical Device (LHD), the complicated three-dimensional (3D) structure of the stochastic magnetic field in the edge region leads to the impurity transport characteristics being quite different from that in tokamaks with 2D magnetic configuration. The transport properties of edge impurity are investigated in LHD by using a space-resolved extreme ultraviolet (EUV) spectrometer system [1-2]. In the present work, the 3D edge transport code EMC3-EIRENE [3-4] is used to study the transport behavior and line emissions of the intrinsic carbon in the stochastic layer of LHD. Recently, the development of the computational grid for the divertor leg regions of LHD has been achieved [5], which results in a good description of the plasma and impurity transport in the divertor leg regions of LHD.

2. Results and discussion

The trajectories of the inboard and outboard X-point regions are indicated with blue dotted lines and magenta solid lines in Fig. 1 (a), respectively. It can be seen that the CIV impurity emission is stronger for the inboard X-point region compared to the outboard one as shown in Fig. 1 (a). Figure 1 (b) shows the 2D distributions of CIV impurity emissions by EMC3-EIRENE modelling for the default case. Figure 1 (b) shows that the CIV impurity emission for the outboard X-point region is stronger between the magenta solid lines compared to the inboard one between the blue dotted lines. Here, a clear discrepancy of the CIV line emission pattern can be seen between the measurement and simulation.

3.1 The effect of the ion thermal force on CIV line emission

First, two important definitions are introduced for studying the difference between the experiment and modelling. The line emission ratio is defined as the ratio of the integrated value of the outboard X-point region emission (between the magenta solid lines in Fig. 1 (b)) to that of the inboard X-point region emission (between the blue dotted lines in Fig. 1 (b)). This line emission ratio can well describe the distribution pattern of inboard and outboard emissions quantitatively. The absolute line emission of CIV impurity is integrated over the area in Fig. 1, which can be used to make a rigorous quantitative comparison with the total intensity of CIV impurity emission measured in the experiment.

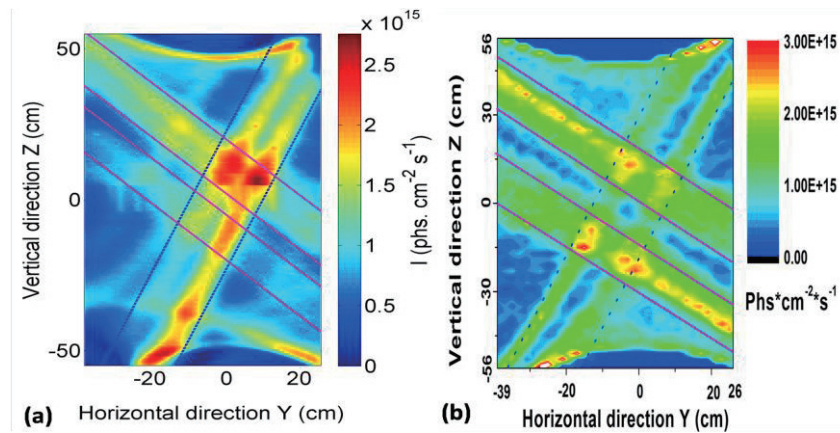


Fig. 1 2D distributions of CIV impurity emissions obtained from the experiment (a) and EMC3-EIRENE simulation (b).

The perpendicular transport is important for impurity transport due to the large connection length and magnetic field stochasticity in LHD compared to tokamaks. The influence of the perpendicular diffusivity D_{imp} is studied in figure 2 which shows the line emission ratios and absolute values of CIV impurity emission as a function of D_{imp} . The black dashed lines indicate the default value of the impurity perpendicular diffusivity ($D_{\text{imp}} = 0.4 \text{ m}^2 \text{ s}^{-1}$) in the modelling. It can be seen that the increase of D_{imp} leads to a reduction of the line emission ratio and an increase of the absolute CIV impurity emission. For the $D_{\text{imp}} \sim 2 \text{ m}^2 \text{ s}^{-1}$, the simulation results can well reproduce the measured pattern of CIV impurity emission.

However, the absolute CIV impurity emission still has a difference between the simulation results and measured value.

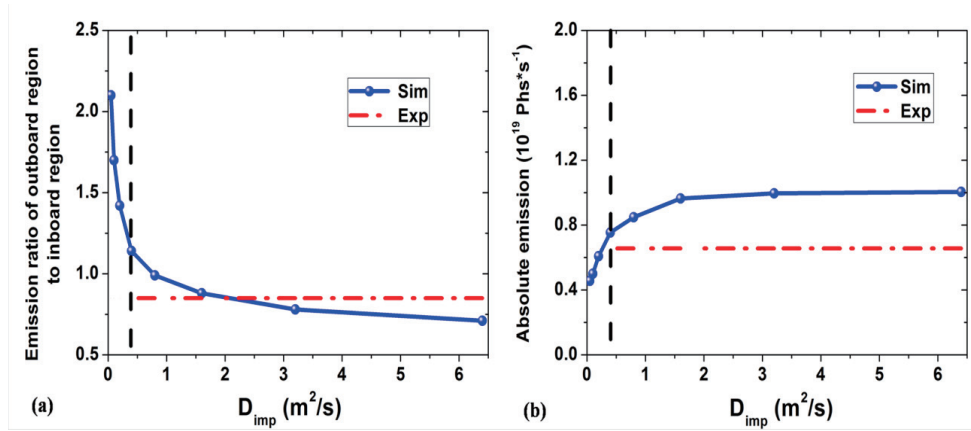


Fig. 2 The line emission ratios (a) and absolute values (b) of CIV line emission as a function of the perpendicular diffusivity D_{imp} . The black dashed lines indicate the default case of $D_{imp} = 0.4 \text{ m}^2 \text{ s}^{-1}$ in the modelling.

Figure 3 presents the 2D distributions of CIV line emission at the toroidal angle of $\varphi=18^\circ$ for the two extreme cases, $D_{imp} = 0.05$ and $6.40 \text{ m}^2 \text{ s}^{-1}$. The open field lines in the stochastic layer of LHD exhibit a rather complicated structure, yielding a mixture of short and long connection lengths from several meters to several hundred meters. The change of flux tubes, along which the parallel transport of C^{3+} is executed, would have an impact on the distribution of CIV impurity emission due to the cross field diffusion. It is seen that the CIV line emission becomes smooth at the outboard region with the larger D_{imp} in figure 3. This is due to the reduction of the peak values of C^{3+} density with enhancing the perpendicular transport. Therefore, the CIV line emission has a wider distribution at the outboard region for $D_{imp} = 6.40 \text{ m}^2 \text{ s}^{-1}$ as shown in figure 3 (b).

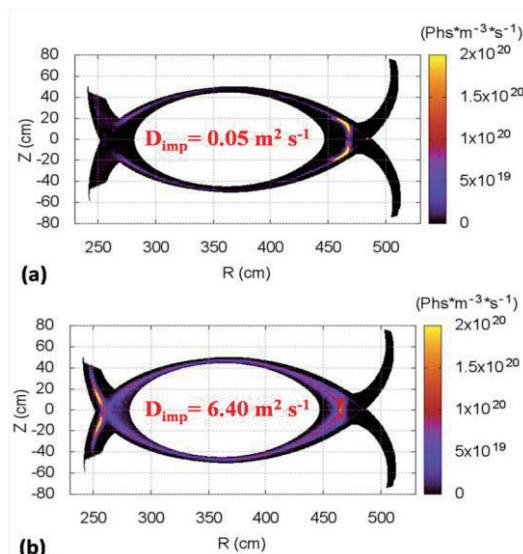


Fig. 3 2D distributions of CIV line emissions at the toroidal angle of $\varphi = 18^\circ$ for $D_{imp} = 0.05 \text{ m}^2 \text{ s}^{-1}$ (a) and $D_{imp} = 6.40 \text{ m}^2 \text{ s}^{-1}$ (b).

3. Summary and outlook

The 3D edge transport code EMC3-EIRENE is used to investigate the transport properties and line emissions of the impurity in the stochastic layer of LHD. The 2D distribution of CIV line emission is simulated and compared with the emission distribution measured by a space-resolved EUV spectrometer system. For the default case of the simulations, the 2D distribution pattern of CIV impurity emissions by EMC3-EIRENE modelling shows a deviation from the experimental measurement. The effects of the impurity perpendicular diffusivity have been studied to check their influences on the CIV line emissions. Increase in D_{imp} leads to the increase of the inboard emission, which brings the simulation results closer to the experiments. This is mainly due to the enhanced penetration of impurity into the high plasma density region at the inboard divertor legs. Thus, the overall intensity also increases slightly with the increasing D_{imp} , by a factor of ~ 1.5 . A more comprehensive study of impurity source distribution at the first wall is foreseen in the future. The contribution of the first wall impurity source perhaps plays an important role to determine the distribution pattern and absolute intensity of CIV impurity emission.

Acknowledgements

This work was partly supported by the JSPS-NRF-NSFC A3 Foresight Program in the field of Plasma Physics (NSFC: No.11261140328).

References

- [1] S. Morita, et al., J. Nucl. Mater. 463, 644-648 (2015).
- [2] H. M. Zhang, et al., Plasma. Fus. Res. 10, 3402038 (2015).
- [3] Y. Feng, et al., Contrib. Plasma Phys. 44, 57 (2004).
- [4] D. Reiter, et al., Nucl. Fusion 47, 172 (2005).
- [5] G. Kawamura, et al, Contrib. Plasma Phys. 54 (4-6), 437-441 (2014).

Long-lived pressure-driven MHD mode in KSTAR plasmas

S. G. Lee¹, J. Seol¹, H. H. Lee¹, A. Y. Aydemir¹, L. Terzolo, K. D. Lee,
Y. S. Bae¹, J. G. Bak¹, G. H. Choe², G. S. Yun², and J. W. Yoo³

¹ National Fusion Research Institute, Daejeon, Korea

² Pohang University of Science and Technology, Pohang, Korea

³ Korea University of Science and Technology, Daejeon, Korea

Email : sglee@nfri.re.kr

An extremely long-lived pressure-driven magnetohydrodynamic (MHD) instability has been observed in KSTAR tokamak under a long-pulse and steady-state operation. The measured long-lived MHD mode is sustained for the full duration of a discharge much longer than any dynamical or dissipative time scales in the system, and it is associated with an $m = 2$ and $n = 1$ mode causing reduction of the toroidal rotation.

1. Introduction

The best-known example of long-lived structure is probably the Jupiter's Red Spot that has been around for many centuries, although the expected life-time of such a vortex pattern is estimated to be in decades [1]. Although on temporal and spatial scales much smaller than Jovian, laboratory plasmas are also known to exhibit long-lived structures that persist for periods much longer than expected from simple dynamical or transport analyses. The physics origin of these observations in fusion plasmas is almost definitely very different from that of the Red Spot; however, their long-time persistence is similarly not very well-understood. The snake modes seen on spatiotemporal plots of soft X-ray signals on rational magnetic surfaces are the earliest examples of long-lived structures in tokamak plasmas [2]. They are attributed to an excess density or impurity concentration trapped in an $m = 1$ magnetic island. Recently, we have reported on the observation of an extremely long-lived MHD mode in the plasma core that is associated with an $m = 2$ and $n = 1$ mode in KSTAR [3]. In this presentation we continuously show further experimental data based on the Ref. 3.

2. Experimental results

Figure 1 shows time traces of the main plasma parameters for a long-pulse discharge with a steady-state operation. The plasma current is 0.5 MA and it is well controlled until the discharge is finished. The electron density (n_e) from a single-channel mm-wave interferometer and total stored energy (W) from a diamagnetic loop are almost constant during the plasma current flat-top period. The core toroidal rotation (V_ϕ) and ion temperature (T_i) from an X-ray imaging crystal spectrometer (XICS) [4] is also shown in Fig. 1. The electron temperature (T_e) from an electron cyclotron emission (ECE) is shown a large coherent oscillation, which is analyzed as a long-lived pressure-driven MHD mode [3]. The toroidal rotation and ion temperature gradually decrease during the time long-lived pressure-driven MHD mode exist as shown in Fig. 1.

Note that the long-lived pressure-driven MHD mode disappears when the ECH is turned off although the ECH turning off time is accidentally coincidence with the plasma current ramp down as shown in Fig. 1. This will be clarified with another similar discharge later. The

central electron temperature and its fluctuations measured from the ECE diagnostic dramatically reduced as soon the ECH is turned off and, the core V_ϕ recovers at the same time. It is noted that the long-lived saturated magnetic fluctuation is measured when on-axis ECH is applied together with early NBI heating during the plasma current ramp-up period, which indicates it originates from the pressure gradient induced by ECH injection [3].

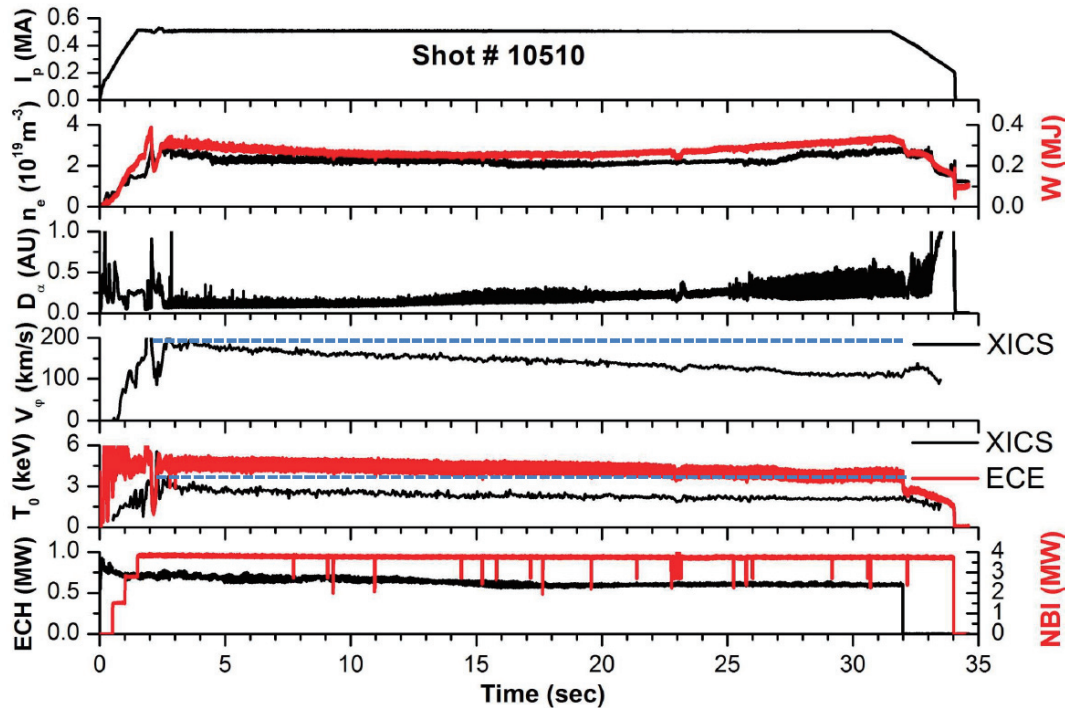


Fig. 1. Characteristic of the plasma parameters for long-pulse and steady-state discharge.

The frequency spectrum of the long-lived pressure-driven MHD mode is illustrated in Fig. 2. The full discharge spectrogram of the electron temperature oscillation measured by the ECE is clearly shown whereas the magnetic fluctuation from the Mirnov coil is shown up to 20 s since the measurement time is limited due to the high sampling rate.

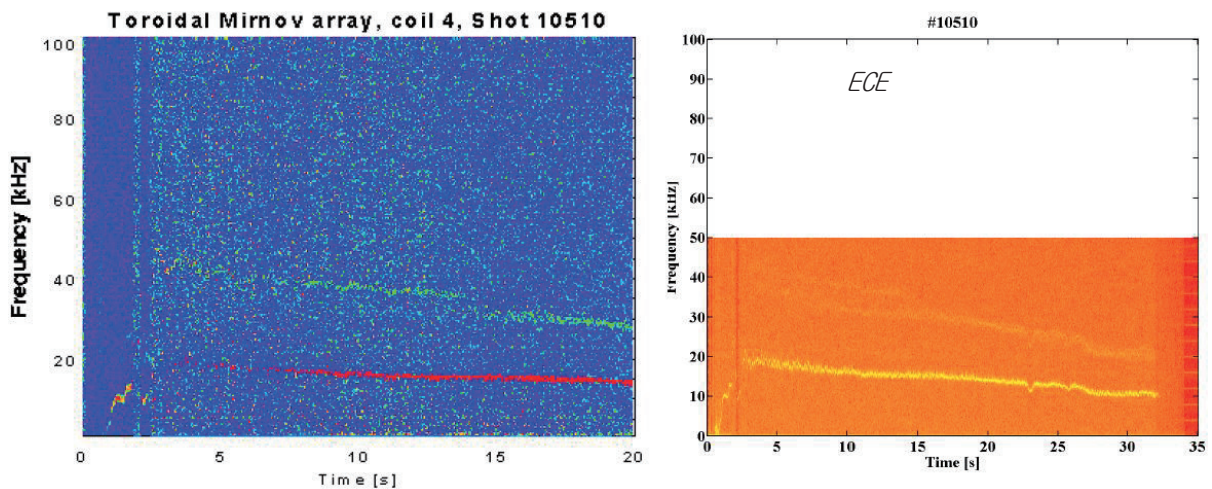


Fig. 2. Time evolution of the frequency spectrum.

Figure 3 shows the plasma parameters under similar steady-state operation such as shot 10510 with ECH off time is conducted during the plasma current flat-top. The long-lived pressure-driven MHD mode is not generated without ECH injection since there are no corresponding modes after ECH off time at 3 s, which is shown in the frequency spectrum of the ECE measurement shown in Fig. 3.

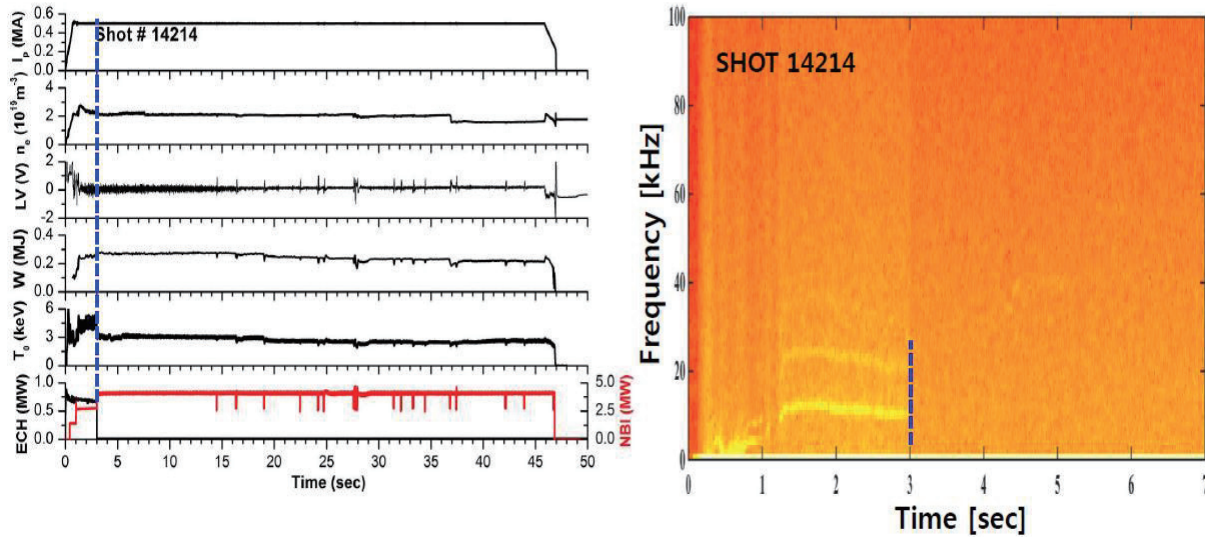


Fig. 3. Time traces of the plasma parameters for long-pulse discharge (left) and time evolution of the frequency spectrum (right).

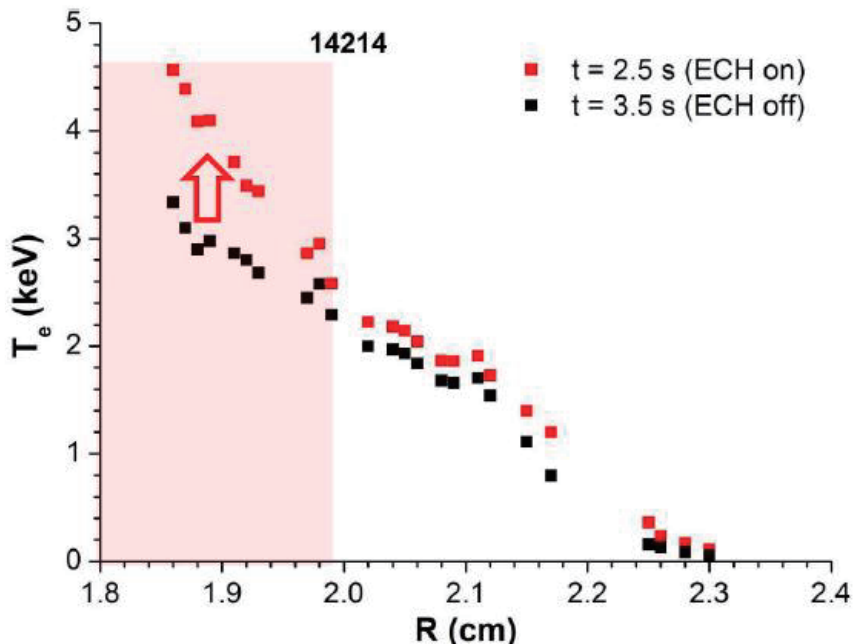


Fig. 4. The electron temperature profiles with and without ECH injection.

The pressure-driven feature for the long-lived MHD mode is elucidated from the electron temperature profiles with and without ECH injection as shown in Figure 4. The electron temperature and temperature gradient in the core region increased a lot during ECH injection.

3. Conclusion

The extremely long-lived pressure-driven MHD instability has been observed in KSTAR tokamak. The measured long-lived pressure-driven MHD mode is sustained for the full duration of a discharge much longer than any dynamical or dissipative time scales in the system, and it is associated with an $m = 2$ and $n = 1$ mode causing reduction of the toroidal rotation and ion temperature. Future fusion-power machines will be operated in the long-pulse and steady-state operation. Therefore, it is important to understand extremely long-lived pressure-driven MHD mode reported in this paper since it makes an essential contribution to core confinement and stability in steady-state burning plasma devices such as ITER and DEMO.

Acknowledgement

This research was supported by Ministry of Science, ICT, and Future Planning under KSTAR project and was partly supported by the JSPS-NRF-NSFC A3 Foresight Program (NRF No. 2012K2A2A6000443).

References

- [1] T. Maxworthy and L. G. Redekopp, *Nature* **260**, 509 (1976).
- [2] A. Weller, A. D. Cheetham, A. W. Edwards, R. D. Gill, A. Gondhalekar, R. S. Granetz, J. Snipes, and J. A. Wesson, *Phys. Rev. Lett.* **59**, 2303 (1987).
- [3] S. G. Lee, J. Seol, H. H. Lee, A. Y. Aydemir et al., *Phys. Plasmas* **23**, 052511 (2016).
- [4] S. G. Lee, J. G. Bak, U. W. Nam, M. K. Moon, Y. Shi, M. Bitter and K. Hill, *Rev. Sci. Instrum.* **81**, 10E506 (2010).

Hamiltonian particle-in-cell methods for Vlasov-Maxwell equations

Y. He^{1,2}, Y. Sun³, J. Liu^{1,2}, H. Qin^{1,4}, R. Zhang^{1,2}, J. Xiao^{1,2}

¹School of Nuclear Science and Technology and Department of Modern Physics, University of Science and Technology of China, Hefei, Anhui, China

²Key Laboratory of Geospace Environment, CAS, Hefei, Anhui, China

³LSEC, Academy of Mathematics and Systems Science, CAS, Beijing, China

⁴Plasma Physics Laboratory, Princeton University, Princeton, New Jersey, USA

Abstract

Hamiltonian particle-in-cell methods are developed for Vlasov-Maxwell equations. The criteria are presented for the spatial discretisation such that the semi-discrete system possesses a discrete non-canonical Poisson structure. We apply a Hamiltonian splitting method to the semi-discrete system in time, then the resulting algorithm is Poisson preserving and explicit. The conservative properties of the algorithm guarantee the efficient and accurate numerical simulation of the Vlasov-Maxwell equations over long-time.

1. Introduction

The collective motion of particles in an electromagnetic fields ($\mathbf{E}(\mathbf{x}, t)$, $\mathbf{B}(\mathbf{x}, t)$) can be described by the Vlasov-Maxwell (VM) equations. The system of dimensionless VM equations regardless of the relativistic effects is

$$\frac{\partial f}{\partial t} + \mathbf{v} \cdot \frac{\partial f}{\partial \mathbf{x}} + (\mathbf{E} + \mathbf{v} \times \mathbf{B}) \cdot \frac{\partial f}{\partial \mathbf{v}} = 0, \quad (1a)$$

$$\nabla \times \mathbf{B} = \int_{\Omega_v} f \mathbf{v} d\mathbf{v} + \frac{\partial \mathbf{E}}{\partial t}, \quad (1b)$$

$$\nabla \times \mathbf{E} = -\frac{\partial \mathbf{B}}{\partial t}, \quad (1c)$$

$$\nabla \cdot \mathbf{E} = \int_{\Omega_v} f d\mathbf{v}, \quad \nabla \cdot \mathbf{B} = 0, \quad (1d)$$

where $f(\mathbf{x}, \mathbf{v}, t)$ is the distribution function of position \mathbf{x} and velocity \mathbf{v} at time t . Solving the VM equation using particle-in-cell (PIC) methods has been an important tool in modern plasma physics and accelerator physics for decades. In the PIC method, the Vlasov equation is solved by following particles' trajectories on Lagrangian grids, and the fields are approximated on Eulerian grids. In most cases, the most concerned characteristics of the VM equations is the long term behaviours and multi-scale structures. Conventionally, the VM equations are solved by standard numerical methods, such as 4-th order Runge-Kutta methods. The local energy-momentum conservation laws can not be preserved, and after long time of computation the accumulation of the error leads to non-reliable results. To overcome this difficulty, we apply geometric integration methods.

Geometric integration methods [1] are designed to conserve the intrinsic properties inherited by the original systems, including the Hamiltonian (symplectic and Poisson) structure, invariant phase space volume, etc. It is known that the continuous VM equations can be written in the Hamiltonian formulation by the Morrison-Marsden-Weinstein (MMW) bracket [3],

$$\frac{\partial \mathcal{F}}{\partial t} = \{\{\mathcal{F}, \mathcal{H}\}\},$$

with \mathcal{F} being any functional defined on $\mathcal{MV} = \{(f, \mathbf{E}, \mathbf{B}) | \nabla \cdot \mathbf{B} = 0, \nabla \cdot \mathbf{E} = \int f d^3\mathbf{v}\}$, and \mathcal{H} being the global energy functional. The MMW bracket is Poisson and is preserved by the exact solution of the VM system. Recently, Hamiltonian (symplectic) algorithms for the VM equations has been developed [4, 5]. In this paper, we further study Hamiltonian methods for the VM equations by combining the PIC technique with finite element methods (FEM).

2. Fully-discrete Vlasov-Maxwell equations

As a start, the distribution function f is discretised using the Klimontovich representation,

$$f(\mathbf{x}, \mathbf{v}, t) = \sum_s f_s = \sum_s \omega_s \delta(\mathbf{x} - \mathbf{X}_s) \delta(\mathbf{v} - \mathbf{V}_s), \quad (2)$$

where $(\mathbf{X}_s, \mathbf{V}_s)$ is the s -th particle's coordinate in phase space. Substituting Eq. (2) into the Vlasov equation (1a) leads to the particles' equations,

$$\dot{\mathbf{X}}_s = \mathbf{V}_s, \quad \dot{\mathbf{V}}_s = \int_{\Omega_x} (\mathbf{E}(\mathbf{x}, t) + \mathbf{V}_s \times \mathbf{B}(\mathbf{x}, t)) \delta(\mathbf{x} - \mathbf{X}_s) d\mathbf{x}, \quad (3)$$

For Maxwell's equations, we discretise the problem by conforming finite element methods. Consider the problem with perfect conducting boundary conditions. Let $\mathcal{T}_h = \{K\}$ be regular partitions of the spatial domain. Suppose that the field variables are approximated by the piecewise polynomials $\mathbf{E}_h \in \mathcal{E}_h$ and $\mathbf{B}_h \in \mathcal{B}_h$ respectively, with

$$\mathbf{E}_h(\mathbf{x}, t) = \sum_{j=1}^{N_e} E_j(t) \mathbf{W}_j^e(\mathbf{x}), \quad \mathbf{B}_h(\mathbf{x}, t) = \sum_{j=1}^{N_b} B_j(t) \mathbf{W}_j^b(\mathbf{x}), \quad (4)$$

where $\{\mathbf{W}^e(\mathbf{x})\}_{j=1}^{N_e}$ are the basis functions. The approximate variational problem is then to solve for $(\mathbf{E}_h, \mathbf{B}_h)$ such that

$$\begin{aligned} (\partial_t \mathbf{E}_h, \Phi) &= (\mathbf{B}_h, \nabla \times \Phi) - \left(\sum_s \mathbf{V}_s \delta(\mathbf{x} - \mathbf{X}_s), \Phi \right), \quad \forall \Phi \in \mathcal{E}_h, \\ (\partial_t \mathbf{B}_h, \Psi) &= -(\nabla \times \mathbf{E}_h, \Psi), \quad \forall \Psi \in \mathcal{B}_h. \end{aligned} \quad (5)$$

Here $(\mathbf{f}, \mathbf{g}) = \int_K \mathbf{f} \cdot \mathbf{g} d\mathbf{x}$ for any two vector functions \mathbf{f} and \mathbf{g} . Substituting Eq. (4) into Eq. (5) and taking $\Phi = \mathbf{W}_i^e$, $\Psi = \mathbf{W}_i^b$ for every $i = 1 \dots N_e(N_b)$ gives the discretisation of Maxwell's equations,

$$\begin{aligned} \sum_{j=1}^{N_e} (\mathbf{W}_j^e, \mathbf{W}_i^e) \partial_t E_j &= \sum_{j=1}^{N_b} (\mathbf{W}_j^b, \nabla \times \mathbf{W}_i^e) B_j - \sum_s (\mathbf{V}_s \delta(\mathbf{x} - \mathbf{X}_s), \mathbf{W}_i^e) \\ \sum_{j=1}^{N_b} (\mathbf{W}_j^b, \mathbf{W}_i^b) \partial_t B_j &= - \sum_{j=1}^{N_e} (\nabla \times \mathbf{W}_j^e, \mathbf{W}_i^b) E_j. \end{aligned} \quad (6)$$

Similar to the continuous system, we can also write the semi-discrete system (3,6) in the form

$$\dot{F} = \{F, H\}(\mathbf{X}_s, \mathbf{V}_s, \mathbf{E}_D, \mathbf{B}_D),$$

where F is any smooth function of the discrete variables. In this case, $\{\cdot, \cdot\}$ is the discrete bracket operator

defined by

$$\begin{aligned}
& \{F, G\}(\mathbf{X}_s, \mathbf{V}_s, \mathbf{E}_D, \mathbf{B}_D) \\
&= \sum_s \frac{1}{\omega_s} \left(\frac{\partial F}{\partial \mathbf{X}_s} \cdot \frac{\partial G}{\partial \mathbf{V}_s} - \frac{\partial G}{\partial \mathbf{X}_s} \cdot \frac{\partial F}{\partial \mathbf{V}_s} \right) \\
&+ \left(\frac{\partial F}{\partial \mathbf{E}_D} \right)^\top \mathcal{W}_e^{-1} \mathcal{K} \mathcal{W}_b^{-1} \frac{\partial G}{\partial \mathbf{B}_D} - \left(\frac{\partial G}{\partial \mathbf{E}_D} \right)^\top \mathcal{W}_e^{-1} \mathcal{K} \mathcal{W}_b^{-1} \frac{\partial F}{\partial \mathbf{B}_D} \\
&+ \sum_s \left(\left(\frac{\partial G}{\partial \mathbf{E}_D} \right)^\top \mathcal{W}_e^{-1} \mathcal{W}_e^S(\mathbf{X}_s) \frac{\partial F}{\partial \mathbf{V}_s} - \left(\frac{\partial F}{\partial \mathbf{E}_D} \right)^\top \mathcal{W}_e^{-1} \mathcal{W}_e^S(\mathbf{X}_s) \frac{\partial G}{\partial \mathbf{V}_s} \right) \\
&+ \sum_s \frac{1}{\omega_s} \mathbf{B}_D^\top \mathcal{W}_b^S(\mathbf{X}_s) \left(\frac{\partial F}{\partial \mathbf{V}_s} \times \frac{\partial G}{\partial \mathbf{V}_s} \right),
\end{aligned} \tag{7}$$

and H is the discrete Hamiltonian,

$$H(\mathbf{X}_s, \mathbf{V}_s, \mathbf{E}_D, \mathbf{B}_D) = \frac{1}{2} \sum_s \omega_s \mathbf{V}_s^2 + \frac{1}{2} \mathbf{E}_D^\top \mathcal{W}_e \mathbf{E}_D + \frac{1}{2} \mathbf{B}_D^\top \mathcal{W}_b \mathbf{B}_D. \tag{8}$$

Here $\mathbf{E}_D := [E_1, E_2, \dots, E_{N_e}]^\top$ and $\mathbf{B}_D := [B_1, B_2, \dots, B_{N_b}]^\top$ denote the values of the approximate fields. The other matrices are defined as follows:

- \mathcal{W}_e is an $N_e \times N_e$ constant symmetric matrix with $(\mathcal{W}_e)_{ij} = (\mathbf{W}_i^e, \mathbf{W}_j^e)$;
- \mathcal{W}_b is an $N_b \times N_b$ constant symmetric matrix with $(\mathcal{W}_b)_{ij} = (\mathbf{W}_i^b, \mathbf{W}_j^b)$;
- $\mathcal{W}_e^S(\mathbf{X}_s)$ is a $N_e \times 3$ matrix function with the j -th row being $\int_{\Omega_x} (\mathbf{W}_j^e)^\top \delta(\mathbf{x} - \mathbf{X}_s) d\mathbf{x}$;
- \mathcal{K} is an $N_e \times N_b$ constant matrix with $(\mathcal{K})_{ij} = (\nabla \times \mathbf{W}_i^e, \mathbf{W}_j^b)$.

It is easy to verify that the discrete bracket in Eq. (7) and Hamiltonian in Eq. (8) are consistent with the continuous ones in Ref. [3].

Moreover, if the discrete bracket (7) is skew-symmetric and satisfies the Jacobi identity, it is Poisson and defines a Poisson structure[1]. This establishes a condition for the basis of the finite element spaces. We have the following theorem.

Theorem 0.1. *If the space of elements $\mathcal{E}_h, \mathcal{B}_h$ for the field variables \mathbf{E} and \mathbf{B} satisfy*

$$\nabla \times \mathcal{E}_h \subset \mathcal{B}_h, \tag{9a}$$

$$\nabla \cdot \mathcal{B}_h = 0, \tag{9b}$$

then the semi-discrete system is a Hamiltonian system with the Poisson bracket defined in Eq. (7).

In the purpose of preserving the structure, it should be stressed here that traditional time integrations generally cannot be applied directly to systems with non-canonical Poisson bracket. However, it is noticed that our concerned system can be decomposed as a summation of solvable parts. Thus we can construct the Poisson-preserving methods by Hamiltonian splitting method presented in [2].

Firstly, we split the Hamiltonian in Eq. (8) as five parts,

$$H = H_E + H_B + H_1 + H_2 + H_3,$$

where $H_E = \frac{1}{2} \mathbf{E}_D^\top \mathcal{W}_e \mathbf{E}_D$, $H_B = \frac{1}{2} \mathbf{B}_D^\top \mathcal{W}_b \mathbf{B}_D$ and $H_i = \frac{1}{2} \sum_s V_s [i]^2$. Here, $V[i]$ denotes the i -th Cartesian component of the velocity \mathbf{V} . Each part of the Hamiltonian associates with a solvable subsystem. We take the subsystem corresponding to the Hamiltonian H_i as an example. For each $i = 1, 2, 3$, the equation $\dot{F} = \{F, H_i\}$ associated with the Hamiltonian H_i is equivalent to

$$\begin{aligned}
\dot{\mathbf{X}}_s &= V_s [i] \mathbf{e}_i, \\
\dot{\mathbf{V}}_s &= V_s [i] \mathbf{e}_i \times (\mathcal{W}_b^S(\mathbf{X}_s) \mathbf{B}_D), \\
\dot{\mathbf{E}}_D &= \mathcal{W}_e^{-1} \left(\sum_s \omega_s V_s [i] \mathcal{W}_e^S(\mathbf{X}_s) \mathbf{e}_i \right), \\
\dot{\mathbf{B}}_D &= 0.
\end{aligned} \tag{10}$$

where \mathbf{e}_i is the unit vector in the i -th Cartesian direction. It is easy to know the exact update of this subsystem with step size Δt is

$$\begin{aligned}
\mathbf{X}_s(t + \Delta t) &= \mathbf{X}_s(t) + V_s[i](t)\mathbf{e}_i, \\
\mathbf{V}_s(t + \Delta t) &= \mathbf{V}_s(t) + \mathbf{e}_i \times (\mathcal{W}_b^S(\mathbf{X}_s)\mathbf{B}_D), \\
\phi^{v_i}(\Delta t) : \mathbf{E}_D(t + \Delta t) &= \mathbf{E}_D(t) - \mathcal{W}_e^{-1} \left(\sum_s V_s[i]\omega_s F_J(\mathbf{X}_s, \Delta t)\mathbf{e}_i \right), \\
\mathbf{B}_D(t + \Delta t) &= \mathbf{B}_D(t). \\
F(\mathbf{X}_s, \Delta t) &= \int_{X_s[i](t)}^{X_s[i](t+\Delta t)} \mathcal{W}_e^S(\mathbf{X}_s) dX_s[i].
\end{aligned} \tag{11}$$

These exact solutions can be composed to get integrators for the semi-discrete system. For example, a second order symmetric method can be derived from

$$\begin{aligned}
\Phi(\Delta t) &= \phi^E(\Delta t/2) \circ \phi^B(\Delta t/2) \circ \phi^{v1}(\Delta t/2) \circ \phi^{v2}(\Delta t/2) \circ \phi^{v3}(\Delta t) \\
&\quad \circ \phi^{v2}(\Delta t/2) \circ \phi^{v1}(\Delta t/2) \circ \phi^B(\Delta t/2) \circ \phi^E(\Delta t/2).
\end{aligned}$$

Higher order methods can be constructed by various ways of compositions[4]. From the above expressing, it is known that the kind of methods can be computed explicitly, hence are easy to be implemented.

It can be verified that all the subsystems are equipped with the same bracket as the semi-discrete system. According to the theory of Lie groups, the numerical magnetic fields are divergence-free, and the discrete non-canonical Poisson structure is preserved by the methods.

Acknowledgements

This work was partly supported by JSPS-NRF-NSFC A3 Foresight Program in the field of Plasma Physics (NSFC-11261140328), the National Science Foundation of China (11271357, 11575186, 11575185, 11505185, and 11505186), the Foundation for Innovative Research Groups of the NNSFC (11321061).

Reference

- [1] E. Hairer, C. Lubich, and G. Wanner, *Geometric Numerical Integration: Structure-Preserving Algorithms for Ordinary Differential Equations*. Springer, New York, 2003.
- [2] Y. He, H. Qin, Y. Sun, J. Xiao, R. Zhang, and J. Liu, *Physics of Plasmas*, 22:124503, 2015.
- [3] J. E. Marsden and A. Weinstein, *Physica*, 4D:394, 1982.
- [4] R. I. McLachlan and G. R. W. Quispel, *Acta Numer.*, 11:341–434, 2002.
- [5] H. Qin, J. Liu, J. Xiao, R. Zhang, Y. He, Y. Wang, Y. Sun, J. W. Burby, L. Ellison, and Y. Zhou, *Nuclear Fusion*, 56:014001, 2016.
- [6] J. Xiao, H. Qin, J. Liu, Y. He, R. Zhang, and Y. Sun, *Physics of Plasmas*, 22:112504, 2015.

Comparison of impurity transport between Al and Fe in LHD based on space-resolved EUV spectroscopy

X.L.Huang¹, S.Morita^{1,2}, T.Oishi^{1,2}, I.Murakami^{1,2}, M.Goto^{1,2}, H.M.Zhang² and Y.Liu²

¹National Institute for Fusion Science, Toki 509-5292, Gifu, Japan (10.5pt)

²Graduate University for Advanced Studies, Toki 509-5292, Gifu, Japan (10.5pt)

Abstract

With impurity pellet injection and a one-dimensional transport code, the transport of Al and Fe ions has been analyzed in the Large Helical Device (LHD) based on extreme ultraviolet (EUV) space-resolved spectroscopy. The total density of Fe ions in the plasma core has been analyzed from the radial profiles of the Fe $n=3-2 L_{\alpha}$ emissions. When the electron density (n_e) profile is peaked or hollow, the Fe density also exhibits a peaked or hollow profile, respectively. The Fe transport analysis shows that the convective velocity (V) is outward in the plasma core and inward near the edge when the n_e profile is hollow. On the other hand, the V takes negative value over the whole radial range in the peaked n_e profile. Therefore, the different Fe density profiles between peaked and hollow n_e profiles can be explained by the significant difference in the V profile. Comparison of the transport coefficients between Al and Fe shows the magnitude of V for Al ions seems to be smaller than that for Fe ions, while the difference in the diffusion coefficient profile is not significant. The difference in the decay time of line emissions between the two species is attributed to the weaker convection for the Al.

1. Introduction

In the Large Helical Device (LHD), the density profile can exhibit a peaked, flat or hollow shape, depending on plasma conditions such as B_t , T_e , and n_e . The formation of hollow and flat density profiles observed in the LHD is quite unique compared with those in tokamaks. The convective velocity of Fe has been found to be highly related to the density gradient in LHD. An outward convective velocity has been observed in the plasma center when a hollow n_e profile occurs. Previous results suggest that the value of inward impurity convection is proportional to the ion charge, which is predicted by the neoclassical theory [1, 2]. If this situation is also identical to the outward convection, the impurity control of heavy impurities will be possible in the plasma core of LHD. In the present work, the transport of Al and Fe are analyzed and compared for the purpose of clarifying the charge dependence of the impurity transport coefficients between different impurity species.

2. Experimental setup

Two extreme ultraviolet (EUV) spectrometers with 2400 grooves/mm holographic gratings work in the wavelength range of 10-130Å in LHD. One spectrometer called EUV-Short works as an impurity monitor [3]. The other spectrometer called EUV-Short2 measures the emission profile from the upper half of a horizontally elongated plasma cross section [4]. The observable wavelength interval of EUV-Short2

is 10\AA at $\lambda=15\text{\AA}$ and 25\AA at $\lambda = 100\text{\AA}$. The radial profiles of Fe $n = 3-2 L_{\alpha}$ transition array consisting of emissions from ionization stages of Ne-like Fe^{16+} through Li-like Fe^{23+} ions are simultaneously measured in the wavelength range of $8-18\text{\AA}$. Figure 1 shows the field of view of the EUV-Short2 spectrometer.

Impurity pellets are injected into the plasma for the purpose of impurity transport study. The impurity pellet injector is installed on an outboard port at horizontally elongated plasma cross section [5]. The pellet velocity is measured by a time-of-flight technique at three pellet chambers for differential pumping. In order to monitor the pellet ablation, emissions of H_{α} , CI and visible bremsstrahlung are measured along the pellet trajectory from the backside of the pellet injection port. The deposition position of the pellet can be determined from the pellet velocity and emission signals.

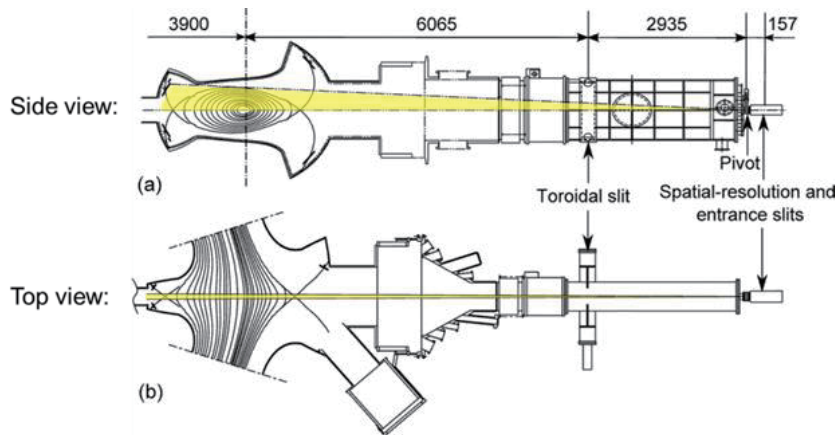


Fig.1 Schematic drawings of the space-resolved EUV spectrometer (EUV-Short2) in (a) side and (b) top

3. Pellet injection experiments and decay time analysis

Typical waveforms of discharges with Al and Fe pellets are shown in Fig. 2 for NBI port-through power, line-averaged electron density, central electron temperature, plasma stored energy, radiation power, and line emission of Al or Fe. The Al and Fe pellets are injected in discharges with $R_{ax} = 3.6\text{m}$ and $B_t = 2.75\text{T}$. The waveforms show that the perturbation caused by the pellets to the bulk plasma is negligibly small.

The line-integrated profiles of Al XII-XIII and Fe XVII-XXIV emissions are measured by EUV-Short2 after the pellet injection. In two discharges with similar density and temperature profiles, Fe XVIII and Fe XXI among all Fe emissions are found to radially distribute most closely to the Al XII and Al XIII emissions, respectively. Therefore, the emission decay time of Fe XVIII and Fe XXI emission can be compared with that of Al XII and Al XIII, respectively.

Decay time of impurity emission after pellet injection directly reflects the impurity confinement time in the plasma. Here, decay time is defined as the time required for the line intensity to decrease to half of its peak value. The decay time of Al and Fe emissions has been calculated for discharges at different densities, as shown in Fig. 3. The Fe XVIII emission has a longer decay time than Al XII at $n_e > 3.5 \times 10^{13}\text{cm}^{-3}$. This means Fe ions are confined longer than Al ions in the plasma edge. Since Fe XXI has a slightly shorter decay time compared to Al XIII, Fe ions have a smaller confinement time compared to Al ions in the plasma core. It should also be noted that the decay time of Fe emissions increases with

density more quickly than that of Al emissions at $n_e > 3.5 \times 10^{13} \text{cm}^{-3}$.

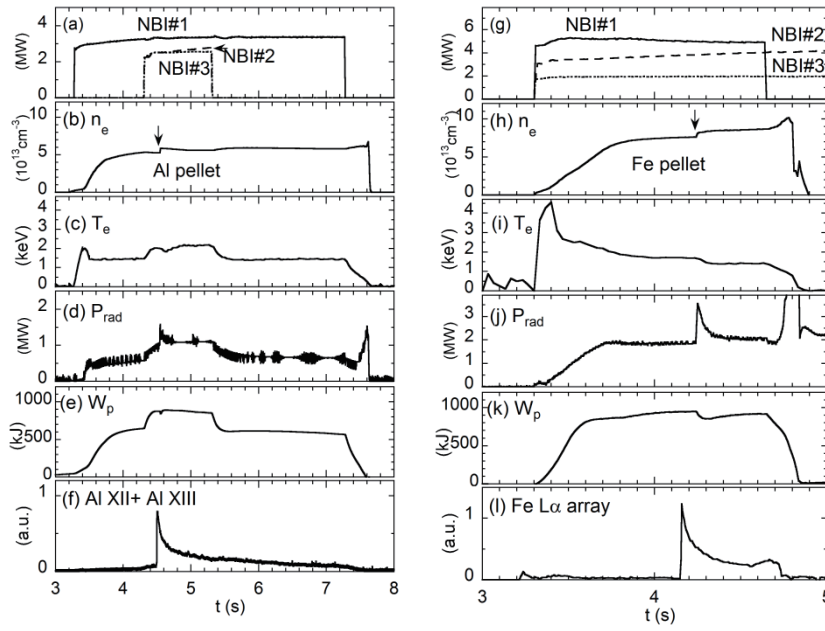


Fig.2 Waveform of discharges with (a) - (f) Al and (g) - (l) Fe pellets.

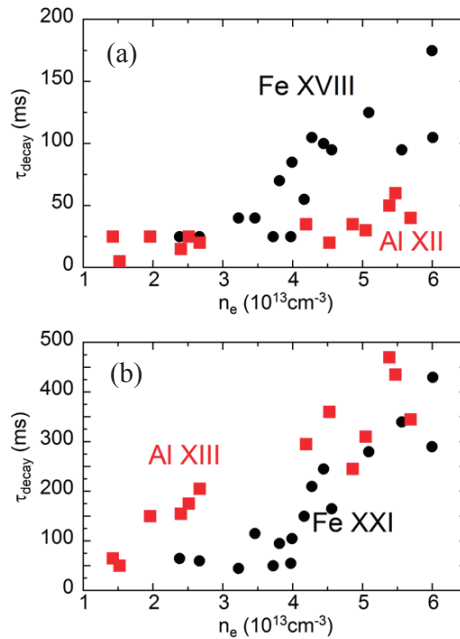


Fig.3. Emission decay times of (a) Al XII (squares) and Fe XVIII (circles) and (b) Al XIII (squares) and Fe XXI (circles) as a function of electron density.

4. Impurity transport simulation

A one-dimensional impurity transport code is employed to determine the transport coefficient [6]. It is assumed that the impurity ions satisfy the following equations of transport and continuity.

$$\Gamma_I^K = -D \frac{\partial n_I^K}{\partial r} + V n_I^K \quad (1)$$

$$\frac{\partial n_I^K}{\partial t} = -\frac{1}{r} \frac{\partial}{\partial r} r \Gamma_I^K + n_e [S_I^{K-1} n_I^{K-1} - (S_I^K + \alpha_I^K) n_I^K + \alpha_I^{K+1} n_I^{K+1}] \quad (2)$$

where Γ_I^K , n_I^K , D , V , S_I^K and α_I^K are the particle flux, the ion density, the diffusion coefficient, the convective velocity, the ionization rate coefficient and the recombination coefficient of impurity ions in the K th ionization stage, respectively. Positive values of V stand for outward and inward convection.

Updated rate coefficients for ionization and recombination have been included in the present transport code [7-9]. With given transport coefficients and radial profiles of plasma parameters, the code yields the impurity ion density profile in all ionization stages as a function of time. The transport coefficient near the emissivity peak can be determined by comparing the emissivity profile between the experiment and the simulation. In order to determine the transport coefficient at the whole plasma radius, the impurity line emission is simultaneously analyzed in several ionization stages. The minimization of deviation between measured and simulated impurity profiles and time evolution of impurity line emissions can determine the transport coefficient profile.

5. Impurity transport coefficients of Fe and Al

Figure 4(b) shows the evaluated transport coefficients of Fe in peaked and hollow n_e profiles as plotted in Fig. 4(a). The V in the figure represents the convective velocity averaged by eight ionization stages of Fe^{16+} through Fe^{23+} . The diffusion coefficient D profile is very similar between peaked and hollow n_e profiles, while the D value gradually increases toward the plasma edge from the center. On the other hand, the V profile is entirely different between the two cases. In the peaked n_e profile, the V is negative, i.e. inward, and increases from the plasma center to the edge. This indicates the impurity accumulation easily occurs with a peaked n_e profile. In the hollow n_e profile, an outward V is obviously observed in the core region of $\rho \leq 0.8$. The V changes from outward to inward near the edge where the n_e gradient changes the sign from positive to negative. The iron ion is pushed back outwards near $\rho = 0.8$ and concentrated near the edge when the n_e profile is hollow. As a result, a hollow iron density profile can be formed with the hollow n_e profile.

Preliminary analysis of Al transport has also been carried out in LHD. The Al transport coefficients are analyzed in a discharge with hollow density profile. The result is compared with Fe transport coefficients (see Fig. 5). The radial profiles of D and V for Al ions are limited at $\rho > 0.6$ because emissions are available only in two charge states, i.e., Al XII and Al XIII. The difference in the D profile is not significant between Al and Fe. The magnitude of V of Al ions seems to be smaller than that of Fe ions. Weaker inward convection of Al leads to shorter confinement time near the edge while weaker outward V of Al leads to longer confinement time in the plasma core. Therefore, the radial profile of V may explain the difference in the decay time between Al and Fe.

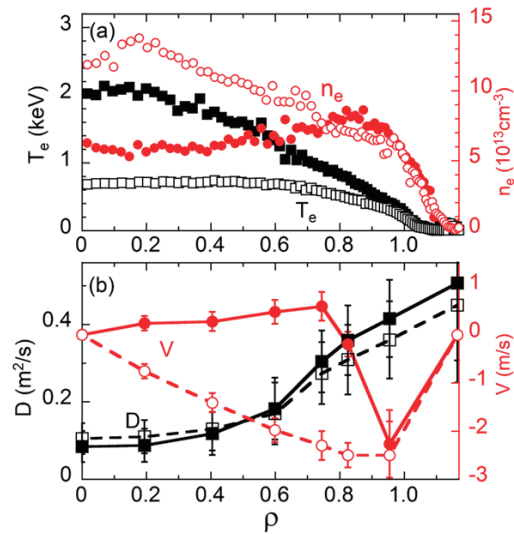


Fig.4 Radial profiles of (a) electron temperature (squares) and density (circles) and (b) diffusion coefficient (squares) and convective velocity (circles) for peaked (open symbols) and hollow (solid symbols) density profiles.

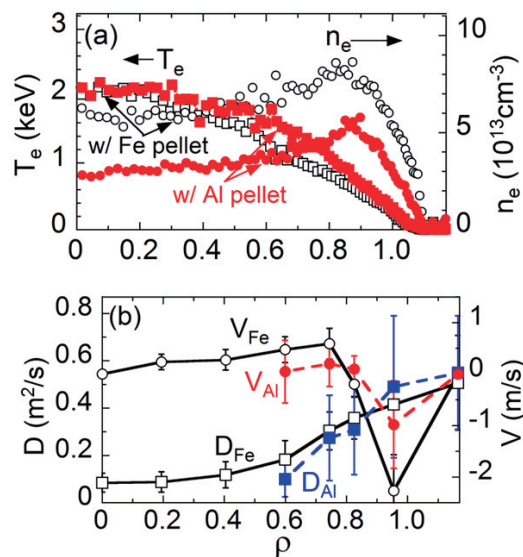


Fig.5. Radial profiles of (a) electron temperature (squares) and density (circles) and (b) diffusion coefficient (squares) and convective velocity (circles) in Fe (open symbols) and Al (solid symbols) pellet experiments.

6. Summary

With help of the transport code, the transport coefficients are successfully obtained for Al and Fe ions based on EUV spectroscopic measurement in LHD discharges with impurity pellet injection. Decay time analysis indicates that Fe ions have a longer confinement time near the edge and a short one in the plasma core compared with Al ions. The Fe transport analysis shows that the convective velocity is outward in

the plasma center and inward near in the edge when a hollow density profile occurs. Comparison of the transport coefficients between Al and Fe shows the difference in the impurity confinement time may be a consequence of the weaker convection of Al compared with Fe. This result is in qualitative agreement with the charge dependence of the convective velocity predicted by the neoclassical theory.

Acknowledgements

This work was partly supported by the JSPS-NRF-NSFC A3 Foresight Program in the field of Plasma Physics (NSFC: No.11261140328, NRF: No.2012K2A2A6000443).

References

- [1] H. Nozato et al., Phys. Plasma **11**(2004), 1920.
- [2] H. Nozato, et al., Phys. Plasma **13**(2006), 092502.
- [3] M. B. Chowdhuri, S. Morita and M. Goto, Applied Optics **47**(2008), 135.
- [4] X. L. Huang, S. Morita, T. Oishi, et al., Rev. Sci. Instrum. **85** (2014) 11E818.
- [5] S. Morita et al., Plasma Sci. Technol. **13**(2011), 290.
- [6] T. Amano, J. Mizuno, and J. Kako, Simulation of impurity transport in tokamak, Int. Rep. IPPJ-616 (1982), Institute of Plasma Physics, Nagoya University.
- [7] N. R. Badnell, Astrophys. J. Suppl. Ser. **167** (2006) 334.
- [8] N. R. Badnell *et al.*, Astron. Astrophys. **406** (2003) 1151.
- [9] K. P. Dere, Astron. Astrophys **466** (2007) 771.

Plasma conditions for gyroviscous cancellation in flowing plasmas

C. Bae¹

¹ National Fusion Research Institute, Gwahak-ro, Yuseong-gu, Daejeon 305-806, South Korea

Abstract

The well-known gyroviscous cancellation in sheared slab geometry is investigated by a systematic perturbative method based on the Mikhailovskii and Tsypin's closure relation and on the large gyrofrequency ordering for flowing plasmas. Systematically perturbed velocity moments of the kinetic equation allow an easier identification of the cancellation mechanism for each perturbed momentum balance equation to investigate the plasma conditions for complete cancellations when the flow (zeroth-order) velocity is considered. The gyroviscous cancellations of each order are presented in the important parallel directions. With the flow velocity considered, the residuals remain in the first-order momentum balance, at an order lower than previously investigated in the literature. The conditions on the lowest order residuals to yield valid gyroviscous cancellation are presented and discussed.

1. Introduction

Gyroviscous cancellation[1-4] between the convective force and the diamagnetic convective contribution in the gyroviscous force is widely used to reduce the momentum balance equation,

$$\partial_t \vec{V}_a + \vec{V}_a \cdot \nabla \vec{V}_a + \frac{1}{m_a n_a} \nabla \cdot \vec{\pi}_a + \frac{1}{m_a n_a} \nabla p_a = \frac{q_a}{m_a} \vec{E} - \Omega_a \hat{b} \times \vec{V}_a + \frac{1}{m_a n_a} \vec{R}_a^{10}, \quad (1)$$

where $\hat{b} \equiv \vec{B}/B$ with \vec{B} being the magnetic field, n_a is the density of species a , \vec{V}_a is the flow velocity, $\vec{\pi}_a = \int d\vec{v} m_a (\vec{w}_a \vec{w}_a - 1/3 w_a^2 \vec{I}) f_a$ is the viscosity tensor with $\vec{w}_a = \vec{v} - \vec{V}_a$ and f_a as its distribution function, Ω_a is the gyrofrequency, and $\vec{R}_a^{10} = \int d\vec{v} m_a \vec{v}_a C_a$ is the collisional friction with C_a being the collision operator. Hereafter a is omitted for simplicity. Since the convective force introduces nonlinearity in (1), its elimination against the similar contribution in the gyroviscous force introduces simplicity in numerical calculation models, especially when the gyroviscous force represents most of the viscous force. However, recent calculations of the convective and gyroviscous forces in practical tokamak plasmas show no indication of valid gyroviscous cancellations [5, 6]. Since all the earlier works[1-4] were done with the flow (zeroth-order) velocity $\vec{V}_{(0)}$ neglected, it is the goal of this research to reinvestigate the cancellation mechanism in sheared slab geometry with $\vec{V}_{(0)}$ retained so that

the detailed conditions for valid gyroviscous cancellation can be examined for practical flowing plasmas.

2. Gyroviscous cancellations in each order

For strongly magnetized plasmas, we can perturb plasma parameters by introducing the smallness parameter δ into the inverse gyrofrequency (Ω^{-1}) since Ω is much larger than other characteristic frequency scales. In this work, we expand any physical quantity in plasma fluid equations, except the magnetic field, as

$$X = X_{(0)}\delta^0 + X_{(1)}\delta^1 + X_{(2)}\delta^2 + \dots \quad (2)$$

where X can be either a scalar, a vector, or a tensor quantity and the corresponding perturbed order is indicated in the parenthesized subscript. With these perturbed parameters, we can apply the perturbative method commonly used in quantum mechanics to systematically represent any force in (1) as the combinations of perturbed parameters. With the lowest order vanishing, the first- and second-order perturbed convective forces are:

$$O(\delta^1): \vec{V}_{(0)} \cdot \nabla \vec{V}_{(1)}, \vec{V}_{(1)} \cdot \nabla \vec{V}_{(0)} \quad (3)$$

$$O(\delta^2): \vec{V}_{(0)} \cdot \nabla \vec{V}_{(2)}, \vec{V}_{(1)} \cdot \nabla \vec{V}_{(1)}, \vec{V}_{(2)} \cdot \nabla \vec{V}_{(0)}. \quad (4)$$

We now try to find the corresponding cancellation mechanisms from the gyroviscous force for each of the perturbed convective forces in (3) and (4). The first-order velocity is

$$\vec{V}_{(1)\perp} = \Omega^{-1} \hat{b} \times \left(\frac{1}{mn_{(0)}} \nabla p_{(0)} - \frac{q}{m} \vec{E}_{(0)} \right) + \Omega^{-1} \hat{b} \times \left(\partial_t \vec{V}_{(0)} - \frac{1}{mn_{(0)}} \vec{C}_{(0)}^{10} \right) \quad (5)$$

and we approximate $\vec{V}_{(1)\perp}$ with the first term in (5) as done in other works[1, 7]. Following the generalized formalism of the gyroviscous force[8, 9], one can find the following perturbed gyroviscous forces:

$$O(\delta^1): \nabla \cdot \vec{\pi}_{(1)}^{\text{gv}} = \Omega^{-1} \nabla p_{(0)} \cdot \hat{b} \times \nabla_{\perp} V_{(0)} \hat{b} = -mn_{(0)} \vec{V}_{d(1)} \cdot \nabla \vec{V}_{(0)} \quad (6)$$

$$O(\delta^2): \nabla \cdot \vec{\pi}_{(2)}^{\text{gv}} = -mn_{(0)} \vec{V}_{d(1)} \cdot \nabla \vec{V}_{(1)} - mn_{(0)} \vec{V}_{d(2)} \cdot \nabla \vec{V}_{(0)} + \nabla \left(\chi_{V(1)} + \chi_{h(1)} \right) + \Omega^{-1} p_{(0)} \left(\hat{b} \times \nabla_{\perp} \partial V_{(1)} \right) \quad (7)$$

where the α th-order diamagnetic drift velocity is defined by

$$\vec{V}_{d(\alpha)} \equiv \frac{1}{mn_{(0)}\Omega} \hat{b} \times \nabla p_{(\alpha-1)}. \quad (8)$$

To investigate the cancellation mechanism in the parallel direction, we add the parallel components of the convective forces in (3) and (4) with the parallel contributions from (6) and (7) respectively to yield

$$O(\delta^1): \vec{V}_{(1)} \cdot \nabla \vec{V}_{(0)} + \vec{V}_{(0)} \cdot \nabla \vec{V}_{(1)} + \frac{1}{mn_{(0)}} \left(\nabla \cdot \vec{\pi}_{(1)}^{\text{gv}} \right) = \vec{V}'_{d(1)} \cdot \nabla \vec{V}_{(0)} + \vec{V}_{(0)} \cdot \nabla \vec{V}_{(1)}, \quad (9)$$

$$\begin{aligned} O(\delta^2): & \vec{V}_{(1)} \cdot \nabla \vec{V}_{(1)} + \vec{V}_{(2)} \cdot \nabla \vec{V}_{(0)} + \vec{V}_{(0)} \cdot \nabla \vec{V}_{(2)} + \frac{1}{m} (n^{-1})_{(1)} \left(\nabla \cdot \vec{\pi}_{(1)}^{\text{gv}} \right) + \frac{1}{mn_{(0)}} \left(\nabla \cdot \vec{\pi}_{(2)}^{\text{gv}} \right) \\ & = \vec{V}'_{d(1)} \cdot \nabla \vec{V}_{(1)} + \vec{V}'_{d(2)} \cdot \nabla \vec{V}_{(0)} + \vec{V}_{(0)} \cdot \nabla \vec{V}_{(2)} + \left(\frac{n_{(1)}}{n_{(0)}} \right) \vec{V}_{d(1)} \cdot \nabla \vec{V}_{(0)} + \frac{1}{mn_{(0)}} \nabla \left(\chi_{V(1)} + \chi_{h(1)} \right) \end{aligned} \quad (10)$$

Here $\vec{V}'_{d(\alpha)} \equiv \vec{V}_{(\alpha)} - \vec{V}_{d(\alpha)}$ is usually considered negligible in the earlier works[1-4] for valid gyroviscous cancellation. With $\vec{V}'_{d(\alpha)}$ contributions neglected, the anisotropic pressure and heat contributions in (10), the last term with $\chi_{V(1)}$ and $\chi_{h(1)}$, are the residuals reported in the earlier works[1-4]. Thus, it is easy to check what terms have survived when $\vec{V}_{(0)}$ is retained. Replacing (9) and (10) with the same forces in the parallel momentum balance equations, a new set of reduced plasma fluid equations with $\vec{V}_{(0)}$ retained can be trivially obtained.

3. Plasma conditions for valid gyroviscous cancellation

To discuss the validity of gyroviscous cancellation in flowing plasmas that one wishes to analyze, an attention must be given to (9) for the residuals at an order lower than investigated in the earlier works[1-4]. The first residual with $\vec{V}'_{d(1)}$ can be neglected when $\vec{V}'_{d(1)} \perp \vec{V}_{(1)\perp}$, $\vec{V}'_{d(1)} \perp \nabla \vec{V}_{(0)}$, and/or $\nabla \vec{V}_{(0)} \approx 0$ while the second neglected when $\vec{V}_{(0)} \perp \nabla \vec{V}_{(1)}$ and/or $\nabla \vec{V}_{(1)} \approx 0$. $\vec{V}'_{d(1)} \perp \vec{V}_{(1)\perp}$ is typically assumed in the literature[1-4] but used to neglect the first term in (10). Thus, $\vec{V}'_{d(1)} \cdot \nabla \vec{V}_{(0)}$ may not be readily negligible for tokamak plasmas with strong velocity gradients in the radial direction, considering that there also is an "augmenting" contribution from the 4th term in (10). The second term in (9), with no cancelling counterpart, may not be negligible when $\nabla \vec{V}_{(1)}$ is significant and perpendicular to $\vec{V}_{(0)}$. Only when these can be neglected, the residuals at a higher order in (10) can now be investigated similarly to the residuals in (9).

4. Conclusion

The viscosity is represented as the sum of its CGL(Chew-Goldberger-Low), collisional, and gyroviscous components[8]. When the CGL and collisional viscosities are neglected, gyroviscous cancellation is a great tool to reduce the momentum balance equation to make computational implementation easier. A caution however must be exercised as shown in this work with the residuals for practical flowing plasmas. When the results in this work are generalized to arbitrary geometry, more restrictions may appear to further limit the validity of gyroviscous cancellation, thus their plasma conditions must be carefully investigated to minimize the computational errors in practical flowing plasmas.

Acknowledgements

This research is based on the note on gyroviscous cancellation written by Dr. Jeong-Young Ji. The author is grateful to him for the note. This work was supported by the JSPS-NRF-NSFC A3 Foresight Program in the field of Plasma Physics (NSFC: No.11261140328, NRF: No.2012K2A2A6000443) and by the Korean Ministry of Science, ICT, and Future Planning (Grant Number GN1513).

References

- [1] Z. Chang and J.D. Callen, *Physics of Fluids B: Plasma Physics* 4 (1992) 1766-1771.
- [2] A.I. Smolyakov, *Canadian Journal of Physics* 76 (1998) 321-331.
- [3] J.J. Ramos, *Physics of Plasmas* 12 (2005) 112301.
- [4] E.V. Belova, *Physics of Plasmas* 8 (2001) 3936-3944.
- [5] C. Bae, W.M. Stacey, W.M. Solomon, *Nuclear Fusion* 53 (2013) 043011.
- [6] C. Bae, W.M. Stacey, S.G. Lee, L. Terzolo, *Physics of Plasmas* 21 (2014).
- [7] R.D. Hazeltine and J.D. Meiss, *Plasma confinement* (Addison-Wesley Pub. Co., Calif., 1992).
- [8] C.T. Hsu, R.D. Hazeltine, P.J. Morrison, *Physics of Fluids* 29 (1986) 1480-1487.
- [9] J.-Y. Ji and E.D. Held, *Physics of Plasmas* 21 (2014) 042102.

Dynamic behavior of cryogenic system under plasma discharge in EAST

L.B.Hu¹, X.F.Lu¹ and Z.Y.Zhang¹

¹Institute of Plasma Physics, Chinese Academy of Sciences, Hefei 230031, Anhui, China

Abstract

The plasma is confined by the magnetic fields generated from a large set of superconducting magnets which are made of cable in-conduit conductor (CICC) in the fusion reactors like EAST Tokamak. Due to plasma discharge and AC loss, superconducting coils and support structures generate a large number of dynamic heat loads during the operation. The pulses heat loads affect the cryogenic system by cooling channels of supercritical helium. The cryogenic system need to remove periodically large heat loads in time. At the same time, the cryogenic system parameters such as helium cooling superconducting magnets, helium refrigerator and helium distribution system are changing. In this paper, dynamic behavior of the cryogenic system under plasma discharge in EAST has been analyzed and simulated in the typical plasma discharge mode. The control scheme has been proposed to smooth the pulse loads and to improve the stability of the operation of the cryogenic system.

1. Introduction

EAST (Experimental Advanced Superconducting Tokamak) is a full superconducting experimental Tokamak fusion device, As one of the important subsystems of the Tokamak, the cryogenic system is mainly responsible for the cooling of the superconducting magnets and related components, ensuring the stable operation of superconducting magnets at various conditions. As shown in Fig 1, the cryogenic system for EAST includes a helium refrigerator and the cryogenic distribution system. The helium refrigerator is composed of gas management system, compressors station, cold box and 10000 liter Dewar. All the heat exchangers, the absorbers and four turbine expanders are installed in the cold box. The design capacity of the helium refrigerator is 1050 W@3.5K +200W@4.5K +13g/s LHe +12~30kW@80K [1]. In order to maintain the proper cryogenic state of the EAST cold components, the helium refrigeration system (HRS) supplies three helium coolants: supercritical helium (SHe), liquid helium, and gaseous helium for the SC coils and their feeder lines, current leads, and thermal shield, respectively. The cryogenic distribution system (CDS) should have sufficient mass flow to operate each of the SC coils.

During the plasma experiments, superconducting magnets suffer the heat loads from the thermal and nuclear radiation from the surrounding components and the plasma, eddy currents and AC losses generated within the magnets, the heat conduction through supports, and the resistive heat generated at the current

lead transitions to room temperature add to the total heat load. The cryogenic system operated in a pulsed heat loads mode requires the helium refrigerator to remove periodically large heat loads in time. At the same time, the relative status of cryogenic system parameters such as helium cooling superconducting magnets, helium refrigerator and helium distribution system are changing. In this paper, dynamic behavior of the cryogenic system under plasma discharge in EAST has been analyzed and simulated in the typical plasma discharge mode. The control scheme has been proposed to smooth the pulse loads and to improve the stability of the operation of the cryogenic system.

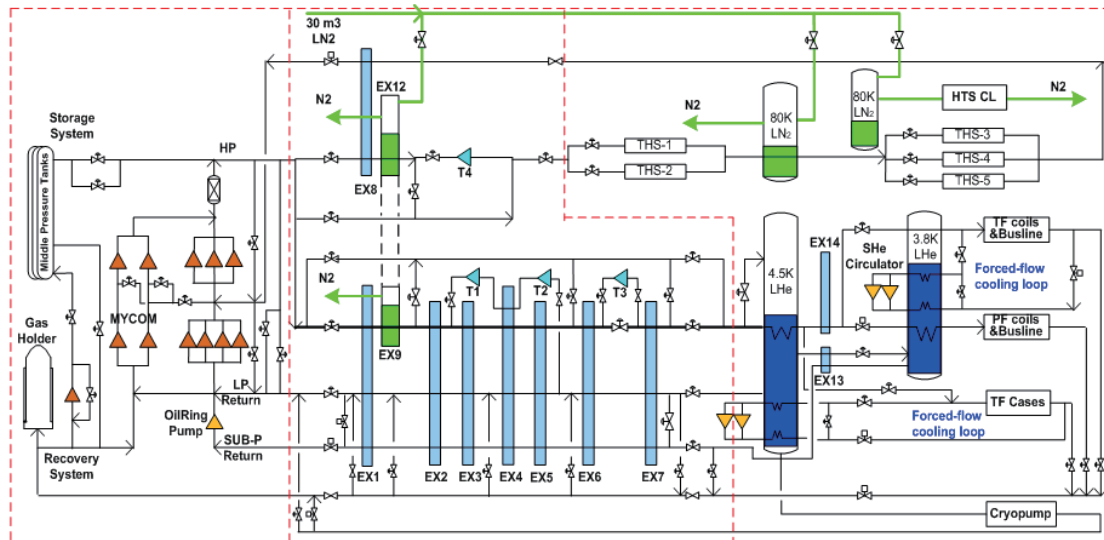


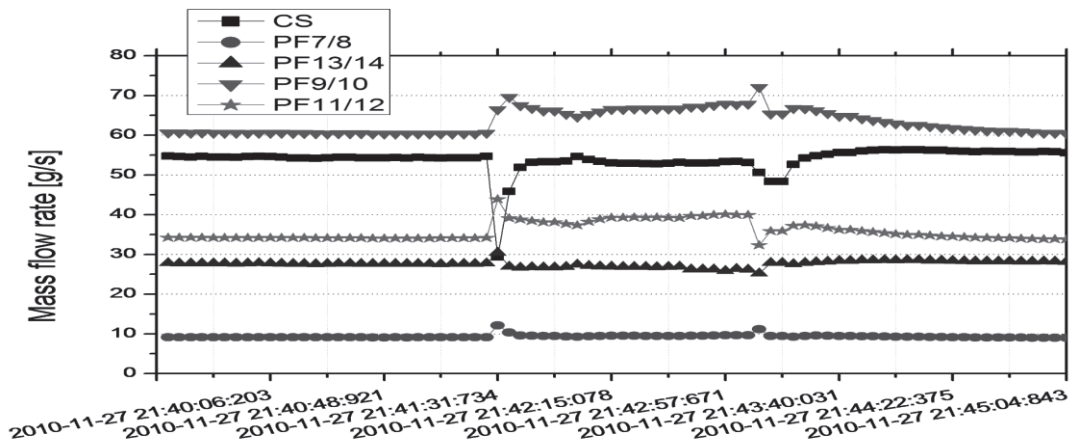
Fig 1. Simplified scheme of EAST cryogenic system

2. Dynamic behavior of cryogenic system during plasma discharge

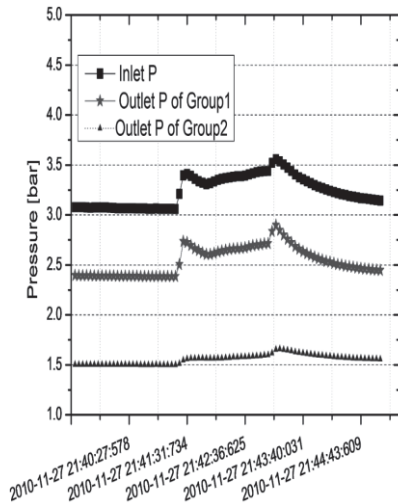
2.1 Variation of cooling parameters for PF magnets

The PF magnet system of EAST consists of three pairs of central solenoid coils and four pairs of big outer rings. PF coils are cooled by the supercritical helium stream from the J-T valve in the helium refrigerator. In order to provide enough mass flow to each cooling channel, the PF coils are divided into two groups and connected in series for cooling. The CS coils and PF13/14 are cooled in parallel in the first group. The helium flowing out of the first group of coils passes through a 3.5K sub-cooler, then to cool the rest of the coils (PF 7~12) in the second group. The helium flowing out of PF 7~12 coils returns to one manifold connected to the liquid helium bath in the cryogenic distribution valve box.

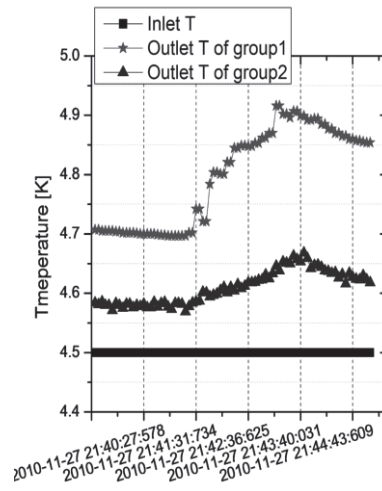
During the plasma experiments, the fast ramping rate of the PF current can generate much heat inside the coil. At this time, the supercritical helium inside the PF coils expands due to the generated heat. As a result, the thermodynamic parameters of the helium cooling channels of the PF magnets fluctuate. Fig 2 shows the variation of cooling parameters of PF at the plasma shot (250kA@100s). According to the experimental observation, the fluctuations of cooling parameters of the PF are subject to the variation of the charge currents in the PF and the plasma current. Furthermore, the temperature of the PF will rise cumulatively during the plasma discharge, which will affect the stability of the superconducting magnets if the interval time between shots is short.



Mass flow rate



Pressure



Temperature

Fig 2. Variation in PF cooling parameters from shot# 34068(250kA@100s)

2.2 Variation of cooling parameters for TF magnets and TF case

The TF coils are cooled with 3.8K SHe in a closed loop. All of the 16 coils are connected in parallel and divided into four groups with the control valves at the outlet of each group. The large mass flow rate is supplied by a SHe circulator with a pressure head of 0.1MPa. The case of the TF coils are cooled with 4.5K SHe in parallel. The cooling SHe is supplied by another circulator of 320 g/s mass flow rate and 0.02MPa pressure head. Two circulators are installed for TF coils. One acts as a spare in case the operating circulator goes out of service. There are also another two circulators installed for the cases of TF coils. An inlet pressure of 0.3MPa ensures the helium is in a supercritical state. In normal discharge mode, the 100s long pulse discharge and 1MA plasma current discharge have been analyzed. Fig 3 shows the fluctuation of outlet temperature and pressure of TF and TF case during the 100s long pulse discharge.

The variation in those parameters during the 1 MA plasma discharge is shown in Fig 4. During the

plasma discharge mode with a 100s pulse, the outlet pressure and temperature of the TF and TF case will rise. The outlet pressure of the TF case rises with about 0.5 bar while that of the TF' rises with 0.2 bar. The outlet temperature rises with about 0.3 K while that of the TF' rises with about 0.1K. The fluctuation trend of the parameters of the TF and TF case during plasma discharge mode with 1MA plasma current is similar with the 100s long pulse mode, but the range of fluctuation of the former is smaller than the latter, due to the accumulation over time.

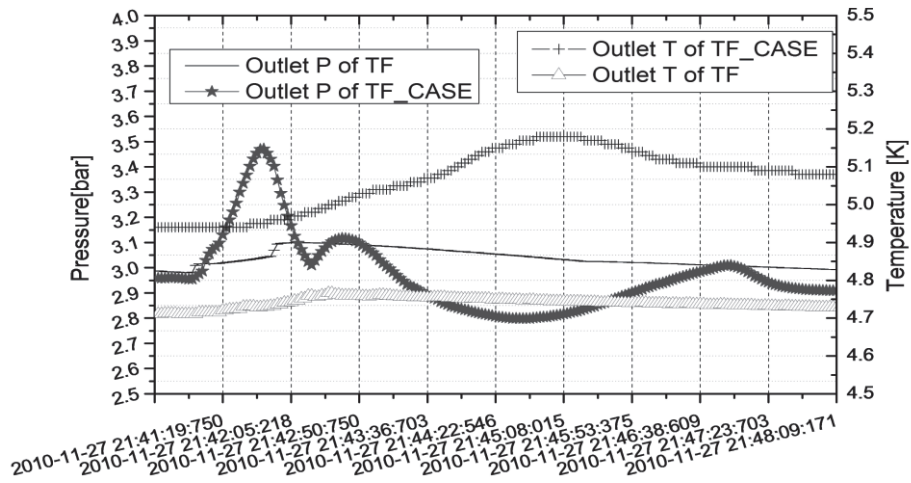


Fig 3. Variation in the outlet parameters of TF and TF case during the 100s long pulse discharge

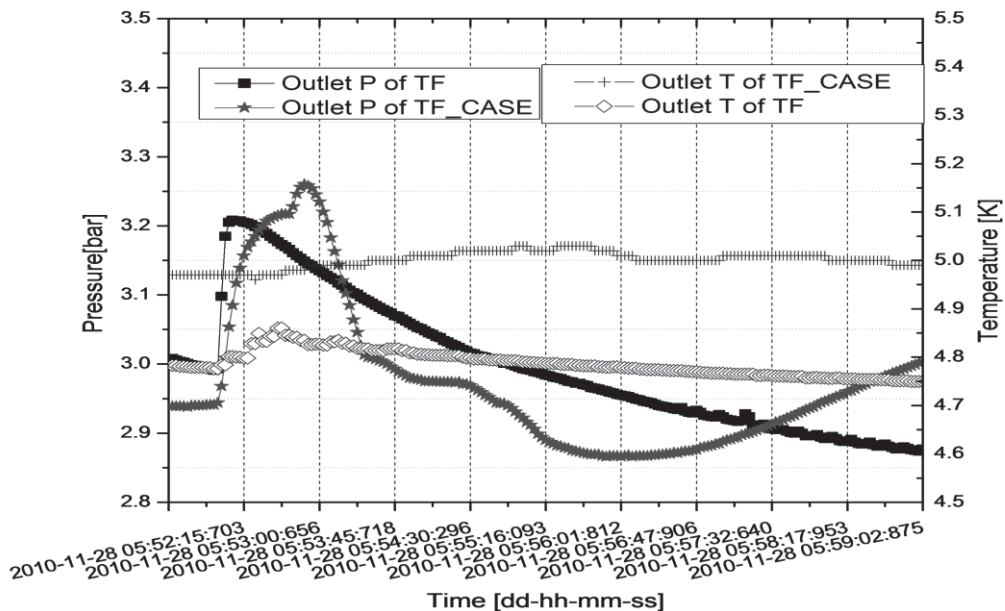


Fig 4. Variation in the outlet parameters of TF and TF case during the 1MA plasma discharge

2.3 Effects of pulsed heat load on helium refrigerator

During the plasma discharge, the heat loads absorbed by the supercritical helium are released into the LHe box and subcooler box, and then the LHe in the two boxes vaporizes and returned to the refrigerator through the low pressure (LP) loop and subcooler loop. Therefore, the immediate effect of the pulsed heat load is the wide fluctuation of mass flow rate returning to the refrigerators. This fluctuation then induces the variation in the parameters of the refrigerator, such as the temperature, the pressure and the mass flow rate. The fluctuation of the mass flow rate also affects the performance and stability of the turbines and the compressors, which are designed to operate in a narrow fluctuating margin of temperature, pressure and mass flow rate.

Due to the cooling of PF magnets directly from the supercritical helium after J-T turbine (T3) of the refrigerator, the AC losses generated in the PF will affect the variation in the inlet pressure of the PF, and then lead to the fluctuation of the outlet pressure, temperature and speed of T3. Therefore, the performance and stability of T3 will be affected during the plasma discharge. Fig 5 shows the variation in the speed of T3 during the continuous plasma discharge. The fluctuations of outlet pressure and temperature are shown in Fig 6. During every plasma discharge shot, the speed of T3 drops, however, the outlet temperature and pressure will rise. Since the outlet temperature will affect the inlet temperature of the cooling magnets of EAST device, the capacity and liquefaction rate of the helium refrigerator will fluctuate. Furthermore, the fluctuation of the speed of T3 will have a significant impact on the stability of T3, increasing the risk of sudden locking of T3 because the brake parameter is substantially constant.

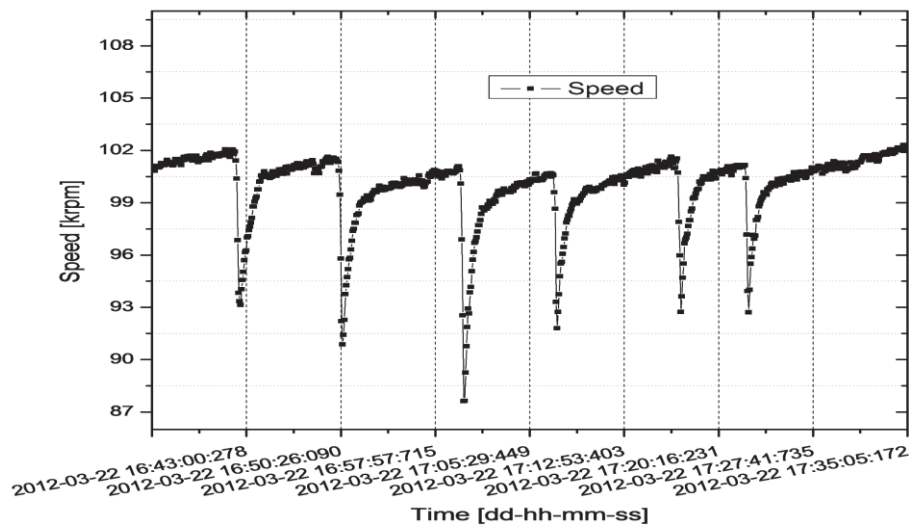


Fig 5. Variation of T3 speed during plasma discharge

During the plasma discharge, the return mass flow rate from the cryogenic distribution box will increase due to the helium vaporization in the cryogenic distribution box. The temperature of the low pressure loop and subcooler loop will drop with the increasing return mass flow rate. Thereby the inlet temperature of turbine 1 (T1) and turbine 2 (T2) will reduce, theoretically increasing the efficiency of the turbine and likely increasing the capacity of refrigerator. However, the inlet temperature of the turbine is in a narrow safety operating range, out of which, the turbine will shutdown thanks to the protection system. For example, the minimum protective value of inlet temperature is 27K, and then the turbine will be locking down in case below 27K. Therefore, the return

mass flow rate from the cryogenic distribution box will affect the inlet temperature of turbine during the plasma discharge. The fluctuations of return mass flow rate and inlet temperature of T1 are shown in Fig 7. When the pulsed heat load is large, the return mass flow rate will increase and the inlet temperature of T1 will reduce and vice versa. Therefore, the return mass flow rate should be controlled to prevent T1 from locking.

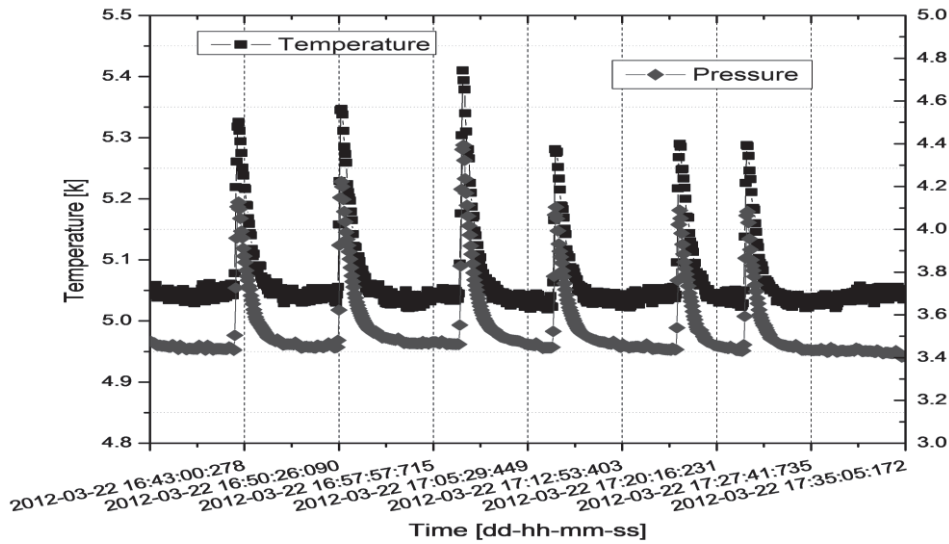


Fig 6. Variation in the outlet temperature and pressure of T3 during plasma discharge

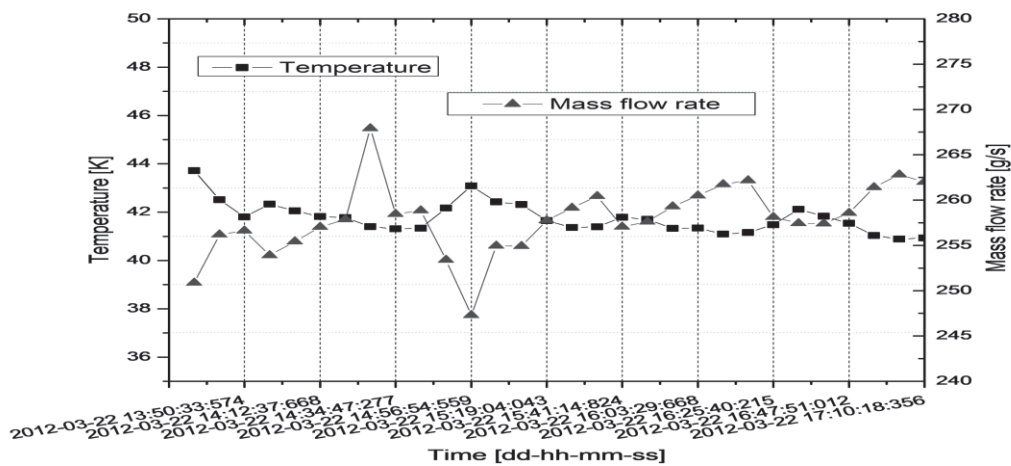


Fig 7. Fluctuation of the return mass flow rate and inlet temperature of T1

3. Dynamic simulation under the pulsed heat loads

Fusion reactors like EAST Tokamak are operated under the condition of long pulsed plasma discharges. Due to intermittent plasma discharge and alternating current, superconducting coils and support structures generate a large number of dynamic thermal depositions. They bring pulsed heat disturbances to the cryogenic system through cooling channels of supercritical helium [1]. A dynamic simulator, CryoPCS (Cryogenic Process and Control Simulator), developed for the helium refrigerator of the EAST Tokamak has been completed. This

process simulator can accurately predict the dynamic behaviors of EAST refrigerator during the operation condition of long pulsed plasma discharge. The dynamic process under a 411s, 250kA plasma discharge on 27th June, 2012 was chosen to demonstrate. Load disturbance made a great effect on EAST refrigerator, deviating from the steady-state. The mass flow of T1&T2_Stream and T3_Stream increased obviously, shown in Fig. 8. In simulation, the mass flows returned to cold-box were provided by experiment data, replacing the heat load of EAST. And the dynamic process of helium refrigerator under this operation condition of long pulsed plasma discharge has been simulated. Variation of mass flows of T1&T2 and T3 were shown in Fig. 8, compared with the experiment data. Without consideration of the jump of mass flow in experiment, the maximum absolute error of mass flow was about 3g/s, and the relative error was less than 2%.

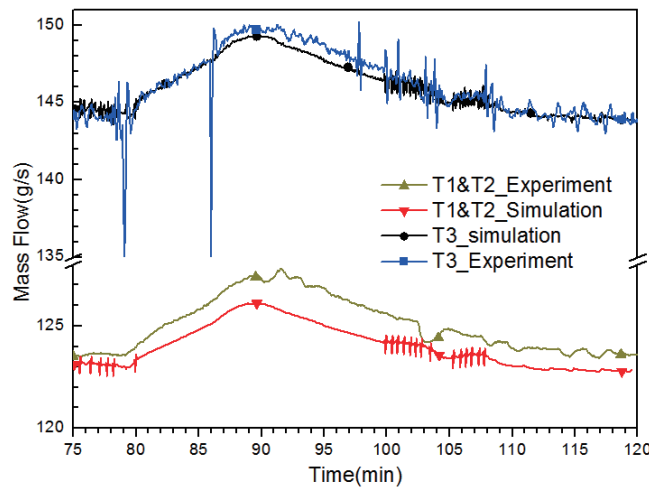


Fig. 8 Mass flow curves of Turbines in simulation compared with experiment data

From the comparison, the dynamic variation of mass flows and temperatures had a good agreement with the real process. Therefore, the CryoPCS is an available platform to design cooperative control strategy to remove periodic heat loads in future work.

4. Control scheme

The variation in the parameters of superconducting magnets and refrigerator has been analyzed in the typical plasma discharge mode. The fluctuation will affect the stability of the cryogenic system for EAST. Therefore, it is necessary to develop a control scheme to smooth the pulse heat load. Some methods have been proposed to mitigate the effects of pulsed heat load from fusion devices [2-3]. Rohan Dutta proposed a novel technique using a supercritical storage Dewar to mitigate the pulse heat load [4], however, this proposal was based on a numerical model and was not yet validated by the experimental operation. In this paper, a control scheme for the pulsed loads characteristic of the cryogenic system has been developed.

The inlet pressure of the PF was controlled by adjusting the inlet valve of the distribution valve box based on the override control method, smoothing the fluctuation of the T3 speed. The inlet temperature of T1 was controlled by adjusting the bypass valve based on a selective control method. The implementation of the control scheme will inhibit the pulse load and improve the stability of the cryoplant.

5. Conclusion

Dynamic behavior of the cryogenic system under plasma discharge in EAST has been analyzed and

simulated in the typical plasma discharge mode. During the plasma discharge, the variation in the response time of temperature is longer than pressure and mass flow rate. Therefore, if the interval time between every shot is short, the temperature was not recovered to a normal range when the next shot discharges. The temperature of the superconducting magnet will cumulatively rise. It is very important to prevent the temperature rising to the critical temperature of the superconducting magnet. Finally, the cooperative control scheme has been proposed to smooth the impact on the cryogenic system due to the pulsed heat load. These methods have been validated during the EAST campaign. Experimental results show it is effective to mitigate the pulse heat load and prevent the quench of superconducting magnets.

Acknowledgements

This work was partly supported by the JSPS-NRF-NSFC A3 Foresight Program in the field of Plasma Physics (NSFC: No.11261140328, NRF: No.2012K2A2A6000443).

References

- [1] Hu L B, Zhuang M, Zhou Z W, et al. 2014, *Advances in Cryogenic Engineering*, 1573:1756
- [2] A. Kuendig and H. Schoenfeld, Helium refrigerator design for pulsed heat load in Tokamak, *AIP Conference Proceedings* 823, 1995-2001 (2006).
- [3] P.Briend, C.Deschildre, Y.Icart, and S.E. Sequeira, Dynamic simulation of a large scale pulsed load helium refrigerator, *AIP Conference Proceeding* 1218, 1453-1459 (2010).
- [4] Rohan Dutta, Parthasarathi Ghosh, and Kanchan Chowdhury, Mitigation of effects of pulsed heat loads in Helium refrigerators for fusion devices using supercritical helium storage-4203712, *IEEE transactions on applied superconductivity* 22(6), 2012.

Tungsten ion distribution analysis based on visible M1 lines of highly charged tungsten ions in LHD

**D.Kato^{1,2}, H.A. Sakaue¹, I. Murakami^{1,2}, M. Goto^{1,2}, T. Oishi^{1,2}, S. Morita^{1,2},
K. Fujii³, N. Nakamura⁴, X.-B. Ding⁵, and C.-Z. Dong⁵**

¹National Institute for Fusion Science, Toki 509-5292, Gifu, Japan

²SOKENDAI, Department of Fusion Science, Toki 509-5292, Gifu, Japan

³Graduate School of Engineering, Kyoto University, Kyoto 615-8540, Japan

⁴Institute for Laser Science, The University of Electro-Communications, Tokyo 182-8585, Japan

⁵College of Phys. and Electronic Eng., Northwest Normal University, Lanzhou, 730070, China

Abstract

Visible emission lines of tungsten ions are useful for analysis of tungsten ion distributions at ITER because the radiation shielding of detectors is not basically necessary by using optical fibers. Here we report the result on observation of visible magnetic-dipole (M1) lines of highly-charged tungsten ions in the Large Helical Device (LHD) with tungsten pellet injection and its first application to the ion distribution analysis. Based on the measured spatial profile of the M1 line intensity, (i) radial distributions of W^{27+} ions in LHD core plasmas are elucidated using an originally developed collisional-radiative model and (ii) strong enhancement of the M1 line intensity due to proton collisions is predicted by the present calculation.

1. Introduction

Tungsten, which is used as divertor materials in ITER, will cause serious radiation loss once it accumulates in the plasma core because it is not fully ionized even in the ITER with $T_e = 15 - 20$ keV. It is, therefore, necessary for the stable operation of ITER to study the influx and edge transport of tungsten ions. Usage of visible line emission of the tungsten ion is useful because the radiation shielding of detectors is not necessary by using optical fibers. However, the knowledge on visible lines of the tungsten from fusion experiments has been extremely limited to neutral atoms and ions in low charge states. The magnetic-dipole (M1) line from ground state highly-charged tungsten ions in the visible range have been observed by using electron-beam-ion-traps (EBITs) [1,2] and the Large-Helical-Device (LHD) with tungsten pellet injection [3] (Fig. 1). These visible M1 lines are useful for measurements of ion temperature, rotation velocity and ion density of tungsten ions in edge plasmas including Scrape-Off Layer (SOL) and divertor regions of ITER. Such visible M1 lines can be investigated in the LHD because the LHD discharge is entirely stable for substantial amount of tungsten density exhibiting no MHD instabilities.

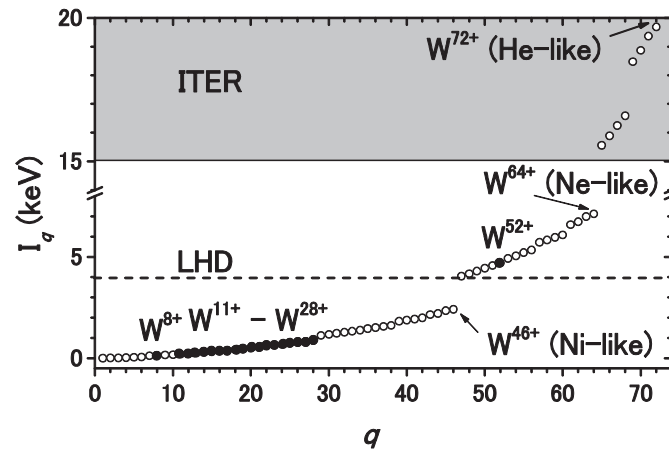


Fig. 1 Ionization potential diagram of tungsten ions. For highly charged W^{q+} ions indicated with solid circles, emission lines in near-UV and visible ranges have been measured using electron-beam-ion-traps (EBITs) [1,2] and the LHD [3]. Shaded region represents core plasma temperatures of ITER and dashed line represents a peak temperature of the LHD NBI discharges.

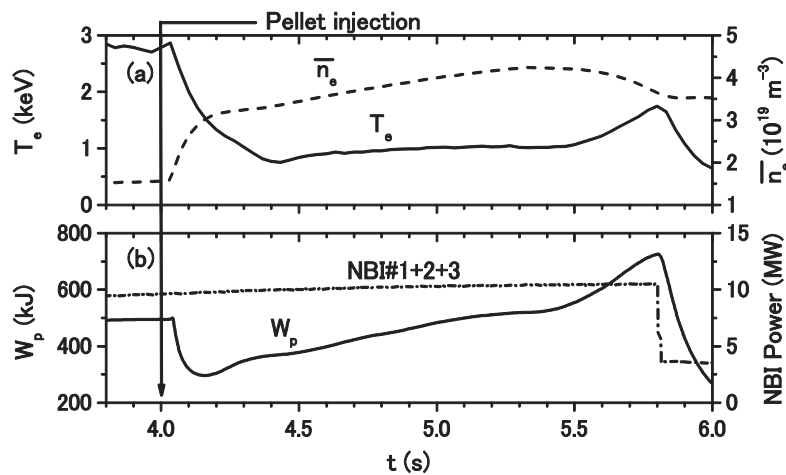


Fig. 2 Time traces of (a) central electron temperature and line-averaged electron density and (b) stored energy (W_p) and NBI port-through powers. A tungsten pellet is injected at 4.0 s.

2. Vertical distributions of an M1 line intensity from W^{27+} ions in LHD

In the present measurement, a polyethylene tube containing a tungsten wire (0.6 mm long and 0.15 mm diameter which reads NW about 6.6×10^{17} /pellet) is injected in the LHD discharge shown in Fig. 2. Line emission was observed at 44 lines of sight along the horizontal axis of a horizontally elongated poloidal cross section of the LHD. Vertical distributions of the M1 line intensity from W^{27+} ions (337.7 nm [2]) are shown in Fig. 3. A collisional-radiative model is constructed to analyze the line intensity profiles. HULLAC code is used to generate tungsten atomic data (energy levels, transition rates, electron collision strengths) in the model.

Proton collision effects are included in our model approximating proton collision strengths as mass scaled electron collision strengths. Ionization excitation from next lower charge state (W^{26+}) is also taken

into account, although the effect has a minor contribution. Our model gives the vertical profile of good agreements with the measured profile. The proton collision effect increases fractional population of the ground state, which results in an enhancement of the M1 line intensity by about 40 %.

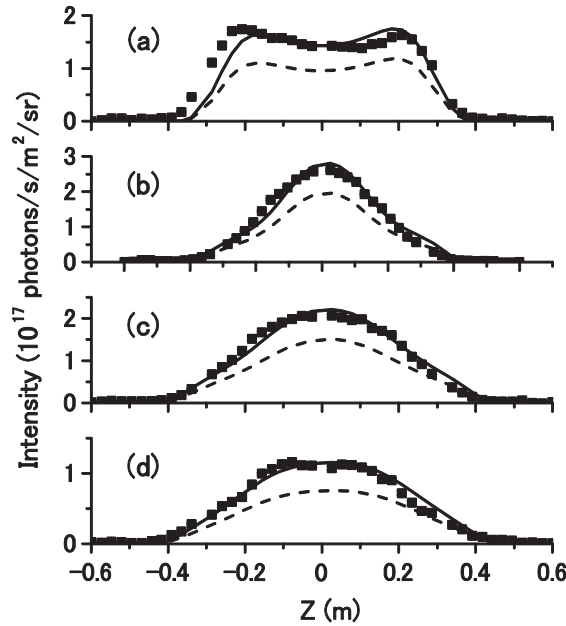


Fig. 3 Vertical distributions of W^{27+} M1 line intensities at (a) $t = 4.1$, (b) 4.3 , (c) 5.0 and (d) 5.6 s. Tungsten pellet is injected at 4.0 s. Solid squares indicate measurement and solid curves calculations, respectively. Dashed lines are the calculation neglecting proton collision effect.

3. Time evolution of radial distribution of W^{27+} ion density

Radial distribution of W^{27+} ions is deduced based on the measured vertical profile (Fig. 4). The initial ion density distribution has a maximum at the effective minor radius of 0.3 m where the fractional W^{27+} ion abundance becomes the maximum at the local electron temperature (about 1.0 keV). The peak position of the radial distribution moves toward the plasma center ($r_{\text{eff}} = 0$) as the temperature at the plasma center decreases with time. The W^{27+} ion density in the core plasma is initially increased after the pellet injection ($4.1 - 4.3$ s)

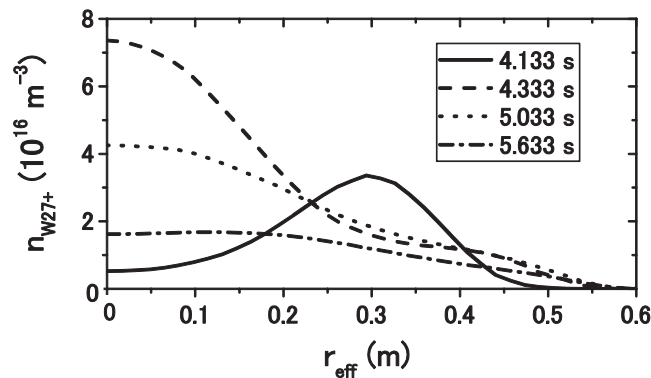


Fig. 4 Radial profile of W^{27+} ion distributions deduced from vertical profiles of the M1 line intensity in Fig. 2. Peak temperatures at the plasma center are 2.0 , 1.0 , 1.0 , and 1.2 keV at 4.1 , 4.3 , 5.0 and 5.6 s, respectively.

accompanying a temperature drop and a density rise. Since the temperature and density are stable in later times (5.0 – 5.6 s), the apparent decrease in the ion density at the core plasma indicates diffusion of the tungsten ions after confinement in the plasma center.

4. Summary

The present work demonstrated for the first time application of visible M1 lines to tungsten ion distribution analysis. Usage of the visible line is advantageous in ITER where serious neutron radiation damage is concerned. In summary, (1) we could successfully obtain the radial ion distribution from the line measurement by using the originally developed atomic model, and (2) strong enhancement of the M1 intensity by proton collisions is predicted.

Acknowledgements

This work was partly supported by the JSPS-NRF-NSFC A3 Foresight Program in the field of Plasma Physics (NSFC: No.11261140328, NRF: No.2012K2A2A6000443). DK is grateful to KAKENHI (15H04235).

References

- [1] A. Komatsu et al., Plasma and Fusion Res.: Rapid Commun. **7** (2012) 1201158.
- [2] Z. Fei et al., Phys. Rev. A **86** (2012) 062501.
- [3] D. Kato et al., Phys. Scr. **T156** (2013) 014081.

Particle-in-cell simulations of parametric decay instability of ion Bernstein wave**Chun-yun Gan^{1,2}, Nong Xiang^{1,2}**¹Institute of Plasma Physics, Chinese Academy of Sciences, Hefei 230031, China²Center for Magnetic Fusion Theory, Chinese Academy of Sciences, Hefei, China**Abstract**

The parametric decay instabilities (PDIs) of ion Bernstein wave with different input power levels are investigated via particle-in-cell simulation. It is found that the number of decay channels increases with the input power. Resonant mode-mode couplings dominate for a low input power. With the input power increasing, the nonresonant PDIs appear which dissipates the energy of the injected wave and gives rise to edge ion heating. In the simulation, the effective ion temperature can reach up to about 60 times of its initial value when the input power is about 0.9 MW. The generated child waves couple with each other as well as the injected wave and/or act as a pump wave to excite new decay channels. As a result, the frequency spectrum is broadened with the increase of the input power.

1. Introduction

The parametric decay instabilities (PDIs) have been detected in many tokamaks during the heating scenarios of radiofrequency (rf) wave in the ion cyclotron range of frequency (ICRF) [1-8]. In some of these experiments, the occurrences of nonresonant parametric decay processes are invoked to interpret the ion heating and/or ion tail formation in the edge region [2, 4-8]. Theoretically, the nonresonant parametric decay processes are predicted to occur according to the calculation of their growth rates and thresholds, and the child waves produced in these nonresonant PDIs may lead to ion heating [9, 10]. Numerically, the generations of resonant and nonresonant parametric decay processes in the ICRF regime have been investigated via the particle-in-cell (PIC) model [11-13]. In Ref. [12, 13], the evidence that the ion cyclotron quasimode (ICQM) produced by the nonresonant decay process leads to the increase of kinetic energy of ions is shown. In addition to the ICQMs, the propagating child waves produced by the resonant or nonresonant PDI processes also dissipate the energy of the injected wave. However, the behavior of PDIs of the ICRF wave with different input power receives little concern. How the PDI processes develop and dissipate the energy of the injected high power ICRF wave is not well understood.

To explore this energy dissipation process, the PIC method implemented in VSim (VORPAL) software [14] has been used to study the dependence of PDI processes of ICRF on input power. To reveal

these effects in relevant experiments, we choose the plasma parameters close to those of the ion Bernstein wave (IBW) heating experiments on HT-7 tokamak [1, 12]. It is demonstrated that more decay channels appear and the frequency spectra broaden as the input power is increased. The characteristics of the spectral broadening and how this broadening come out will be presented. Furthermore, the effective ion temperature varies with the input power will be shown.

2. Simulation setup

For simplicity, a plasma with a single ion species, hydrogen, is taken into account. The ion and electron temperatures are 30 eV and 50 eV, respectively. We take the computational domain as follows. The simulation size $l_x = 0.06$ m. The plasma density profile is $n(x) = n_0(0.43 \operatorname{atan}(5x/l_x - 2) + 0.47)$ with $n_0 = 2 \times 10^{17} \text{ m}^{-3}$. The injected wave with the frequency ω_0 is launched by a perturbation current with the form $J(x, t) = J_0(1 - e^{-\gamma t})^2 e^{-(x-0.006)^2/0.006^2} \sin(\omega_0 t)$, where $\gamma = 0.02\omega_0$. The perturbation current amplitude J_0 denotes the level of input power. Typically, $J_0 = 6 \times 10^2 \text{ Am}^{-2}$ corresponds to the input power of roughly one hundred kilowatts. The external magnetic field is constant in y-direction (toroidal direction in a tokamak geometry) and the cyclotron frequency of hydrogen satisfies $\Omega_H \approx 0.57\omega_0$ in the simulation region. The other parameters are the same as the resonant PDI case in Ref. [18] in which the second and third harmonic waves are generated.

3. Simulation results

In this section, we will demonstrate the simulation results for different input powers. In figure 1, the spectral energy density $|E_x|^2$ for four typical perturbation amplitudes $J_0 = (6, 9, 12, 24) \times 10^2 \text{ Am}^{-2}$ are plotted versus the normalized frequency at $x = 0.023$ m and $t = 406/\omega_0$. As the input power increase, the broadening of the frequency spectra is clearly demonstrated. In figure 1(a), the second and third harmonic modes of the driving frequency are detected in the $J_0 = 6 \times 10^2 \text{ Am}^{-2}$ case. It has been indicated in Ref. [12] that the second and third harmonic modes of the driving frequency are generated by the resonant parametric decay channels $\omega_0 + \omega_0 \rightarrow 2\omega_0$ and $\omega_0 + 2\omega_0 \rightarrow 3\omega_0$, respectively. For a low input power in this level, the resonant mode-mode couplings dominate.

As the amplitude of the perturbation current is increased to $J_0 = 9 \times 10^2 \text{ Am}^{-2}$, new peaks with frequencies $0.57\omega_0$, $1.43\omega_0$ and $1.86\omega_0$ appear in the spectrum as shown in figure 1(b). When the perturbation current amplitude rises to a higher level at $J_0 = 12 \times 10^2 \text{ Am}^{-2}$, the waves observed in the $J_0 = 9 \times 10^2 \text{ Am}^{-2}$ case are also present, together with a new sideband occurring at frequency $2.43\omega_0$ (figure 1(c)). Except the frequencies mentioned above, the peaks of $1.6\omega_0$ and $4\omega_0$ add to the spectrum of the $J_0 = 24 \times 10^2 \text{ Am}^{-2}$ case as shown in figure 1(d). However, how these sidebands be generated is not clear. The temporal evolution of the frequency spectrum and the distribution of particles in phase space

are helpful to identify the generation mechanism of these frequency peaks. In order to explain the decay pattern of these observed frequency peaks, we take the $J_0 = 12 \times 10^2 \text{ Am}^{-2}$ case for instance.

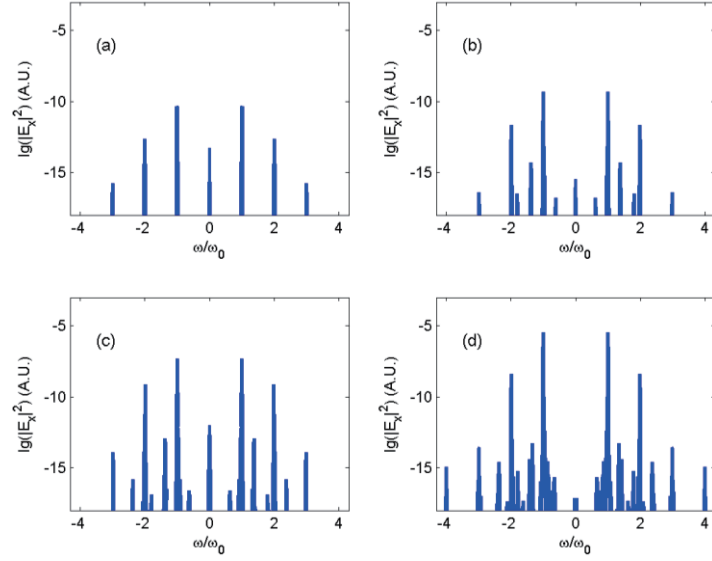


Fig. 1. The frequency spectrum at $x=0.023 \text{ m}$ and $t=406/\omega_0$ in the simulations with different amplitudes of perturbation current: (a) $J_0 = 6 \times 10^2 \text{ Am}^{-2}$, (b) $J_0 = 9 \times 10^2 \text{ Am}^{-2}$, (c) $J_0 = 12 \times 10^2 \text{ Am}^{-2}$ and (d) $J_0 = 24 \times 10^2 \text{ Am}^{-2}$.

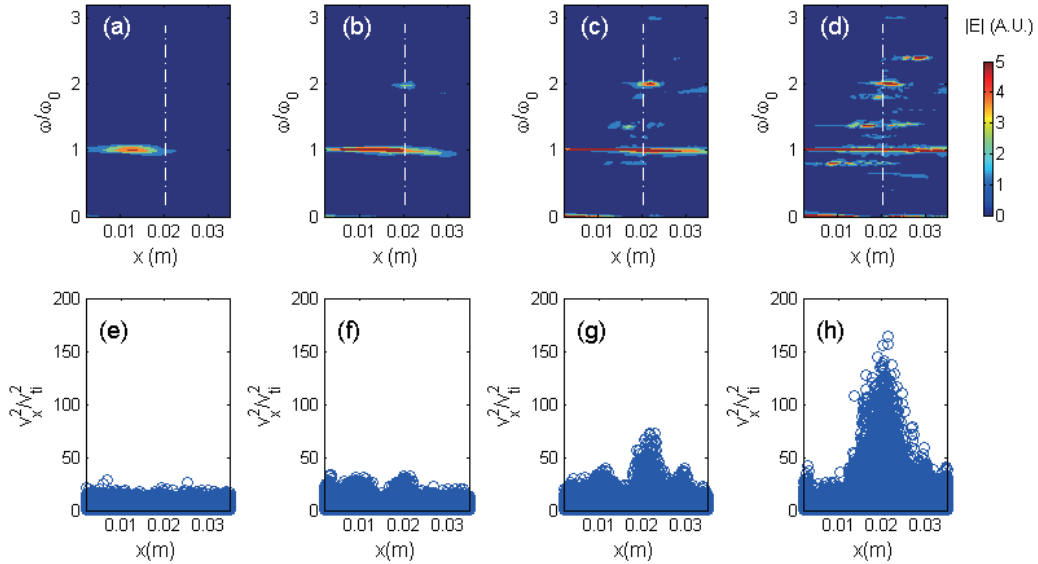


Fig. 2. Contours of the amplitude of $|E|$ in the $x-\omega$ plane for the $J_0 = 12 \times 10^2 \text{ Am}^{-2}$ case at (a) $t = 65/\omega_0$, (b) $t = 122/\omega_0$, (c) $t = 203/\omega_0$ and (d) $t = 406/\omega_0$. The vertical dash-dot line labels the position where the match condition $k_{2\omega_0} = 2k_{\omega_0}$ is satisfied. The spatial distributions of normalized kinetic energy of ions for the $J_0 = 12 \times 10^2 \text{ Am}^{-2}$ case at (e) $t = 65/\omega_0$, (f) $t = 122/\omega_0$, (g) $t = 203/\omega_0$ and (h) $t = 406/\omega_0$.

Figure 2 shows the history of the contours of the amplitude of electric field $|E|$ in the $x-\omega$ plane and the normalized kinetic energy of ions in the perpendicular direction for the $J_0 = 12 \times 10^2 \text{ Am}^{-2}$ case. At early stage in figure 2(a), only the injected wave is generated in the simulation. As the injected wave passes through the coupling point where the match condition of wavenumber $k_{2\omega_0} = 2k_{\omega_0}$ is satisfied, the second harmonic wave is generated nearby (figure 2(b)). Thereafter, the amplitude of the second harmonic wave grows and other sidebands with frequencies $0.86\omega_0, 1.14\omega_0, 1.43\omega_0, 1.86\omega_0$ and $3.0\omega_0$ appear in the spectrum, as shown in figure 2(c). Simultaneously, the ions are heated in the vertical direction as displayed in figure 2(g). No heating is observed in the parallel direction for ions and in all the directions for electrons. Since there is no ion cyclotron resonance layer located in our simulation region, we conjecture that the ion heating is caused by the nonresonant parametric decay process as presented in Ref. [14, 15].

According to the observed frequency peaks and their occurring times, the most probable nonresonant decay channels are $2\omega_0 \rightarrow \Omega_H + (2\omega_0 - \Omega_H)$ (i.e. $2\omega_0 \rightarrow 0.57\omega_0 + 1.43\omega_0$) and $2\omega_0 \rightarrow 2\Omega_H + (2\omega_0 - 2\Omega_H)$ (i.e. $2\omega_0 \rightarrow 1.14\omega_0 + 0.86\omega_0$). The produced ICQMs with frequencies $\Omega_H = 0.57\omega_0$ and $2\Omega_H = 1.14\omega_0$ may be heavily damped on ions, and thus their amplitudes are much smaller than that of the IBWs with frequencies $1.43\omega_0$ and $0.86\omega_0$. The region of ion heating is consistent with the one where these two nonresonant decay pairs occur. However, no ion heating is observed in the earlier time in the $J_0 = 12 \times 10^2 \text{ Am}^{-2}$ case (figure 2(e) and (f)) when these nonresonant decay pairs are absent in their corresponding spectra (figure 2(a) and (b)). Furthermore, the ions are not heated in the $J_0 = 6 \times 10^2 \text{ Am}^{-2}$ case, but they are heated in the $J_0 = 9 \times 10^2 \text{ Am}^{-2}$ and $J_0 = 24 \times 10^2 \text{ Am}^{-2}$ cases in the region where the nonresonant decay channels appear. Therefore, it is confirmed that these nonresonant parametric decay processes are excited and give rise to the ion heating observed in the simulation.

On the other hand, the IBW with frequency $1.86\omega_0$ may be excited via the resonant mode-mode coupling by the decay channel $\omega_0 + 0.86\omega_0 \rightarrow 1.86\omega_0$. The dispersion curves, i.e. the perpendicular wavenumbers versus the radial position, for the wave with frequencies $0.86\omega_0$ and $1.86\omega_0$ are plotted in figure 3. One can see that the selection condition of the wavenumber $k_{1.86\omega_0} = k_{\omega_0} + k_{0.86\omega_0}$ can be satisfied around $x \approx 0.016 \text{ m}$, indicating that the wave with frequency $1.86\omega_0$ can be produced by the resonant decay process if the amplitudes of the pump waves are large enough.

At a later time as illuminated in figure 2(d), the amplitudes of the decay waves described above increase and a new sideband with frequency $2.43\omega_0$ appears. Similarly, the dispersion curves for the sidebands with frequencies $1.43\omega_0$ and $2.43\omega_0$ shown in figure 3 indicate that the selection condition $k_{2.43\omega_0} = k_{\omega_0} + k_{1.43\omega_0}$ can be satisfied around $x \approx 0.021 \text{ m}$. Thus the IBW with frequency $2.43\omega_0$ is

triggered by the resonant decay channel $\omega_0 + 1.43\omega_0 \rightarrow 2.43\omega_0$. In addition, we have checked the dispersion curve for the fourth harmonic wave and found that the selection condition $k_{4\omega_0} = 2k_{2\omega_0}$ is satisfied around $x \approx 0.02$ m. The fourth harmonic mode detected in the $J_0 = 24 \times 10^2$ Am⁻² case is generated by the self-interaction of the second harmonic wave.

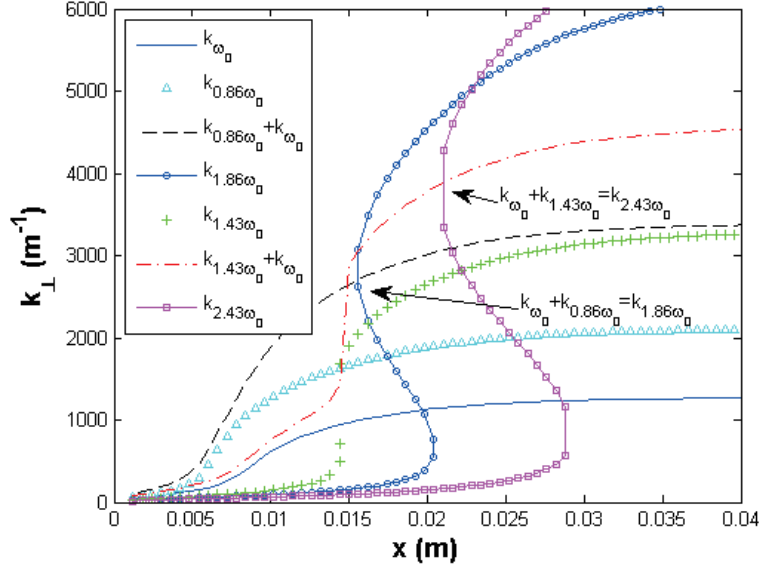


Fig. 3. Dispersion curves k_{\perp} versus x for the IBWs with frequencies ω_0 (blue solid line), $0.86\omega_0 = 2\omega_0 - 2\Omega_H$ (cyan triangles), $1.43\omega_0 = 2\omega_0 - \Omega_H$ (green crosses), $1.86\omega_0$ (blue-circle solid line) and $2.43\omega_0$ (magenta-square solid line). The black dash and red dash-dot lines denote $k_{\omega_0} + k_{0.86\omega_0}$ and $k_{\omega_0} + k_{1.43\omega_0}$, respectively.

According to the time evolution of the frequency spectrum as well as the kinetic energy distribution of the particles, the development of the PDI spectrum in a high input power is clearly demonstrated. In this $J_0 = 12 \times 10^2$ Am⁻² case, the self-interaction of the injected wave excites the second harmonic mode initially. Then this generated child wave couples with the injected wave and acts as a pump wave, leading to the generation of the other sidebands. These new sidebands couple with each other as well as the pump waves and/or act as a pump wave and thus excite more sidebands. Therefore, the frequency spectra is broadened. It is found that the waves observed in the simulation are generated via the three-wave coupling process rather than the four-wave or higher order interaction.

In figure 4, the effective ion temperature in different input power levels are shown. Clearly, the effective ion temperature can reach up to about 60 times of its initial value when the amplitude of injected wave rises to about 2×10^5 V/m, corresponding to about 0.9 MW. For the initial ion temperature at 30eV in our simulation, the effective ion temperature may be increased to about 1.8 keV.

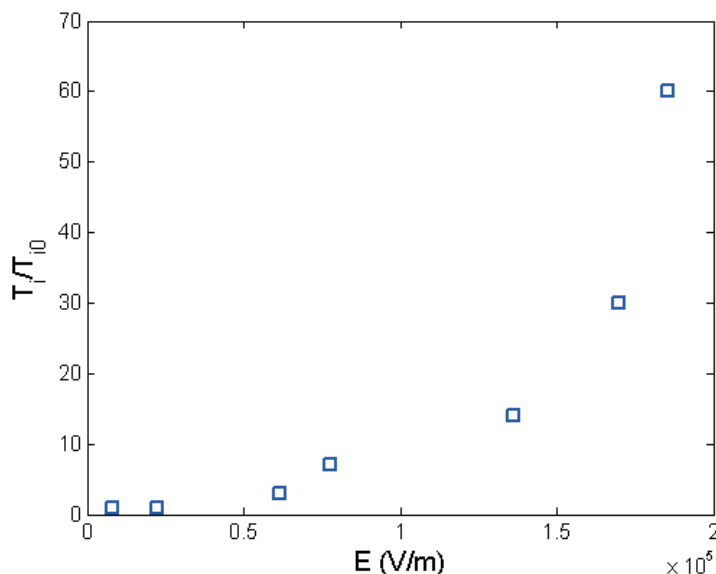


Fig. 4. The effective ion temperature varies with the amplitude of the injected wave.

4. Summary

In summary, we have illustrated that more decay channels appear in the PIC simulation of ion Bernstein wave when the input power is increased. For a low input power, the resonant mode-mode couplings dominate. The nonresonant PDIs occur at a higher input power level and lead to the ion heating. With the plasma parameters close to those of IBW heating experiments on HT-7 tokamak, the normalized effective ion temperature (T_i / T_{i0}) can reach up to about 60. The generated child waves couple with each other as well as the injected wave and/or act as a pump wave to excite new decay channels. As a result, the frequency spectrum is broadened with the increase of the input power. During the range of input power in our simulations, only three-wave couplings are observed, no four-wave or higher order interaction is found.

Acknowledgements

This work was partly supported by the JSPS-NRF-NSFC A3 Foresight Program in the field of Plasma Physics (NSFC: No.11261140328, NRF: No.2012K2A2A6000443).

References

- [1] Li J, Bao Y, Zhao Y P, Luo J R, Wan B N, Gao X, Xie J K, Wan Y X and Toi K 2001 *Plasma Phys. Control. Fusion* **43** 1227-38.
- [2] Pace D C, Pinsker R I, Heidbrink W W, Fisher R K, Van Zeeland M A, Austin M E, McKee G R and Garcia-Munoz M 2012 *Nucl. Fusion* **52** 063019.

- [3] Myra J R, D'Ippolito D A, Russell D A, Berry L A, Jaeger E F and Carter M D 2006 *Nucl. Fusion* **46** S455-S68.
- [4] Wilson J R, Bernabei S, Biewer T, Diem S, Hosea J, LeBlanc B, Phillips C K, Ryan P and Swain D W 2005 *AIP Conference Proceedings* **787** 66-73.
- [5] Rost J C, Porkolab M and Boivin R L 2002 *Phys. Plasmas* **9** 1262-70.
- [6] Pinsker R I, Petty C C, Mayberry M J, Porkolab M and Heidbrink W W 1993 *Nucl. Fusion* **33** 777-93.
- [7] Fujii T, et al. 1990 *Fusion Eng. Des.* **12** 139-48.
- [8] Vannieuwenhove R, Vanoost G, Noterdaeme J M, Brambilla M, Gernhardt J and Porkolab M 1988 *Nucl. Fusion* **28** 1603-9.
- [9] Porkolab M 1990 *Fusion Eng. Des.* **12** 93-103.
- [10] Porkolab M 1985 *Phys. Rev. Lett.* **54** 434-7.
- [11] Jenkins T G, Austin T M, Smithe D N, Loverich J and Hakim A H 2013 *Phys. Plasmas* **20** 012116.
- [12] Gan C, Xiang N, Ou J and Yu Z 2015 *Nucl. Fusion* **55** 063002.
- [13] Kuley A, Bao J, Lin Z, Wei X S and Xiao Y 2015 *AIP Conf. Proc.* **1689** 060008.
- [14] Nieter C and Cary J R 2004 *J. Comput. Phys.* **196** 448-73.

Participants of the 9th A3 Workshop at Yinchuan
May. 17-20, 2016, yinchuan, China

No	Affiliation & Name			M / F	e-mail
1	NFRI	오영국	Yeong-Kook OH	M	ykoh@nfri.re.kr
2	NFRI	홍석호	Suk-Ho HONG	M	sukhhong@nfri.re.kr
3	NFRI	곽종구	Jong-Gu KWAK	M	jgkwak@nfri.re.kr
4	NFRI	배천호	Cheonho BAE	M	cbae@nfri.re.kr
5	NFRI	박준교	Jun-Gyo BAK	M	jgbak@nfri.re.kr
6	NFRI	이상곤	Sang Gon LEE	M	sglee@nfri.re.kr
7	NFRI	서성현	Seong-Heon SEO	M	shseo@nfri.re.kr
8	NFRI	아이데미러	Ahmet AYDEMIR	M	aydemir@nfri.re.kr
9	NFRI	고원하	Won-ha KO	F	whko@nfri.re.kr
10	NFRI	김재현	Jayhyun KIM	M	jayhyunkin@nfri.re.kr
11	Daegu Univ.	권오진	Ohjin KWON	M	ojkwon@daegu.ac.kr
12	NFRI	오노영	Noh-Yeong OH	F	ony55@nfri.re.kr
13	NIFS	森田繁	Shigeru MORITA	M	morita@nifs.ac.jp
14	NIFS	芦川直子	Naoko ASHIKAWA	F	ashikawa@nifs.ac.jp
15	NIFS	東井和夫	Kazuo TOI	M	toi@nifs.ac.jp
16	NIFS	大石鉄太郎	Tetsutarou OISHI	M	oishi@nifs.ac.jp
17	NIFS	大館暁	Satoshi OHDACHI	M	ohdachi@nifs.ac.jp
18	NIFS	鈴木康浩	Yasuhiro SUZUKI	M	suzuki.yasuhiro@nifs.ac.jp
19	NIFS	黄賢礼	Xianli HUANG	M	huang.xianli@nifs.ac.jp
20	NIFS	坂東隆宏	Takahiro BANDO	M	bando.takahiro@nifs.ac.jp
21	NIFS	加藤太治	Daiji KATO	M	kato.daiji@nifs.ac.jp
22	NIFS	藤堂泰	Yasushi TODO	M	todo@nifs.ac.jp
23	NIFS	庄司主	Mamoru SHOJI	M	shoji@nifs.ac.jp
24	NIFS	戴舒宇	Shuyu DAI	M	dai.shuyu@nifs.ac.jp
25	NIFS	磯部光孝	Mitsutaka ISOBE	M	isobe@nifs.ac.jp
26	NIFS	細川秀男	Hideo HOSOKAWA	M	hosokawa.hideo@nifs.ac.jp
27	NIFS	神谷良志夫	Yoshio KAMIYA	M	kamiya.yoshio@nifs.ac.jp
28	ASIPP	胡立群	Liqun HU	M	lqhu@ipp.ac.cn
29	ASIPP	董少华	Shaohua Dong	F	shdong@ipp.ac.cn
30	ASIPP	席莹琨	Yingkun XI	F	xiyingkun@ipp.ac.cn
31	ASIPP	周瑞杰	Ruijie ZHOU	M	rjzhou@ipp.ac.cn

32	ASIPP	郭后扬	Houyang GUO	M	hyguo@ipp.ac.cn
33	ASIPP	胡友俊	Youjun HU	M	yjhu@ipp.cas.cn
34	ASIPP	张启勇	Qiyong ZHANG	M	zhangqy@ipp.ac.cn
35	ASIPP	陆小飞	Xiaofei LU	M	xiaofeilu@ipp.ac.cn
36	ASIPP	肖炳甲	Bingjia XIAO	M	bjxiao@ipp.ac.cn
37	ASIPP	沈飙	Biao SHEN	M	biaoshen@ipp.ac.cn
38	ASIPP	陈大龙	Dalong CHEN	M	cdalong@ipp.ac.cn
39	ASIPP	刘海庆	Haiqing LIU	M	hqliu@ipp.ac.cn
40	ASIPP	王守信	Shouxin WANG	M	wangshouxin@ipp.ac.cn
41	ASIPP	连辉	Hui LIAN	M	lianhui@ipp.ac.cn
42	ASIPP	周登	Deng ZHOU	M	dzzhou@ipp.ac.cn
43	ASIPP	胡建生	Jiansheng HU	M	hujs@ipp.ac.cn
44	ASIPP	姚星佳	Xingjia YAO	M	xjyao@ipp.ac.cn
45	ASIPP	丁伯江	Bojiang DING	M	bjding@ipp.ac.cn
46	ASIPP	王茂	Mao WANG	M	mwang@ipp.ac.cn
47	ASIPP	张凌	Ling ZHANG	F	zhangling@ipp.ac.cn
48	SWIP	高金明	Jinming GAO	M	gaojm@swip.ac.cn
49	SWIP	董春风	Cunfeng DONG	F	dongcf@swip.ac.cn
50	SWIP	张轶泼	Yipo ZHANG	M	zhangyp@swip.ac.cn
51	SWIP	林静	Jing LIN	F	linj@swip.ac.cn
52	ASIPP	陈竞博	Jingbo CHEN	M	chenjingbo@ipp.ac.cn
53	USTC	王雨雷	Yulei Wang	M	wyulei@mail.ustc.edu.cn
54	USTC	何洋	Yang He	F	heyang14@ustc.edu.cn
55	Tsinghua University	谭熠	Yi TAN	M	tanyi@mail.tsinghua.edu.cn
56	ASIPP	项农	Nong XIANG	M	xiangn@ipp.ac.cn
57	ASIPP	甘春芸	Cunyun GAN	F	cygan@ipp.ac.cn
58	ASIPP	夏天阳	Tianyang XIA	M	xiaty@ipp.ac.cn
59	Beifang University of Nationalities	马天鹏	Tianpeng MA	M	13709515425@163.com
60	USTC	徐国梁	Guoliang XU		
61	USTC	刘利	Li LIU		
62	USTC	王华杰	Huajie WANG		
63	ASIPP	钟国强	Guoqiang ZHONG	M	gqzhong@ipp.ac.cn
64	ASIPP	肖敏	Min XIAO	M	minxiao@ipp.ac.cn
65	HUST	庄革	Ge ZHUANG	M	ge-zhuang@mail.hust.edu.cn
66	ASIPP	陈俊凌	Junling CHEN	M	jlch@ipp.ac.cn
67	ASIPP	张晓东	Xiaodong ZHANG	M	xdzhang@ipp.ac.cn
68	ASIPP	刘松林	Songlin LIU	M	slliu@ipp.ac.cn
69	ASIPP	彭姣	Jiao PENG	F	pengjiao@ipp.ac.cn

70	ASIPP	杨秀达	Xiuda YANG	M	xdyang@ipp.ac.cn
71	ASIPP	张寿彪	Shoubiao ZHANG	M	bszhang@ipp.ac.cn
72	ASIPP	季振山	Zhenshan JI	M	jizh@ipp.ac.cn
73	ASIPP	吴莎	Sha WU	F	wusha@ipp.ac.cn
74	ASIPP	胡良兵	Liangbing HU	M	huliangbing@ipp.ac.cn